

Conference Proceedings of the Society for Experimental Mechanics Series

Dario Di Miao · Pablo Tarazaga · Paolo Castellini *Editors*

Special Topics in Structural Dynamics, Volume 6

Proceedings of the 34th IMAC, A Conference and Exposition
on Structural Dynamics 2016



 Springer

The Springer logo consists of a white chess knight piece on a pedestal, positioned to the left of the word 'Springer' in a white serif font.

Conference Proceedings of the Society for Experimental Mechanics Series

Series Editor

Kristin B. Zimmerman, Ph.D.
Society for Experimental Mechanics, Inc.,
Bethel, CT, USA

More information about this series at <http://www.springer.com/series/8922>

Dario Di Miao • Pablo Tarazaga • Paolo Castellini
Editors

Special Topics in Structural Dynamics, Volume 6

Proceedings of the 34th IMAC, A Conference and Exposition
on Structural Dynamics 2016

Editors

Dario Di Miao
University of Bristol
Bristol, UK

Pablo Tarazaga
Virginia Polytechnical Institute
Blacksburg, VA, USA

Paolo Castellini
DIISM, Università Politecnica delle Marche
Ancona, Italy

ISSN 2191-5644 ISSN 2191-5652 (electronic)
Conference Proceedings of the Society for Experimental Mechanics Series
ISBN 978-3-319-29909-9 ISBN 978-3-319-29910-5 (eBook)
DOI 10.1007/978-3-319-29910-5

Library of Congress Control Number: 2016935842

© The Society for Experimental Mechanics, Inc. 2016

This work is subject to copyright. All rights are reserved by the Publisher, whether the whole or part of the material is concerned, specifically the rights of translation, reprinting, reuse of illustrations, recitation, broadcasting, reproduction on microfilms or in any other physical way, and transmission or information storage and retrieval, electronic adaptation, computer software, or by similar or dissimilar methodology now known or hereafter developed. The use of general descriptive names, registered names, trademarks, service marks, etc. in this publication does not imply, even in the absence of a specific statement, that such names are exempt from the relevant protective laws and regulations and therefore free for general use. The publisher, the authors and the editors are safe to assume that the advice and information in this book are believed to be true and accurate at the date of publication. Neither the publisher nor the authors or the editors give a warranty, express or implied, with respect to the material contained herein or for any errors or omissions that may have been made.

Printed on acid-free paper

This Springer imprint is published by Springer Nature
The registered company is Springer International Publishing AG Switzerland

Preface

Special Topics in Structural Dynamics represents one of ten volumes of technical papers presented at the 34th IMAC, A Conference and Exposition on Structural Dynamics, organized by the Society for Experimental Mechanics and held in Orlando, Florida, on January 25–28, 2016. The full proceedings also include volumes on *Nonlinear Dynamics; Dynamics of Civil Structures; Model Validation and Uncertainty Quantification; Dynamics of Coupled Structures; Sensors and Instrumentation; Structural Health Monitoring, Damage Detection & Mechatronics; Rotating Machinery, Hybrid Test Methods, Vibro-Acoustics and Laser Vibrometry; Shock & Vibration, Aircraft/Aerospace, Energy Harvesting, Acoustics & Optics*; and *Topics in Modal Analysis & Testing*.

Each collection presents early findings from experimental and computational investigations on an important area within structural dynamics. *Special Topics in Structural Dynamics* represents papers on enabling technologies for modal analysis measurements and applications of modal analysis in specific application areas.

The organizers would like to thank the authors, presenters, session organizers, and session chairs for their participation in this track.

Bristol, UK
Blacksburg, VA, USA
Ancona, Italy

Dario Di Maio
Pablo Tarazaga
Paolo Castellini

Contents

1	Online Input and State Estimation in Structural Dynamics	1
	K. Maes, G. De Roeck, A. Iliopoulos, W. Weijtjens, C. Devriendt, and G. Lombaert	
2	Modeling and Testing of the Anti-Vibration Base for Michelangelo’s Pietà Rondanini	11
	Alfredo Cigada, Edoardo Sabbioni, Ali Siami, and Emanuele Zappa	
3	Estimation of Frequency and Damping of a Rotating System Using MEOT and Virtual Sensor Concept	23
	Sharang Inamdar, Randall J. Allemang, and Allyn W. Phillips	
4	Multibody/FEM Numerical Tool for HIL Scaled Offshore Wind Turbine	37
	H. Giberti, M. Belloli, I. Bayati, and E. Fiore	
5	Detection and Identification of Firearms Upon Discharge Using Floor-Based Accelerometers	45
	M. Kasarda, P. Tarazaga, M. Embree, S. Gugercin, A. Woolard, B. Joyce, and J. Hamilton	
6	An Adaptive Markov Chain Monte Carlo Method for Bayesian Finite Element Model Updating	55
	I. Boulkaibet, T. Marwala, M.I. Friswell, and S. Adhikari	
7	Modal Parameters of Multiple-Disk Shaft System from Multiple Reference Impact Test	67
	Naim Khader and Mohammad Ramadan	
8	Identification of Aerodynamic Properties of Bridge Decks in Arbitrary Motion	79
	Bartosz Siedziako, Ole Øiseth, and Nils Erik Anders Rønquist	
9	A Multiphysical Modelling Approach for Virtual Shaker Testing Correlated with Experimental Test Results	87
	S. Waimer, S. Manzato, B. Peeters, M. Wagner, and P. Guillaume	
10	Characterizing the Dynamics of Systems Incorporating Surrogate Energetic Materials	101
	Jelena Paripovic and Patricia Davies	
11	Multimodal Damping of a Plate with a Passive Piezoelectric Network	111
	B. Lossouarn, M. Aucejo, J.-F. Deü, and K.A. Cunefare	
12	State Estimation: A Model-Based Approach to Extend Test Data Exploitation	119
	Herman Van der Auweraer, Steven Gillijns, Stijn Donders, Jan Croes, Frank Naets, and Wim Desmet	
13	Generation of Traveling Waves in a 2D Plate for Future Drag Reduction Manipulation	129
	Patrick F. Musgrave, V.V.N. Sriram Malladi, and Pablo A. Tarazaga	
14	Surrogate Granular Materials for Modal Test of Fluid Filled Tanks	139
	Pierre-Louis Chiambaretto, Miguel Charlotte, Joseph Morlier, Philippe Villedieu, and Yves Gourinat	
15	Dynamics of a Hydroelastic Oscillating Cylinder with Added Viscoelastic Damping for Passive Control of Vibrations	147
	Bruno Sousa Carneiro Da Cunha, Antônio Marcos Gonçalves de Lima, and Alice Rosa da Silva	

16	Dynamic Analysis of Fluid-Filled Piping System on Flexible Foundation	155
	Longlong Ren, Xiuchang Huang, Zhengguo Zhang, and Hongxing Hua	
17	Incremental Dynamic Analyses of Steel Moment Resisting Frames with Superelastic Viscous Dampers	165
	Baikuntha Silwal, Osman E. Ozbulut, and Robert J. Michael	
18	Structural Control Using a Semiactive Friction Damper	175
	Juan S. Mantilla, Daniel Gómez, and Peter Thomson	
19	Seismic Response of SMA Reinforced Shear Walls	185
	Marina Maciel, Dan Palermo, and Alaa Abdulridha	
20	Stability of MIMO Controllers for Floor Vibration Control	193
	Donald Nyawako, Paul Reynolds, and Emma Hudson	
21	Extraction of Wave Dispersion Characteristics in a Discrete Chain Using Complex Modal Decomposition	205
	Rickey A. Caldwell Jr., Smruti Panigrahi, and Brian F. Feeny	
22	Approximate General Responses of Multi-Degree-of-Freedom Systems with Parametric Stiffness	211
	Gizem Acar and Brian F. Feeny	
23	Harmonic Forcing of a Two-Segment Elastic Rod	221
	Arnaldo J. Mazzei Jr. and Richard A. Scott	
24	An Unified Framework for Studying Gear Dynamics Through Model Reduction Techniques	233
	Carlo Rosso and Elvio Bonisoli	
25	Application of the Harmonic Balance Method to Centrifugal Pendulum Vibration Absorbers	243
	Mustafa A. Acar and Steven W. Shaw	
26	Development of Multi-Physics Dynamics Models for High-Frequency Large-Amplitude Structural Response Simulation	253
	Armen Derkevorkian, Lee Peterson, Ali R. Kolaini, Terry J. Hendricks, and Bill J. Nesmith	
27	An Efficient Simulation Method for Large-Scale Systems with Local Nonlinearities	259
	Yousheng Chen, Andreas Linderholt, and Thomas Abrahamsson	
28	A Modal Superposition Method for the Analysis of Nonlinear Systems	269
	Erhan Ferhatoğlu, Ender Ciğeroğlu, and H. Nevzat Özgüven	
29	Adaptive Harmonic Balance Methods, A Comparison	279
	Onur Sert and Ender Ciğeroğlu	

Chapter 1

Online Input and State Estimation in Structural Dynamics

K. Maes, G. De Roeck, A. Iliopoulos, W. Weijtjens, C. Devriendt, and G. Lombaert

Abstract This paper presents two applications of joint input-state estimation in structural dynamics. The considered joint input-state estimation algorithm relies upon a limited set of response measurements and a system model, and can be applied for online input and state estimation on structures. In the first case, the algorithm is applied for force identification on a footbridge. The second case shows an application where strains in the tower of an offshore monopile wind turbine are estimated. In both cases, real measured data obtained from in situ measurements are used for the estimation. The dynamic system model, used in the estimation, is for both case studies obtained from a finite element model of the structure. The quality of the force and response estimates is assessed by comparison with the corresponding measured quantities.

Keywords Joint input-state estimation • Force identification • Response estimation • System identification • Application

1.1 Introduction

The knowledge of the loads applied to structures and the corresponding system response is very important for many engineering applications. Often, however, the dynamic forces acting on a structure cannot be obtained by direct measurements, e.g. for wind loads. In addition, the response of a structure cannot be measured at all physical locations, due to practical and economical considerations. System inversion techniques allow combining available vibration data from a limited number of sensors with the information obtained from a dynamic model of the structure, hereby estimating the forces acting to the structure and the response at unmeasured locations.

Several force identification algorithms have been proposed in the literature [4, 10, 11]. Additionally, several state estimation algorithms have been proposed, for linear as well as for non-linear systems [8]. A common approach in state estimation consists of modeling the system input as zero mean Gaussian white noise, where a Bayesian framework is applied for state estimation [16]. In order to overcome the assumption of white noise system input, joint input-state estimation algorithms have been developed, that combine both input and state estimation, e.g. [2, 15]. Gillijns and De Moor [7] have proposed an algorithm where the input estimation is performed prior to the state estimation step. The algorithm was introduced in structural dynamics by Lourens et al. [12], and further extended in [14].

This paper presents a full scale verification of the joint input-state estimation algorithm introduced in [14], using data obtained from two in situ measurements. The algorithm is first applied for force identification on a footbridge. Next, the algorithm is applied for strain estimation in the tower of an offshore monopile wind turbine. The dynamic system model, used in the estimation, is for both case studies obtained from a finite element model of the structure. The estimated forces and response are verified by comparing them to the actual measured quantities.

The outline of the paper is as follows. Section 1.2 gives a brief overview of the joint input-state estimation algorithm. Next, Sect. 1.3 shows the application of the algorithm for force identification on the footbridge. Section 1.4 shows the application of the algorithm for strain estimation on the offshore wind turbine. Finally, Sect. 1.5 concludes the paper.

K. Maes (✉) • G. De Roeck • G. Lombaert

Department of Civil Engineering, KU Leuven, Kasteelpark Arenberg 40, B-3001 Leuven, Belgium
e-mail: kristof.maes@bwk.kuleuven.be

A. Iliopoulos

Mechanics of Materials and Constructions, Vrije Universiteit Brussel, Pleinlaan 2, B-1050 Brussels, Belgium

W. Weijtjens • C. Devriendt

Acoustics and Vibration Research Group, Vrije Universiteit Brussel, Pleinlaan 1, B-1050 Brussels, Belgium

1.2 Joint Input-State Estimation Algorithm

Consider the following linear discrete-time combined deterministic-stochastic state-space description of a system:

$$\mathbf{x}_{[k+1]} = \mathbf{A}\mathbf{x}_{[k]} + \mathbf{B}\mathbf{p}_{[k]} + \mathbf{w}_{[k]} \quad (1.1)$$

$$\mathbf{d}_{[k]} = \mathbf{G}\mathbf{x}_{[k]} + \mathbf{J}\mathbf{p}_{[k]} + \mathbf{v}_{[k]} \quad (1.2)$$

where $\mathbf{x}_{[k]} \in \mathbb{R}^{n_s}$ is the state vector, $\mathbf{d}_{[k]} \in \mathbb{R}^{n_d}$ is the output vector, assumed to be measured, and $\mathbf{p}_{[k]} \in \mathbb{R}^{n_p}$ is the unknown input vector, with n_s the number of system states, n_d the number of outputs, and n_p the number of inputs. In many cases, modally reduced order models are applied, constructed from a limited number of structural modes. The state vector $\mathbf{x}_{[k]}$ then consists of the modal displacements and velocities. The deterministic system behavior is described by the system matrices \mathbf{A} , \mathbf{B} , \mathbf{G} , and \mathbf{J} , that are obtained from a model based on first principles, e.g. a finite element model, or alternatively are identified from experimental vibration data using system identification techniques, see e.g. [18]. The process noise $\mathbf{w}_{[k]}$ compensates for modeling errors and unknown stochastic excitation, i.e. excitation which is not accounted for by $\mathbf{p}_{[k]}$ in Eq. (1.1). The measurement noise $\mathbf{v}_{[k]}$ compensates for modeling errors, unknown stochastic excitation, and measurement errors.

Joint input-state estimation consists of estimating the forces $\mathbf{p}_{[k]}$ and system states $\mathbf{x}_{[k]}$, from a set of response measurements $\mathbf{d}_{[n]}$. A state estimate $\hat{\mathbf{x}}_{[k|l]}$ is defined as an estimate of $\mathbf{x}_{[k]}$, given the output sequence $\mathbf{d}_{[n]}$, with $n = 0, 1, \dots, l$. An input estimate $\hat{\mathbf{p}}_{[k|l]}$ is defined similarly. This section gives a brief summary of the joint input-state estimation algorithm introduced in [14].

The system model used in the estimation is given by Eqs. (1.1) and (1.2). Throughout the derivation of the joint input-state estimation algorithm, the system matrices \mathbf{A} , \mathbf{B} , \mathbf{G} , and \mathbf{J} are assumed known. In addition, it is assumed that the sensor network meets the conditions for instantaneous system inversion derived in [13]. The noise processes $\mathbf{w}_{[k]}$ and $\mathbf{v}_{[k]}$ are assumed to be zero mean and white, with known covariance matrices \mathbf{Q} , \mathbf{R} , and \mathbf{S} , defined by:

$$\mathbb{E} \left\{ \begin{pmatrix} \mathbf{w}_{[k]} \\ \mathbf{v}_{[k]} \end{pmatrix} \begin{pmatrix} \mathbf{w}_{[l]}^T & \mathbf{v}_{[l]}^T \end{pmatrix} \right\} = \begin{bmatrix} \mathbf{Q} & \mathbf{S} \\ \mathbf{S}^T & \mathbf{R} \end{bmatrix} \delta_{[k-l]} \quad (1.3)$$

with $\mathbf{R} > 0$, $\begin{bmatrix} \mathbf{Q} & \mathbf{S} \\ \mathbf{S}^T & \mathbf{R} \end{bmatrix} \geq 0$, and $\delta_{[k]} = 1$ for $k = 0$ and 0 otherwise. $\mathbb{E}\{\cdot\}$ is the expectation operator.

Finally, it is assumed that an unbiased estimate $\hat{\mathbf{x}}_{[0|-1]}$ of the initial state is available, with error covariance matrix $\mathbf{P}_{\mathbf{x}[0|-1]}$ (i.e. $\mathbb{E}\{\mathbf{x}_{[0]} - \hat{\mathbf{x}}_{[0|-1]}\} = 0$, $\mathbf{P}_{\mathbf{x}[0|-1]} = \mathbb{E}\{(\mathbf{x}_{[0]} - \hat{\mathbf{x}}_{[0|-1]})(\mathbf{x}_{[0]} - \hat{\mathbf{x}}_{[0|-1]})^T\}$). The estimate $\hat{\mathbf{x}}_{[0|-1]}$ is assumed independent on the noise processes $\mathbf{w}_{[k]}$ and $\mathbf{v}_{[k]}$ for all k .

The joint input-state estimation algorithm consists of a three-step recursive filter:

$$\hat{\mathbf{p}}_{[k|k]} = \mathbf{M}_{[k]} (\mathbf{d}_{[k]} - \mathbf{G}\hat{\mathbf{x}}_{[k|k-1]}) \quad (1.4)$$

$$\hat{\mathbf{x}}_{[k|k]} = \hat{\mathbf{x}}_{[k|k-1]} + \mathbf{K}_{[k]} (\mathbf{d}_{[k]} - \mathbf{G}\hat{\mathbf{x}}_{[k|k-1]} - \mathbf{J}\hat{\mathbf{p}}_{[k|k]}) \quad (1.5)$$

$$\hat{\mathbf{x}}_{[k+1|k]} = \mathbf{A}\hat{\mathbf{x}}_{[k|k]} + \mathbf{B}\hat{\mathbf{p}}_{[k|k]} \quad (1.6)$$

The first step in Eq. (1.4), referred to as the ‘‘input estimation step’’, yields a filtered estimate of the unknown input vector $\mathbf{p}_{[k]}$, given the measured output $\mathbf{d}_{[k]}$ up to time step k . The second step in Eq. (1.5), referred to as the ‘‘measurement update’’, yields a filtered estimate of the state vector $\mathbf{x}_{[k]}$. The third step in Eq. (1.6), referred to as the ‘‘time update’’, yields a one step ahead prediction of the state vector $\mathbf{x}_{[k+1]}$. The gain matrices $\mathbf{M}_{[k]} \in \mathbb{R}^{n_p \times n_d}$ and $\mathbf{K}_{[k]} \in \mathbb{R}^{n_s \times n_d}$ are determined such that both the input estimates $\hat{\mathbf{p}}_{[k|k]}$ and the state estimates $\hat{\mathbf{x}}_{[k|k]}$ are minimum variance and unbiased (MVU) [7], i.e. the uncertainty on the force and state estimates is minimized, and the error on the estimated forces $\hat{\mathbf{p}}_{[k|k]}$ and states $\hat{\mathbf{x}}_{[k|k]}$ does not depend on the actual forces $\mathbf{p}_{[k]}$. The gain matrices depend on the noise covariance matrices \mathbf{Q} , \mathbf{R} , and \mathbf{S} , on the forces to be estimated, as well as on the sensor configuration.

After applying the joint input-state estimation algorithm, the estimated state vector $\hat{\mathbf{x}}_{[k|k]}$ and force vector $\hat{\mathbf{p}}_{[k|k]}$ can be used to estimate the response $\mathbf{d}_{e[k]} \in \mathbb{R}^{n_{d,e}}$ at any location in the structure, using the following modified output equation:

$$\hat{\mathbf{d}}_{e[k|k]} = \mathbf{G}_e \hat{\mathbf{x}}_{[k|k]} + \mathbf{J}_e \hat{\mathbf{p}}_{[k|k]} \quad (1.7)$$

where the matrices $\mathbf{G}_e \in \mathbb{R}^{n_{d,e} \times n_s}$ and $\mathbf{J}_e \in \mathbb{R}^{n_{d,e} \times n_p}$ relate the state vector $\mathbf{x}_{[k]}$ and force vector $\mathbf{p}_{[k]}$ to the vector of estimated output quantities $\mathbf{d}_{e[k]}$, respectively.

In the case where the location or spatial distribution of the forces acting on the structure is unknown, e.g. for wind loads, the forces $\mathbf{p}_{[k]}$ assumed for response estimation are equivalent loads acting at predefined locations, rather than the actual loads. In this sense, the forces assumed generally account for any source of vibration.

1.3 Force Identification on a Footbridge

The structure under consideration in the first verification example is a footbridge located in Ninove (Belgium). The two-span cable-stayed steel bridge, shown in Fig. 1.1, has a main and secondary span of 36 m and 22.5 m, respectively [19].

1.3.1 Measurement Setup and Data Acquisition

The structure is excited by a sequence of hammer impacts, applied vertically on the bridge deck. The sensor configuration is shown in Fig. 1.2. The acceleration response of the footbridge has been recorded in three orthogonal directions at 12 locations on the bridge deck, using 12 wireless GeoSIG GMS-18 units. In addition, a National Instruments (NI) data acquisition system has been used to record (1) the vertical acceleration at nodes 27 and 48, obtained from PCB 393B04 uniaxial accelerometers, (2) the vertical displacement of the bridge deck at nodes 27 and 40, obtained from AWLG 008M optical displacement sensors, and (3) the impact loads applied vertically at nodes 27 and 48 using PCB 086D50 instrumented hammers (mass 5.5 kg).

A sampling frequency of 200 Hz and 1000 Hz is used for the GMS-18 units and the NI system, respectively. The GMS-18 acceleration data and the measurement data obtained from the NI system are synchronized by maximizing the correlation between the acceleration obtained from the GMS-18 unit at node 48 and the acceleration at node 48 obtained from the cabled uniaxial accelerometer. The measured response and force signals used in the analysis are all digitally lowpass filtered by means of an eighth-order Chebyshev type I lowpass filter with a cut-off frequency of 16 Hz, in both the forward and the



Fig. 1.1 The footbridge in Ninove, Belgium

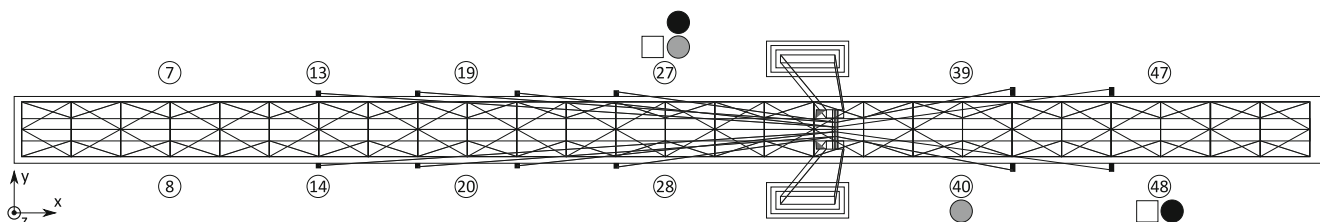


Fig. 1.2 Sensor configuration Ninove footbridge (white circle: GMS-18 unit, black circle: uniaxial accelerometer, gray circle: optical displacement sensor, white square: instrumented hammer)

Table 1.1 Comparison between the experimentally identified modal characteristics and the modal characteristics calculated from the calibrated FE model (j : No. identified mode, \tilde{f}_j : identified undamped natural frequency, $\tilde{\xi}_j$: identified modal damping ratio, j_{item} : No. corresponding mode calibrated FE model, f_j : undamped natural frequency FE model, ε_j : relative error f_j w.r.t. \tilde{f}_j , MAC: MAC-value)

j	\tilde{f}_j (Hz)	$\tilde{\xi}_j$ (%)	j_{item}	f_j (Hz)	ε_j (%)	MAC (-)	Description
1	2.93	1.16	2	3.07	4.70	1.00	1st lateral bending main span
2	2.97	0.39	1	2.87	-3.64	1.00	1st vertical bending main span
3	3.81	0.77	3	3.73	-2.11	0.99	1st combined lateral bending
4	5.79	1.04	4	5.50	-4.98	0.89	1st lateral bending secondary span
5	6.00	0.52	5	5.81	-3.09	0.98	1st vertical bending secondary span
6 [†]	7.06	0.20	7	7.07	0.08	0.94	1st torsional main span
7	7.27	1.26	6	6.84	-5.95	0.96	2nd lateral bending main span
8	8.02	0.56	8	7.62	-5.00	0.99	2nd vertical bending main span
9	9.83	0.73	11	9.97	1.38	0.94	2nd combined lateral bending
10 [†]	11.06	1.28	12	10.80	-2.39	0.96	1st torsional secondary span
11	11.44	2.09	13	11.60	1.38	0.94	2nd torsional main span
12	12.57	1.40	14	12.92	2.72	0.97	3rd combined lateral bending
13	13.59	0.41	15	13.07	-3.85	0.98	3rd vertical bending main span
14 [†]	14.08	0.47	16	14.07	-0.12	0.93	3rd lateral bending main span
15	14.72	0.34	17	14.18	-3.68	0.98	2nd vertical bending secondary span
16	16.20	0.94	19	16.84	3.98	0.97	4th lateral bending main span
17	17.55	1.33	21	18.71	6.61	0.90	2nd torsional secondary span
18 [†]	18.63	0.68	20	17.86	-4.17	0.93	4th vertical bending main span

The identified modes indicated with a dagger are not included in the calibration and are used for cross validation

reverse direction to remove all phase distortion, and then re-sampled at 40 Hz. Next, the acceleration signals obtained from the NI system and the GMS-18 units are additionally digitally highpass filtered by means of a fifth order Butterworth filter with a cut-off frequency of 0.5 Hz and 0.1 Hz, respectively, in both the forward and the reverse direction. The aim of the filter is to remove the low frequency components from the signals that are contaminated by measurement noise. Finally, a detrend operation is applied to all acceleration signals to remove the (physically meaningless) DC component. The measured displacement signals are relative to the displacement at the start of the experiment.

1.3.2 System Model

The force identification is based on a state-space description of the system, given by Eqs. (1.1) and (1.2). The system model used in the present analysis is based on a detailed finite element (FE) model of the structure. The FE model of the footbridge is calibrated using a set of experimental modal parameters that have been obtained through operational modal analysis (OMA) [17, 18]. In total 18 modes of the bridge deck have been identified in the frequency range from 0 to 20 Hz. Table 1.1 gives the natural frequencies, the modal damping ratios, and a description of the mode shapes corresponding to the identified modes. Comparison of the experimental modal parameters with the modal parameters obtained from the initial FE model shows some discrepancies. A model calibration is therefore performed. The calibration parameters considered in this analysis are (1) the stiffnesses of the neoprene bearings, (2) the Young's modulus of the bridge deck, (3) the Young's modulus of the pylons, and (4) the effective Young's modulus of the cables. The natural frequencies and mode shapes corresponding to 14 identified modes are used as the observed quantities in the calibration procedure, i.e. modes 1–5, 7–9, 11–13, and 15–17, listed in Table 1.1. The remaining modes, i.e. modes 6, 10, 14, and 18, are used for cross validation of the model after calibration.

Figure 1.3 shows modes 1, 3, and 7 obtained from the calibrated FE model. Table 1.1 shows the modal characteristics obtained from the FE model after calibration and a comparison to the corresponding observed quantities. The relative error on the natural frequency ε_j for mode j is defined as $\varepsilon_j = (f_j - \tilde{f}_j) / \tilde{f}_j$, where f_j is the undamped natural frequency corresponding to mode j , obtained from the FE model, and \tilde{f}_j is the corresponding value obtained from the system identification. In general very high MAC-values ($\text{MAC} \geq 0.89$) are obtained, both for the modes included in the model calibration and the modes used for cross validation. This indicates a good overall agreement between the identified dynamic behavior of the footbridge and the one predicted by model.

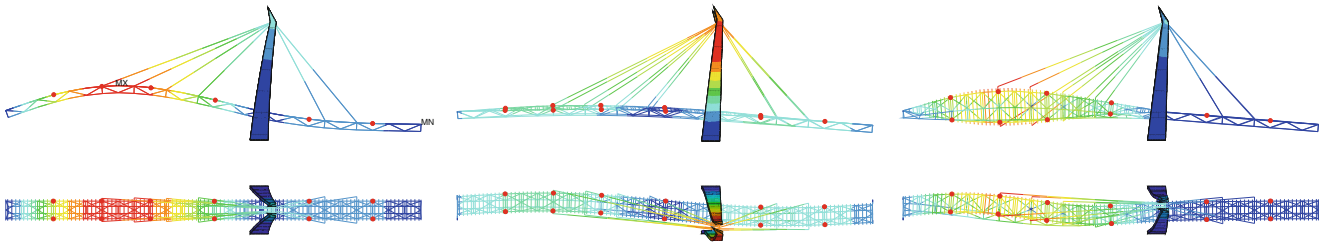


Fig. 1.3 Mode shape mode 1 (*left*), mode 3 (*middle*), and mode 7 (*right*) obtained from the calibrated FE model (*top*: side view, *bottom*: top view). The measurement locations are indicated by *red dots*

A reduced-order discrete-time state-space model is constructed from the modal characteristics of the structure. The model includes all bending modes of the bridge deck with a natural frequency that falls within the frequency range 0–20 Hz, i.e. the 18 modes listed in Table 1.1. For each mode, the mass normalized mode shape of the FE model is used. The natural frequency and modal damping ratio are taken as the experimentally identified values. A zero order hold assumption is applied on the input vector $\mathbf{p}_{[k]}$ in the time discretization. The reader is referred to [14] for the expression of the system matrices **A**, **B**, **G**, and **J**.

1.3.3 Results Force Identification

The forces corresponding to hammer impacts applied at nodes 27 and 48 are estimated using a data set consisting of two vertical displacements (nodes 27 and 40) and two vertical accelerations that are collocated with the applied forces (nodes 27 and 48). The sensor configuration is determined such that (1) the conditions for instantaneous system inversion presented in [13] are met, and (2) the uncertainty on the force estimates introduced by measurement noise and wind loads is (sufficiently) small [14]. Quantification of the uncertainty requires the power spectral density (PSD) of the unknown stochastic excitation, that has been obtained from the response of the structure under ambient loading. The noise covariance matrices **Q**, **R**, and **S** used for joint input-state estimation are based on the PSD of the unknown stochastic excitation and the noise characteristics of the sensors. The initial state estimate vector $\mathbf{x}_{[0|-1]}$ and its error covariance matrix $\mathbf{P}_{[0|-1]}$ are both assumed zero.

Figure 1.4 shows the results of the identification for a sequence of hammer impacts applied at nodes 27 and 48. Firstly, a fairly good estimate of both forces is seen from both the time history and the frequency content. Three time intervals can be distinguished in Fig. 1.4b, e for a single hammer impact applied to the bridge deck; (1) the impact, (2) free vibration, and (3) ambient vibration. During the impact, the broad band hammer force excites the entire frequency range considered. The errors introduced by ambient forces (i.e. unknown stochastic forces) are small, since the hammer impact is far more important than the ambient loading. During the free vibration phase, the structure vibrates at its natural frequencies and modeling errors result in errors on the estimated force time history that generally decay exponentially over time. After the free vibration phase, the measured response is predominantly due to ambient loads. The ambient vibration phase is for example seen in Fig. 1.4b, e for $t < 104$ s. During this phase, the errors on the estimated forces originates from ambient excitation and measurement noise. The force levels observed during this phase (i.e. the force error levels) are small. It is concluded that the errors introduced by ambient excitation and measurement noise are small compared to the peak values generated by the impact forces. From the time history of the forces in Fig. 1.4b, e it is also seen that in this case of broadband excitation, the algorithm is able to properly distinguish between the two forces.

1.4 Strain Estimation on an Offshore Monopile Wind Turbine

The structure considered in the second verification example is a Vestas V90 3 MW wind turbine on a monopile foundation (Fig. 1.5) [5]. The wind turbine is located at the Belwind offshore windfarm in the North Sea, 46 km off the Belgian coast. The hub-height of the wind turbine is on average located at 72 m above the lowest astronomical tide (LAT). The wind turbine is mounted on a monopile foundation with a diameter of 5 m. The water depth at the turbine location is 24 m w.r.t. LAT and the monopile has a penetration depth of 21 m.

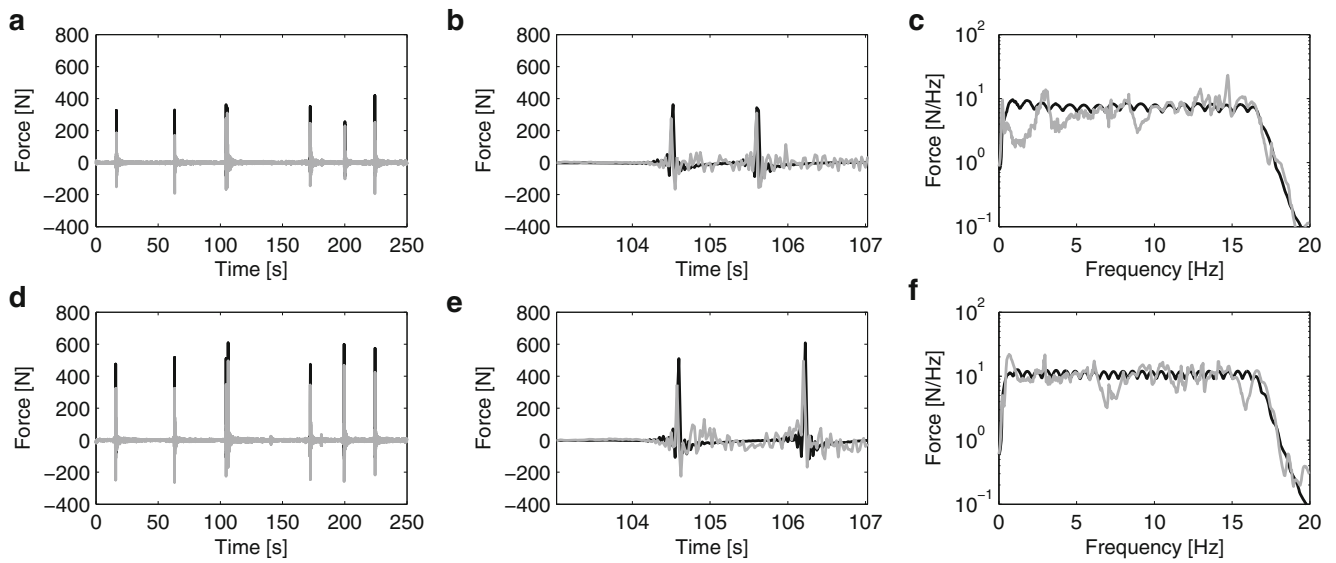


Fig. 1.4 Time history (*left*), detail of the time history (*middle*), and averaged amplitude of the narrow band frequency spectrum (*right*) of the hammer forces applied at node 27 [(a)–(c)] and node 48 [(d)–(f)]. The measured force signals are shown in *black*, the identified force signals are shown in *gray*

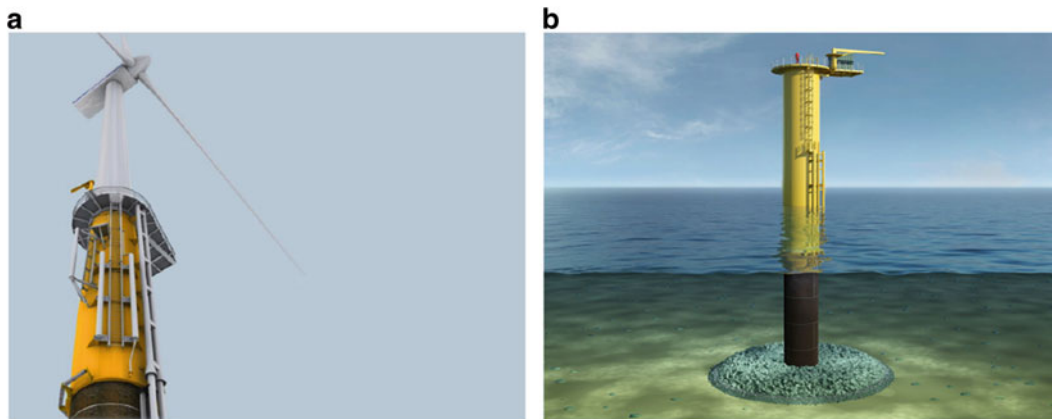


Fig. 1.5 (a) Vestas V90 3 MW wind turbine on a monopile foundation and (b) mud-line, hotspot for fatigue

Offshore wind turbines (OWTs) are exposed to continuous wind and wave excitation and loads originating from the rotor, a.k.a. rotor harmonics. These cyclic loads and their interaction with the turbine dynamics make fatigue life a design driver for offshore wind turbines. The continuous monitoring of the strain response time histories at fatigue hot spots, e.g. at the mud-line, is important to assess the remaining lifetime of the structure. For (offshore) wind turbines, two distinctive components in the strain response time history and consequently in the fatigue spectra can be identified. The low-frequent, near-static (<0.5 Hz) strain cycles are related to variations in the thrust loading of the turbine, e.g. due to gusts. This component can be estimated using the 1 Hz turbine SCADA-data [3] and thus in theory requires no direct strain measurements. The second component is linked to the turbine's dynamics and modal behavior. The corresponding dynamic strains are situated in a higher frequency-range (>0.1 Hz) and originate from additional sources of vibrations, such as turbulence, rotor harmonics, and wave-loading. The focus in this section is on the monitoring of dynamic strains. For some critical locations, a direct measurement of the strains is not feasible. For example, direct measurements of the strains at the mud-line (Fig. 1.5b) require sensors installed prior to the pile-driving of the monopile foundation. As a consequence, the sensors cannot be installed on existing OWTs. Experience in the field has also shown that strain sensors are harder to maintain, are less reliable

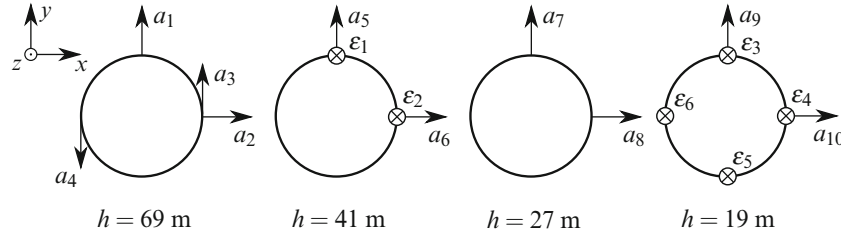


Fig. 1.6 Sensor configuration wind turbine (levels h relative to LAT)

than accelerometers over long periods, and are more susceptible to installation errors. As an alternative to direct strain measurements, response estimation techniques can be applied in order to estimate the (unmeasured) strain response, based on a limited number of response measurements above the water surface (accelerations, strains) and a system model.

1.4.1 Measurement Setup and Data Acquisition

The measurement data considered in the verification consist of two data sets with a duration of 10 min each. The first data set corresponds to rotating conditions of the turbine (wind speed ± 11 m/s, rotation speed turbine ± 16 rpm), the second data set corresponds to parked conditions of the turbine (wind speed ± 2 m/s, rotation speed turbine < 1 rpm).

In total, ten accelerometers and six strain gauges have been installed on the wind turbine; four accelerometers at a height of 69 m (LAT), two accelerometers and two optical fiber Bragg grating strain sensors at a height of 41 m (LAT), two accelerometers at a height of 27 m (LAT), and two accelerometers and four optical fiber Bragg grating strain sensors at a height of 19 m (LAT). Figure 1.6 shows the sensor configuration. The data at all levels are transformed in respectively the Fore-Aft (FA) direction and the Side-Side (SS) direction using the known yaw direction. FA motion is parallel to the wind direction and SS motion is perpendicular to the wind direction. The acceleration and strain data obtained are hereafter referred to as $a_{\alpha\beta}$ and $\epsilon_{\alpha\beta}$, respectively, where α indicates the level in m LAT and β indicates the direction (FA or SS).

A sampling rate of 20 Hz is used in the data acquisition. For each data block of 10 min, the frequency content below 0.05 Hz and above 5 Hz has been removed.

1.4.2 System Model

A system model is constructed from a FE model of the wind turbine, developed by OWI/VUB. The FE model has been updated using a set of experimental modal parameters, which have been obtained through an output-only system identification procedure using data collected in parked conditions [6, 9]. The displacement mode shapes corresponding to the first six modes calculated using the updated FE model are shown in Fig. 1.7. Table 1.2 shows the experimentally identified natural frequencies and modal damping ratios [6], as well as the natural frequencies obtained from the FE model and the MAC-values, which indicate the agreement between the measured and computed displacement mode shapes [1]. For nearly all bending modes of the wind turbine, a high MAC-value is obtained. Note that the FE model is symmetric, whereas the actual behavior of the wind turbine is different in the FA and SS directions and will vary for different wind directions [20].

A reduced-order discrete-time state-space model is constructed from the FE model of the wind turbine, applying a zero order hold assumption on the force. The model includes the six modes listed in Table 1.2. For each mode, the mass normalized mode shape and natural frequency are assumed to be known from the FE model, whereas the modal damping ratio is taken as the experimentally identified value.

1.4.3 Results Strain Estimation

The applicability of joint input-state estimation for response estimation is now verified by predicting the FA and SS strain at the lowest measurement level ($h = 19$ m LAT). The data set consists of six accelerations at the three highest levels (a_{69FA} ,

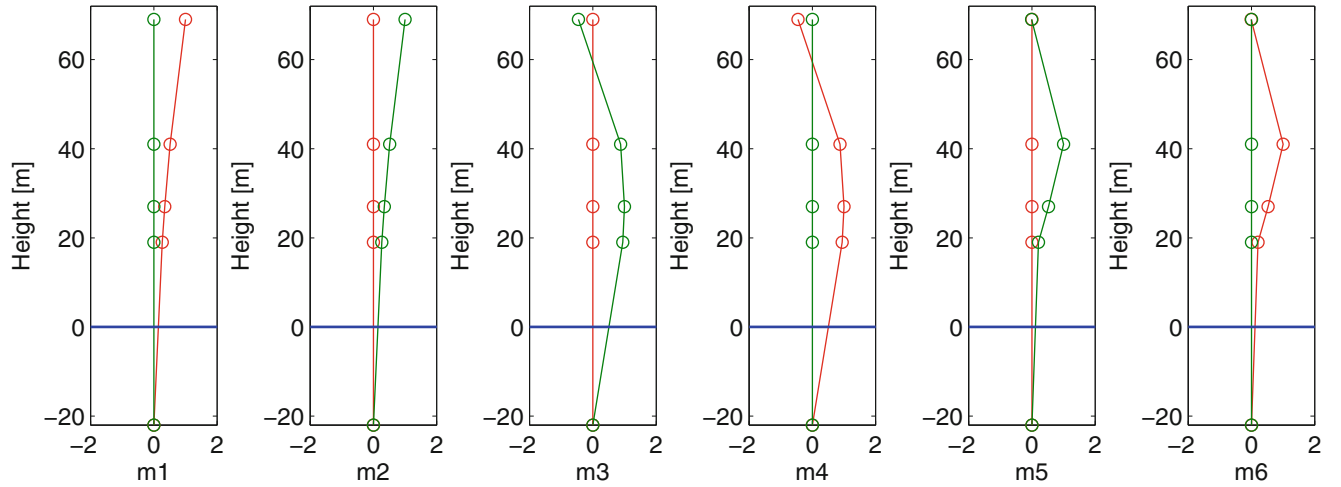


Fig. 1.7 First six displacement mode shapes obtained from the FE model, FA-direction (*red*) and SS-direction (*green*). From left to right: FA1, SS1, SS2, FA2, SS3, FA3

Table 1.2 Experimentally identified modal characteristics and comparison to the modal characteristics obtained from the FE model (f_{id} : identified natural frequency, f_{fem} : natural frequency obtained from FE model, ξ_{id} : identified modal damping ratio, MAC: MAC-value)

No.	f_{id} (Hz)	f_{fem} (Hz)	ξ_{id} (%)	MAC	Description
1	0.361	0.374	1.86	0.99	First FA bending mode
2	0.365	0.374	2.49	0.99	First SS bending mode
3	1.448	1.440	1.38	0.99	Second SS bending mode
4	1.560	1.440	1.14	0.98	Second FA bending mode
5	3.610	3.636	0.56	0.96	Third SS bending mode
6	3.910	3.636	0.92	0.92	Third FA bending mode

a_{69SS} , a_{41FA} , a_{41SS} , a_{27FA} , a_{27SS}) and two strains at level $h = 41$ m LAT (ϵ_{41FA} and ϵ_{41SS}). The force vector $\mathbf{p}_{[k]}$ assumed for joint input-state estimation consist of six independent modal forces. For the stability of the joint input-state estimation algorithm and the uniqueness of the estimated quantities, at least n_p displacements or strains are required as part of the output vector $\mathbf{d}_{[k]}$, in addition to the measured accelerations [13], where n_p is the number of forces ($n_p = 6$). In this analysis, no displacements have been measured and a set of displacements is calculated by (offline) numerical integration of the acceleration data. The signals obtained by integration have been highpass filtered applying a cutoff frequency of 0.25 Hz. The aim of the filter is to remove the low frequency components from the signals which are contaminated by measurement noise. Six displacements are added to the data set (d_{69FA} , d_{69SS} , d_{41FA} , d_{41SS} , d_{27FA} , d_{27SS}).

The (equivalent) forces $\mathbf{p}_{[k]}$ are assumed to cover all sources of excitation. The noise covariance matrices \mathbf{Q} , \mathbf{R} , and \mathbf{S} assumed for joint input-state estimation, characterizing the noise processes $\mathbf{w}_{[k]}$ and $\mathbf{v}_{[k]}$ in Eqs. (1.1) and (1.2), respectively, are calculated in accordance to the sensor noise statistics. The initial state vector $\hat{\mathbf{x}}_{[0|-1]}$ and the corresponding error covariance matrix $\mathbf{P}_{[0|-1]}$ are assumed zero. The estimated strain signals are characterized by spurious low frequency components that originate from measurement noise on the acceleration data. The estimated strain signals have therefore been highpass filtered applying a cutoff frequency of 0.25 Hz. The 0.25 Hz low frequency boundary is chosen to focus on dynamic strains.

Figure 1.8 compares the measured and estimated strain response for data set 1 (rotating conditions). Very accurate strain estimates are obtained both for the FA and SS direction. It is expected that small estimation errors mainly result from errors on the mode shapes. The measured (unfiltered) strain signals are characterized by an important low frequency content (frequencies < 0.25 Hz), which is not present in the estimated strain signals (see Fig. 1.8c, f).

Figure 1.9 compares the measured and estimated strain response for data set 2 (parked conditions). The measured strain response for parked conditions is mainly dominated by the first bending mode, both for the FA and SS direction, as seen from the strain PSD. For frequencies between 0.3 and 0.6 Hz, there is a very good agreement between the measured and

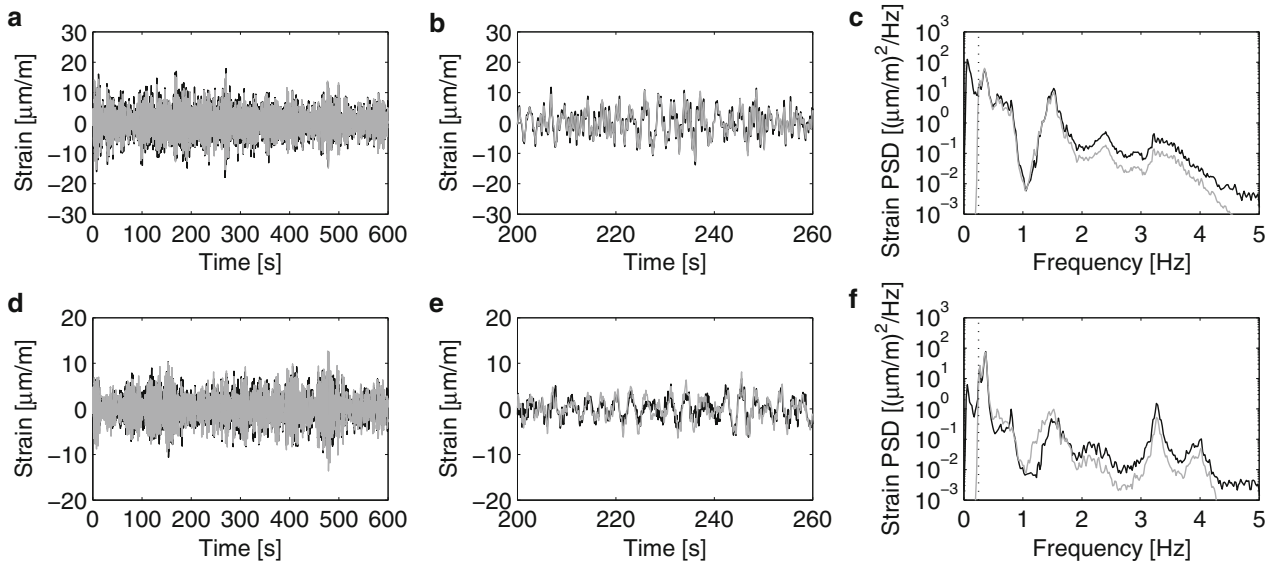


Fig. 1.8 Time history (*left*), detail time history (*middle*) and estimated PSD (*right*) of the FA strain (*top, a–c*) and SS strain (*bottom, d–f*) at level $h = 19$ m LAT for data set 1 (rotating conditions). The measured strains are shown in *black*, the estimated strains are shown in *gray*

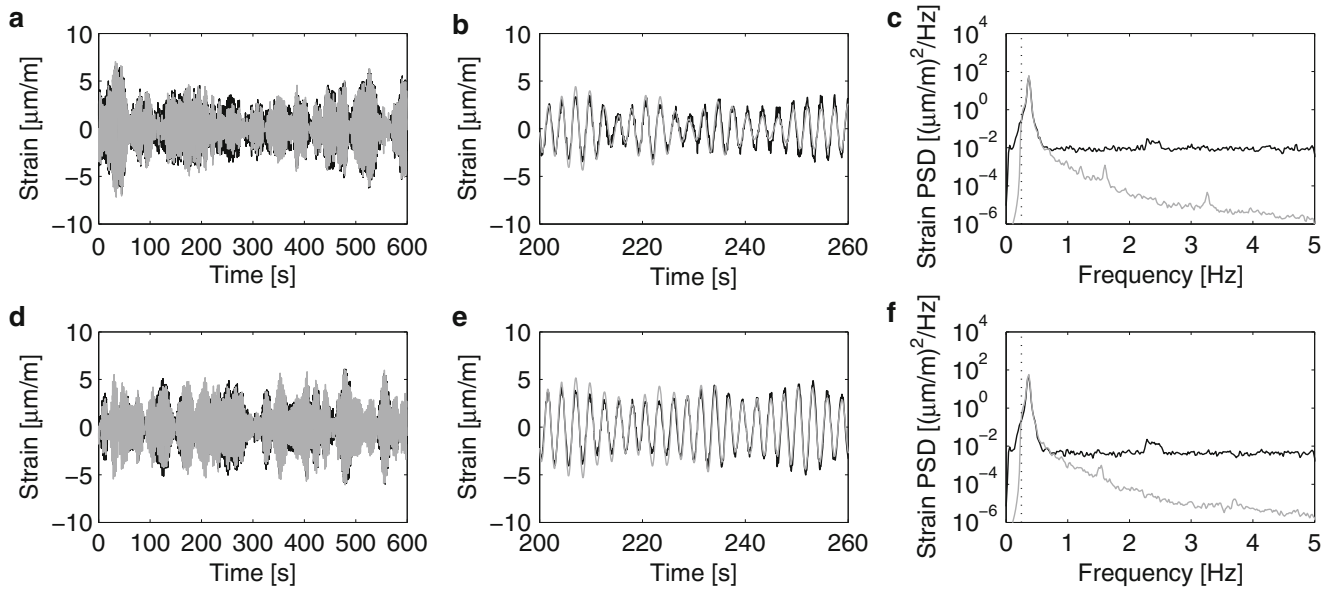


Fig. 1.9 Time history (*left*), detail time history (*middle*) and estimated PSD (*right*) of the FA strain (*top, a–c*) and SS strain (*bottom, d–f*) at level $h = 19$ m LAT for data set 2 (parked conditions). The measured strains are shown in *black*, the estimated strains are shown in *gray*

estimated strain signals (see Fig. 1.9c, f). It can clearly be seen how the measured strain signals (black) are hitting the noise floor of the strain gauges beyond the first mode at frequencies larger than 0.9 Hz. The predicted strains (gray) dive beneath the noise floor of the strain gauges. From the predicted strains, the noise floor of the accelerometers, multiplied with $1/\omega^2$ from the double integration, and following $1/\omega^4$ behavior in the PSD, is clearly visible at higher frequencies. Higher order dynamics still appear in the predicted strain signals, however. The observed peaks, e.g. near 1.5 Hz, correspond to the natural frequencies given in Table 1.2. The peaks are not observed in the measured strains, since at the peak frequencies, the strains are below the noise level of the strain gauges.

1.5 Conclusions

In this paper, a state-of-the-art-joint input-state estimation algorithm is applied for two case studies, using data obtained from full scale experiments. In the first case study, the algorithm is applied for the identification of impact loads applied at the deck of a footbridge. In the second case, the algorithm is applied for strain estimation in the tower of an offshore monopile wind turbine. For both cases, comparison of the estimated forces/strains to the actual measured quantities shows a good agreement. Focus in further research is on the integration of joint input-state estimation techniques in the framework of real-time and online monitoring of civil engineering structures.

Acknowledgements The research presented in this paper has been performed within the framework of the project G.0738.11 “Inverse identification of wind loads on structures”, funded by the Research Foundation Flanders (FWO), Belgium. Their financial support is gratefully acknowledged. The authors affiliated to KU Leuven are all members of the KU Leuven—BOF PFV/10/002 OPTEC—Optimization in Engineering Center. The authors would also like to acknowledge the Offshore Wind Infrastructure Application Lab, Parkwind and Belwind for providing the data used in the offshore wind turbine application.

References

1. Allemang, R.J., Brown, D.L.: A correlation coefficient for modal vector analysis. In: Proceedings of the 1st International Modal Analysis Conference, pp. 110–116, Orlando (1982)
2. Azam, S.E., Papadimitriou, C., Chatzi, E.: A dual Kalman filter approach for state estimation via output-only acceleration measurements. *Mech. Syst. Signal Process.* **60–61**, 866–886 (2015)
3. Baudisch, R.: Structural health monitoring of offshore wind turbines. Master’s thesis, Danmarks Tekniske Universitet (2012)
4. Bernal, D., Ussia, A.: Sequential deconvolution input reconstruction. *Mech. Syst. Signal Process.* **50–51**, 41–55 (2015)
5. Devriendt, C., Magalhães, F., Weijtjens, W., De Sitter, G., Cunha, Á., Guillaume, P.: Structural health monitoring of offshore wind turbines using automated operational modal analysis. In: Chang, F.-K. (ed.) Proceedings of the 9th International Workshop on Structural Health Monitoring, IWSHM 2013, vol. 1, pp. 2415–2422, Stanford (2013)
6. Devriendt, C., Weijtjens, W., El Kafafy, M., De Sitter, G.: Monitoring resonant frequencies and damping values of an offshore wind turbine in parked conditions. *IET Renew. Power Gener.* **8**(4), 433–441 (2014). doi: [10.1049/iet-rpg.2013.0229](https://doi.org/10.1049/iet-rpg.2013.0229)
7. Gillijns, S., De Moor, B.: Unbiased minimum-variance input and state estimation for linear discrete-time systems with direct feedthrough. *Automatica* **43**(5), 934–937 (2007)
8. Hernandez, E.M.: A natural observer for optimal state estimation in second order linear structural systems. *Mech. Syst. Signal Process.* **25**(8), 2938–2947 (2011)
9. Iliopoulos, A., Shirzadeh, R., Weijtjens, W., Guillaume, P., Van Hemelrijck, D., Devriendt, C.: A modal decomposition and expansion approach for prediction of dynamic responses on a monopile offshore wind turbine using a limited number of vibration sensors. *Mech. Syst. Signal Process.* **68–69**, 84–104 (2016)
10. Klinkov, M., Fritzen, C.P.: An updated comparison of the force reconstruction methods. *Key Eng. Mater.* **347**, 461–466 (2007)
11. Liu, Y., Shepard, W.S.: Dynamic force identification based on enhanced least squares and total least squares schemes in the frequency domain. *J. Sound Vib.* **282**, 37–60 (2005)
12. Lourens, E., Papadimitriou, C., Gillijns, S., Reynders, E., De Roeck, G., Lombaert, G.: Joint input-response estimation for structural systems based on reduced-order models and vibration data from a limited number of sensors. *Mech. Syst. Signal Process.* **29**, 310–327 (2012)
13. Maes, K., Lourens, E., Van Nimmen, K., Reynders, E., De Roeck, G., Lombaert, G.: Design of sensor networks for instantaneous inversion of modally reduced order models in structural dynamics. *Mech. Syst. Signal Process.* **52–53**, 628–644 (2015)
14. Maes, K., Smyth, A.W., De Roeck, G., Lombaert, G.: Joint input-state estimation in structural dynamics. *Mech. Syst. Signal Process.* **70–71**, 445–466 (2016)
15. Niu, Y., Klinkov, M., Fritzen, C.-P.: Online force reconstruction using an unknown-input Kalman filter approach. In: Proceedings of the 8th International Conference on Structural Dynamics, EUROODYN 2011, pp. 2569–2576, Leuven (2011)
16. Papadimitriou, C., Fritzen, C.-P., Kraemer, P., Ntotsios, E.: Fatigue predictions in entire body of metallic structures from a limited number of vibration sensors using Kalman filtering. *Struct. Control Health Monit.* **18**, 554–573 (2011)
17. Peeters, B., De Roeck, G.: Reference-based stochastic subspace identification for output-only modal analysis. *Mech. Syst. Signal Process.* **13**(6), 855–878 (1999)
18. Reynders, E., De Roeck, G.: Reference-based combined deterministic-stochastic subspace identification for experimental and operational modal analysis. *Mech. Syst. Signal Process.* **22**(3), 617–637 (2008)
19. Van Nimmen, K., Lombaert, G., De Roeck, G., Van den Broeck, P.: Vibration serviceability of footbridges: evaluation of the current codes of practice. *Eng. Struct.* **59**, 448–461 (2014)
20. Weijtjens, W., Verbelen, T., De Sitter, G., Devriendt, C.: Foundation structural health monitoring of an offshore wind turbine - a full-scale case study. *Struct. Health Monit.* (2015)

Chapter 2

Modeling and Testing of the Anti-Vibration Base for Michelangelo's Pietà Rondanini

Alfredo Cigada, Edoardo Sabbioni, Ali Siami, and Emanuele Zappa

Abstract The famous statue Pietà Rondanini by Michelangelo Buonarroti (sculpted in the second half of 1500) was recently moved to a new position in a museum in Castello Sforzesco, Milan. In this new location, the vibration levels, due to the close presence of underground tracks, has been considered worthy of specific attention; therefore both the Municipality of Milan and the Cultural Heritage ministry asked for the design of a new base capable of mitigating the vibration input to the statue. In addition, since Milan is a seismic area (although with moderate risk), it was also required to include in the base design an anti-seismic device. The protection from the underground action (which is in the range between 16 and 80 Hz) requires the development of a system with low natural frequency and rather limited damping, to have a steep filtering after resonance. However in case of an earthquake, the low frequency range would be strongly excited, with the eventual risk of an extreme event like rocking. A second device is thus introduced to protect the statue from earthquakes, consisting in a low friction slide of the same type as those used to protect buildings from the same kind of events. The coupling between the two types of protection imposed a careful design and testing of the complete system made up of the base and the statue. The design of the base was developed by means of an experimental-numerical approach. A measuring campaign using a large 6 degrees of freedom shaking table was used to test a full scale prototype of the base supporting a marble 1:1 copy of the statue. A multibody model of the full installation (complete base and statue) was developed, qualified by means of experimental data, and used to optimize the parameters, such as the mass distribution, positions of the elastomeric supports and the damping of the devices. The final system is now installed in the museum, protecting the Pietà.

Keywords Cultural heritage • Vibration protection • Anti-seismic device • Elastomeric support • Multibody model

2.1 Introduction

Preserving historical statues from earthquakes and repeated ambient vibrations is a crucial issue for many museums and historical sites. One among the most effective methods introduced in recent years has been the use of sliding isolators to protect historical monuments from earthquake shakes. Only in a very few cases [1, 2] the requirements were for a statue protection from both earthquakes and ambient vibrations. Vestorni et al. [3] investigated the capability of a base isolation system constituted of multi-stage high damping laminated rubber bearings to reduce the seismic risk for statues. Specifically, a parametric analysis was carried out to determine the sensitivity of system response to the variation of base isolation system parameters. Petrovic et al. [4] instead studied the applicability of base isolation systems made of elastomeric bearings for the protection of cultural heritage. The performed analysis defined the maximum height-to-width ratio of the objects to be mounted on the elastomeric isolators in order to prevent rocking and considering different soil conditions.

Several sliding isolator devices are instead compared in [5], while Jampole et al. [6] developed and tested a low-cost sliding isolation system for protecting light-frame residential structures from earthquakes.

The device described in this paper instead combines a sliding isolator to mitigate seismic vibrations due to earthquakes with passive anti-vibration rubbers for filtering ambient vibrations.

The main issue concerned with this kind of devices consists in the interaction between the two mitigating systems, which are designed to filter out different vibration kinds, acting with different frequency, amplitude and probability of occurrence. In fact ambient vibrations are certain and continuous, they have low levels and are present in a wider band, while earthquakes have lower frequencies, higher amplitudes but they occur rarely.

A. Cigada • E. Sabbioni (✉) • A. Siami • E. Zappa
Department of Mechanical Engineering, Politecnico di Milano, via La Masa 1, Milan, Italy
e-mail: edoardo.sabbioni@polimi.it

That's why, after a thorough examination of the specific shape and size for each statue, the proper isolation system has to be tailored to each different artifact, to optimize the best effectiveness and safety of the adopted final isolating system.

In this research, the new vibration isolation system for Michelangelo's Pietà Rondanini has been numerically investigated.

The statue was in fact recently moved to a new location, to give this masterpiece its proper value inside a new museum: however the proximity to a subway has required the designers of the new museum to face the not yet known problem of the marble response to a daily vibration dose. A fit to the purpose isolation system has then been set-up.

Based on a series of vibration tests carried out on a prototype of the base, also relying on the use of a 1:1 marble copy of the statue, a multibody model of the whole system has been developed.

The validation of the model allows not just to reproduce the observed base-statue behavior, but also to go on trying a further optimization, to eventually increase the system effectiveness, by working on a proper combination of stiffness and damping of the elements making up the base, or modifying the actual geometry.

The final results show a good agreement between the model and the experimental results and allow to verify the choices adopted in modeling the system. It should be noted that the main target of this research is to develop a model for the isolating system and to verify its performance. The details of the isolating system are thus not included in this work.

2.2 The Isolating System

The isolation system was designed to accomplish the following requirements: (1) to separate the statue from any kind of ground vibration, (2) to sustain the weight of the statue and its supporting structure, (3) to damp any eventual higher amplitude motion and (4) to restore the statue to its original position after an earthquake. To achieve these targets, the isolation system consists of two parts: a sliding unit for mitigation of the seismic vibrations; these low friction slides are equipped with devices to restore the statue to its initial position in case of displacement from the rest position. The second part consists of a vibration-mechanical filter, placed on top of the sliding unit, made up of anti-vibration rubbers for isolating ground-borne vibrations generated by the underground trains. A sketch of the whole system is given in Fig. 2.1.

The sliding unit is made up of two orthogonal low-friction linear motion bearings, allowing the displacement of the system made up of the base and the statute in the horizontal plane. The restoring function is provided by a belt connecting the sliding plates. The sliding unit was designed so to have a response to displacements induced by an earthquake lower than 2 mm/s and a natural frequency in the horizontal direction of about 0.3 Hz (the global mass of the base and the statue is approximately 2850 kg). To avoid undesired movements of the base and statue in absence of an earthquake, the belts of the sliding unit are preloaded: no relative movements occur if the applied force is lower than 500 N.

The ambient vibration-isolation is achieved by means of 13 rubber elements fixed between the sliding unit (lower base, Fig. 2.1) and a plate sustaining the statue support (upper base, Fig. 2.1). The position of the rubber bearings is shown in Fig. 2.2. As it can be seen, a modular layout was adopted, made up of nine modules, some of them connected to the slides, while the others are dummy elements. This allows to easily change position and type of the rubber bearings to reach the target performance for the vibrations-isolating system and to make any eventual maintenance an easier task.

To guarantee the best mechanical filtering action for all kinds of vibrations, a compromise solution has been looked for by selecting rubber bearings allowing to get a natural frequency in the vertical (i.e. perpendicularly to the ground) and horizontal directions of approximately 8 and 3 Hz, respectively.

The main characteristics of the isolating system are given in Table 2.1.

2.3 Experimental Tests

In this section a summary of the measurement results relevant to this paper will be presented. The measurements were carried out by using a shaking table capable of exciting the structure in the vertical and the horizontal directions at the same time.

Figure 2.3 shows the experimental setup: a 1:1 marble copy of the Pietà Rondanini statue is placed on a support, which is positioned on the previously described isolation system. The lower part of the sliding unit of the isolation system is rigidly connected with a shaking table (called in the following seismic base). The shaker, from CESI Ricerche, can be actuated and controlled independently over 6 axes.

Figure 2.3 also shows some of the accelerometers used to reconstruct the vibration path from the table to the statue. Two independent measurement systems were adopted with different resolution and full scale.

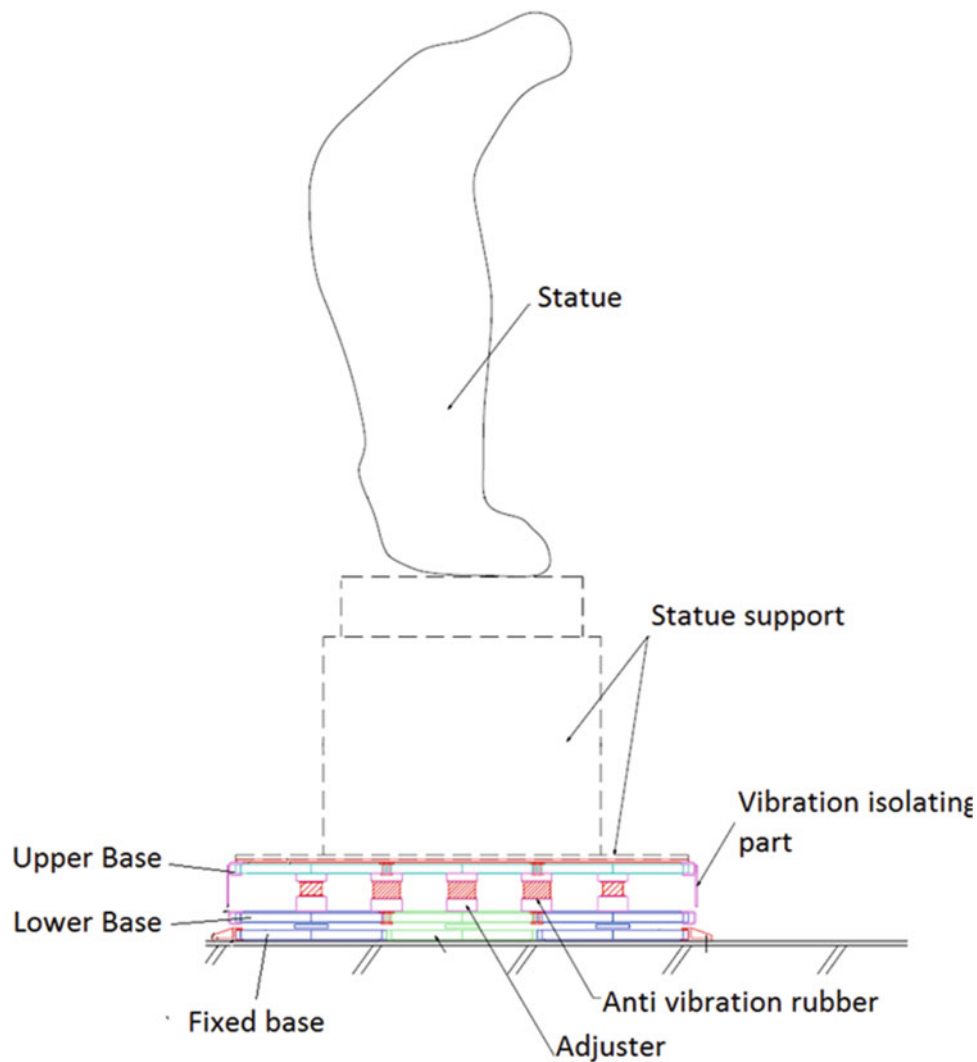


Fig. 2.1 Schematic plan of the statue and the isolating system

Table 2.1 Main characteristics of the isolating system

Design mass (kg)	2800–3100
Stiffness of restoring belts (N/mm)	1.26
Vertical stiffness of rubber bearings ($\times 13$) (N/mm)	568
Horizontal stiffness of rubber bearings ($\times 13$) (N/mm)	128

Several input signals were applied by means of the shaking table to the statue and the isolating system. In the following, the results concerned with sweep sine tests are reported. Imposed sweep sine test consisted in a chirp signal having a constant displacement amplitude (25 mm) in the range of 0.1–0.45 Hz and then a constant acceleration profile in the range 0.63–50 Hz with rate of 1 oct/min.

The FRFs (Frequency Response Functions) in the X-direction and Z-direction are respectively shown in Figs. 2.4 and 2.5. The acceleration of the shaking table (point 1 in Fig. 2.3) is used as reference.

More in detail, Fig. 2.4 shows the FRFs (amplitude and phase) between the acceleration imposed by the shaking table and the acceleration of points 2, 3 and 6 (make reference to Fig. 2.3) along the X-axis when the excitation is imposed along the same direction. Point 2 and 3 are respectively placed on the lower (lower base, Fig. 2.1) and the upper base (upper base, Fig. 2.1) of the vibrations-isolating system. Point 6 is instead placed on the support of the statue, near to its feet.

As it can be seen, the natural frequency of the horizontal motion of the whole system is about 0.3 Hz and it is governed by the restoring system. Below this frequency the whole system moves together.

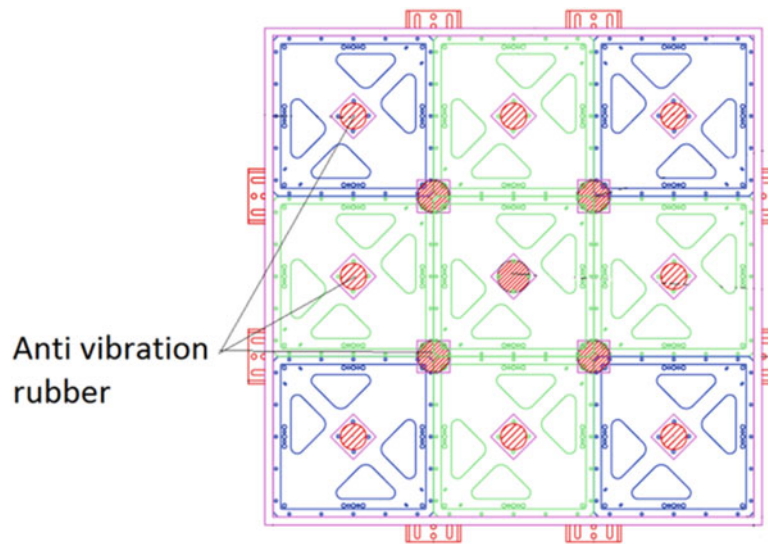


Fig. 2.2 Position of rubber bearings

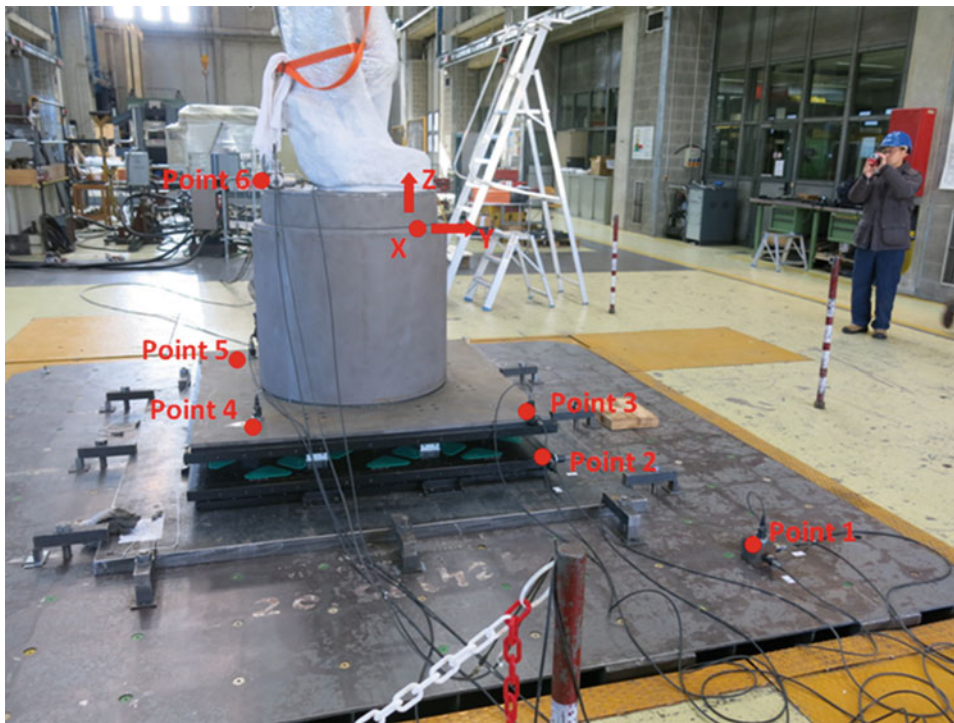


Fig. 2.3 Experimental setup, position of accelerometers and reference system

Frequencies of the pitch and horizontal motions of the part of the system above the sliding unit are located in the range 0.3–6 Hz. Above 6 Hz vibrations along the X-direction of the statue support are filtered out by the vibrations-isolation system (red line and black dashed-dotted line), while the lower base of the vibrations-isolating system (which is above the sliding unit) and the seismic base (i.e. the shaking table) move together (blue solid line), i.e. there is no sliding between them.

Figure 2.5 shows the FRFs (amplitude and phase) between the acceleration imposed by the shaking table and the acceleration of points 3, 4, 5 and 6 (make reference to Fig. 2.3) along the Z-axis when the excitation is imposed along the same direction. A resonance peak at 8.7 Hz can be clearly seen concerned with the motion along the Z-axis of the whole system. Above this frequency, vibrations are filtered out by the vibrations-isolation system.

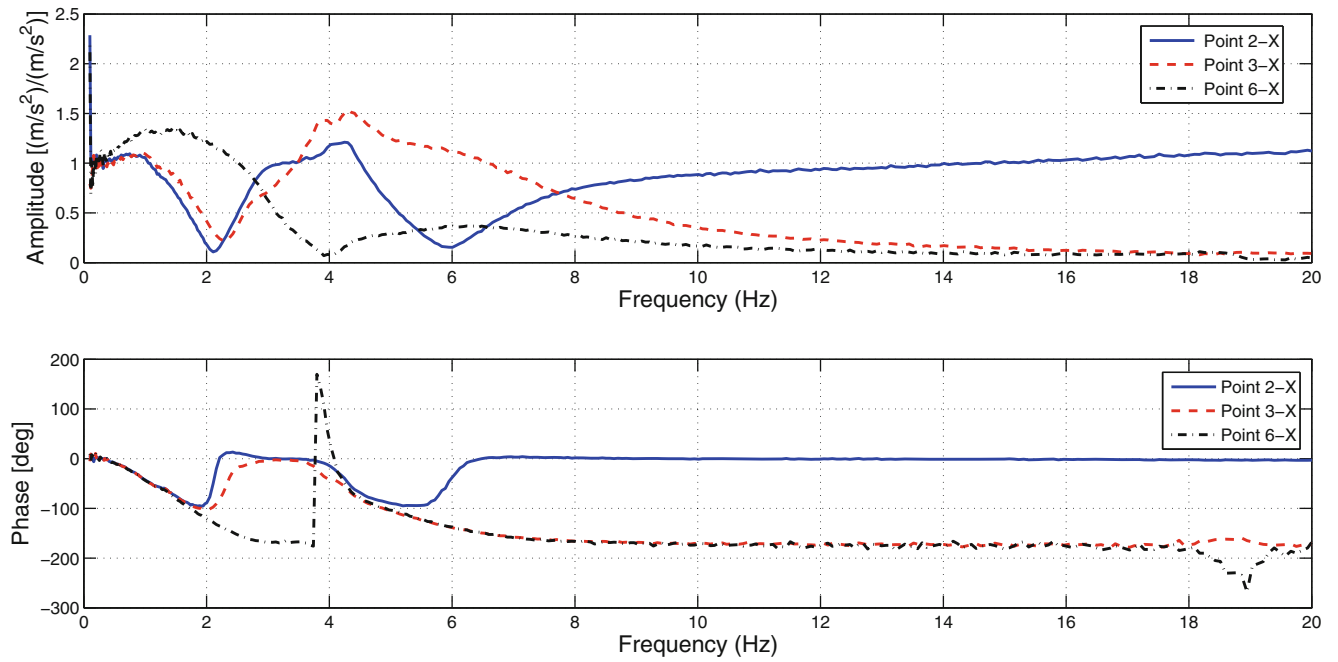


Fig. 2.4 Amplitude and phase of the FRFs between the X-acceleration of the seismic base (point 1) and the X-acceleration of points 2, 3 and 6 (see Fig. 2.3). Sweep test along the X-direction

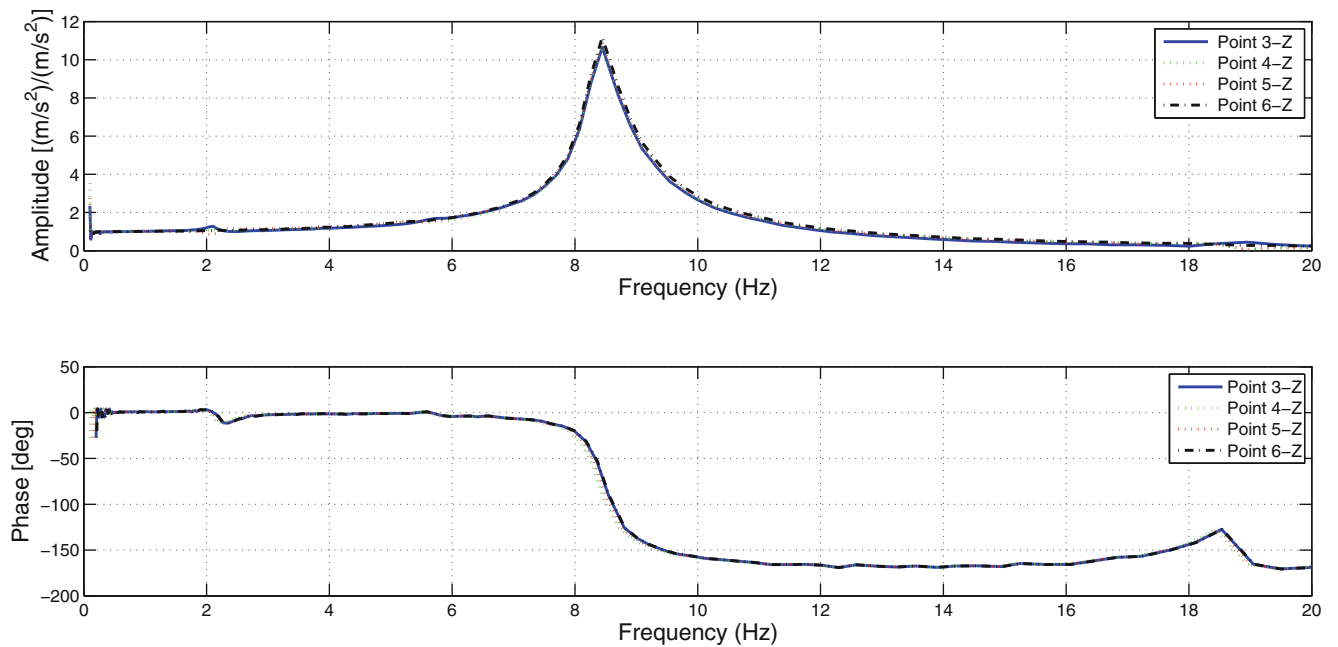


Fig. 2.5 Amplitude and phase of the FRFs between the Z-acceleration of the seismic base (point 1) and the Z-acceleration of points 3, 4, 5 and 6 (see Fig. 2.3). Sweep test along the Z-direction

2.4 Multibody Model of the Isolating System

To investigate any possible improvements of the isolating device, a multibody (MB) model of the whole system, including the statue and its support, was developed in ADAMS/View environment.

The developed model aims at reproducing the experimental set-up used during the above described tests.

The model consists of three rigid bodies respectively representing (Figs. 2.6 and 2.7):

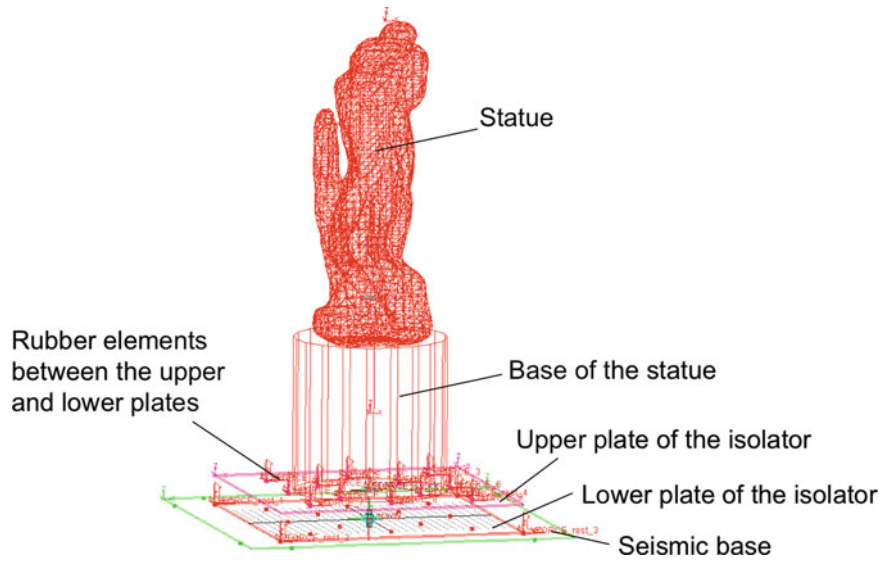


Fig. 2.6 Multibody model of the isolating system

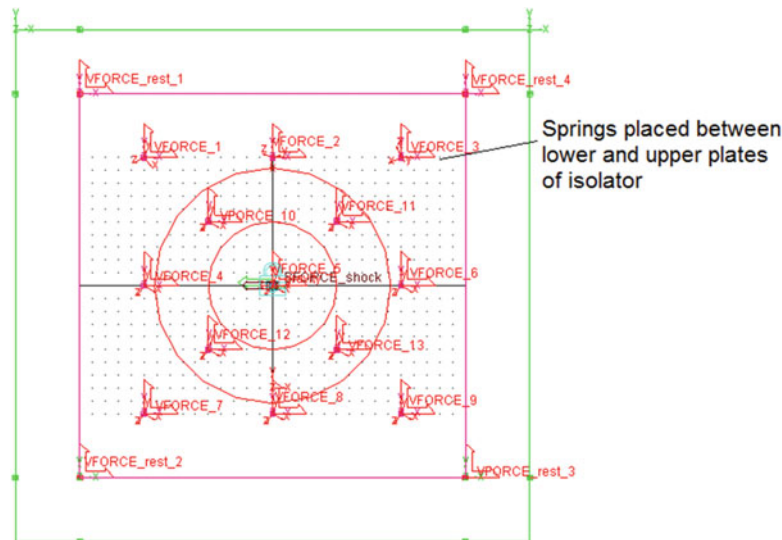


Fig. 2.7 Multibody model of the isolating system, top view

- the seismic base, which imposes the motion to the isolating system and the statue;
- the lower base of the vibrations-isolating system (lower base, Fig. 2.1), which is placed above the linear motion bearings;
- the assembly of the upper plate of the vibrations-isolating system (upper base, Fig. 2.1), the support of the statue and the Rondanini Pietà statue, which is placed above the rubber bearings. This part consists of the cylindrical parts and the pink plate according to the Fig. 2.1.

Inertial properties of the bodies constituting the model were estimated through direct measurements or 3D solid models.

The sliding unit was modeled as a nonlinear three-component force field. Into details, a linear spring-damper system reproduces the vertical damping and stiffness of the linear motion bearings.

The global force in the horizontal direction is instead given by:

$$F_H = F_k + F_d + F_\mu \quad (2.1)$$

where F_μ represents the Coulomb sliding friction force of the linear motion bearings, while F_k and F_d are the elastic and the dissipative components of the restoring force respectively. While the elastic force is linear (the belt stiffness is given in

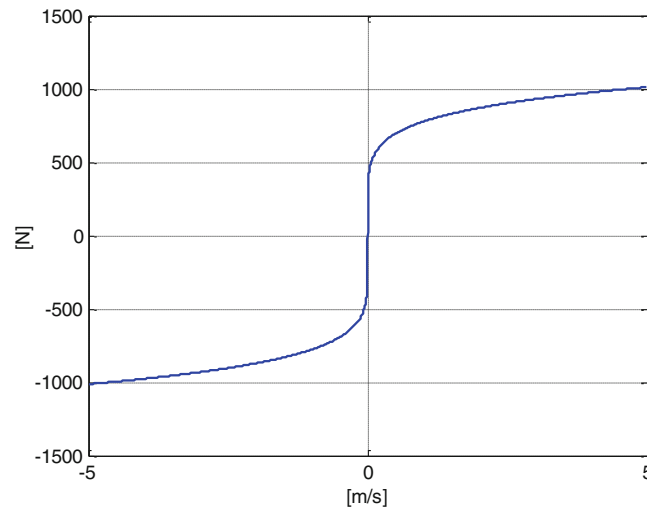


Fig. 2.8 Dissipative component of the restoring force as a function of the sliding speed

Table 2.1), the dissipative force is a nonlinear function of the sliding speed, as depicted in Fig. 2.8. As it can be seen, to reproduce the preload of the restoring belt avoiding undesired movements of the statue, a force of 500 N is provided when the sliding speed is equal to zero.

The vibrations-isolating device was modeled by means of 13 bushings reproducing stiffness and damping properties of the rubber bearings (see Table 2.1).

Input to the model is the motion imposed to the seismic base.

2.4.1 Numerical-Experimental Comparison

To verify the capability of the developed MB model to reproduce the response of the isolating system, numerical results were compared with experimental data collected during the tests described in Sect. 2.3. On this purpose, the same input displacement imposed to the seismic base during the experimental tests was provided to the MB model.

As an example of the obtained results, the comparison between numerical and experimental data obtained during a sweep tests along the Z and the X directions is presented in the following. Specifically Fig. 2.9 refers to the sweep test along the Z direction, while Figs. 2.10, 2.11, and 2.12 are concerned with the sweep test along the X direction. Into details, Fig. 2.9 shows the FRF between the Z-acceleration of the seismic base (point 1 in Fig. 2.3 and input to the model) and the one at the upper base of the vibrations-isolating system (point 3 in Fig. 2.3).

Figures 2.10, 2.11, and 2.12 respectively show the FRFs between the acceleration along the X-direction of the seismic base (point 1 in Fig. 2.3 and input to the model) and those of (a) the lower base of the vibrations-isolating system (point 2 in Fig. 2.3), (b) the upper base of the vibrations-isolating system (point 3 in Fig. 2.3), and (c) the statue support which is point 6 of Fig. 2.3.

In all the figures, results of the MB model are depicted in red, while dashed blue lines represent the experimental data. A good agreement between numerical and experimental data can be seen for all the reported FRFs in the frequency range 0–20 Hz, where the rigid vibration modes of the system are found.

2.4.2 Sensitivity Analysis

To investigate any possible improvement of the isolating system, a sensitivity analysis was carried out by varying some parameters of the model. On this purpose, it must be considered that the stiffness of the restoring belts and of the rubber bearings cannot be significantly varied, since they have to guarantee the functions for which they have been introduced. They must work only in case of an earthquake (belts) and filter out at best the ground-borne vibrations under normal operating

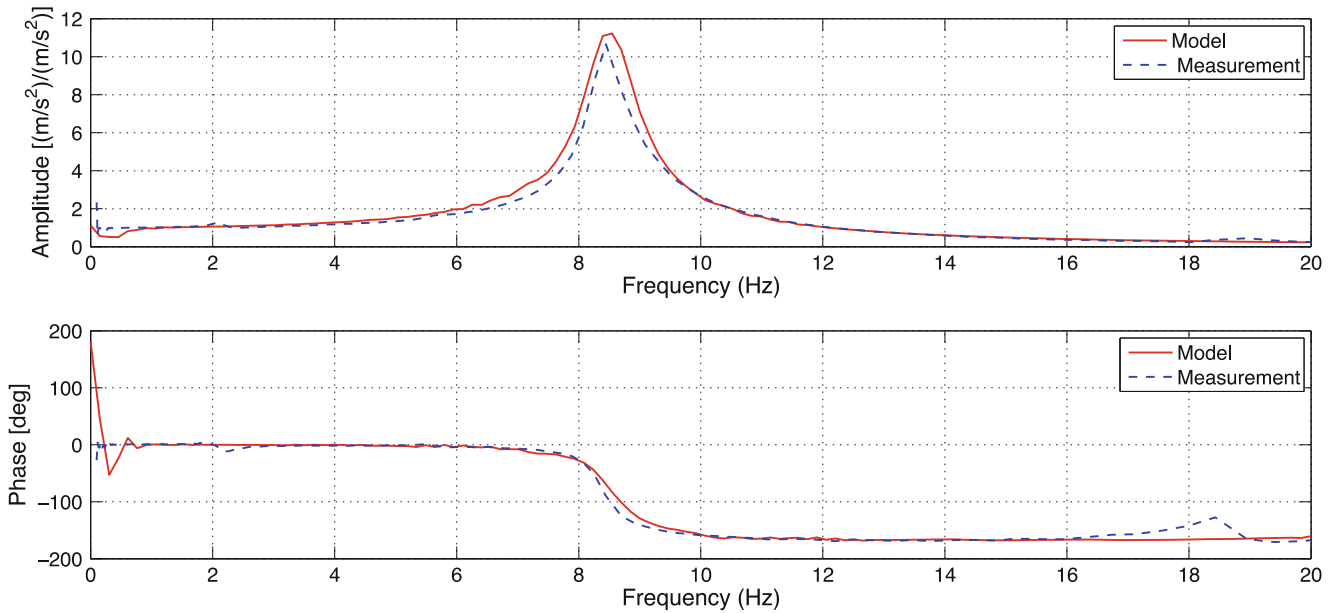


Fig. 2.9 Numerical-experimental comparison: FRF between the acceleration along the Z direction of the seismic base (point 1) and the upper base (point 3)

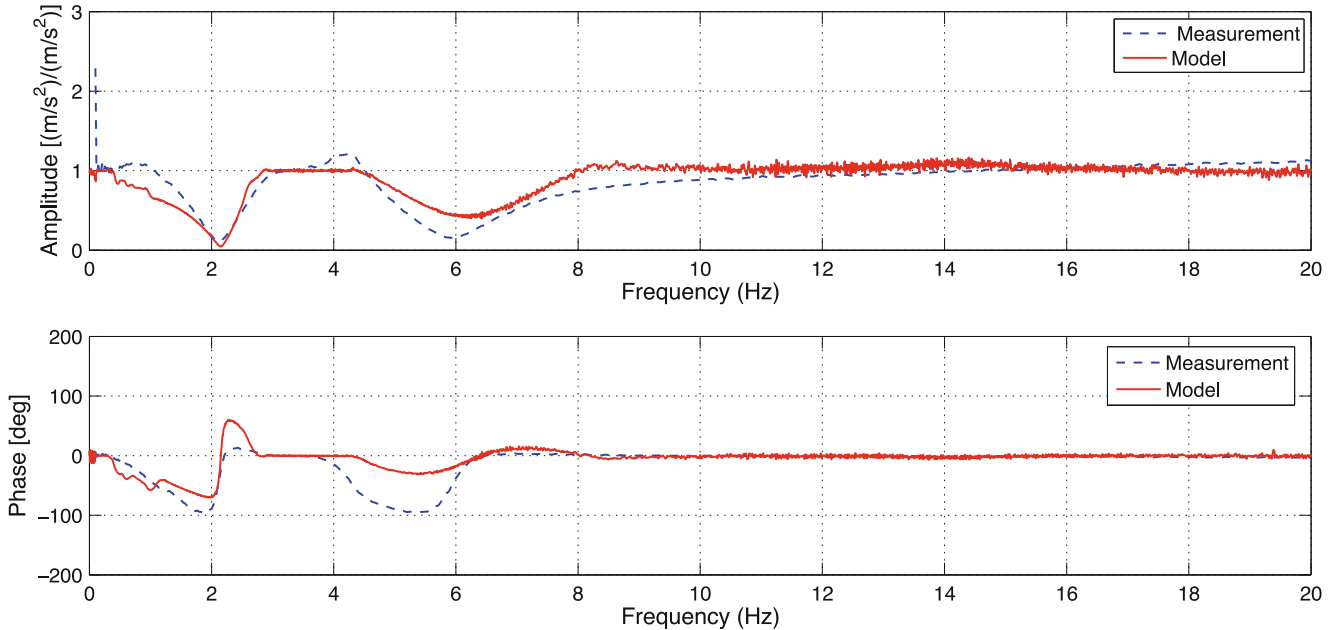


Fig. 2.10 Numerical-experimental comparison: FRF between the acceleration along the X direction of the seismic base (point 1) and the lower base (point 2)

conditions, therefore requiring the lowest possible stiffness (rubber elements). Moreover, the vertical damping of the rubber bearings has to be kept as low as possible to filter out at best vibration frequencies higher than 10 Hz.

So, for a first sensitivity analysis the following parameters were varied:

- the height of the support of the statue, i.e. the height of the assembly above the upper plate of the vibrations-isolating system; in particular the height of the support was varied in a range ± 20 cm;
- distribution of stiffness between the rubber bearings constituting the vibrations-isolating system. Specifically, vertical stiffness of rubber bearings placed at the four corners of the isolation system (specified by blue color module in Fig. 2.2) were increased, while stiffness of the other rubbers was decreased in order to maintain the frequency of the vertical motion at about 8.7 Hz, but reducing the pitch motion of the statue support.

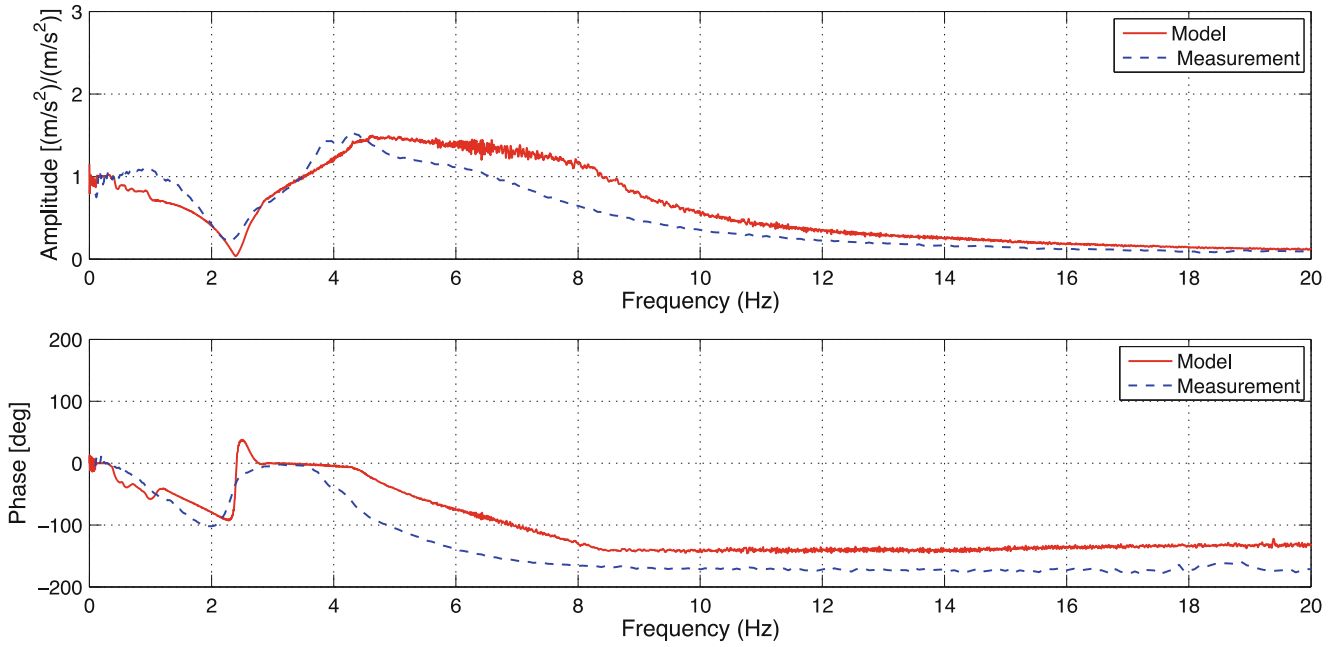


Fig. 2.11 Numerical-experimental comparison: FRF between the acceleration along the X direction of the seismic base (point 1) and the upper base (point 3)

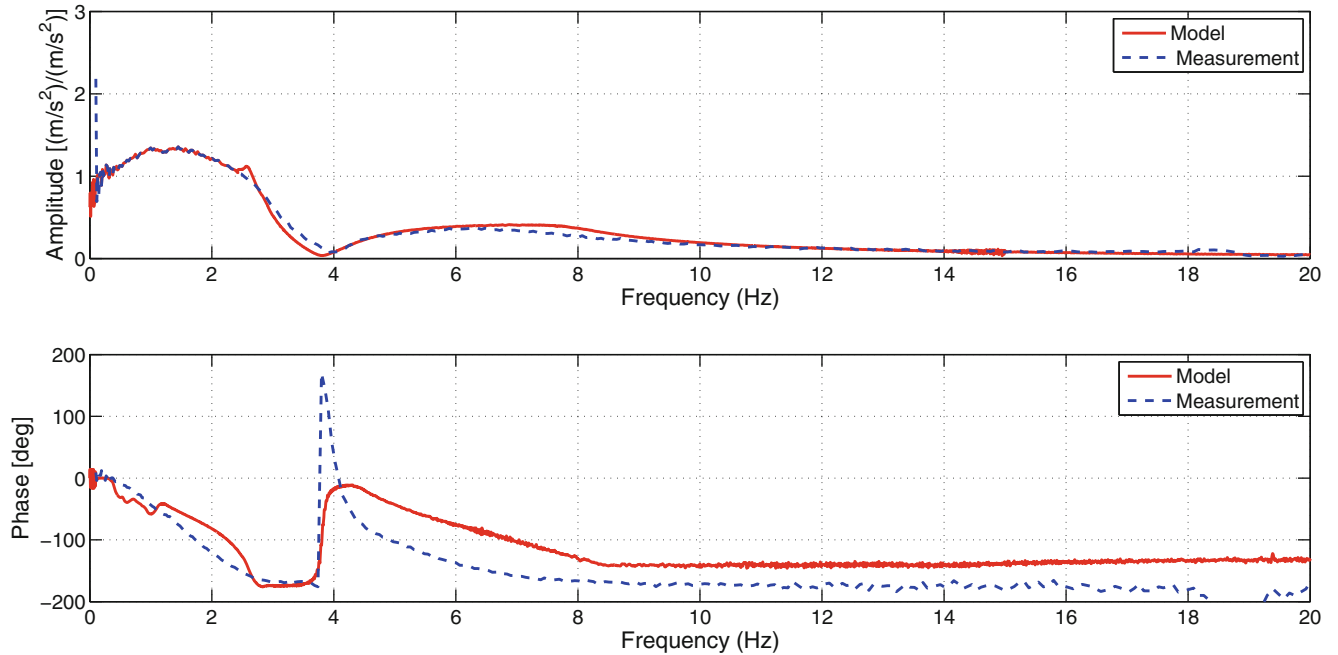


Fig. 2.12 Numerical-experimental comparison: FRF between the acceleration along the X direction of the seismic base (point 1) and statue support (point 6)

In Fig. 2.13 the result of the sensitivity analysis on the height of the statue support is shown. The FRFs between the acceleration along the X direction of the seismic base and those of point 6 (i.e. the statue support, blue lines) and of the head of the statue (black lines) are reported. A sweep sine test along the X direction is applied. Measurements are also reported (red lines).

It can be clearly seen that by decreasing the height of the support, the resonance frequencies increase, although the maximum amplitudes remain quite similar. It is worth remembering that simulations were carried out considering the statue perfectly fixed to the support, which might not be the case as the statue bottom cannot be perfectly flat.

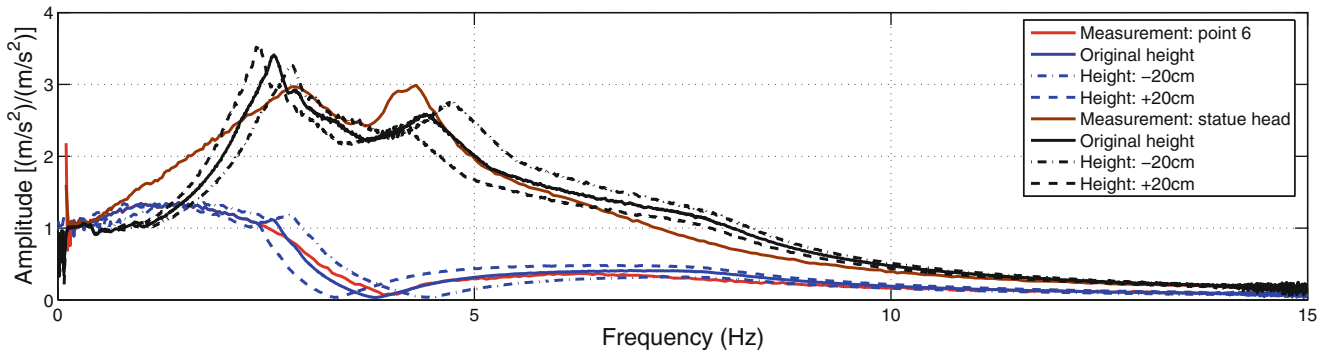


Fig. 2.13 Sensitivity analysis on the height of the statue support: FRFs between the acceleration of the seismic base (point 1 in Fig. 2.3) along the X direction and the acceleration of statue support (point 6 in Fig. 2.3, blue lines) and statue head (black lines)

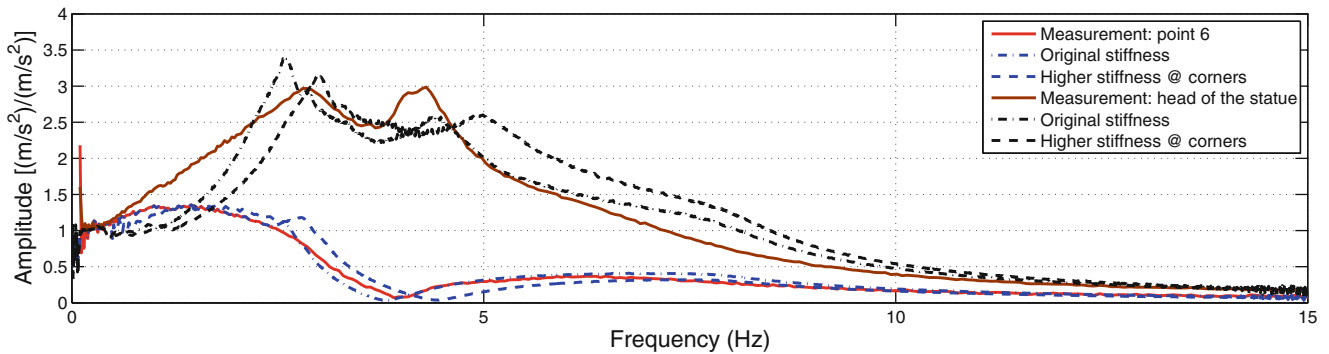


Fig. 2.14 Sensitivity analysis on the rubbers stiffness: FRFs between the acceleration of the seismic base (point 1 in Fig. 2.3) along the X direction and the acceleration of statue support (point 6 in Fig. 2.3, blue lines) and statue head (black lines)

The effect of changing the spring stiffness of the rubber bearings placed at the four corners of the vibrations-isolating system is presented in Fig. 2.14. In this figure, the FRFs between the acceleration along the X direction of the seismic base and those of point 6 (blue lines) and of the head of the statue (black lines) are reported. A sweep sine test along the X direction is applied. Measurements are also reported (red lines).

The stiffness along the Z-direction of the four rubber bearings placed at the corners of the vibrations-isolating system was increased by three times and at the same time the overall stiffness in the Z-direction was kept equal to the original value by decreasing the stiffness of the others rubber bearings. In other words the ratio between the vertical stiffness and torsional stiffness of the vibrations-isolating system was changed. It can be clearly seen in Fig. 2.14 that by increasing the stiffness of the rubber bearings placed at the corners, the resonance frequency associated with the pitch motion (at about 2.7 Hz) increases and this effect is more evident on the head of statue, where a reduction in the peak amplitude is also observed.

2.5 Conclusions

In this research the new isolating system for the famous statue Pietà Rondanini by Michelangelo was investigated. As mentioned earlier, the aim of this research was to develop a model of the isolating system and to verify the performance of the designed one. Vibration measurements were carried out to evaluate the performance of the designed system for an earthquake and in case of ground-borne vibrations due to the close presence of the underground. In other words, the target of these measurements was first of all to validate the model and to achieve further information to optimize the performance of the isolating system. According to the difficulties and costs of repeating tests under different scenarios, a multibody model was developed to predict the dynamic performance of the complete system by means of parameter sensitivity. The model was implemented in ADAMS/View according to the information received from the isolating system manufacturer. Results of the developed MB model are in good agreement with the experimental data in Z and X directions, although some improvements may be introduced for a better reproduction of the behavior of the system in the X-direction according to the complexity of

the real structure (especially the nonlinear damping of the restoring system). The developed model was then used to perform a sensitivity analysis on the isolation system parameters, such as stiffness and damping of rubber bearings of the vibrations-isolation device, geometry of the statue supporting base, etc. The performed analysis showed that decreasing the height of statue support leads to an increase of pitch natural frequency, but a reduction of peak amplitudes. Moreover, varying stiffness distribution of rubber bearings by increasing stiffness at corners limits pitching of the statue.

Acknowledgements The authors gratefully acknowledge the Municipality of Milano for the financial support and the precious control role, then CESI Ricerche, THK, Miyamoto and the Conservation Institute of the Italian Ministry of Cultural Heritage (ISCR) for the precious cooperation offered through the different activities of the project.

References

1. Silva, *Vibration and Noise Handbook*, Taylor & Francis Group, LLC, 2005
2. Zhong-Ming, X., Xuan, C., Zi-Liang, Y.: The study displacement spectrum on sliding base isolation. In: 6th International Conference on Advance in Experimental Structural Engineering, University of Illinois, Urbana-Champaign, United States, 2015
3. Vestorni, F., Di Cintio, S.: Base isolation for seismic protection of statues. In: 12th World Conference on Earthquake Engineering, Auckland, New Zealand, 2000
4. Petrovic, S., Koren, D., Kilar, V.: Applicability of base isolation made of elastomeric isolators for the protection of cultural heritage. *Urban Challenge*, **20**(1), 220–228 (2009)
5. Girish, M., Pranesh, M.: Sliding isolation systems: state-of-the-art review. *J. Mech. Civil Eng.* **2278–1684**, 30–35 (2013)
6. Jampole, E.A., Swensen, S.D., Fell, B., Miranda, E., Deierlein, G.G.: Dynamic testing of a low-cost sliding isolation system for light-frame residential structures. In: Tenth U.S. National Conference on Earthquake Engineering, Frontiers of Earthquake Engineering, Anchorage, Alaska, 21–25 July 2014

Chapter 3

Estimation of Frequency and Damping of a Rotating System Using MEOT and Virtual Sensor Concept

Sharang Inamdar, Randall J. Allemang, and Allyn W. Phillips

Abstract Currently, to obtain an understanding of the frequency and damping of the modes of a rotating system, an impact test or a shaker test is done to find the frequency at which the modes of the system exist. Then, an operating test is done to obtain an understanding of the orders of the system. A Mode Enhanced Order Track (MEOT) can be used to obtain the frequency and damping of various modes directly from the operating data of a rotating system but it cannot find modes which are very close together in frequency or those that are repeated. The MEOT is a method described in Dr J.R. Blough's PhD dissertation, which has not been tested on data obtained from an actual rotating system. This data was taken from a Toro Leaf Blower, using a laser tachometer and 7 triaxial sensors. Using Mode enhanced Order Tracking, the frequency and damping of different modes was found. These were then compared to the results obtained from an Impact Test performed on the Toro Leaf Blower. This method was also tested after using the virtual sensor concept on the data. A virtual sensor was created for each triaxial sensor. The results obtained from the impact test, MEOT and the MEOT performed on the virtual sensor data were then compared and analysed.

Keywords MEOT • Virtual dominant sensors • Rotating systems • Frequency estimation • Damping estimation

Nomenclature

Δt	Discrete sampling time interval
F_{samp}	Sampling frequency of the DSA
F_{nyq}	Nyquist frequency
F_{max}	Maximum frequency that can be observed
O_{samp}	Sampling order
O_{nyq}	Nyquist order
O_{max}	Maximum order that can be observed
Δo	Delta Order—order resolution
t	Time variable
T	Total sample time analyzed
N	Data block size/total number of spectral lines
Δf	Delta frequency—frequency resolution
$[A]$	Base matrix
$[U]$	Left singular matrix
$[V]$	Right singular matrix
$[\Sigma]$	Singular value matrix
$[I]$	Identity matrix
$[Q]$	Eigen vector matrix
$[E]$	Eigen value matrix
σ	Singular value

S. Inamdar (✉) • R.J. Allemang • A.W. Phillips

Structural Dynamics Research Laboratory, Department of Mechanical Engineering, University of Cincinnati, Cincinnati, OH 45221-0072, USA
e-mail: inamdasg@mail.uc.edu

3.1 Introduction

Rotational system analysis needs to be done for many reasons. It can be used in health monitoring of machinery, diagnosis of faults, damage detection, etc. The information obtained from the various technique used to obtain and analysing data from rotating systems, is then used to make informed design choices, perform suitable maintenance operations or predict the failure of a part before it occurs.

The analysis of rotational systems is usually done in two steps, the first step is to analyse the dynamic characteristics of the system, i.e. to perform either a shaker test or an impact test on the system to gathering information about the modal parameters of the system. The second step is to perform a test under operational (rotating) conditions, i.e. while the rotating machine is running. This second step provides an understanding of the different orders at different RPMs and frequencies. Using the information gathered from these steps, the system can be either designed or modified so as to have a longer life or damage to the internal components of the system can be detected. The problem here is, due to various factors such as non-linearities, the characteristics of the system under dynamic conditions may vary from the characteristics of the system under operational conditions. This will cause there to be errors in the information obtained from the combination of the two tests. Therefore, a method of acquiring all required information from the structure in one test under dynamic conditions is required. The MEOT concept can be used to acquire the required parameters from the order tracks of the structure. To improve the quality of the MEOT, the virtual sensor concept can be used.

3.2 Background

3.2.1 Operating Shape Decomposition by RPM

Operating shape decomposition is done on an RPM by RPM basis. Using this method, the number of operating shapes that can be found in the system are equal to the number of orders in the system. This is done by performing a singular value decomposition (SVD) on the order tracking data.

In this data, the singular values (Σ) represent how well excited the operating shapes are at various RPMS. The left singular (U) vector contains a set of linearly independent operating shapes. These operating shapes approximate the mode shapes in the system [1, 2]. The right singular vector (V) contains the participation factor and the linearity between the linearly independent operating shapes and the orders [1, 2].

The singular values can then be plotted with RPM. This plot is read similar to the complex mode indicator function (CMIF) plot. The number of singular value curves will be equal to the number of orders present in the system. The number of singular value curves that peak at any RPM is equal to the number of linearly independent operating shapes getting excited at that RPM. The highest singular value curve represents the best excited linearly independent operating shape. If the lowest singular value curve also peaks up at a certain RPM, then there are as many linearly independent operating shapes excited as there are orders in the system [1, 2].

3.2.2 Order Track Autopower

The Order Track Autopower shows the amount of energy each order of the system contains at various RPMs. Different orders will have high or low energy at different RPMs. The order with the highest energy at a given RPM can be targeted to solve noise and vibration problems occurring at that RPM.

$$OA_{i,r} = \left(\sum_{k=1}^n (O_{ik})^2 \right)_r \quad (3.1)$$

Where:

n is the number of measured Degrees of Freedom (DOFs).

$OA_{i,r}$ is the order track autopower of order i at RPM r.

O_{ik} is the Order i at DOF k at RPM r.

The order track autopower is a useful way of reducing a large number of DOFs into a composite measurement per order. Thus, making handling large datasets much easier [1, 2].

3.2.3 Mode Enhanced Order Tracking

The left and right singular vector of a singular value from any RPM can be used to obtain the Mode Enhanced Order Track (MEOT) of a singular vector being analysed. This is similar to the enhanced FRF [3, 4] calculated to find the frequency and damping of the mode in question in the CMIF parameter estimation method. These order tracks are estimated from orthogonal functions, therefore the system can be considered to have linearly independent inputs. This will result in the MEOT resembling the frequency response function (FRF) of a single degree of freedom (SDOF) system. Thus, SDOF parameter estimation methods can be used to estimate the frequency and damping of the system [1, 2].

$$MEOT_{l,r} = \{U_l\}^H_{1 \times n} (\{O\} \{O\} \dots \{O\})_{n \times m} \{V_l\} \quad (3.2)$$

Where:

$MEOT_{l,r}$ is the mode enhanced order track of singular vector l at RPM r .

$\{U_l\}^H$ is the Hermitian of the left singular vector that the MEOT is being calculated with respect to.

$\{V_l\}$ is the right singular vector that the MEOT is being calculated with respect to.

3.2.4 Virtual Sensor Concept

The virtual sensor concept is an SVD based method of observing and understanding the responses recorded by the various sensors on the structure. The crosspower matrix of the frequency response vector is calculated. This square matrix will contain autopower terms as the diagonal elements of the matrix. The off-diagonal terms in this matrix are the crosspower terms. An SVD is then performed on this matrix. The resulting singular value matrix contains the virtual sensor data.

The order track data from the sensors can be condensed into virtual data using two approaches, the first approach is using response data from one location on the structure, but in the three principle directions. The second approach is to use the order track data from multiple locations on the structure. Through this approach a better understanding of the response of the structure can be obtained [5].

$$R_{k,O} = \left(\begin{array}{c} \left[\begin{array}{c} a_1 + ib_1 \\ a_2 + ib_2 \\ \vdots \\ \vdots \\ a_m + ib_m \end{array} \right]_{m \times 1} \end{array} \right)_{k,O} \quad (3.3)$$

$$C_{k,O} = R_{k,O} \times R_{k,O}^H \quad (3.4)$$

Where:

$R_{k,O}$ is the Response of order O at RPM k .

m is the number of measured degrees of freedom

$C_{k,O}$ is the crosspower matrix.

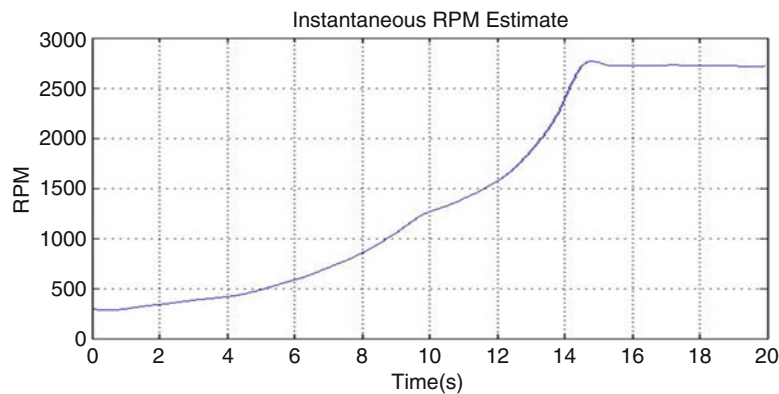


Fig. 3.1 Instantaneous RPM estimate of data from the Toro Leaf Blower

3.3 Estimation of Frequency and Damping from Order Track Data

Data was collected from a Toro Leaf Blower which was run using a DC motor. Details on the apparatus used and the DSP parameters used can be found in the thesis work that this paper is based on [6].

3.3.1 Instantaneous RPM

For any data collected from a rotating system, the most important information is the Instantaneous RPM estimate. The tachometer data was collected using an infrared tachometer while collecting data from a Toro Leaf Blower. Spline fitting and the shaving algorithm were used to get a good instantaneous RPM Estimate [2, 7].

The profile of the RPM curve used is an important consideration. This can determine the readability of the singular value map when plotted against RPM. This is explained more in detail while discussing the order tracks (Fig. 3.5).

3.3.2 RPM Spectral Maps

The instantaneous RPM curve and the data from the leaf blower is used to plot an RPM spectral map. This gives a good overview of the response of the structure at different RPMs. Figure 3.2 shows the RPM spectral map at one location on the Toro Leaf Blower.

The spectral map in Fig. 3.2 is created from data obtained from a Toro leaf blower. The region between 200 and 250 Hz shows high magnitude. This is because of the presence of a natural frequency in this region. The orders that show dominance in this region seem to be the 6th and 7th order. Smearing can be observed around this natural frequency due to leakage. As a result, pinpointing this natural frequency with any good amount of accuracy from the spectral map is not possible. The presence of non-integer orders is also observed.

3.3.3 Order Tracking

Order tracking was done using Time Variant Discrete Fourier Transform (TVDFFT). A large number of orders were tracked at all the available DOFs. The RPM spectral map was used to choose which orders need to be analysed

In Fig. 3.3, it is observed that the 6th order has a high magnitude region between 200 and 250 Hz. This corresponds to the RPM spectral map shown in Fig. 3.2, where a high magnitude region is observed in the same frequency range. This high magnitude region can also be observed in the order track for the 6.5th and 7th order. Therefore, the orders that should be focussed on for the data acquired from the Toro Leaf Blower are the 6th, 6.5th and 7th order.

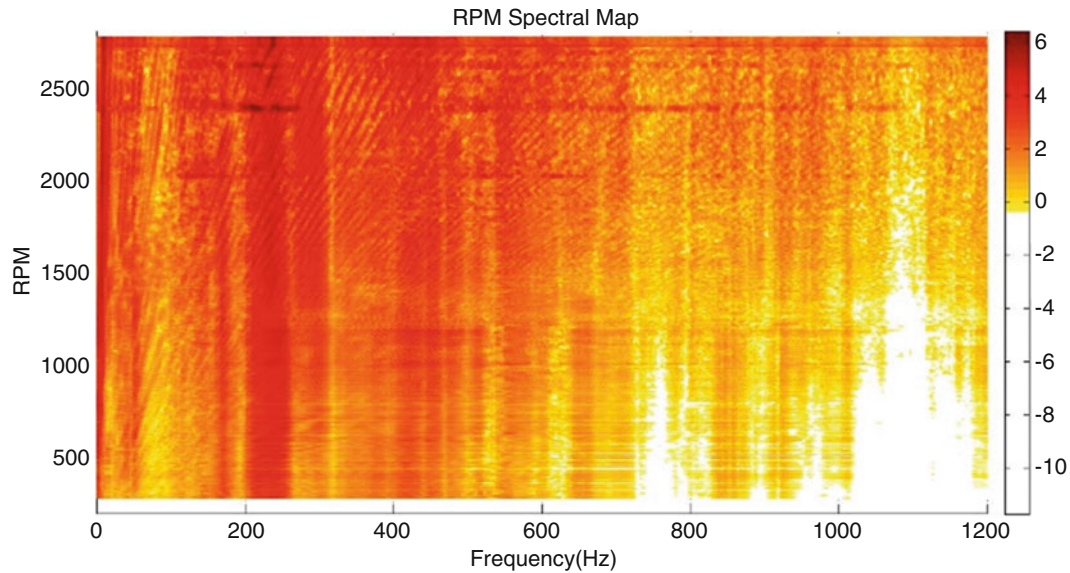


Fig. 3.2 RPM spectral map for data from Toro Leaf Blower

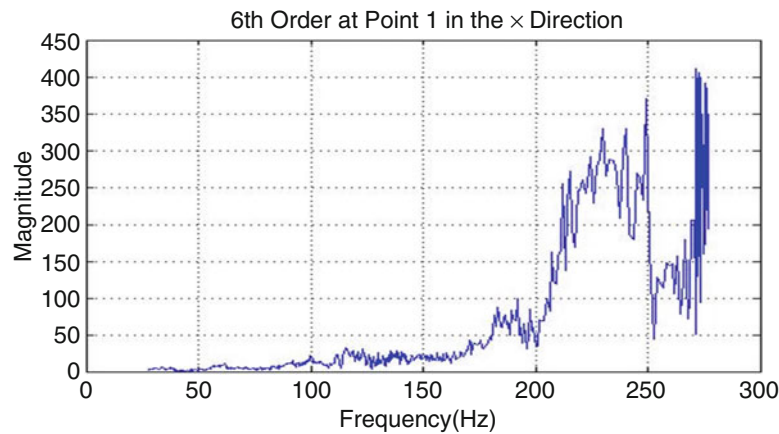


Fig. 3.3 Order track of the 6th order at point 1 in the X direction

The data towards the end of all the orders was collected at a constant RPM, as seen in the highlighted area in Fig. 3.4. This causes there to be many data points at the same RPM/frequency, causing this noisy region. The speed of the Toro Leaf Blower was not taken further than this frequency for fear of causing damage to it.

As observed above, the shape of the instantaneous RPM curve is extremely important for the order track. It was also observed that having a single upward or downward RPM sweep resulted in more useable data than multiple RPM sweeps going up and down in the same data set.

In Fig. 3.5, the result of having RPM data with the characteristics mentioned. The order track ends up having more than one data point at the same RPM. If this happens at an RPM where the order in question crosses a natural frequency, it can cause problems in analysing the data.

3.3.4 Operating Shape Decomposition by RPM

Operating shape decomposition was done to identify the RPMs at which the first singular value curve (σ_1) peaked. This was done by plotting the singular values, obtained by performing an SVD, against RPM. The exact RPM Bins in which these peaks were located were also identified by plotting the singular values against the RPM Bins (Fig. 3.6).

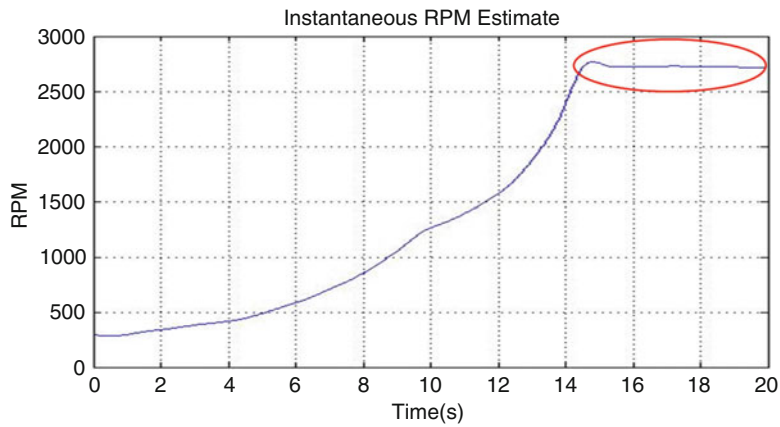


Fig. 3.4 Instantaneous RPM estimate of Toro Leaf Blower data

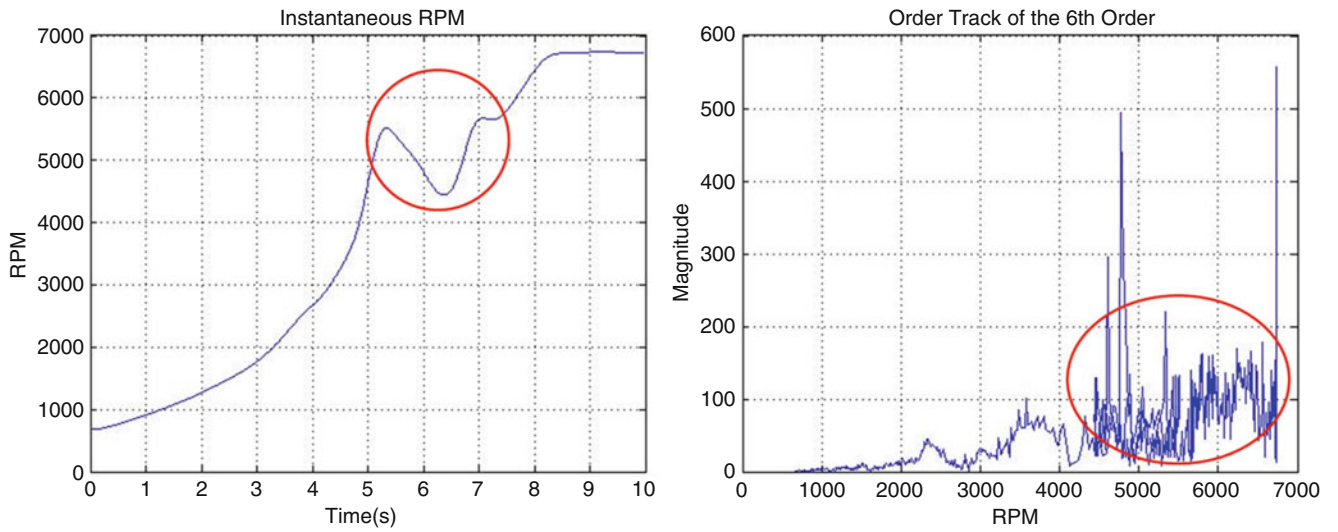


Fig. 3.5 Order track of the 6th order of the Toro Leaf Blower with upward and downward swept RPM

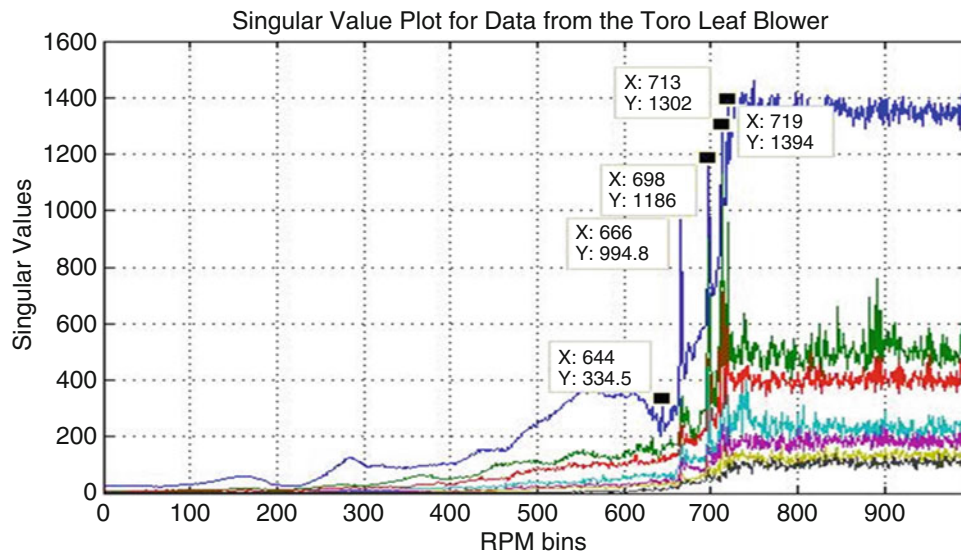


Fig. 3.6 Plot of singular values with RPM Bins for the data acquired from the Toro Leaf Blower

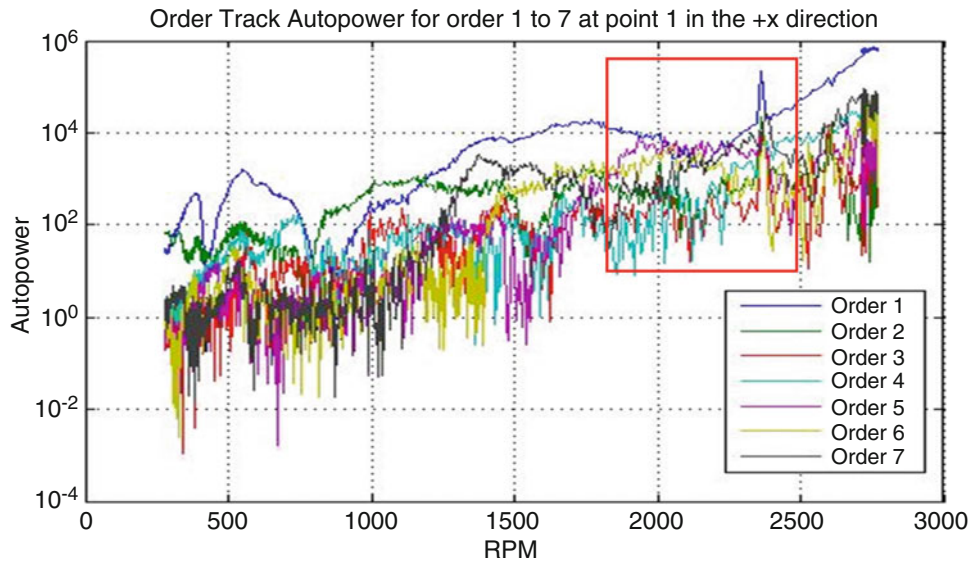


Fig. 3.7 Plot of singular values with RPM Bins for the data acquired from the Toro Leaf Blower

Five distinct peaks are present at the 644th, 666th, 698th, 713th and 719th RPM Bins are found at 1834 RPM, 2009 RPM, 2375 RPM, 2594 RPM and 2677 RPM.

3.3.5 Order Track Autopower

From Fig. 3.7, it can be seen that the first order is dominant in the RPM range of interest (highlighted in Fig. 3.6). However, from the RPM spectral map in Sect. 3.3.2, it can be observed that the first order does not reach the desired frequency within this frequency range while Order 5, 6 and 7 do. Therefore, it can be concluded that the first order cannot be used in this particular case. Figure 3.7 also shows orders 5, 6 and 7 are very well excited in this RPM range.

It was also observed that the 6.5th order is also excited in this RPM and frequency range. To determine the orders that should be used to estimate the frequency and damping of the operating shapes, the Order Track Autopower of the orders with the RPM Bins can be plotted. Plotting with the RPM Bins should show the exact order that should be used for each peak. Initially the existence of the 6.5th order was ignored. Later a comparison between results using the 6.5th order vs without using the 6.5th order will be done.

Figure 3.8 can be used to choose the dominant order at each RPM Bin of interest. For the RPM Bin 666, the 6th order is dominant, for the remaining RPM Bins of interest, the 7th Order is prominent. If the 6.5th order is included, it would be the dominant order for RPM Bin 698, as seen in Fig. 3.9.

Similarly for the peak at RPM Bin 644, the 5.5th order would be the dominant order if it were taken into consideration.

3.3.6 Mode Enhanced Order Track

The Mode Enhanced Order Track (MEOT) is a method similar to the enhanced FRF. The MEOT is in a form similar to a FRF of a SDOF system which peaks at a specific RPM Bin. This property can be used to calculate the frequency and damping of the four peaks found in Sect. 3.3.4 at the 644th, 666th, 698th, 713th and 719th RPM Bins using any SDOF parameter estimation method. Sometimes, the MEOT may peak slightly at other RPM Bins, this is because the same operating shape can be excited at other RPMs by other orders.

In Eq. (3.2), the left and right singular vectors used are those that are obtained from the SVD of the RPM Bin of interest. In this case, the 666th RPM Bin. The singular vector matrix is used is for each RPM Bin. Figure 3.10 shows the MEOT of the 666th RPM Bin overlapping the primary (σ_1) singular value curve as well as the MEOTs calculated w.r.t. RPM Bins 644, 698, 713 and 719. The MEOT calculated with respect to the 666th RPM Bin will only be equal to the σ_1 singular value curve at the 666th RPM Bin. The same procedure is followed for the other MEOTs and the results can be interpreted similar to the MEOT calculated with respect to the 666th RPM Bin.

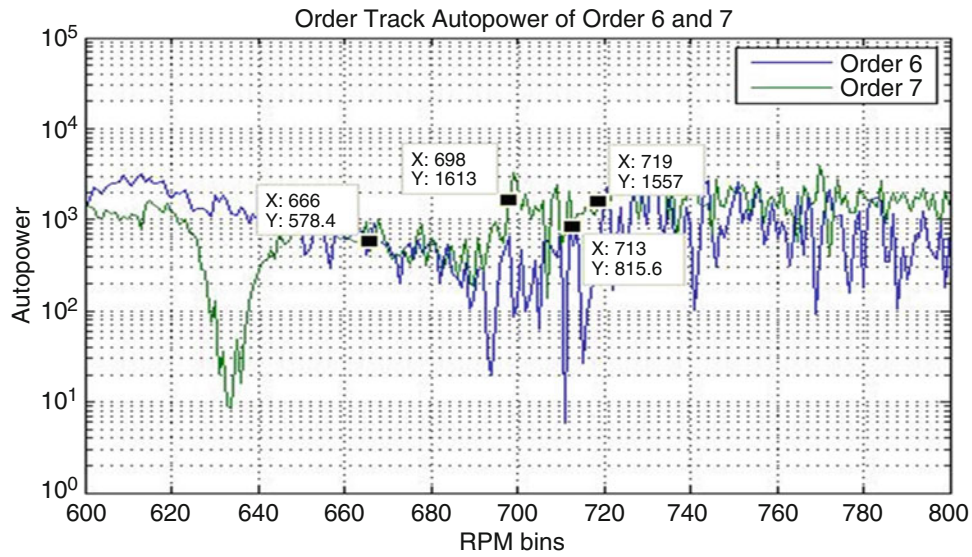


Fig. 3.8 Order track autopower at point 3 in the +x direction for orders 6 and 7 from RPM Bin 600 to RPM Bin 800

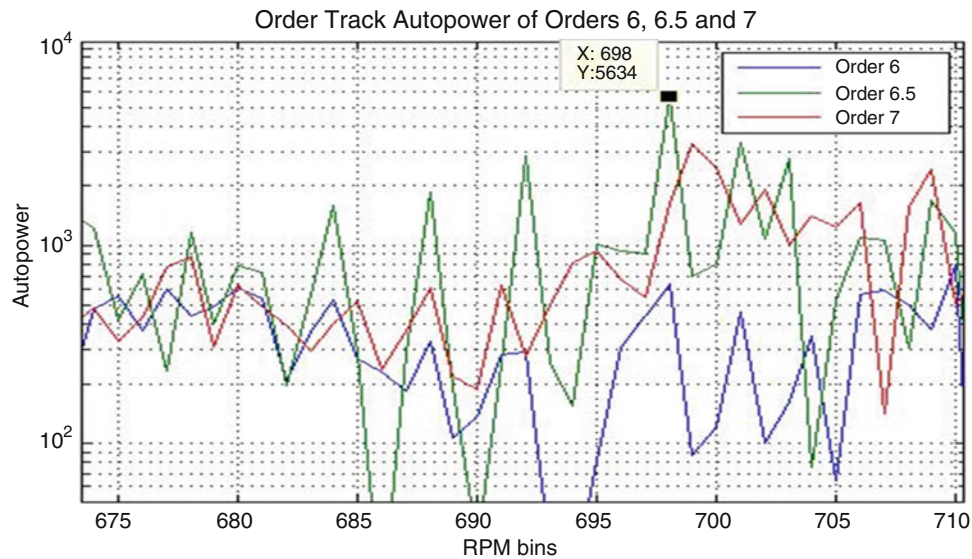


Fig. 3.9 Order track at point 3 in the +x direction for orders 6, 6.5 and 7 between RPM Bins 675 and 710

3.3.7 Obtaining Frequency and Damping using SDOF Parameter Estimation Methods

Using the least square local SDOF parameter estimation algorithm [8], the frequency and damping for the selected peaks can be found. The frequency (ω) is found using the dominant orders at the respective RPM Bins. These dominant orders are found using the information gained from the order track autopower and the RPM spectral map. A more detailed explanation of this is provided in the thesis work that this paper is based on [6].

Using this technique, the following results were obtained (Table 3.1).

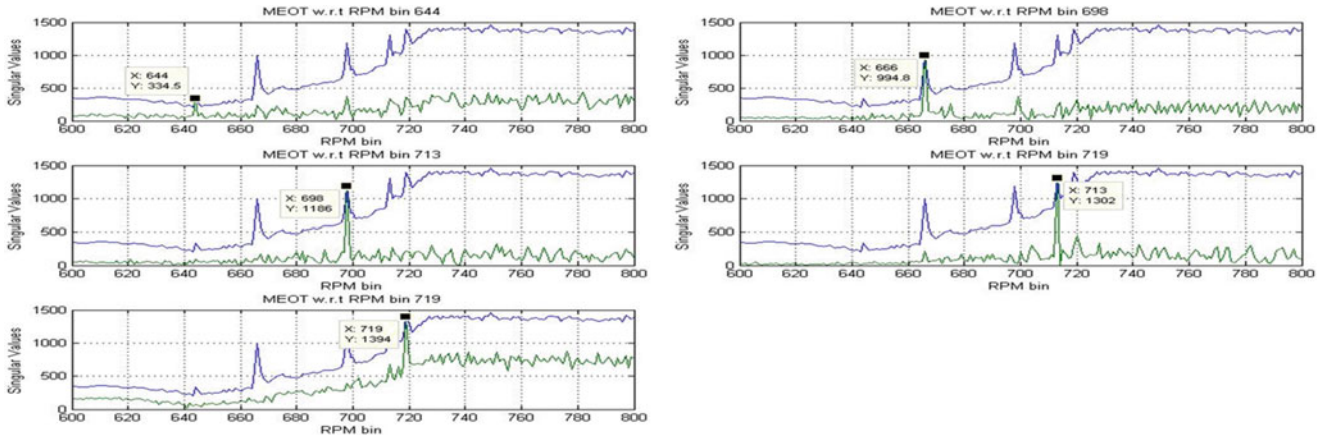


Fig. 3.10 MEOTs of RPM Bins 644, 666, 698, 713 and 719

Table 3.1 Frequency and damping estimates from using the MEOT

RPM Bin	Frequency (Hz)	Damping ratio (%)
644	168.1413	0.0363
666	200.9454	0.0532
698	257.3778	0.0484
713	302.6949	0.0078
719	311.1453	0.2509

3.4 Estimation of Frequency and Damping from Virtual Sensor Order Track Data

3.4.1 Virtual Sensor Order Track Data

A singular value matrix can be calculated from the cross power matrix at each order of interest. The order track data used to acquire the virtual sensor data was obtained from the Toro Leaf Blower data. The virtual sensors created represented data from one location on the structure but in three DOFs. The singular values calculated represent the magnitude data of the virtual sensor order track. The phase information is divided between the left and right singular vectors. To compensate for this, the left singular vector is multiplied with one value from the right singular vector. A similar process is done while dealing with Modal Parameter Estimation (MPE) using the CMIF [3, 4], but in this case the right singular value used is a value from the driving point of the system. Since the data captured is from a rotating system, there is no driving point available. As a result, the right singular value used was chosen through trial and error.

The left singular vector consists of the operating shapes of the system. These operating shapes can be complex-valued instead of purely real-valued. This complexity can be reduced using central axis rotation. Figure 3.11a and b shows the left singular vector of one virtual sensor from one location on the structure before and after central axis rotation is performed.

The three points in Fig. 3.11a and b represent the three DOFs available at every location on the Toro Leaf Blower. This technique is performed on single complex modal vector at a time. So, in the context of this report, it is performed one operating shape (left singular vector) at a time at each RPM Bin. The real and imaginary part of the complex vector are separated into two real valued vectors [9].

$$\{\psi\} = \{\psi_{real}\} + i \{\psi_{imag}\} \quad (3.5)$$

Where:

$\{\psi\}$ is the left singular vector.

$\{\psi_{real}\}$ and $\{\psi_{imag}\}$ are the real and imaginary vectors created from the real and imaginary parts of each value of the left singular vector.

After these real valued vectors are created, a matrix containing real and imaginary vectors is created as shown in Eq. (3.6). After this a SVD is performed on this matrix as shown in Eq. (3.7) [9].

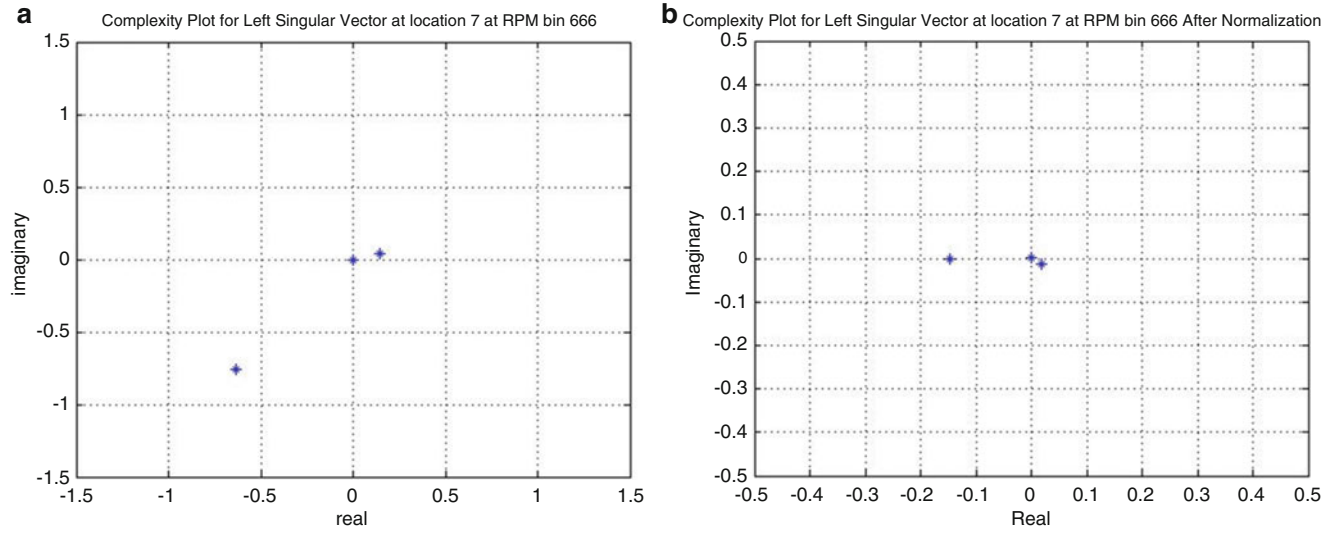


Fig. 3.11 Complexity plots of the left singular vector at location 7 on the Toro Leaf Blower before (a) and after complex axis rotation (b)

$$[\{\psi_{imag}\} \{\psi_{real}\}] \quad (3.6)$$

$$[U, \Sigma, V] = svd\left([\{\psi_{imag}\} \{\psi_{real}\}]^t [\{\psi_{imag}\} \{\psi_{real}\}]\right) \quad (3.7)$$

The matrix on which the SVD is performed will be a 2 by 2 matrix irrespective of the number of DOFs available. After this the angle of the central axis is found using the components of the right singular vector. This is done using an arctangent function so that the signs of the denominator and numerator are taken into account [9].

After this angle is found, it is used in a complex rotational phasor to rotate the central axis so that the left singular vector is now real valued [9].

$$\bar{\phi} = \tan^{-1}\left(\frac{V_{2,2}}{-V_{1,2}}\right) \quad (3.8)$$

$$\{\hat{\psi}\} = (\cos\bar{\phi} - j\sin\bar{\phi}) \{\psi\} \quad (3.9)$$

The plot on the right of Fig. 3.11 shows the close to real-valued left singular vector. It can be seen that the complex rotation of this vector is greatly reduced. After this is done, the left singular vector is then multiplied with the values of the singular vector. This then causes the phase information to also be stored in the singular values, thus acquiring virtual sensor data with both magnitude and phase information.

3.4.2 Comparison Between Order Track Data and Virtual Sensor Order Track Data

From Fig. 3.12a and b, it can be observed that a peak present in the Fig. 3.12a is at RPM Bin 719 is not present in Fig. 3.12b. The significance of this will be explained in a later section. It is also observed that the magnitude of the singular values in Fig. 3.12b is much more than that of the singular values in Fig. 3.12a. This is because when the virtual sensor data is synthesized, there is a difference in the magnitudes of the order tracks from the original order tracks. Since the absolute magnitude of the data is not as important, this difference in magnitude was ignored. Overall, the virtual sensor data leads to ‘cleaner’ MEOT plots as seen in Fig. 3.13a and b.

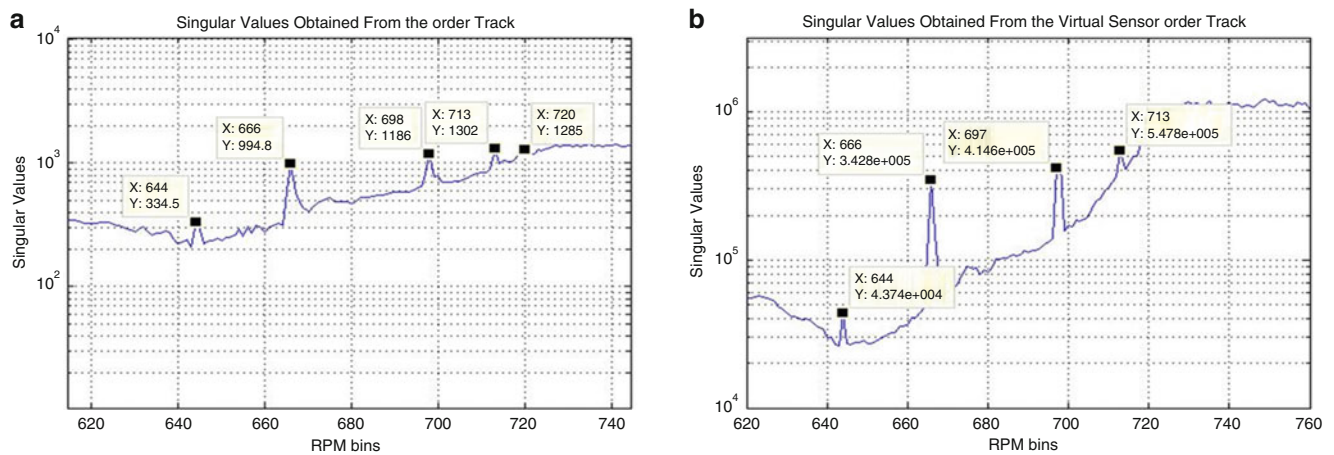


Fig. 3.12 Comparison of σ_1 singular value plots obtained using order track data (a) and virtual sensor data (b)

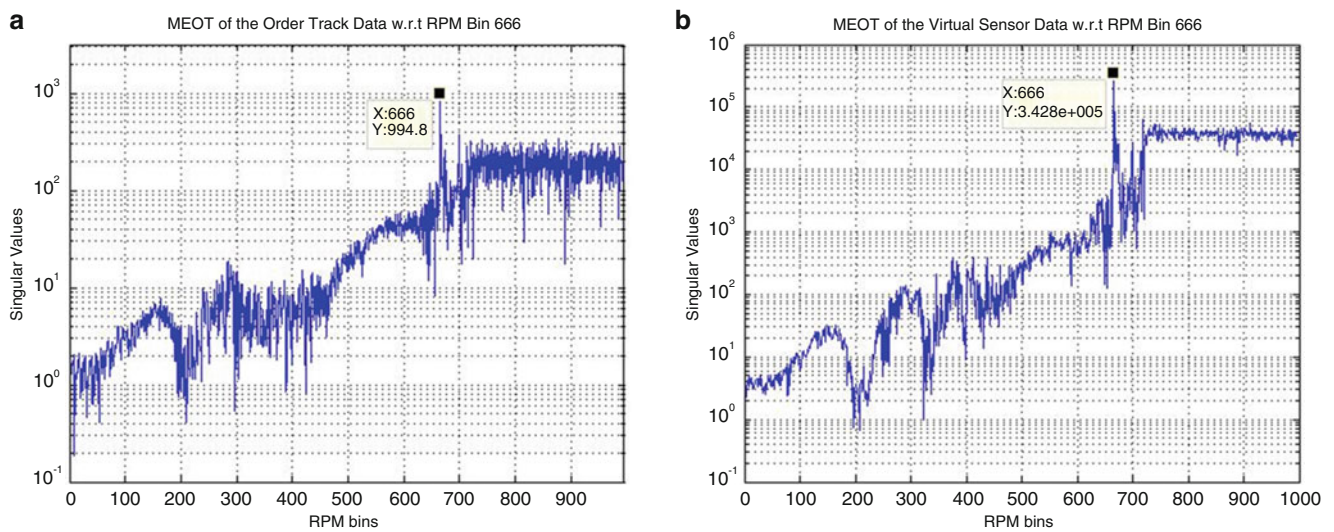


Fig. 3.13 Comparison of the MEOT Plots w.r.t the 666th RPM Bin using order tracking data (a) and virtual sensor data (b)

Table 3.2 Comparison of results obtained from order track data and virtual sensor order track data

RPM Bin	Frequency estimate from order track data (Hz)	Frequency estimate from virtual sensor order track data (Hz)	Percentage difference (%)	Damping ratio estimate from order track data (%)	Damping ratio estimate from virtual sensor order track data (%)	Percentage difference (%)
640	168.1413	168.1804	0.023	0.0363	0.0012	96.69
666	200.9454	200.886	0.029	0.0532	0.0059	88.91
698	257.3778	257.2597	0.045	0.0484	0.0016	96.69
713	302.6949	302.5388	0.005	0.0078	0.0034	56.41
719	311.1453	–	–	0.2509	–	–

Finally the estimated values of frequency and damping for the two sets of data do not vary much. The main difference between the two estimates is the absence of the peak at RPM Bin 719.

As can be seen from Table 3.2, the frequencies estimates are very similar using both types of data but the damping ratio estimates have a large amount of difference. Also there is the issue of the extra peak in the order track data.

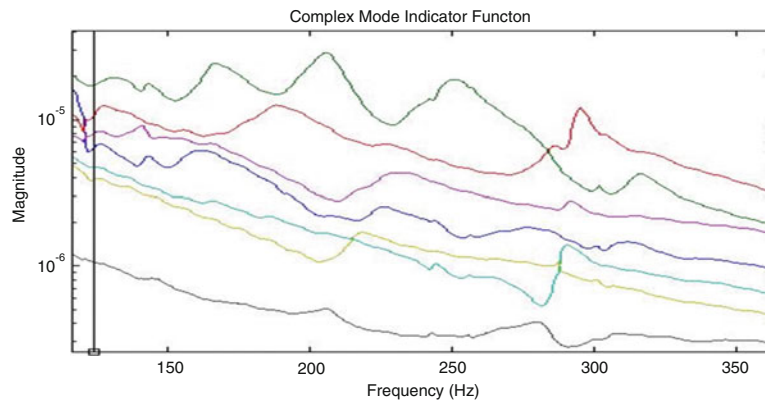


Fig. 3.14 CMIF plot of impact test data from the Toro Leaf Blower

Table 3.3 Comparison of frequency estimates

RPM Bin	Frequency estimate from order track data (Hz)	Impact test (Hz)	Percentage difference (%)	Frequency estimate from virtual sensor order track data (Hz)	Percentage difference (%)
644	168.1413	164.6201	2.138985458	168.1804	2.162737114
666	200.9454	207.6498	3.228705253	200.886	3.257311107
698	257.3778	249.7797	3.04192054	257.2597	2.994638876
713	302.6949	293.3494	3.185791415	302.5388	3.13257842
719	311.1453	–	–	–	–

Table 3.4 Comparison of damping estimate

RPM Bin	Damping ratio estimate from order track data (%)	Damping ratio estimate from impact test (%)	Percentage difference (%)	Damping ratio from virtual sensor order track data (%)	Percentage difference (%)
644	0.0363	4.926	99.2651	0.0012	99.9756
666	0.0532	2.4581	97.8357	0.0059	99.7599
698	0.0484	2.5264	98.0842	0.0016	99.9367
713	0.0078	1.2902	99.3954	0.0034	99.7364
719	0.2509	–	–	–	–

3.4.3 Comparison with Impact Test Results

An impact test was performed to understand the static characteristics of the Toro Leaf Blower. The results obtained were then compared with the results obtained from the MEOT using the two types of order tracks. The CMIF plot of the impact test data is shown in Fig. 3.14. Here too it can be seen that only four peaks instead of five exist in the frequency range of interest.

Tables 3.3 and 3.4 compares the results from the impact test to the results obtained from the order tracks and virtual sensor order tracks. It can be seen that the frequencies are accurately estimated while the damping ration has a very large error.

3.5 Conclusion

This paper has looked at the potential of the MEOT to be used as a method to estimate the frequency and damping of a system. The effects of integration of the Virtual Dominant Sensor Concept with order tracking was also explored. It has been noted that the accuracy frequency estimates using the MEOT, with and without the application of the Virtual Dominant Sensor Concept, is very good when compared to the impact test while the accuracy of the estimated damping was poor. The

MEOT without the use of virtual sensors order tracks, found an extra peak which was not found in the other cases. It was also found that the Virtual Sensor Order Tracks resulted in a 'cleaner' MEOT plot than the MEOT plot obtained from the standard order tracks. The reasons for the differences between the two sets of data needs to be investigated further.

References

1. Blough, J.R.: Improving the Analysis of Operating Data on Rotating Automotive Components. University of Cincinnati, Cincinnati (1998)
2. Blough, J.R., Brown, D.L., VanKarsen, C.: Independent Operating Shape Determination on Rotating Machinery, Based on Order Track Measurements. IMAC XVI proceedings (1998)
3. Allemang, R.J., Brown, D.L.: A Complete Review of Complex Mode Indicator Function (CMIF) with Applications. University of Cincinnati, Cincinnati (2006)
4. Phillips, A.W., Allemang, R.J., Fladung, W.A.: The Complex Mode Indicator Function (CMIF) as a Parameter Estimation Method. IMAC XVI proceedings (1998)
5. Deshpande, S.: Improving Observability in Experimental Analysis of Rotating Systems. University of Cincinnati, Cincinnati (2014)
6. Inamdar, S.: Estimation of Frequency and Damping of a Rotating System using MEOT and Virtual Sensor Concept. University of Cincinnati, Cincinnati (2015)
7. Structural Dynamics Research Laboratory, Rotating System Measurements. University of Cincinnati, Cincinnati
8. Structural Dynamics Research Laboratory: Vibrations: Experimental Modal Analysis. University of Cincinnati, Cincinnati (2007)
9. Hiremaglur, R.: Real-Normalisation of Experimental Complex Modal Vectors with Modal Vector Contamination. University of Cincinnati, Cincinnati (2007)

Chapter 4

Multibody/FEM Numerical Tool for HIL Scaled Offshore Wind Turbine

H. Giberti, M. Belloli, I. Bayati, and E. Fiore

Abstract Nowadays the study of the renewable sources of energy is one of the most important lines of research. For this reason the wind tunnel researchers of Politecnico di Milano want to apply new hardware in the loop approach to study floating offshore wind turbines scale models by reproducing at the same time both the aerodynamic and hydrodynamic phenomena involved. These experiments allow to have a better understanding of the operating conditions of these structures and to properly set the control algorithm for the blades pitch in order to have a better exploitation of the wind stream. In addition the results of the experimental phase could be used to validate the numerical codes. While it is possible to physically reproduce the wind profile with a good approximation, the sea waves effect has to be simulated by means of a 6-DoF parallel kinematic machine. The result is a coupled system in which two flexible structures, the turbine and the robot, cannot be regarded as two separate entities. The aim of this paper is to provide a multibody model to perform dynamic analysis of this coupled system and to study how the pose of the manipulator and the wind profile affect the results.

Keywords Parallel kinematic machines • Robot • Offshore wind turbines • Flexible multibody systems

4.1 Introduction

One of the most important line of research in the field of renewable energies is represented by floating offshore wind turbines. In order to increase the power generation the tendency is to move towards bigger sizes and deeper water. With the aim of properly simulate new turbine designs with appropriate applied loads, new codes that take into account all the involved phenomena (aerodynamics, hydrodynamics, elasticity) have been developed. Whereby they need to be validated through experimental tests in controlled environments such as wind tunnels. For this reason Politecnico di Milano wants to equip its civil-environmental large wind tunnel with a 6-DoF parallel kinematic machine called Hexaslide to perform HIL simulations [1]. Thanks to this robot it will be possible to reproduce the sea wave motion at the bottom of a scale model of a floating offshore wind turbine: the mobile platform reference motion should be computed in real time on the basis of a mathematical model of the sea whose inputs are the forces and moments exerted on the robot and that are the results of the inertial and aerodynamic loads coming from the scale model. The attachment point between mobile platform and scale model is denoted as TCP (*tool-center-point*) should be kept as low as possible since the scale model takes up almost all the vertical space of the wind tunnel section. Furthermore the zone near the ceiling is characterized by a turbulent flow and it's important that the scale model, in particular the tip of the blades, stay outside of this zone. In the beginning the hypothesis of using a serial robot have been considered. Indeed these manipulators are definitely the most diffused commercially speaking and moreover do not suffer any problem in terms of workspace dimensions. However in serial manipulators the errors of each joint add up to those of the successive joints with the result of worsening the accuracy of the positioning of the end-effector. Due to their intrinsic embossed structure they have to bear with high bending loads and so the links that connect one actuated joint to the other become increasingly bulky starting from the end-effector towards the base joint. These considerations in addition to the need of having an attachment point between scale model and robot which is as low as possible, lead to consider parallel kinematic manipulators (PKM) as a valid alternative. The performances of these machines strictly depend on their dimensions and so making a comparison between different architectures is a difficult task as stated by Merlet in [2]. However it is still possible to highlight their general peculiarities. For sure the size of their working volume is lower than that of serial robots, but these machines are characterized by a high stiffness thanks to the fair distribution among the links of the loads acting on the endeffector. Furthermore some PKMs like the Hexaslide are characterized by having spherical or cardanic

H. Giberti (✉) • M. Belloli • I. Bayati • E. Fiore

Mechanical Engineering Department, Politecnico di Milano, Via La Masa 1, 20156 Milano, Italy
e-mail: hermes.giberti@polimi.it

joints at the ends of the links, and so the loads the links are subjected to are exclusively of axial nature. In parallel kinematic manipulators the interaction mechanisms between the errors of each joint and those of the end-effector are far too complex with respect to serial robots with the result of having a lower sensitivity of the positioning errors of the end-effector. The turbine is scaled respecting all the similarity condition with respect to the real one. By the way due to the intrinsic flexible nature of the machine, the scale model and the robot can't be regarded as two separate entities. There's the risk that the modes of vibration of the turbine scale model are affected by the presence of the robot. In PKMs the modes of vibration are strongly affected by the pose of the end effector as described in [3]. This paper presents a coupled flexible multibody model of the Hexaslide with the turbine scale model mounted on its mobile platform. Through this useful tool it is possible to quantitatively evaluate the change in the dynamic behavior of the scale model coupled with the robot with respect to the model alone.

The following sections are organized as follow: Sect. 4.2 describes the inverse kinematics of the Hexaslide; Sect. 4.3 describes the desired workspace and the actual workspace that the optimized machine is able to reach; Sect. 4.4 introduces the coupled flexible multibody model describing: (1) robot model with links treated as discrete beam elements (2) turbine model with flexible tower and blades and aerodynamic forces computed by means of a subroutine. Results are given in Sect. 4.5.

4.2 Hexaslide Kinematics

The Hexaslide robot is made of a mobile platform connected to six linear guides by means of six links of fixed length, so that six independent kinematic chains can be identified belonging to the PUS family. A detailed description of 6-DoF PUS PKMs is provided by Bonev in [4, 5]. The six linear guides are organized into three couples of parallel transmission units, each one out of phase by 120° with respect to the z axis.

Given the TCP position and the mobile platform orientation, $\Theta = \{\alpha, \beta, \gamma\}$, it is possible to find each slider position, q_i , by performing the inverse kinematics analysis. With reference to Fig. 4.1, for the i th kinematic chain it is possible to write:

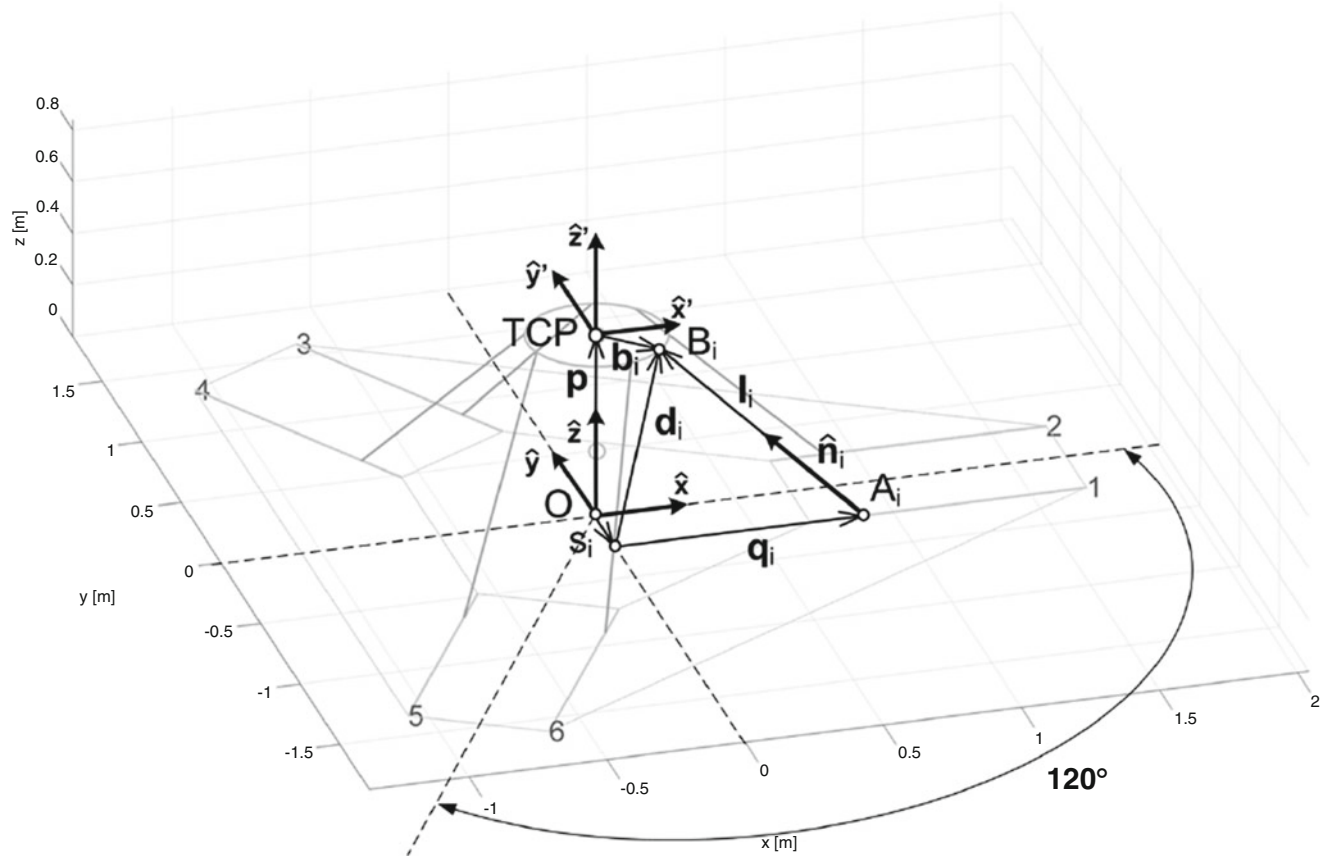


Fig. 4.1 Hexaslide kinematics

$$\mathbf{l}_i = \mathbf{d}_i + q_i \hat{\mathbf{u}}_i \quad \text{with} \quad \mathbf{d}_i = \mathbf{p} + [R]\mathbf{b}'_i - \mathbf{s}_i \quad (4.1)$$

The $[R]$ matrix is the rotational matrix used to switch from the mobile frame to the fixed one, and it is function of the platform orientation Θ . After some simple mathematical passages you get:

$$q_i = \mathbf{d}_i^T \hat{\mathbf{u}}_i \pm \sqrt{\mathbf{d}_i^T (\hat{\mathbf{u}}_i \hat{\mathbf{u}}_i^T - [I]) \mathbf{d}_i + l_i^2} \quad (4.2)$$

Once solved the inverse kinematics it is possible to find the relationship between the slider velocity and the velocity of the TCP. It can be shown that for the i th kinematic chain the following expression holds:

$$\hat{\mathbf{n}}_i^T \hat{\mathbf{u}}_i \dot{q}_i - [\hat{\mathbf{n}}_i^T \quad (\mathbf{b}_i \times \hat{\mathbf{n}}_i)^T] \mathbf{W} = 0 \quad (4.3)$$

where $\mathbf{W} = [\dot{x}, \dot{y}, \dot{z}, \omega_x, \omega_y, \omega_z]^T$ is a vector containing both the translational and angular components of TCP velocity. Considering all the six links the previous relationship can be expressed through the Jacobian matrix $[J]$ as:

$$\mathbf{W} = [J] \dot{\mathbf{q}} \quad (4.4)$$

The Jacobian matrix represents the relationship intercurring between the sliders velocity and the TCP velocity. Under the hypothesis of small displacements it is possible to use the Jacobian matrix to relate the small variations of the sliders position to the variation of the robot pose as follows:

$$\Delta \mathbf{X} = [J] \Delta \mathbf{q} \quad (4.5)$$

This relationship allows to compute the TCP positioning error due to the linear units accuracy.

4.3 Workspace

The desired workspace is the portion of space in which the TCP (and consequently the bottom of the turbine scale model) should be able to move, and can be represented as a parallelepiped whose dimensions are represented in Fig. 4.2a and whose center is located in $\{0, 0, z_{wsd}\}^T$ with respect to the inertial reference system. This position defined as *home position* is the location occupied by the TCP when all the sliders have the same stroke with respect to their corresponding guides. As mentioned before due to the limited vertical space in wind tunnel and to dimensions of the scale model the TCP should be kept as low as possible during the experimental tests; for this reason the parameter z_{wsd} is not a priori defined but is the result of an optimization process described in [6, 7]. During the optimization the isotropy of the robot has been taken into account following the theory presented in [8, 9]. After the optimization process the value of z_{wsd} is set to 0.48 m, which is the minimum value that still allows to have a total coverage of the desired workspace. It's worth to note that the TCP must be able to reach each point of the desired workspace with any possible combination of $\{\alpha, \beta, \gamma\}$ that define the orientation of the mobile platform and of the scale model. The actual machine workspace versus the desired one is represented in Fig. 4.2.

4.4 Multibody Model

In order to investigate its behavior all over the working space, a flexible multibody model of the coupled system has been set up in ADAMS[®]. Reference markers have been used both for the modeling and the analysis phases. All markers used for the creation of bodies, constraints, and forces, have been parametrized in such a way that by changing the TCP coordinates all the elements that constitute the manipulator and the scale model would move to the new configuration. In particular for the development of the turbine model an expressly developed plug-in called AdWiMo[®] is used.

4.4.1 Robot Model

As regards the robot the only source of flexibility is considered to be the links due to their slender shape. Even if the platform has not been designed it is reasonable to assume that it can be regarded as a rigid structure. As a matter of fact it is possible to

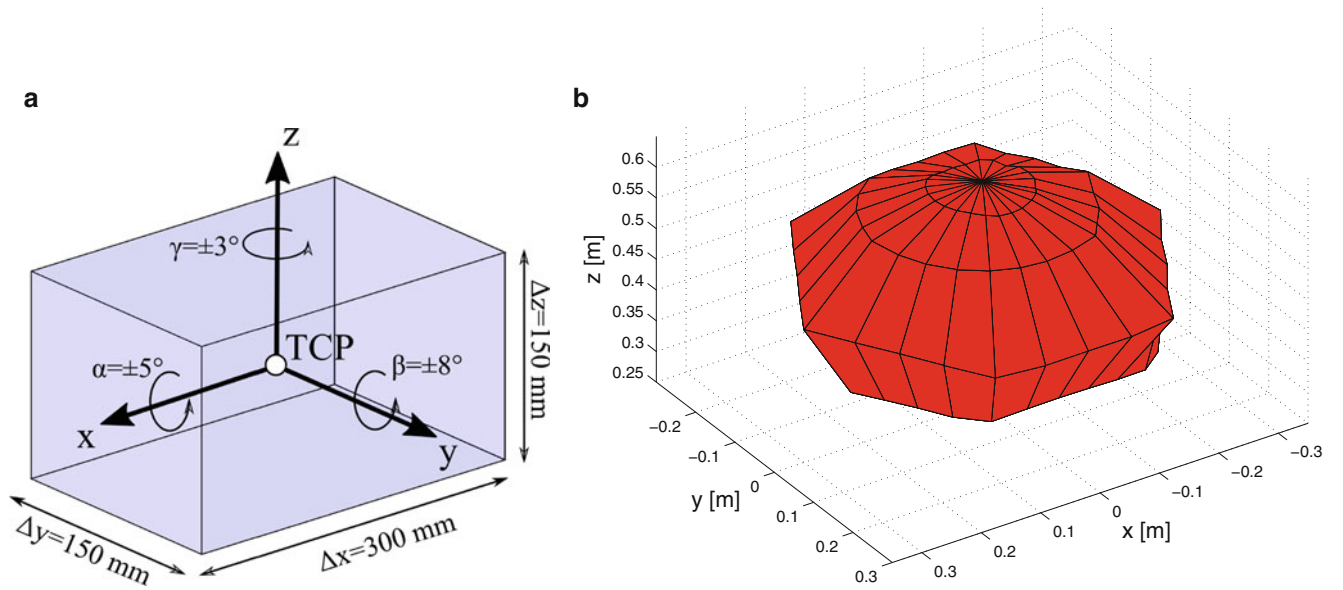


Fig. 4.2 Desired workspace vs. optimized machine workspace. (a) Desired workspace. (b) Hexaslide workspace

realize a very stiff element by means of a reticular structure. At the moment the platform is represented through a cylindrical shaped rigid body; by the way at the end of the design process of the machine this rigid body will be replaced by an FEM model of the as-built construction drawings in order to check the validity of the rigid body approximation. In order to model the flexible behavior of the links they are modeled using discrete beam elements, that is a sequence of rigid segments, each of them with its inertia properties, connected by means of force fields that simulate the sectional stresses arising in the beam section due to external loads. The relationship between the forces arising between two adjacent segments and their relative displacements is expressed as follows:

$$\begin{pmatrix} F_x \\ F_y \\ F_z \\ T_x \\ T_y \\ T_z \end{pmatrix} = - \begin{bmatrix} \frac{EA}{L} & 0 & 0 & 0 & 0 & 0 \\ 0 & 12\frac{EI_{zz}}{L^3} & 0 & 0 & 0 & -6\frac{EI_{zz}}{L^2} \\ 0 & 0 & 12\frac{EI_{yy}}{L^3} & 0 & 6\frac{EI_{yy}}{L^2} & 0 \\ 0 & 0 & 0 & \frac{GI_{xx}}{L} & 0 & 0 \\ 0 & 0 & 6\frac{EI_{yy}}{L^2} & 0 & 4\frac{EI_{yy}}{L} & 0 \\ 0 & -6\frac{EI_{zz}}{L^2} & 0 & 0 & 0 & 4\frac{EI_{zz}}{L} \end{bmatrix} \begin{pmatrix} \Delta x \\ \Delta y \\ \Delta z \\ \Delta\phi_x \\ \Delta\phi_y \\ \Delta\phi_z \end{pmatrix} \quad (4.6)$$

For each segment three different markers are created: one *center of mass marker* that defines the location of the center of mass of the corresponding marker and the orientation of its principal axes of inertia; two *force markers* whose aim is to define the position and orientation of their corresponding segment with respect to the previous and next ones. It's worth to notice that all these markers are parametrized with respect to those positioned at the two ends of each link. In turns these markers are parametrized with respect to the one representing the TCP so that by changing its location and orientation every single element in model is brought to the new configuration respecting the kinematics constraints.

PKMs are really complex structures in which many mechanical elements coexist. Very often the interaction between these elements are difficult to be modeled. Among these interaction phenomena backlashes and frictions play a crucial role. ADAMS[®] allows to take into account joints friction by means of a simple friction coefficient or even through a user defined function.

As mentioned before the actuation of the Hexaslide is achieved through six linear transmission units. The choice is restricted to two different kinds of transmission unit: (1) belt-driven transmission units which are relatively cheap and present a quite low additional inertia but whose elasticity contributes to worsen the overall performances of the machine; (2) ball-screw transmission units that for sure are stiffer with respect to the previous mentioned belt-driven ones and moreover allow precise positioning and ensure a great efficiency; the main drawback of this kind of transmission unit is their great rotational inertia which means having bigger and so more expensive drive systems. The effects of transmission units on the performances of the robot have been investigated in [3]. In order to reduce these negative effects proper control algorithm were proposed in [10].

4.4.2 Turbine Model

AdWiMo[®] allows the user to independently model the various components of the turbine model. All the elements are modeled as flexible bodies, created with the help of NASTRAN[®] which takes as input a *.bdf* file (bulk data file). The *.bdf* file stores all the information related to material properties, nodes position, the nodes each element is made of, as well as their stiffness and mass properties. Both the tower and the blades are defined by means of NASTRAN[®] CBEAM elements. The *.bdf* file is used to launch the NASTRAN[®] analysis SOL 103, whose output is a *.mnf* file that once imported in ADAMS[®] allows to create the desired flexible body. In addition to the structural properties the *.mnf* file contains the attachment points that will be used to create the constraints with the other bodies and the points to which the aerodynamic forces will be applied.

Once all the turbine components have been set up, AdWiMo[®] automatically creates the constraints between them, as well as the *general forces* that simulate the aerodynamic loads. AdWiMo[®] defines the aerodynamic forces are calculated using the external subroutine “aerodyn13” developed by NREL.

4.5 Results

The final model is shown in Fig. 4.3. With this model it is possible to get all the desired information about the coupled system. Indeed thanks to this model it is possible to perform both static-modal and dynamic analyses: in the first case the aim

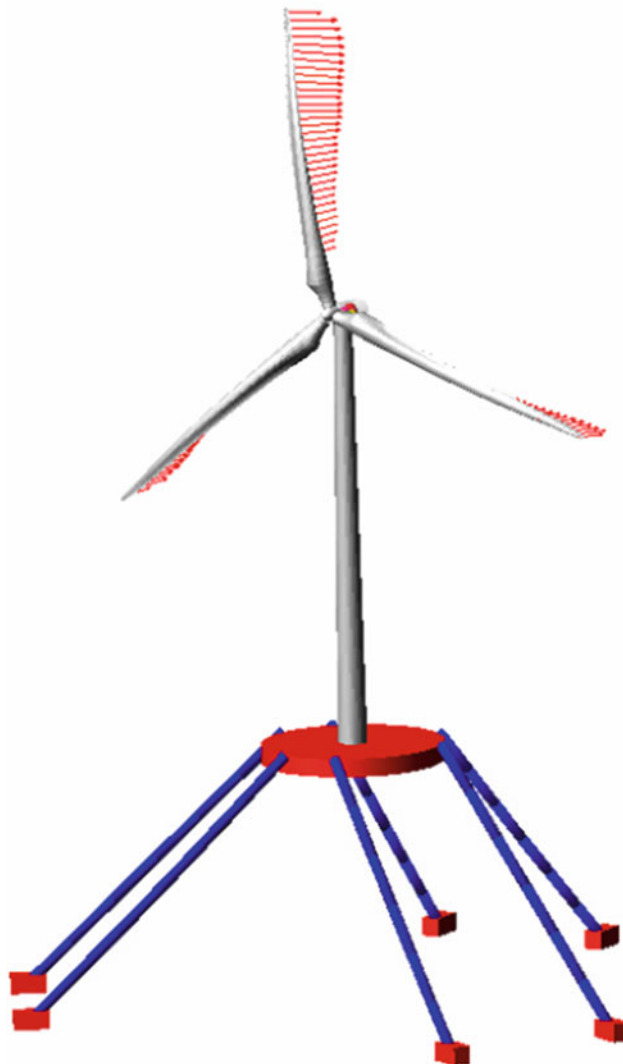


Fig. 4.3 Coupled flexible multibody model

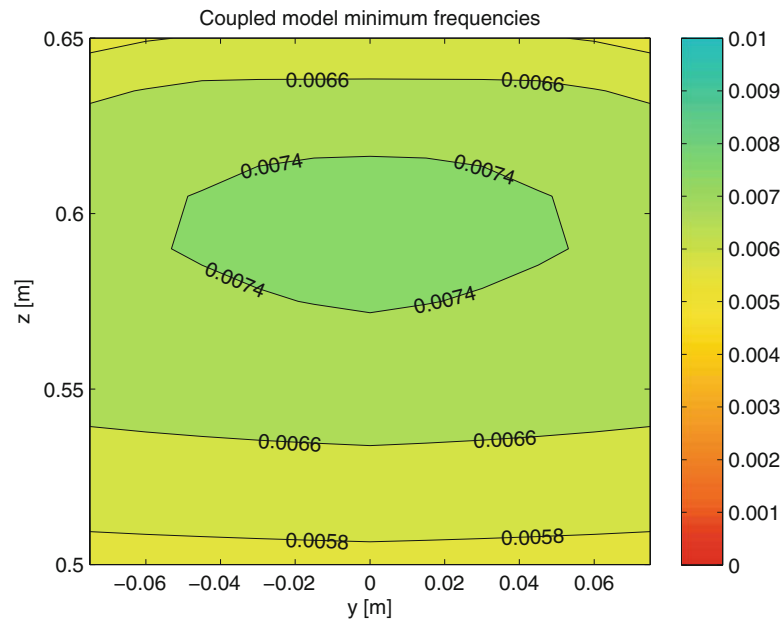


Fig. 4.4 Map of the frequency associated to the first mode of vibration of the system on the $y - z$ plane

is to investigate how the modes of vibration of the system are affected by various factors such as robot pose and wind profile; while in the second one the ideal turbine motion coming from the mathematical model of the sea waves can be compared with the true one due to links elasticity, frictions, backlashes. In addition the co-simulation between ADAMS[®] and other programs such as MATLAB[®] allows to test different control algorithm in order to achieve the desired performances. By imposing to the sliders the motions the real robot will be subjected to, it's easy to compute the motor-reducer requirements in terms of requested torque and accelerations so that the driving system can be properly sized following an approach similar to the one described in [11–14].

As an example in Fig. 4.4 is shown a map of the system frequency associated to its first mode of vibration on the global $y - z$ plane.

4.6 Conclusions

This paper presents a coupled flexible multibody model of an offshore wind turbine scale model and 6-DoF parallel kinematic manipulator. The model is created using the commercial code ADAMS[®] and a particular plug-in developed with the purpose of setting up wind turbines flexible multibody models. The thus built model can be used to explore the coupled system behavior all over the workspace of the machine and with different wind profiles. The information obtained by the all possible simulations are essential during the design phase of the robot since they allow to select the proper size of the structural elements the machine is made of, so that its worsening effects on the scale model can be made negligible.

References

1. Bayati, I., Belloli, M., Ferrari, D., Fossati, F., Giberti, H.: Design of a 6-DoF robotic platform for wind tunnel tests of floating wind turbines. *Energy Procedia J.* **53**, 313–323 (2014)
2. Merlet, J.P.: *Parallel Robots*, 2 edn. Springer, Heidelberg (2006)
3. Fiore, E., Giberti, H., Ferrari, D.: Dynamics modeling and accuracy evaluation of a 6-DoF hexaslide robot. In: *Proceedings of the 33rd IMAC*, pp. 473–479 (2015)
4. Bonev, I.A.: *Analysis and design of a 6-DOF 6- PRRS parallel manipulators?* M.Sc. thesis, GIST, South Korea (1998)
5. Bonev, I.A.: A geometrical method for computing the constant-orientation workspace of 6-PRRS parallel manipulators? *Mech. Mach. Theory* **36**, 1–13 (2001)

6. Ferrari, D., Giberti, H.: A genetic algorithm approach to the kinematic synthesis of a 6-DoF parallel manipulator. In: IEEE Multi-Conference on Systems and Control, Antibes, 8–10 October 2014
7. Cinquemani, S., Ferrari, D.: A genetic algorithm optimization for independent modal space control technique. In: IEEE Multi-Conference on Systems and Control, Antibes, 8–10 October 2014
8. Legnani, G., Tosi, D., Fassi, I., Giberti, H., Cinquemani, S.: The point of isotropy and other properties of serial and parallel manipulators. *Mech. Mach. Theory* **45**(10), 1407–1423 (2010)
9. Legnani, G., Fassi, I., Giberti, H., Cinquemani, S., Tosi, D.: A new isotropic and decoupled 6-DoF parallel manipulator. *Mech. Mach. Theory* **58**, 64–81 (2012)
10. Giberti, H., Ferrari, D., Negahbani, N.: A belt-driven 6-DoF parallel kinematic machine. In: IMAC XXXIII A Conference and Exposition on Structural Dynamics, Orlando, 2–5 February 2015
11. Giberti, H., Ferrari, D.: Drive system sizing of a 6-DoF parallel robotic platform. In: Proceedings of ASME 12th Biennial Conference on Engineering Systems Design and Analysis, ESDA2014, Copenhagen, 25–27 June 2014
12. Giberti, H., Cinquemani, S., Legnani, G.: A practical approach to the selection of the motor-reducer unit in electric drive systems. *Mech. Based Des. Struct. Mach.* **39**(3), 303–319 (2011)
13. Giberti, H., Cinquemani, S., Legnani, G.: Effects of transmission mechanical characteristics on the choice of a motor-reducer. *Mechatronics Elsevier J.* **20**, 604–610 (2010)
14. Giberti, H., Clerici, A., Cinquemani, S.: Specific accelerating factor: one more tool in motor sizing projects. *Mechatronics Elsevier J.* **24**(7), 898–905 (2014)

Chapter 5

Detection and Identification of Firearms Upon Discharge Using Floor-Based Accelerometers

M. Kasarda, P. Tarazaga, M. Embree, S. Gugercin, A. Woolard, B. Joyce, and J. Hamilton

Abstract Vibration monitoring and analysis techniques have significant potential to improve security and threat detection in the built environment. The cornerstone of the Virginia Tech Smart Infrastructure Laboratory (VTSIL) is the highly instrumented Goodwin Hall on the VT campus. This 5-story classroom and laboratory building is instrumented with over 200 accelerometers hard-wired throughout its 160,000 square feet, providing a platform for research and education in structural health monitoring, dynamic model validation, and occupancy studies, among other smart building applications. One of the major research goals for VTSIL is to utilize vibration data to develop advanced security strategies, including threat detection, identification, and localization. Toward realizing this goal, a mobile cement and I-beam platform was built and instrumented with accelerometers. This test-bed recorded vibration signatures during the event of a person discharging a firearm while standing atop the platform. This paper includes initial results that demonstrate there are detectable differences in sensor measurements between a handgun, rifle, and shotgun. Initial analysis of this vibration data using the singular value decomposition demonstrates that one can deduce the type of firearm discharged regardless of differences in the shooter (male, female, weight, etc.), thus justifying the pursuit of advanced vibration-based threat detection and identification systems.

Keywords Firearm • Vibration • Smart building • Shooter event • Accelerometer • Singular value decomposition

5.1 Introduction and Motivation

According to a 2013 FBI report [1], there were 1043 casualties (killed and wounded) from 160 active shooting events in the United States between 2000 and 2013; 60 % of these events ended before police arrived. Highly instrumented smart buildings have the potential to rapidly detect a shooting event and then communicate accurate details and/or instructions in real time to both occupants and first responders, thus saving many lives. Goodwin Hall is a new 160,000 sq ft 5-story building on the Virginia Tech (VT) campus that has been highly instrumented by the VT Smart Infrastructure Laboratory. The building is currently outfitted with over 200 high-fidelity accelerometers (with over 20 more in the installation and commissioning process at the time of this writing) that will be used for structural health monitoring, verification of building models, and the study of human activity in the building, including threat detection and improving occupant safety. Earlier pilot studies have used vibration data from the building accelerometers to locate a hammer strike (mimicking the impact of a footstep) [2, 3], and to classify occupant characteristics from vibrations induced by footsteps down a corridor. In this paper we present results from a new pilot study that uses vibration data to detect when a firearm is discharged, and to classify the weapon (handgun, rifle, or shotgun).

Two traits distinguish an active shooter event from general building activity. (1) Firearm discharges give distinct vibration signatures that can be used to locate the shots, identify the number of shooters and how many shots they have fired, and identify the types of firearms. (2) The shooter may be evasive, making vibration data a particularly appealing alternative

M. Kasarda (✉) • P. Tarazaga • A. Woolard • B. Joyce
Department of Mechanical Engineering, Virginia Tech Smart Infrastructure Laboratory, Virginia Polytechnic Institute and State University,
Blacksburg, VA 24061, USA
e-mail: maryk@vt.edu

M. Embree • S. Gugercin
Virginia Tech Department of Mathematics and Division of Computational Modeling and Data Analytics, Virginia Polytechnic Institute and State
University, Blacksburg, VA 24061, USA

J. Hamilton
Optimal CAE, Plymouth, MI 48170, USA

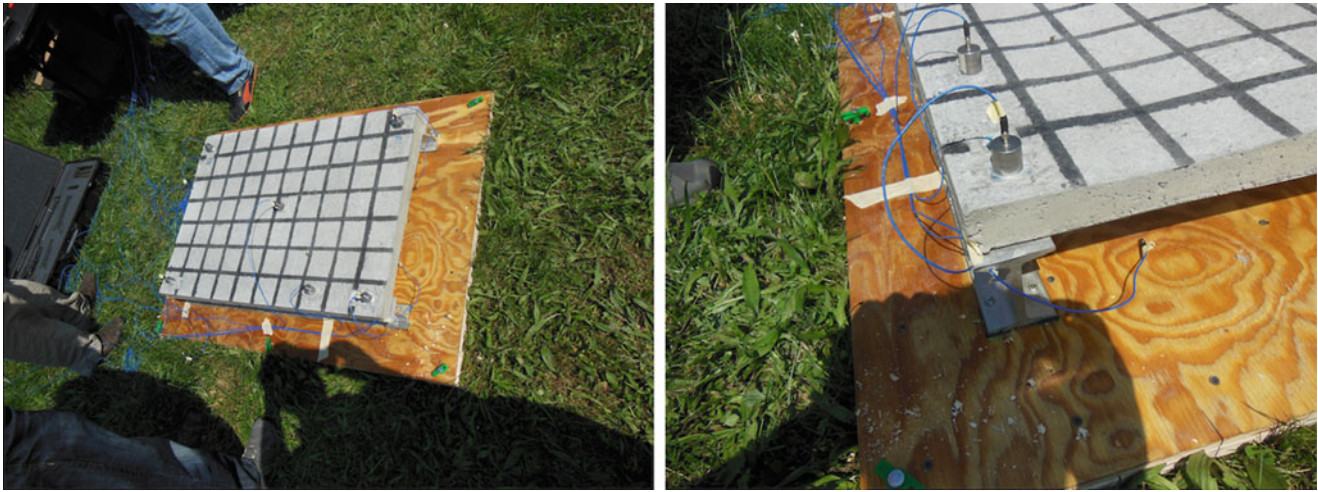


Fig. 5.1 Instrumented concrete and I-beam platform used for collecting firearm discharge vibration data at the VT Police Shooting Range

to cameras, which can be tampered with or destroyed relatively easily. The energy dissipated from a discharged firearm is channeled through the environment as well as through the shooter's body into the floor, where accelerometers detect the vibration characteristics. Although it is beyond the scope of this pilot study, using an accelerometer for sensing and locating the discharge of a weapon may hold advantages over acoustic approaches that are subject to complications, such as echoes and reflections of the sound signature from a discharge [4].

To explore and verify methods for detecting and identifying a firearm discharge using floor accelerometers, experimental data was obtained using an instrumented 3 ft-by-2 ft concrete platform designed to mimic a building floor (in Goodwin Hall) with 10 accelerometers mounted on it. The platform was taken to the VT Police Shooting Range in McCoy, Virginia, where multiple individuals (male and female, different weight and height, different levels of experience with firearms) stood on the platform and fired each of three firearms (a 5.56 mm caliber AR15 rifle, a 20-gauge shotgun, and a 9 mm caliber handgun). The pilot study presented here applies the singular value decomposition to effectively classify vibration signals based on sets of training test data, which allows for efficient and accurate comparison to other firearm discharge data to identify the type of gun used. The results of this study demonstrate significant promise for the detection and identification of a shooting event as it happens in a building equipped with an accelerometer network. Further work is required to enrich the training set for real in-building shot characterization, and to enhance the system to discriminate non-gunshot signals (e.g., a door closing or a book dropping) from actual gunshots.

5.2 Experimental Test Set-Up

Tests were conducted at the VT Police shooting range using a 3 ft-by-2 ft concrete pad that was 3 in thick and supported by two aluminum I-beams, simulating a scaled building floor; see Fig. 5.1. The platform was not intended to fully represent a building floor structure, but was designed for proof-of-concept work to verify the use of accelerometers in detecting and identifying gunshots in a relatively heavy floor structure typical of a public building, while avoiding the considerable complications of conducting live tests within a high-use building. This also provided the sensors a rigid mounting location from which to gather data.

The platform was instrumented with 10 accelerometers of three different types, two of which are actively used in Goodwin Hall. The schematic in Fig. 5.2 shows the locations of the 10 accelerometers on the platform. The four corners and center of the platform were instrumented with single-axis PCB 393B04 accelerometers that have a bandwidth of 500 Hz and 1000 mV/G sensitivity. Directly next to each of the four corner accelerometers, single-axis PCB U352C67 accelerometers were placed for comparison; these sensors have a bandwidth of 10 kHz and a sensitivity of 10 mV/G. Additionally, a single axis Measurement Specialties 7114A accelerometer with a bandwidth of 8 kHz and 100 mV/G sensitivity was placed

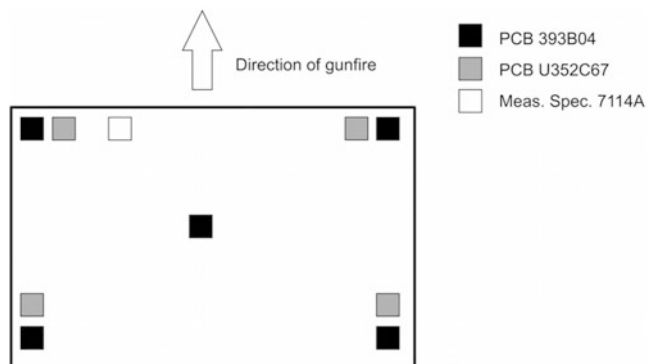


Fig. 5.2 Configuration of accelerometers on the concrete platform



Fig. 5.3 Three different shooters firing shotgun (a) and (b) and rifle (c) while standing on the instrumented platform

approximately 2 in. away from a corner pair. Data was recorded at a sample rate of 25.6 kHz for all channels simultaneously using three NI-9234 DAQs connected to a single 8 slot c-DAQ chassis. Acceleration amplitudes ranged from 1 to 5 G depending on the firearm used. Typical accelerations were found to be within 1–2 G for the shotgun, 2–4 G for the pistol, and 4–5 G for the rifle.

Three different firearms were tested: a 5.56 mm caliber AR15 rifle, a 20-gauge shotgun, and a 9 mm handgun. These tests involved three individuals (male and female, different heights and weights, and different levels of experience with each of the firearms, among other differences), who took turns shooting each of the three weapons. Figure 5.3 shows examples of test firings.

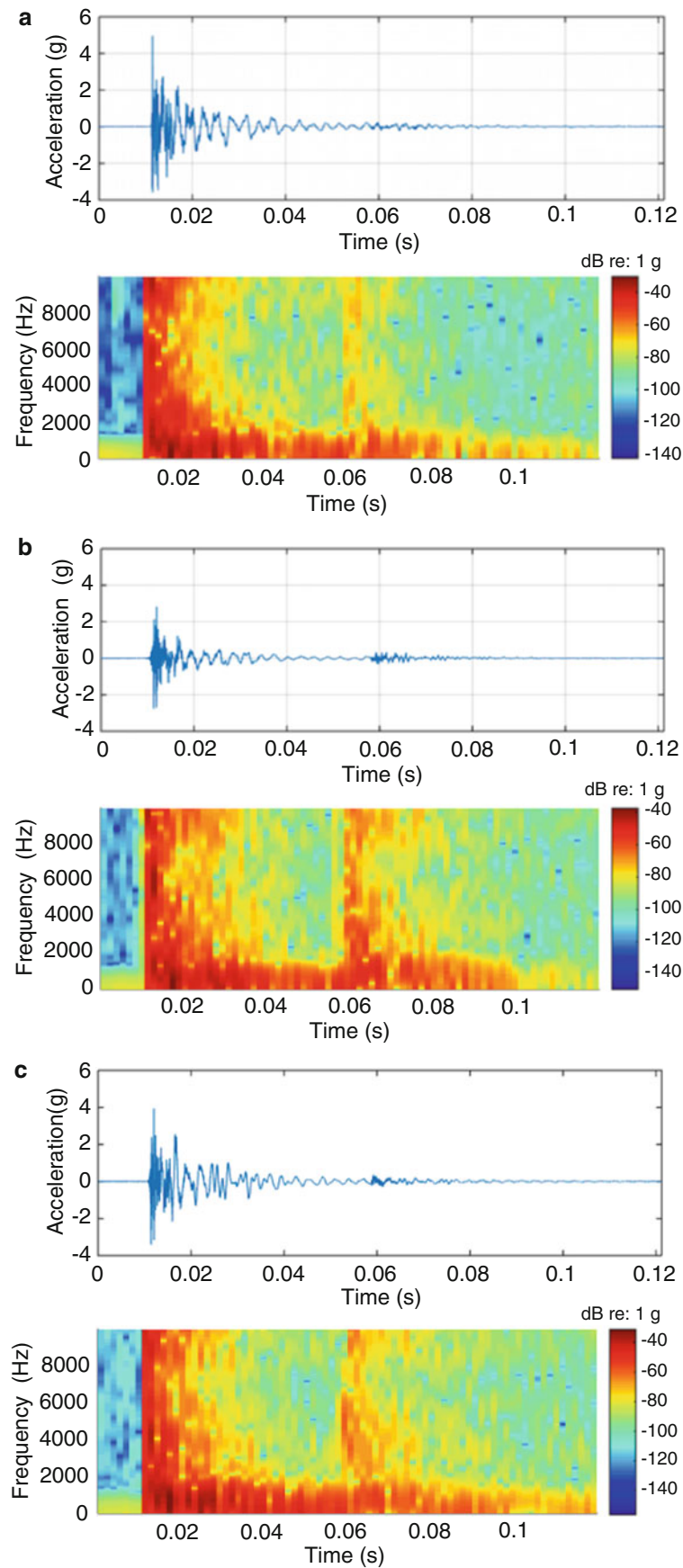


Fig. 5.4 Vibration response recorded from an accelerometer on the cement test platform for (a) a rifle discharge (b) a shotgun and (c) pistol discharge (Weaver stance) for same shooter

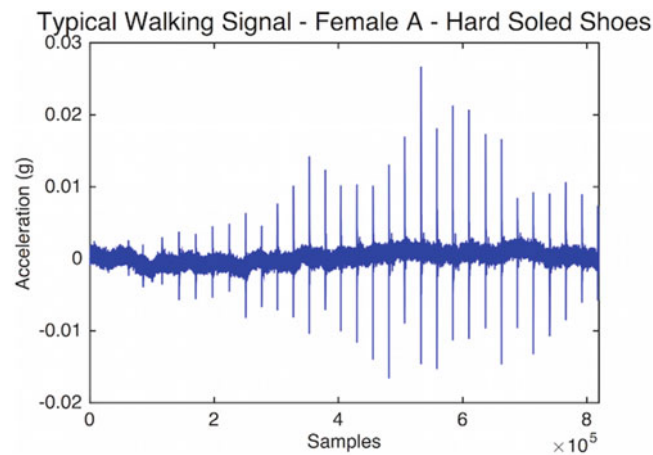


Fig. 5.5 Walking signal from an under-floor mounted accelerometer in Goodwin Hall for a female walking down a hallway over approximately 15 s of total elapsed time

During the platform testing, individual shooters took turns shooting each of the three firearms. Each subject took three shots each with these four scenarios: (1) pistol, isosceles stance; (2) pistol, Weaver stance; (3) shotgun; (4) rifle. (The isosceles and Weaver stances are two common positions from which to fire a handgun, prescribing the positioning of the shooter's legs and manner of gripping the gun.) Thus, the data set consists of readings from 10 accelerometers for 3 subjects and 4 scenarios; each experiment was recorded for 1 s, giving 25,600 data points per experiment.

Figure 5.4 shows sample time series vibration data from the discharge of the AR15 rifle, the 20-gauge shotgun, and the 9-mm pistol, all with the same shooter. Each of the time series shows a distinct increase in vibration amplitude for a short period of time (0.01 s for all firearms) followed by a decreasing amplitude for about 0.05 s, before settling down to an ambient vibration level. The maximum magnitude of the rifle, shotgun and handgun discharges are 5 G, 2 G, and 4 G, respectively. This data suggests that there may exist enough variation between the discharge of a firearm and ambient vibration characteristics to identify the occurrence of a shooting event. For example, Fig. 5.5 shows a time series from one accelerometer in Goodwin Hall as an individual walks down a hallway, showing a maximum amplitude of 30.0 mG over the 15 s of data presented. Note in this figure the distinct pattern associated with a typical human gait as the walker approaches the location of the under-floor accelerometer, walks over it (maximum vibration amplitude), and then continues past. While it is incorrect to make a quantitative comparison between the firearm discharge event vibrations (from the platform test-bed) shown in Fig. 5.4 with the Goodwin Hall building vibration data in Fig. 5.5, an initial visual comparison suggests the potential of using accelerometers to detect shooting events in a building, because they likely have distinct measurable vibration characteristics that are different from typical ambient vibrations in the building.

5.3 Identification of Discharged Firearm Using a Singular Value Decomposition (SVD) Approach

The similarities between the discharge of a rifle, a shotgun, or a pistol, each incurring high amplitude vibrations of short duration, can potentially be detected using a continuous vibration monitoring system in a smart building, such as the one deployed in Goodwin Hall. Looking closer at the sample accelerometer data shown in Fig. 5.4, a comparison shows that the rifle (a), shotgun (b), and pistol (c) each have distinctive characteristics that can be seen even with the naked eye. Therefore, the possibility exists to not only detect a shot from a firearm, but also identify the type of firearm using accelerometer data.

One approach for inferring information efficiently from vibration data applies the singular value decomposition (SVD) and the closely related statistical technique of principal component analysis to a matrix whose columns contain sampled vibrations induced by gunshots from a given weapon. This matrix-based approach can be used for breaking down large data sets into simpler meaningful pieces. It has been used in countless diverse applications, including determination of dominant modes of vibration from spatially distributed data for structural health monitoring [6], and for an advanced method to identify useful information from a vibration signal contaminated by noise [7], to name just two applications involving vibrations.

For our scenario, we build a matrix $G \in \mathbb{R}^{m \times n_g}$, each column of which contains a vibration time series comprising m measurements; each column corresponds to one of n_g firearm test fires (centered about its mean). The SVD of G (see, e.g., [8]) has the form

$$G = U\Sigma V^T = \sum_{j=1}^r \sigma_j u_j v_j^T, \quad (5.1)$$

where $r = \text{rank}(G)$ denotes the number of linearly independent columns of G . (In typical cases, $r = n_g \ll m$.) The columns u_1, \dots, u_r of U , the *singular vectors*, give an orthonormal basis for the column space of G . The singular values, $\sigma_1, \sigma_2, \dots, \sigma_r$, are ordered by decreasing magnitude, $\sigma_1 \geq \sigma_2 \geq \dots \geq \sigma_r > 0$, and hence the singular vectors are ordered from most important to least important. Suppose we are given a new vector of (mean-centered) vibration measurements, $x \in \mathbb{R}^m$. We can test how well x agrees with the data in G by projecting x onto the dominant singular subspace of G . The projection of x onto the d dominant singular vectors is given by

$$Px := \sum_{j=1}^d u_j u_j^T x. \quad (5.2)$$

We can measure the quality of this approximation by the norm of the mismatch between x and Px , normalized to scale for amplitude (e.g., to account for varying distance of the gunshot from the sensors):

$$\frac{\|x - Px\|}{\|x\|}. \quad (5.3)$$

A small value of this residual indicates that the new signal x is consistent with the existing data that made up G . The dimension d can be chosen as large as n_g , but in many circumstances one might choose it to be rather smaller; the singular values $\{\sigma_j\}$ can guide the selection of d : the faster the singular values decay, the smaller one can take d while still capturing the essence of the training data in G . To classify a new signal from an unknown gun, one can build a matrix G and compute its SVD (Eq. 5.1) for each firearm, compute the best approximation of the new signal from each firearm subspace (Px), and identify the unknown firearm as the one that gives the smallest residual (Eq. 5.3).

To demonstrate the power of this approach, we build matrices G for each of the pistol, shotgun, and rifle. We reserve all the data from one of the three shots from each shooter on each weapon, leaving two shots per shooter per weapon as training data. In this case, $m = 25,600$ for one second of vibration amplitude data sampled at 25.6 kHz (e.g., see the data in Fig. 5.4). Each of the columns is centered about its mean. For the pistol, we have $n_g = 120$ (10 accelerometers per shot, 2 shots per shooter, 3 shooters, 2 stances). We reserve $n_t = 60$ samples for use in testing (10 accelerometers, 1 shot per shooter, 3 shooters, 2 stances). For the shotgun we have $n_g = 42$ (3 accelerometers were offline, so we use 7 accelerometers, 2 shots per shooter, 3 shooters, 1 stance) with $n_t = 21$. For the rifle, we have $n_g = 48$ (2 accelerometers were offline) with $n_t = 24$.

To make for a fair comparison, we set $d = 42$, meaning that we use all singular vectors for the shotgun, and only the dominant 42 singular vectors for the pistol and rifle. Figure 5.6 shows the singular values for these three cases. Figure 5.7 shows the results of the algorithm for identifying the weapon associated with 105 new trials. The top plot shows the residual measure $\|(I - P)x\|/\|x\|$ for projection onto each of the three training data sets, for the 105 different trials. Dark blue indicates a small residual (good fit); yellow indicates a large residual (poor fit). The bottom plot highlights the training set that gave the smallest residual for each trial. We see that this algorithm correctly classifies 104 of the 105 test cases, with only one mismatch. These results are very encouraging; however, we note that some of the test cases (especially for shotgun and rifle shots) give relatively poor residual norms (around 0.5) for all three weapons. A more extensive set of training images will likely improve this outcome.

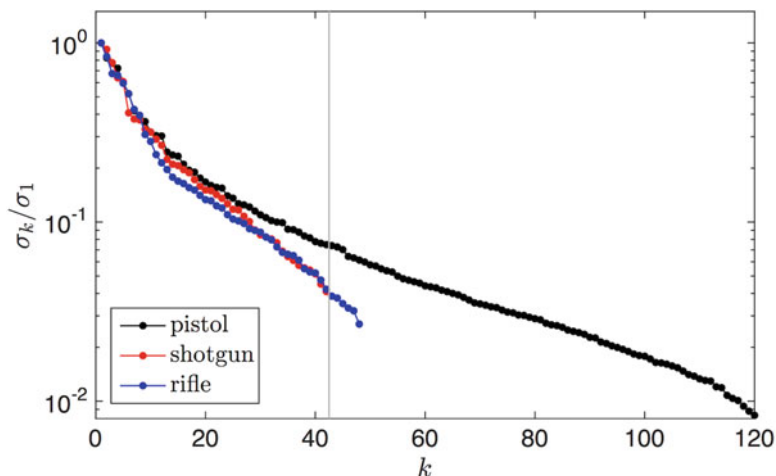


Fig. 5.6 Singular values of G for the pistol, shotgun, and rifle, showing steady decay with the index k . The results in Fig. 5.7 use the first 42 singular vectors from each data set

5.4 Conclusion

A 3 ft-by-2 ft cement and I-beam platform was instrumented with accelerometers and taken to the VT police shooting range, where it was used to measure the vibrations caused when various individuals fired three distinct firearms. Broad characteristics of this vibration data allow for visual discrimination of a gunshot from other common causes of vibration in a building, while finer characteristics of the data allow for classification of the type of weapon fired as well as properties of the shooter. This latter analysis applied the singular value decomposition to a dictionary of typical gunshots to create a tool that could be used to classify new vibration signals. This pilot study demonstrates the significant potential to detect the discharge of a firearm in a building as well as to identify the type of firearm discharged through the utilization of accelerometer-based vibration data. While the preliminary results are encouraging, further tests are required with a more extensive training set. In particular, a robust algorithm should be able to automatically process signals, identify potential gunshots, and discriminate true shots from other sharp vibrations (doors closing, books dropping, etc.). The work described here provides a first step toward a vibration monitoring system that can identify and locate an active shooter in a public building, and help direct first responders to the incident and the occupants to safety.

Acknowledgements The authors would like to thank the VT Police for the use of their shooting range facility for performing the tests presented here, and also for their support of this project and ongoing research for improving threat detection and identification. The authors wish to acknowledge the support and the close collaborative efforts provided by our sponsors, VTI Instruments, PCB Piezotronics, Inc.; Dytran Instruments, Inc.; Oregano Systems; and Measurement Specialties, Inc. The authors are particularly appreciative for support provided by the College of Engineering at Virginia Tech through Dean Richard Benson and Associate Dean Ed Nelson as well as VT Capital Project Manager, Todd Shelton, and VT University Building Official, William Hinson. The authors would also like to acknowledge Gilbane, Inc. and in particular, David Childress and Eric Hotek. We want to give a special thanks to the Student Engineering Council (SEC) at Virginia Tech and their financial commitment to the Goodwin Hall instrumentation work. The specific project work presented here was conducted through the support of the Virginia Tech Smart Infrastructure Laboratory and its members.

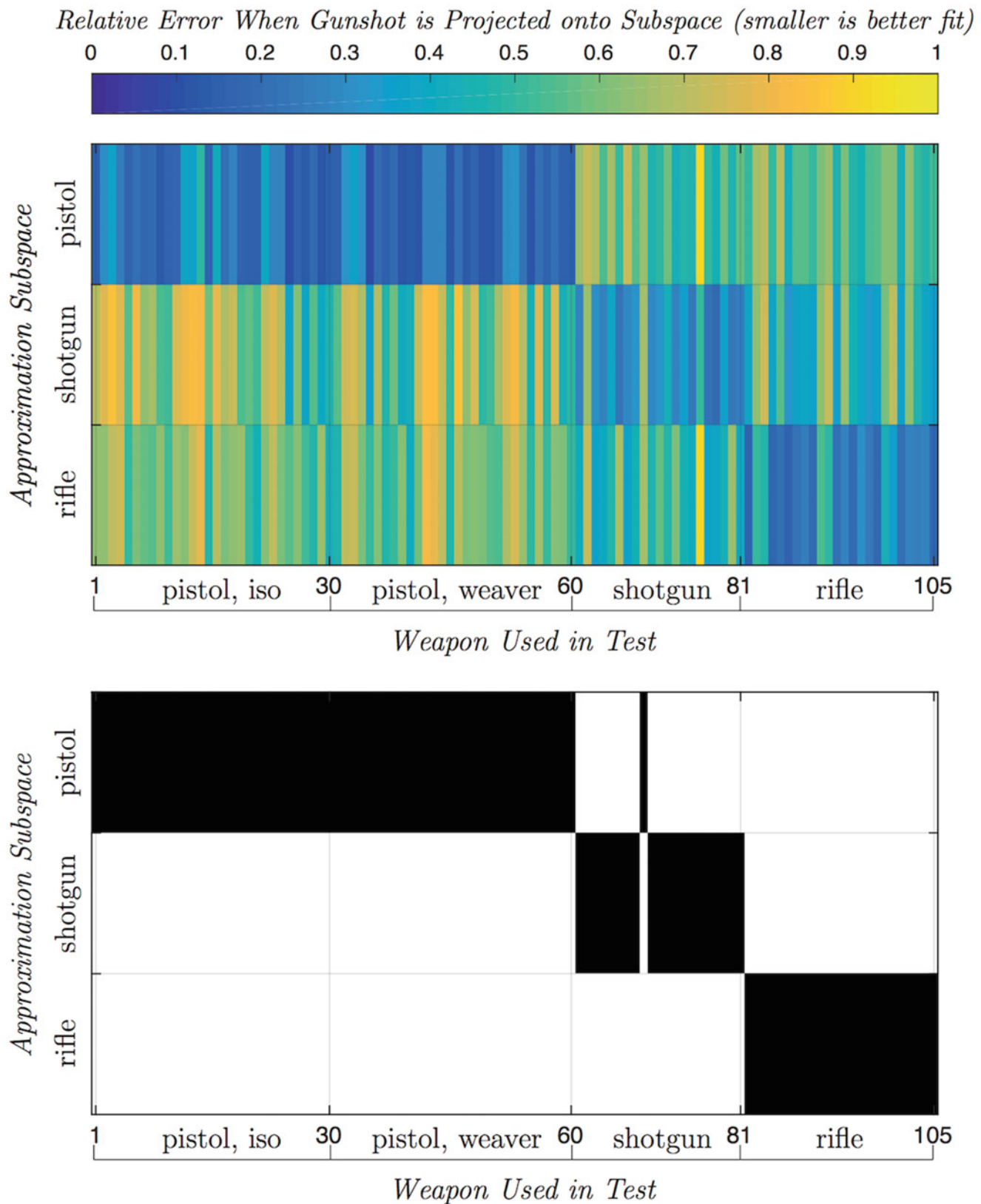


Fig. 5.7 The identification of firearms via floor accelerometer sensing and subspace projections

References

1. Federal Bureau of Investigation (FBI): A study of active shooter events in the United States between 2000 and 2013. <https://www.fbi.gov/news/stories/2014/september/fbi-releases-study-on-active-shooter-incidents/pdfs/a-study-of-active-shooter-incidents-in-the-u.s.-between-2000-and-2013>
2. Poston, J.D., Schloemann J., Buehrer, R.M., Malladi, V.S., Woolard, A.G., Tarazaga, P.A.: Towards indoor localization of pedestrians via smart building vibration sensing. In: International Conference on Localization and GNSS, 22–24 June 2015
3. Schloemann, J., Malladi, V.V.N.S., Woolard, A.G., Hamilton, J.M., Buehrer, R.M., Tarazaga, P.A.: Vibration Event Localization in an Instrumented Building. In: International Modal Analysis Conference (IMAC) XXXIII, Orlando, Florida, 2–5 Feb 2015
4. Valenzise, G., et al.: Scream and gunshot detection and localization for audio-surveillance systems. In: Advanced Video and Signal Based Surveillance, 2007. AVSS 2007. IEEE Conference on. IEEE, 2007
5. Maher, R.C.: Acoustical characterization of gunshots. In: Signal Processing Applications for Public Security and Forensics, 2007. SAFE'07. IEEE Workshop on. IET, 2007
6. Kerschen, G., Golinval, J.-C.: Physical interpretation of the proper orthogonal modes using the singular value decomposition. *J. Sound Vib.* **249**(5), 849–865 (2002)
7. Yang, W.-X., Tse, P.W.: Development of an advanced noise reduction method for vibration analysis based on singular value decomposition. *NDT & E Int.* **36**(6), 419–432 (2003)
8. Golub, G.H., Van Loan, C.F.: *Matrix Computations*, 4th edn. Johns Hopkins University Press, Baltimore (2012)

Chapter 6

An Adaptive Markov Chain Monte Carlo Method for Bayesian Finite Element Model Updating

I. Boulkaibet, T. Marwala, M.I. Friswell, and S. Adhikari

Abstract In this paper, an adaptive Markov Chain Monte Carlo (MCMC) approach for Bayesian finite element model updating is presented. This approach is known as the Adaptive Hamiltonian Monte Carlo (AHMC) approach. The convergence rate of the Hamiltonian/Hybrid Monte Carlo (HMC) algorithm is high due to its trajectory which is guided by the derivative of the posterior probability distribution function. This can lead towards high probability areas in a reasonable period of time. However, the HMC performance decreases when sampling from posterior functions of high dimension and when there are strong correlations between the uncertain parameters. The AHMC approach, a locally adaptive version of the HMC approach, allows efficient sampling from complex posterior distribution functions and in high dimensions. The efficiency and accuracy of the AHMC method are investigated by updating a real structure.

Keywords Finite element model updating • Bayesian • Markov Chain Monte Carlo • Hybrid Monte Carlo • Adaptive

6.1 Introduction

The Finite Element Model (FEM) [1–3] is one of the famous numerical methods that can be useful in numerous engineering areas such as Mechanical, Civil and Electrical Engineering. This approach derives approximate numerical models for real systems (or structures). The obtained numerical models are very accurate for simple structures or systems; however, the approximation degrades when the modelled system is sufficiently complex, and the results obtained from the Finite Element Models (FEMs) are different from those obtained from experiments. Several factors can cause the accuracy degradation of the FEMs, such as the variability of certain model parameters and the errors resulting from the modelling process. To improve the FEMs, some of the uncertain model parameters need to be adjusted to reduce the error between the measured data and the numerical model [4, 5]. The process of adjusting these uncertain parameters, to determine the most probable parameters that accurately describes the structure in the presence of the measured responses of the system, is known as “model updating” [4, 5].

There are two main strategies to perform FEM updating: the direct and indirect (iterative) updating strategies [4]. To perform a direct updating strategy, the FEM output is directly equated to the measured data. However, in the iterative strategy the differences between the measured data and the FEM output are minimized by adjusting some “flexible” uncertain variables [4]. The most used iterative algorithms are the sensitivity-based methods [4, 5] and the metaheuristics algorithms [5–7]. These methods are typically optimization problems and their objective functions are described by the error between the analytical and experimental data. The objective functions of an iterative updating strategy are then minimized by finding the optimal solution of the updated parameters of the FEM.

Other approaches used in FEM updating are to implement statistical theories [8–10]. Statistical methods (or uncertainty quantification methods) are very useful mathematical tools that can be used to update FEMs and to provide more information about the variability of the updated parameters. The use of statistical theories in model updating problems has become very attractive in the last 10 years. The statistical methods that have been used in updating FEMs are divided into two main classes: the class of non-probabilistic (possibilistic) methods such as the fuzzy logic method [11, 12], which can be used to estimate the uncertainty of the model parameters where the uncertain parameters are characterized by membership functions. The second class describes the probabilistic methods where these methods treat the uncertain parameter as a

I. Boulkaibet (✉) • T. Marwala

Electrical and Electronic Engineering Department, University of Johannesburg, 524, Auckland Park 2006, South Africa
e-mail: ilyes@aims.ac.za

M.I. Friswell • S. Adhikari

College of Engineering, Swansea University, Singleton Park, Swansea SA2 8PP, UK

random distribution with a joint probability density function (PDF) [8, 9]. The Bayesian approach [5, 10, 13–17], which is one of the most common probabilistic methods along with perturbation methods [9], has become very attractive in system identification and uncertainty quantification. This approach has been used numerous times for FEM updating and showed promising results for uncertainty quantification [17]. The uncertain parameters, in the Bayesian method, are modelled as random parameters with joint probability density functions (PDFs), which is also known as the *posterior* PDF. In the case that the posterior PDF is analytically unavailable, sampling methods can be implemented to obtain numerical solutions for the posterior PDF. The most attractive sampling techniques are the Markov chain Monte Carlo (MCMC) methods. The MCMC methods have been widely used for FEM updating where the most recognized MCMC algorithm is the Metropolis–Hastings (M-H) algorithm. This algorithm has been implemented numerous times in the FEM updating problems and uncertainty quantifications [10, 13, 16, 17]. Moreover, several MCMC algorithms were used to solve Bayesian model updating problems. A Monte-Carlo inverse approach was used by Mares et al. [18] for stochastic (or Bayesian) model updating. Nichols et al. [19] applied an MCMC algorithm to sample from the posterior PDF of some nonlinear systems. The Gibbs sampling technique was implemented by Ching et al. [20] for model updating problems. Ching and Cheng [21] introduced a modified version of the M-H algorithm called the Transitional Markov Chain Monte Carlo (TMCMC) algorithm. The TMCMC algorithm was used by Muto and Beck [22] to update hysteretic structural models. Cheung and Beck [23] implemented the Hybrid Monte Carlo (HMC) method to update a structural dynamic linear system with 31 uncertain parameters. The updating process was successfully able to characterize uncertainties associated with the underlying structural system.

The HMC method had shown promising results to solve higher-dimensional complex problems. The trajectory of the HMC algorithm, which is guided by the derivative of the posterior log-density, facilitates the convergence to areas of high probability in a limited time (or limits the number of iterations) during the searching process [17, 24–26]. In the HMC algorithm, a Molecular Dynamic (MD) system is created and its total energy, or the Hamiltonian function, is used to draw samples. The total energy is evaluated through time numerically by using the leapfrog integrator (or algorithm). Unfortunately, this integrator (or even other integrators that can be used by the HMC algorithm) does not conserve the Hamiltonian function, especially when a relatively large time step is needed to speed up the convergence process or when the system size is relatively large. Boulkaibet et al. tried to solve this problem by implementing two modified versions of the HMC algorithm called the shadow hybrid Monte Carlo (SHMC) [13] and the separable shadow hybrid Monte Carlo (S2HMC) [15] algorithms for Bayesian finite element model updating. Both of these algorithms produced samples with a relatively large time step and give more accurate results than the HMC algorithm.

In this paper, another modification of the HMC algorithm is proposed. The idea is to deal with the acceptance rate (AR) degradation and to improve the results accuracy. First, the algorithm will adaptively choose the trajectory length to obtain a good Acceptance Rate (AR) without wasting computation time. This can be done by adjusting the trajectory length at every iteration to keep the AR acceptable (and controlled), and with relatively large trajectory length. Secondly, the algorithm should deal with separated regions (two high probability areas are isolated by regions of low probability). Most of the MCMC algorithms (including the HMC) have difficulties to move from one search region to another when these two regions are separated by other regions with low probability. This can be a problem when the obtained samples are only obtained from the regions with local minima. To overcome this problem, the trajectory of the AHMC algorithm is adjusted and the samples are obtained from a sequence of distributions that are more diffuse than the original posterior PDF. In this paper, an Adaptive HMC algorithm is introduced to sample the posterior PDF. This method is investigated by updating two structural examples: a 3 degree of freedom (DOF) linear system and an unsymmetrical H-shaped structure. The advantages and disadvantages of the AHMC technique will be discussed.

This paper is organized as following: first, the posterior distribution function of the uncertain parameters is presented in Sect. 6.2. Section 6.3 discusses the AHMC algorithm. Section 6.4 shows the implementation of Bayesian FEM updating on a 3 DOF linear system. In Sect. 6.5, the AHMC algorithm is used to update an unsymmetrical H-shaped structure with real measured data. Section 6.6 concludes the paper.

6.2 The Bayesian Theory

The Bayesian approach is governed by Bayes rule [13, 15, 17, 27]:

$$P(\boldsymbol{\theta} | \mathcal{D}, \mathcal{M}) \propto P(\mathcal{D} | \boldsymbol{\theta}, \mathcal{M}) P(\boldsymbol{\theta} | \mathcal{M}) \quad (6.1)$$

where $\boldsymbol{\theta} \in \Theta \subset \mathcal{R}^d$ is the uncertain parameter vector that needs to be updated. The \mathcal{M} notation indicates the model class of the target system to be updated. Usually, the model classes are separated by the updating vector $\boldsymbol{\theta}$. \mathcal{D} represents the experimental measurements (frequencies f_i^m , mode shapes ϕ_i^m , ...). The $P(\boldsymbol{\theta}|\mathcal{M})$ PDF is the prior knowledge of the uncertain parameters when the model class is known. $P(\mathcal{D}|\boldsymbol{\theta}, \mathcal{M})$ represented the likelihood function, which is obtained by the difference between the measurements and the FEM data when both $\boldsymbol{\theta}$ and \mathcal{M} are given. The term $P(\boldsymbol{\theta}|\mathcal{D}, \mathcal{M})$ is The posterior PDF which represents the probability of update parameters when both \mathcal{D} and \mathcal{M} are given. Since only a single model class is considered in this paper, the notation \mathcal{M} will be ignored for the remaining equations.

The posterior $P(\boldsymbol{\theta}|\mathcal{D})$ PDF used in this paper is the same one used in [13, 15, 17]:

$$P(\boldsymbol{\theta}|\mathcal{D}) = \frac{1}{Z_s(\alpha, \beta_c)} \exp\left(-\frac{\beta_c}{2} \sum_i^{N_m} \left(\frac{f_i^m - f_i}{f_i^m}\right)^2 - \sum_i^Q \frac{\alpha_i}{2} \|\boldsymbol{\theta}^i - \boldsymbol{\theta}_0^i\|^2\right) \quad (6.2)$$

where $Z_s(\alpha, \beta_c)$ is a normalizing constant given by [13, 15, 17]

$$Z_s(\alpha, \beta_c) = \left(\frac{2\pi}{\beta_c}\right)^{N_m/2} \prod_{i=1}^{N_m} f_i^m (2\pi)^{Q/2} \prod_{i=1}^Q \frac{1}{\sqrt{\alpha_i}} \quad (6.3)$$

β_c is a constant that can be used to give more weight to the likelihood terms, f_i and f_i^m are the i th analytical natural frequency and the i th measured natural frequency. N_m is the number of measured modes used for the updating process. Q is the size of the parameter vector, $\boldsymbol{\theta}_0$ is the vector of initial values of the parameters, which are usually the mean values. α_i is the i th coefficient of the i th updating variable and these coefficients can be used to weight the prior PDF. The notation $\|\cdot\|$ represents the Euclidean norm of the quantity *. In complex structures, obtaining an analytical solution from the posterior PDF is not possible. Sampling techniques however can provide a numerical solution of the PDF in Eq. (6.1) [13, 15, 17]. In this work, the adaptive HMC algorithm is implemented to sample from the posterior PDF.

6.3 Adaptive Hybrid Monte Carlo

The main idea of the AHMC algorithm is to improve the HMC trajectory by providing an adaptive trajectory length as well as a tempered trajectory. The AHMC algorithm [28, 29] is based on the original HMC algorithm (which is introduced by Duane et al. [24]). The HMC algorithm has shown encouraging results for solving higher-dimensional complex engineering problems [13, 15–17, 23, 28]. The main idea of the HMC algorithm is to combine the Molecular Dynamic (MD) trajectory and the Monte Carlo (MC) accept/rejection step. The same concepts are used for the AHMC algorithm where a new dynamical system is constructed by introducing a new auxiliary variable, called momentum, $\mathbf{p} \in \mathcal{R}^d$. The uncertain vector $\boldsymbol{\theta}$ will be treated as the system displacement while the total energy (the Hamiltonian function) of the new dynamical system can be defined as: $H(\boldsymbol{\theta}, \mathbf{p}) = V(\boldsymbol{\theta}) + W(\mathbf{p})$. The potential energy is defined by $V(\boldsymbol{\theta}) = -\ln(P(\boldsymbol{\theta}|\mathcal{D}))$ while the kinetic energy of the dynamic system is given by $W(\mathbf{p}) = \mathbf{p}^T \mathbf{M}^{-1} \mathbf{p} / 2$, where the matrix $\mathbf{M} \in \mathcal{R}^{d \times d}$ is positive definite.

The Hamiltonian dynamics are then governed by:

$$\frac{d\boldsymbol{\theta}}{dt} = \mathbf{M}^{-1} \mathbf{p}(t), \quad \frac{d\mathbf{p}}{dt} = -\nabla V(\boldsymbol{\theta}(t)) \quad (6.4)$$

In this paper, the joint density function $\rho(\boldsymbol{\theta}, \mathbf{p})$ follows a Boltzmann distribution [15, 28] where $\rho(\boldsymbol{\theta}, \mathbf{p}) \propto \exp(-\beta_B H(\boldsymbol{\theta}, \mathbf{p}))$, where $\beta_B = \frac{1}{T}$ and T is a constant temperature (the Boltzmann constant is neglected). It is easy to see that $\rho(\boldsymbol{\theta}, \mathbf{p})$ can be rewritten as $\rho(\boldsymbol{\theta}, \mathbf{p}) \propto \exp\left(-\frac{V(\boldsymbol{\theta})}{T}\right) \cdot \exp\left(-\frac{W(\mathbf{p})}{T}\right)$, or

$$\rho(\boldsymbol{\theta}, \mathbf{p}) \propto P(\boldsymbol{\theta}|\mathcal{D}) \cdot \exp\left(-\frac{1}{T} \mathbf{p}^T \mathbf{M}^{-1} \mathbf{p} / 2\right) \quad (6.5)$$

Equation (6.5) shows that sampling the vector $\boldsymbol{\theta}$ from the posterior PDF can also be achieved by sampling the pair of vectors $(\boldsymbol{\theta}, \mathbf{p})$ from the joint PDF $\rho(\boldsymbol{\theta}, \mathbf{p})$. The pair $(\boldsymbol{\theta}, \mathbf{p})$ is evaluated through time t by using the following leapfrog integrator [13, 15–17, 23, 28]:

$$\mathbf{p}\left(t + \frac{\delta t}{2}\right) = \mathbf{p}(t) - \frac{\delta t}{2} \nabla V(\boldsymbol{\theta}(t)) \quad (6.6)$$

$$\boldsymbol{\theta}(t + \delta t) = \boldsymbol{\theta}(t) + \delta t \mathbf{M}^{-1} \mathbf{p}\left(t + \frac{\delta t}{2}\right) \quad (6.7)$$

$$\mathbf{p}(t + \delta t) = \mathbf{p}\left(t + \frac{\delta t}{2}\right) - \frac{\delta t}{2} \nabla V(\boldsymbol{\theta}(t + \delta t)) \quad (6.8)$$

where δt is the time step and ∇V is the gradient which can be obtained numerically by finite difference as [15, 23]

$$\frac{\partial V}{\partial \theta_i} \cong \frac{V(\boldsymbol{\theta} + \Delta h) - V(\boldsymbol{\theta} - \Delta h)}{2h\Delta_i} \quad (6.9)$$

h is a scalar that dictates the size of the perturbation of $\boldsymbol{\theta}$, while $\Delta = [\Delta_1, \Delta_2, \dots, \Delta_N]$ is the perturbation vector. After the evaluation of Eqs. (6.6, 6.7, and 6.8), an MC accept-reject step is added to satisfy the property of Eq. (6.4). Thus, if the pair $(\boldsymbol{\theta}, \mathbf{p})$ is the initial vector while the pair $(\boldsymbol{\theta}^*, \mathbf{p}^*)$ is the vector after evaluating Eqs. (6.6, 6.7, and 6.8), then the candidate $(\boldsymbol{\theta}^*, \mathbf{p}^*)$ is accepted with probability $\min(1, \exp\{-\frac{\Delta H}{T}\})$, $\Delta H = H(\boldsymbol{\theta}^*, \mathbf{p}^*) - H(\boldsymbol{\theta}, \mathbf{p})$. Since the AHMC algorithm has the same basics as the HMC algorithm, all previous equations and properties will be used by the AHMC algorithm. However, the AHMC algorithm has certain modifications that improves the sampling performance. To *avoid the non-ergodicity problem* and to ensure a good performance of the AHMC algorithm, the evaluation of the leapfrog algorithm needs to be done L steps during each iteration. This will increase the algorithm trajectory and ensure large steps. The value of L can be uniformly chosen from the interval $\{1, L_{max}\}$. *Moreover, since* the time step used by the leapfrog integrator is bounded ($\delta t_{min} < \delta t < \delta t_{max}$), the time step will be careful adjusted after a number of iterations. Adjusting the time step after a fixed number of iterations avoids a large rejection rate when the time step is large [28, 29]. Also, the adaptation of the time step avoids using a small trajectory length and therefore more iteration are needed to converge. To adapt the time step, a random value of the δt is chosen from the interval $[\delta t_{min}, \delta t_{max}]$. Then the Eqs. (6.6, 6.7, and 6.8) will be evaluated for N_b iterations. The N_b samples obtained will be used to calculate the acceptance rate $\bar{\alpha}^b$ and used to decide if the time step has to increased or decreased as following:

$$\delta t^{i+1} = \begin{cases} \delta t^i + \gamma^i \delta t^i, & \bar{\alpha}^b < \bar{\alpha} \\ \delta t^i - \gamma^i \delta t^i, & \bar{\alpha}^b \geq \bar{\alpha} \end{cases} \quad (6.10)$$

where γ^i is a random variable selected from the interval [0.01 0.05] and $\bar{\alpha}$ is the target acceptance rate. The value of the target acceptance rate can be selected high to ensure more different samples are involved in computing the mean values of the uncertain parameters. Then, after each N_b samples (or iterations) the time step will be adapted by increasing or decreasing the time step by a small value (between 1 and 5 %). This strategy will ensure that the time step does not produce small trajectory moves and is not relatively large (significant numbers of iterations are not wasted). The second modification proposed in this algorithm is to sample from distributions that are more diffuse than the original posterior PDF [30]. This strategy can facilitate the movement between high probability areas separated by regions of low probability. This can be done by increasing the temperature T which will eventually give more diffuse distribution (the posterior PDF is when $T = 1$) [30]. In this paper, the temperature is changed at each iteration by a small value according to: $T(i+1) = \bar{\alpha}^T T(i)$, where $\bar{\alpha}^T > 1$. The AHMC algorithm is than summarised as:

1. A value $\boldsymbol{\theta}_0$ is used to initiate the algorithm
2. Initiate \mathbf{p}_0 such that $\mathbf{p}_0 \sim N(0, \mathbf{M})$
3. Run the following steps N_b times:
 - (a) Initiate the leapfrog integrator by the previously accepted pair $(\boldsymbol{\theta}, \mathbf{p})$ and run the algorithm for L time steps to obtain $(\boldsymbol{\theta}^*, \mathbf{p}^*)$.
 - (b) Update the FEM and use the obtained analytical frequencies to compute $H(\boldsymbol{\theta}^*, \mathbf{p}^*)$.

- (c) Accept (θ^*, \mathbf{p}^*) with probability $\min\left(1, \exp\left\{-\frac{\Delta H}{T(i)}\right\}\right)$.
- (d) Change the temperature according to: $T(i+1) = \bar{\alpha}^T T(i)$
4. Use the N_b samples to obtain the acceptance rate $\bar{\alpha}^b$
 5. Adjust the time step according to Eq. (6.10)
 6. Repeat steps (6.3, 6.4, and 6.5) to for N_s samples.

In the next sections, the performance of the AHMC algorithm is discussed when two different systems are updated.

6.4 Application 1: A 3 DOF Linear System

To investigate the AHMC algorithm, a simulation of a 3 DOF mass-spring linear system is considered. The system is shown in Fig. 6.1. The deterministic parameters of this system are: $m_1 = 2$ kg, $m_2 = 1$ kg, $m_3 = 3$ kg. The nominal mean values of the uncertain parameters are: $k_1 = 10$ N/m, $k_2 = 6$ N/m, $k_2 = k_3$ and $k_4 = 10$ N/m, and these values are used to obtain the following natural frequencies of interest of this structure: $\omega_1 = 1.12$ Hz, $\omega_2 = 3.5$ Hz and $\omega_3 = 4.1$ Hz. However, the initial values of the uncertain parameters are: $k_1 = 12$ N/m, $k_2 = 4$ N/m, $k_2 = k_3$ and $k_4 = 7$ N/m. Thus, the parameters to be updated are: k_1 , k_2 and k_4 , and can be represented by a vector of $d = 3$ variables $\theta = \{\theta_1, \theta_2, \theta_3\}$.

6.4.1 Updating the Stiffness Parameters

In this subsection, the 3 DOF linear system is updated by adjusting a vector of 3 parameters $\theta = \{\theta_1, \theta_2, \theta_3\}$ using the Bayesian approach, while the AHMC algorithm is used to sample from the posterior PDF. The number of samples is set to $N_s = 5000$, the coefficients α_i in Eq. (6.2) were set equal to $\frac{1}{\sigma_i^2}$, where σ_i^2 is the variance of θ_i . Since only the stiffness parameters are updated, the σ_i $\{i = 1, 2, 3\}$ have equal values and are set to 500. The constant β_c , the weight of the likelihood term, in Eq. (6.2) was set equal to 1. The updating parameters θ_i were bounded with a maximum value of 14 N/m and a minimum value of 2 N/m.

The initial vector of θ is set to $\theta_0 = \{12, 4, 7\}$. The initial time step used in the HMC algorithm is $\delta t^0 = 1 \times 10^{-3}$ s while the time step is bounded with a minimum value of $\delta t^0 = 0.001 \times 10^{-3}$ s and a maximum value of $\delta t^0 = 15 \times 10^{-3}$ s. L is uniformly distributed on the interval $\{1, 30\}$, the target acceptance rate is $\bar{\alpha} = 0.95$ (95 %), the initial value of the temperature is $T(1) = 1$, and $\bar{\alpha}^T$ is set to 1.0012. N_b is set to 50, and the results of the updating are given in Tables 6.1 and 6.2.

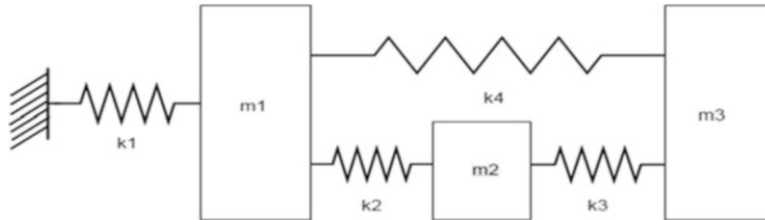


Fig. 6.1 The 3 DOF mass-spring linear system

Table 6.1 The updated vector of the stiffness parameters using AHMC technique

Stiffness parameters (N/m)					
	Initial	Nominal values	Error (%)	AHMC algorithm (μ_i)	$\frac{\sigma_i}{\mu_i}$ (%) c.o.v
θ_1	12.00	10.00	20	9.89	1.77
θ_2	4.00	6.00	50	5.99	2.82
θ_3	7.00	10.00	30	10.05	5.79

Table 6.2 Frequencies and errors when AHMC techniques used to update stiffness parameters

Modes	Nominal frequency (Hz)	Initial frequency (Hz)	Error (%)	Frequency AHMC method (Hz)	c.o.v values (%)	Error (%)
1	1.120	1.122	0.16	1.119	0.43	0.05
2	3.500	2.932	16.23	3.498	0.48	0.07
3	4.100	3.649	11.01	4.100	0.45	0.01
Total average error	–	–	9.13	–	–	0.04

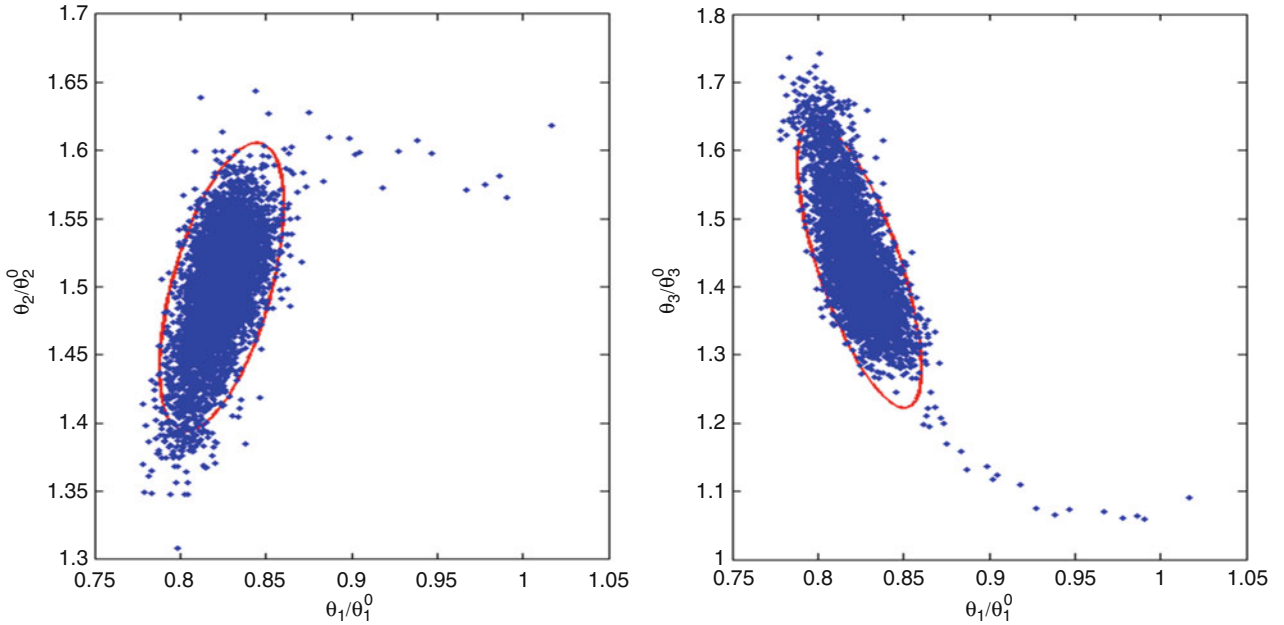
**Fig. 6.2** The scatter plots with the error ellipses using the AHMC method

Figure 6.2 shows the scatter plots for the three uncertain parameters using the AHMC algorithm. The uncertain parameters plotted in Fig. 6.2 are normalised by dividing their values by the initial value θ_i^0 . Also, an error ellipse (or confidence ellipse) for the obtained samples is shown in the same figure. The error ellipse represents a contour that allows the visualization of the confidence interval, given as the region that contains 95 % of the parameter samples. The plot shows that the AHMC algorithm has found the high probability areas after a few iterations.

The updated values of the uncertain parameters are presented in Table 6.1 along with their initial values, nominal values and the coefficient of variation (c.o.v) values. The c.o.v values are obtained by dividing the obtained standard deviation by the updated vector θ , and can be used to describe the errors in the updated parameters. Table 6.1 shows that the c.o.v values are small for the AHMC algorithm (less than 6 %) which indicates that the AHMC algorithm has efficiently estimated the uncertain parameters. This can be seen from the updated parameters which are nearly identical to the nominal values.

Table 6.2 shows the initial and updated natural frequencies, together with the absolute errors obtained by $\frac{|f_i^m - f_i|}{f_i^m}$, the total

average error (TAE) as a percentage, where $TAE = \frac{1}{N_m} \sum_{i=1}^{N_m} \frac{|f_i^m - f_i|}{f_i^m}$ ($N_m = 3$), and the coefficient of variation which is obtained

by dividing the standard deviation of the natural frequencies by the updated values. The results obtained by the AHMC algorithm are, on average, better than the initial natural frequencies. The initial error for the first frequency was 0.16 %, and when the AHMC algorithm is applied to update the FEM the error was reduced to 0.05 %. The same comment can be made for the other frequencies. In general, using the AHMC algorithm to update the system reduces the total average error from 9.13 % to only 0.04 %. Also, the coefficient of variation obtained by the AHMC algorithm indicates that the error for all modes is very small.

Figure 6.3 displays the total average error versus the iteration number for the first 5000 iterations. Figure 6.3 is obtained by computing the mean values of samples at every iteration as $\hat{\theta} = E(\theta) \cong \frac{1}{N_s} \sum_{j=1}^i \theta^j$, where i represents the current iteration.

Then, the obtained mean value is used to obtain the new natural frequencies from the FEM and the absolute total average

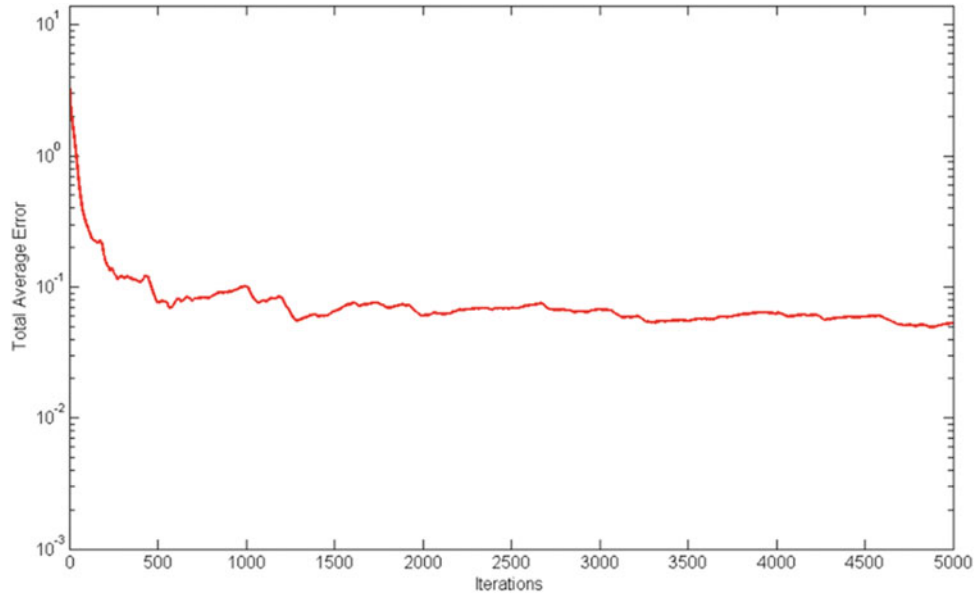


Fig. 6.3 The total average error using the AHMC algorithm

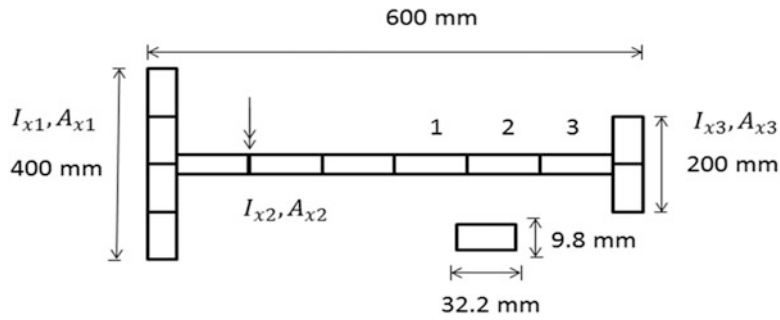


Fig. 6.4 The H-shaped aluminium structure

error is computed by $TAE(i) = \frac{1}{N_m} \sum_{j=1}^{N_m} \left| \frac{f_j^m - f_j}{f_j^m} \right|$. The result plotted in Fig. 6.3 shows that the AHMC algorithm converges reasonably fast and within the first 300 iterations.

In the next section, an unsymmetric H-shaped aluminium structure with real measured data is used to test the AHMC algorithm and the results obtained will be compared with those obtained previously with the HMC algorithm.

6.5 The Unsymmetric H-Shaped Structure

In this section, an unsymmetric H-shaped aluminium [5, 17] structure with real measured data is updated using the AHMC algorithm. This structure is shown in Fig. 6.4. The structure was modelled by assembling 12 beam elements where each element was modelled as an Euler-Bernoulli beam. The position specified by the double arrow in the middle beam (see Fig. 6.4) showed the location where the structure was excited. An electromagnetic shaker was used to excite the structure, and an accelerometer was used to measure the response. A set of 15 frequency-response functions were measured. More details about the structure can be found in [5].

The measured natural frequencies are: 53.9, 117.3, 208.4, 254.0 and 445.0 Hz. In this example, the uncertain parameters are the moments of inertia and the section areas of the three beams (as shown in Fig. 6.4). The AHMC algorithm will be used to obtain the updated vector $\theta = \{I_{x1}, I_{x2}, I_{x3}, A_{x1}, A_{x2}, A_{x3}\}$.

6.5.1 The Unsymmetric H-Shaped Structure Simulation

The parameters of the unsymmetric H-shaped aluminium structure are given as follows: the Young's modulus is set at 7.2×10^{10} N/m², the density is set to 2785 kg/m³. The same simulation sets and boundaries used in [13–17] are used for the AHMC algorithm. To help to keep the uncertain parameters physically realistic, the updated parameter vector is bounded by maximum and minimum values equal to: $[3.73 \times 10^{-8}, 3.73 \times 10^{-8}, 3.73 \times 10^{-8}, 4.16 \times 10^{-4}, 4.16 \times 10^{-4}, 4.16 \times 10^{-4}]$ and $[1.73 \times 10^{-8}, 1.73 \times 10^{-8}, 1.73 \times 10^{-8}, 2.16 \times 10^{-4}, 2.16 \times 10^{-4}, 2.16 \times 10^{-4}]$, respectively.

The likelihood weight β_c (see Eq. (6.2)) is set equal to 10. The coefficients α_i are set equal to $\frac{1}{\sigma_i}$ where $\sigma = [5 \times 10^{-8}, 5 \times 10^{-8}, 5 \times 10^{-8}, 5 \times 10^{-4}, 5 \times 10^{-4}, 5 \times 10^{-4}]$. The number of samples N_s is set to 1000, the initial time step used in the HMC algorithm is $\delta t^0 = 4.5 \times 10^{-3}$ s while the time step is bounded with a minimum value of $\delta t^0 = 0.001 \times 10^{-3}$ s and a maximum value of $\delta t^0 = 7 \times 10^{-3}$ s. L is uniformly distributed on the interval $\{1, 30\}$, the target acceptance rate is $\bar{\alpha} = 0.95$ (95 %), the initial value of the temperature is $T(1) = 1$, and $\bar{\alpha}^T$ is set to 1.0081. N_b is set to 20. The results obtained using the AHMC algorithm, namely the updated parameters and the updated frequencies, are presented in Tables 6.3 and 6.4, respectively.

Figure 6.5 shows the Kernel smoothing density estimation of the updating parameters along with the updated values of the uncertain parameters. The θ_i refers to the sequential numbering of the updating parameters while the normalisation constants θ_i^0 are the initial values of the updated parameters. The obtained results show that the AHMC algorithm identified the high probability region. Moreover, the shapes of the density functions are not Gaussian.

The updated parameter values, the initial values of these parameters and their c.o.v values are given in Table 6.3. The total acceptance rate for the AHMC algorithm is 96.3 % which is very good (only 3.7 % of the computational time was wasted). The AHMC algorithm successfully updated the uncertain parameters (the updated values are different to the initial θ_0). The coefficients of variation obtained by the AHMC algorithm shows that the estimation for the middle beam parameters are better than those of the left and the right beams parameters (the c.o.v of the middle beam is smaller than that for the other two beams). This is obvious since structure was excited in the middle beam, and more information on the middle beam was used in the updating process.

The correlation between all updated parameters, when the AHMC algorithm is used to update the structure, is shown in Fig. 6.6. The uncertain parameters are weakly correlated except for the pair (I_{x2}, A_{x2}) which are highly correlated (the correlation is equal to 0.73).

The unsymmetric H-shaped aluminium structure has been updated many times by different (deterministic and statistic) methods [5]. The Nelder Mead (NM) Simplex method gave a total average error equal 2.14 % [5] while the Genetic Algorithm (GA) [5] reduced the TAE to 1.1 %. On the other hand, the Response-Surface (RS) method [5] produced a higher TAE than the GA algorithm (the total average error was equal to 1.84 %). The Particle Swarm Optimization (PSO) algorithm [5] gave better results and the error was reduced to 0.4 %. Moreover, three MCMC algorithms were applied to this structure, the M-H, SS and HMC algorithms [17], and the results were 3.01, 2.98 and 0.73 %, respectively. Another two modified versions of the HMC algorithm (SHMC and S2HMC algorithms) were also applied to update this structure and the results were 0.66 and 0.58 %, respectively.

Table 6.3 Initial and updated parameters using the AHMC algorithm

	θ_0 vector Initial	θ vector, AHMC method	$\frac{\sigma_i}{\theta_i}$ (%)
I_{x1}	2.73×10^{-8}	3.51×10^{-8}	15.56
I_{x2}	2.73×10^{-8}	2.30×10^{-8}	2.80
I_{x3}	2.73×10^{-8}	3.12×10^{-8}	14.50
A_{x1}	3.16×10^{-4}	3.79×10^{-4}	1.35
A_{x2}	3.16×10^{-4}	2.45×10^{-4}	2.83
A_{x3}	3.16×10^{-4}	2.28×10^{-4}	3.98

Table 6.4 Natural frequencies and errors when AHMC algorithm is used to update the structure

Mode	Measured frequency (Hz)	Initial frequency (Hz)	Error (%)	Frequencies AHMC method (Hz)	Error (%)
1	53.90	51.40	4.63	53.44 (0.87 %)	0.85
2	117.30	116.61	0.59	118.96 (0.96 %)	1.42
3	208.40	201.27	3.42	208.38 (1.04 %)	0.01
4	254.00	247.42	2.59	254.30 (1.40 %)	0.12
5	445.00	390.33	12.28	445.08 (1.21 %)	0.02
Total average error	–	–	4.70	–	0.48

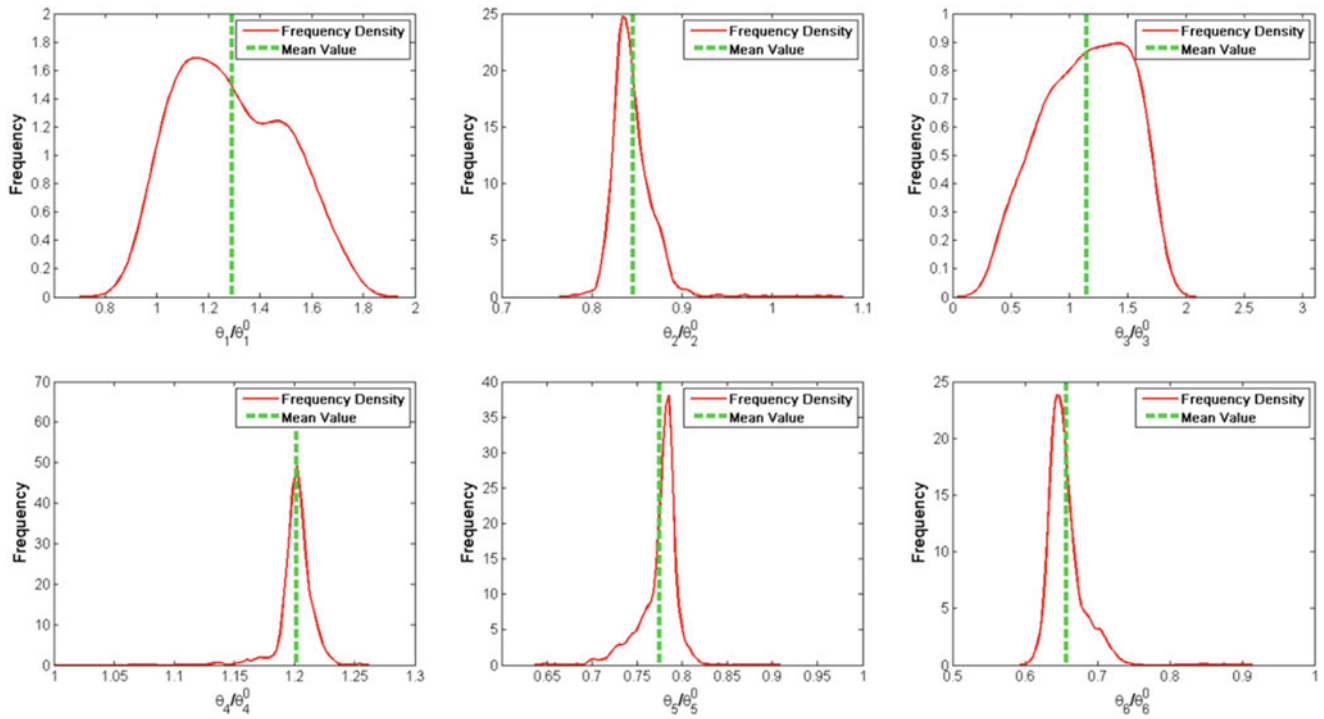


Fig. 6.5 The Kernel smoothing density estimation of updating model parameters using the AHMC method

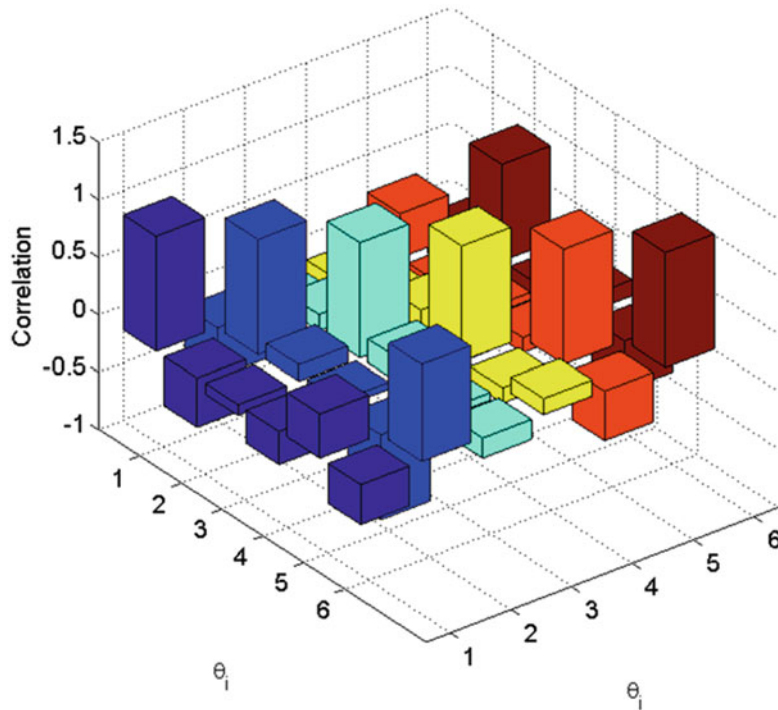


Fig. 6.6 The correlation between uncertain parameters

Table 6.4 presents the updated frequencies obtained by the AHMC algorithm. The initial error for the first measured natural frequency was 4.63 %. When the AHMC algorithm was used to update the structure the error was reduced to 0.85 %. In general, the results obtained by the AHMC algorithm are far better than the initial FEM. The AHMC algorithm reduced the total error to 0.48 % which is good compared to the results obtained in previous works (better than all algorithms except for the PSO algorithm).

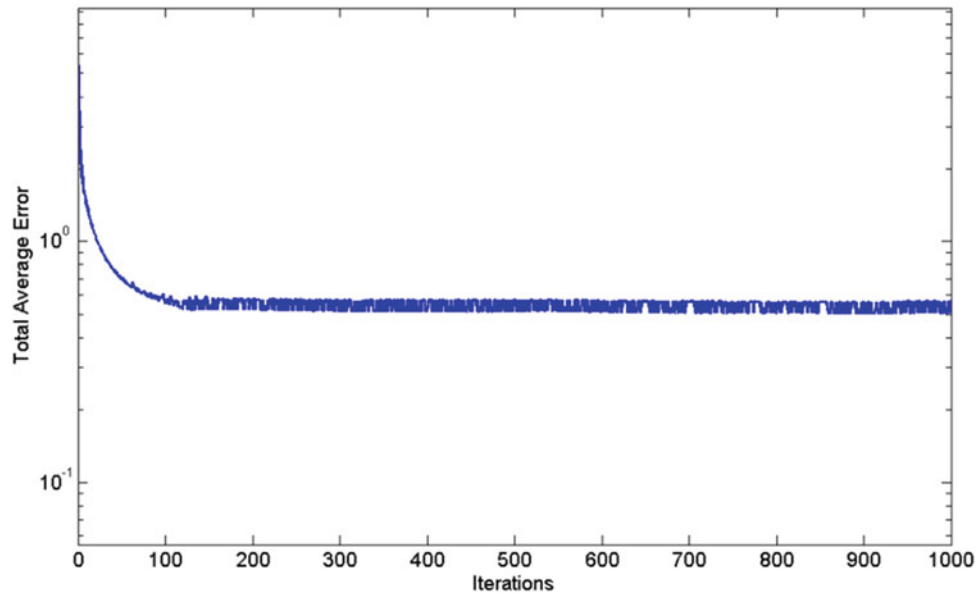


Fig. 6.7 The total average error for the AHMC algorithm

Figure 6.7 shows the variation in the total average error through time (iterations). The strategy used in the first example to plot Figure 6.3 is used again to plot Figure 6.7. The plotted results show that AHMC algorithm converges fast and within the first 100 iterations (100 samples will be enough for the structure to be updated).

6.6 Conclusion

In this paper, an adaptive MCMC algorithm, the Adaptive Hybrid Monte Carlo algorithm, is proposed to solve the Bayesian FEM updating formulation. In this method, the time step was adaptively selected to improve the trajectory length of the algorithm. The method was tested by updating two structural systems: a simulated 3 DOF linear system and an unsymmetric H-shaped aluminium structure. In the first simulation the AHMC technique gave good results and reduced the error to less than 0.05 %. In the second example, the AHMC method also gave good results and reduced the total error to 0.48 %. The results obtained by the AHMC algorithms are better than those obtained by HMC, SHMC and S2HMC algorithms in previous works. The SHMC and S2HMC methods use relatively larger time steps (which means large trajectory moves in the search space), whereas the AHMC algorithm adjusts its time step and temperature at each iteration and this gave the algorithm a significant advantage to escape local solutions. Further work will consider the differences between the above method and other adaptive MCMC algorithms. Also, the AHMC algorithm will be used to update more complex structures.

References

1. Bhatti, M.A.: *Fundamental Finite Element Analysis and Applications*. Wiley, New York (2005)
2. Onâte, E.: *Structural Analysis with the Finite Element Method. Linear Statics, vol. 1: Basis and Solids*. Springer, Dordrecht (2009)
3. Rao, S.S.: *The Finite Element Method in Engineering, 4th edn*. Elsevier Butterworth Heinemann, Burlington (2004)
4. Friswell, M.I., Mottershead, J.E.: *Finite Element Model Updating in Structural Dynamics*. Kluwer, Academic Publishers, Dordrecht (1995)
5. Marwala, T.: *Finite Element Model Updating Using Computational Intelligence Techniques*. Springer, London, UK (2010)
6. Boulkaibet, I., Mthembu, L., De Lima Neto, F., Marwala, T.: Finite element model updating using fish school search optimization method. In: 1st BRICS & 11th CBIC Brazilian Congress on Computational Intelligence, Brazil, 2013
7. Boulkaibet, I., Mthembu, L., De Lima Neto, F., Marwala, T.: Finite element model updating using fish school search and volitive particle swarm optimization. *Integr. Comput. Aid. Eng.* **22**(4), 361–376 (2015)
8. Yuen, K.V.: *Bayesian Methods for Structural Dynamics and Civil Engineering*. Wiley, New York (2010)

9. Haddad Khodaparast, H.: Stochastic Finite Element Model Updating and its Application in Aero-Elasticity. Ph.D. Thesis, University of Liverpool (2010)
10. Marwala, T., Sibisi, S.: Finite element model updating using Bayesian approach. In: Proceedings of the International Modal Analysis Conference, Orlando, Florida, USA, 2005. ISBN: 0-912053-89-5
11. Moens, D., Vandepitte, D.: Recent advances in non-probabilistic approaches for non-deterministic dynamic finite element analysis. Arch. Comput. Meth. Eng. **13**(3), 389–464 (2006)
12. Hanss, M., Willner, K.: A fuzzy arithmetical approach to the solution of finite element problems with uncertain parameters. Mech. Res. Commun. **27**(3), 257–272 (2000)
13. Boulkaibet, I., Mthembu, L., Marwala, T., Friswell, M.I., Adhikari, S.: Finite element model updating using the shadow hybrid Monte Carlo technique. Mech. Syst. Sig. Process. **52**, 115–132 (2015)
14. Boulkaibet, I., Marwala, T., Mthembu, L., Friswell, M.I., Adhikari, S.: Finite element model updating using an evolutionary Markov Chain Monte Carlo algorithm. Dyn. Civil Struct. **2**, 245–253 (2015)
15. Boulkaibet, I., Mthembu, L., Marwala, T., Friswell, M.I., Adhikari, S.: Finite element model updating using the separable shadow hybrid Monte Carlo technique. Top. Modal Anal. II **8**, 267–275 (2014)
16. Boulkaibet, I., Marwala, T., Mthembu, L., Friswell, M.I., Adhikari, S.: Sampling techniques in bayesian finite element model updating. Top. Model Validat. Uncertain. Quantif. **4**, 75–83 (2012)
17. Boulkaibet, I.: Finite element model updating using Markov Chain Monte Carlo techniques. Ph.D. Thesis, University of Johannesburg (2015)
18. Mares, C., Mottershead, J.E., Friswell, M.I.: Stochastic model updating: part 1—theory and simulated example. Mech. Syst. Sig Process. **20**(7), 1674–1695 (2006)
19. Nichols, J., Link, W., Murphy, K., Olson, C.: A Bayesian approach to identifying structural nonlinearity using free-decay response: application to damage detection in composites. J. Sound Vib. **329**(15), 2995–3007 (2001)
20. Ching, J., Muto, M., Beck, J.L.: Structural model updating and health monitoring with incomplete modal data using Gibbs Sampler. Comput. Aid. Civil Infrast. Eng. **21**(4), 242–257 (2006)
21. Ching, J., Chen, Y.J.: Transitional Markov chain Monte Carlo method for Bayesian model updating, model class selection, and model averaging. J. Eng. Mech. **133**(7), 816–832 (2007)
22. Muto, M., Beck, J.L.: Bayesian updating and model class selection for hysteretic structural models using stochastic simulation. J. Vib. Control **14**, 7–3 (2008)
23. Cheung, S.H., Beck, J.L.: Bayesian model updating using hybrid Monte Carlo simulation with application to structural dynamic models with many uncertain parameters. J. Eng. Mech. **135**(4), 243–255 (2009)
24. Duane, S., Kennedy, A.D., Pendleton, B.J., Roweth, D.: Hybrid Monte Carlo. Phys. Lett. B **195**(2), 216–222 (1987)
25. Kennedy, A.D., Pendleton, B.: Acceptances and autocorrelations in hybrid Monte Carlo. Nucl. Phys. B Proc. Suppl. **20**, 118–121 (1991)
26. Beskos, A., Pillai, N.S., Roberts, G.O., Sanz-Serna, J.M., Stuart, A.M.: Optimal tuning of the hybrid Monte-Carlo algorithm. Bernoulli, **319**(5A), 1501–1534 (2011)
27. Bishop, C.M.: Pattern Recognition and Machine Learning. Springer, New York (2006)
28. Neal, R.M., MCMC using Hamiltonian dynamics. Handbook of Markov Chain Monte Carlo, volume 2, pp. 113–162. Chapman & Hall/CRC Press, Boca Raton, FL (2011)
29. Andrieu, C., Thoms, J.: A tutorial on adaptive MCMC. Stat. Comput. **18**(4), 343–373 (2008)
30. Neal, R.M.: Annealed importance sampling. Stat. Comput. **11**(2), 125–139 (2001)

Chapter 7

Modal Parameters of Multiple-Disk Shaft System from Multiple Reference Impact Test

Naim Khader and Mohammad Ramadan

Abstract The proposed work is intended for Experimental Modal Analysis (EMA) of a multi-disk shaft system to estimate its modal parameters, i.e., natural frequencies, damping ratios, and mode shapes. The considered system is excited by a roving impact hammer at a set of excitation points, and the vibration response is measured at a number of response points (taken as reference points) using piezoelectric accelerometers. The Frequency Response Function (FRF) matrix and the corresponding Impulse Response Function (IRF) matrix are estimated, which allows the detection and estimation of repeated or closely coupled modes, known to exist in the considered structure. The estimated FRF and IRF matrices are employed with both time and frequency domain algorithms to estimate the desired modal parameters. Modal frequencies are estimated from Finite Element analysis using ANSYS and compared with the experimentally obtained frequencies.

Keywords Mechanical vibrations • Modal analysis • Structural dynamics • Rotor dynamics • Modal parameter estimation

7.1 Introduction

The multi disk-shaft system is found in numerous mechanical and aerospace applications, such as compressors, turbines, and hard disk drives. Stringent requirements on such systems resulted in highly flexible structure with strong coupling between modes of constituent components, i.e., modes of the shaft and individual disks. It is therefore of great importance to accurately predict their modal parameters to come up with a reliable design, free from resonance vibration during operation. This subject was examined by several researchers who employed different theoretical, numerical and experimental approaches to address this problem. Shahab and Thomas [1] developed a thick sector element to investigate the coupling effects between disks and shaft modes on the dynamic characteristics of the multiple-disk shaft system. Wu and Flowers [2] developed a transfer matrix procedure to account for disk flexibility and to investigate how it might influence the natural frequencies and critical speeds of practical rotors. Lee et al. [3] also used the substructure synthesis and the assumed modes method to calculate the natural frequencies of the coupled vibration of flexible shaft-multiple flexible disk systems, typically found in computer hard disk drives. They introduced some tuning parameters to accurately model the considered system, which resulted in close agreement between theoretical and experimental results of the examined hard disk drive spindle system. Lee and Chun [4] studied the effect of multiple flexible disks on the vibration modes of a flexible shaft using the assumed modes method, which was applied to computer hard disk drive spindle system and to a simple flexible rotor system with two flexible disks. Jia [5] used the substructure synthesis technique to examine the coupled bending vibration of a multi span shaft, modeled as a Timoshenko beam, carrying several flexible circular disks and supported by multiple isotropic journal bearings. Jang et al. [6] used the finite element method and substructure synthesis technique to examine the free vibration of a spinning flexible disk-spindle system supported by ball bearing and flexible shaft and performed modal testing to verify theoretical results. Shen et al. [7] studied the vibration of a rotating spindle carrying multiple flexible disks mounted on a flexible housing-stator assembly through ball bearings or hydrodynamic bearings. They measured the natural frequencies of a ball bearing spindle with different housing configurations to verify the presented mathematical model. Hili et al. [8] analyzed the free vibration of a spinning disk-shaft system using finite element method and evaluated the effect of rotor speed, disk flexibility, and boundary conditions on the system's natural frequencies. Khader et al. [9] presented a theoretical model based on the

N. Khader (✉)

Department of Mechanical Engineering, Jordan University of Science & Technology, (JUST), P.O. Box 3030, Irbid 22110, Jordan
e-mail: nkhader@just.edu.jo

M. Ramadan

Department of Aeronautical Engineering, Jordan University of Science & Technology, (JUST), P.O. Box 3030, Irbid 22110, Jordan

assumed modes method to examine the coupled multiple disk-flexible shaft system, and compared theoretical results with the experimentally determined natural frequencies, which were identified from the peaks of the obtained Frequency Response Functions (FRF), relating a single measured response with a single excitation from an impact hammer. It is known that the considered system has repeated frequencies, and the single input/single output scheme is not the appropriate choice, and one has to employ a multiple input/multiple output estimation scheme to predict the modal parameters of such systems. Khader [10] employed a multiple input/multiple output modal parameter estimation scheme in the frequency domain to estimate modal parameters of the coupled vibration of a flexible disk-flexible shaft system from theoretically generated FRF matrix, obtained from simulated excitation and response data.

This work presents an estimate of the modal parameters of a multiple disk-shaft structure, which consists of three flexible disks, rigidly attached to a flexible shaft. The disk shaft assembly is supported by soft supports at its free ends.

Multi Reference Impact Testing (MRIT) is adopted, where the structure is hit by a roving impact hammer at a number of excitation points and the acceleration is measured at another number of response points. A force window is applied to the captured signal from the impact hammer, with subsequent application of an exponential window to both impact hammer and accelerometer signals. The H_1 approach is used to estimate the FRF with ten averages for each excitation. Seven accelerometers were used to collect the response signal and 36 points were impacted by the hammer, resulting in a FRF matrix $[H]_{N_o \times N_i}$ with $N_o = 36$ and $N_i = 7$. The corresponding IRF matrix is obtained by the Inverse Fast Fourier Transform (IFFT) of the FRF matrix. A low order Unified Matrix Polynomial Approach (UMPA) and Eigensystem Realization Algorithm (ERA) were applied in the time domain, and the Polyreference Least Squares Complex Frequency (LSCF) algorithm, known as PolyMax, was applied in the frequency domain to estimate the desired modal parameters of the tested structure.

7.2 Multiple Reference Impact Testing

The presented work employs the Multiple Reference Impact Testing (MRIT) [11–13], which is a modal testing method, where the tested system is excited by a roving hammer (at a number of input dofs) and the response is measured at number of fixed response points (output dofs). By the principle of reciprocity of the FRFs, the output dofs are taken as the references and the input dofs are used to estimate system mode shapes.

For each impact point, a set of FRFs is estimated to relate the impact force to the measured responses at the fixed response points, which is equivalent a set of single-input multiple-output FRFs for each input dof. Thus, multiple impact points result in a multiple reference FRF matrix and multiple reference estimation algorithms can be used to estimate the desired modal parameters of the considered system.

The required equipment to employ the MRIT in the presented work is restricted to an instrumented impact hammer; seven PCB accelerometers model 352C03, and an 8-channel USB dynamic acquisition system with built-in signal conditioning. The dynamic acquisition system is connected to a host PC, which hosts Labview software for data acquisition. The acquired force and response signals are subsequently analyzed in MATLAB.

7.3 Experimental Setup and Procedure

The experimental setup used in the present work is shown in Fig. 7.1, where one can identify the following main components:

1. The test structure, which consists of three flexible disks clamped at their inner radius to the outer radius of the supporting shaft. The complete system is supported by soft supports at the free ends of the shaft.
2. An impact hammer, instrumented with a load cell is used to excite the test system. Force signal from the hammer is fed to the first channel of the dynamic acquisition system.
3. Seven piezoelectric accelerometers with built-in charge amplifiers are used to capture the response at reference dofs. The accelerometers are attached at the selected reference dofs by magnetic mounting studs. Response signal captured by the accelerometers are fed to the remaining seven channels of the dynamic signal acquisition system.
4. An USB 8-channel dynamic acquisition system (CompatDaq)
5. Personal Computer which hosts the data acquisition software, signal processing software, and modal parameter estimation algorithm.

When the test setup is complete, one proceeds to collect force and response data to estimate FRFs between reference dofs and the input dof, associated with the roving hammer. Ten averages are completed for each impact location with emphasis



Fig. 7.1 Experimental setup

to impact at the same location, along the same normal direction to the surface of test structure at impact location and with almost the same force level for each average as possible.

During data collection, a pretrigger delay is specified so no part of the impact pulse is lost, which results in distorted impulse spectrum and adversely affects the estimated FRFs. The same pretrigger delay is specified for all channels. Each impact test is examined before being accepted to make sure there is no double hit and the magnitude of the input spectrum does not decrease more than 20 dB in the frequency range of interest.

7.4 Frequency Response Functions

Force and exponential windows have been used in the estimation of FRFs from impact test. The force window is used to improve the signal-to-noise ratio of the impulsive force, and the exponential window is used to reduce leakage errors. For the same purpose, i.e., to reduce leakage errors, a longer time record was collected to make sure that the response completely decays in the observed time. Details about the used force and exponential windows can be found in [14, 15].

Response and excitation signals $x_i(t)$ and $f_j(t)$ are acquired and digitized by the dynamic signal acquisition system. Frequency spectra of these signals $X_i(\omega)$ and $F_j(\omega)$ are obtained by Discrete Fourier Transforms (DFT), which are used to estimate the FRF relating these dofs H_{ij} , and the corresponding coherence function γ_{ij}^2 . According to the H_1 algorithm, the FRF is given by:

$$H_{ij} = G_{X_i F_j} / G_{F_j F_j} \quad (7.1)$$

The coherence function is given by:

$$\gamma_{ij}^2(\omega) = |G_{F_j X_i}(\omega) G_{X_i F_j}(\omega)| / G_{X_i X_i}(\omega) G_{F_j F_j}(\omega) \quad (7.2)$$

Where:

$G_{X_i F_j}(\omega) = X_i(\omega) F_j^*$, $G_{F_j X_i}(\omega) = F_j(\omega) X_i^*$, $G_{F_j F_j}(\omega) = F_j(\omega) F_j^*$, and $G_{X_i X_i}(\omega) = X_i(\omega) X_i^*$ are the auto- and cross-power spectra of the force and response signals, and (*) denotes complex conjugate.

Examples of the estimated FRFs and coherence functions are presented in Figs. 7.2 and 7.3.

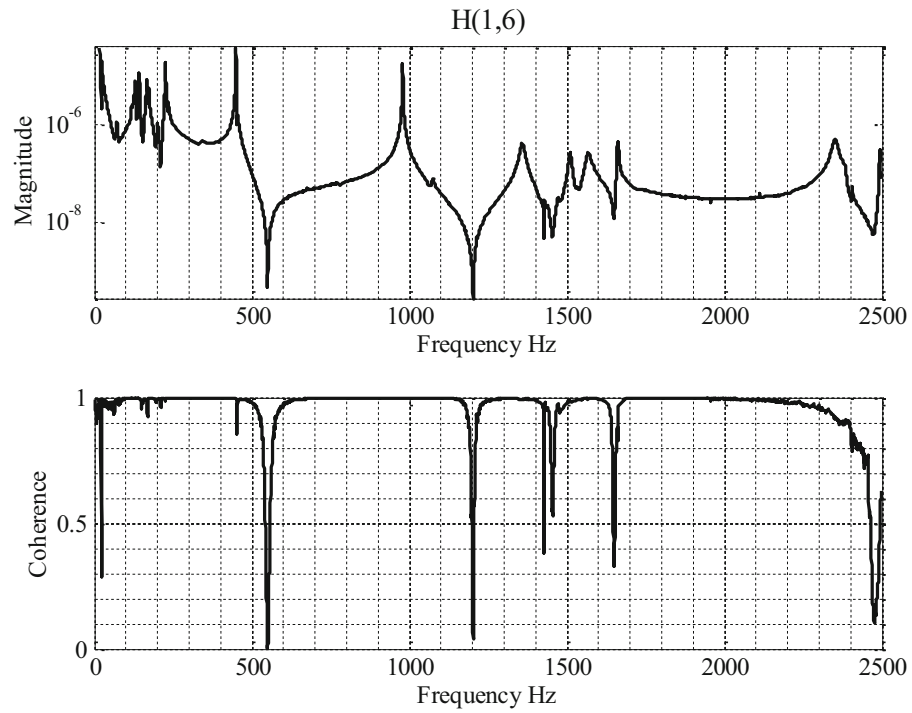


Fig. 7.2 Driving point FRF and coherence between excitation 1 and reference 6

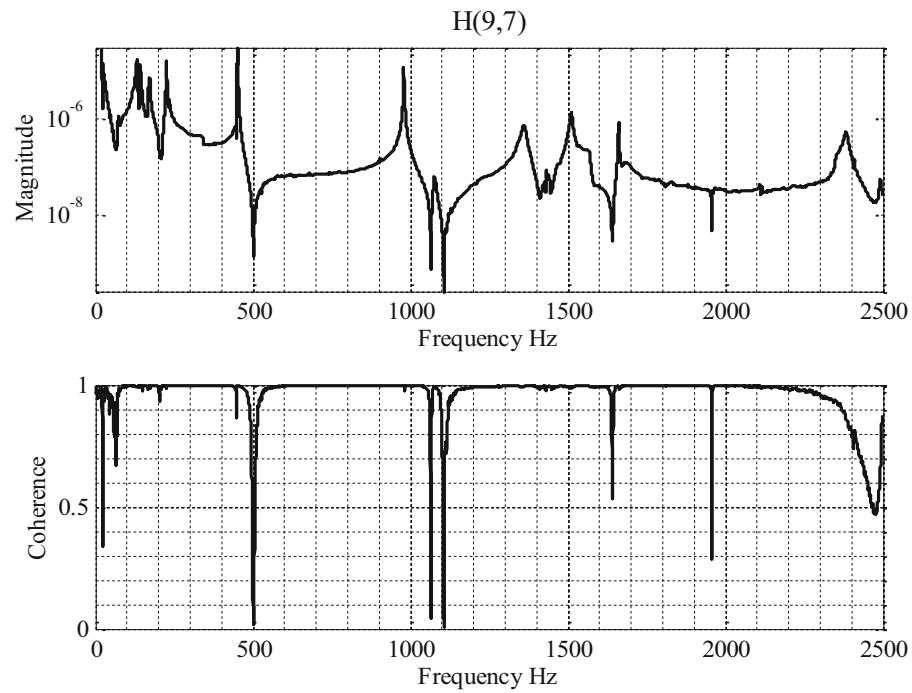


Fig. 7.3 Driving point FRF and coherence between excitation 9 and reference 7

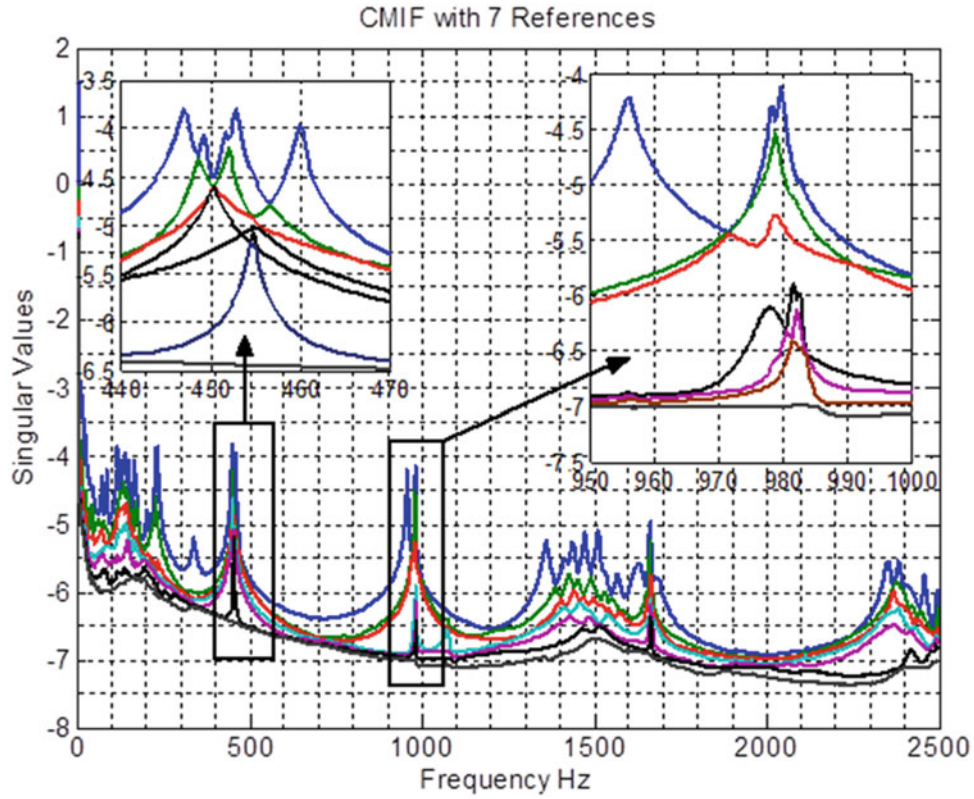


Fig. 7.4 CMIF with 7 reference dofs

7.5 Modal Parameter Estimation

The Complex Mode Indicator Function (CMIF) of the estimated FRF matrix is examined first. The CMIF [16, 17] is a plot of the singular values (Σ_k) of the FRF matrix, obtained from Singular Value Decomposition (SVD) for each spectral line, i.e.

$$[H(\omega_k)]_{(N_o \times N_i)} = [U_k]_{(N_o \times N_i)} [\Sigma_k]_{(N_i \times N_i)} [V_k]^H_{(N_i \times N_i)} \quad (7.3)$$

Where $[U_k]_{(N_o \times N_i)}$ is the matrix of left singular vectors, $[\Sigma_k]_{(N_i \times N_i)}$ is a diagonal matrix of the singular values, and $[V_k]_{(N_i \times N_i)}$ is the matrix of right singular vectors at the k -th spectral line. Peaks in the CMIF curves occur at the damped natural frequencies of the considered structure, and the left and right singular vectors associated with these peaks give approximation to the corresponding mode shapes and modal participation factors, respectively. CMIF gives insight about the appropriate model order, the existence of repeated or closely related modes, and how modes are distributed in the frequency range of interest. CMIF for two cases, one with 7 and the other with 4 reference dofs are shown in Figs. 7.4 and 7.5, respectively.

7.6 Time Domain Algorithm

In the time domain, the Eigensystem Realization Algorithm (ERA), which was originally developed by Juang [18, 19] and its equivalent first order UMPA algorithm in the time domain [20–22] are employed. The ERA algorithm was originally developed by NASA to construct a state space model from MIMO test data, and UMPA was developed as a general estimation approach, with the different estimation algorithms being special cases of this general approach in both time and frequency domains.

Formulation of the UMPA time domain is based on the following general equation:

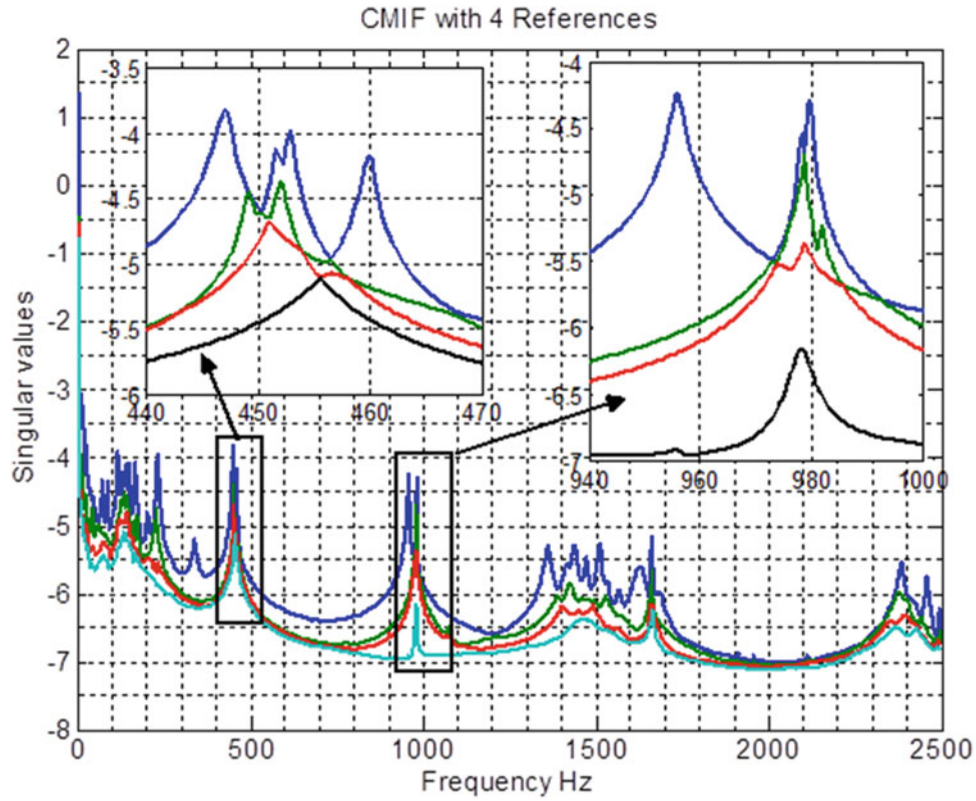


Fig. 7.5 CMIF with 4 reference dofs

$$\sum_{k=0}^n [\tilde{\alpha}_k]_{N_o \times N_o} [h_{t+k}]_{N_o \times N_i} = [0]; \quad \text{for } t = 0 \cdots N \quad (7.4)$$

Where $[\tilde{\alpha}_k]$, is the k-th polynomial coefficient matrix and $[h_{t+k}]$ is the IRF at the k-th time shift. In the employed first order UMPA model, only $[\tilde{\alpha}_0]$ and $[\tilde{\alpha}_1]$ are used in the expansion. Additional time shifts are added to this basic form to make sure the size of the coefficient matrix is enough to determine the desired number of modes, which results in following expanded form of the equation:

$$[\alpha_0] \begin{bmatrix} h_0 & h_1 & h_2 & \cdots & h_N \\ h_1 & h_2 & \cdots & h_N & h_{N+1} \\ \vdots & & & & \vdots \\ h_{n-1} & & & & h_{N+n-1} \end{bmatrix} = -[\alpha_1] \begin{bmatrix} h_1 & h_2 & h_3 & \cdots & h_{N+1} \\ h_2 & h_3 & \cdots & h_{N+1} & h_{N+2} \\ \vdots & & & & \vdots \\ h_n & & & & h_{N+n} \end{bmatrix} \quad (7.5)$$

This can be expressed in the following compact form:

$$[\alpha_0] [H_0] = -[\alpha_1] [H_1] \quad (7.6)$$

Both $[\alpha_0]$ and $[\alpha_1]$ are rectangular matrices of order $n \times N_o$, $[H_0]$ and $[H_1]$ are the Hankel matrices, constructed from the IRF matrix $[h(t)]_{N_o \times N_i}$. The corresponding matrix coefficient characteristic polynomial is given by:

$$[\alpha_1] z^{(1)} + [\alpha_0] z^{(0)} = 0 \quad (7.7)$$

Where $z = e^{\lambda \Delta t}$ and Δt is the time between consecutive samples.

For high order normalization i.e., $[\alpha_1] = [I]$, the companion matrix is simply $[\alpha_0]$ and the resulting eigenvalue problem is:

$$[\alpha_0] \{\phi\} = \lambda_z \{\phi\} \quad (7.8)$$

$$\text{Where } \{\phi\} = \begin{Bmatrix} \lambda_z^{n-1} \psi \\ \lambda_z^{n-2} \psi \\ \vdots \\ \lambda_z \psi \\ \psi \end{Bmatrix}$$

The desired eigenvalues $\lambda_r = \sigma_r + j\omega_r$ of considered system are obtained from eigenvalues $(\lambda_z)_r$ of the formulated eigenvalue problems above with $\sigma_r = \text{Re}\left(\frac{\ln(\lambda_z)_r}{\Delta t}\right)$ and $\omega_r = \text{Im}\left(\frac{\ln(\lambda_z)_r}{\Delta t}\right)$.

7.7 Frequency Domain Algorithm

In the frequency domain, the Polyreference Least-Squares Complex Frequency algorithm, known as ‘‘PolyMAX’’ is employed. The Polyreference Least-Squares Complex Frequency algorithm uses the right matrix-fraction description to represent the estimated FRF matrix from measured data

$$\widehat{H}(\Omega_f, \theta) = B(\Omega_f, \theta) A^{-1}(\Omega_f, \theta) \quad (7.9)$$

Where $\widehat{H}(\Omega_f, \theta) \in \mathbb{C}^{N_o \times N_i}$ is the model FRF matrix, $B(\Omega_f, \theta) \in \mathbb{C}^{N_o \times N_i}$ is the numerator matrix polynomial, and $A(\Omega_f, \theta) \in \mathbb{C}^{N_i \times N_i}$ is the denominator matrix polynomial for N_o output and N_i input dofs. The row corresponding to the o -th output dof in the right matrix-fraction description model is expressed as

$$\left[\widehat{H}_o(\Omega_f, \theta) \right] = \left[B_o(\Omega_f, \theta) \right] A^{-1}(\Omega_f, \theta) \quad (o = 1, 2, \dots, N_o)$$

Numerator $B_o(\Omega_f, \theta)$ and dominator $A(\Omega_f, \theta)$ matrix polynomials are assumed in the form:

$$B_o(\Omega_f, \theta) = \sum_{j=0}^n b_{oj} \Omega_f^j, \quad b_{oj} \in \mathbb{R}^{1 \times N_i}$$

$$A(\Omega_f, \theta) = \sum_{j=0}^n a_j \Omega_f^j, \quad a_j \in \mathbb{R}^{N_o \times N_i}$$

For a frequency domain model, which is derived from a discrete time model, basis functions are expressed as $\Omega_f = e^{-j\omega_f T_s}$ where T_s is the sampling period. The unknown matrix coefficients b_{oj} and a_j , which need to be determined, are grouped in one parameter matrix $\theta = [\beta_1^T, \beta_2^T, \dots, \beta_{N_o}^T, \alpha^T]^T$ where $\beta_o = [b_{o0}, b_{o1}, b_{o2}, \dots, b_{on}]^T \in \mathbb{R}^{(n+1) \times N_i}$ and $\alpha = [\alpha_o, \alpha_1, \alpha_2, \dots, \alpha_n]^T \in \mathbb{R}^{(n+1)N_i \times N_i}$ with n being the model order. If the model FRF is replaced by the measured FRF and right multiplying with the denominator matrix polynomial, a linearized weighted error function is obtained

$$\varepsilon_o(\Omega_f, \theta, H_o) = W_o(\omega_f) B_o(\Omega_f, \theta) - H_o(\omega_f) A(\Omega_f, \theta) \quad (7.10)$$

$W_o(\omega_f)$ is a weighting function. The least-squares cost function

$$\ell(\theta) = \sum_{o=1}^{N_o} \sum_{f=1}^{N_f} \varepsilon_o \varepsilon_o^T \quad (7.11)$$

is minimized to estimate the unknown matrix polynomial coefficients. A reduced normal equation is formulated and solved for the denominator matrix polynomials, which are used in the companion matrix to solve for system poles and participation factors. Stability diagrams are constructed by solving for different model orders to distinguish between physical and mathematical poles. Details about the Polyreference least-squares complex frequency-domain method can be found in [23, 24].

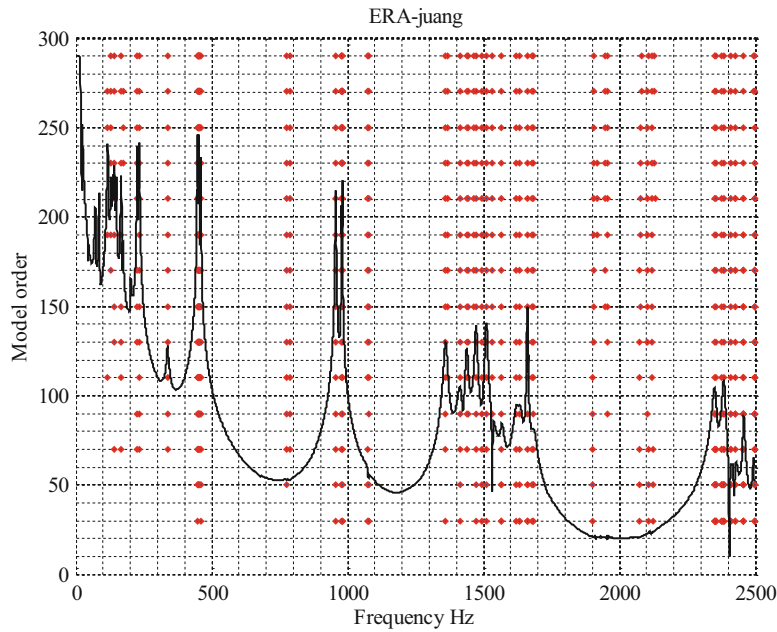


Fig. 7.6 Stability diagram obtained from ERA algorithm

7.8 Results and Discussions

The test structure consists of three identical flexible disks clamped to the shaft at the nondimensional spanwise positions $Z = Z_d/L_s = 0.23, 0.5, \text{ and } 0.77$. The geometric and material properties of the shaft and disks are: $L_s = 0.80\text{ m}$, $R_{out\ disk} = 0.129\text{ m}$, $R_{inner\ disk} = R_{out\ shaft} = 0.01\text{ m}$, $h_{disk} = 0.005\text{ m}$, $E_s = E_d = 200\text{ Gpa}$, $\rho_s = \rho_d = 7850\frac{\text{kg}}{\text{m}^3}$, $\nu_d = \nu_s = 0.3$.

The collected response from 7 reference dofs and 36 excitation dofs (roving hammer) with sampling rate of 5000 Hz and number of collected samples is set to 15k samples. An FRF matrix $[H(\omega)]_{36 \times 7}$ is estimated and representative examples are shown in Figs. 7.2 and 7.3. The CMIF for the cases with 7 and 4 reference dofs are shown in Figs. 7.4 and 7.5. Since the structure comprises three identical disks, and since each disk has repeated modes due its polar symmetry, it is expected to see six closely coupled modes, and this is clearly demonstrated in Fig. 7.4. However, if less than six reference dofs are used (for example 4 reference dofs), the estimated FRF matrix $[H(\omega)]_{36 \times 4}$ results only in four closely coupled modes, as shown in Fig. 7.5. This means it is essential to employ enough reference dofs in the test to reveal all possible closely coupled modes of the test structure, and for the considered three disk-shaft system, the considered 7 reference dofs are sufficient to reveal up to six closely coupled modes.

The corresponding IRF matrix is obtained for the case with 7 dofs, i.e. $[h(t)]_{36 \times 7}$, which is employed in the ERA and its equivalent first order UMPA time domain algorithms. The resulting stability diagrams for these time domain algorithms are shown in Figs. 7.6 and 7.7. In the frequency domain, the estimated FRF matrix is employed with the Polyreference Least Squares Complex Frequency (LSCF) algorithm, and the resulting stability diagram is shown in Fig. 7.8.

Once the poles (and the corresponding modal participation factors) of the tested structure are determined by interpreting the stability diagrams, the corresponding mode shapes can be calculated from the pole-residue model

$$[H(\omega)] = \sum_{r=1}^N \left(\frac{\{v_r\}\langle L_r^T \rangle}{j\omega - \lambda_r} + \frac{\{v_r^*\}\langle L_r^H \rangle}{j\omega - \lambda_r^*} \right) + \frac{LR}{\omega^2} + UR, \text{ where } \{v_r\} \text{ and } \langle L_r^T \rangle \text{ are } r\text{-th mode shape and participation factor,}$$

corresponding to the r -th pole. $(\)^*$, and $(\)^H$ mean complex conjugate and Hermitian of a quantity. LR , and UR represent lower and upper residual effects of the out-of-band modes.

The experimentally obtained results are compared with results from a Finite Element model of the examined three disk-shaft system, where disks were modelled by the shell element SHELL281, which has 8-nodes and with 6 DOFs at each node. The shaft was modelled by the beam element BEAM188, which has 2 nodes with 6 DOFs at each node. Low-stiffness springs were added to simulate the soft support of the shaft at its ends. The employed Finite Element model is shown in Fig. 7.9. The obtained natural frequencies from the Finite Element model are presented on the stability diagram, obtained from the Polyreference Least squares Complex Frequency algorithm in Fig. 7.10. In the Finite Element modelling, perfectly polar symmetric disks are assumed, which are attached to the shaft in the same way. However, life is not perfect, and this

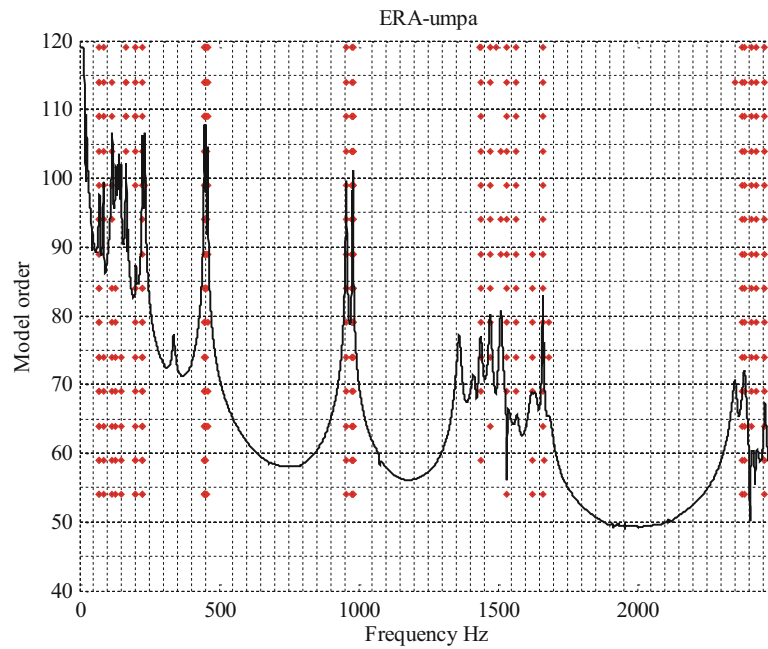


Fig. 7.7 Stability diagram obtained from first order time domain UMPA algorithm

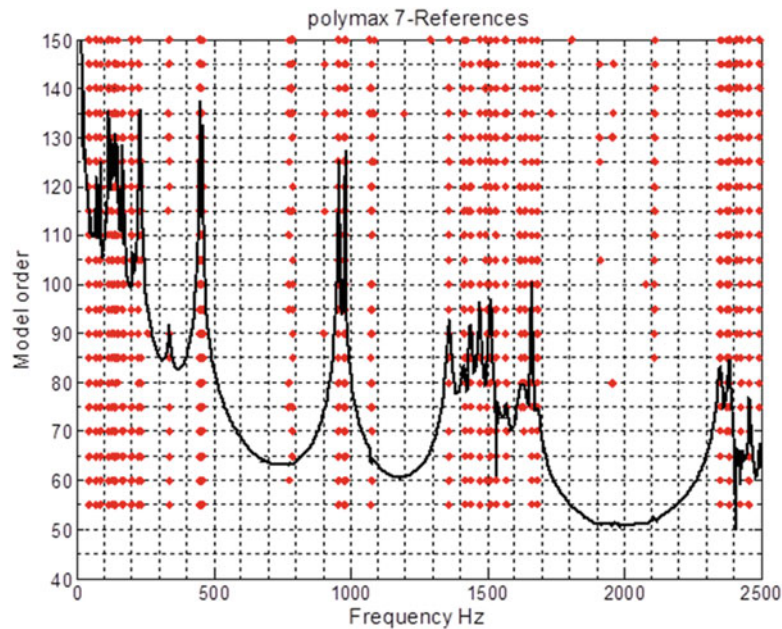


Fig. 7.8 Polymax stability diagram 7-reference dofs

assumption is not satisfied in real life. Therefore, we see in Fig. 7.10, for example, three zero nodal diametral modes with the same frequency of 358.17 Hz, with three different experimental frequencies around 338 Hz, which correspond to this mode. Similarly, there are six identical Finite Element frequencies of 450.24 Hz, which correspond to two identical 2-nodal diametral modes for each of the three identical disks with a total of six identical frequencies. On the other hand, there are six different, but close experimental frequencies in the range 447–460 Hz which correspond these Finite Element frequencies. This is also noticed for higher 3-nodal and 4-nodal diametral modes. The 1-nodal diametral modes are known to be the only disk modes which couple with shaft flexible modes, and this is observed in the range 1350–1570 Hz, with eight coupled modes that correspond to two shaft modes and two modes for each disk with total of eight coupled shaft-disk modes. This is clearly demonstrated in Fig. 7.10.

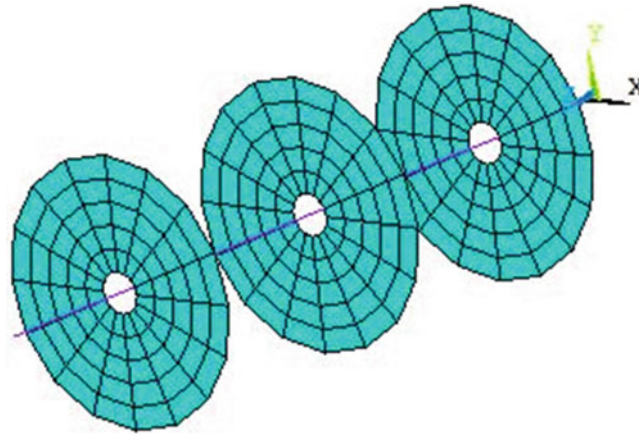


Fig. 7.9 Finite element mesh used in ANSYS

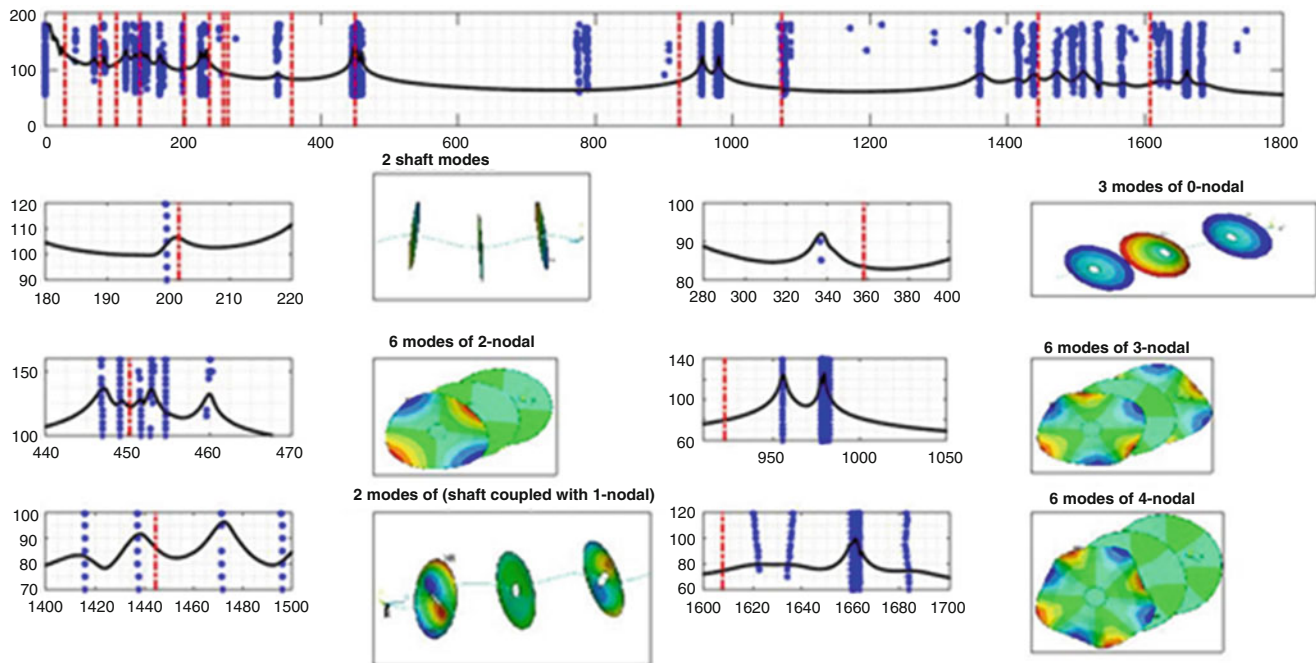


Fig. 7.10 Frequencies from PolyMAX and FE with mode shapes

7.9 Conclusions

The MRIT is used to estimate an FRF matrix of a three-flexible disk-flexible shaft system. Seven reference and 36 excitation dofs are used. CMIF is estimated and gives an initial estimate of the possible modes available in the considered frequency band. ERA and its equivalent first order UMPA time domain algorithms use the estimated IRF matrix, and the Polyreference Least-Squares Frequency Domain algorithm uses the calculated FRF matrix to estimate system poles and modal participation factors in a first step, and the corresponding mode shapes are estimated in a second step from the pole-residue model in a Least-Squares Frequency Domain approach.

Acknowledgement The authors acknowledge support provided the Deanship of Research at Jordan University of Science & Technology (JUST) under grant 2013/198, as well as the valuable discussion with Dr. M. El-Kafay from Vrije Universiteit Brussel, Belgium

References

1. Shahab, A.S., Thomas, J.: Coupling effect of disk flexibility on the dynamic behavior of multi disk-shaft system. *J. Sound Vib.* **114**(3), 435–446 (1987)
2. Wu, F., Flowers, G.T.: A transfer matrix technique for evaluating the natural frequencies and critical speeds of a rotor with multiple flexible disks. *J. Vib. Acoust.* **114**, 242–248 (1992)
3. Lee, C.W., Jia, H.S., Kim, C.S., Chun, S.B.: Tuning of simulated natural frequencies for a flexible shaft-multiple flexible disk system. *J. Sound Vib.* **207**(4), 435–451 (1997)
4. Lee, C.-W., Chun, S.-B.: Vibration analysis of a rotor with multiple flexible disks using assumed modes method. *J. Vib. Acoust.* **120**, 87–94 (1998)
5. Jia, H.S.: On the bending coupled natural frequencies of a spinning, multispan Timoshenko shaft carrying elastic disks. *J. Sound Vib.* **221**, 623–649 (1999)
6. Jang, G.H., Lee, S.H.: Free vibration analysis of a spinning flexible disk-spindle system supported by ball bearing and flexible shaft using the finite element method and substructure synthesis. *J. Sound Vib.* **251**(1), 59–78 (2002)
7. Shen, J.-Y., Tseng, C.-W., Shen, I.Y.: Vibration of rotating disk/spindle system with flexible housing/stator assemblies. *J. Sound Vib.* **271**, 725–756 (2004)
8. Hili, M.A., Fakhfakh, T., Haddar, M.: Vibration analysis of a rotating flexible shaft-disk system. *J. Eng. Math.* **57**, 351–363 (2007)
9. Khader, N., Atoum, A., Al-Qaisia, A.: Theoretical and Experimental modal analysis of multiple flexible disk-flexible shaft system. Paper presented at 2007 SEM annual conference, Springfield, Massachusetts, USA, 3–6 June 2007
10. Khader, N.: Modal parameters of a flexible disk-flexible shaft system from simulated data. *Int. J. Veh. Noise Vib.* **8**(1), 60–73 (2012)
11. Fladung, Jr, W.A.: The development and implementation of multiple reference impact testing. Dissertation, University of Cincinnati (1990)
12. Catbas, F.N., Lenett, M., Brown, D.L., Doebling, S.W., Farrar, C.R., Turer, A.: Modal analysis of multi-reference impact test data for steel stringer bridges. In: Proceedings of the 15th International Modal Analysis Conference, February 1997
13. Brown, D.L., Matthew, C.W.: Review of recent developments in multiple-reference impact testing. *Sound Vib.* **45-1**, 8–17 (2011)
14. Fladung, B.: Windows used for impact testing. In: Proceedings of the 15th International Modal Analysis Conference (IMAC), vol. 2, 1662–1666, February 1997
15. Sohaney, R.C., Nieters, J.M.: Proper use of weighting functions for impact testing. In: Proceedings, of the 3rd International Modal Analysis Conference, Orlando, FL, January 1985
16. Allemang, R.J., Brown, D.L.: A Complete review of the complex mode indicator function (CMIF) with applications. In: Proceedings International Conference on Noise and Vibration Engineering (ISMA), Katholieke Universiteit Leuven, Belgium, 2006
17. Shih, C.Y., Tsuei, Y.G., Allemang, R.J., Brown, D.L.: Complex mode indication function and its application to spatial domain parameter estimation. *J. Mech. Syst. Sig. Process.* **2**, 367–372 (1988)
18. Juang, J.N., Pappa, R.S.: An eigensystem realization algorithm for modal parameter identification and model reduction. *AIAA J. Guid. Control Dyn.* **8**(5), 8620–627 (1985)
19. Juang, J.N.: Mathematical correlation of modal parameter identification methods via system realization theory. *J. Anal. Exp. Modal Anal.* **2**, 1–18 (1987)
20. Allemang, R.J., Brown, D.L.: A unified matrix polynomial approach to modal identification. *J. Sound Vib.* **211**(3), 301–322 (1987)
21. Phillips, A.W., Allemang, R.J.: The unified matrix polynomial approach to understanding modal parameter estimation: an update. In: Proceedings, International Conference on Noise and Vibration Engineering, Katholieke Universiteit Leuven, Belgium, 2004
22. Brown, D.L., Phillips, A.W., Allemang, R.J.: A first order extended state vector expansion approach to experimental modal parameter estimation. Proceedings, International Modal Analysis Conference, 2005
23. Guillaume, P., et al.: A poly-reference implementation of the least-squares complex frequency-domain estimator. Proceedings of IMAC, vol. 21, 2003
24. Peeters, B., et al.: The PolyMAX frequency-domain method: a new standard for modal parameter estimations. *Shock Vib.* **11**(3–4), 395–409 (2004)

Chapter 8

Identification of Aerodynamic Properties of Bridge Decks in Arbitrary Motion

Bartosz Siedziako, Ole Øiseth, and Nils Erik Anders Rønnquist

Abstract Flutter, buffeting response and vortex shedding are crucial factors when designing long-span bridges. An analysis of these phenomena requires experimental data, which can be provided by wind tunnel tests. The forced vibration method is chosen in this study because it is considered to be more reliable and better suited to provide data at high velocities, large amplitudes and more intense turbulence. The models currently used to describe self-excited forces in bridge engineering are linear. However, it is a well-known fact that the principle of superposition does not hold in fluid dynamics. Several case studies have shown that it is a fair approximation when predicting wind-induced dynamic response of bridges if the response is dominated by one vibration mode in each direction. Yet, it is uncertain how well the current models will be able to predict the self-excited forces for a more complicated motion. Currently developing experimental setup will enable the performance of forced vibration tests by applying an arbitrary motion. This paper focuses on extending three identification methods developed for single harmonic motion such that they can be applied in more complex motion patterns. Numerical simulations of forced vibration tests were performed to test the performance of those extended methods.

Keywords Forced vibration test • Arbitrary motion • Aerodynamics • Bridges • System identification

8.1 Introduction

The aerodynamic properties of the bridge deck play an important role in long span bridge design. Wind tunnel tests are therefore commonly carried out in the design process. Currently, sectional model tests, where only a part of the bridge deck is considered, are the most commonly used [1–3]. Compared to other available testing techniques, sectional models are low cost, easy to build and are suitable for relatively small wind tunnels. Moreover, details of the bridge deck known to have significant impact on aerodynamic performance, such as handrails, can be easily reproduced. The main outputs from the tests are static force coefficients and aerodynamic derivatives, which define the self-excited and static wind forces and characterize the overall aerodynamic behavior of the bridge deck.

There exist two main types of sectional model tests. Either the bridge deck is suspended in springs in a free vibration test or it is forced in an oscillatory motion in a forced vibration test. The free vibration method has been the most common method in the past. However, in recent years this trend seems to be changing. Data from forced vibration test are by some researchers considered to be much more reliable and repeatable, [4]. In particular, the forced vibration test outperforms the free vibration test when considering large reduced velocities, large motion amplitudes, high turbulence intensities and cross sections sensitive to vortex shedding [5, 6].

The load models most commonly used in bridge aerodynamics are linear engineering approximations. It has been shown in several case studies that the models are working well when the response of the bridge is dominated by one vibration mode in each direction. Taking into account that the principle of superposition does not hold in fluid dynamics, it is unknown if the models will be able to predict reliable results for a more complex motion. Thus, there is a need to develop a new setup where it is possible to test the accuracy of the linear assumption introduced in the modelling of the self-excited forces. This paper focus on the identification of aerodynamic derivatives by forced vibration tests. Three different methods that work very well for pure harmonic motion have been extended such that a more arbitrary motion can be considered. Chen et al. [7] presented a very convenient and relatively simple frequency domain approach to estimate eight aerodynamic derivatives. The time domain method presented by Han et al. [8] provides the same information, while Cao & Sarkar [5] presented an algorithm to identify rational functions directly from time domain data. The researchers mentioned above developed their

B. Siedziako (✉) • O. Øiseth • N.E.A. Rønnquist

Department of Structural Engineering, Norwegian University of Science and Technology, Richard Birkelandsvei 1a 7491, Trondheim, Norway
e-mail: bartosz.siedziako@ntnu.co

own experimental setups for forced vibration tests and measured accuracy of methods. The motion was however limited to pure harmonic vertical or torsional motion in [8, 9] or coupled vertical-torsional motion in [6]. The presented three approaches are extended here to the 3 Degrees Of Freedom (DOF) case, so that lateral, vertical, and torsional motions can be simultaneously applied.

8.2 Identification Methods

As described in [8, 9], the identification methods commonly used in forced vibration testing have been developed for a pure harmonic motion. Herein these methods are further developed by assuming that the motion is given as sums of harmonic components.

$$p = \sum p_k e^{i\omega_k t} \quad h = \sum h_j e^{i\omega_j t} \quad \alpha = \sum \alpha_l e^{i\omega_l t} \quad (8.1)$$

Here, p , h and α are the lateral, vertical and torsional motions, respectively; p_k , h_j , and α_l are motion amplitudes; ω_k , ω_j , and ω_l are circular frequencies. All of the presented techniques are based on the Scanlan & Tomko [9] representation of the self-excited aerodynamic forces:

$$D_{se} = \frac{1}{2} \rho U^2 B K \left[P_1^*(K) \frac{\dot{p}}{U} + P_5^*(K) \frac{\dot{h}}{U} + P_2^*(K) \frac{B\dot{\alpha}}{U} + KP_4^*(K) \frac{p}{B} + KP_6^*(K) \frac{h}{B} + KP_3^*(K) \alpha \right] \quad (8.2)$$

$$L_{se} = \frac{1}{2} \rho U^2 B K \left[H_5^*(K) \frac{\dot{p}}{U} + H_1^*(K) \frac{\dot{h}}{U} + H_2^*(K) \frac{B\dot{\alpha}}{U} + KH_6^*(K) \frac{p}{B} + KH_4^*(K) \frac{h}{B} + KH_3^*(K) \alpha \right] \quad (8.3)$$

$$M_{se} = \frac{1}{2} \rho U^2 B^2 K \left[A_5^*(K) \frac{\dot{p}}{U} + A_1^*(K) \frac{\dot{h}}{U} + A_2^*(K) \frac{B\dot{\alpha}}{U} + KA_6^*(K) \frac{p}{B} + KA_4^*(K) \frac{h}{B} + KA_3^*(K) \alpha \right] \quad (8.4)$$

Here, ρ is the air density; U denotes the mean wind velocity; B is the bridge deck width; $K = B\omega/U$ is the reduced frequency; P_i^* , H_i^* , and A_i^* , where $i = 1, \dots, 6$ are the so-called aerodynamic derivatives. The equations above provide the motion induced forces for a pure harmonic motion with reduced frequency K . The self-excited forces for a more complicated motion can be obtained applying the principle of superposition.

Chen et al. (2005) This frequency domain method is relatively straight forward. The section model was forced in a pure harmonic motion with reduced frequency K and certain amplitude. The three self-excited force components can then be measured and since the motion is purely horizontal, vertical or torsional it is very easy to calculate the aerodynamic derivatives by considering the complex Fourier amplitudes of the measured self-excited forces. By introducing the arbitrary motion defined in Eq. (8.1) into Eqs. (8.2), (8.3), and (8.4) the method can be extended. Next, by separating the real and imaginary parts of the drag force, $D(K)$, the lift force, $L(K)$ and the pitching moment, $M(K)$, the following expressions are obtained:

$$\text{Re}[D] = \frac{1}{2} \rho U^2 B \left[\sum K_k^2 P_4^*(K_k) \frac{p_k}{B} + \sum K_j^2 P_6^*(K_j) \frac{h_j}{B} + \sum K_l^2 P_3^*(K_l) \alpha_l \right] \quad (8.5)$$

$$\text{Im}[D] = \frac{1}{2} \rho U^2 B \left[\sum K_k^2 P_1^*(K_k) \frac{p_k}{B} + \sum K_j^2 P_5^*(K_j) \frac{h_j}{B} + \sum K_l^2 P_2^*(K_l) \alpha_l \right] \quad (8.6)$$

$$\text{Re}[L] = \frac{1}{2} \rho U^2 B \left[\sum K_k^2 H_6^*(K_k) \frac{p_k}{B} + \sum K_j^2 H_4^*(K_j) \frac{h_j}{B} + \sum K_l^2 H_3^*(K_l) \alpha_l \right] \quad (8.7)$$

$$\text{Im}[L] = \frac{1}{2} \rho U^2 B \left[\sum K_k^2 H_5^*(K_k) \frac{p_k}{B} + \sum K_j^2 H_1^*(K_j) \frac{h_j}{B} + \sum K_l^2 H_2^*(K_l) \alpha_l \right] \quad (8.8)$$

$$\operatorname{Re}[M] = \frac{1}{2}\rho U^2 B^2 \left[\sum K_k^2 A_6^*(K_k) \frac{p_k}{B} + \sum K_j^2 A_4^*(K_j) \frac{h_j}{B} + \sum K_l^2 A_3^*(K_l) \alpha_l \right] \quad (8.9)$$

$$\operatorname{Im}[M] = \frac{1}{2}\rho U^2 B^2 \left[\sum K_k^2 A_5^*(K_k) \frac{p_k}{B} + \sum K_j^2 A_1^*(K_j) \frac{h_j}{B} + \sum K_l^2 A_2^*(K_l) \alpha_l \right] \quad (8.10)$$

The aerodynamic derivatives can then be obtained from the complex Fourier amplitudes of the measured self-excited forces just like in the pure harmonic motion case. The only difference is that there will be several Fourier amplitudes that contribute to the total self-excited forces. In order to easily separate contributions from different aerodynamic derivatives it is important that each selected reduced frequency is only used for horizontal, vertical or torsional motion. Otherwise the Fourier amplitude of the self-excited forces at this reduced frequency will contain contributions relevant to several aerodynamic derivatives, which will make the identification process harder. If $K_k \neq K_j \neq K_l$, the following aerodynamic derivatives can be obtained from the real part of the measured lift force.

$$H_6^*(K_k) = \frac{2}{\rho B^2 \omega_k^2 \rho_k} \operatorname{Re}[L(K_k)] \quad (8.11)$$

$$H_4^*(K_j) = \frac{2}{\rho B^2 \omega_j^2 h_j} \operatorname{Re}[L(K_j)] \quad (8.12)$$

$$H_3^*(K_l) = \frac{2}{\rho B^3 \omega_l^2 \alpha_l} \operatorname{Re}[L(K_l)] \quad (8.13)$$

It is clear that the more reduced frequencies are used to define the motion of the sectional model, the more data points will be provided for the aerodynamic derivatives. Thus, in theory, it is possible to obtain a full set of aerodynamic derivatives from one test in the wind tunnel. This is however not recommended since the principle of superposition does not hold in fluid dynamics and that the load model outlined in Eqs. (8.2), (8.3), and (8.4) is an engineering approximation.

Han et al. (2014) The primary goal of their study was to investigate the influence of traffic flow on bridges on the aerodynamic performance of bridge decks under different wind attack angles using forced vibration tests. A time-domain identification method was applied to identify the aerodynamic derivatives. The researchers claimed that, although time-domain analysis is more complex than frequency domain methods, it provides more accurate results [8]. The aerodynamic derivatives were obtained from the measured aerodynamic forces and the motion time-histories by least-square fitting. First, measurements performed when the wind velocity was equal to zero were used to estimate the structural properties in still air. In the following tests, dynamic forces related to the still-air properties of the model were subtracted from the total forces to obtain the self-excited forces. In order to determine the parameters by least squares fitting the self-excited forces are expressed as

$$\mathbf{Q}_{se,U} = \mathbf{X}_U \mathbf{E} \quad (8.14)$$

$$\mathbf{X}_U = \begin{bmatrix} \dot{p}_1 & \dot{h}_1 & \dot{\alpha}_1 & \alpha_1 & h_1 & p_1 \\ \dot{p}_2 & \dot{h}_2 & \dot{\alpha}_2 & \alpha_2 & h_2 & p_2 \\ \vdots & \vdots & \vdots & \vdots & \vdots & \vdots \\ \dot{p}_n & \dot{h}_n & \dot{\alpha}_n & \alpha_n & h_n & p_n \end{bmatrix} \quad \mathbf{Q}_{se,U} = \begin{bmatrix} D_{se,1} & L_{se,1} & M_{se,1} \\ D_{se,2} & L_{se,2} & M_{se,2} \\ \vdots & \vdots & \vdots \\ D_{se,n} & L_{se,n} & M_{se,n} \end{bmatrix} \quad (8.15)$$

Here, n is the number of data points, $\mathbf{Q}_{se,U}$ symbolizes the vector of self-excited forces, \mathbf{E} contains the unknown parameters, while \mathbf{X}_U contains the displacement and velocity time histories. The matrix \mathbf{E} can then be obtained as follows:

$$e = \mathbf{Q}_{se,U} - \mathbf{X}_U \mathbf{E} \quad (8.16)$$

$$\mathbf{E} = (\mathbf{X}_U^T \mathbf{X}_U)^{-1} \mathbf{X}_U^T \mathbf{Q}_{se,U} \quad (8.17)$$

$$\mathbf{E} = \frac{1}{2}\rho U^2 B \begin{bmatrix} K_p P^*_1/U & K_h P^*_5/U & BK_\alpha P^*_2/U \\ K_p H^*_5/U & K_h H^*_1/U & BK_\alpha H^*_2/U \\ BK_p A^*_5/U & BK_h A^*_1/U & B_2 K_\alpha A^*_2/U \\ K_p^2 A^*_6 & K_h^2 A^*_4 & BK_\alpha^2 A^*_3 \\ K_p^2 H^*_6/B & K_h^2 H^*_4/B & K_\alpha^2 H^*_3 \\ K_p^2 P^*_4/B & K_h^2 P^*_6/B & K_\alpha^2 P^*_3 \end{bmatrix} \quad (8.18)$$

To consider arbitrary motion as defined in Eq. (8.1), the design matrix \mathbf{X}_U must be extended to size $n \times 6N_f$, where n is the number of data points in the time series and N_f is the number of harmonic components used to define the motion.

$$\mathbf{Q}_{se,U} = \mathbf{X}_U^* \mathbf{D}^* \quad \mathbf{X}_U^* = [\mathbf{X}_{U,1} \mathbf{X}_{U,2} \dots \mathbf{X}_{U,f}] \quad \mathbf{D}^* = [\mathbf{D}_1 \mathbf{D}_2 \dots \mathbf{D}_f]^T \quad (8.19)$$

As in the method presented by Chen et al. [7] all the parameters cannot be determined by the pseudo inverse of the design matrix if the same frequency component is used twice, because two columns in \mathbf{X}_U matrix provide same data. In other words, the method can only be applied for a small number of harmonic components and it is required that the frequencies used to define the horizontal, vertical and torsional motion are strictly different.

Cao & Sarkar (2012) This method differs from the two previous since the goal is not to obtain data points for the aerodynamic derivatives at discrete reduced velocities. Instead, main objective is to directly identify the rational function coefficients (RFC) that define the motion to self-excited force transfer functions. The rational function approximation was first used in aerodynamics by Roger [10] and subsequently improved by Karpel [11] and has more recently been applied to predict wind induced dynamic response of bridges by Chen et al. [12], Øiseth et al. [13] and Neuhaus et al. [14]. Chowdhury and Sarkar [15] have recently proposed a method to directly extract the rational function coefficients RFC from free vibration tests. They have also developed a method for forced vibration tests [5], that will be considered in this paper, see also references [16–18] for further details. The self-excited forces can in the Laplace domain be expressed as:

$$\begin{bmatrix} \widehat{\mathbf{D}}_{se} \\ \widehat{\mathbf{L}}_{se} \\ \widehat{\mathbf{M}}_{se} \end{bmatrix} = \begin{bmatrix} 0.5\rho U^2 B & 0 & 0 \\ 0 & 0.5\rho U^2 B & 0 \\ 0 & 0 & 0.5\rho U^2 B^2 \end{bmatrix} \mathbf{Q} \widehat{\mathbf{q}}, \quad \widehat{\mathbf{q}} = \begin{bmatrix} \widehat{p}/B \\ \widehat{h}/B \\ \widehat{\alpha} \end{bmatrix} \quad (8.20)$$

$$\mathbf{Q} = \begin{bmatrix} (A_0)_{11} + (A_1)_{11}p + \frac{F_{11}p}{p+\lambda} & (A_0)_{12} + (A_1)_{12}p + \frac{F_{12}p}{p+\lambda} & (A_0)_{13} + (A_1)_{13}p + \frac{F_{13}p}{p+\lambda} \\ (A_0)_{21} + (A_1)_{21}p + \frac{F_{21}p}{p+\lambda} & (A_0)_{22} + (A_1)_{22}p + \frac{F_{22}p}{p+\lambda} & (A_0)_{23} + (A_1)_{23}p + \frac{F_{23}p}{p+\lambda} \\ (A_0)_{31} + (A_1)_{31}p + \frac{F_{31}p}{p+\lambda} & (A_0)_{32} + (A_1)_{32}p + \frac{F_{32}p}{p+\lambda} & (A_0)_{33} + (A_1)_{33}p + \frac{F_{33}p}{p+\lambda} \end{bmatrix} \quad (8.21)$$

Here, A_0 and A_1 and F represent unknown coefficients, λ denotes an unknown lag term, while $p = iK$ represents the dimensionless Laplace variable. The hat “ $\widehat{}$ ” indicates that the variable is in the Laplace domain. Multiplying Eq. (8.20) by $p + \lambda$ and applying the inverse Laplace transform, the following time-domain equations are obtained:

$$\mathbf{A}_D \mathbf{X}(t) = \dot{\mathbf{D}}(t) \quad \mathbf{A}_L \mathbf{X}(t) = \dot{\mathbf{L}}(t) \quad \mathbf{A}_M \mathbf{X}(t) = \dot{\mathbf{M}}(t) \quad (8.22)$$

$$\mathbf{A}_D = \begin{bmatrix} \psi_1 \\ \psi_2 \\ \psi_3 \\ -\lambda_D \end{bmatrix}^T \quad \mathbf{A}_L = \begin{bmatrix} \psi_4 \\ \psi_5 \\ \psi_6 \\ -\lambda_L \end{bmatrix}^T \quad \mathbf{A}_M = \begin{bmatrix} \psi_7 \\ \psi_8 \\ \psi_9 \\ -\lambda_M \end{bmatrix}^T \quad \mathbf{X}_{D(L)} = \begin{bmatrix} 0.5\rho U^3 \mathbf{q} \\ 0.5\rho U^2 B \dot{\mathbf{q}} \\ 0.5\rho UB^2 \ddot{\mathbf{q}} \\ \mathbf{D}(L)_{se} U/B \end{bmatrix} \quad \mathbf{X}_M = \begin{bmatrix} 0.5\rho U^3 B \mathbf{q} \\ 0.5\rho U^2 B^2 \dot{\mathbf{q}} \\ 0.5\rho UB^3 \ddot{\mathbf{q}} \\ \mathbf{M}_{se} U/B \end{bmatrix} \quad (8.23)$$

Here, the \mathbf{A}_n , $n \in \{D, L, M\}$ matrices contain unknown rational function coefficients that can be identified by least-squares fitting. Each ψ_i is a 1×3 vector since $\mathbf{q} = [p/B \ h/B \ \alpha]^T$. This method is superior to the other methods discussed since it can be used for arbitrary motion directly. The only requirement is that the horizontal, vertical and torsional motions are different such that the matrices \mathbf{X}_n , $n \in \{D, L, M\}$ do not have identical rows.

Table 8.1 Frequency and amplitudes of the harmonic components

Motion	Horizontal			C&S	Vertical			C&S	Torsional			C&S
Frequencies (Hz)	0.75	1.1	1.7	0.6	0.5	0.9	1.8	0.4	0.8	1.2	1.5	0.7
Amplitudes (cm), (rad)	5.0	5.0	5.0	20	20	5.0	5.0	10	0.05	0.05	0.05	0.2

8.3 Numerical Results

The bridge deck of the largest suspension bridge in Norway, the Hardanger Bridge, has been used as a case study in this paper. Experimental data of the aerodynamic derivatives of the cross section are presented in Fig. 8.1 together with a rational function approximation based on experimental data. These data have been obtained by free vibration tests and presented in [19]. Numerical simulations of forced vibration tests have been performed to test the capabilities of the identification methods discussed in this paper. The time histories of the self-excited-forces have been generated using a discrete state space model based on the rational function approach presented by Øiseth et al. [20].

The sectional model motion was generated using frequencies and amplitudes as presented in Table 8.1. Nine harmonic components were used to generate the motion when evaluating the extended version of methods presented by Chen et al. and Han et al. while 12 components (3 additional components are placed in the C&S columns) were used when the method developed by Cao and Sarkar was considered. The frequencies were carefully chosen to fulfill the criteria discussed in the preceding chapters and to ensure that the obtained aerodynamic derivatives were in a range in which they could be compared with the experimental results from the free vibration tests. The simulated time histories of the self-excited forces were contaminated by white noise, such that the ratio between the standard deviation of the noise and the signal is equal to 10 %.

The identified aerodynamic derivatives are presented in Fig. 8.1 together with the rational function approximation used to generate the self-excited forces. Two mean wind velocities, 3 and 5 m/s, were considered when testing the methods developed by Chen et al. and Han et al. while only one mean wind velocity of 4 m/s was considered when the method developed by Cao and Sarkar was considered. As can be seen in this figure, the methods developed by Chen et al. and Han et al. provided identical results that correspond to the rational function approximation used to generate the time histories of the self-excited forces. The method developed by Cao and Sarkar with one lag term provided results of slightly lower accuracy since it cannot obtain the values of the aerodynamic derivatives at discrete reduced frequencies independently, but needs to cover the entire frequency range using the same coefficients for the real and the imaginary part of the transfer functions. However, it is a huge advantage that the method can be easily used for random motion.

8.4 Concluding Remarks

The models currently used to describe self-excited forces in bridge engineering are linear. It is a well-known fact that the principle of superposition does not hold in fluid dynamics. Several case studies have shown that it is a fair approximation when predicting wind-induced dynamic response of bridges if the response is dominated by one vibration mode in each direction. However, it is uncertain how well the current models will be able to predict the self-excited forces for a more complicated motion. Currently developing experimental setup will be capable of forcing the section model of a bridge deck in an arbitrary motion to investigate the accuracy of the current models for self-excited forces. In this paper, several identification techniques were studied to assess whether they can be used for a more random motion of the sectional model. Numerically generated forced vibration test confirmed that all the methods considered can be used for a more general motion than the pure harmonic case. It is also clear that the method suggested by Cao and Sarkar outperforms the others in this setting since far less requirements need to be considered when the random motion is generated.

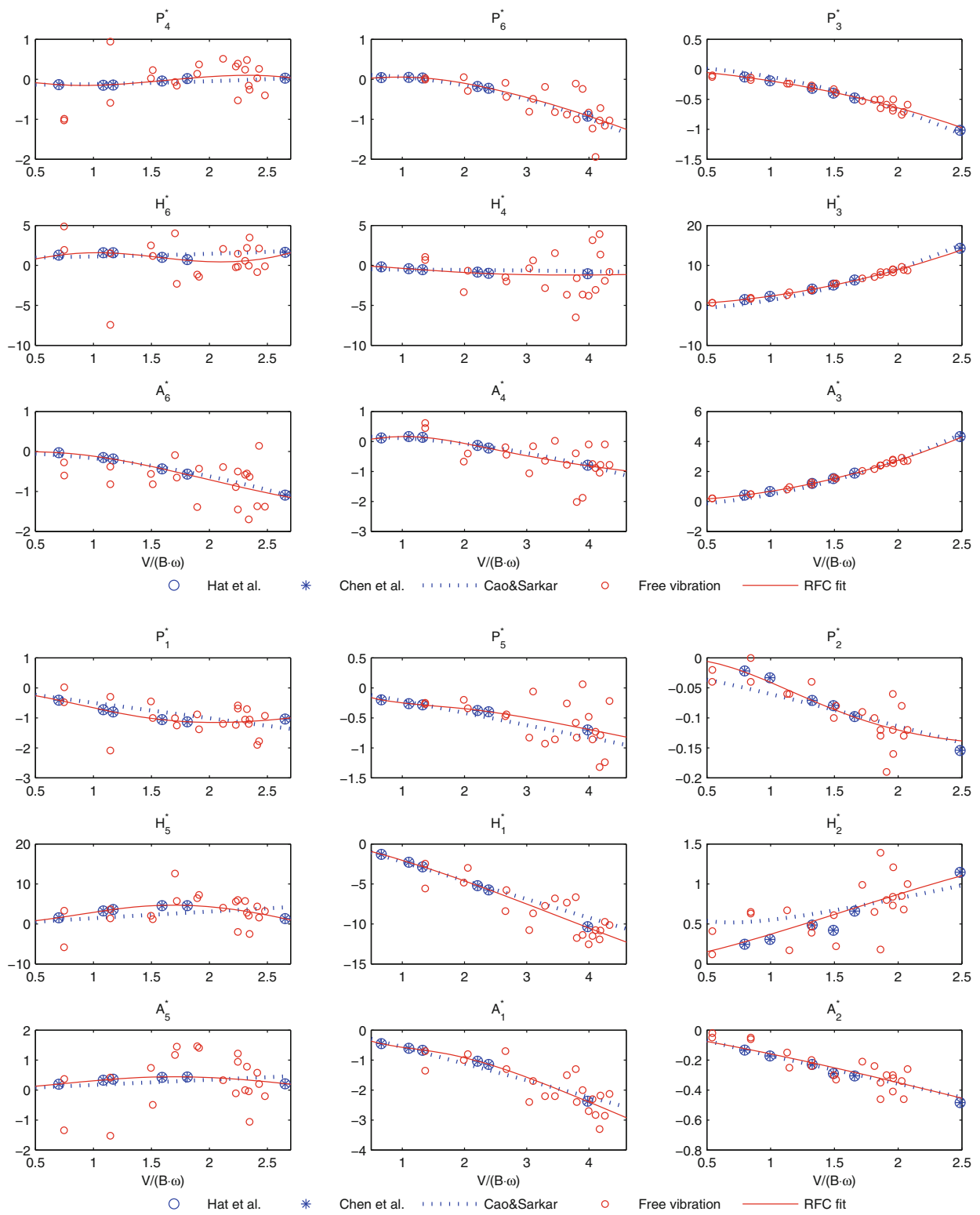


Fig. 8.1 Aerodynamic identified by considering the multi-harmonic motion

References

1. Diana, G., Fiammenghi, G., Belloli, M., Rocchi, D.: Wind tunnel tests and numerical approach for long span bridges: the Messina bridge. *J. Wind Eng. Ind. Aerodyn.* **122**, 38–49 (2013)
2. Zasso, A., Belloli, M., Argentini, T., Flamand, O., Knapp, G., Grillaud, G., Klein, J.F., Virlogeux M. de Ville, V.: Third Bosphorus Bridge aerodynamics: Sectional and full-aerolastic model testing. *Proceedings of the Istanbul Bridge Conference.* (2014)
3. Ge, Y.J., Xiang, H.F.: Recent development of bridge aerodynamics in China. *J. Wind Eng. Ind. Aerodyn.* **96**, 736–768 (2008)
4. Diana G., Rocchi D., Belloli M.: Wind tunnel: a fundamental tool for long-span bridge design. *Struct. Infrastruct. Eng.* **11**(4), 533–555 (2015)
5. Cao, B., Sarkar, P.P.: Identification of Rational Functions using two-degree-of-freedom model by forced vibration method. *Eng. Struct.* **43**, 21–30 (2012)
6. Sarkar, P.P., Caracoglia, L., Haan, F.L., Sato, H., Murakoshi, J.: Comparative and sensitivity study of flutter derivatives of selected bridge deck sections, part 1: analysis of inter-laboratory experimental data. *Eng. Struct.* **31**(1), 158–169 (2009)
7. Chen, Z.Q., Yu, X.D., Yang, G., Spencer, B.F.: Wind-induced self-excited loads on bridges. *J. Struct. Eng.* **131**, 1783–1793 (2005)
8. Han, Y., Liu, S., Hu, J.X., Cai, C.S., Zhang, J., Chen, Z.: Experimental study on aerodynamic derivatives of a bridge cross-section under different traffic flows. *J. Wind Eng. Ind. Aerodyn.* **133**, 250–262 (2014)
9. Scanlan, R.H., Tomko, J.: Airfoil and bride deck flutter derivatives. *J. Eng. Mech. Div.* **97**(6), 1717–33 (1971)
10. Roger, K.L.: Airplane math modeling and active aeroelastic control design[C]. *Agard-Cp-228228* AGARD, 4.1–4.11 (1977)
11. Karpel, M.: Design for active and passive flutter suppression and gust alleviation. NASA contractor report No. 3482 (1981)
12. Chen, X., Matsumoto, M., Kareem, A.: Time domain flutter and buffeting response analysis of bridges. *J. Eng. Mech.* **126**(1), 7–16 (2000)
13. Øiseth, O., Rönquist, A., Sigbjörnsson, R.: Time domain modeling of self-excited aerodynamic forces for cable-supported bridges: A comparative study. *Comput. Struct.* **89**(13–14), 1306–1322 (2011)
14. Neuhaus, C., Mikkelsen, O., Bogunovi, J., Höffer, R., Zahlten, W.: Time domain representations of unsteady aeroelastic wind forces by rational function approximations. In: *EACWE 5 Florence, Italy 19th–23rd July 2009*, vol. 49, July 1–12 2009
15. Chowdhury, A.G., Sarkar, P.P.: Experimental identification of rational function coefficients for time-domain flutter analysis. *Eng. Struct.* **27**, 1349–1364 (2005)
16. Cao, B., Sarkar, P.P.: Identification of Rational Functions by Forced Vibration Method for Time-Domain Analysis of Flexible Structures. In *Proceedings of The Fifth International Symposium on Computational Wind Engineering* (2010)
17. Cao, B.: Time-domain parameter identification of aeroelastic loads by forced-vibration method for response of flexible structures subject to transient wind. *Graduate Theses and Dissertations. Paper 12290* (2012)
18. Chowdhury, A.G.: Identification of frequency domain and time domain aeroelastic parameters for flutter analysis of flexible structures. *Retrospective Theses and Dissertations. Paper 778* (2004)
19. Svend Ole Hansen ApS. The Hardanger Bridge. Static and dynamic wind tunnel tests with a section model. Prepared for: Norwegian Public Roads Administration, Revision 2, March 2009
20. Øiseth, O., Rönquist, A., Sigbjörnsson, R.: Finite element formulation of the self-excited forces for time-domain assessment of wind-induced dynamic response and flutter stability limit of cable-supported bridges. *Finite Elem. Anal. Des.* **50**, 173–183 (2012)

Chapter 9

A Multiphysical Modelling Approach for Virtual Shaker Testing Correlated with Experimental Test Results

S. Waimer, S. Manzato, B. Peeters, M. Wagner, and P. Guillaume

Abstract A virtual shaker testing simulation environment aims to predict the outcome of a spacecraft vibration test numerically, prior to its physical execution at the environmental test facility. Therefore, it needs to comprise the complex dynamical characteristic of the test setup and facility in order to calculate and predict the interaction between the electrodynamic shaker system, test specimen, and vibration controller as it occurs during tests of large spacecraft. A currently derived one-dimensional multiphysical shaker model with three degrees-of-freedom, e.g. the 160 kN electrodynamic shaker of the European Space Agency (ESA), is based on a tailored experimental system identification methodology to estimate the system's parameter. The model is validated by subsequent simulations to recalculate and predict the test results. The main focus of the paper is the enhancement of the shaker model to encompass additionally, lateral and rotational dynamics of the shaker table as well as the coupling with test specimen dynamics and control system performance. The improvements are based on analytical modelling steps in conjunction with the exploitation of experimental test results of hammer impact excitations, and closed-loop random and sine control testing performed on the shaker, loaded with a dummy specimen and excited with different excitation levels.

Keywords Environmental spacecraft testing • Multiphysical system • Modelling and simulation • Experimental system identification • Active control

9.1 Introduction

Environmental testing plays a crucial role in spacecraft engineering to ensure and demonstrate that the designed spacecraft (S/C) will properly perform its intended mission under its operational dynamical loads experienced during its lifecycle. In detail, S/C are tested for vibrations on ground for two main reasons, (1) qualification of the structure by subjecting it to vibration environments representative for launcher loads or operational conditions plus a qualification margin, and (2) validation of the correct workmanship and assembly, so called acceptance testing. In both cases test results are correlated with mathematical models [1, 2].

The main objective of virtual shaker testing [3] is to predict the outcome of a S/C vibration test numerically and especially to improve its accuracy by taking into account the dynamic coupling between the vibration test facility, the S/C structural model and the vibration control system active during test. The outputs of such a simulation environment can be used to assess possible problems during test of the coupled, complex and dynamic system, e.g. beating phenomena which usually occur at structural resonances, and can result in over- or under testing, or even damage of the S/C [4–6]. If the virtual test simulation is performed prior to its physical execution the numerical results can be used to tackle these issues by optimising control parameters and apply notching strategies to improve the entire test performance. As consequence, the virtual shaker testing

S. Waimer (✉)

Siemens Industry Software NV, Researchpark 1237, Interleuvenlaan 68, 3001 Leuven, Belgium

Vrije Universiteit Brussel, Pleinlaan 2, 1050 Brussels, Belgium

e-mail: steffen.waimer@siemens.com

S. Manzato • B. Peeters

Siemens Industry Software NV, Researchpark 1237, Interleuvenlaan 68, 3001 Leuven, Belgium

P. Guillaume

Vrije Universiteit Brussel, Pleinlaan 2, 1050 Brussels, Belgium

M. Wagner

European Space Agency, ESA/ESTEC, Keplerlaan 1, PO Box 299, NL-2200 AG Noordwijk, The Netherlands

methodology results in a tailored test control of complex test specimen and an enhanced correlation between numerical S/C models and physical test results. The simulation environment needs to comprise the main contributors of the vibration test chain: (1) the S/C or structure being tested including all test brackets and adapters, (2) the excitation system (electrodynamic or hydraulic vibration system), and (3) the vibration control system active during test.

This paper summarises the current work which has been performed to derive and validate an electrodynamic numerical shaker model in open and closed loop configuration coupled to a dedicated vibration controller. The coupled shaker and controller numerical model represents the fundamental basis to couple a structural dynamic S/C model in subsequent modelling and simulation tasks. Following, it comprises all contributors of the vibration test chain and being capable to perform virtual shaker testing. Therefore the paper is divided into two basic parts. Section 9.2 presents a review of the currently derived one-dimensional, three degrees-of-freedom (DoF) lumped parameter electrodynamic shaker model in Sect. 9.2.1 and its coupling to a sine sweep testing vibration controller in Sect. 9.2.2. The model is based on test data of a tailored experimental system identification methodology and validated by subsequent simulations to recalculate and predict the results. Section 9.3 contains the main part of the paper which highlights the limitations of the model derived in Sect. 9.2 by exploiting experimental test data of hammer impact excitations in Sect. 9.3.2. Based on these observations an enhanced shaker model is presented in Sect. 9.3.3 and verified in terms of numerical simulations in Sect. 9.3.4.

9.2 Review of Current Work

9.2.1 Part I: Shaker Modelling Theory and Practice

The derivation and validation of the numerical shaker model is based on the technical roadmap as shown in Fig. 9.1. The lumped-parameter, one-dimensional, three DoFs, electromechanical shaker model is derived from [7] and describes a basic model of a Modal shaker which has already been introduced in detail in previous research activities [4, 5, 8]. The physical shaker model consists of a coil which is suspended by rollers or an elastic suspension system in the air gap of a radial magnetic field of an electromagnet. When an electrical current i is conducted through the coil, an axial force, according to the electromagnetic Lorentz Force, is produced,

$$F = Bln \cdot i = k_1 \cdot i \quad (9.1)$$

with the magnetic flux density B in T, the coil length l per turn in m and the number of turns n . This force is transmitted through the suspension system to the table structure resulting in a vertical motion of the table as well as to the test specimen mounted on top. Consequently, a voltage e_{back} is induced back to the electrical system according to Faraday's law due to the relative dynamic motion of the coil \dot{z}_C and body \dot{z}_B in the axial magnetic field of the air gap:

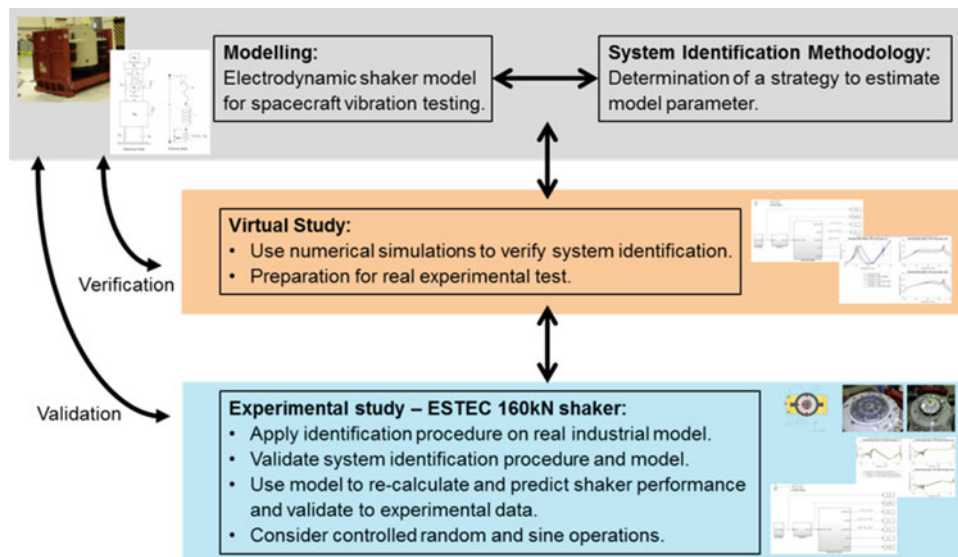


Fig. 9.1 Technical roadmap of the subsequent modelling, simulation and testing steps to derive a numerical shaker model

$$e_{back} = Bln(\dot{z}_C - \dot{z}_B) = k_2 \cdot (\dot{z}_C - \dot{z}_B) \quad (9.2)$$

Hence, the interplay between the shaker's mechanical and electrical system is defined by Eqs. (9.1) and (9.2), whereas, small motion amplitudes are assumed resulting in constant proportionality coupling factors: force-current coupling k_1 in N/A and voltage-velocity coupling k_2 in V/(ms⁻¹). The compliant connection between the armature assembly and the body forms a mass, spring and damper system defining a single DoF system. Adding two more DoFs completes the mechanical model: firstly, the armature structure is modelled as being elastic and not rigid by treating the coil and table as separate masses, connected by a spring and damper system, and secondly, the isolation system of the shaker to the ground is modelled with a second spring and damper system. Consequently, the entire mathematical model in time domain is defined as,

$$\begin{bmatrix} m_c & 0 & 0 & 0 \\ 0 & m_T & 0 & 0 \\ 0 & 0 & m_B & 0 \\ 0 & 0 & 0 & 0 \end{bmatrix} \begin{bmatrix} \ddot{z}_c \\ \ddot{z}_T \\ \ddot{z}_B \\ 0 \end{bmatrix} + \begin{bmatrix} c_c & -c_c & 0 & 0 \\ -c_c & c_C + c_S & -c_S & 0 \\ 0 & -c_S & c_B + c_S & 0 \\ k_2 & 0 & -k_2 & L \end{bmatrix} \begin{bmatrix} \dot{z}_c \\ \dot{z}_T \\ \dot{z}_B \\ \partial i / \partial t \end{bmatrix} + \begin{bmatrix} k_c & -k_c & 0 & -k_1 \\ -k_C & k_C + k_S & -k_S & 0 \\ 0 & -k_S & k_B + k_S & k_1 \\ 0 & 0 & 0 & R \end{bmatrix} \begin{bmatrix} z_c \\ z_T \\ z_B \\ i \end{bmatrix} = \begin{bmatrix} 0 \\ 0 \\ 0 \\ e \end{bmatrix}. \quad (9.3)$$

The mass, stiffness, damping, displacement, velocity and acceleration of the shaker coil, table and body are indicated by the subscripts C , T and B . For heavy test objects, e.g. S/Cs, the shaker is hard mounted to a large seismic block. In this case, the shaker isolation system is clamped and the shaker body mass couples with the mass of the seismic block. The assembly of coil and table is often called armature and represents the moving elements of the electrodynamic shaker. Under these assumptions, the shaker is characterised by three modes of vibration:

- The isolation mode occurs in the low frequency range, where the compliant isolation system allows the entire shaker to translate as a rigid body with almost no relative motion between the components.
- The suspension mode dominates in the low end of the operating range, where the armature assembly moves as a rigid body relatively to the shaker body.
- The coil mode is encountered at or beyond the high frequency limit of operation, where the coil moves out-of-phase with the table as the elastic armature structure is deformed.

At this status, Eq. (9.3) is directly implemented in Matlab/Simulink representing an open-loop system of the vibration control chain. An arbitrary input voltage $u(t)$ represents the output voltage of the vibration controller of the real case, which is amplified by G_V through the amplifier and drives the lumped-parameter shaker model with the shaker input voltage $e(t) = G_V u(t)$. The amplifier is assumed to be in voltage mode resulting in a constant amplification factor G_V and any cut-off frequency of the amplifier is assumed to be much higher than the coil mode frequency to avoid significant phase shifts [9]. An additional loading of the shaker table m_i is modelled as rigid mass. In this case, the shaker table mass in Eq. (9.3) represents the sum of the empty shaker table m_T and the loading m_i .

In parallel, a tailored system identification methodology according to [4, 5, 8] is derived and applied to estimate the physical shaker parameter of Eq. (9.3). The procedure requires test results of at least two different loading configurations on the shaker table (rigid masses) to calculate frequency response functions (acceleration- and voltage-over-current transfer functions, FRF). Subsequently, PolyMAX [10] is applied to estimate the modal parameters of the suspension and coil mode, and using this information to approximate the test results and modes with analytical models to estimate the shaker's mechanical parameter. The electrical system is fully determined by the last line of the matrix formulation in Eq. (9.3) resulting in the estimation of the parameters by solving a least square problem in the Laplace domain.

The system identification is verified in terms of a virtual simulation study [12] and applied to real test data gathered at the system identification test campaign using the 160 kN shaker of the European Research and Technology Centre (ESTEC). A comprehensive test campaign was performed (see Table 9.1) using multiple tri-axial acceleration sensors (low and high frequency performance) mounted on the shaker table and body to record the acceleration responses of different excitations techniques (hammer excitation, controlled sine and random operations) and levels. At this point, only the FRFs based on the acceleration sensor T1, centred on the shaker table in sine and random control testing are used to estimate the shaker parameter to avoid any additional dynamics introduced by lateral or rotational effects. More information about the test results (centred and not-centred sensor location and excitation), sensor setup and instrumentation is presented in [11] and Sect. 9.3.2. The results of the system identification are summarised in Fig. 9.2 using a global approach as reported in [12]. In this case, the experimental results of the first two loading configurations (Empty shaker table and Interface disc) are applied to determine the shaker parameters and used to predict the test performance of the third loading configuration (Interface disc/cuboid). Two different sets of parameter are estimated and applied for the simulation:

Table 9.1 160 kN shaker system identification—test procedure, loading configuration, excitation levels and parameter

Loading configuration	Excitation	Comments		
Empty shaker table $m_i = 0.02$ kg	Hammer impacts	Multiple locations (centred and not-centred)		
Interface disc $m_i = 20.70$ kg	Random control testing, 10–2500Hz	Low level	0.1	$\cdot 10^{-3}$ g rms
		Medium level	1.0	
		High Level	10.0	
Interface disc/cuboid $m_i = 31.15$ kg	Sine control testing, 3–200Hz	Level	0.5	g oct/min
		Sweep rate	0.5	
		Compression factor	8	

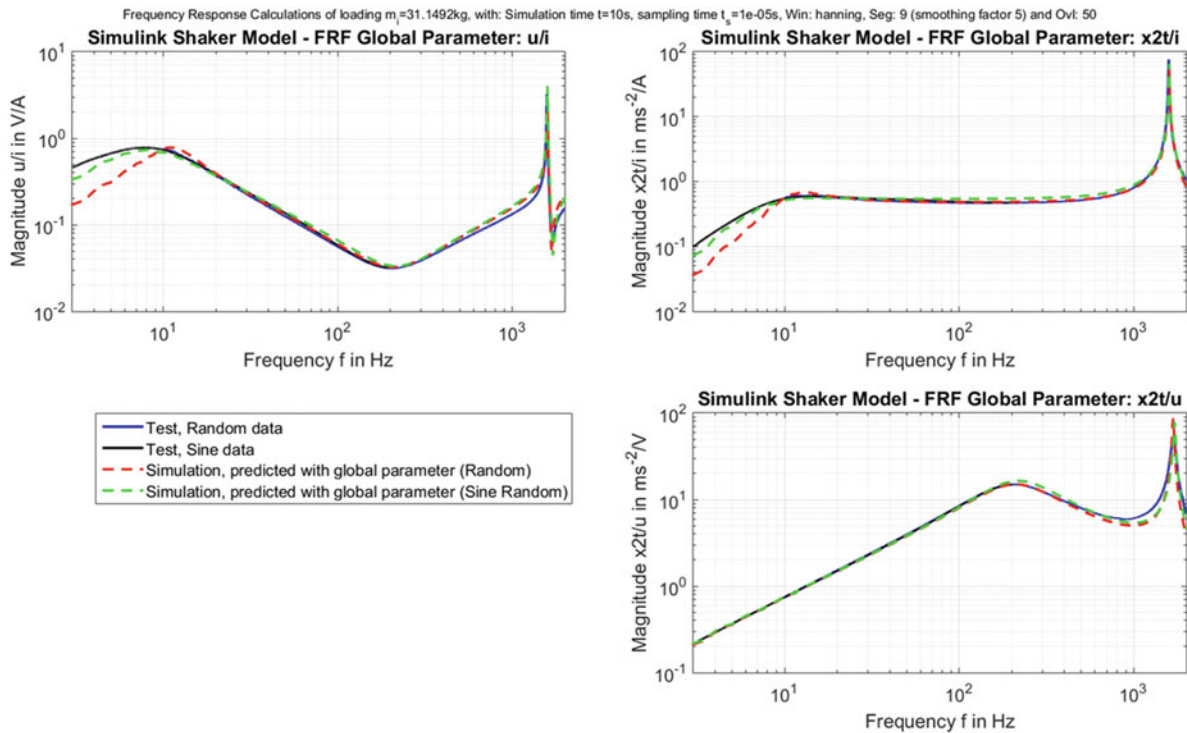


Fig. 9.2 Results of the system identification of ESTEC's 160 kN shaker to predict test results of the Interface disc/cuboid configuration $m_i = 31.149$ kg. Test results random (blue) and sine (black) control testing. Red - numerical prediction of test results using random control data only. Green - numerical prediction of test results using combined sine and random control data for system identification

- Only the high level random control data ($10 < f < 2000$ Hz, $10 \cdot 10^{-3}$ g rms) is used for the estimation of the suspension and coil mode characteristic and the solution of the least square problem for the electrical parameter determination. The results are shown by the dashed-red FRFs in Fig. 9.2.
- An enhanced system identification is applied combining experimental results of the sine and random control testing. The sine control data ($3 < f < 200$ Hz, 0.5 oct/min, 0.5 g) is used to estimate the suspension mode characteristic. The high level random control data ($10 < f < 2000$ Hz, $10 \cdot 10^{-3}$ g rms) is used to estimate the coil mode characteristic as well as solving the least square equations for the electrical parameter estimation. This is represented by the dashed-green FRFs in Fig. 9.2.

Figure 9.2 shows the FRFs of voltage- and acceleration-over-current, and acceleration-over-voltage calculated directly from the time series of the simulations (dashed red and green) and validate these to the corresponding experimental test FRFs of the sine (black) and random (blue) control test. It is obvious that the numerical simulation results show a good correlation with respect to the experimental test data, whereas the low frequency deviation is minimised by using the combination of sine and random control results of the enhanced system identification.

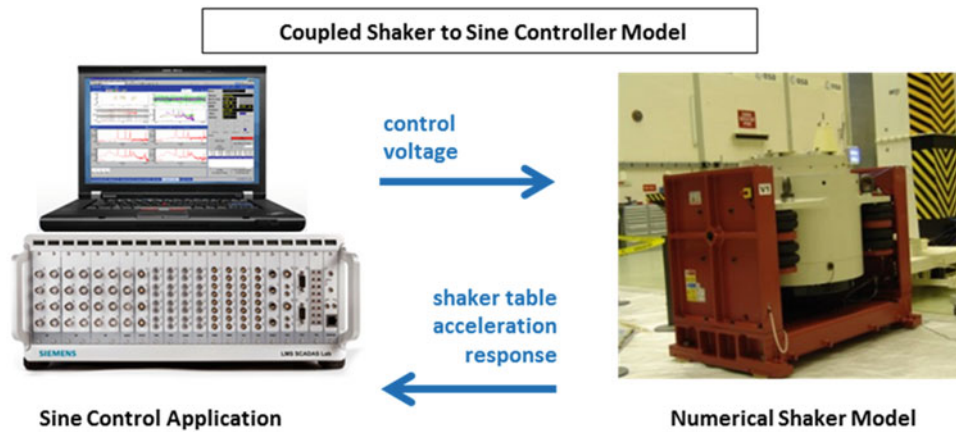


Fig. 9.3 Sketch of the LMS Test.Lab sine control model coupled to the numerical representation of ESTEC's 160 kN shaker. The input (control voltage) and output (shaker table acceleration) signals are closing the vibration test loop

9.2.2 Part II: Shaker to Sine Controller Coupling

After the shaker model derivation in Sect. 9.2.1, the shaker model is coupled to a vibration test controller by closing the loop with an acceleration feedback to be capable to control the shaker table acceleration w.r.t. required specifications see Fig. 9.3. Due to its large number of installations at vibration space testing centres, LMS Test.Lab Sine Control is implemented and used to conduct controlled virtual sine sweep tests. The sine controller model has been derived and extensively validated to the existing hardware and software implementation [13, 14] as reported in previous works [4, 5]. The estimated set of shaker parameter derived in the previous section is used to validate the coupled shaker and sine controller model. In detail, the coupled model is used to predict the test performance of the Interface disc/cuboid loading configuration in sine control testing. Therefore, the numerical calculation uses the same control settings as applied during the real sine control test as mentioned in Table 9.1. Figure 9.4 shows a good agreement between the test results and numerical prediction for both, the shaker drive voltage and the shaker table acceleration control spectrum. This correlation is also expected, since no dominant dynamics of the coupled sine controller and shaker model appears in the considered frequency range (3–200 Hz). In detail, some deviations are observable when evaluating the acceleration control spectrum. First, measurement noise is present in the experimental results whereas the numerical ones exhibit a clear characteristic. This is also clear, since no noise is modelled or simulated in the numerical calculations. Second, although a centred mass is considered in the test, the shaker table lateral or rotational dynamics are present in the acceleration control spectrum of the test. Consequently, it results in a deviation between the experimental and numerical spectra for frequencies $f > 100$ Hz, as these dynamics are not yet modelled in the numerical shaker model.

9.3 Shaker Model Enhancement

9.3.1 Motivation for Shaker Model Enhancement

At the current status, the shaker table specifically consists of one translational DoF which is capable to represent the shaker's dynamical characteristic for an idealised test case as it is shown in Sect. 9.2. The ideal test case assumes that a rigid mass is attached at the centred position on the shaker table. For these cases the current shaker model can be used to recalculate and predict test results in open and closed loop random and sine control operations. However, considering centred conditions some deviations occur between the test and simulation results especially in the sine control shaker table acceleration and drive voltage spectra as shown in Fig. 9.4. In practice, these deviations will increase, if complex test structures are attached to the shaker and idealised conditions cannot be applied anymore which explains the discrepancies between the experimental and simulation results in Fig. 9.4. Especially for S/C vibration testing, the centre-of-gravity (CoG) of the S/C and shaker table is rarely aligned to each other w.r.t. the main vertical axis of motion. As consequence, the entire system tends to be subjected to undesired rotational and lateral dynamical movements during test. A first main problem is the dynamical coupling between the first bending mode of the structure under test and the rocking (rotational) mode of the shaker table.

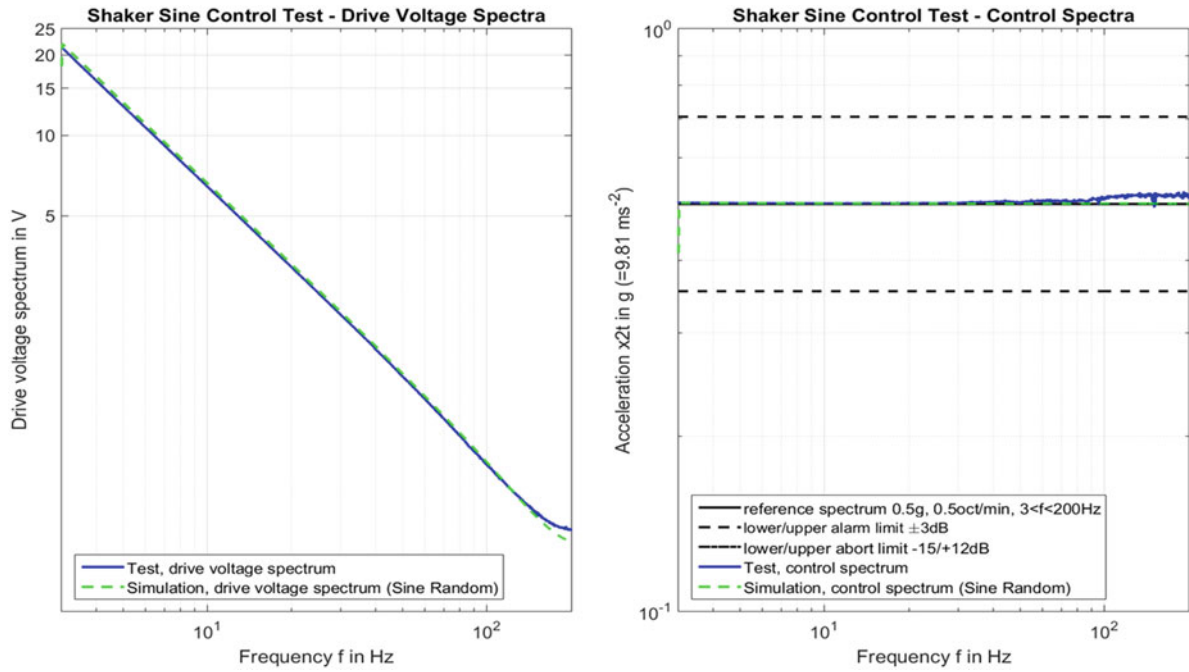


Fig. 9.4 Sine control test spectra (*left* - shaker drive voltage, *right* - shaker table control acceleration) for closed loop validation testing of the numerical shaker model coupled to the sine controller implementation against experimental sine control results (*blue*)

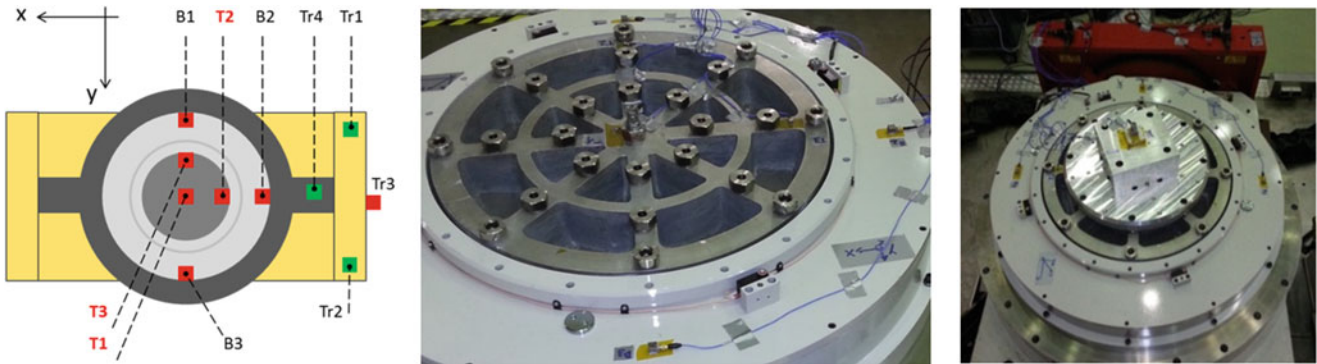


Fig. 9.5 *Left* - 160 kN shaker sensor plan for system identification (*red* squares represent tri-axial acceleration sensors; *green* squares indicate tri-axial seismic accelerometers). *Centre* - Source ESA [15]: empty 160 kN shaker table loaded with centred control sensor. *Right* - Source ESA [15]: shaker table loaded with interface disc, cuboid and control sensor

This is a main reason, for virtual shaker testing and to follow a multi-domain modelling and simulation approach, including the test structure, excitation system and control system in order to assess the global performance [3]. To predict this in the future, it is intended to enhance the current shaker model with additional DoFs.

9.3.2 Enhanced Test Data Exploitation

A principle sketch and pictures of the shaker sensor instrumentation and loading configurations of the 160 kN shaker system identification are shown in Fig. 9.5. To assess rotational and higher order shaker table dynamics, impact excitations were performed on centred (T1) and not-centred (T2 at -x-axis and T3 at -y-axis) sensor and impact positions. Additionally, impact positions were selected to be T4 and T5 at opposing points of T3 and T2, respectively.

Figure 9.6 shows the driving point FRFs for the three loading configurations and specific sensor and impact combinations. The top plot presents the results of the centred impact and sensor location T1 for the empty shaker table in red, Interface disc in green and Interface disc/cuboid loading configuration in blue. The corresponding off-centred impact and sensor considerations are presented by the plots at the centre (T2,-x-axis) and bottom (T3,-y-axis) in the same colour as T1 for the

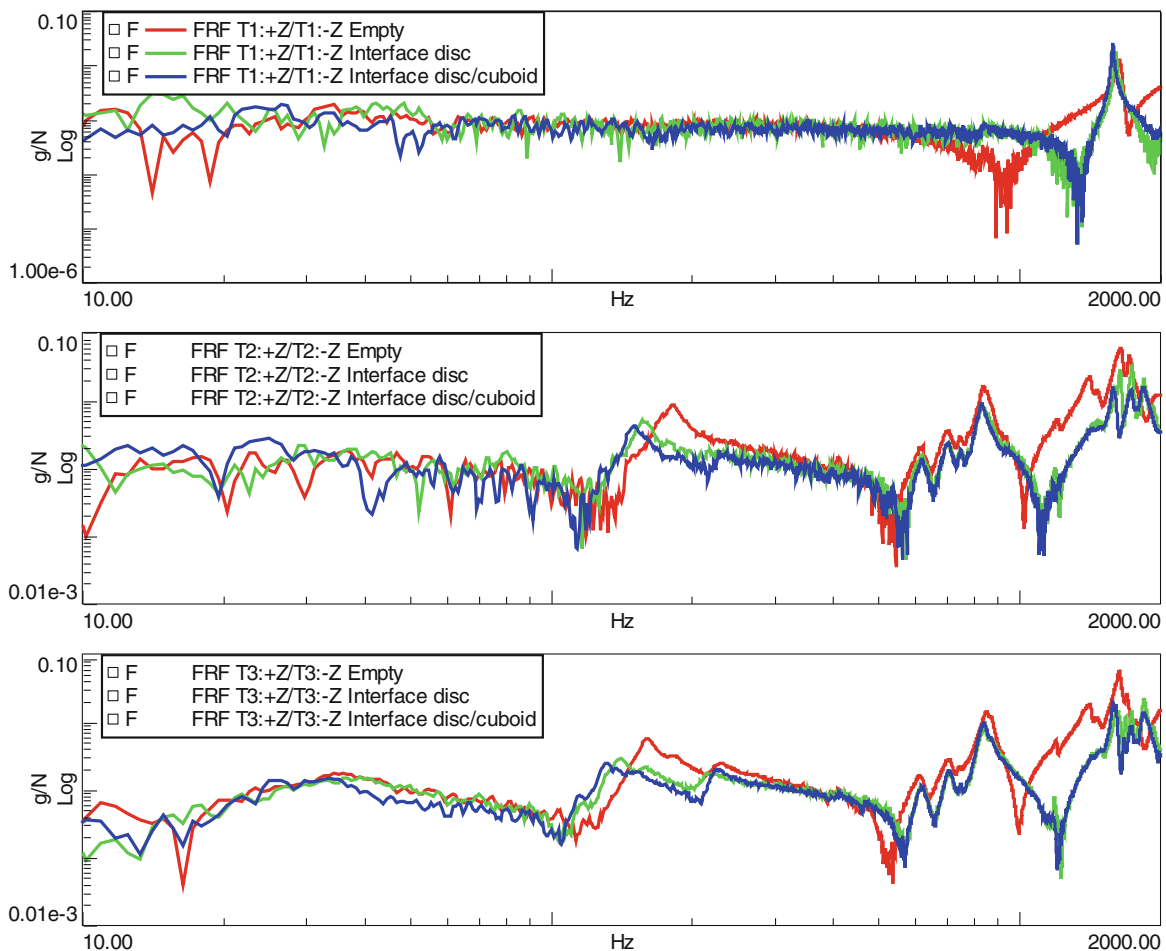


Fig. 9.6 FRFs of hammer excitation tests on the shaker table at centred (T1, *top*) and not-centred (T2, *centre* and T3, *bottom*) sensor and impact locations considering different loading configurations (Empty in *red*, Interface disc in *green* and Interface disc/cuboid in *blue*)

different loadings. As a first check, the reciprocity of the shaker table was successfully validated by using cross-coupled FRFs of all inputs and outputs, and comparing these to the corresponding FRFs of the reversed equivalent cases, e.g. T2/T1 to T1/T2 (note: results are shown in [12]). The entire set of FRFs including the driving point FRFs shown in Fig. 9.6 and all cross-coupled FRFs were processed in LMS Test.Lab, using PolyMAX least square technique to estimate the mode shapes, frequencies and damping. The results are summarised in Table 9.2 and correlated to the FRFs of Fig. 9.6 in the following. As expected, it can be seen that applying impacts at multiple locations reveal more modes and rotational dynamics when the shaker table is excited at not-centred positions (T2, T3). In the following part, the modes are identified by visualisation of the FRFs and post-processing steps, applying Modal analysis. The main goal is to identify and evaluate their performance and consider this in the derivation of an enhanced model. For these cases, the rotational modes are directly excited as it shown by the first modes between 100 and 200 Hz and are slightly different for the two orthogonal directions x and y ; rotation around x -axis if excited on T3 ([159.8, 138.4, 132.4] Hz) and rotation around y -axis if excited on T2 ([178.9, 156.1, 148.9] Hz), respectively. Additionally, the modes exhibit a dependency to the loading configuration which results in a decreasing natural frequency for increasing mass, as it is also the case for the high frequency coil modes ([1625.0, 1609.6, 1585.2] Hz). The coil mode frequencies are clearly identified for the centred sensor case (T1, top). For the not-centred sensor considerations the coil mode frequency is surrounded by many adjacent modes with similar behaviour.

In between the first rotational and coil modes at approx. 615, 700, and ± 850 Hz, there are three higher order modes detected. The modes exhibit coupled translational and rotational components in the mode shapes and are not significantly affected by any change of the mass loading. To identify these modes, a very high order for the modal model (≥ 150) is required.

Two more modes at approx. 1200 and 1400–1500 Hz are detected for the empty shaker table whereas only the second one has also been calculated for the two loading configurations. The modes are similar to torsional shaker table dynamics.

Table 9.2 Modal analysis results of shaker table in different loading configurations, considering 3×5 FRF matrix of inputs at T1–T5 and outputs on T1–T3

Mode description	Empty		Interface disc		Interface disc/cuboid	
	Hz	%	Hz	%	Hz	%
Low level, noisy	33.2 Hz	16.6 %	36.4 Hz	9.4 %	26.2 Hz	5.3 %
1st rocking, x-rotation	159.8 Hz	3.6 %	138.4 Hz	4.1 %	132.4 Hz	4.0 %
1st rocking, y-rotation	178.9 Hz	4.0 %	156.1 Hz	3.7 %	148.9 Hz	3.2 %
Higher order coupled modes: rocking and translational	616.7 Hz	2.1 %	610.9 Hz	1.7 %	615.9 Hz	1.1 %
	701.5 Hz	2.4 %	700.3 Hz	1.8 %	700.2 Hz	1.7 %
	842.8 Hz	1.7 %	834.5 Hz	1.9 %	830.8 Hz	1.7 %
	852.0 Hz	0.8 %	845.3 Hz	1.5 %	846.7 Hz	1.6 %
	865.2 Hz	1.6 %	871.7 Hz	1.8 %	870.6 Hz	0.8 %
Small effect of higher modes on empty table FRFs	1204.1 Hz	0.5 %	–	–	–	–
	1214.1 Hz	0.9 %	–	–	–	–
Dominant modes prior to coil mode, on empty table FRFs	1397.5 Hz	0.8 %	–	–	–	–
	1424.9 Hz	1.1 %	–	–	1446.0 Hz	1.9 %
	1463.5 Hz	2.2 %	1475.5 Hz	2.3 %	1476.6 Hz	1.5 %
Coil mode	1625.0 Hz	2.2 %	1609.6 Hz	0.5 %	1585.2 Hz	0.5 %

The hammer impacts were performed also to identify the coil mode at high frequency. Hence, some noise persists in the FRFs due to difficulties in properly exciting the entire frequency range. As a consequence, the first low frequency modes ([33.2, 36.4, 26.2] Hz) show no direct dependency to the loading configuration with an obvious trend. A high model order is required to estimate this mode and it is only visible in the FRFs shown on the bottom of Fig. 9.6, which are calculated on sensor responses and impacts at position T3.

As summary, during vibration control experiments and considering idealised conditions, none of these modes are significantly excited, even when the not-centred sensor responses (T2, centre and T3, bottom) are considered for the FRF calculations. In this case the hammer impact results with centred excitation and sensor location (T1, top) represents the dynamic system characteristic with a flat magnitude, as shown by the top plots in Fig. 9.6. This difference is a result of the perfectly aligned electromagnetic force of the shaker combined with the centred loading, but will change with CoG misalignments as reported.

9.3.3 Modelling of Rotational Shaker Table Dynamics

Figure 9.7 shows a schematic representation of the shaker table, allowing to modify the differential equation of the shaker table by adding two differential equations characterising rotational dynamics. The proposed derivation describes the system in terms of linear algebra to calculate forces and moments, whereas vectors (small) and matrices (capital) are written in bold letters. As it relies on vector calculus, this approach ensures a high flexibility in the model. It is not restricted to actual geometry settings or the consideration of specific misalignments in the setup. The following assumptions are set to define the physical model:

- The rotation point x_{CoG} is assumed to be equal to the CoG of the coupled system of the shaker table and structure under test or it can be assumed as the connection point between both systems. At the current status, the rotation point's position vector \mathbf{x}_{CoG} in the local coordinate system of the shaker table is assumed to be,

$$\mathbf{x}_{CoG} = [x_{CoG}, y_{CoG}, 0]^T. \quad (9.4)$$

- The spring and damper system (c_s, k_s) between the shaker table/armature and body is spatially distributed in a circular shape according to the shaker table's geometry and lateral axis, x and y . Consequently, the entire force $\sum_i \mathbf{f}_i$ acting between the shaker table and body is calculated by the sum of the distributed forces,

$$\mathbf{f}_i = \left[0, 0, -\frac{1}{4} \{ (\dot{z}_T - \dot{z}_B) c_s + (z_T - z_B) k_s \} \right]^T, \quad (9.5)$$

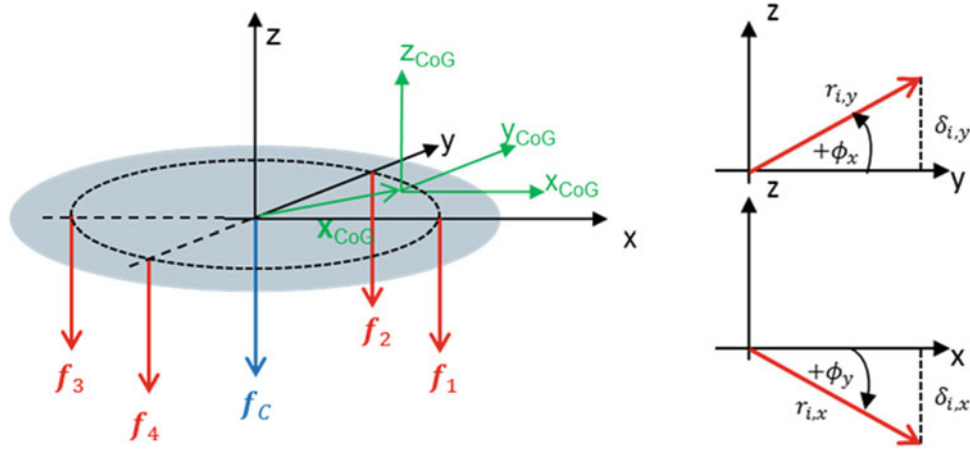


Fig. 9.7 Sketch of the shaker table to add rotational dynamics around orthogonal x- and y-axis

for each spring and damper system $i = 1, 2, 3, 4$. The position vectors \mathbf{p}_i describe the location of the suspension forces \mathbf{f}_i defined in the local coordinate system of the shaker table. Due to this spatial distribution, mechanical moments $\mathbf{r}_i \times \mathbf{f}_i$ are induced with active lever arms $\mathbf{r}_i = \mathbf{p}_i - \mathbf{x}_{CoG}$. These moments occur as first sum in the rotational model in Eqs. (9.10) and (9.11), and represent the first translational to rotational coupling due to the geometry.

- The mass spring and damper system (c_c, k_c) between the shaker table and coil driven by the electromagnetic Lorentz force acting on the coil is assumed to be centred. Consequently, no rotational dynamics of the coil is modelled and the influence of the shaker table rotation at the centre is neglected. The resulting force,

$$\mathbf{f}_c = [0, 0, -\{(\dot{z}_T - \dot{z}_c) c_c + (z_T - z_c) k_c\}]^T = [0, 0, ki - m_c \ddot{z}_T]^T, \quad (9.6)$$

acting on the centre of the shaker table induces a mechanical moment $\mathbf{r}_c \times \mathbf{f}_c$ w.r.t. the rotation point \mathbf{x}_{CoG} and active lever $\mathbf{r}_c = \mathbf{0} - \mathbf{x}_{CoG}$. This moment occurs as second sum in the rotational model in Eqs. (9.10) and (9.11), and represents a further translational to rotational coupling.

- The rotational dynamics are described by rotation angles $\phi_{x,y}$, angular velocities $\dot{\phi}_{x,y}$ and accelerations $\ddot{\phi}_{x,y}$ around the local axis \mathbf{x}_{CoG} and \mathbf{y}_{CoG} in parallel to the shaker table axis x and y . The signs of the rotations are defined as in the right sketch of Fig. 9.7. The coupling of rotational angles and angular velocities to an angular spring and damping force is only assumed for the shaker table suspension system. The resulting forces $\mathbf{f}_{i,x}$ and moments $\mathbf{M}_{i,x}$ for an rotation ϕ_x are calculated as,

$$\mathbf{f}_{i,x} = \frac{1}{4} (c_S \dot{\delta}_{i,x} + k_S \delta_{i,x}) = \frac{1}{4} (c_S r_{i,y} \dot{\phi}_x + k_S r_{i,y} \phi_x), \quad (9.7)$$

$$\mathbf{M}_{i,x} = \frac{1}{4} (c_S \dot{\delta}_{i,x} r_{i,y} + k_S \delta_{i,x} r_{i,y}) = \frac{1}{4} (c_S r_{i,y}^2 \dot{\phi}_x + k_S r_{i,y}^2 \phi_x), \quad (9.8)$$

considering small angles: $\delta_{i,x} = r_{i,y} \sin \phi_x \approx r_{i,y} \phi_x$. The resulting forces $\mathbf{f}_{i,y}$ and moments $\mathbf{M}_{i,y}$ as a function of ϕ_y are calculated respectively, but by considering the x-components of the active lever arm $r_{i,x}$ and the rotation ϕ_y in Eqs. (9.7) and (9.8), $\delta_{i,y} \approx r_{i,x} \phi_y$. This calculation and positive rotation directions are shown by the right sketches in Fig. 9.7. This approach is applied to define the mathematical equations describing the rotational to translation coupling in Eq. (9.10) and to derive the purely rotational system equations represented by the last sum of the right hand side of Eq. (9.11).

Under these assumptions, the shaker table model in translational direction considering rotational effects is derived to,

$$\begin{aligned}
 (m_T + m_D) \ddot{z}_T &= - \underbrace{[(\dot{z}_T - \dot{z}_B) c_S + (z_T - z_B) k_S]}_{\sum f_i} - \underbrace{[(\dot{z}_T - \dot{z}_c) c_c + (z_T - z_c) k_c]}_{f_c} \\
 &\quad - \frac{1}{4} \underbrace{\left\{ c_S \left[\dot{\phi}_x \sum_i r_{iy} + \dot{\phi}_y \sum_i r_{ix} \right] + k_S \left[\phi_x \sum_i r_{iy} + \phi_y \sum_i r_{ix} \right] \right\}}_{\text{rotational to translational coupling}}
 \end{aligned} \tag{9.9}$$

The equation comprises the original shaker table translational model of Eq. (9.3) and is extended by an additive term describing the rotational to translational coupling, as described by (9.7). The global approach for the rotational dynamics in terms of calculation of the resulting moment is given by,

$$\mathbf{M} = \mathbf{J} \ddot{\boldsymbol{\phi}} = \sum_i \mathbf{r}_i \times \mathbf{f}_i + \mathbf{r}_c \times \mathbf{f}_c - [\mathbf{R}_C \dot{\boldsymbol{\phi}} + \mathbf{R}_K \boldsymbol{\phi}]. \tag{9.10}$$

It comprises the translational to rotational coupling by the first two sums at the right hand side. The rotational terms of the shaker table to body suspension system is derived by applying Eq. (9.8), considered as uncoupled and represented by the rotational differential equation of the last two sums,

$$\begin{aligned}
 \begin{bmatrix} J_{xx} & 0 \\ 0 & J_{yy} \end{bmatrix} \begin{pmatrix} \ddot{\phi}_x \\ \ddot{\phi}_y \end{pmatrix} &= - \frac{1}{4} \underbrace{[(\dot{z}_T - \dot{z}_B) c_S + (z_T - z_B) k_S] \sum_i \begin{pmatrix} r_{i,y} \\ -r_{i,x} \end{pmatrix} - [(\dot{z}_T - \dot{z}_c) c_c + (z_T - z_c) k_c] \begin{pmatrix} r_{C,y} \\ -r_{C,x} \end{pmatrix}}_{\text{translational to rotational coupling}} \\
 &\quad - \underbrace{\left\{ \frac{c_S}{4} \begin{bmatrix} \sum_i r_{iy}^2 & 0 \\ 0 & \sum_i r_{ix}^2 \end{bmatrix} \begin{pmatrix} \dot{\phi}_x \\ \dot{\phi}_y \end{pmatrix} + \frac{k_S}{4} \begin{bmatrix} \sum_i r_{iy}^2 & 0 \\ 0 & \sum_i r_{ix}^2 \end{bmatrix} \begin{pmatrix} \phi_x \\ \phi_y \end{pmatrix} \right\}}_{\text{rotational dynamics}}
 \end{aligned} \tag{9.11}$$

By implementing these modifications in Eq. (9.9) and by adding the rotational shaker table dynamics of Eq. (9.11), the existing three DoFs shaker model is extended to represent a five DoFs model, with three translational and two rotational DoFs. The moments of inertias (MoI) J_{xx} and J_{yy} , around the x- and y-axis, need to be derived as additional parameters w.r.t. the existing model. At the current status, the MoIs are estimated experimentally rather than deriving them analytically. Therefore, based on the purely rotational model in Eq. (9.11), the angular acceleration-over-input moment transfer functions in the Laplace domain are derived as,

$$\frac{\ddot{\phi}_x(s)}{M_x(s)} = \frac{s^2}{J_{xx}s^2 + \frac{c_S}{4} \sum_i r_{iy}^2 s + \frac{k_S}{4} \sum_i r_{iy}^2}, \quad \frac{\ddot{\phi}_y(s)}{M_y(s)} = \frac{s^2}{J_{yy}s^2 + \frac{c_S}{4} \sum_i r_{ix}^2 s + \frac{k_S}{4} \sum_i r_{ix}^2}, \tag{9.12}$$

considering the rotations about the two orthogonal axis to be decoupled. From (9.12) it follows, that two angular frequencies

$$\omega_x^2 = \frac{\frac{k_S}{4} \sum_i r_{iy}^2}{J_{xx}}, \quad \omega_y^2 = \frac{\frac{k_S}{4} \sum_i r_{ix}^2}{J_{yy}}, \tag{9.13}$$

exist in the model. Subsequently, the MoIs are estimated by rearranging Eq. (9.13), considering an idealised case: the distributed forces \mathbf{f}_i are assumed to be located on the shaker table \pm x- and \pm y-axis under decoupled conditions, with a radial distance r and the experimentally measured angular resonance frequencies of the shaker table rocking modes as summarised in Table 9.2.

9.3.4 Simulation and Verification

As a first application, the enhanced shaker model is implemented and verified against hammer impact results of the Interface disc/cuboid loading configuration. Therefore, the hammer impacts are numerically approximated and simulated by defining an input moment \mathbf{M}_{in} as excitation on the shaker table, similarly to the experimental conditions. The input moment is added to the rotational shaker model of Eq. (9.11). It is defined as the vector product between the direction vector \mathbf{r}_{in} representing the active lever arm and the input force, which is modelled as Dirac function $\delta(t)$ in negative z-direction. The direction vector \mathbf{r}_{in} is defined as vector pointing from the CoG offset \mathbf{x}_{CoG} to the impact location \mathbf{p}_{in} defined by the position vectors \mathbf{x}_{CoG} and \mathbf{p}_{in} in the local frame of the shaker table. The Dirac function $\delta(t)$ is mathematically described as difference between two step functions $\sigma(t)$ and $\sigma(t - mt_s)$ shifted in time by a multiple m of the sampling time t_s .

$$\mathbf{M}_{in} = \mathbf{r}_{in} \times [0, 0, \delta(t)]^T = [\mathbf{p}_{in} - \mathbf{x}_{CoG}] \times \left[0, 0, -\frac{1}{mt_s} [\sigma(t) - \sigma(t - mt_s)] \right]^T \quad (9.14)$$

The amplitude scaling needs to be introduced so that the Dirac function fulfils the requirement,

$$\int \delta(t) dt = 1. \quad (9.15)$$

For this testing application the shaker model is completely decoupled from the input voltage $e(t) = G_V u(t)$, contrary to the open loop or controlled sine control testing described in Sect. 9.2. In the analysis, the shaker model response is simulated for two different cases:

- The shaker is switched off: the electrical shaker model is completely disconnected from the mechanical shaker model in the Simulink simulation. This means, that the only shaker input is defined by the Dirac function of Eq. (9.15).
- The shaker is switched on: the electrical shaker model is kept unchanged and coupled to the mechanical shaker model. This means, that the electrical and mechanical shaker systems interact according to Eqs. (9.1) and (9.2) due to the resulting movement of the coil in the electromagnetic field of the air gap, even if no input voltage $e(t) = 0$ is applied.

At this point the higher order modes at approx. 615, 700, and ± 850 Hz are added to the simulation model based on the modal analysis results in Table 9.2. These modes are only mathematically modelled without any physical representation, as to improve the predictive capabilities of the model when compared to the measured data. Hence, the FRFs of the simulation study shown in Fig. 9.8 are used to recalculate the experimental data of the hammer impact excitations on the shaker table at location T2 ($-x$ -axis). Therefore, the position vector of the excitation in Eq. (9.14) is defined as $\mathbf{p}_{in} = [-r, 0, 0]^T$, with the shaker table radius $r = 0.3\text{m}$. The test results are plotted in green. The simulation results of the shaker in switched-off and switched-on configuration in red and black, respectively. Additionally, the dashed blue curve represents the synthesised FRF which is fitted to the test results using PolyMAX.

The results show that the numerical simulation well approximates the experimental test results and all modes are visible in the considered frequency range. Due to the excitation at T2 ($-x$ -axis) the shaker table rocking mode with a rotation around the y-axis at 150 Hz, is excited more significantly than the rocking mode around the x-axis which occurs at a lower frequency at 131 Hz. This is the case for the numerical simulation as well as for the physical test. Additionally, it is shown that the lower rocking mode is also clearly excited in the simulation. This is a result of the simulation settings: a small CoG offset $\mathbf{x}_{CoG} \neq 0$ is assumed to overcome and simulate minor misalignments and shows the presence of the two rocking modes in the simulation results. The test results do not show this mode distinctively due to the noisy characteristic and the excitation on T2. The higher order modes are well recalculated in the simulation model and synthesised FRFs.

As further option, the simulation enables the observation of the shaker system in switched on and off configuration. While testing this was not possible due to the fact, that the sensor signals were disturbed by the strong electromagnetic field of the shaker. This disturbance vanished if the shaker was operated in open or closed loop random and sine control testing. Consequently, the simulation model is used to study the effect numerically. By comparing the results (switched off-red, switched on-black) it is obvious that the shaker suspension mode which is already highly damped in the switched off configuration does not appear anymore if the shaker is switched on. On the contrary, the shaker table rotational (rocking) modes are not affected significantly by switching off/on the shaker as it is already been reported in [9]. Hence, it is important to model and understand the presence of these rotational modes. The higher order modes show no dependency to the impact location or loading configuration. The coil mode moves to a higher frequency if the shaker is switched on with a slight magnitude reduction. This has also been investigated in the test results shown in Fig. 9.2 and in Sect. 9.2.1: it originates from the coupling between the shaker's electrical and mechanical systems. Especially, the transfer function of the shaker's

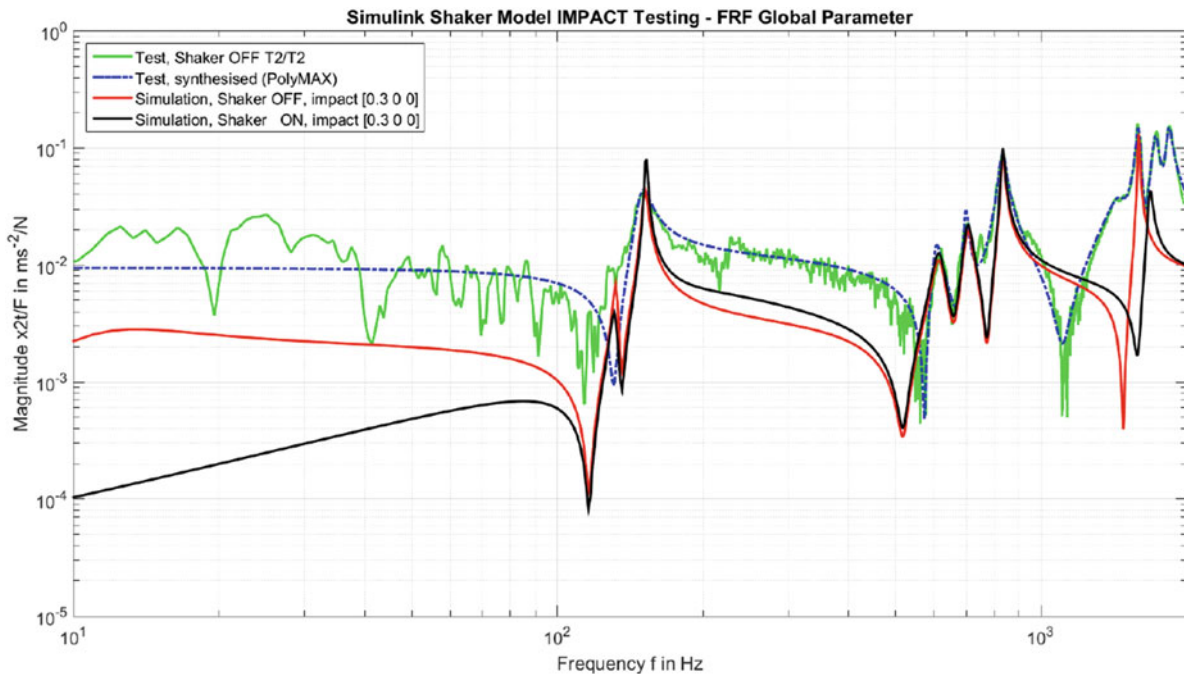


Fig. 9.8 Correlation between hammer impact excitation test results on impact location T2 ($-x$ -axis) and simulated results with enhanced shaker model

complex impedance $Z(s)$ induces this change [11, 12]. As main observation, the analogy between the hammer test results and controlled operations are summarised: it is observed that the FRFs of the shaker switched off are similar to the acceleration-over-current FRFs in the controlled operations. This behaviour satisfies also the condition which is set during the system identification, that the mechanical parameters are estimated by considering the acceleration-over-current FRFs. The FRFs with the shaker switched on behave similarly to the acceleration-over-voltage FRF, with the coupled mechanical and electrical system.

9.4 Conclusions

This paper summarises the work which has been performed to develop and validate a virtual shaker testing environment implemented in Matlab/Simulink. It starts with the summary of the existing lumped-parameter electromechanical shaker model. The shaker model is based on experimental data gathered to determine the shaker parameter and to estimate physical mechanical, electrical and coupling parameters. Additionally, a closed loop simulation environment is defined by coupling the shaker model to a validated sine controller model with acceleration feedback. The 160 kN electrodynamic shaker of the European Space Research and Technology Centre (ESTEC) was used to perform extended tests in random and sine control operations as well as hammer impact excitations. The experimental test data in controlled operation is used to validate the numerical shaker model for both cases, open and closed loop shaker configuration. As main results, it has been shown that the numerical shaker model is capable to recalculate and predict the physical shaker performance for certain loading configurations. The results of the closed loop sine control application for validation show that the current shaker model needs to be improved in terms of rotational shaker table dynamics to minimise the deviations in the shaker acceleration spectra and FRF estimations. Hence, an enhanced shaker model is derived, including rotational shaker table rocking modes and higher frequency modes which were detected with hammer impact excitations and Modal analysis on the measured FRFs. Hence, the shaker model represents a coupled translational and rotational system with five DoFs; three translational DoFs of the shaker table, coil and body, and two rotational DoFs of the shaker table around its lateral, orthogonal x - and y -axis. In final simulations, the shaker model is correlated to hammer impact excitations gathered on the 160 kN shaker. The results show a good agreement between the experimental and numerical results, although some deviations are observable which will be investigated in more detail in the future. Additionally, the simulation model is used to show the dynamical differences if the shaker is switched off/on. The main differences are, that the suspension mode is highly damped and it is only

observable with the shaker turned off, the rocking modes are unchanged and the coil mode is slightly increased if the shaker is switched on. As main conclusion it is observed that the FRFs with shaker off are similar to the acceleration-over-current FRFs in controlled operations, while the FRFs with shaker switched on correspond to the acceleration-over-voltage FRF. In the future, the shaker model will be validated with experimental results in controlled operations considering an off-centred test object mounted on top of the shaker table. It will also be analysed how the physical and virtual models behave since only centred loading cases have been considered. To reliably perform these analyses in a numerical environment, methodologies need to be investigated to couple the controller/shaker model with representative spacecraft structural dynamical models. Additionally, lateral dynamic effects of the shaker table and the shaker trunnion, will also need to be included.

Acknowledgements The authors of this work gratefully acknowledge the European Space Agency under the Network/Partnering Initiative PhD programme (contract No. 4000110039/14/NL/PA) in collaboration with Siemens Industry Software NV and Vrije Universiteit Brussel. A special thank you also to Alessandro Cozzani, Matteo Appolloni and Steffen Scharfenberg from ESTEC for their support and discussions. This research was also performed in the frame of the project IWT 130936 ADVENT (Advanced Vibration Environmental Testing). The financial support of the IWT (Flemish Agency for Innovation by Science and Technology) is gratefully acknowledged.

References

1. NASA Technical Handbook. Spacecraft Dynamic Environments Testing. NASA-HDBK-7008, 2014
2. ESA-ESTEC. European Cooperation for Space Standardization, Space Engineering, Spacecraft Mechanical Loads Analysis Handbook. ECSS-E-HB-32-26A, Noordwijk, The Netherlands, 2013
3. Appolloni, M., Cozzani, A.: Virtual testing simulation tool for the new quad head expander electrodynamic Shaker. In: Proc. 6th Int. Symp. on Environmental Testing for Space Programmes, ESA-ESTEC, June 2007
4. Ricci, S., Peeters, B., Fetter, R., Boland, D., Debille, J.: Virtual shaker testing for predicting and improving vibration test performance. In: Proc. IMAC 2009, Orlando (FL), USA, Feb 2009
5. ESA-ESTEC study, TN-3: Assessment of the Shaker Performance in Presence of Non-linear Dynamic Effects, LMS International in framework of ESA Study Advancement of Mechanical Verification Methods for Non-linear Spacecraft Structures. TEC-MCS/2007/1558/In/AN
6. Bettacchioli, A.: Simulation of satellite vibration test. In: Proc. 13th European Conference on Spacecraft Structures, Materials and Environmental Testing, Braunschweig, Germany, April 2014
7. Fox Lang, G., Snyder, D.: Understanding the physics of electrodynamic shaker performance. *Sound Vib.* **35**, 24–33 2001
8. Ricci, S., Peeters, B., Debille, J., Britte, L., Faignet, E.: Virtual shaker testing: a novel approach for improving vibration test performance. In: Proc. ISMA 2008 International Conference on Noise and Vibration Engineering, Leuven, Belgium, September 2008
9. McConnell, K.G., Varoto, P.S.: *Vibration Testing: Theory and Practice*. Wiley, New York (1995)
10. Peeters, B., Van Der Auweraer, H., Guillaume, P., Leuridan, J.: The PolyMAX frequency-domain method: a new standard for modal parameter estimation? *Shock Vib.* **11**, 395–409 (2004)
11. Waïmer, S., Manzato, S., Peeters, B., Wagner, M., Guillaume, P.: Derivation and Implementation of an electrodynamic shaker model for virtual shaker testing based on experimental data. In: 29th Aerospace Testing Seminar, Los Angeles (CA), USA, October 2015
12. Waïmer, S., Manzato, S., Peeters, B., Wagner, M., Guillaume, P.: Experimental system identification of an electrodynamic shaker for virtual shaker testing. In: Proc. ICEDyn 2015 International Conference on Structural Engineering Dynamics, Lagos, Portugal, June 2015
13. Siemens Industry Software NV, LMS Test.Lab Environmental. Leuven, Belgium. www.siemens.com/plm/lms (2015)
14. Siemens Industry Software NV. LMS SCADAS III Data Acquisition Front-end. Breda, The Netherlands. www.siemens.com/plm/lms (2015)
15. European Space Agency (ESA). www.esa.int

Chapter 10

Characterizing the Dynamics of Systems Incorporating Surrogate Energetic Materials

Jelena Paripovic and Patricia Davies

Abstract It is hypothesized that by understanding the mechanical behavior of explosive materials it may be possible to use an object's mechanical response to distinguish between objects that contain explosive materials and those that do not. While the materials will typically be embedded in a system and the system behavior will play a role in the response, the focus here is on the identification of mechanical material properties and behavior of surrogate explosive materials. Base excitation swept sine tests were conducted to characterize the uniaxial dynamic response of a mass-surrogate material system. The tests were conducted to gain an understanding of the dynamic behavior near resonance, repeatability of measured responses, and how these change over long periods of time. Linear and nonlinear viscoelastic models were fitted to the data and changes to material parameter estimates were examined as excitation levels changed and also as the composition of the surrogate materials changed. Recommendations for future development of the model structure are given.

Keywords Nonlinear • Dynamic • Low-frequency • Base-excitation • Material modeling • Viscoelastic • HTPB

10.1 Introduction

The mechanical response of energetic material is of great interest for defense applications. With very little existing data in reported literature, there is a need to investigate and tabulate the mechanical material properties [1, 2]. Here we investigate the vibratory response of surrogate energetic materials at low frequencies (less than 500 Hz) to determine the materials macroscopic dynamic properties. By having the ability to predict the system's response, one may optimize the acoustic or vibratory excitation to increase the identification of these energetic materials [3]. Despite the focus on energetic materials, the experimental set-up, modeling techniques and system identification methodologies can be used in other applications.

10.2 Low Frequency Base Excitation

In this section the material samples, experimental set up and measurements are described.

10.2.1 Sample Preparation

The surrogate energetic materials were cast in cylindrical molds. The samples are comprised of hydroxyl-terminated polybutadiene (HTPB) binder and inert ammonium-chloride (NH₄CL) crystals. The HTPB binder is a common constituent of IEDs; the matrix polymer acts as a fuel for the energetic material while also providing structure. The inert crystals were selected due to their resemblance in both particle size and density to Ammonium Perchlorate (AP) another common energetic constituent. To fabricate the samples a mold was machined out of an Acetal resin. This homopolymer's stiffness, dimensional stability and resistance to fuels and solvents make it very suitable for this application. The cylindrical samples were 7.62 cm with varying diameters (1.27, 2.54, 7.62 cm) and crystal-to-binder volume ratios (0 %, 50 % and 75 %). The focus of this paper is on the low frequency response of the samples 7.62 cm in diameter and on the HTPB 0 and 50 % HTPB samples.

J. Paripovic (✉) • P. Davies

Ray W. Herrick Laboratories, Purdue University, 177 South Russel Street, West Lafayette, IN 47906, USA
e-mail: jparipov@purdue.edu; daviesp@purdue.edu

Table 10.1 Surrogate samples geometric properties for 0 % HTPB and 50 % HTPB

Sample (%)	Diameter (cm)	Height (cm)	Weight (kg)
HTPB 0	7.62	6.1	0.193
HTPB 50	7.62	7.62	0.400

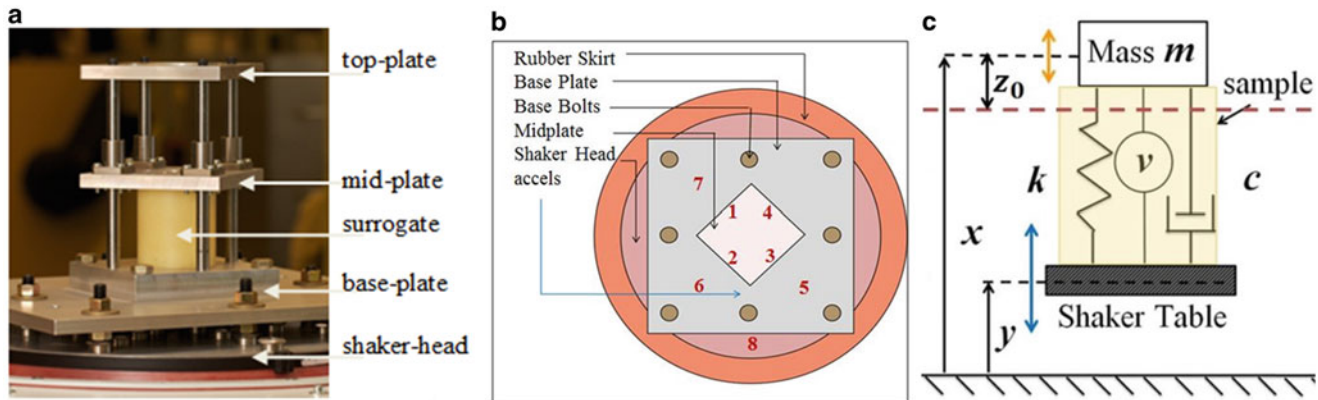


Fig. 10.1 (a) Experimental test-rig with surrogate test sample, (b) top view of the test-rig showing the positions of the accelerometers, and (c) a graphical representation of experimental set-up

The geometry of the samples subjected to the low frequency base excitation data can be found in Table 10.1. Note that the 0 % HTPB sample is slightly shorter than its 50 % HTPB counterpart; this is due to an air void formed in the casting process which was removed, thus shortening the sample; this is taken into account in the subsequent modeling.

10.2.2 Experimental Test Rig

The goal of these tests is to observe and characterize the mechanical material behavior of the HTPB surrogate samples. This was achieved, by conducting low frequency sinusoidal base excitation sweeps on mass-material systems. A TIRA vib 34 kN uni-axial shaker provided the base excitation. The system placed on the shaker is shown in Fig. 10.1a; it is comprised of the cylinder of the material attached to a mass. Frequency ranges were chosen such that the mass-material system went through resonance in the center of the sweep. Tests were conducted at various excitation levels: 5, 10, and 15 g. For the 0 % HTPB the excitation frequency range was 50 to 110 Hz, and for the 50 % HTPB sample the frequency range was from 150 to 330 Hz; all the sweeps lasted 60 s. The mass-material system was designed to constrain the sample to uniaxial (vertical) motion. The test-rig consists of a base plate and four vertical posts that allow a midplate (0.98 kg) to traverse vertically. A top plate is fixed to the top of the four studs, to ensure they remain vertical thus minimizing friction. To fix the samples into the test rig, thin (7 mm) aluminum plates were epoxied to the top and bottom of the cylindrical samples. The plates have a small threaded hole in the center that is used to bolt the aluminum plates to the mid-plate and base-plate constraining the sample, see Fig. 10.1a.

10.2.3 Instrumentation and Signal Post Processing

To measure the acceleration of the mid-plate, shaker head, and base plate, an independent data acquisition set up was employed to acquire the signals. Eight PCB 353B68 accelerometers were fixed to the test rig, 4 were places on the mid-plate, 3 on the baseplate and 1 on the shaker head. The layout of the accelerometers is illustrated in Fig. 10.1b. The acceleration signals were passed through a low-pass analog filter (Wavetek 852) with a cut-off frequency set at 600 Hz. These filters have a 48 dB/Octave roll off. The filtered signals were sampled at 6000 samples/second. Of interest is the relative acceleration between the acceleration of the mid-plate mass (\ddot{x} -accelerometers 1,2,3,4) and the base plate (\ddot{y} -accelerometers 5,6,7). The top plate accelerometer signals were averaged to reduce any effects due to noise and non-unilateral motion (slight rocking motions) and the base acceleration measurements were also averaged. The relative displacement of the mid-plate is denoted by z .

Additional signal post processing includes the use of multiple digital filters (low pass, high pass, differentiator, and integrator) to calculate the relative displacement, velocity and instantaneous frequency and instantaneous amplitude (signal envelope). A 255 point finite impulse response (FIR) digital filter that works well over the range of 30–2970 Hz was designed to calculate the Hilbert transform of the signal and 121 point FIR filter was designed so that it behaved well over a frequency range from 0 to 1000 Hz so the that derivative of the signal and its Hilbert transform could be calculated. These signals were used to calculate the instantaneous frequency and amplitude using the following relationships. In continuous time, if the acceleration signal is $x(t)$ and its Hilbert transform is $\hat{x}(t)$ then the instantaneous amplitude and frequency can be calculated by using:

$$A(t) = \sqrt{x^2(t) + \hat{x}^2(t)} \quad \text{m/s}^2, \quad (10.1)$$

and

$$\omega(t) = \frac{x(t)\dot{\hat{x}}(t) - \hat{x}(t)\dot{x}(t)}{x^2(t) + \hat{x}^2(t)} \quad \text{rad/s}, \quad (10.2)$$

respectively [4]. The FIR digital filters described above were used to estimate these quantities these from the sampled relative acceleration signals.

10.2.4 Test Procedure

A series of tests was conducted over a 138 day period (Day 1, Day 2, Day 19 . . . Day 138) to investigate the repeatability of the measurements and to determine how the sample behavior changes over time. The sample was not tested until 180 days after fabricated allowing time for it to cure. On each day the sample was placed in the fixture with the mass attached and the vibration testing commenced. Three tests were conducted and the starts of each test were 30 min apart, allowing the mass to rest on the sample between excitations (1 min of excitation followed by 29 min of resting for each test). At the end of testing for that day, the sample was removed from the system. This procedure was followed on each day of testing unless otherwise noted. The added mass attached to the material sample was 0.98 kg. Base excitations for the HTPB 0 % sample were sinusoidal sweeps from 50 to 110 Hz in 60 s (1 Hz/s) and for the HTPB 50 % sample were sinusoidal sweeps from 150 to 330 Hz in 60 s (3 Hz/s). Tests were conducted at 5 and 10 g excitation levels for both materials.

10.3 Results

In Figs. 10.2 and 10.3, the envelope (instantaneous amplitude) of the relative acceleration response of the top plate is plotted. The results for the 0 % HTPB sample for a base excitation of 5 g are shown in Fig. 10.2a. In all of the plots in Figs. 10.2 and 10.3, each color represents a different day of testing; the different color shades correspond to the three tests done on each day from dark to light. The frequency where maximum acceleration is observed remains between 80.5 and 83.1 Hz for the 0 % HTPB sample over a 138 day period. Same day repeatability is very good for the pure binder sample as evident by all three shades of the same color lying on top of one another in the plots. The results for the test at 10 g base excitation (not shown here) are similar in terms of repeatability.

Also of interest is the linearity of the material response. Two tests at 5 g base excitation were conducted 30 min apart followed by two 10 g base excitation tests. The results for the HTPB 0 % sample are shown in Fig. 10.2b. In this plot, the envelopes of the response were normalized by the forcing signal, for a linear system the normalized profiles would be identical. As shown in Fig. 10.2b, with the HTPB 0 % sample the normalized responses are very close to each other with a slight shift to lower frequencies for the higher forcing level test.

The results of the tests on the 50 % HTPB samples for base excitations of 5 g are shown in Fig. 10.3a. Unlike the pure binder sample, the resonance of the system with the 50 % HTPB shifts from 220 Hz on Day 1 to 260 Hz on Day 120. This shift suggests the material is stiffening over this time, this could be a result of the material settling, drying out, or some internal damage due to the low frequency base excitation, or a combination of all. A similar shifting to the right effect was observed when the excitation level was 10 g.

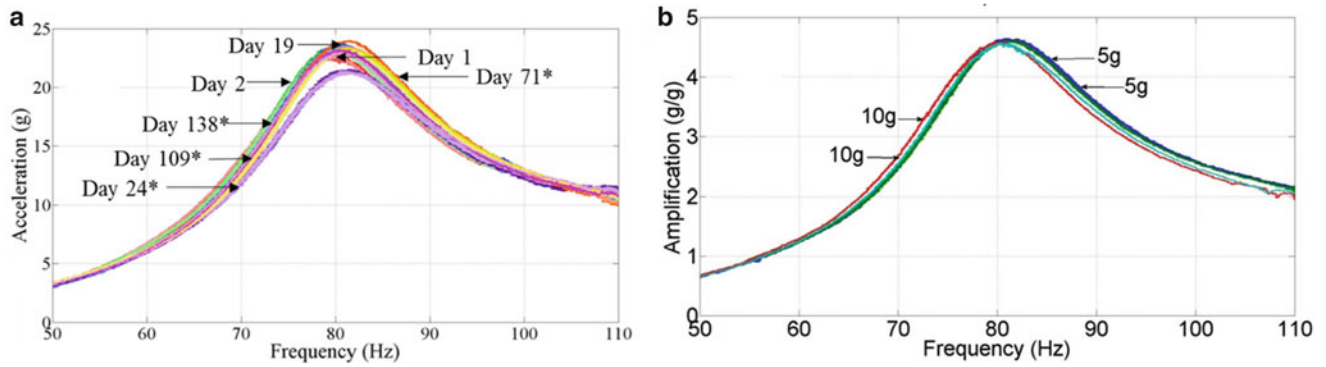


Fig. 10.2 (a) Response of HTPB 0 % sample excited at 5 g and (b) normalized response of HTPB 0 % from 50 to 110 Hz in 60 s over 138 days, where * means the samples was allowed to rest unweighted between tests

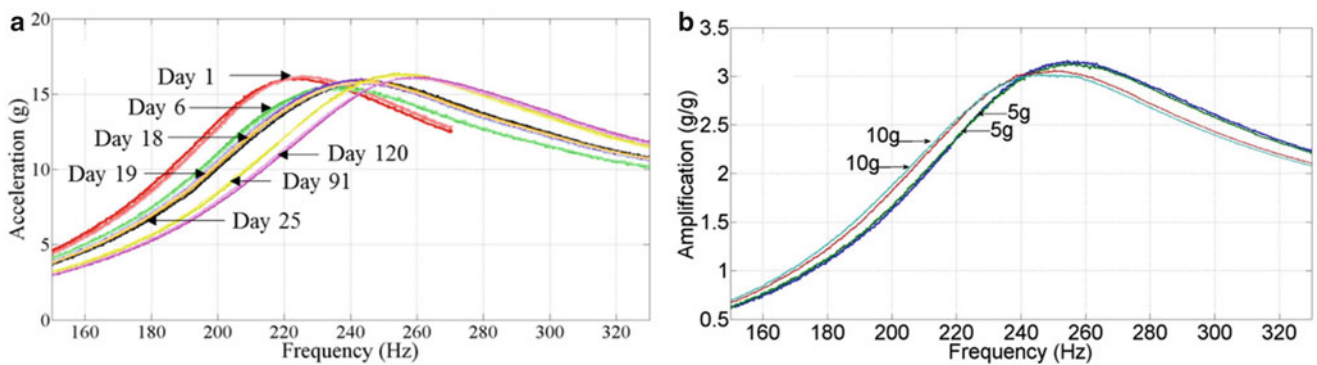


Fig. 10.3 (a) Response of HTPB 50 % sample excited at 5 g and (b) normalized response of HTPB 0 % from 150 to 330 Hz in 60 s over 138 days, where * means the samples was allowed to rest unweighted between tests

The normalized response envelopes from a 5 g and a 10 g test performed on the same data are shown in Fig. 10.3b. Here there is a much more pronounced nonlinear effect than in the HTPB 0 % case. The 10 g responses (red and cyan) are shifted to the left by about 10 Hz. This presence of the crystals in the binder promotes nonlinear behavior—the peak response shift to the left is consistent with a softening stiffness nonlinearity or a nonlinear damping mechanism that produces higher damping as excitation (and therefore response) levels increase.

10.4 System Model, System Identification and Parameter Estimation

In this section a model of the mass-material system is proposed and a continuous-time system identification technique that was used to estimate the parameters in the model is described.

10.4.1 Model of the Mass-Material System

The mass-material system is modeled as a mass-spring-damper with an additional viscoelastic term; see Fig. 10.1c. Recall that for a harmonic base excitation system the most generic form of equation of motion is a sum of viscoelastic, damping, stiffness, mass and forcing terms, it is of the form:

$$m\ddot{z} + c(z, \dot{z}) + k(z) + v(z, \dot{z}) = -m\ddot{y}, \quad (10.3)$$

where z is the relative motion of the mass, k the stiffness term which may be nonlinear, c is the damping term which also may be nonlinear, \ddot{y} the base acceleration, $v(t)$ is the viscoelastic term and m is the mass of the mid-plate (0.98 kg) plus a

third of the sample mass (see Table 10.1). The damping and stiffness terms may be functions of the relative displacement and velocity. Potential damping terms considered were a simple viscous damping term

$$c(z, \dot{z}) = c\dot{z}, \quad (10.4)$$

and a hysteretic damping term [7]:

$$c(z, \dot{z}) = c\dot{z} |\dot{z}|^\alpha. \quad (10.5)$$

For nonlinearities related to elasticity the stiffness term may be modeled by using a polynomial [5] or the more complex Ogden's hyperplastic model [6]. Here we chose a polynomial stiffness term for $k(z)$.

10.4.2 Continuous-Time System Identification

To illustrate the approach in the continuous-time system identification, the model in a simpler form is considered. This simpler model is chosen to have linear viscous damping term, a 3rd order polynomial stiffness term and no viscoelastic term ($v(t) = 0$), this simplifies Eq. (10.3) to the following form:

$$m\ddot{z} + c\dot{z} + k_1z + k_2z^2 + k_3z^3 = -m\ddot{y}. \quad (10.6)$$

Even though Eq. (10.6) is nonlinear it is linear in parameters, and in this case continuous time system identification is straightforward to implement. To estimate the parameters, k_1, k_2, k_3 , and c , the signals z, z^2, z^3 , and \dot{z} are used with Eq. (10.6) to produce:

$$\begin{bmatrix} -m\ddot{y}(1\Delta) - \ddot{z}(1\Delta) \\ -m\ddot{y}(2\Delta) - \ddot{z}(2\Delta) \\ \vdots \\ -m\ddot{y}(N\Delta) - \ddot{z}(N\Delta) \end{bmatrix} = \begin{bmatrix} \dot{z}(1\Delta) & z(1\Delta) & z^2(1\Delta) & z^3(1\Delta) \\ \dot{z}(2\Delta) & z(2\Delta) & z^2(2\Delta) & z^3(2\Delta) \\ \vdots & \vdots & \vdots & \vdots \\ \dot{z}(N\Delta) & z(N\Delta) & z^2(N\Delta) & z^3(N\Delta) \end{bmatrix} \begin{bmatrix} c \\ k_1 \\ k_2 \\ k_3 \end{bmatrix}, \quad (10.7a)$$

which can be written in matrix form as

$$q = Ap. \quad (10.7b)$$

where Δ is the time step [8]. To improve the accuracy of the parameter estimates, care was taken to ensure that all the columns in \mathbf{A} and \mathbf{q} were treated to equal amounts of filtering. A challenge of implementing the continuous time system identification approach is the need to derive the necessary time signals (displacement, and velocity) from the measured experimental acceleration and the sensitivity of these transformations to measurement noise [9].

10.4.3 Viscoelastic Term

A hereditary viscoelastic model was chosen for the viscoelastic term $v(t)$. The general expression is a convolution of a relaxation kernel with an arbitrary function $f(t)$ that may be dependent on the displacement, velocity or both, it is of the form:

$$v(t) = \int_{-\infty}^t f(\tau) \sum_i^M \beta_i e^{-\alpha(t-\tau)} d\tau, \quad (10.8)$$

where M is the order of the kernel and β and α are the system parameters. Here we consider the viscoelastic model where $f(t) = \dot{z}(t)$ and $M = 1$. To incorporate the viscoelastic term into Eq. (10.3) and set up the equations so we can use the

Table 10.2 Model considered to characterize the HTPB 0 % and HTPB 50 % experimental profiles

Model	Stiffness $k(z)$	Damping $c(z, \dot{z})$	Viscoelastic term $f(t)$
1	$k_1 z$	$c \dot{z}$	
2	$\sum_j^N k_j z^j, N = 1, 3, 5$	$c \dot{z}$	
3	$\sum_j^5 k_j z^j$	$c \dot{z} \dot{z} ^\alpha$	
4	$\sum_j^5 k_j z^j$	$c \dot{z}$	\dot{z}

continuous-time approach for estimating the parameters, first we recast the convolution in the $v(t)$ term as an ordinary differential equation. Recall that a convolution in time is a multiplication in the s domain. By taking the Laplace transform of Eq. (10.8), rearranging the terms and taking the inverse Laplace transform this convolution can be put in the differential equation form shown in Eq. (10.9). Putting

$$\dot{v}(t) + \alpha_1(t)v(t) = \beta_1 \dot{z} \quad (10.9)$$

Rearranging the original differential equation as:

$$v(t) = -\ddot{y}m - m\ddot{z} - c\dot{z} - k(z),$$

and differentiated to give an expression for $dv(t)/dt$ in terms of derivatives of v . The expressions for $v(t)$ and its derivative can be substituted back into Eq. (10.9) to form a single differential equation. When $k(z) = k_1 z$, it is of the form:

$$m\ddot{z} + (c + \alpha_1 m)\dot{z} + (k + \alpha_1 c + \beta_1)\dot{z} + \alpha_1 k z + \alpha_1 m\ddot{y} = -m\dot{y}. \quad (10.10)$$

The continuous time system identification approach described above can now be applied based on Eq. (10.10). It is still linear in parameters. Following the process with other forms of the viscoelastic model, the only word of caution is to make sure that the columns of the matrix \mathbf{A} are not linearly dependent when the estimation matrix is set up. Four different models were considered with different stiffness, damping and viscoelastic terms. The form of the stiffness, damping and viscoelastic terms for each of the four models are shown in Table 10.2.

10.5 Results

With estimated Models 1 and 2 we see the effects of increasing the order of the stiffness polynomial ($N = 1, 3$, and 5). R^2 was calculated for the different models for both the tests on HTPB 0 % and 50 % at both excitation levels. Note here the data gathered in a test is used to estimate the parameters in the model for that test. There is no improvement in the HTPB 0 % when the stiffness term order is increased from 1 to 3 to 5. There is a slight improvement for the HTPB 50 % case from $R^2 = 0.9975$ to $R^2 = 0.9980$. An effective linear stiffness term: k_{linear} was calculated for each of the models; which is a linear approximation to the estimated polynomial expression of the stiffness in the response displacement range in the test. How k_{linear} of Model 2 (with $N = 5$) changes as a function of the base excitation for the different samples and tests is shown in Fig. 10.4. The k_{linear} terms derived from the tests at the higher excitation level (10 g) are consistently lower than their 5 g excitation test counterparts. Possible explanations are that there is a softening nonlinearity playing a role or that the damping and viscoelastic terms are of insufficient structure to capture the complex damping/viscoelastic behavior and the resulting lowering of the location of the resonance frequency in this case is being modeled with a lower stiffness.

To improve the fit between the response envelope predicted from the estimated models and the experimental envelope, a nonlinear damping term was considered (Model 3). For Model 3, the 5th order nonlinear stiffness term was kept and the linear damping term was replaced with the term shown in Eq. (10.5). Note that if $\alpha = 0$ the system simplifies to Model 2 with $N = 5$. To be able to employ the described continuous time system identification approach (linear in parameters), α was set to a value and the other parameters (c and k_j) were estimated. This was done for a range of values of α from 0 to 3. The results for the HTPB 50 % sample excited at 10 g can be seen in Fig. 10.5. Including the nonlinear damping term altered the shape of the simulated profile; the peak is no longer pronounced. While $\alpha = 1.8$ improves the fit between 240 and 300 Hz the fit worsen at low frequencies (150–230 Hz).

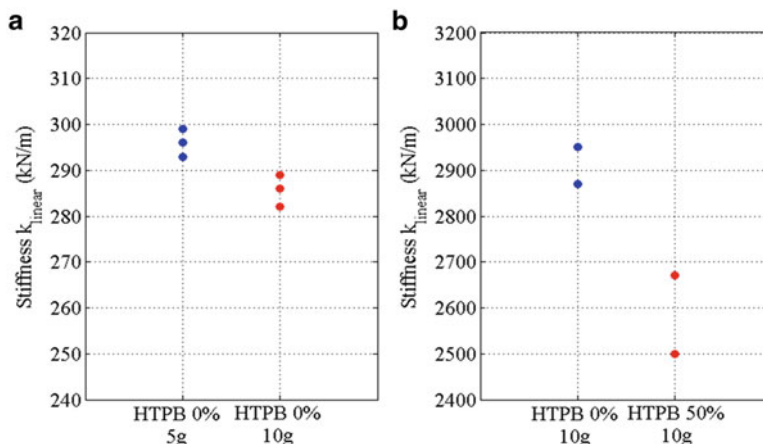


Fig. 10.4 The estimated linear stiffness (k_{linear}) derived from a fit of a model with a 5th order polynomial stiffness term (Model 2, $N = 5$) to the data for (a) HTPB 0 % and (b) HTPB 50 %. Blue indicates 5 g and red indicates 10 g base excitation. The three values in (a) and two in (b) come from the repeated tests on the same day

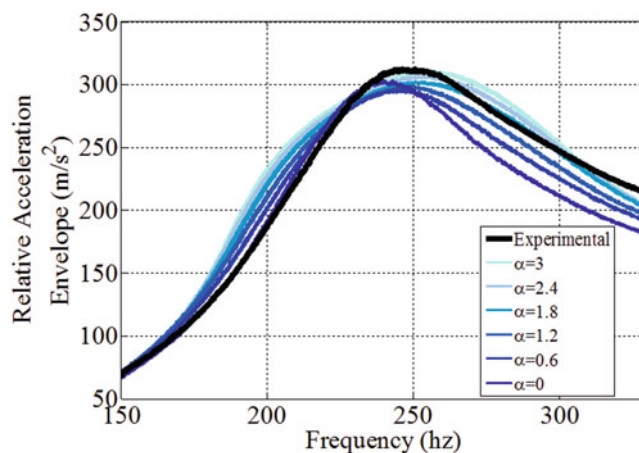


Fig. 10.5 Envelope of the relative acceleration of the HTPB 50 % excited at 10 g (black) and the Model 3 results with $\alpha = 0$ to $\alpha = 3$ (varying shades of blue from dark to light as α is increased). Note the model parameters c and k_i are re-estimated for each α

Next, the inclusion of a viscoelastic term was considered (Model 4). The model was fitted to data from both HTPB 0 % and HTPB 50 % experimental tests. The estimated and experimental response envelopes for HTPB 0 % and 50 % can be found in Fig. 10.6. Model 2 predictions (blue) are also included in the plots because the model structure is the same except for the viscoelastic term, $v(t)$ which is set to 0.

Overall, including a viscoelastic term improves the fit compared to Model 2 without a viscoelastic term: $v(t) = 0$. Unlike Model 2, Model 4 does a good job characterizing the behavior at frequencies above resonance as well as the lower frequency behavior. The effective linear stiffness term is calculated from the stiffness terms in all the different tests. These results are shown in Table 10.3. Note that the linear stiffness for Model 1 is just k_1 , and for Model 2, 3 and 4 it is a linear approximation to the 5th order polynomial stiffness over the response range in the tests. Also since the geometric properties of the sample are known, the Young's Modulus can be calculated from k_{linear} using the relation $E = Lk_{linear}/A$ [10]; these are given in Table 10.3.

The models estimated using data from a single experiment produced response predictions that were close to the experimental response in that experiment. However the parameters are different for each testing condition. When the 10 g parameter estimates were used to simulate the 5 g response (and vice versa) the fit worsened, particularly in the tests with the HTPB 50 %. Additionally, if multiple data sets were used in the estimation (base excitation tests of 5 and 10 g) the model did not predict the response envelope very accurately. This suggests that more terms are needed in the model and one approach would be to include much higher order viscoelastic models ($M > 1$) [11].

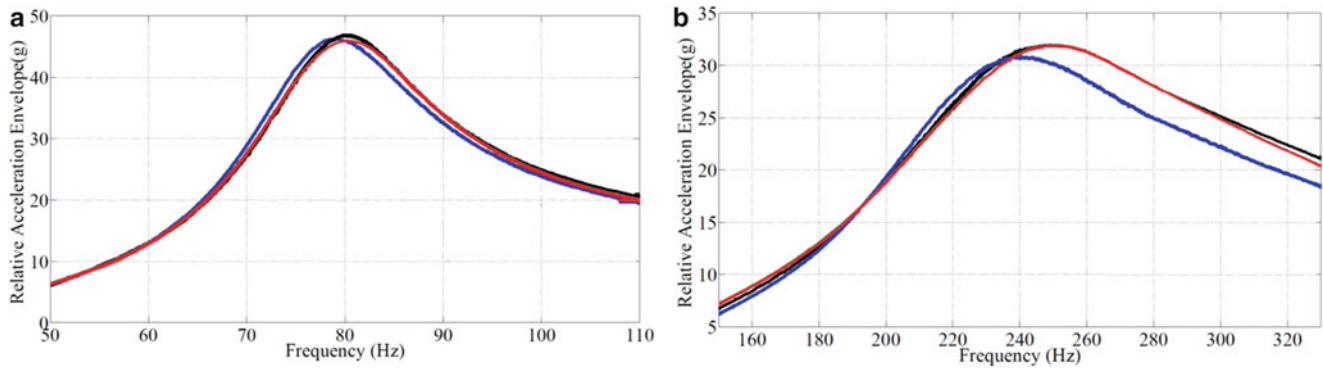


Fig. 10.6 Envelope of the relative acceleration of (a) HTPB 0 % and (b) HTPB 50 % excited at 10 g. *Black* is the experimental response envelope, *blue* is the predicted response envelope from Model 2 (without a viscoelastic term) and *red* is the predicted response envelope from Model 4, which included a viscoelastic term

Table 10.3 Estimated damping coefficient, effective linear stiffness and Young's modulus estimates for HTPB 0 % and HTPB 50 % surrogate explosive materials

			Model 1	Model 2 ($N = 5$)	Model 3 ($\alpha = 1.8, N = 5$)	Model 4 ($N = 5, M = 1$)
HTPB 0 %	5 g	c (Ns/m)	133.7	133.7		77.66
		k_{linear} (kN/m)	297.8	227.5		305.8
		E (MPa)	4.329	2.67		4.446
	10 g	c (Ns/m)	129.9	129.9		76.39
		k_{linear} (kN/m)	292.6	498.8		292.4
		E (MPa)	4.254	7.251		4.251
HTPB 50 %	5 g	c (Ns/m)	626.9	626.9	12605	158.5
		k_{linear} (kN/m)	2855	2197	2870	3150
		E (MPa)	47.7	36.71	47.96	52.64
	10 g	c (Ns/m)	619.9	619.9	15202	37.78
		k_{linear} (kN/m)	2646	1773	2710	3458
		E (MPa)	44.21	29.63	45.28	57.75

Material sample is a described in Table 10.2

10.6 Conclusions and Future Work

The low frequency (50–350 Hz) dynamics and repeatability of tests on surrogate energetic materials were examined. The binder surrogate (HTPB 0 %) had very good same day and day-to-day repeatability. The HTPB 50 % sample did not show good day-to-day repeatability despite have good same-day repeatability. The location of the resonance of a mass-material system when the material was HTPB 50 % shifted from 220 to 260 Hz over a 120 day period, suggesting the material is stiffening with time. Doubling the forcing and comparing the normalized responses in the two tests showed that the system with the HTPB 50 % material exhibited clear nonlinear behavior, the results are characteristic of materials with softening nonlinearities or of systems whose damping changes with forcing levels. Four different models were considered and fitted to the experimental data by using a continuous-time estimation procedure. These models contained different combinations of different stiffness, damping and viscoelastic terms. Overall Model 4, the only model with a viscoelastic term, produced the best response predictions amongst all the different models. The inclusion of a viscoelastic term greatly improves the predictions of the response. For each model the equivalent linear stiffness was calculated, along with the damping. The Young's Modulus was then calculated from the linear approximation of the stiffness. The Young's Modulus for HTPB 0 % ranges from 2.67 to 7.25 MPa and 29.63 to 66.29 MPa for HTPB 50 %. These values are in the range of stiffness identified in compression testing of these materials [1].

Further investigation consists of modifying the model by including a higher order viscoelastic kernel ($M > 1$) and different viscoelastic forcing functions, $f(t)$, other than the relative velocity forcing function considered here. This may allow prediction of the mass-material system response under different loading conditions [11].

Acknowledgments This material is based upon work supported by the U.S. Office of Naval Research as a Multi-disciplinary University Research Initiative on Sound and Electromagnetic Interacting Waves under grant number N00014-10-1-0958.

References

1. Cady, C.M., Blumenthal, W.R., Gray III, G.T., Idar, D.J.: Mechanical properties of plastic-bonded explosive materials as a function of strain-rate and temperature. *Polym. Eng. Sci.* **46**(6), 812–819 (2006)
2. Siviour, C.R., Gifford, M.J., Walley, S.M., Proud, W.G., Field, J.E.: Particle size effects on the mechanical properties of a polymer bonded explosive. *J. Mater Sci.* **39**(4), 1255–1258 (2004)
3. Paripovic, J.: Characterization and modeling of materials used in improvised explosive devices. Master's thesis, Purdue University, West Lafayette, IN 47907 (2013)
4. Oppenheim, A.V., Schaffer, R.W.: *Digital Signal Processing*, Englewood cliffs. Prentice Hall (1975)
5. Rong, D.: Modeling and characterization of flexible polyurethane foams. Ph.D. thesis, Purdue University, West Lafayette, IN 47907 (2004)
6. Ogden, R.W.: *Nonlinear Elastic Deformations*. Dover Publications, Mineola (1984) Print
7. Doughty, T.: System identification of modes in non linear structures. Ph.D. thesis, Purdue University, West Lafayette, IN 47907 (2002)
8. Doughty, T., Davies, P., Bajaj, A.K.: A comparison of three techniques using steady-state data to identify nonlinear modal behavior of an externally excited cantilever beam. *J. Sound Vib.* **249**(4), 785–813 (2002)
9. Garnier, H., Wang, L.: *Identification of Continuous-Time Models From Sampled Data*. London, Springer (2008)
10. Chau, K.: Young's modulus interpreted from compression tests with end friction. *J. Eng. Mech.* **123**(1), 1–7 (1997)
11. Azizi, Y., Bajaj, A.K., Davies, P.: Identification and investigation of nonlinear viscoelastic models of flexible polyurethane foam from uniaxial compression data. In: *Proceedings of ASME International Mechanical Engineering Conference and Exposition*, Paper Number: IMECE2012-88190, Houston, Texas, 447–454 October 2012

Chapter 11

Multimodal Damping of a Plate with a Passive Piezoelectric Network

B. Lossouarn, M. Aucejo, J.-F. Deü, and K.A. Cunefare

Abstract Multimodal vibration reduction can be obtained by coupling a mechanical structure to an electrical network approximating its modal properties. This strategy is applied to the control of a clamped plate with a 2D network of passive electrical components. The plate and the network are coupled through a periodic array of piezoelectric patches that enables the energy conversion. The network is experimentally implemented with inductors and transformers in order to create electrical resonances that present a spatial distribution approaching the first mode shapes of the plate. By tuning electrical resonances to mechanical ones, it becomes possible to introduce the equivalent of a tuned mass effect. This effect only occurs if the electrical and mechanical mode shapes are sufficiently close, which requires specific network topology and boundary conditions. Once the network is tuned, adding resistors introduces damping that can lead to a broadband vibration reduction of the plate. It is thus shown that a 2D control can be implemented with a purely passive solution, which could be of great interest for many embedded applications.

Keywords Multimodal damping • Piezoelectric coupling • Periodic array • Resonant network • Passive control

11.1 Introduction

Arrays of piezoelectric patches enables the implementation of efficient control strategies focusing on large wavelength compared to the dimension of the patches. Indeed, using multiple patches of reduced dimensions limits the charge cancellation that would happen with longer patches, which allows a control over a wider frequency range. Several solutions involving an array of piezoelectric shunts have been proposed to damp vibration of plates. Resonant shunts [1, 2] exhibit performance around the electrical resonance but a multimodal control would require the addition of several electrical resonances for each shunt, which would lead to an impractical number of components. Broadband wave attenuation can be obtained with negative capacitance circuits [3] but this solution requires an external power supply. So, the passive implementation of a robust multimodal control of a plate is still an open problem.

A theoretical concept was proposed by Vidoli and dell'Isola [4], who presented an interconnection of piezoelectric patches through a 2D electrical network. An efficient energy transfer is obtained by tuning analogous plate-like electrical modes to the corresponding mechanical modes of the plate. The coupling of two structures exhibiting similar resonances acts as a tuned mass damping of several modes simultaneously. A suitable topology of the electrical network can be determined from the electrical analogue of a plate. Alessandrini et al. [5] used a Lagrangian formulation to find an electrical network as a discrete analogue of a plate unit cell. Unfortunately, the large number of electrical components required for each unit cell of the network makes its practical implementation difficult.

In the present contribution, we focus on a new electrical topology that reduces the number of required components. The proposed electrical network is obtained by extending a procedure previously applied to rods and beams [6–9]. It consists of a finite difference formulation of the equations describing the mechanical medium, followed by a direct electromechanical analogy. A 2D electrical topology involving capacitors, inductors and transformers is thus defined. This network is implemented with passive components in a case focusing on the analogue of a clamped plate. The electrical modes are observed experimentally, which validates the analogous electrical topology. Afterward, the control of a clamped plate is considered by a coupling to the electrical network through an array of piezoelectric patches. A significant vibration

B. Lossouarn (✉) • M. Aucejo • J.-F. Deü
Structural Mechanics and Coupled Systems Laboratory, CNAM, 2 Rue Conté, 75003 Paris, France
e-mail: boris.lossouarn@cnam.fr

K.A. Cunefare
Woodruff School of Mechanical Engineering, Georgia Institute of Technology, 813 Ferst Dr, Atlanta, GA 30332, USA

reduction is observed over a broad frequency range. Depending on the application, the electrical network is then tuned by adding resistors or by modifying the values of the inductors. In the end, a passive and tunable solution for the control of a plate is proposed and experimentally validated.

11.2 Electrical Analogue of a Plate

An electrical analogue of a plate is found from a discretization of the mechanical medium followed by a direct electromechanical analogy. The resulting electrical network is implemented with passive components and the topology is validated by observing electric modal properties that are analogous to what can be obtained for a clamped plate.

11.2.1 Direct Electromechanical Analogy

As a two-dimensional extension of the Euler-Bernoulli beam theory, the Kirchhoff-Love plate theory gives a relation between the spatial and temporal derivatives of the transverse displacement w through the equation

$$D \left(\frac{\partial^4 w}{\partial x^4} + 2 \frac{\partial^4 w}{\partial x^2 \partial y^2} + \frac{\partial^4 w}{\partial y^4} \right) = -\rho h \frac{\partial^2 w}{\partial t^2}, \quad \text{where } D = \frac{Yh^3}{12(1-\nu^2)}. \quad (11.1)$$

Y , ν , ρ and h are respectively the Young's modulus, the Poisson's ratio, the density and the thickness of the plate. $\partial[.]/\partial x$ and $\partial[.]/\partial y$ represent the partial derivative along the principal directions x and y . It can be shown that a finite difference procedure applied to those differential operators in Eq. (11.1) leads to a set of discrete equations that can be represented under the electrical scheme in Fig. 11.1.

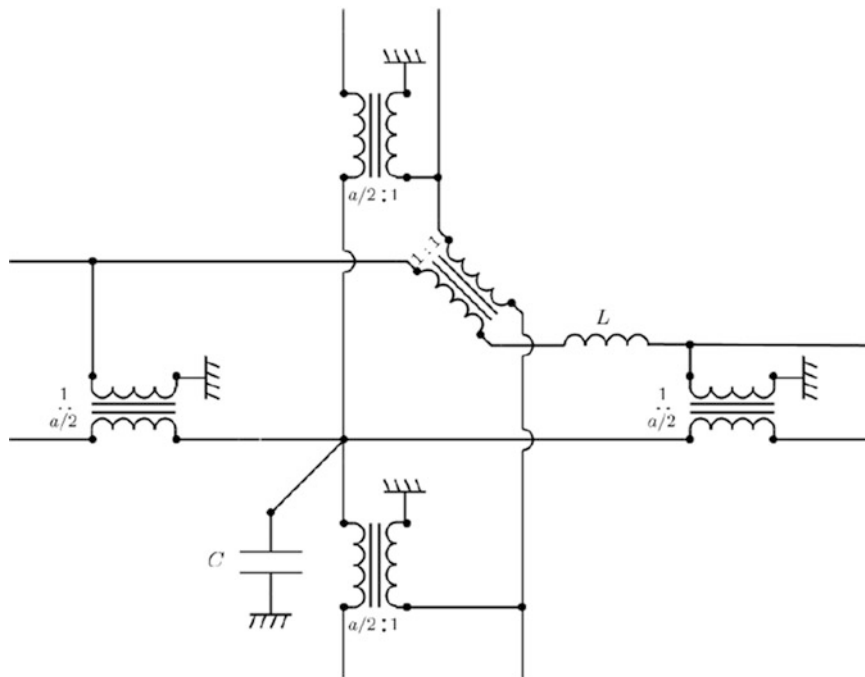


Fig. 11.1 Electrical unit cell corresponding to the analogue of a discretized square plate

The proposed topology is based on the direct electromechanical analogy, which assumes an equivalence between mass and inductance and between stiffness and the inverse of a capacitance. The inductance L is then equal to ρha^2 , which corresponds to the mass of a square unit cell of side a . C is equal to $1/D$, the inverse of the bending stiffness of the square plate element. The analogous electrical unit cell can thus be implemented with only one inductor, one capacitor and five transformers.

Note that the connection of adjacent unit cells reduces the number of components. Indeed, a series of two transformers of ratio $a/2$ can be replaced by a single transformer with a ratio equal to a . This simplification does not apply to the boundaries, but the average number of transformers per unit cell still tends to 3 when the number of unit cells is increasing. A simpler network is finally obtained compared to the topology proposed by Alessandroni et al. [5], which involves three inductors, one capacitor and six transformers per unit cell. As a consequence, the new topology simplifies the practical implementation of the analogous network for experimental validation and application to piezoelectric damping.

11.2.2 Experimental Validation

In order to validate the electrical topology, we focus on the analogue of a clamped plate discretized with 20 unit cells. The clamped boundary conditions require zero displacement and zero rotation along the four edges of the plate. The direct analogue in the electrical domain corresponds to zero current flowing through the edges of the electrical network. Those electrical boundary conditions simplify the network to an electrical analogue made of 6 inductors, 16 capacitors and 23 transformers.

As the proposed electrical network represents the analogue of a clamped plate, it was decided to validate the electrical behavior with classical instrumentation normally dedicated to mechanical modal analysis. The setup is represented in Fig. 11.2 where a clamped plate and its electrical analogue appear together in order to show the analogy in term of data acquisition. If the considered structure is the mechanical plate, we acquire the input force and the velocity, which is scanned on several points with a vibrometer. If the electrical network is analyzed, the signals of interest are not force and velocity but their direct analogues: an input voltage and the current flowing through the inductors. The direct measurement of the current would require the introduction of instruments in the network, but this could modify its electrical properties. A less intrusive solution consists in measuring the voltage drop across the inductors, which is finally the analogue of the acceleration. This differential voltage is measured by using a low noise preamplifier offering a differential function. The resulting signal and the voltage input are sent to the workstation, where the electrical frequency response function (FRF) is computed.

Electrical mode shapes can be determined by scanning several points of the electrical network. This requires the use of two preamplifiers and a switch, which allows changing the measurement location without any delay. While the voltage drop is measured on one inductor, we have time to prepare the electrical connections for the next measurement. This is crucial, as the scanning process is controlled by the vibrometer software that generates an instantaneous switching between measurement points.

The electrical mode shapes are represented in Fig. 11.3 together with an electrical FRF measured at locations that are analogous to the points of excitation and measurement represented in Fig. 11.2 for the clamped plate. The presence of six inductors in the network naturally yields six electrical resonances. Compared to classical FRFs obtained for a plate, each resonance exhibits a low quality factor, which is due to the internal damping in the electrical components. The spatial distributions of the electrical current are similar to the first six mode shapes of a clamped plate. This validates the proposed network topology that comes from the Kirchhoff-Love plate theory.

11.3 Multimodal Piezoelectric Damping

Once the design of the electrical network is validated, it can be applied to the damping of a clamped plate. The network is coupled to the plate with an array of piezoelectric patches. When electrical modes match their mechanical analogues, significant multimodal vibration reduction is observed.

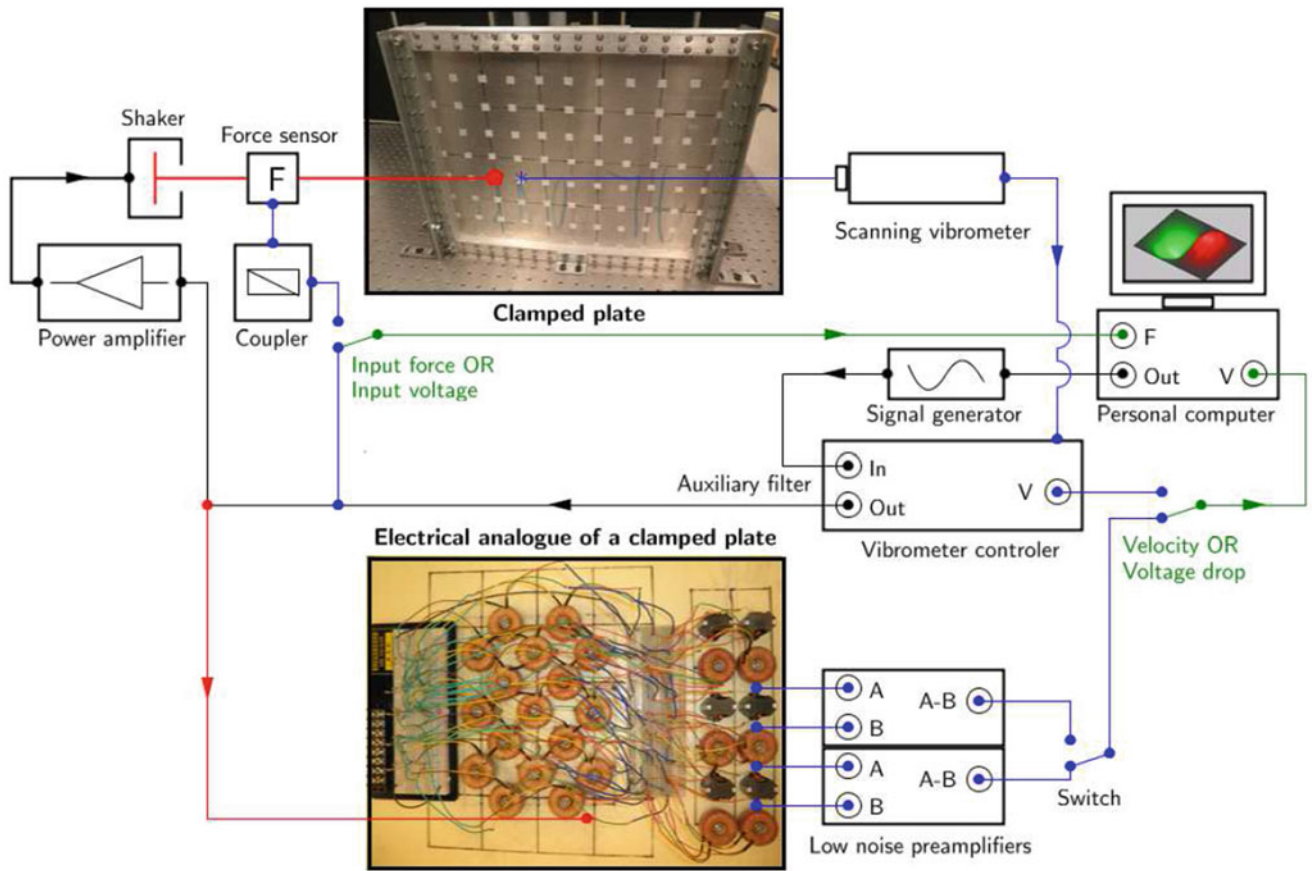


Fig. 11.2 Experimental setup for the modal analysis of a clamped plate or for its analogous electrical network

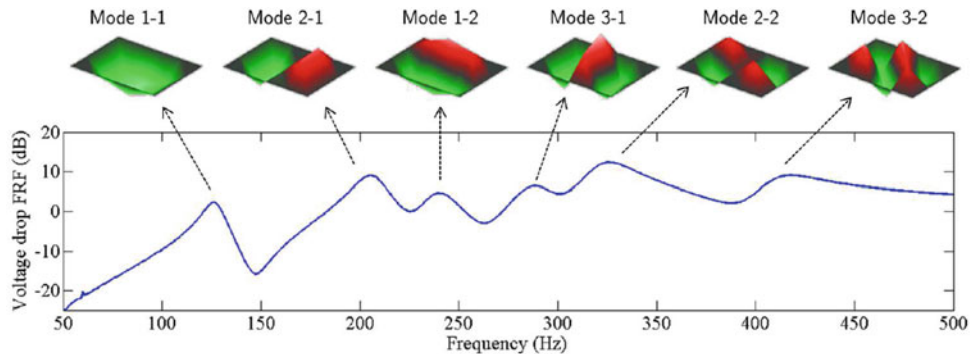


Fig. 11.3 Electrical frequency response function of the network and the corresponding electrical mode shapes

11.3.1 Clamped Plate

The mechanical structure to control is a clamped aluminum plate 400 mm long, 320 mm wide and 1.9 mm thick. The clamping frame is made of square aluminum bars reinforced with steel angle channels. Two rows of bolts are equally tightened with a torque wrench to ensure zero deflection and zero slope boundary conditions. A white noise excitation is generated from a shaker and the transverse velocity of the plate is measured with a laser vibrometer, as represented in Fig. 11.2. The input force is measured with a force sensor placed between the shaker and the plate. The force signal is then processed together with the velocity signal to compute the velocity FRF.

As seen in Fig. 11.4, the aluminum plate is covered with an array of 20 square piezoelectric patches of side 72.4 and 0.27 mm thickness. The patches are made of PZT-5H, which is a soft piezoceramic. As a reference, it is observed that the

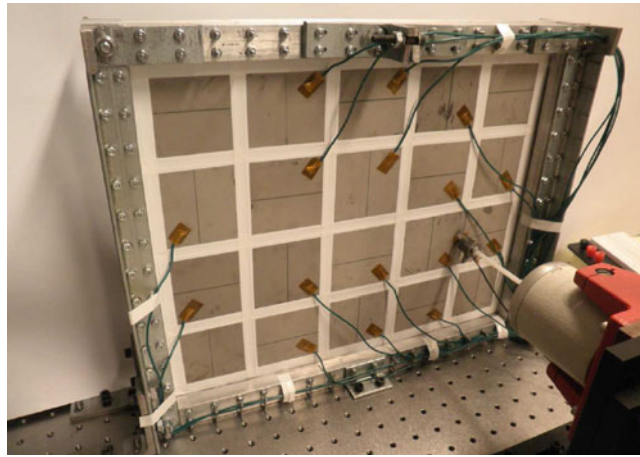


Fig. 11.4 Clamped aluminum plate covered with 20 square piezoelectric patches

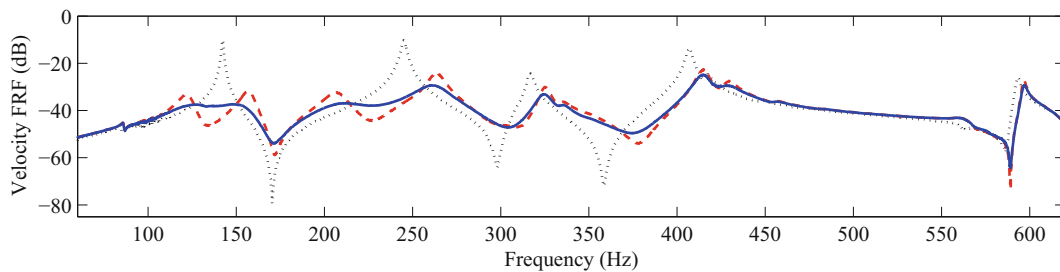


Fig. 11.5 Effect of the multimodal control on the velocity frequency response function of the plate: (*dotted line*) with open-circuited patches, (*red dashed line*) with coupling to the analogous electrical network and no external resistance: (*blue solid line*) with coupling to the analogous electrical network and $180\ \Omega$ in series with each inductor

first mode of the plate is around 140 Hz with open-circuited patches and this frequency is decreased by 3.5 % once the patches are short-circuited. The frequency range of the analysis was defined according to the number of plate-like modes that can be generated with the electrical network to influence the mechanical frequency responses. We thus focus on the first six modes of the plate, which spread until 600 Hz. The open-circuited FRF is presented in Fig. 11.5, where six resonances are observed. The distinction between the fourth and fifth resonances is not straightforward because they occur at almost the same frequency.

11.3.2 Coupling to the Electrical Network

The electrical network is connected to the plate by replacing the capacitance C , represented in Fig. 11.1, by the piezoelectric capacitance offered by the patches. Consequently, no external capacitors are required. According to the discrete network topology obtained for a clamped plate, the patches on the corners do not play any role. Only 16 of the 20 patches are thus connected to the electrical network for the present application. Once the network is engaged, it is seen in Fig. 11.5 that the coupling provides a strong modification of the modal behavior of the plate.

For the measurements presented in Fig. 11.5, the value of the six inductors is equal to 1 H, which leads to a suitable tuning of the network around the first mode of the plate. Indeed, we can observe a local minimum around 140 Hz surrounded by two local maximum that present approximately the same amplitude. This is a characteristic of an underdamped tuned mass control, which is here generated by the resonant network. It is remarked that the vibration reduction is also significant for the higher modes. However, the network does not offer a tuning that is optimized on all the modes simultaneously. This is due to the fact that the electrical network is a discrete structure that only approximates the continuous plate behavior. The lower electrical resonances occur at frequencies that are close to the corresponding mechanical resonances but for higher modes the frequency error becomes non-negligible. It is possible to more closely match the first six resonances of the plate with the same network topology by increasing the number of unit cells.

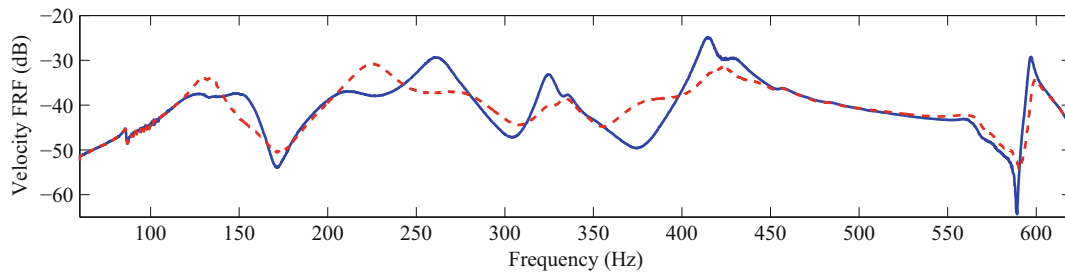


Fig. 11.6 Tuning of the network: (*blue solid line*) minimization of the amplitude around the first mode with $L = 1$ H, (*dashed line*) optimization over a broader frequency range with $L = 0.8$ H

11.3.3 Tuning Procedures

The network can be tuned in different ways depending on the considered application. For example, if a control is required at one specific frequency which is near a mechanical resonance, the inductors can be adjusted to move the corresponding electrical resonance closer. This would induce an antiresonance, as seen in Fig. 11.5 around the first and second modes. Then, the internal damping in the components should be minimized in order to increase the depth of the antiresonance.

On the other hand, a control on a broader frequency range requires the introduction of additional damping in the network. Indeed, it is shown in Fig. 11.5 that $180\ \Omega$ resistors in series with the six inductors flatten the frequency response function. A vibration reduction close to 27 dB is then obtained around the first mode. It is noticed that the addition of resistance does not necessarily increase the number of components as it can be included into the design of the inductors. It is seen in Fig. 11.5 that the introduction of resistors mainly affects the first two modes because of the discretization of the electrical network that yields inaccurate tuning at higher frequencies. However, a solution for a broadband vibration reduction with the considered discrete network can be to detune the first modes to better tune higher modes. This strategy is presented in Fig. 11.6, where the previous case involving a network with 1 H inductors and $180\ \Omega$ resistors is compared to a second case with 0.8 H inductors and the same resistors. By decreasing the inductance, the electrical resonances move to higher frequencies. In this case, it can be noticed that the second electrical resonance is moved from a frequency below the second mechanical resonance to a frequency above it. Even if the modification of the tuning is not beneficial for the first mode, the maximum of the amplitude over the frequency range of interest is minimized. The detuning of the first mode moves the higher electrical resonances closer to their mechanical analogues, which clearly reduces the amplitude of the frequency response function around the higher modes. It is thus finally shown that the proposed passive damping can induce substantial vibration reduction over a broad frequency range.

11.4 Conclusions

A new electrical topology that approximates the modal properties of a plate was obtained from a finite difference procedure applied to the Kirchhoff-Love equation, followed by a direct electromechanical analogy. The resulting network was implemented with passive components and validated experimentally through a modal analysis procedure similar to what is normally performed for a mechanical structure. Plate-like mode shapes are observed when looking at the distribution of the current over the electrical network. To the best knowledge of the authors, this work presents the first practical implementation of a plate electrical analogue based on the direct electromechanical analogy. It is thus also the first time that such a passive network is connected to a plate for a piezoelectric damping purpose. It is observed that the coupling induces a significant modification of the mechanical response. Depending on the application, a suitable tuning of the electrical network can then optimize the vibration reduction around one specific frequency or over a broad frequency range.

Acknowledgments The authors would like to thank the French Ministry of National Education, Higher Education and Research for providing a 3 year scholarship for doctoral studies related to piezoelectric damping. The authors also sincerely acknowledge the Fulbright Program, which made possible a 9-month visit at the Georgia Institute of Technology.

References

1. Casadei, F., Ruzzene, M., Dozio L., Cunefare, K.A.: Broadband vibration control through periodic arrays of resonant shunts: experimental investigation on plates. *Smart Mater. Struct.* **19**(1), 015002 (2010)
2. Chen, S., Wang, G., Wen, J., Wen, X.: Wave propagation and attenuation in plates with periodic arrays of shunted piezo-patches. *J. Sound Vib.* **332**(6), 1520–1532 (2013)
3. Tateo, F., Collet, M., Ouisse, M., Cunefare, K.A.: Design variables for optimizing adaptive metacomposite made of shunted piezoelectric patches distribution. *J. Vib. Control* in press, doi: 10.1177/1077546314545100 (2014)
4. Vidoli, S., Dell’Isola, F.: Vibration control in plates by uniformly distributed PZT actuators interconnected via electric networks. *Eur. J. Mech. A. Solids* **20**(3), 435–456 (2001)
5. Alessandrini, S., Andreus, U., Dell’Isola, F., Porfiri, M.: A passive electric controller for multimodal vibrations of thin plates. *Comput. Struct.* **83**(15), 1236–1250 (2005)
6. Lossouarn, B., Aucejo, M. and Deü, J.-F.: Multimodal coupling of periodic lattices and application to rod vibration damping with a piezoelectric network. *Smart Mater. Struct.* **24**(4), 045018 (2015)
7. Lossouarn, B., Aucejo, M., Deü, J.-F.: Multimodal vibration damping through a periodic array of piezoelectric patches connected to a passive network. *Proc. SPIE* **9431**, 94311A–94311A-14 (2015)
8. Porfiri, M., Dell’Isola, F., Mascioli, F.M.F.: Circuit analog of a beam and its application to multimodal vibration damping, using piezoelectric transducers. *Int. J. Circuit Theory Appl.* **32**(4), 167–198 (2004)
9. Lossouarn, B., Deü, J.-F., Aucejo, M.: Multimodal vibration damping of a beam with a periodic array of piezoelectric patches connected to a passive electrical network. *Smart Mater. Struct.* **24**(11), 115037 (2015)

Chapter 12

State Estimation: A Model-Based Approach to Extend Test Data Exploitation

Herman Van der Auweraer, Steven Gillijns, Stijn Donders, Jan Croes, Frank Naets, and Wim Desmet

Abstract Design models can drastically improve the applicability of testing and allow measuring previously unmeasurable quantities and designing reduced test configurations. A common workflow is followed: a multiphysics system model provides a prediction of the system states which is corrected by the estimation algorithms using the measurement data. The model can then generate data of the non-measurable quantities (e.g. virtual sensors). A wide range of models can be used, including analytical, 1D lumped parameter and 3D distributed parameter models. Key is that they are easy to evaluate and have a small number of states, while capturing the dominant physics. Novel model order reduction techniques enable the use of more complex models. A wide range of state estimation approaches has been developed such as the (linear, extended, unscented, . . .) Kalman Filter and the Moving Horizon Estimator. All approaches require a trade-off between accuracy and computational load so that conventional estimators must be tailored to deal with high-fidelity nonlinear models of industrial complexity. The approach is illustrated with two cases: the estimation of hard-to-measure vehicle body forces using the extended Kalman filter and the application to an electro-mechanical drivetrain subject to unknown input forces. Methodological aspects are evaluated and different estimators are compared.

Keywords State estimation • Simulation • Testing • Multiphysics • Virtual sensing

12.1 Introduction: Industrial Needs to Measure the Unmeasurable

In all phases of the product life cycle, from design to development, commissioning and operation, experimental analysis plays a key role. Benchmark tests help to set targets and validate requirements, simulation models need to be verified and updated, prototypes to be checked and refined, final products to be certified and commissioned and during operation performance must be monitored. The task of the hereto required experiments is to measure the quantities of the selected parameters or variables which can then be checked against targets, analysed in the time or frequency domain, processed into black box models (such as EMA modal models) or used to validate numerical models. The physical quantities of interest in the applications investigated for the present study are all highly dynamic and hence take the form of measurement signals.

The basic assumption however of this process is that the concerned signals can effectively be measured. This is often far from trivial for a variety of reasons. Quantities such as forces and moments are often hard to obtain without affecting the structure under test or without using complex and expensive sensors. This is in particular the case for internal load variables in composed structures, for example the force transmitted between a car suspension and the car body or the torque in a driveshaft. It may also be that the quantities of interest have to be measured at physical locations which are hard or even impossible to access such as in a wheel spindle or in bearings or gears or the contact surface between the road and a tyre. Next to advanced sensors and sensor systems (such as complex and expensive torque sensors), inverse procedures have been developed that use off-line measured non-parametric models in combination with operating response data to estimate the loads acting on the system under evaluation. In most cases, frequency domain frequency response function models are

H. Van der Auweraer (✉)
Siemens Industry Software NV, Researchpark 1237, Interleuvenlaan 68, 3001 Leuven, Belgium

KU Leuven – PMA, Celestijnenlaan 300 – bus 2420, 3001 Leuven, Belgium
e-mail: herman.vanderauweraer@siemens.com

S. Gillijns • S. Donders
Siemens Industry Software NV, Researchpark 1237, Interleuvenlaan 68, 3001 Leuven, Belgium

J. Croes • F. Naets • W. Desmet
KU Leuven – PMA, Celestijnenlaan 300 – bus 2420, 3001 Leuven, Belgium

used, processed through matrix inversion with all related noise sensitivity and numerical conditioning problems. The force identification procedures in Transfer Path Analysis belong to this category, leading to continued research efforts focused on adequate load identification methods [1–3]. When time domain loads are needed, these are derived from the spectra either by transforming the spectral loads in time series or by transforming the inverse FRF matrix functions into filters. In the case of non-linear or multiphysics systems, these approaches face additional challenges. Finally, in industrial systems to be tested during normal life operation, cost considerations as well as robustness and reliability requirements make that the number and complexity of sensors must be minimized within the limits of the observability characteristics of the system under test. Hence a strong need exists for feasible methods that allow to deduce the values of physical quantities from other measurement data and this for dynamically varying signals.

In the control systems domain where the above sketched problem is also strongly present, a model based approach is adopted to derive the values of unmeasured quantities, based on the state estimation methodology [4, 5]. In the present study, the application of the state estimation methodology to the product life cycle measurement problem is explored.

12.2 State Estimation: Capitalize on Industrial Models to Measure the Unmeasurable

12.2.1 Matching Models with State Estimation Needs

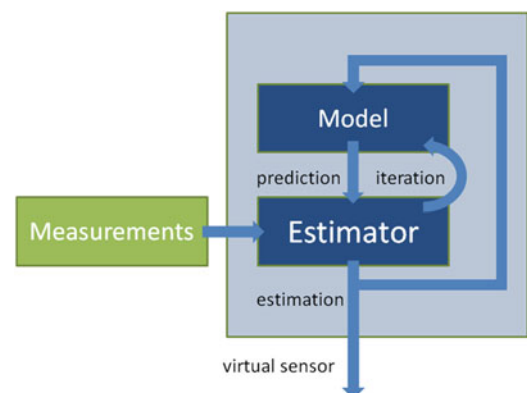
Over the past decades a range of methods have been developed to exploit the (combined) knowledge from different measurements as effectively as possible. However, in those approaches the inherent physics-based knowledge available in design models is typically overlooked. Exploiting this information in data processing can drastically improve the robustness and applicability of measurement processing. In this respect multiphysical models can be exploited during the design phase to define a measurement campaign to identify the dominant physics influencing the system performance. Once the measurement campaign has finished, state/input/parameter estimation techniques can be used to quantify the model discrepancy, identify uncertain parameters and provide ‘**virtual sensor**’ data of quantities that cannot be measured directly. The strength of such an approach is that the knowledge of both the measurements and model combined is far better than the individual sources.

In general these estimation techniques follow a global workflow depicted in Fig. 12.1. The model provides a prediction of the states at the next time step which is corrected by the estimation algorithms using the measurement data. As the updated set of states fully represents the system, the model can generate data of the non-measurable quantities (e.g. virtual sensors).

The measurements which are employed in standard testing practice are typically dictated by available sensor technology and test environment requirements or limitations. Model-based estimators open new possibilities depending on the nature of the model and estimator. A wide range of models is already available for design purposes. These models vary from analytical models to lumped parameter (1D) descriptions and detailed (3D) distributed parameter models that contain all the geometric information. Not all these models are directly suitable for state estimation, due to computational cost, observability limitations or lack of gradient information. Also, the exact (numerical) formulation often has to be adapted to allow interfacing with state estimation approaches (for instance, standard recursive techniques as the Extended Kalman Filter are not equipped to handle differential algebraic equations (DAEs)). Three points of attention are:

1. the computational load of the models,
2. the interfacing strategy between the estimator and the model
3. the amount of information as compared to the number of states (observability).

Fig. 12.1 Model based estimation overview



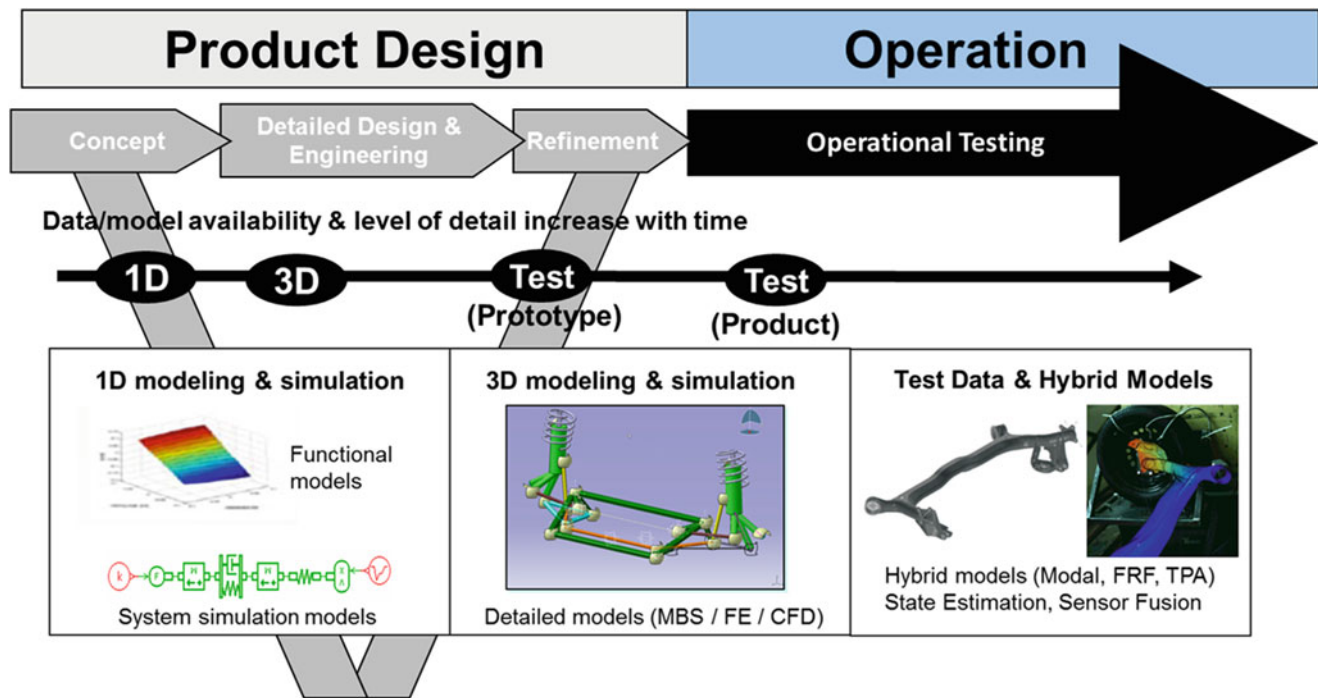


Fig. 12.2 Extended V-cycle for product design & operation process, with the use of models and test data along the timeline

One of the prime challenges in this research field is to build models that are easy to evaluate and that have a small number of states, while still capturing the most dominant physics. In this respect novel advanced model order reduction techniques can enable the use of more advanced models than previously possible [6, 7]. On the other hand an estimator approach has to be selected as well. Since the introduction of the linear Kalman filter in the 1950s, a wide range of estimator approaches have been developed [4]. For these approaches often a **trade-off** between accuracy and computational load has to be made: while high end estimators provide a much higher **accuracy** of the state, inputs and parameter predictions and more information on the estimated uncertainty distribution, they often come with a heavy **computational burden** due to the iterative nature of these algorithms. As the performance of the state estimation algorithms is highly dependent on the quality of the model, the conventional estimators have to be tailored to be able to deal with high-fidelity nonlinear models of industrial complexity. Section 12.2.3 discusses some of the most common estimator methods and how they can be coupled to different design models.

12.2.2 Industrial Modeling Approaches

Figure 12.2 shows the extended V-cycle (i.e. the “square-root sign”) that represents the product design & operation process for instance for vehicles [8, 9]. The vertical direction in the V-cycle diagram ranges from ‘system level’ (top) via ‘subsystem level’ to ‘component level’ (bottom).

- The left arm of the “V” represents the design phase. Based on the system-level requirements (at the top of the “V”), the design engineers must move downward (along the left side of the “V”) to translate the system requirements into the subsystem-level targets of the individual subsystems, which are then possibly broken down further into component-level targets. The models made in the design phase can serve their purpose for the use of state estimation algorithms in the validation phase and the definition of the test campaign.
- The right arm of the “V” is the validation phase, where the requirements that have been put forward during the design are verified against (prototype) test data. This starts with the components’ performance validation, followed by the detailed engineering & validation of subsystem-level and finally system-level performance.
- After successful validation, the product is released on the market and starts its operation phase (horizontal arrow after the “V”). During the operational lifetime, the product is monitored for proper operation and for maintenance.

The horizontal axis represents the timeline of the design and operations process, consisting of four main phases: concept definition, detailed design, engineering refinement engineering and the operational phase. The data quality and model availability increases with time, and the level of detail increases with time. Throughout the timeline of the design and operation phase, the aim is to exploit the available models and test data at any time.

- In a 1D modelling approach, the system is divided in a set of discrete entities that are linked together via its input/output behaviour. Each entity is a sub-model that provides a relationship between the interface points with the rest of the model. As such, 1D subsystem models can have a functional representation (data tables, maps, splines, surface matrices . . .) or simulate a system, built up of components and subsystems in a functional scheme, with interaction typically based on power exchange—adopting the bond graph methodology for interfacing models of different multiphysical nature [10]. The benefit of a 1D modelling approach is that the system level architecture is independent of the submodel complexity. By describing the different entities into ‘equivalent’ bond graph blocks, the system equations generally leads to a minimal set of states, which is desirable in a state estimation framework.
- 3D modelling approaches become possible from the detailed engineering phase onwards, as detailed 3D CAD models become available. A continuous description for the spatial distribution of geometrical and material properties is taken into account into the governing equations, which are typically solved numerically through a discretization in space and possibly in time. From a practical viewpoint, 3D modelling & simulation comprises the use of detailed simulation models, built from a detailed geometry base. Examples are multi-body simulation (MBS) models, flexible finite element (FE) models, boundary element (BE) models and computational fluid dynamics (CFD) models. As these models are computationally very expensive in their full geometry-based representation, model reduction techniques often have to be applied to derive reduced models that can be used in-the-loop [11–13], and thus ensure fast evaluation and the representation of the relevant physics with a limited set of states. These reduced models have several important advantages over nonreduced models. First of all they allow an important speed up in model evaluation. On the one hand this is caused by an important reduction in the number of degrees-of-freedom which is typically also coupled to a more suitable truncation in the frequency content of the model (enabling larger timesteps in the integration). On the other hand, these techniques can also improve the structure of the model equations. The model reduction can lead to an ordinary differential equation (ODE) description for an original differential-algebraic equation (DAE) description (e.g. in multibody simulation), making them more suitable for the integration in a state estimation environment [6]. Secondly, model reduction can also lead to better observability properties. The selected limited set of motion modes can be selected to omit the unobservable behaviour of the system, such that a more stable estimator can be obtained.
- Hybrid Test-CAE modelling approaches are possible from the refinement engineering stage onwards, with the availability of first test prototypes [4]. One example is the creation of hybrid models in which a 3D model of a newly designed component is combined with an experimentally identified model of an already existing component (prototype). Especially in case of re-using complex components with nonlinear behavior in a future design, such hybrid modelling approaches can be very interesting. In this phase, also the correlation and updating user scenario is relevant, for instance by improving a Finite Element Model (FEM) based on Experimental Modal Analysis (EMA) results from a vibration test. Moreover, the reduced EMA model can also have a value to be used directly in a state estimation environment, representing part of the realistic physics of the system in a concise representation.

12.2.3 State Estimation Methods

This section presents a more detailed account on the algorithms behind the state estimation methods. State estimation is a time domain approach to predict the true values of states of a model, given a set of measurements. The basic idea is to use a weighted sum of both the measurements and model predictions to make an overall optimal prediction of the true value of the states. These states can be states internal to the physical system, or augmented states: states that are added to the system equation, and that can represent inputs/parameters that are unknown or cannot be measured directly. Virtual sensors can be introduced via numerical calculations on top of internal system states, or as augmented states. The choice of the weights in the weighted sum is often inspired by the noise level on the measurements and the accuracy of the model. In this way, the model is continuously synchronized with the measurement data and can be used for analysis and control.

All state estimation techniques employ a model formulation that describes the dependencies between the internal states x_k over time (1) and a measurement equation that governs the relationship between the states x_k and the measurement data y_k . Each equation has a respective noise term w_k and v_k that is weighted to represent its accuracy.

Model equation:

$$x_{(k+1)} = f(x_k, u_k, w_k) \quad (12.1)$$

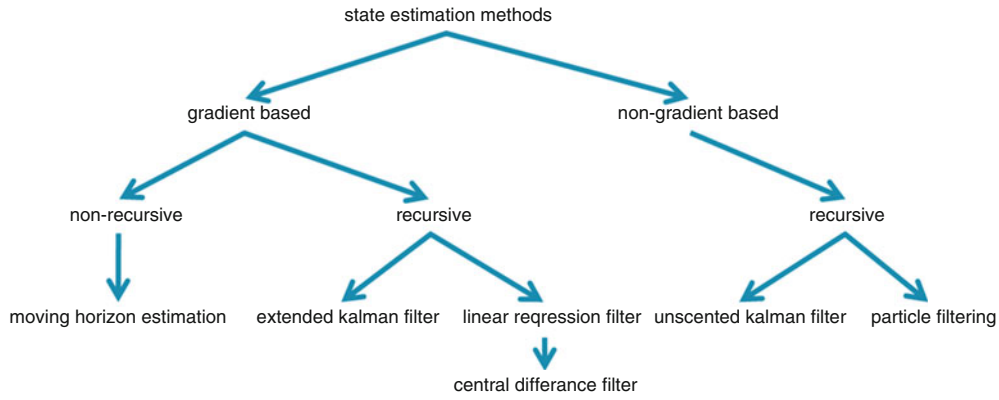


Fig. 12.3 Classification of different state estimation methodologies

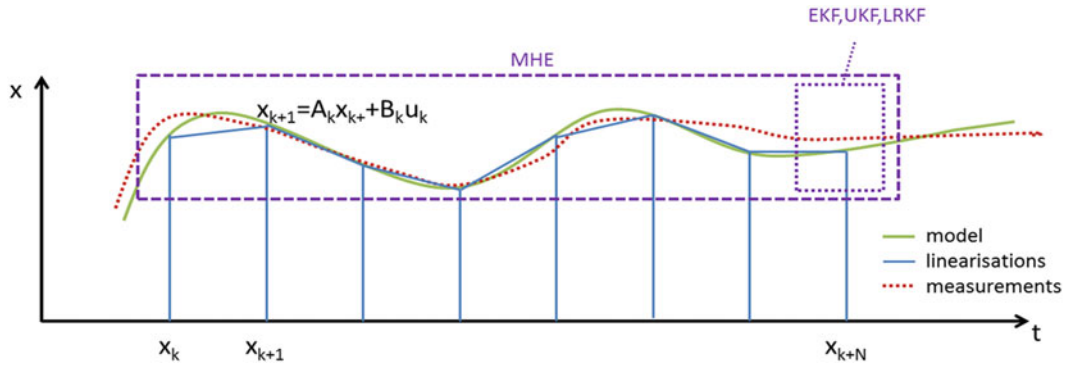


Fig. 12.4 Schematic illustration between recursive and non recursive filters

Measurement equation:

$$y_{(k+1)} = h(x_k, u_k, v_k w_k) \tag{12.2}$$

If the problem is approached from a statistical point of view, the weights are inversely proportional to the covariance of the noise terms. Most often, the assumption of Gaussian noise with zero mean is used:

$$\begin{cases} w_k = N(0, Q_k) \\ v_k = N(0, R_k) \end{cases} \tag{12.3}$$

The respective model and measurement equations are used to propagate the covariance of the noise terms to the covariance of the states and the virtual sensors over time. All the states have a corresponding mean and covariance at each time step. This means that not only the mean estimate of the true value is given but also information about its respective spread. A classification of the most popular industrially applicable methodologies is depicted in Fig. 12.3.

The most important distinction is whether or not model gradients are used in the estimator calculations. The gradient information allows us to provide a linearized relationship between the states over time. If the algorithm takes into account only the information at the current time step without any iteration, it is called a recursive method. This is in contrast with a non-recursive method that uses measurement and model info over a larger time interval to make a prediction at the last measurement timestamp. The main workhorse of the recursive gradient based estimators is the Extended Kalman (EKF) filter [4] while its non-recursive counterpart is the moving horizon estimator (MHE) [14]. If the gradient is not readily available, it can be approximated numerically as in the approach of a linear regression Kalman filter (LRKF). In Fig. 12.4 an illustration of the MHE filter is shown. The states at time x_k till x_{k+N} are estimated simultaneously, given the linearized model and measurement equation around each working point and all the known measurements within this window. An optimization procedure is used till the prediction is converged. Afterwards, the window is shifted over 1 time interval.

A counterpart of the gradient based filters are the non-gradient based filters based on the reasoning that it is better to approximate the mean and covariance of the distribution through sampling than approximating the model via linearization. In this case multiple perturbed variations of the states are simulated to create an approximate probability distribution. The most general approach is the particle filter and a scaled down approach that simplifies the distribution to a Gaussian shape is called the ‘unscented’ filter. Although these methods are initially developed to perform predictions of the states, the framework can be extended to include the prediction of unknown inputs and parameters through the state augmentation.

A final remark should be made regarding the observability. Observability means that the measurement data has to contain sufficient information to predict all the states/inputs and parameters. This is one of the main challenges of model-based state estimation, as there is no overall method to evaluate observability for nonlinear systems in a certain estimator and it is therefore not straightforward to define a good measurement campaign that will ensure all the physical phenomena in the model can be evaluated. It is important to note that model reduction can be exploited to obtain better observability properties.

12.3 Case Studies

In this paper, two cases are presented involving a coupled input/state estimation example using a 1D modeling approach. The first example is specifically dedicated to the estimation of body forces in a vehicle using the extended Kalman filter while the second example puts more emphasis on the methodological side where the different estimators are compared.

12.3.1 Body Force Estimation

An attractive application for state estimation is the identification of the forces acting between two or more bodies. These forces can in many cases not be measured directly using force transducers because the transducers would influence the forces or because the location of interest is difficult or even impossible to access. Hence, there is a need for estimating these forces. This section considers the problem of estimating the forces acting in the interface between the body and the suspension of a car. For automotive manufacturers, accurate knowledge of the body forces is important to assess the handling performance of a car. The traditional approach for assessing and optimizing vehicle dynamics performance is to rely heavily on subjective evaluation based on full system-level testing of a vehicle prototype. However, such evaluations can only be applied very late in the development timeline and by highly experienced test drivers. The forces acting in the interface between the body and the suspension of a car, on the other hand, yield an objective evaluation of vehicle dynamics performance.

An approach was developed for estimating the forces between a body and suspension of a vehicle based on a Kalman filter. The Kalman filter employs a 1D full vehicle model developed in LMS Imagine.Lab AMESim. This vehicle model (shown in Fig. 12.5) consists of sub-models for the chassis, the suspension (spring-damper model), the tires, and the road adherence. The chassis model is devoted to longitudinal and lateral vehicle dynamics and is in fact a simple multi-body model.

A limitation of this approach is that a 1D full vehicle model does not have geometric information embedded. Therefore, only the so-called ‘corner forces’ can be estimated. Although these forces are rather abstract, they provide a first level of insight in handling performance of the vehicle. The corner forces in the AMESim model are known nonlinear functions of the state variables. Hence, the estimation of the corner forces boils down to a nonlinear state estimation problem that is, as shown in Fig. 12.6, addressed using an Extended Kalman filter.

The Extended Kalman filter assimilates sensor data in the 1D model, built in LMS Imagine.Lab AMESim. The sensor data were selected by two criteria. First, it must be easy to mount the sensors in a car. Second, the Kalman filter needs to be observable. A trial-and-error study to ensure a good balance between model content and number of sensors led to selecting the wheel angles & speeds and velocity & position of the center-of-gravity. Wheel speeds (and angles) are readily available on a car. To measure the position and orientation of the car body, an inertial measurement unit is mounted in the vehicle.

The feasibility of the Kalman filter for estimating corner forces was assessed using simulations. In a first step, the LMS Imagine.Lab AMESim model was simulated using some pre-defined input profiles. During the simulation, the time history of the corner forces, the position and orientation of the car body and the rotation angles of the wheels are recorded and written to a file. These corner forces are considered to be “truth” and are to be estimated by the Kalman filter. In the second step, the Kalman filter is employed to estimate the corner forces. The same input profiles as in the previous step are applied to the 1D model. In order to make the simulations as realistic as possible, noise was added to the sensor data and slightly different parameters are used for the tire models than in the previous step. Figure 12.7 shows some results.

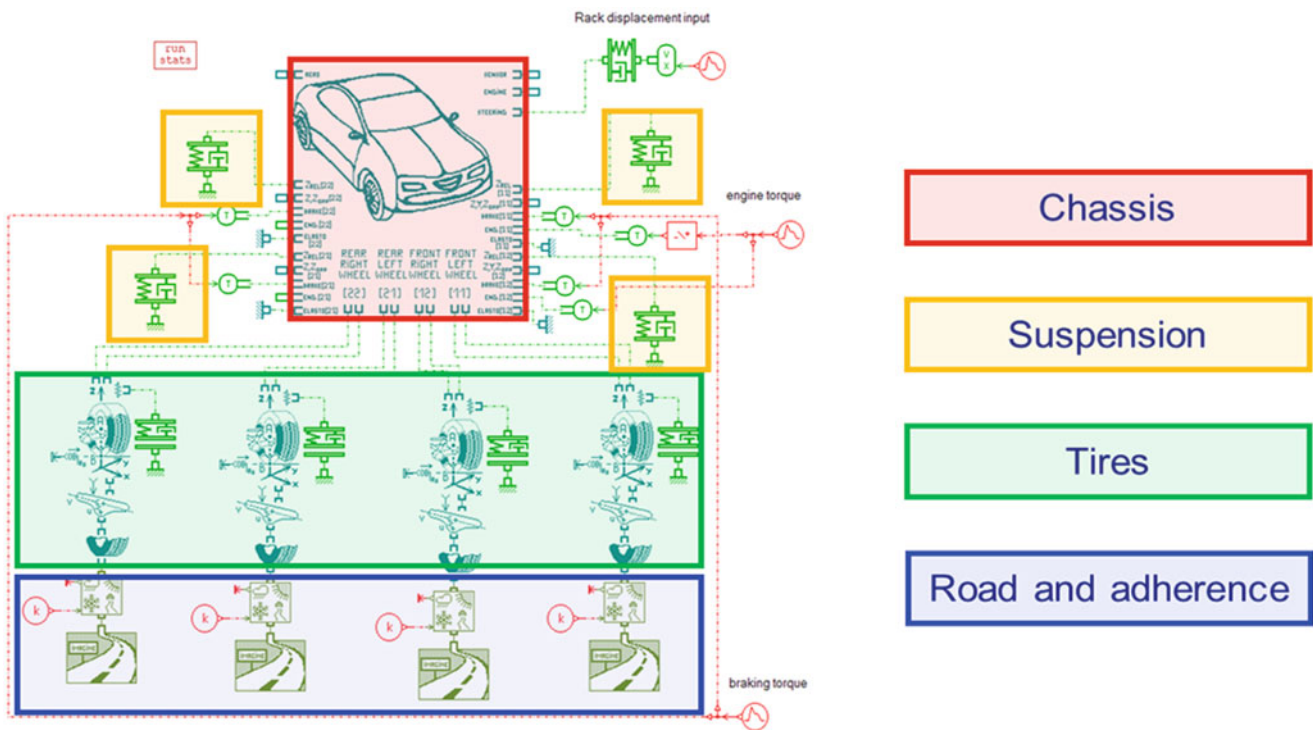


Fig. 12.5 1D Full vehicle model developed in LMS AMESim

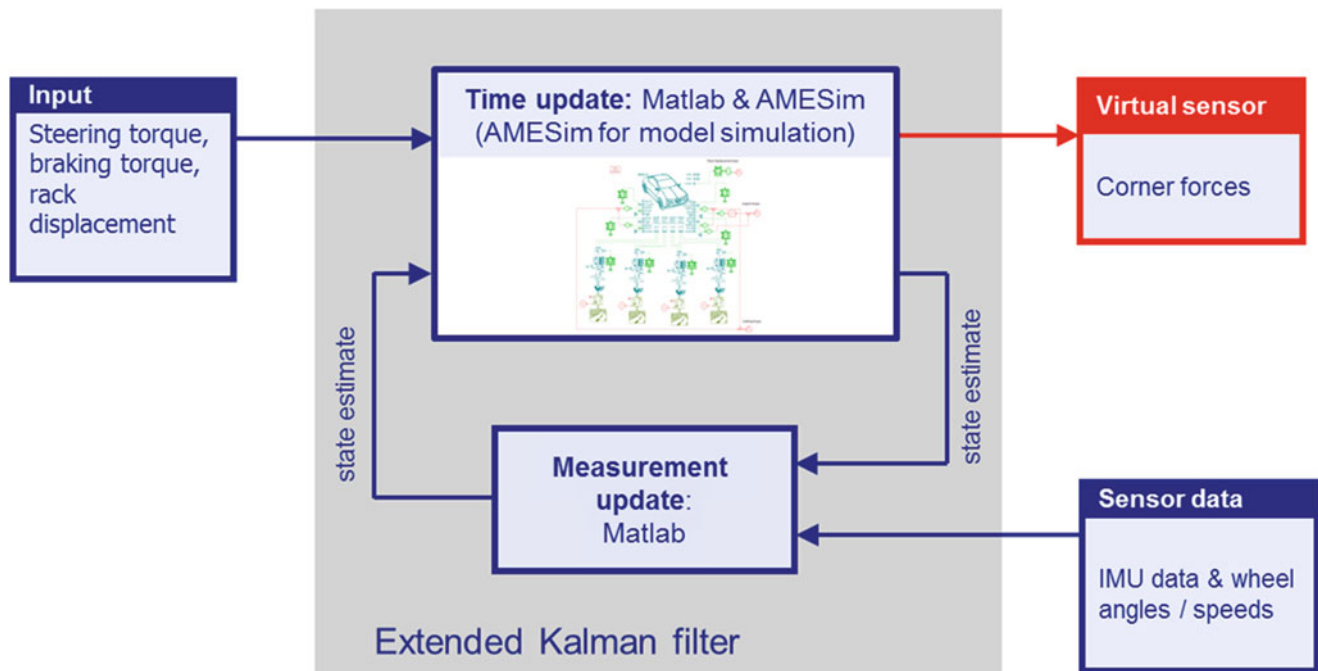


Fig. 12.6 Schematic of an Extended Kalman filter for corner force estimation. The Kalman filter is based on the 1D full vehicle model presented in Fig. 12.5

In the figure, “Estimated” refers to the results of the Extended Kalman filter, “Modified” refers to a Kalman filter using perturbed model parameters. “True” refers to the results that would be obtained by performing a simulation from the same initial state as the Kalman filter and using the same numerical model as the Kalman filter. The use of the Kalman filter

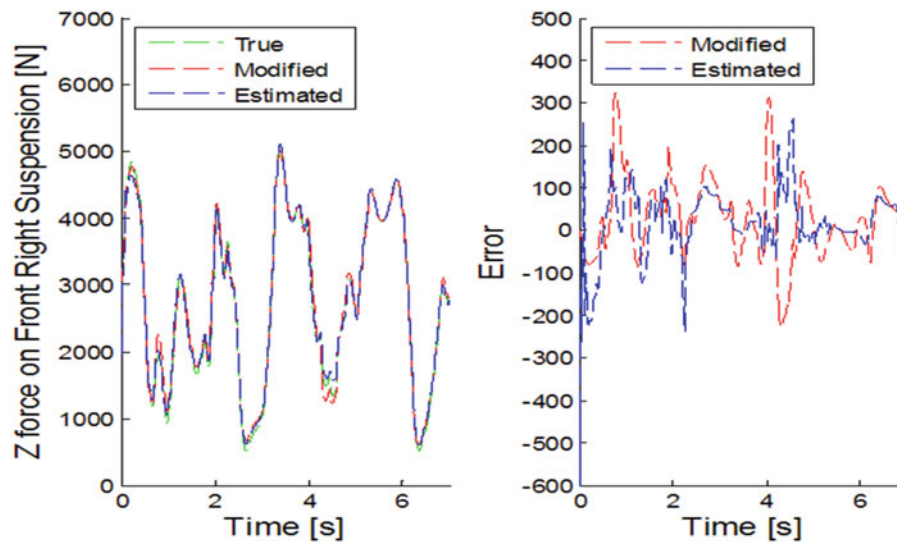


Fig. 12.7 Example of corner force estimate obtained using Extended Kalman filter

clearly decreases the peaks. An error of around 250 N is obtained for force peaks up to 5 kN, which is good enough to draw engineering conclusions about the handling performance of a vehicle.

12.3.2 Case: Drive Train Input Estimation for Production Machinery

In this section, a case study is presented of an electro-mechanical drivetrain which is subject to an unknown input force. As the purpose of this case is to illustrate the different methodologies, this example is based on a physical system but the measurements are generated by simulation with additive noise.

The challenges in such an example are:

- The system is inherently multi-physical as the model contains phenomena from the electrical, mechanical, tribological domain and a control loop;
- The end-effector which slides over a linear slide is constraint to move only within its predefined action range;
- The input force is unknown and hence needs to be estimated simultaneously.

Figure 12.8 shows the model of the example built in the multiphysical environment LMS Imagine.Lab AMESim. Each subsystem is framed within a colored rectangle to distinguish the different parts. The control loop steers the end-effector towards a reference trajectory. The control is performed by a position feedback loop which determines the output of the voltage source in the DC circuit. This electrical energy is transformed into a mechanical torque and velocity by the DC motor. The mechanical system consist of a dual mass-spring system with an ideal rack and pinion, some friction losses between the end-effector and the ground plus a force that has to be estimated, which is a saw tooth profile.

The state estimation aim is to estimate five states and the unknown input at the end effector, using one position measurement and the voltage and current measurements of the electrical circuit. The end-effector collides with its boundaries around $t = 0.9$ s, which brings non-linearity into the system response.

Figure 12.9 illustrates the result of the state estimation exercise where different estimators have been tested. The recursive filters like the unscented Kalman filter and extended Kalman filter are not able to deal with inequality constraints even though they have been extended with projection methods available in literature. As their respective formulas are based on the linear Kalman filter, the estimation has a deterministic solution and has difficulties with strong nonlinearities like inequality constraints. This is clear from the sharp peak in the estimated input force for both the recursive filters. A less obvious way to see their inability to deal with constraint is in the velocity profile where they do not have the discontinuity due to the sudden impact. The moving horizon filter however is especially equipped to deal with constraint since the constraints are naturally embedded in the estimation algorithm. A moving horizon filter with a window length of one timestep is already able to satisfactory deal with the constraints with only a slightly higher computation cost. Increasing the window size in this particular example does not increase the accuracy of the estimation much as the model is fairly linear if the state bounds and

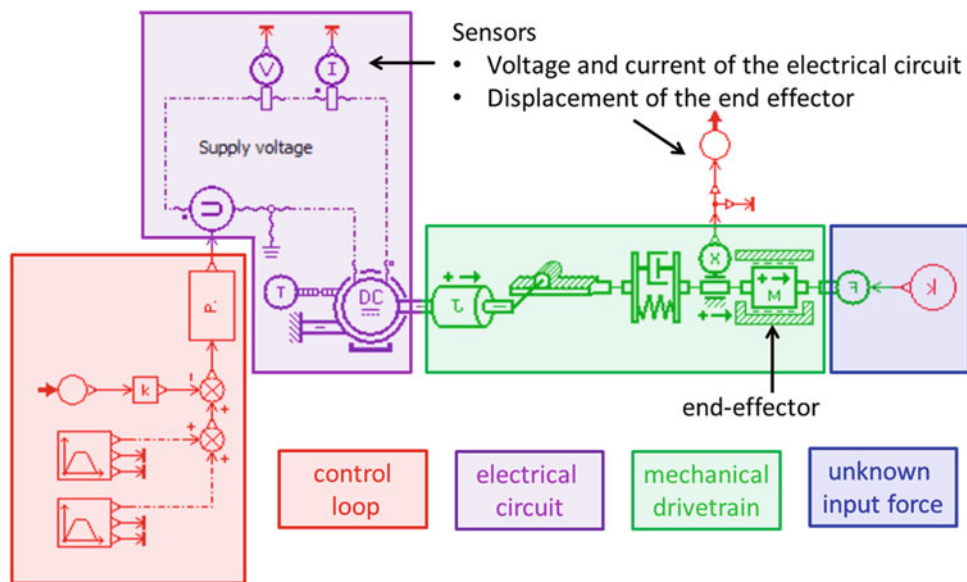


Fig. 12.8 Illustration of the nonlinear drive train model with state constraints and an unknown input force

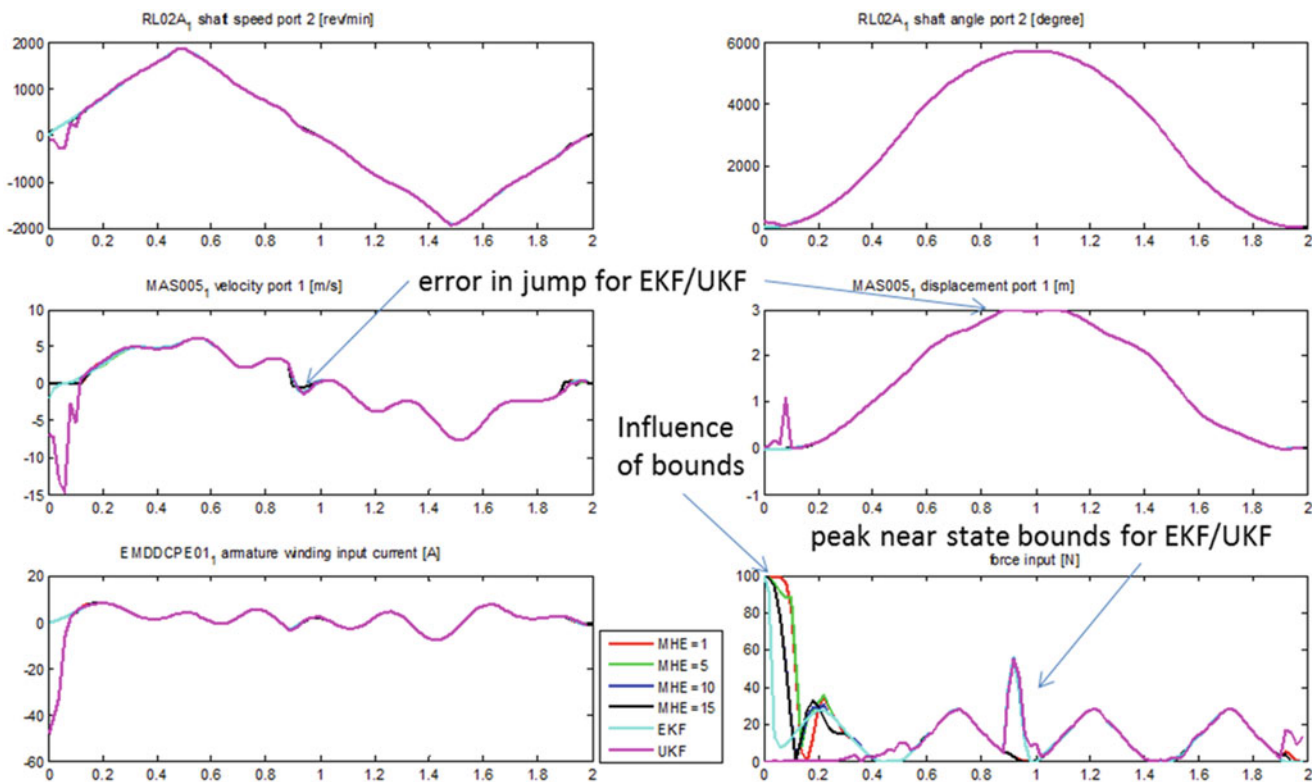


Fig. 12.9 Results of the state/input estimation exercise. (Upper left) angular velocity of the motor shaft in [rev/min], (upper right) angular position of the motor shaft in [°], (middle left) linear velocity of the end-effector in [m/s], (middle right) linear position of the end-effector in [m], (lower left) current in the electromotor [A], (lower right) estimated input force at the end-effector

end-effector friction are not taken into account. In parameter estimation exercises where the parameter can be approximated as a constant value over the full window, an increase in the window length does however have a significant impact on the quality of the estimation.

To conclude this example, there is a clear need to adopt iterative estimators like the Moving Horizon Estimator when severe nonlinearities enter the model. The recursive filters still serve their purpose as they are fast and have a fixed computation time but it comes with a decreased accuracy.

12.4 Conclusions and Discussion

A main conclusion of this paper is that there exists significant potential for enhanced data exploitation using state estimation methods in mechanical and mechatronic systems engineering. The availability of powerful and accurate modelling methods as used in 1D system simulation and 3D geometry based simulation offers a perfect basis to adopt the state estimation methodology in mechanical product testing. The main investigated state estimation approaches are the Kalman Filter and the Moving Horizon Estimator. It was demonstrated that through application of state estimation with design engineering models, estimates for critical internal parameters can be obtained. This was illustrated with two engineering cases.

Future work will be focusing on the further extension of the approach to use high-fidelity 3D models in the state estimation loop. This will involve including more realistic physics (force cross-coupling, flexibilities, ...). Furthermore a more methodological view will be taken to include sensors into the model and to explore new ways to exploit the corresponding measurements. An example is “Sensor Expansion” to generate distributed information with computer vision (as alternative to “Sensor Fusion” where you combine multiple measurements into 1 data point).

Acknowledgements The research presented in this paper was partly performed in the context of the ITEA2 project 11004 MODRIO. The authors gratefully acknowledge the support of VLAIO, the Flemish government agency for Innovation.

References

1. van der Linden, P., Floetke, H.: Comparing inverse force identification and mount stiffness force identification methods for noise contribution analysis. In: Proceedings of ISMA 2004, Leuven, Belgium, September 2004
2. Blau, M.: Inverse force synthesis: state of the art and future research. In: Proceedings Inter-Noise 2000, Nice, France, August 2000
3. Van der Auweraer, H., Mas, P., Dom, S., Vecchio, A., Janssens, K., Van de Ponsseele, P.: Transfer path analysis in the critical path of vehicle refinement: the role of fast, hybrid and operational path analysis. In: Proceedings of the SAE Noise and Vibration Conference, Paper No. 2007-01-2352, Leuven, Belgium, May 2007
4. Simon, D.: Optimal State Estimation—Kalman, H-infinity and Nonlinear Approaches. Wiley, Hoboken NJ (2006)
5. De Bruyne, S., Van Der Auweraer, H., Anthonis, J.: Improving active suspension performance by means of advanced vehicle state and parameter estimation. In: Proceedings IEEE-ICM International Conference on Mechatronics, Istanbul (Turkey), April 2011
6. Naets, F., Pastorino, R., Cuadrado, J., Desmet, W.: Online state and input force estimation for multibody models employing extended Kalman filtering. In: Multibody Sys. Dyn. (2013)
7. Naets, F., Croes, J., Desmet, W.: An online coupled state/input/parameter estimation approach for structural dynamics. *Comput. Meth. Appl. Mech. Eng.* **283**, 1167–1188 (2015)
8. International Council On Systems Engineering (INCOSE). *Systems Engineering Handbook Version 3.1*, August 2007
9. Van der Auweraer, H., Anthonis, J., De Bruyne, S., Leuridan, J.: Virtual engineering at work: the challenges for designing mechatronic products. *Eng. Comput.* **29**(3), 389–408 (2013). doi:[10.1007/s00366-012-0286-6](https://doi.org/10.1007/s00366-012-0286-6)
10. Dean, C., Karnopp, D.L., Margolis, R., Rosenberg, R.C.: *System Dynamics: Modeling and Simulation of Mechatronic Systems*. Wiley, Hoboken, NJ (2006)
11. Donders, S., Hermans, L., Nauwelaerts, E., Chojin, S., Pluymers, B., Desmet, W.: CAE technologies for efficient Vibro-Acoustic vehicle design modification and optimization. In: Proceedings ISMA 2008, Leuven, Belgium, 4127–4142 September 2008
12. Naets, F., Tamarozzi, T., Heirman, G., Desmet, W.: Real-time flexible multibody simulation with global modal parameterization. *Multibody Syst. Dyn.* **27**(3), 267–284 (2012)
13. Van der Auweraer, H., Leuridan, J.: The new paradigm of testing in today's product development process. In: Proceedings of ISMA 2004, Leuven, Belgium, 1151–1170 September 2004
14. Rawlings, J.B., Mayne, D.Q.: *Model Predictive Control: Theory and Design*. Nob Hill Publishing, Madison, WI (2009)

Chapter 13

Generation of Traveling Waves in a 2D Plate for Future Drag Reduction Manipulation

Patrick F. Musgrave, V.V.N. Sriram Malladi, and Pablo A. Tarazaga

Abstract In most systems, friction drag is an obstacle to be hurdled and is a large source of energy inefficiency in airplanes, ships, pipes, etc. By reducing the amount of friction drag between a fluid and a surface, large energy savings are possible. This study investigates the generation of traveling surface waves propagating in the spanwise direction (perpendicular to flow) that can later be applied to decrease the friction drag in turbulent flow. A thin plate with C-F-C-F boundary conditions is excited by two piezoelectric actuators at the same frequency but with a phase difference between them. The operational deflection shapes are captured at five different frequencies where one to four regions of traveling waves exist in the plate at each frequency, with some moving in opposing directions. The traveling waves have standing waves superimposed, where the form of the standing waves are determined by the participation of nearby modes. This work provides initial assessment on the generation of traveling waves in 2D structures that can potentially be used for drag reduction in the future.

Keywords Traveling waves • Drag reduction • Piezoelectric • Turbulent flow • Waves

13.1 Introduction

Skin friction drag is a major source of energy loss in transportation, from cars to boats to airplanes. As a result, a large amount of research has focused on reducing the amount of skin friction drag experienced, via both passive and active means. In the early 1980s, small v-shaped grooves known as riblets were first researched and yielded drag reductions of 5–8 % [1, 2]. Research then progressed to utilizing various active methods, with one such method involving the generation of in-plane oscillations on a surface in order to interrupt the turbulent vortex production [3, 4]. Among other active drag reduction methods, one of the most recent involves the use of spanwise (perpendicular to flow) traveling waves with out-of-plane wall deformation. Under initial experiments, Itoh [5] experimentally achieved a drag reduction of 7.5 % when compared to a non-actuated surface. These results were then validated via numerical simulation by Klumpp et al. [6], achieving a 6 % drag reduction. Additional experimental studies [7–9] have resulted in drag reductions of up to 13 % [7]. However, the focus has been driven mainly from a fluids standpoint and the traveling waves themselves are not well-characterized, have frequency limitations, or require discrete highly intrusive actuators. Thus, the goal is to generate well-understood and controlled, variable-frequency traveling waves with minimal actuation for application to drag reduction in turbulent flow.

The proposed traveling wave method is an extension of the two-mode excitation method [10], where in the case of a beam, two actuators are excited at the same frequency and magnitude but with a phase difference. Similarly, traveling waves were generated by Bucher in [11], with actuators excited at frequencies halfway between modes and with a phase difference of 90° . Traveling waves were then theoretically and experimentally verified in beams of varying boundary conditions using piezoelectric actuators as the excitation with an applied 90° phase difference between actuation points [12]. Further research into beams showed that a 90° phase difference between actuators is simply a particular case for when the frequency is halfway between modes [13]. It was shown that traveling waves can be theoretically generated at any frequency when the proper phase difference is used. As a result, to generate a traveling wave at a given frequency there should be an optimal phase difference between actuators. In addition to beams, a model for 2D traveling waves in plates has been developed [14] and traveling waves have been experimentally generated moving circumferentially around a cylinder [15]. However, traveling waves have not yet been experimentally generated in plates using these methods.

P.F. Musgrave (✉) • V.V.N.S. Malladi • P.A. Tarazaga
Vibration, Adaptive Structures, and Testing Laboratory, Department of Mechanical Engineering, Virginia Tech,
635 Prices Fork Road, Blacksburg, VA 24061, USA
e-mail: pfm@vt.edu

This paper presents the experimental results of traveling waves generated in a thin plate clamped along two parallel edges and excited using two piezoelectric actuators. Traveling waves at different frequencies are generated to move from one clamped-edge to another for eventual application to drag reduction in turbulent flow. The next section discusses the experimental setup, including boundary conditions and the chosen traveling wave frequencies. The experimental results are then presented and discussed.

13.2 Experimental Setup

In order to generate traveling waves, an aluminum plate with dimensions of $8'' \times 12''$ and a thickness of $0.016''$ is used. The plate is clamped along the $12''$ edges by epoxying aluminum spacers to the plate as seen on the top and bottom of Fig. 13.1a. Two Macro-Fiber Composite (MFC) actuators with 85 mm active length (model M8507-P1) are attached symmetrically about the vertical axis of the plate next to the fixed boundaries. This plate is then bolted to a mounting frame as seen in Fig. 13.1b to generate the clamped-free-clamped-free (C-F-C-F) boundary conditions. The entire assembly is then mounted inside of a larger plate ($24'' \times 36'' \times 0.5''$) as shown in Fig. 13.2. This setup will eventually be placed in a wind tunnel for drag reduction testing; however, all of the current tests take place under ambient conditions in a laboratory.

Before traveling waves were generated, the frequency response and operational deflection shapes (ODSs) [16] of the plate were experimentally measured. A one dimensional Polytec scanning laser vibrometer (PSV-400-1D) was used to measure the out-of-plane velocity at chosen points along the plate when excited by a burst chirp signal sent to one of the MFC actuators. The average frequency response for the plate was determined and is shown in Fig. 13.3. Since the plot shows the average response of the plate, only the resonant peaks appear. While the first mode of the plate occurs at approximately 30 Hz, the frequency range of interest in this study is from 100–600 Hz, since this is the region that will be used to generate traveling waves.

Although previous studies [13] indicate that traveling waves can be generated at any frequency through proper actuator placement and phase difference, the frequencies of interest are limited in this application since only waves traveling from one

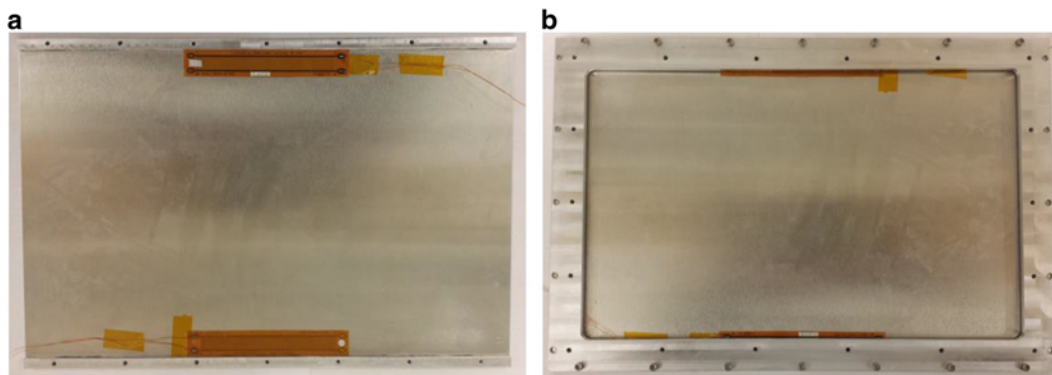


Fig. 13.1 Bottom of plate on which traveling waves are generated. (a) The plate is fixed along the long dimensions using aluminum spacers and has two MFC actuators attached. (b) The plate and spacers are bolted down to a mounting frame

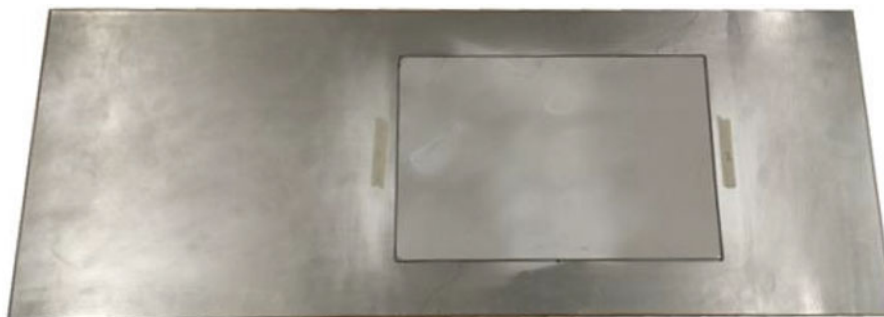


Fig. 13.2 Traveling wave plate (white) mounted inside of larger plate for future installation into wind tunnel for drag reduction testing; current testing in this paper takes place outside of the tunnel

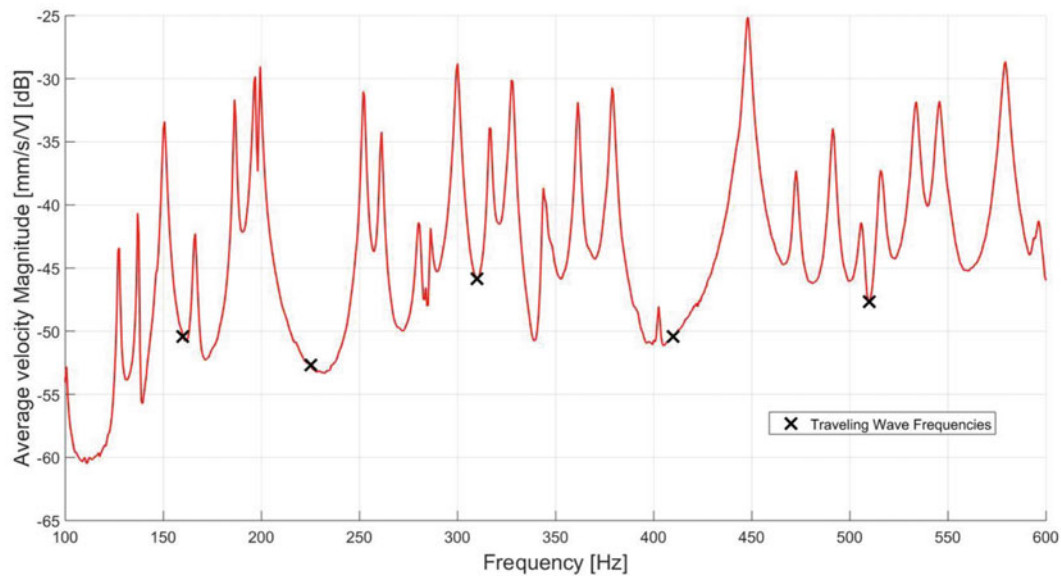


Fig. 13.3 Average frequency response of plate with marked traveling wave frequencies shown with an X

clamped boundary to the other clamped boundary (spanwise) are desired. At the frequencies between two natural frequencies (particularly those marked with an X), the highest mode participation is expected to come from the neighboring two mode shapes, assuming that the other natural frequencies are far enough apart. Thus, in order to generate spanwise traveling waves, the surrounding modes should have nodal lines perpendicular to the desired direction of the traveling wave. As a result, the frequencies marked with an X shown in Fig. 13.3 are chosen to generate traveling waves since all the participating modes, as shown in Table 13.1, have nodal lines parallel to the clamped edges, with the exception being the (0,7) mode at 491 Hz. For the case of 160 Hz, both mode shapes in Table 13.1 (150 and 166 Hz) have one horizontal node line. While there is also a vertical node line, traveling waves in the spanwise direction are expected on either side of this node line.

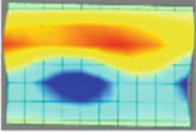
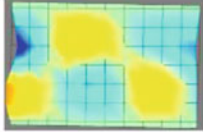
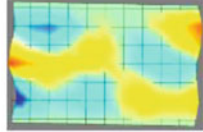
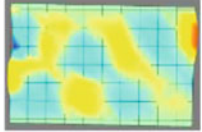
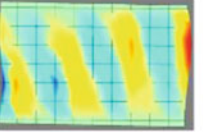
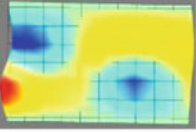
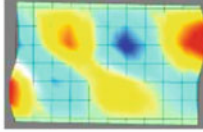
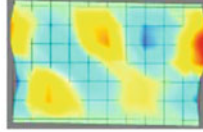
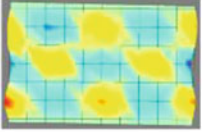
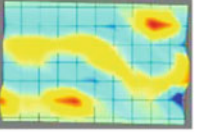
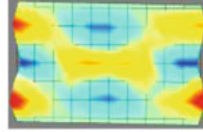
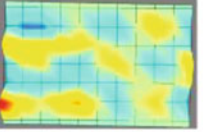
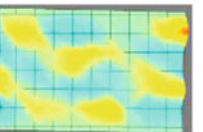
Since the chosen frequencies are roughly halfway between modes, the actuators are excited with a phase difference of approximately 90° for each case. The scanning laser vibrometer is then used to collect time data at various points along the plate in order to analyze the wave propagation. The response of the plate is visualized in a time-step animation generated by the vibrometer software. The location and direction of traveling waves are then determined by analyzing the time-steps and also the root mean square (RMS) velocity magnitude of the plate.

13.3 Experimental Results

The first traveling wave frequency case chosen (Fig. 13.3) is generated when the plate is excited at 160 Hz with an actuator phase difference of 95° , as shown in Fig. 13.4. Thus, the ODS at 160 Hz is made up of the (1,0) mode at 150 Hz and the (1,1) mode at 166 Hz (Table 13.1). Two separate traveling wave regions were generated at this ODS mainly due to the vertical nodal line created by mode (1,1). The waves are indicated by boxes A and B in Fig. 13.4, where both waves travel in the same direction. These two traveling waves are visualized in subplots 1–6, which show sequential contour plots of the out-of-plane velocity with a time step of 0.4 ms between each plot. Outside of regions A and B, the plate vibrates with a standing wave about the horizontal nodal line given by the (1,0) and (1,1) mode shapes. Inside both regions A and B, the magnitude decreases along the standing wave nodal line, indicating that this region does not contain a pure traveling wave, rather a combination of both traveling and standing waves. Thus, the strength of the traveling wave can be denoted by the reduction in velocity magnitude along the standing wave nodes. For region A, the magnitude at the node is approximately 37 % of the peak, and in region B, it is approximately 54 %.

The next traveling wave analyzed resulted from exciting the plate at 225 Hz with a phase difference of 110° , and is shown in Fig. 13.5. The ODS for this frequency has participation from the (1,2) mode at 199 Hz and the (1,3) mode at 252 Hz, see Table 13.1. Looking outside the traveling wave regions in Fig. 13.5, the (1,2) and (1,3) modes both have a single horizontal nodal line and thus a standing wave about it results. At this frequency there are two traveling wave regions. The waves in region A travel from bottom to top and can be visualized in subplots 1–6, while the waves in region B travel from top to bottom with the progression seen on the right side of subplots 3–6. Once again, in both regions A and B, the velocity

Table 13.1 This table illustrates the prominent mode shapes surrounding the frequencies at which traveling waves are generated (Fig. 13.3) in this study

Traveling Wave at 160Hz	Traveling Wave at 225Hz	Traveling Wave at 310Hz	Traveling Wave at 410Hz	Traveling Wave at 510Hz
Mode (1,0): 150 Hz 	Mode (1,2): 199 Hz 	Mode (2,1): 300 Hz 	Mode (1,5): 403 Hz 	Mode (0,7): 491 Hz 
Mode (1,1): 166 Hz 	Mode (1,3): 250 Hz 	Mode (1,4): 317 Hz 	Mode (2,4): 448 Hz 	Mode (3,1): 506 Hz 
		Mode (2,2): 328 Hz 		Mode (3,2): 516 Hz 
				Mode (3,3): 534 Hz 

Each mode shape is defined by (i,j), where i is the number of horizontal node lines and j the number of vertical ones. Mode shapes (1,5), (3,2), and (3,3) were defined by the most prominently observed node lines

magnitudes decrease along the nodal line, indicating that both traveling and standing waves are present. Within region A, there is a larger 1-node standing wave on the left and a 2-node standing wave on the right side of the region; however, in the middle, the magnitude is relatively constant, meaning that this area contains almost a pure traveling wave. In region B, there is a 1-node standing wave in addition to the traveling wave, with the velocity magnitude decreasing to approximately 75 % at the node.

The next traveling frequency is at 310 Hz and a phase difference of 100° is used between the two inputs. The result is shown in Fig. 13.6. The (2,1) mode at 300 Hz and (1,4) mode at 317 Hz, see Table 13.1, will have the largest modal participation values in the ODS; however, the (2,2) mode at 328 Hz may have a non-negligible participation value. Outside of the traveling wave regions, all of the standing waves have two nodes, as indicated by the nearby (2,1) and (2,2) mode shapes. Within region A, the traveling waves move from top to bottom with the progression shown in subplots 2–6. These traveling waves in this region contain a 2-node standing wave component, with the velocity magnitude decreasing to approximately 45 % at the nodal line. In region B, the wave does not travel vertically, as previously seen, rather there is a slight angle as the wave travels from bottom to top as seen in subplots 1–4. In addition, the traveling wave is overlaid with a 1-node standing wave where the magnitude at the node is roughly 20 % of the peak value within the wave, meaning that the traveling wave is relatively weak in this region.

The next set of traveling waves analyzed occurs when the plate is excited at 410 Hz and with a phase difference of 100° , as seen in Fig. 13.7. Looking at Fig. 13.3, there is a natural frequency at 403 Hz, given in Table 13.1 as the (1,5) mode; however, that peak is very small, so despite its proximity its modal participation value at 410 Hz is expected to be relatively small. In addition, the peak at 448 Hz is much larger than those surrounding it, thus its mode shape (2,4) should have the greatest participation in this ODS. Figure 13.7, confirms that the (2,4) mode is the largest component in the RMS velocity plot, since the (2,4) nodal lines are clearly visible. There is only one traveling wave region for this frequency where the progression is clearly seen in subplots 1–6 moving from the bottom to the top of the plate. Within the traveling wave region there is a 2-node standing and the velocity magnitude decreases to roughly 64 % at the node, resulting in a fairly strong traveling wave.

The final traveling wave frequency analyzed is when the plate is excited at 510 Hz with a phase difference of 100° , as seen in Fig. 13.8. Looking back to Fig. 13.3, the natural frequencies are not well separated in this region; thus, the ODS will have participation from more than the two closest modes. The mode shapes that have non-negligible participation values are the (0,7) mode at 491 Hz, the (3,1) mode at 506 Hz, the (3,2) mode at 516 Hz, and the (3,4) mode at 534 Hz, see Table 13.1. The 3 horizontal nodal lines have a strong effect on the ODS with this fact visible in Fig. 13.8. In terms of traveling waves, there are four separate regions at this frequency. Region A visually progresses in subplots 2–6 and includes a standing wave with two nodes, resulting in a decrease to 40 % magnitude along one of the nodes. The other three regions contain a traveling wave with a 3-node standing wave overlaid. For region C the traveling wave progresses visually in subplots 1–6 with the RMS velocity magnitude at the nodes decreasing a fairly large amount to 30 % of the peak RMS velocity for that region.

The work here has shown that several types of traveling waves can be generated with the use of piezoceramic actuation on a rectangular plate. While traveling waves were successfully generated, additional research is necessary before they can be utilized for drag reduction applications. These steps include, but are not limited to, correlating these experimental results with a simulated model, maximizing achievable amplitude, and varying the experimental setup in terms of boundary conditions, number of actuators, location, and optimization of frequency and phase difference. As shown in Fig. 13.2 the plate forms part of a wind tunnel section that will be used to study the effects that traveling waves can have on drag reduction. The future studies will try and minimize drag by perturbing the flow using these traveling waves and understanding what role amplitude and frequency play on the coupled fluid structure dynamics.

13.4 Conclusions

Traveling waves were successfully generated within a thin plate under C-F-C-F boundary conditions. The operational deflection shapes were analyzed at five different frequencies. Depending on the frequency of actuation used one to four concurrent traveling waves were found to exist in the plate. In most cases, the traveling waves also contained components of standing waves, where the form of the standing wave was determined by the modal participation of nearby mode shapes. Prior to the end application of drag reduction in turbulent flow, further research is required in order to reduce the standing wave content in the traveling waves and increase the plate area over which the waves travel.

Acknowledgments The authors acknowledge the support of the Air Force Office of Scientific Research through the 2015 Young Investigator Program.

References

- Walsh, M.J.: Riblets as a viscous drag reduction technique. *AIAA J.* **21**(4), 485–486 (1983)
- Viswanath, P.R.: Aircraft viscous drag reduction using riblets. *Prog. Aerosp. Sci.* **38**(6), 571–600 (2002)
- Jung, W.J., Mangiavacchi, N., Akhavan, R.: Suppression of turbulence in wall-bounded flows by high-frequency spanwise oscillations. *Phys. Fluids A Fluid Dyn.* (1989–1993) **4**(8), 1605–1607 (1992)
- Baron, A., Quadrio, M.: Turbulent drag reduction by spanwise wall oscillations. *Appl. Sci. Res.* **55**(4), 311–326 (1995)
- Itoh, M., et al.: Drag reduction in a turbulent boundary layer on a flexible sheet undergoing a spanwise traveling wave motion. *J. Turbul.* **7**, N27 (2006)
- Klumpp, S., Meinke, M., Schröder, W.: Drag reduction by spanwise transversal surface waves. *J. Turbul.* **11**, N22 (2010)
- Tamano, S., Itoh, M.: Drag reduction in turbulent boundary layers by spanwise traveling waves with wall deformation. *J. Turbul.* **13**, N9 (2012)
- Bai, H.L., et al.: Active control of a turbulent boundary layer based on local surface perturbation. *J. Fluid Mech.* **750**, 316–354 (2014)
- Li, W., et al.: Turbulent drag reduction by spanwise traveling ribbed surface waves. *Eur. J. Mech. B/Fluids* **53**, 101–112 (2015)
- Loh, B.-G., Ro, P.I.: An object transport system using flexural ultrasonic progressive waves generated by two-mode excitation. *IEEE Trans. Ultrason. Ferroelectr. Freq. Control* **47**(4), 994–999 (2000)
- Bucher, I.: Estimating the ratio between travelling and standing vibration waves under non-stationary conditions. *J. Sound Vib.* **270**(1), 341–359 (2004)
- Avirovik, D., Malladi, S., Priya, S., Tarazaga, P.A.: Theoretical and experimental correlation of mechanical wave formation on beams. *J. Intell. Mater. Syst. Struct.* (2016). doi:[10.1177/1045389X15615967](https://doi.org/10.1177/1045389X15615967)
- Malladi, V.V.N.S., Avirovik, D., Priya, S., Tarazaga, P.: Characterization and representation of mechanical waves generated in piezo-electric augmented beams. *Smart Mater. Struct.* **24**(10), 105026 (2015)
- Malladi, S., Albakri, M., Gugercin, S., Tarazaga, P.A.: Reduced plate model used for 2D traveling wave propagation. In: ASME Conference on Smart Materials, Adaptive structures and Intelligent Systems, Colorado Springs, Co., 21–23 September 2015
- Phoenix, A., Malladi, S., Tarazaga, P.A.: Traveling wave phenomenon through piezoelectric actuation of a free-free cylindrical tube. In: ASME Conference on Smart Materials, Adaptive structures and Intelligent Systems, Colorado Springs, Co., 21–23 September 2015
- Richardson, M.H.: Is it a mode shape, or an operating deflection shape? *SV Sound Vib.* **31**(1), 54–61 (1997)

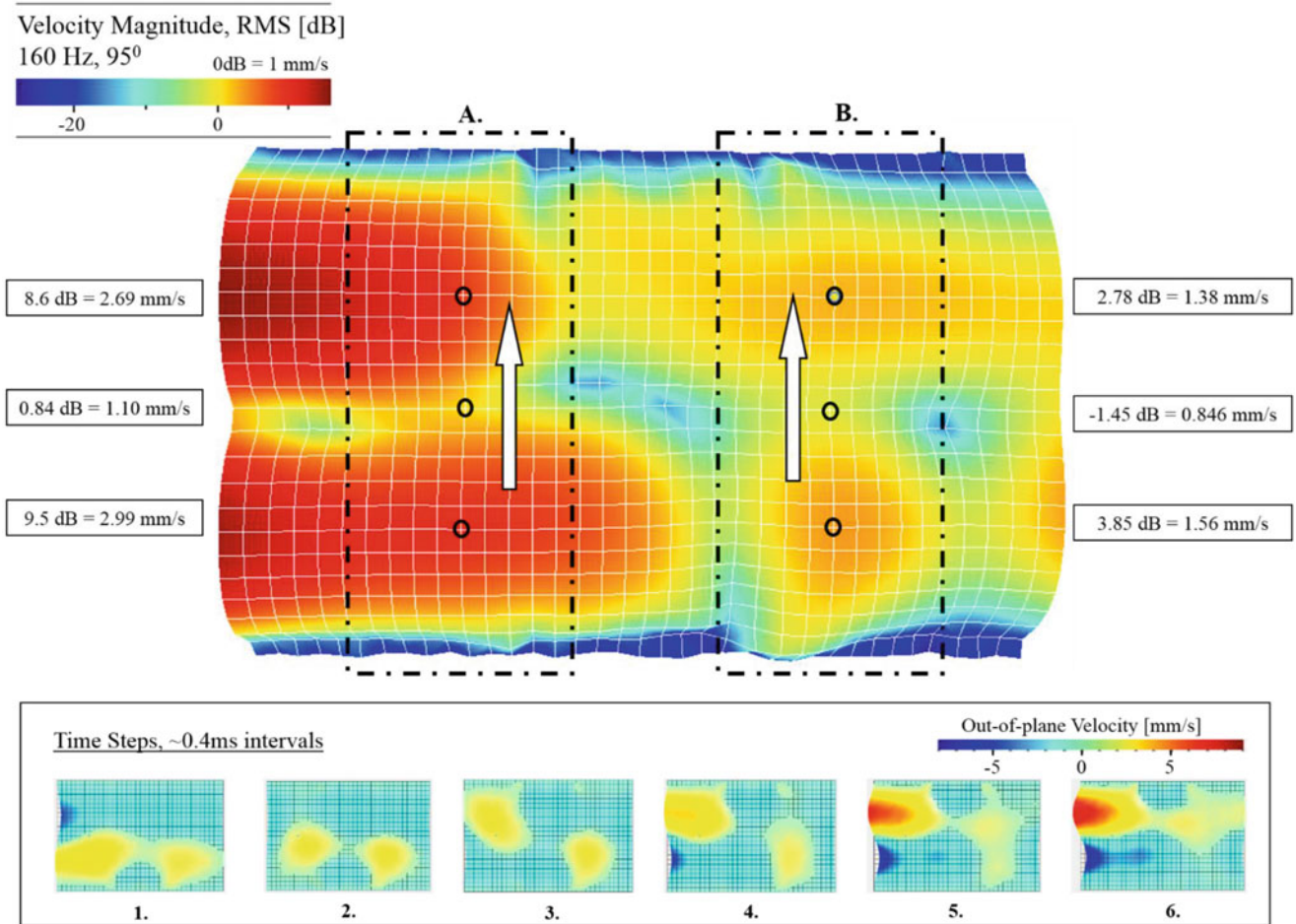


Fig. 13.4 Contour plot of RMS velocity values for the plate excited at 160 Hz with a 95° phase difference between actuators. Traveling waves exist within the boxes and move in the directions shown. RMS velocity values are given for the circled points. The plots 1–6 show the out-of-plane velocity values at six sequential time-steps

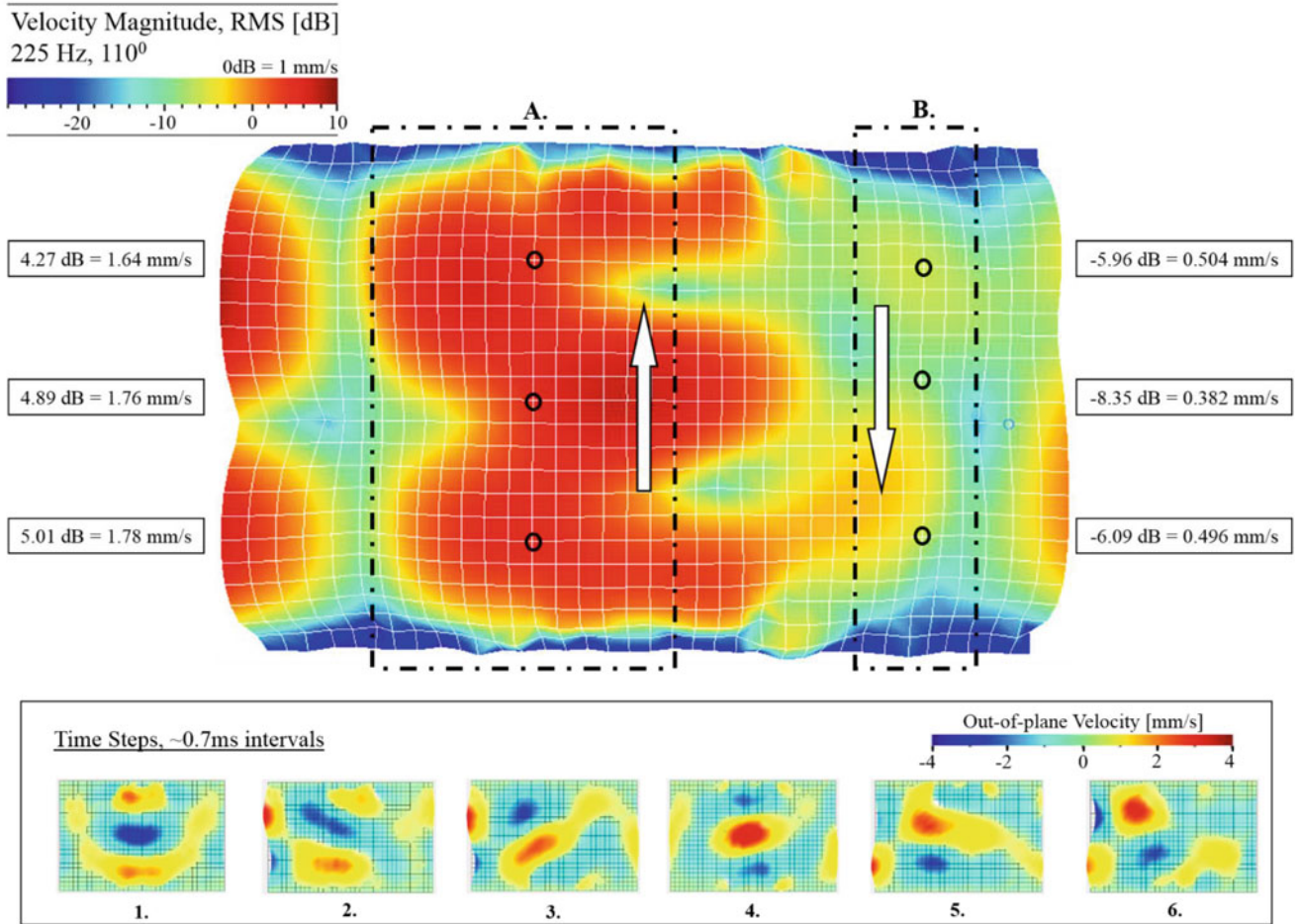


Fig. 13.5 Contour plot of RMS velocity values for the plate excited at 225 Hz with a 110° phase difference between actuators. Traveling waves exist within the boxes and move in the directions shown. RMS velocity values are given for the circled points. The plots 1–6 show the out-of-plane velocity values at six sequential time-steps

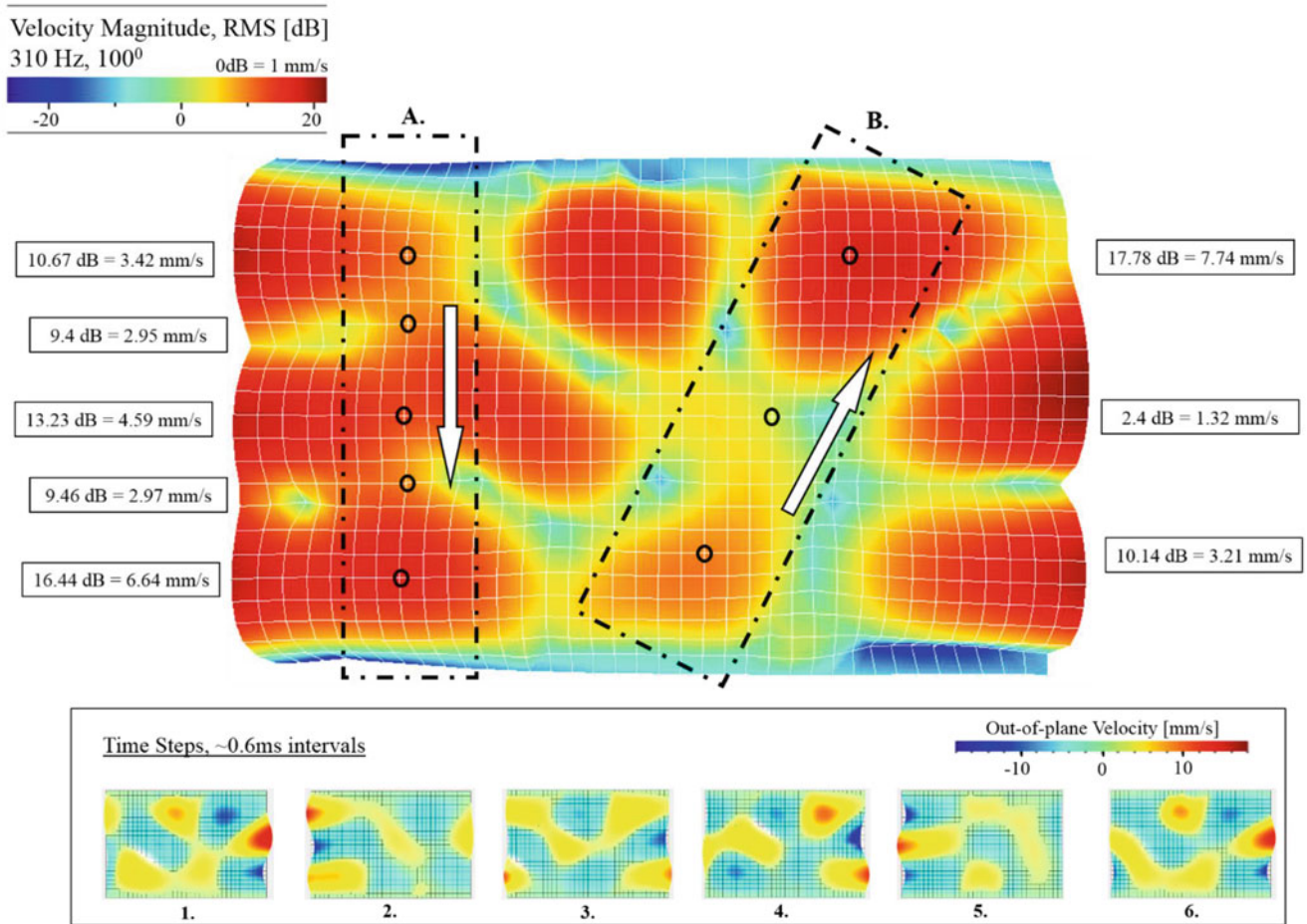


Fig. 13.6 Contour plot of RMS velocity values for the plate excited at 310 Hz with a 100° phase difference between actuators. Traveling waves exist within the boxes and move in the directions shown. RMS velocity values are given for the circled points. The plots 1–6 show the out-of-plane velocity values at six sequential time-steps

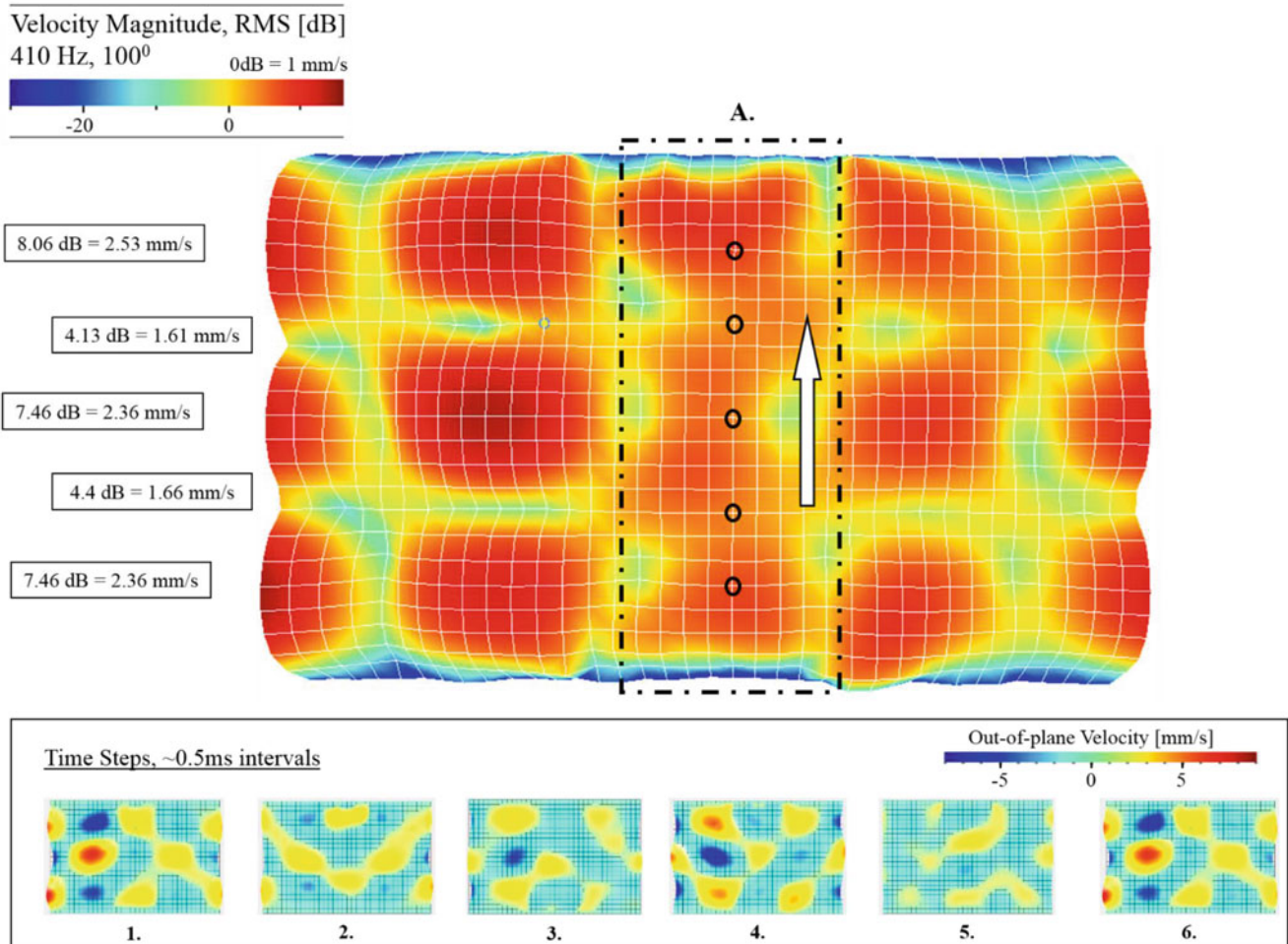


Fig. 13.7 Contour plot of RMS velocity values for the plate excited at 410 Hz with a 100° phase difference between actuators. Traveling waves exist within the box and move in the directions shown. RMS velocity values are given for the circled points. The plots 1–6 show the out-of-plane velocity values at six sequential time-steps

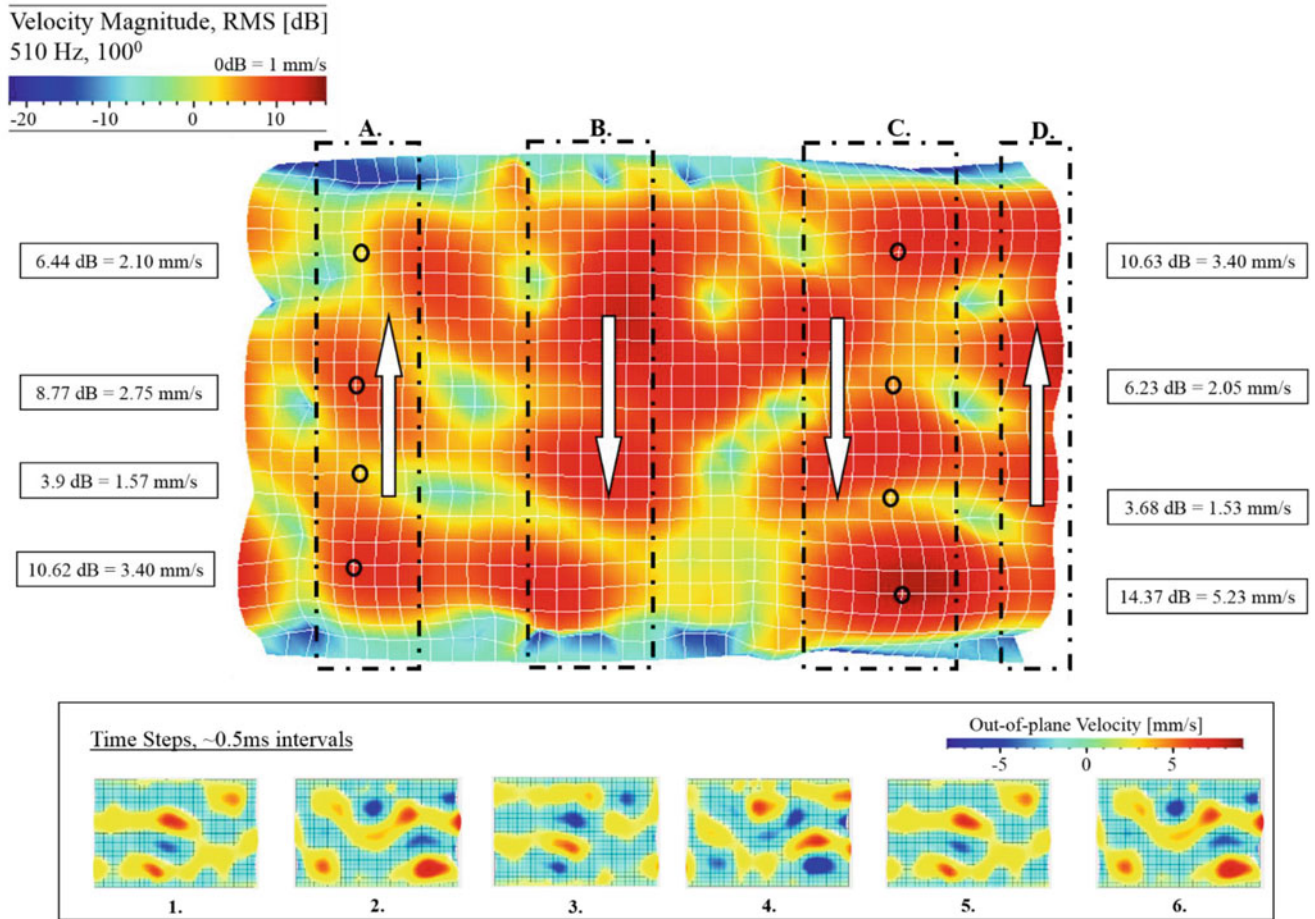


Fig. 13.8 Contour plot of RMS velocity values for the plate excited at 510 Hz with a 100° phase difference between actuators. Traveling waves exist within the boxes and move in the directions shown. RMS velocity values are given for the circled points. The plots 1–6 show the out-of-plane velocity values at six sequential time-steps

Chapter 14

Surrogate Granular Materials for Modal Test of Fluid Filled Tanks

Pierre-Louis Chiambaretto, Miguel Charlotte, Joseph Morlier, Philippe Villedieu, and Yves Gourinat

Abstract Experimental vibration certification of launcher cryogenic tanks is an important issue in the aerospace industry. Liquid hydrogen is indeed too dangerous to be used in tank vibration tests. Unlike most fluids used in aerospace industry such as liquid oxygen, surrogate fluids cannot be used to approach the modal behavior of a tank filled with liquid hydrogen because of its particularly low mass density. However granular materials could safely replace liquid hydrogen for vibration testing of tanks.

This work aims at proposing an innovative methodology to determine the geometry and the material properties of substitution grains in order to keep the same mode shape and eigen frequencies of a vertical cylindrical tank studied considering 2D horizontal slices. Assuming that the tank slices are sufficiently far enough from the free-surface not to be affected by sloshing effects, the fluid-structure interaction is purely inertial. This methodology is based on the homogenization of a granular material composed of spheres with an elastic behavior. Thus the tank filled with grains can be modeled by a membrane surrounded by a circular beam. An experimental test bench developed to validate the methodology, as well as analytical and numerical simulation results of fluid-beam and membrane-beam interactions, are presented on the first modes.

Keywords Cryogenic tank • Modal analysis • Rayleigh-Ritz • Granular materials

14.1 Introduction

Cryogenic stages are commonly used for launchers due to their efficiency. However, several technical issues make their development tough. One of these challenges is to determine the dynamic responses of tanks entirely or partially filled with cryogenic fluids. Indeed, it is dangerous and expensive to perform vibration tests on tanks filled with these fluids. Therefore, for some fluids such as liquid oxygen, surrogate fluids with close thermodynamic constants can be used. As explained by NASA [1], this approach is also used for liquid hydrogen, by using water even if the density ratio of these fluids is around 14. Looking for alternatives, this innovative work deals with the possibility to use pre-stressed granular materials to fill the tank in order to obtain experimentally the same modal response as a tank filled with liquid hydrogen for low frequencies.

A methodology based on a semi-analytical resolution to choose the granular material and the pre-development of an experimental test bench is presented: After the justification of 2D hypothesis, the aim will be to validate the modal equivalence between fluid filled tanks and grains filled tanks. In order to achieve this, another model based on a homogenization of the granular material is used as sketched in Fig. 14.1. After explaining the hypotheses associated with this homogeneous model, eigen-vectors and eigen-frequencies of the proposed mechanical model are determined thanks to the Rayleigh-Ritz method. To obtain the same modal parameters as fluid filled tank, grain material can be chosen. A test bench is under development to confirm this approach and identify some parameters such as the *coordination number* of the granular material.

P.-L. Chiambaretto (✉) • M. Charlotte • J. Morlier • Y. Gourinat
Université de Toulouse, CNRS, ISAE-Supaero, Institut Clément Ader, 10 avenue Edouard Belin, Toulouse, 31055 Cedex 4, France
e-mail: pierre-louis.chiambaretto@isae.fr

P. Villedieu
DMAE, ONERA, Centre de Toulouse, 2 avenue Edouard Belin, Toulouse, 31055 Cedex 04, France

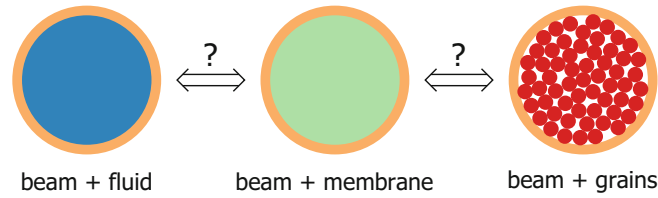


Fig. 14.1 Modal equivalence between fluid filled beam and grains filled beam using an homogeneous model for granular material

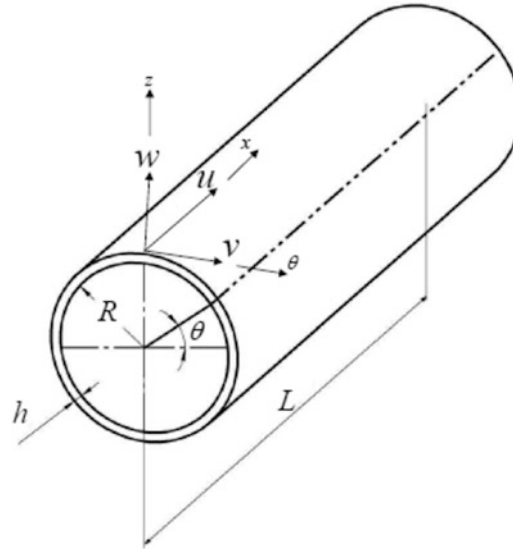


Fig. 14.2 Cylindrical shell parametrization: $(\vec{u}, \vec{v}, \vec{w})$ is the local base of a current point defined by its cylindrical coordinates: (R, θ, x)

14.2 Modeling

This work focuses on cylindrical tanks such as the Ariane 5 cryogenic main stage tank. The first step is to define a model of tank filled with liquid hydrogen, in order to obtain an expression of the first eigen modes intended for the equivalence with the tank filled with grains.

14.2.1 Fluid-Structure Interaction

The tank is mainly composed of a long hollow cylinder closed by two spherical caps. Since the thickness is considerably smaller than the other dimensions, consequently the tank can be modeled by a shell. Moreover, the two spherical caps are non-developable surfaces, therefore the rigidity of these caps is much larger than the cylinder's one. We assume the caps do not participate in the first modes. Then, the model can be reduced to a cylindrical shell clamped. The shell geometry is defined by the radius R and the thickness h and its homogeneous, isotropic material by the Young modulus E_1 and the density ρ_1 .

The first modes of this structure are flexural radial-orthoradial modes. Regardless of the shell theory chosen, with the parametrization of the Fig. 14.2, using the method of separation of variables and the invariance to rotation, the displacement can be written in the form:

$$\begin{cases} u(\theta, x, t) = \sum_{ij} u_{ij}(\theta, x, t) = \sum_{ij} \mathcal{F}_{ij}^u(x) \cos(i\theta) \cos(\omega t) \\ v(\theta, x, t) = \sum_{ij} v_{ij}(\theta, x, t) = \sum_{ij} \mathcal{F}_{ij}^v(x) \sin(i\theta) \cos(\omega t) \\ w(\theta, x, t) = \sum_{ij} w_{ij}(\theta, x, t) = \sum_{ij} \mathcal{F}_{ij}^w(x) \cos(i\theta) \cos(\omega t) \end{cases} \quad (14.1)$$

The relation between i, j and ω depends on the shell theory used. In order to solve analytically the problem, an assumption of plane motion is used; accordingly $u(\theta, x, t) \ll v(\theta, x, t)$ and $w(\theta, x, t)$. Then, the tank can be studied slice by slice with an amplitude function of x . A tank's slice is modeled by a circular beam. As the radius is much larger than the thickness, the beam theory used is the Euler-Bernoulli's one [2]; Love determined the flexural modes of a circular beam. These modes were obtained by adding to the Euler-Bernoulli equations, a closure relation imposing: $\epsilon_{\theta\theta} = 0 \Leftrightarrow \frac{\partial v}{\partial \theta} - w = 0$. This relation imposes that the work done by normal forces (membrane forces) is null. The i th eigen-modes functions and eigen-frequencies equations are:

$$\begin{cases} v_i(\theta, t) &= V_i(\theta) \cos(\omega t) = A_x \sin(i\theta) \cos(\omega t) \\ w_i(\theta, t) &= W_i(\theta) \cos(\omega t) = iA_x \cos(i\theta) \cos(\omega t) \quad \forall i \in \mathbb{N} . \\ \omega &= \frac{i(i^2-1)}{R^2(i^2+1)^{1/2}} \left(\frac{E_1 h}{12\rho_1} \right)^{1/2} \end{cases} \quad (14.2)$$

Thanks to these expressions, the generalized mass and stiffness for each mode by unit of length can be obtained as follows:

$$\begin{cases} K_g^B|_i &= \frac{E_1 h^3}{12R^3} \int_0^{2\pi} \left(\frac{d^2 W_i}{d\theta^2} + W_i \right)^2 d\theta = \frac{E_1 h^3 \pi}{12R^3} (1 - i^2)^2 \\ M_g^B|_i &= \rho_1 h R \int_0^{2\pi} (V_i^2 + W_i^2) d\theta = \rho_1 h R \pi \left(1 + \frac{1}{i^2} \right) \end{cases} . \quad (14.3)$$

In this work, the tank is assumed totally filled, so there is no sloshing effect. To determine the importance of acoustic effects, orders of magnitude are used. The celerity of sound c is about 1000 m/s, the first frequency f of our system is about 10 Hz and the characteristic $2R$ is about 1 m. The Helmholtz number is defined for example in [3] as: $He = \left(\frac{2\pi f R}{c} \right)^2 \approx 10^{-2}$. As a consequence, the hypothesis **H1** is made:

- **H1**: Acoustic effects are negligible.

The Helmholtz equations simplify to Laplace equation in pressure [3]:

$$\Delta(p) = 0 \quad . \quad (14.4)$$

To model the entire system, equations of elastic beams and Eq. (14.4) are used. The interaction is defined on the boundary of the liquid domain by:

$$\begin{cases} \vec{\sigma}(\vec{n}) &= -p \vec{n} \\ \vec{grad}(p) \cdot \vec{n} &= \rho_F \omega^2 w \end{cases} \quad (14.5)$$

\vec{n} representing the normal vector from the fluid to the beam and ρ_F the density of the fluid. As shown for example by Axisa in [4] for each mode, the mode shapes remain the same than for the beam without fluid, and the frequency decreases due to the inertia added by fluid. This phenomenon can be decreased by an added mass due to the fluid on each mode. In the case of a ring, this added mass by unit of length is defined by: $M_a^F|_{i,j} = \left(\mathcal{F}_{ij}^w(x) \right)^2 \frac{\rho_F \pi R^2}{i}$. Here $\mathcal{F}_{ij}^w(x)$ denotes the amplitude of the beam radial motion for the slice. In this 2D approach, it is a constant. Eigen-frequencies, can be obtained thanks to Rayleigh ratio with $M_a^F|_i = M_a^F|_{i,j}$ with $\mathcal{F}_{ij}^w(x) = 1$:

$$f_i = \frac{1}{2\pi} \sqrt{\frac{K_g^B|_i}{M_g^B|_i + M_a^F|_i}} \quad . \quad (14.6)$$

Thanks to this analysis, it is possible to sum up on modal objectives for the tank filled with grains as follows:

- mode shapes of the tank filled with grains must be the same as the empty tank's one;
- eigen-frequencies must follow relation (14.6), this paper focuses only on the first mode.

14.2.2 Homogenization of Elastic Granular Materials

A granular material is composed of a lot of grains. The understanding of its different behaviours and the transitions between them, for such materials, constitutes an important research field. In this study the granular material is in its “static material” state: meaning the grains cannot flow. As explained for example by Nedderman [5], this state can exist if the material is pre-compressed and the amplitude of pressure oscillations is low enough to prevent the formation of slip planes. According to the Mohr-Coulomb theory [5], this failure mode happens when:

$$\left(\frac{1 - \sin(\delta)}{1 + \sin(\delta)} \right) \sigma_1 > \sigma_2 > \left(\frac{1 + \sin(\delta)}{1 - \sin(\delta)} \right) \sigma_1 \quad . \quad (14.7)$$

Here σ_1 and σ_2 are the principal stresses (the third principal stress being null in this 2D approach, the same kind of relation exists in 3D). δ is the effective angle of internal friction computed thanks to the geometry of grains and their assembly and to the friction coefficient between grains.

Given the foregoing hypothesis on principal stresses, the granular material can be described like a non-linear elastic solid. Indeed, even if the grain material is linearly elastic, according to Hertz theory [6] the stiffness is non-linear due to the increase of contact area. If the grain's sizes is very small in front of the tank size, an homogeneous theory could be used. In this preliminary work, Boussinesq theory [7] is used. The behaviour law is Hooke's law with material parameters depending on the pre-compression of grains: $\sigma_{ij} = K(\Delta)\Delta\delta_{ij} + 2G(\Delta)\tilde{\epsilon}_{ij}$ with Δ the volumic variation: $\Delta = -\frac{\delta V}{V} = -\epsilon_{kk}$. Material coefficients can be approximated combining both Hertz contact theory in 2D and Duffy-Mindlin model [8] (pressure P is evenly distributed on contacts) as follows: $K \simeq A_1 Z E \Delta^{1/2} \simeq A_1 (Z E)^{2/3} P^{1/3}$ and $G \simeq A_2 Z E \Delta^{1/2} \simeq A_2 (Z E)^{2/3} P^{1/3}$. Where Z is the *coordination number* characterizing the average number of contacts by grain. The Z value depends on the assemblage configuration and the size disparity of grains. For a 2D model, $Z \in [3, 4]$ and for a 3D model, $Z \in [4, 6]$ as explained by Andreotti et al. [9]. A_1 and A_2 are constants depending on grain materials. To sum up, three hypotheses are made:

- **H2:** Pre-stressed pressure is high enough to prevent relative motions between grains.
- **H3:** Granular material can be described as an elastic material with material coefficient depending on pressure.
- **H4:** Pressure variation during vibration tests is low enough to linearize material coefficients.

The equivalent solid is described by its density ρ_2 , its Lamé parameters λ_2 and μ_2 . Referring to Fig. 14.1, the modal equivalence between a “beam+grains” model and a “beam+membrane” model in 2D is now possible. To obtain the modal equivalence between a “beam+membrane” model and the “beam+fluid” model in 2D, it's necessary to determine the mode shapes and eigen frequencies of the “beam+membrane” model. Thus the granular material properties and the pre-stress pressure could be determined to fit with this model's responses to the fluid structure developed in Sect. 14.2.1

14.2.3 2D Analytical Modal Determination of a Circular Membrane Surrounded by a Beam

The methodology developed to approximate the eigen modes of a circular membrane surrounded by a beam is based on the Rayleigh-Ritz method. A mode shape form is assumed, then by calculating the mass and stiffness operator, eigen-frequencies are determined. To validate the supposed mode shape form, these frequencies are compared to numerical results. With the currently used assumption of separation of spatial variables (r, θ) for mode shapes of disk and using the 2π -periodicity of the structure on θ , the following hypothesis **H5** can be made:

- **H5:** The radial displacements of the mode shape of a free circular beam, of a circular membrane on its free edge and of a beam filled by this circular membrane are the same.

To validate this assumption, a modal analysis has been made by the finite element method using COMSOL. The Fig. 14.3 shows the third mode of a beam, a membrane and a membrane circled by a beam obtained. The deformed shape of the free beam, of the membrane on free edge and of the beam on the coupled system seem to be quit close. Therefore, mode shapes of a free circular beam are the same as for a beam filled by a membrane. This result is coherent with the fluid filled beam.

As the mode shapes of the free beam and of the free membrane are barely compatible, for the coupled system these two mode shapes are used for the Rayleigh-Ritz approach with an holonomic condition of same amplitude in radial motion. Mode shapes of the beam have already been computed in Sect. 14.2.1 as well as the mass and stiffness operators $K_g^B|_i$ $M_g^B|_i$. In-plane mode shapes of a free edge circular membrane have been less studied than out-plane vibration. In plane mode shapes of a circular membrane with elastic boundary conditions have been analytically obtained by Kim et al. [10]. By using the

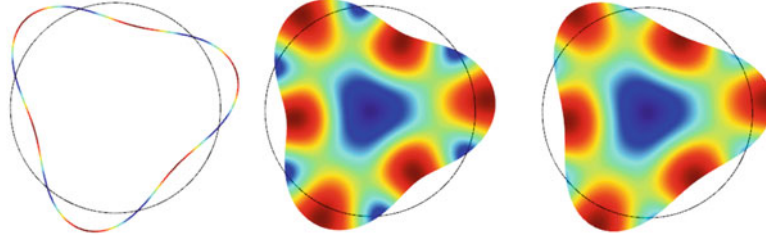


Fig. 14.3 Third mode of a circular beam, a circular membrane and circular membrane surrounded by a beam obtained by COMSOL to validate the hypothesis **H5**

separation of variables in polar coordinates, the i th eigen-vector can be written as: $\vec{U} = \begin{pmatrix} U_r(r)|_i \cos i\theta \\ U_\theta(r)|_i \sin i\theta \\ 0 \end{pmatrix}$, with:

$$\begin{cases} U_r(r)|_i &= \frac{R}{2} \{A_1 [J_{i+1}(\alpha \frac{r}{R}) - J_{i-1}(\alpha \frac{r}{R})] + A_2 [J_{i+1}(c\alpha \frac{r}{R}) + J_{i-1}(c\alpha \frac{r}{R})]\} \\ U_\theta(r)|_i &= \frac{R}{2} \{A_1 [J_{i+1}(\alpha \frac{r}{R}) + J_{i-1}(\alpha \frac{r}{R})] + A_2 [J_{i+1}(c\alpha \frac{r}{R}) - J_{i-1}(c\alpha \frac{r}{R})]\} \\ c &= \sqrt{2/(1-\nu_1)} \\ \alpha &= \omega R \sqrt{\rho(1-\nu_2^2)/E_2} \end{cases} \quad (14.8)$$

where J_i is Bessel function of first kind of order i . The values of α are determined thanks to the dispersion relation:

$$2J_{n+2}(\alpha)J_{n-2}(c\alpha) + 2J_{n+2}(c\alpha)J_{n-2}(\alpha) - 2(c^2 - 1)J_n(\alpha) [J_{n+2}(c\alpha) + J_{n-2}(c\alpha)] = 0 \quad (14.9)$$

The amplitudes A_1 and A_2 are linked by the relation: $D_{22}D_{12}A_2 = -A_1D_{11}D_{21}$ with:

$$\begin{cases} D_{11} &= -\frac{\lambda}{2} [J_{i+2}(\lambda) + J_{i-2}(\lambda) - 2(c^2 - 1)J_i(\lambda)] \\ D_{22} &= -\frac{c\lambda}{2} [J_{i+2}(c\lambda) + J_{i-2}(c\lambda)] \\ D_{12} &= -\frac{c\lambda}{2} [J_{i+2}(c\lambda) - J_{i-2}(c\lambda)] \\ D_{21} &= -\frac{\lambda}{2} [J_{i+2}(\lambda) - J_{i-2}(\lambda)] \end{cases} \quad (14.10)$$

Using classical elasticity theory, the stiffness and mass operators per unit of length can be obtained as follows:

$$\begin{aligned} K_g^M|_i &= \pi \int_0^R \frac{1}{r} [r^2 (U_r'|_i)^2 (\lambda_2 + 2\mu_2) + 2\lambda_2 r (U_r|_i + iU_\theta|_i) U_r'|_i + \mu_2 r^2 (U_\theta'|_i)^2 \\ &\quad - 2\mu_2 r U_\theta'|_i (iU_r|_i + U_\theta|_i) + U_r|_i^2 ((2 + i^2)\mu_2 + \lambda_2) + 2i(\lambda_2 + 3\mu_2) U_r|_i U_\theta|_i \\ &\quad + (i^2 + (\lambda_2 + 2\mu_2) + \mu_2) U_\theta|_i^2] dr \end{aligned} \quad (14.11)$$

and

$$M_g^M|_i = \pi \rho_2 \int_0^R (U_r^2 + U_\theta^2) r dr \quad (14.12)$$

To evaluate $U_r'|_i$ and $U_\theta'|_i$ recurrence relation on Bessel functions is used: $J_{i+1}(x) - J_{i-1}(x) = -2\frac{dJ_i(x)}{dx}$ with $x = \alpha$ or $x = c\alpha$.

$$\begin{cases} U_r'(r)|_i &= \frac{\alpha}{4} \{A_1 [2J_i(\alpha \frac{r}{R}) - J_{i-2}(\alpha \frac{r}{R}) - J_{i+2}(\alpha \frac{r}{R})] + cA_2 [J_{i-2}(c\alpha \frac{r}{R}) - J_{i+2}(c\alpha \frac{r}{R})]\} \\ U_\theta'(r)|_i &= \frac{\alpha}{4} \{A_1 [J_{i-2}(\alpha \frac{r}{R}) - J_{i+2}(\alpha \frac{r}{R})] + cA_2 [2J_i(c\alpha \frac{r}{R}) - J_{i-2}(c\alpha \frac{r}{R}) - J_{i+2}(c\alpha \frac{r}{R})]\} \end{cases} \quad (14.13)$$

Integration of $M_g^M|_i$ and $K_g^M|_i$ are made numerically. Knowing $M_g^B|_i$, $K_g^B|_i$, $M_g^M|_i$ and $K_g^M|_i$, it is possible using Rayleigh-Ritz theory to determined eigen frequencies of the circular membrane surrounded by the beam:

$$f_i = \frac{1}{2\pi} \sqrt{\frac{K_g^B|_i + K_g^M|_i}{M_g^B|_i + M_g^M|_i}} \quad (14.14)$$

For the first mode of ovalization, this analytical frequency is compared to the frequency obtained by the finite element model for different radius and materials of membrane and beam. The maximal error obtained is around 5 %. Therefore, this model can be used to find a modal equivalence between the circular membrane surrounded by the beam and the fluid filled beam.

14.3 Methodology of Choice for Granular Material and Future Experimental Test Bench

The objective is to choose a granular material in order to get the same eigen frequencies. Using expression (14.6) and (14.14), this objective can be written as:

$$\begin{aligned} \frac{K_g^B|_i + K_g^M|_i}{M_g^B|_i + M_g^M|_i} &= \frac{K_g^B|_i}{M_g^B|_i + M_a^F|_i} \Leftrightarrow K_g^M|_i \\ &= \frac{K_g^B|_i}{M_g^B|_i + M_a^F|_i} M_g^M|_i + \frac{K_g^B|_i}{M_g^B|_i + M_a^F|_i} M_g^B|_i - K_g^B|_i \quad . \end{aligned} \quad (14.15)$$

Fluid acts only as an added mass for the beam whereas the membrane acts as an added mass and an added stiffness. Therefore, the density of the membrane must be greater than the one of the liquid in a proportion depending on the membrane's stiffness as shown in relation (14.15). To choose the grain material, a density-Young modulus Ashby diagram [11], on the Fig. 14.4, can be used. This graph represents the main material families, densities and young modulus. For a granular material, the average density ρ_2 is linked to the density of the material ρ thanks to the packing fraction c by the relation: $\rho_2 = c\rho$. The packing fraction value depends on the organisation of the grains. For a random compact arrangement, the value is closed to 0.7. Young modulus of a granular material E_2 is proportional to $E^{2/3}$ with E the material Young modulus. Moreover, $K_g^M|_i$ is proportional to E_2 and $M_g^M|_i$ is proportional to ρ_2 .

To verify Eq. (14.15) with existing materials, Young modulus needs to be quite low. According to Ashby diagram, foams and elastomer could be interesting. By calculating the mass and stiffness operators of the membrane, for an aluminium beam with a radius of 1 m, it is possible to determine the pre-stress pressure on grains needed to verify (14.15). To finalize the choice the pre-stress pressure obtained must be verified at several points during vibration tests:

- Each grain must remain in its elastic domain: $\sigma_{max} < Re \Rightarrow P_{Max}$
- Pressure must prevent slipping grain motions: Eq. (14.7) $\Rightarrow P_{Min}$

In order to validate the methodology and the semi-analytical approach, a test bench is under development. Even if the model is mainly 2D, it is quite difficult to realize a 2D experimentation. The model presented on Fig. 14.1 of a granular material surrounded by a beam is unstable due to the possibility of out of slice-plane motions. To deal with this issue a solution is to use a long cylindrical tank to be in plane strain state for slices far away from boundaries conditions. The tank is fully filled with spherical grains pressurized by a membrane to get, thanks to a Jassen theory [12], the pressure needed for the slice of interest. The tank is embedded on a horizontal plate directly connected to the shaker. Accelerometers are settled on the slice of interest. The Fig. 14.5 represents a schematic design of the test bench.

14.4 Conclusion

This work has presented a new approach to perform vibration tests on liquid hydrogen filled tanks. Due to liquid hydrogen's low density, the use of surrogate fluid, as done up to now, presents some important issues. By using a granular material instead of water to fill the tank for vibration tests, it seems possible to reach mode shapes and eigen-frequencies which are unreachable with water.

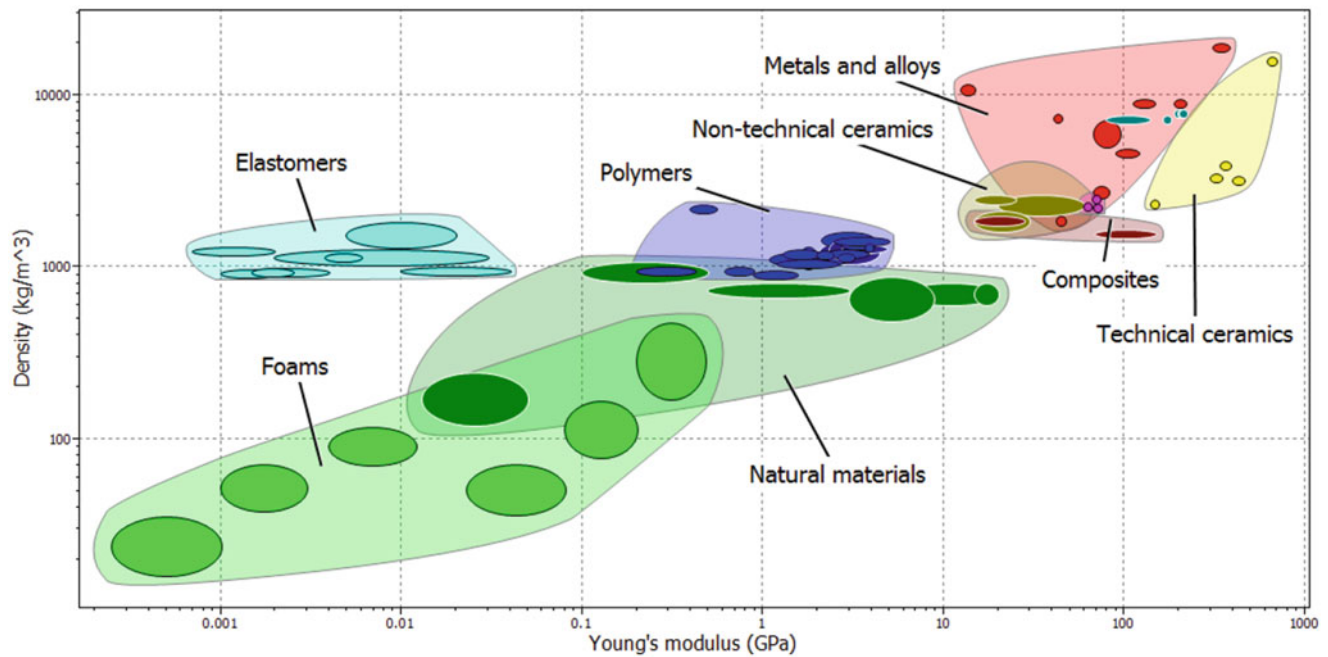


Fig. 14.4 Density-Young modulus Ashby diagram obtained using CES-EduPack

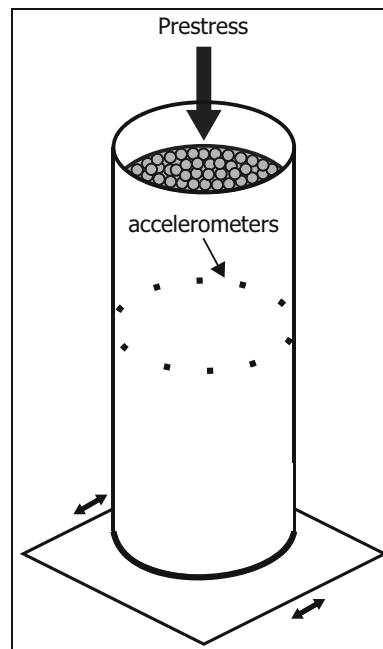


Fig. 14.5 Schematic design of the test bench

After the justification of a 2D approach, the first mode of a cylindrical tank filled with liquid were analytically obtained under the hypothesis **H1** (incompressible fluid). Once these objective modes are known, an homogeneous approach of granular material based on several hypotheses (mainly **H2**, **H3** and **H4**) has been developed in order to semi-analytically find the modes of a tank filled with grains using assumption **H5**. At last, in order to fit the modes obtained for each tank, a methodology for choosing material and pre-stress pressure has been exposed. A test bench, currently under development, has been presented to validate this analytical approach. Theories used in this study are easy-to-apply like the Boussinesq's one. This choice was made to facilitate the analytical approach in order to get orders of magnitude to choose grain properties. The test bench could help us determine the validation range of these theories and to improve modeling if necessary. In future works, we will focus mainly on the impact and the modeling of damping in granular material using experimental results.

References

1. Tuma, M., Chenevert, D.: Ensuring safe exploration: ares launch vehicle integrated vehicle ground vibration testing. In: AIAA SpaceOps Conference, pp. 2010–2026 (2010)
2. Love, A.E.H.: A Treatise on the Mathematical Theory of Elasticity. Cambridge University Press, Cambridge (1927)
3. Sigrist, J.-F.: Interaction Fluide-Structure: Analyse Vibratoire Par Éléments Finis. Ellipses, Paris (2011)
4. Axisa, F., Antunes, J.: Modelling of Mechanical Systems: Fluid-Structure Interaction, vol. 3. Butterworth-Heinemann, Oxford (2006)
5. Nedderman, R.M.: Statics and Kinematics of Granular Materials. Cambridge University Press, Cambridge (2005)
6. Hertz, H.: Über die Berührung fester elastischer Körper. Journal für die reine und angewandte Mathematik **92**, 156–171 (1882)
7. Boussinesq, J.: Essai théorique sur l'équilibre des massifs pulvérulents: comparé à celui de massifs solides, et sur la poussée des terres sans cohésion, F. Hayez (1876)
8. Duffy, J., Mindlin, R.: Stress-strain relation and vibrations of a granular medium. J. Appl. Mech. **24**, 585–593 (1957)
9. Andreotti, B., Forterre, Y., Pouliquen, O.: Les milieux granulaires-entre fluide et solide: Entre fluide et solide. EDP Sciences, Les Ulis (2012)
10. Kim, C.-B., Cho, H.S., Beom, H.G.: Exact solutions of in-plane natural vibration of a circular plate with outer edge restrained elastically. J. Sound Vib. **331**(9), 2173–2189 (2012)
11. Ashby, M.F., Cebon, D.: Materials selection in mechanical design. Le J. Phys. IV **3**(C7), C7–1 (1993)
12. Janssen, H.: Versuche über getreidedruck in silozellen. Z. Ver. Dtsch. Ing. **39**(35), 1045–1049 (1895)

Chapter 15

Dynamics of a Hydroelastic Oscillating Cylinder with Added Viscoelastic Damping for Passive Control of Vibrations

Bruno Sousa Carneiro Da Cunha, Antônio Marcos Gonçalves de Lima, and Alice Rosa da Silva

Abstract In the scope of flow around cylindrical structures, the vortex shedding phenomena are those that have attracted considerable attention from many mechanical and civil engineering domains. Since, these phenomena—dependent on a number of factors—may have disastrous effects in engineering practice, such as economic loss, damage of installations, loss of power-generating time, etc. This is a reason for which in the last decades, a great deal of effort has been devoted to the development of numerical and computational procedures for dealing with the problem of vortex shedding phenomena. Among the various new developments for dealing with the problem of vortex-induced vibration, the use of viscoelastic materials is considered as an interesting strategy, since they present great efficiency in mitigating vibrations levels at moderate application and maintenance costs. In this paper, the Immersed Boundary Method combined with the Virtual Physical Model is used to investigate the forces and response associated with the vortex-induced vibration of a rigid oscillating cylinder incorporating viscoelastic damping. In the context of fluid-structure interactions, an important issue addressed herein is the modeling procedure of the viscoelastic behavior in the time domain, which is performed by using a fractional-order constitutive model. After the presentation of the underlying theoretical foundations related to the various aspects of the numerical modeling procedure, numerical simulations with a viscoelastically damped oscillating cylinder performed in a wide range of oscillating amplitude and forcing frequency are presented and discussed aiming at demonstrating the influence of viscoelastic damping on the flow structure and fluid forces.

Keywords Immersed boundary method • Virtual physical method • Oscillating cylinder • Vortex shedding modes • Viscoelastic damping

15.1 Introduction

Incompressible viscous flows over circular cylinders have been studied by many researchers [3, 7, 8, 14]. However, nowadays it is also important to appreciate the numerical studies involving vortex-induced vibrations (VIV) of a circular cylinder due to its great importance both academic and industrial domains. It is especially true if the main interest is to investigate control strategies of the undesirable induced vibrations with the aim of increasing the fatigue life of engineering systems subjected to the VIV problem.

In practice, the VIV problem can occur in many engineering fields, such as bridges, transmission lines, maritime structures, drilling and petroleum production, hydrodynamic and hydro-acoustic applications. Thus, several methods have been developed to overcome this class of flow problem to increase the understanding, the prevention and the prediction of the VIV phenomenon and to quantify the relation between the structure response and the most important parameters related to it. As an example, the behavior of long cylindrical structures immersed in water has been extensively investigated due to development of the hydrocarbons sources in depth greater than 1000 m [19]. Within this context, experimental and numerical efforts have been made to characterize the vortex shedding frequency, the response frequency, the induced forces, the damping effects [25], the time histories of the displacement, the acceleration and the total force acting on elastically mounted circular cylinders in uniform flows [23]. The wake vortices [1] and the response amplitude of the cylinder have been also addressed by many authors [10–12, 20].

B.S.C. Da Cunha (✉) • A.M.G. de Lima
Federal University of Uberlândia, School of Mechanical Engineering, Campus Santa Mônica, Uberlândia, MG, Brazil
e-mail: brunocarneirocunha@gmail.com; amglima@mecanica.ufu.br

A.R. da Silva
Federal University of Uberlândia, School of Civil Engineering, Campus Santa Mônica, Uberlândia, MG, Brazil
e-mail: alicers@feciv.ufu.br

Thus, several works have been proposed for performing fluid-structure interaction analyses of systems, as reported in the references. However, few studies have addressed the problem of estimating the VIV problem of systems incorporating viscoelastic damping devices, which motivates the study reported in this paper.

Several approaches have been developed for performing dynamic responses of simple and more complex engineering structures containing viscoelastic damping devices, as reported in Anagnostopoulos [2], Da Silva et al. [8] and Lima et al. [14]. Among the widely used mathematical representations accounting for the typical dependence of the viscoelastic properties with respect to frequency and temperature, in this paper the four-parameter fractional derivative model (FDM) originally proposed by Bagley and Torvik [4] and modified by Galuci et al. [9] for the transient analysis of viscoelastically damped systems, has been retained to be combined with the VIV problem in order to mitigate undesired levels of vibration. In this context, it is used the Immersed Boundary Methodology (IBM) combined with the Virtual Physical Model (VPM) to simulate the flow around the viscoelastically mounted circular cylinder composed by one degree of freedom in an uniform flow.

Therefore, the motivation intended for the present study is to provide a detailed analysis of the flow features over a two-dimensional viscoelastically mounted circular cylinder with one degree of freedom based on the vortex shedding mechanism visualized by the vorticity contours, the drag and lift coefficients aiming to investigate the influence of the viscoelastic damping on the cylinder response.

15.2 Mathematical Methodology

The Immersed Boundary Method [17] with the Virtual Physical Model [14] is used to simulate two-dimensional, incompressible, isothermal and viscous flow. This methodology is based on the Navier-Stokes equations added a force term, which acts upon the fluid so that it notice the existence of interface, thus making the exchange of information between fluid and solid. In this method, there are two meshes, one called Eulerian, which represents the calculation domain and other called Lagrangian that represents the immersed body [14].

These meshes are geometrically independent and coupled through the force term. This methodology characteristic enables the study of flows over simple, complex and even mobile and deformable geometry without remeshing process. We can observe the Fig. 15.1 that shows an illustrative scheme of the both meshes for a two-dimensional domain, with the presence of an arbitrary interface [13].

15.2.1 Mathematical Formulation for the Fluid

The Navier-Stokes can be expressed in the tensor form, as follow:

$$\frac{\partial u_i}{\partial t} + \frac{\partial (u_i u_j)}{\partial x_j} = -\frac{1}{\rho} \frac{\partial p}{\partial x_i} + \frac{\partial}{\partial x_j} \left[\nu \left(\frac{\partial u_i}{\partial x_j} + \frac{\partial u_j}{\partial x_i} \right) \right] + f_i \quad (15.1)$$

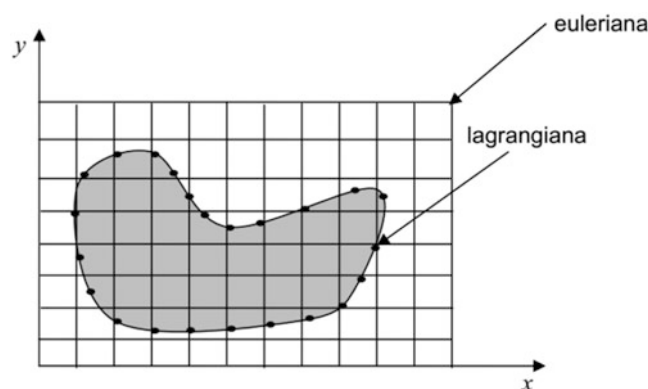


Fig. 15.1 Representation of the Eulerian and Lagrangian meshes for an arbitrary interface

$$\frac{\partial u_i}{\partial x_i} = 0 \quad (15.2)$$

where ρ is the specific mass of fluid, ν kinematic viscosity of fluid, u_i are the velocity vector components, p is the pressure and f_i are the components of the Eulerian force vector components.

The source term of Eulerian force only exists in the Eulerian points coincident or near the Lagrangean grid, being null for the order points of the calculation domain. This term is calculated through the distribution of the components of the Lagrangean interfacial force vector [18].

15.2.2 Virtual Physical Model (VPM)

The Virtual Physical Model (VPM) allows the calculation of the Lagrangean force based on physical interaction of the fluid and the solid surface immersed structure in the flow. The mathematical calculation is based on the application of the balance of the momentum equation of the fluid particles located in the Lagrangean points by observing the following expression [13]:

$$\vec{F}(\vec{x}_k, t) = \vec{F}_a + \vec{F}_i - \vec{F}_v + \vec{F}_p \quad (15.3)$$

where \vec{F}_a is the acceleration force, \vec{F}_i is the inertial force, \vec{F}_v is the viscous force and \vec{F}_p is the pressure force.

15.2.3 Fractional Step Model

The Fractional Step Method (FSM) [6] is used here with the aim of coupling the pressure-velocity fields. The FSM is a non-iterative method that form the velocity components, pressure and force of the previous iteration in which the velocity components fields are estimated. After obtained, the pressure correction is then calculated through the solution of the linear system. Next, the Poisson equation for the pressure correction is that it makes the connection between the momentum and continuity equations. Therefore, it has values of pressure that allow to calculated the components of velocities (u^{n+1} and v^{n+1}), obtained from Navier-Stokes equations and lastly it needs to test the mass conservation in the time $n + 1$.

15.2.4 Description of the Problem

The present study is focused on the flow over a circular viscoelastically damped cylinder subjected to one degree of freedom. The computational domain is chosen to be $40D \times 30D$ with the cylinder located at $16.5D$ from the inlet boundary. Numerical investigations [5] have shown that the downstream boundary located at least $20D$ away from the cylinder center do not influence the numerical solution. The results reported by Prasanth et al. [22] showed that the outflow boundary has no significant effect on the flow and on the cylinder response if it is located at least $25.5D$ away from the cylinder center. In this work this distance is assumed to $23.5D$. The lateral boundaries are located at $15D$ from the cylinder center at each side, where $D [m]$ is the cylinder diameter.

The transverse response of the viscoelastically damped cylinder is modeled using a mass-visco-spring-damper model as illustrated in Fig. 15.2, where the motion of the cylinder is in the normal direction of the free-stream velocity $U [m/s]$ only. Also, the cylinder is assumed to be a rigid body. Therefore, the equation of motion generally used to represent the vortex-induced vibration problem is given as [15, 21]:

$$m\ddot{y}(t) + c\dot{y}(t) + k_v^*y(t) = F_\ell(t) \quad (15.4)$$

where $m [kg]$ is the mass, $c [Ns/m]$ is the damping coefficient, $k_v^* [N/m]$ is the frequency- and temperature-dependent viscoelastic stiffness value, $y [m]$ is the transverse displacement, and $F_\ell(t) [N]$ is the lift force generated by the flow.

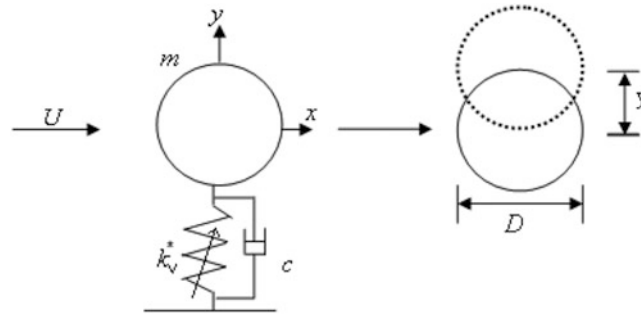


Fig. 15.2 Illustration of the one viscoelastically damped degree of freedom system under consideration

15.2.5 Fractional Derivative Model Incorporated into the Equation of Motion

In the context of the present study Eq. (15.4) must be solved in order to generate the dynamic responses of viscoelastic cylinder in a flow. Also, it must be taking into account the dependency of the material *moduli* with respect to the frequency and temperature. Various mathematical models have been developed to represent the viscoelastic behavior and have been shown to be suitable to be used in combination with the discretization procedures. In this paper, as the interest is confined to time-domain analyses of VIV problem, the *Fractional Derivative Model* (FDM) initially proposed by Bagley and Torvik [4] is used in combination with the Grünwald discretization technique [9] to approximate the fractional operator appearing in the following one-dimensional stress state constitutive equation for linear viscoelastic materials:

$$\bar{\varepsilon}(t) + \tau^\alpha \frac{d^\alpha \bar{\varepsilon}(t)}{d t^\alpha} = \frac{E_\infty - E_0}{E_\infty} \varepsilon(t) \quad (15.5)$$

where E_0 and E_∞ are, respectively, the relaxed or static modulus, and non-relaxed or high-frequency limit value of the modulus, τ is the relaxation time, and α represents the fractional order of the time derivative ($0 < \alpha < 1$).

One important aspect regarding the use of the complex modulus function, $E_v^* = (E_0 + E_\infty(i\omega\tau)^\alpha) / (1 + (i\omega\tau)^\alpha)$, obtained by applying the Fourier transform to Eq. (15.5) is the identification of the four parameters (E_0 , E_∞ , τ , α) from experimental data-sheets provided by the manufactures containing the material storage modulus and loss factor as functions of frequency and temperature. Thus, from the complex modulus definition, the determination of the values of the material parameters can be carried out by formulating an optimization problem in which the objective function represents the difference between the experimental data points and the corresponding model predictions in the frequency band of interest for a fixed temperature value [9]. Also, it must be emphasize that Eq. (15.5) was obtained by introducing the following internal variable as a strain function, $\bar{\varepsilon}(t) = \varepsilon(t) - \sigma(t)/E_\infty$, in the standard one-dimensional stress state constitutive equation for viscoelastic materials [16]. As a result, Eq. (15.5) contains only one fractional derivative term, $d^\alpha \bar{\varepsilon}(t)/d t^\alpha$, instead of two presented in the classical constitutive equation, and can be approximated by the Grünwald definition, $d^\alpha \bar{\varepsilon}(t)/d t^\alpha \approx \Delta t^{-\alpha} \sum_{j=0}^{n_p} A_{j+1} \bar{\varepsilon}(t - j\Delta t)$, noting that $A_1 = 1$, to generate the following discretized form of the anelastic strain:

$$\bar{\varepsilon}(t) = (1 - c) \frac{E_\infty - E_0}{E_\infty} \varepsilon(t) - c \sum_{j=1}^{n_p} A_{j+1} \bar{\varepsilon}(t - j\Delta t) \quad (15.6)$$

In Eq. (15.6), $\Delta t = t/n$ is the time step, $n_p \leq n$ is the number of discretization points, $c = \tau^\alpha / (\tau^\alpha + \Delta t^\alpha)$ and A_{j+1} represents the Grünwald coefficients given by the following recurrence formulae, $A_{j+1} = (j - \alpha - 1) A_j / j$.

At this point, if the viscoelastic stiffness value is considered to be frequency- and temperature-independent, the term $k_v^* y(t)$ appearing in Eq. (15.4) is defined as $k_v^* y(t) = \int B^T(y) \sigma(y, t) dy$ where the vector $\sigma(y, t)$ can be written in terms of the anelastic strain Eq. (15.6) and the strain relation, $\bar{\varepsilon}^y(t) = \varepsilon(t) - \sigma(t)/E_\infty$, as follow:

$$\sigma(y, t) = \left(1 + c \frac{E_\infty - E_0}{E_0}\right) \varepsilon(y, t) - c \frac{E_\infty}{E_0} \sum_{j=1}^{n_p} A_{j+1} \bar{\varepsilon}(y, t - j\Delta t) \quad (15.7)$$

By combining the Eq. (15.7) with the elastic and anelastic strain-displacement relations, $\varepsilon(y, t) = B(y) y(t)$ and $\bar{\varepsilon}(y, t) = B(y) \tilde{y}(t)$, the resulting modified elementary viscoelastic stiffness matrix assumes the following form:

$$k_v^* y(t) = \tilde{k}_v y(t) + \tilde{f}_v(t - j\Delta t) \quad (15.8)$$

Where $\tilde{k}_v = \left(1 + c \frac{E_\infty - E_0}{E_0}\right) k_v$ and $\tilde{f}_v(t - j\Delta t) = c \frac{E_\infty}{E_0} k_v \sum_{j=1}^{n_p} A_{j+1} \tilde{y}(t - j\Delta t)$.

Upon introduction of the Eq. (15.8) into Eq. (15.4), the resulting equation of motion of the viscoelastically mounted one degree of freedom cylinder in a flow can be written as:

$$m\ddot{y}(t) + c\dot{y}(t) + \tilde{k}_v y(t) = F_\ell(t) - \tilde{f}_v(t - j\Delta t) \quad (15.9)$$

Where $\tilde{f}_v(t - j\Delta t)$ is the viscoelastic loading dependent on the anelastic displacements $\tilde{y}(t)$, and the Grünwald coefficients which represent the fading memory phenomenon in the viscoelastic material.

15.3 Numerical Results

In this section, numerical simulations are presented to illustrate the interaction of the fluid-structure with and without the viscoelastic damping. Now, we considered the follows values of dimensionless parameters: $m^* = 10.30$, $\zeta = 0.07736$, $V_r = 3.5$ and $R_e = 10.000$.

In the same way, we have fixed the value of temperature to investigate the behavior of viscoelastic material in the structure. So, the value of temperature was $T = 10^\circ\text{C}$. Therefore, the characteristic of the viscoelastic material in this temperature of work is: $E_0 = 1.2526$ MPa, $E_\infty = 572.44$ MPa, $\tau = 0.0034$ ms and $a = 0.6682$.

15.3.1 Vorticity Fields

The flow visualization by the vorticity contours is presented in the Fig. 15.3a (without viscoelastic damping) and Fig. 15.3b (with viscoelastic damping). It can be seen a different mode of vortex shedding comparing the two figures. Where there is a '2P' and '2S', respectively, in Fig. 15.3a and b. This classification is taking into account [24].

15.3.2 Time Histories of the Hydrodynamic Coefficients

Now, as another illustration, Fig. 15.4a and b shows the time evolution of the drag and lift coefficients for the flow in the cylinder, that the red color represents the simulation without viscoelastic and the blue color with viscoelastic material. It can be verified in Fig. 15.4a that mode of the fluctuations of amplitudes for the drag coefficient is different and more stable when we used the viscoelastic damping.

Then, observing the Fig. 15.4b, that represents the study of lift coefficient, it can be provided a significant reduction of the oscillation in the inclusion of viscoelastic damping. Moreover, the stability over time of this coefficient must be considered an advantage to structure.

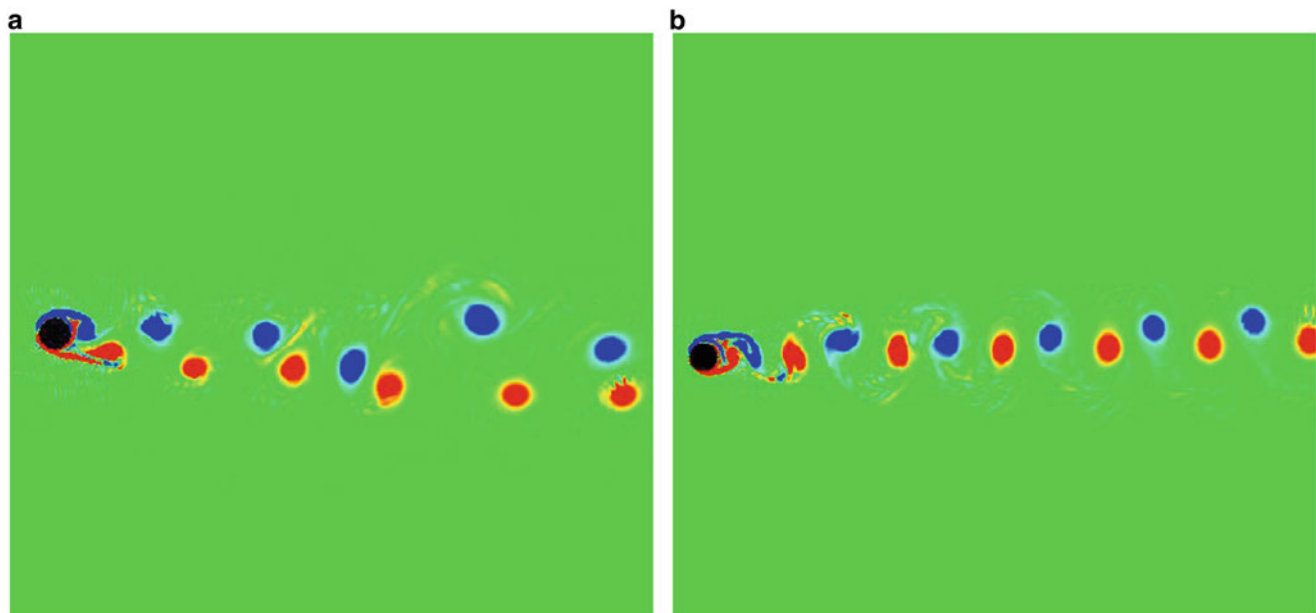


Fig. 15.3 Vorticity contours for number Reynolds equal to 10,000, (a) without viscoelastic; (b) with viscoelastic

The Fig. 15.4c, represents the displacement of the structure. It can be noted that simulation without viscoelastic material the system has a beating condition. So, when is inserted the damping in the system, it can be verified the decrease and stability for the displacement of the structure.

15.4 Concluding Remarks

In the present work, the numerical simulations over a single circular cylinder immersed in two-dimensional, incompressible, viscous and isothermal flows were carried out at Reynolds number equal to 10,000. In the same way, has been suggested a modeling of viscoelastic structural system containing translational mount.

The first step of simulations, it was illustrated the vorticity fields and compared the structure with and without viscoelastic damping. Then, it can be observed a different mode of vortex shedding, that to the structure with viscoelastic damping obtained a '2S' and the other one '2P'. So, for the second results, has been showed the different amplitudes of the drag and lift coefficients, that the simulations of the viscoelastic damping improve the both coefficients and turn its more stable. The third outcome, it can be observed the decrease of displacement and the end of the beating condition when is used the viscoelastic material.

This paper has purpose an alternative and efficient model of passive control of vibrations induced by vortex (VIV), that the next steps will be analysis the influence of temperature in the system as well as mass ratio and reduced speed. Therefore, it is believed that this strategy can be advantageously used for the next studies of VIV or same applications.

Acknowledgements The authors are grateful to the Minas Gerais State Agency FAPEMIG for the financial support to their research activities and the Brazilian Research Council—CNPq for the continued support to their research work, especially through research projects 303020/2013-0 (A.M.G. de Lima). Also, the authors express their acknowledgements to the INCT-EIE, jointly funded by CNPq, CAPES and FAPEMIG.

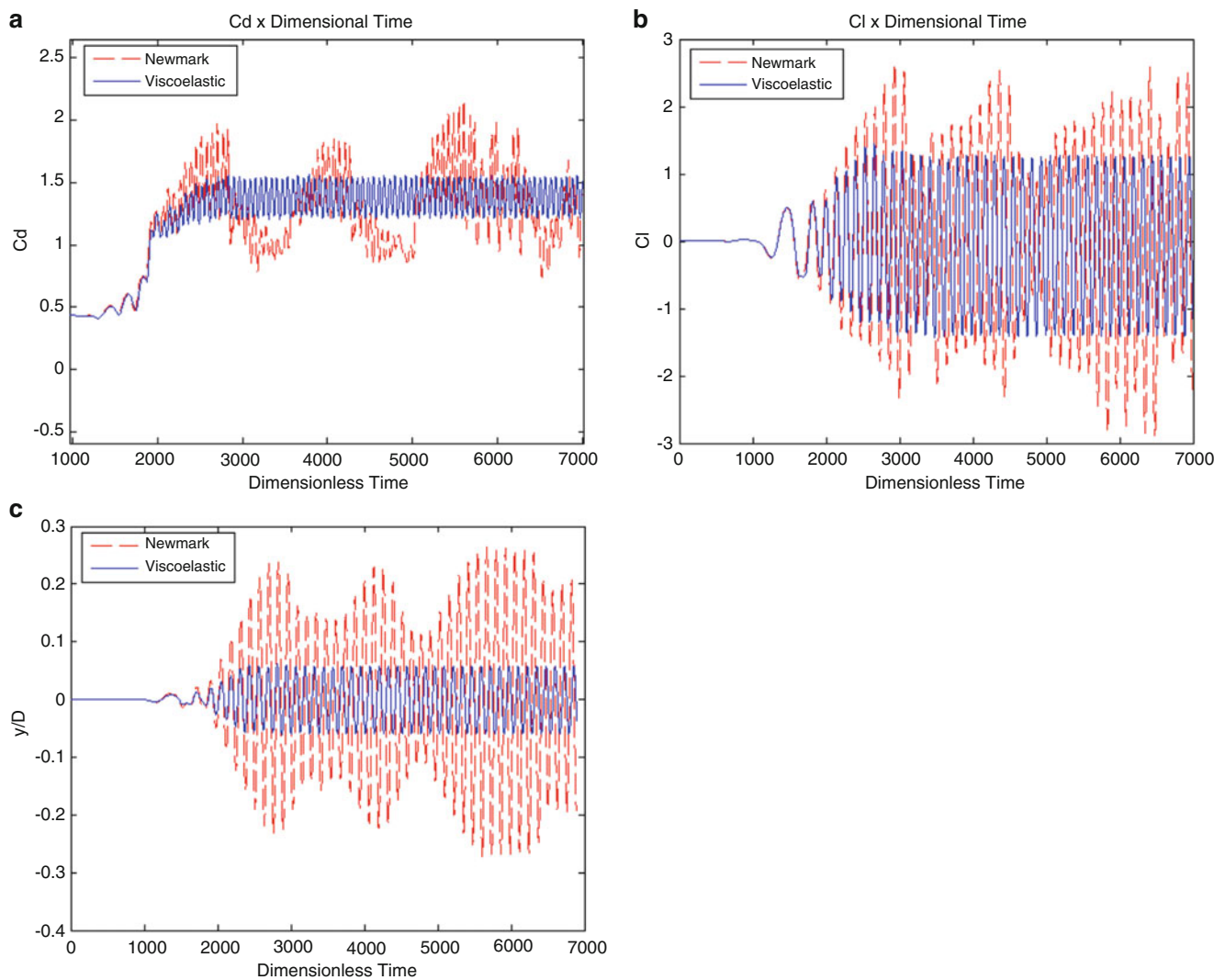


Fig. 15.4 Time histories of the coefficients and displacement with number Reynolds equal to 10,000, (a) Drag Coefficient (b) Lift Coefficient and (c) Displacement of the structure

References

1. Al-Jamal, H., Dalton, C.: Vortex induced vibrations using Large Eddy simulation at a moderate Reynolds number. *J. Fluid Struct.* **9**, 73–92 (2004)
2. Anagnostopoulos, P.: Numerical investigation of response and wake characteristics of a vortex-excited cylinder in a uniform stream. *J. Fluid Struct.* **8**, 367–390 (1994)
3. Bao, Y., Zhou, D., Huang, C.: Numerical simulation of flow over three circular cylinders in equilateral arrangements at low Reynolds number by a second-order characteristic-based split finite element method. *Comput. Phys.* **39**(5), 882–899 (2010)
4. Bagley, R.L., Torvik, P.J.: Fractional calculus—A different approach to the analysis of viscoelastically damped structures. *AIAA J.* **21**, 741–748 (1983)
5. Chen, X.Y., Zha, G.C.: Fully coupled fluid-structural interactions using an efficient high resolution upwind scheme. *J. Fluid Struct.* **20**, 1105–1125 (2005)
6. Chorin, A.J.: Numerical Solution of the Navier-Stokes equations. *Math. Comput.* **22**(104), 745–762 (1968)
7. Da Silva, A.R., Silveira-Neto, A., de Lima, A.M.G., Rade, D.A.: Numerical simulations of flows over a rotating circular cylinder using the immersed boundary method. *J. Braz. Soc. Mech. Sci. Eng.* **33**(1), 99–106 (2011)
8. Da Silva, A.R., Silveira-Neto, A., Rade, D.A., Francis, R., Santos, E.A.: Numerical simulations of flows over a pair of cylinders at different arrangements using the immersed boundary method. *Comput. Model Eng.* **50**, 285–303 (2009)
9. Galucio, A.C., Deü, J.F., Ohayon, R.: Finite element formulation of viscoelastic sandwich beams using fractional derivative operators. *Comput. Mech.* **33**, 282–291 (2004)

10. Khalak, A., Williamson, C.H.K.: Fluid forces and dynamics of a hydroelastic structure with very low mass and damping. *J. Fluid Struct.* **11**, 973–982 (1997)
11. Khalak, A., Williamson, C.H.K.: Motions, forces and mode transitions in vortex-induced vibrations at low mass-damping. *J. Fluid Struct.* **13**, 813–851 (1999)
12. Klamro, J.T., Leonard, A., Roshko, A.: The effects of damping on the amplitude and frequency response of a freely vibrating cylinder in cross-flow. *J. Fluid Struct.* **22**, 845–856 (2006)
13. Lima, A.M.G., Silva, A.R.: Numerical simulations of incompressible and two-dimensional flow around a rotating cylinders pair. In: XXXV Iberian Latin-American Congress on Computational Methods in Engineering, Ceará, Brazil, 23–28 November 2014
14. Lima, A.M.G., Silva, A.R., Silveira-Neto, A.: Numerical simulation of two-dimensional complex flows around bluff bodies using the immersed boundary method. *J. Braz. Soc. Mech. Sci. Eng.* **4**, 378–386 (2007)
15. Meirovitch, L.: *Dynamics and Control of Structures*. Wiley, New York (1989)
16. Nashif, A.D., Jones, D.I.G., Henderson, J.P.: *Vibration Damping*. Wiley, New York (1985)
17. Peskin, C.S.: Numerical analysis of blood flow in the heart. *J. Comput. Phys.* **25**, 220–252 (1977)
18. Peskin, C.S., McQueen, D.M.: A general method for the computer simulation of biological systems interacting with fluids. In: *Symposium on Biological Fluid Dynamics (SEB)*, Leeds, England, 5–8 July 1994
19. Sarpkaya, T.: A critical review of the intrinsic nature of vortex-induced vibrations. *J. Fluid Struct.* **19**, 389–447 (2004)
20. Singh, S.P., Mittal, S.: Vortex-induced oscillations at low Reynolds numbers: hysteresis and vortex-shedding modes. *J. Fluid Struct.* **20**, 1085–1104 (2005)
21. Thomson, W.T., Dahleh, M.D.: *Theory of Vibration with Applications*. Prentice Hall, New Jersey (1998)
22. Prasanth, T.K., Behara, S., Singh, S.P., Kumar, R., Mittal, S.: Effect of blockage on vortex-induced vibrations at low Reynolds numbers. *J. Fluid Struct.* **22**, 865–876 (2006)
23. Vikestad, K., Vandiver, J.K., Larsen, C.M.: Added mass and oscillation frequency for a circular cylinder subjected to vortex-induced vibrations and external disturbance. *J. Fluid Struct.* **14**, 1071–1088 (2000)
24. Williamson, C.H.K., Roshko, A.: Vortex formation in the wake of an oscillating cylinder. *J. Fluids Struct.* **2**, 355–381 (1988)
25. Zhou, C.Y., So, R.M.C., Lam, K.: Vortex-induced vibrations of an elastic circular cylinder. *J. Fluid Struct.* **13**, 165–189 (1999)

Chapter 16

Dynamic Analysis of Fluid-Filled Piping System on Flexible Foundation

Longlong Ren, Xiuchang Huang, Zhengguo Zhang, and Hongxing Hua

Abstract In this paper, dynamic modeling of fluid-filled piping system coupled with general flexible foundation by discrete springs has been investigated. A method combined the transfer matrix method (TMM) and frequency response function (FRF)-based substructure method has been proposed to enhance the computation efficiency. Fluid-structure interaction of the fluid-filled piping system has been taken into consideration in the TMM by variable separation. By using this method, the natural frequencies and FRFs of the coupled system can be obtained. The engineering applications with plate-like foundation have been simulated. Very good agreement has been obtained compared with the results by finite element method (FEM). Parametric studies are carried out to illustrate the influences of stiffness of spring and plate on the dynamic behaviors of the coupled system. This study will shed some light on designing fluid-filled piping system on flexible foundation in engineering practice.

Keywords Fluid-filled • Piping system • Flexible foundation • Transfer matrix method • Substructure method

16.1 Introduction

Piping system is widely used in many fields such as nuclear industries, marine engineering, and civil engineering and so on. As is well-known, the vibration of piping system is induced by excitation from inside and outside, of which the former is caused by the fluid in the piping system through fluid-structure interaction (FSI). A great number of researches indicates that the FSI is very important and should be considered in the dynamic analysis of piping system.

Over the past 60 years, many theoretical models of the piping system such as beam model and shell model have been developed. Tijsseling et al. [1] and Li et al. [2] have carried out detailed review about the early and recently development. The theoretical model based on beam model mainly include the 4-equations model [3]; the 6-equations model [4]; the 8-equations model [5]; 12-equations model [6]; and the 14-equations model [7]. In order to solve these models, the method of characteristic (MOC) is widely used in the time domain [8]; the methods such as transfer matrix method (TMM) are proposed in the frequency domain [9]. Although many results have been achieved in recent years, most of these studies have not established the whole model containing pipe system and the foundation, in other words, the foundation is considered as rigid. Yang et al. [10] studied the longitudinal vibration of multi-span pipe by using TMM. Liu et al. [11] analyzed the vibration of liquid-filled pipe line with elastic constraints. The foundation in reality is flexible and the dynamics of the pipe system are apparently influenced by the foundation. Many works about the modeling of the whole system have been done in similar systems such as the rotor-foundation system. Bonello et al. [12] developed an analytical model based on the impedance technique to predict the responses of a coupled rotor-bearing-foundation system. Zhang et al. [13] developed an efficient analytical framework to study the transverse vibration of double-beam system.

Substructure synthesis method is usually used for a system consisted of many substructures, Liu and Ewins [14] presented a brief review of previous developments in substructure synthesis methods and proposes a new coupling analysis approach which takes into account the effect of elastic media between substructures. Huang et al. [15] studied the vibration transmission from vibrating machines to the base by using the frequency-response function (FRF)-based substructure method. The FRF matrix is an important medium when using the substructure synthesis method, it can be determined by three methods which are analytical method, experimental method and numerical method. Usually the flexible foundation is

L. Ren (✉) • X. Huang • Z. Zhang • H. Hua

Institute of Vibration, Shock & Noise, Shanghai Jiaotong University, Dongchuan Road 800, 200240 Shanghai, China

State Key Laboratory of Mechanical System and Vibration, Shanghai Jiaotong University, Dongchuan Road 800, 200240 Shanghai, China

e-mail: renlonglong@sjtu.edu.cn

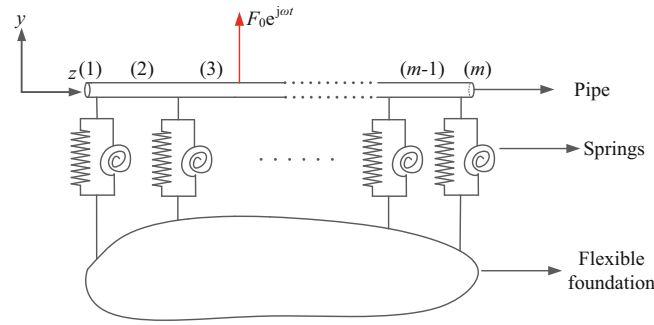


Fig. 16.1 Model of the coupled pipe-spring-foundation system

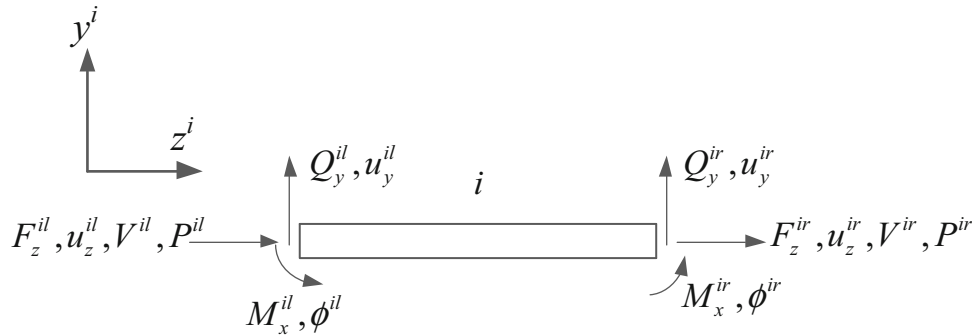


Fig. 16.2 Projection of pipe segment i in y - z plane

a complex structure, the analytical method is inapplicability, and the latter two methods are more frequently used to obtain the FRF matrix of the flexible foundation. The FRF matrix of the pipe substructure can be obtained by analytical method.

This paper develops a model based on the TMM and FRF-based substructure method to predict the dynamic characteristics of a coupled pipe-spring-foundation system. The FRF matrix of the pipe substructure and flexible foundation are obtained by TMM and FEM, respectively. The proposed method is validated by finite element method (FEM). The influence of flexibility of the foundation and the stiffness of the springs on the vibration transmission due to the FSI by the pipe system is discussed.

16.2 Theoretical Development

16.2.1 Model Description

The coupled system is divided into two substructures as shown in Fig. 16.1, the pipe substructure and the flexible foundation, where the z -axis is along the pipe. The two substructures are connected by springs. According to the position of the springs and other interested points such as the excitation point, the pipe subsystem can be divided into m segments; each segment is modeled as a fluid-filled pipe based on the Timoshenko beam model. For studying the coupled system conveniently, the model is simplified as a 2D planar problem.

16.2.2 Pipe Substructure

16.2.2.1 Model of Pipe Segment

The governing differential equations for transverse vibration and axial vibration in the y^i - z^i plane of any pipe segment i as show in Fig. 16.2 can be written as

Lateral motion:

$$\frac{\partial \dot{u}_y^i}{\partial t} + \frac{1}{\rho_p^i A_p^i + \rho_f^i A_f^i} \frac{\partial Q_y^i}{\partial z} = 0 \quad (16.1)$$

$$\frac{\partial \dot{u}_y^i}{\partial z} + \frac{1}{(\kappa^i)^2 G^i A_p^i} \frac{\partial Q_y^i}{\partial t} = -\dot{\theta}_x^i \quad (16.2)$$

$$\frac{\partial \dot{\theta}_x^i}{\partial t} + \frac{1}{\rho_p^i I_p^i + \rho_f^i I_f^i} \frac{\partial M_x^i}{\partial z} = \frac{1}{\rho_p^i I_p^i + \rho_f^i I_f^i} Q_y^i \quad (16.3)$$

$$\frac{\partial \theta_x^i}{\partial z} + \frac{1}{E^i I_p^i} \frac{\partial M_x^i}{\partial t} = 0 \quad (16.4)$$

Axial motion:

$$\frac{\partial \dot{u}_z^i}{\partial t} - \frac{1}{\rho_p^i} \frac{\partial \sigma_z^i}{\partial z} = 0 \quad (16.5)$$

$$\frac{\partial \dot{u}_z^i}{\partial z} - \frac{1}{E^i} \frac{\partial \sigma_z^i}{\partial t} = -\frac{\nu r^i}{E^i e^i} \frac{\partial P^i}{\partial t} \quad (16.6)$$

$$\frac{\partial V^i}{\partial t} + \frac{1}{\rho_f^i} \frac{\partial P^i}{\partial z} = 0 \quad (16.7)$$

$$\frac{\partial V^i}{\partial z} + \left(\frac{1}{K^i} + (1 - \nu^2) \frac{2r^i}{E^i e^i} \right) \frac{\partial P^i}{\partial t} = 2\nu \frac{\partial \dot{u}_z^i}{\partial z} \quad (16.8)$$

where, Q_y^i is lateral shear force of the i th pipe segment; u_y^i is the lateral displacement; M_x^i is the bending moment; θ_x^i is the slope; ρ_p^i , ρ_f^i are density of the pipe and the fluid, respectively; A_p^i , A_f^i are cross section area of the pipe and the fluid, respectively; I_p^i , I_f^i are moment of inertial of pipe and fluid, respectively; $\kappa^i = 2(1 + \nu)/(4 + 3\nu)$ is shear coefficient; E^i is Young modulus of pipe; G^i is shear modulus of pipe; P^i is fluid fluctuating pressure, V^i is cross-sectional average velocity; u_z^i is axial displacement of the pipe; r^i is inner radius of the pipe; e^i is thickness of the pipe; K^i is fluid bulk modulus; ν is Poisson's ratio.

By the derivation, the conventional pipe equation in terms of u_y^i corresponding to Eqs. (16.1), (16.2), (16.3), and (16.4) is

$$\begin{aligned} E^i I_p^i \frac{\partial^4 u_y^i}{\partial z^4} - (\rho_p^i I_p^i + \rho_f^i I_f^i) \frac{\partial^4 u_y^i}{\partial z^2 \partial t^2} - \left(E^i I_p^i \frac{\rho_p^i A_p^i + \rho_f^i A_f^i}{(\kappa^i)^2 G^i A_p^i} \right) \frac{\partial^4 u_y^i}{\partial z^2 \partial t^2} \\ + (\rho_p^i A_p^i + \rho_f^i A_f^i) \frac{\partial^2 u_y^i}{\partial t^2} + \frac{(\rho_p^i I_p^i + \rho_f^i I_f^i)(\rho_p^i A_p^i + \rho_f^i A_f^i)}{(\kappa^i)^2 G^i A_p^i} \frac{\partial^4 u_y^i}{\partial t^4} = 0 \end{aligned} \quad (16.9)$$

And the wave equation in terms of u_z^i corresponding to Eqs. (16.5), (16.6), (16.7), and (16.8) is

$$\frac{\partial^4 u_z^i}{\partial t^4} - \left((a_p^i)^2 + (a_f^i)^2 + \frac{2\nu^2 b^i K^{*i}}{\rho_p^i} \right) \frac{\partial^4 u_z^i}{\partial z^2 \partial t^2} + (a_p^i)^2 (a_f^i)^2 \frac{\partial^4 u_z^i}{\partial z^4} = 0 \quad (16.10)$$

where $\frac{1}{K^{*i}} = \frac{1}{K^i} + (1 - \nu^2) \frac{2r^i}{E^i e^i}$; $b^i = \frac{r^i}{e^i}$; $d^i = \frac{\rho_p^i}{\rho_f^i}$; $(a_p^i)^2 = \frac{E^i}{\rho_p^i}$; $(a_f^i)^2 = \frac{K^{*i}}{\rho_f^i}$.

By using the method of separation of variables, assuming $u_y^i = U_y^i(z)e^{j\omega t}$ and $u_z^i = U_z^i(z)e^{j\omega t}$, Eqs. (16.9) and (16.10) lead to the spatial equations as follows

$$E^i I_p^i \frac{\partial^4 U_y^i}{\partial z^4} + \omega^2 \left(E^i I_p^i \frac{\rho_p^i A_p^i + \rho_f^i A_f^i}{(\kappa^i)^2 G^i A_p^i} + \rho_p^i I_p^i + \rho_f^i I_f^i \right) \frac{\partial^2 U_y^i}{\partial z^2} - \omega^2 \left(\rho_p^i A_p^i + \rho_f^i A_f^i \right) U_y^i + \omega^4 \frac{(\rho_p^i I_p^i + \rho_f^i I_f^i)(\rho_p^i A_p^i + \rho_f^i A_f^i)}{(\kappa^i)^2 G^i A_p^i} U_y^i = 0 \quad (16.11)$$

$$(a_p^i)^2 (a_f^i)^2 \frac{\partial^4 U_z^i}{\partial z^4} + \omega^2 \left((a_p^i)^2 + (a_f^i)^2 + \frac{2\nu^2 b^i K^{*i}}{\rho_p^i} \right) \frac{\partial^2 U_z^i}{\partial z^2} + \omega^4 U_z^i = 0 \quad (16.12)$$

where ω is the angular frequency and $j = \sqrt{-1}$. The general solution of Eqs. (16.11) and (16.12) is

$$U_y^i = A_1^i e^{\lambda_{1,2}^i z} + A_2^i e^{\lambda_{3,4}^i z} + A_3^i e^{\lambda_{1,2}^i z} + A_4^i e^{\lambda_{3,4}^i z} \quad (16.13)$$

$$U_z^i = B_1^i e^{q_{1,2}^i z} + B_2^i e^{q_{3,4}^i z} + B_3^i e^{q_{1,2}^i z} + B_4^i e^{q_{3,4}^i z} \quad (16.14)$$

where

$$\lambda_{1,2}^i = \pm \left(\frac{-\omega^2 C^i + \sqrt{(D^i)^2 \omega^4 + 4\omega^2 A^i E^i I_p^i}}{2E^i I_p^i} \right)^{1/2}, \quad \lambda_{3,4}^i = \pm \left(\frac{-\omega^2 C^i - \sqrt{(D^i)^2 \omega^4 + 4\omega^2 A^i E^i I_p^i}}{2E^i I_p^i} \right)^{1/2},$$

$$q_{1,2}^i = \pm \left(\frac{-\omega^2 R^i + \sqrt{\omega^4 \left[(R^i)^2 - 4(a_p^i)^2 (a_f^i)^2 \right]}}{2(a_p^i)^2 (a_f^i)^2} \right)^{1/2}, \quad q_{3,4}^i = \pm \left(\frac{-\omega^2 R^i - \sqrt{\omega^4 \left[(R^i)^2 - 4(a_p^i)^2 (a_f^i)^2 \right]}}{2(a_p^i)^2 (a_f^i)^2} \right)^{1/2}.$$

$$A^i = \rho_p^i A_p^i + \rho_f^i A_f^i, \quad B^i = \rho_p^i I_p^i + \rho_f^i I_f^i, \quad C^i = \frac{E^i I_p^i A^i}{(\kappa^i)^2 G^i A_p^i} + B^i, \quad D^i = \frac{E^i I_p^i A^i}{(\kappa^i)^2 G^i A_p^i} - B^i, \quad R^i = (a_p^i)^2 + (a_f^i)^2 + \frac{2\nu^2 b^i K^{*i}}{\rho_p^i}.$$

Combining with Eqs. (16.1), (16.2), (16.3), (16.4), (16.5), (16.6), (16.7), and (16.8), and the state vectors of the i th pipe segment can be expressed as

$$\Psi^i = \mathbf{P}^i [A_1^i, A_2^i, A_3^i, A_4^i, B_1^i, B_2^i, B_3^i, B_4^i]^T \quad (16.15)$$

where $\Psi^i = [U_y^i(z), \Phi_x^i(z), M_x^i(z), Q_y^i(z), U_z^i(z), P^i(z), V^i(z), F_z^i(z)]^T$, \mathbf{P}^i is a 8×8 matrix.

Applying the displacement/slope and force/moment boundary conditions at $z = 0$ and L^i to Eq. (16.15), gives

$$\Psi^{ir} = \mathbf{T}^i \Psi^{il} \quad (16.16)$$

where \mathbf{T}^i is the field transfer matrix of the i th pipe segment and its size is 8×8 ; $\sum_{i=1}^m L^i = L$, L^i and L are, length of the i th pipe segment and the piping subsystem, respectively; the superscript r and l , denote the right and left side of the i th pipe segment, respectively.

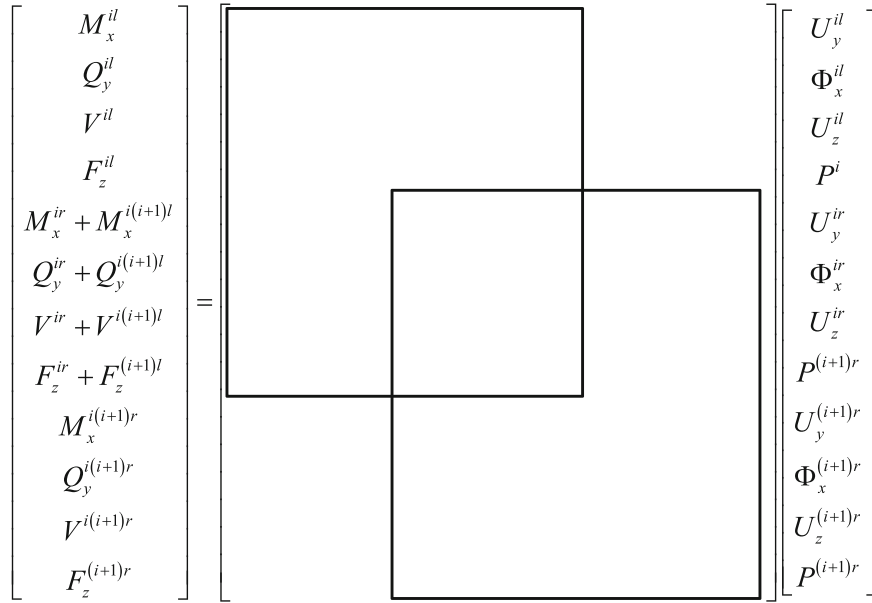


Fig. 16.3 Assembly of FRF matrix of two pipe segments

16.2.2.2 FRF Matrix of Piping System Substructure

The FRF matrix of the piping system substructure can be obtained by assembling transmission matrices of pipe segment elements and continuity of displacement/slope and force/moment at each pipe station. Based on Eq. (16.16), the impedance matrix of the i th pipe segment can be expressed as

$$f_p^i = Z_p^i x_p^i \quad (16.17)$$

where Z_p^i is a 8×8 matrix, $x_p^i = [U_y^{il}(z), \Phi_x^{il}(z), U_z^{il}(z), P^i(z), U_y^{ir}(z), \Phi_x^{ir}(z), U_z^{ir}(z), P^{ir}(z)]^T$, $f_p^i = [M_x^{il}(z), Q_y^{il}(z), V^{il}(z), F_z^{il}(z), M_x^{ir}(z), Q_y^{ir}(z), V^{ir}(z), F_z^{ir}(z)]$. An example of the assembly of two pipe segments i and $i+1$ is shown as Fig. 16.3. In order to assemble them, the two matrices have been extended, and they are added at the appropriate locations.

By using this method, a matrix consisted of quantities of the m pipe segments is finally obtained as follows

$$\Gamma = KW \quad (16.18)$$

where Γ and W are, force/moment and displacement/slope column vectors of the pipe subsystem, K is a $(m+1) \times (m+1)$ matrix. Since every element of K is known, if we set each row of Γ equals 1 while other rows equal 0 in turn, then W can be obtained. We could get $m+1$ column vectors, and assemble these column vectors as a matrix, the FRF matrix is obtained as follows.

$$x_p = H_p f_p \quad (16.19)$$

where f_p is the vector of load on the interested points on piping subsystem; x_p is the vector of displacement and slope of the interested points on piping system substructure.

16.2.3 Flexible Foundation Subsystem

Since the force and moment input from the piping system substructure to the flexible foundation subsystem are located at the springs, the flexible foundation impedance matrix can be expressed as a FRF matrix H_f whose size is $3N \times 3N$

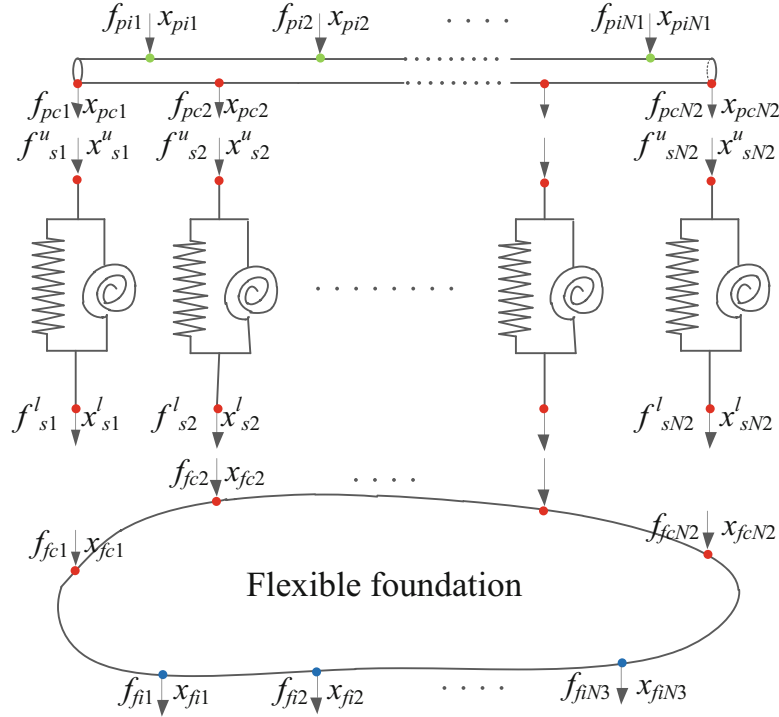


Fig. 16.4 Force and displacement vectors of substructures

$$x_f = H_f f_f \quad (16.20)$$

where $f_f = [Q_{fy1}, Q_{fz1}, M_{fx1} \cdots Q_{fyN}, Q_{fzN}, M_{fxN}]$ is the vector of load on the interested points on flexible foundation; $x_f = [u_{fy1}, u_{fz1}, \phi_{fx1} \cdots u_{fyN}, u_{fzN}, \phi_{fxN}]$ is the vector of displacement and slope of the interested points on flexible foundation.

In this paper, the FRF matrix H_f of the flexible foundation is obtained by using FEM. First we achieve the modal data of the flexible foundation through normalizing the mass, and then the FRF matrix H_f can be obtained as

$$H_f(\omega) = \Phi_{dn} [\omega_r^2 - \omega^2 + 2j\omega\omega_r\zeta_r]_{n \times n}^{-1} \Phi_{dn} \quad (16.21)$$

where the subscript d is the number of the degree of freedom; the subscript n is the number of modal frequencies reserved; ω_r is the r th modal frequency; ζ_r is the r th modal damping ratio. It's worth mentioning that according to the Nyquist Sample Criterion, the highest order of the reserved modal frequencies should be more than 2.5 times the analysis frequency.

16.2.4 The Coupled System

Dynamic modeling of the piping system with flexible foundation is based on the FRF-based substructure method. As shown in Fig. 16.4, there are $(N1 + N2)$ points on the piping system containing $N1$ interested points (called internal points) and $N2$ coupling points, and $(N2 + N3)$ points on the flexible foundation subsystem containing $N3$ interested points (internal points) and $N2$ coupling points.

The FRF matrix of the pipe system and the flexible foundation before synthesizing can be expressed as

$$x_p = \begin{Bmatrix} x_{pi} \\ x_{pc} \end{Bmatrix} = \begin{bmatrix} H_{pii} & H_{pic} \\ H_{pci} & H_{pcc} \end{bmatrix} \begin{Bmatrix} f_{pi} \\ f_{pc} \end{Bmatrix} = f_p, x_f = \begin{Bmatrix} x_{fi} \\ x_{fc} \end{Bmatrix} = \begin{bmatrix} H_{fii} & H_{fic} \\ H_{fci} & H_{fcc} \end{bmatrix} \begin{Bmatrix} f_{fi} \\ f_{fc} \end{Bmatrix} = f_f, H_{pic} = H_{pci}^T, H_{fic} = H_{fci}^T \quad (16.22)$$

where the subscript i and c represents the internal degree of freedom (dof) and the coupling dof, respectively. According to the number of internal points and coupling points, $x_{pi} = \{x_{pi1}, x_{pi2}, \dots, x_{piN1}\}$, $x_{pc} = \{x_{pc1}, x_{pc2}, \dots, x_{pcN2}\}$, $f_{pi} = \{f_{pi1}, f_{pi2}, \dots, f_{piN1}\}$, $f_{pc} = \{f_{pc1}, f_{pc2}, \dots, f_{pcN2}\}$, $x_{fi} = \{x_{fi1}, x_{fi2}, \dots, x_{fiN3}\}$, $x_{fc} = \{x_{fc1}, x_{fc2}, \dots, x_{fcN2}\}$, $f_{fi} = \{f_{fi1}, f_{fi2}, \dots, f_{fiN3}\}$, $f_{fc} = \{f_{fc1}, f_{fc2}, \dots, f_{fcN2}\}$.

After rearranging the elements of the vectors, a new FRF matrix describing two uncoupled substructures is written as

$$\begin{Bmatrix} x_{pi} \\ x_{fi} \\ x_{pc} \\ x_{fc} \end{Bmatrix} = \begin{bmatrix} H_{pii} & 0 & H_{pic} & 0 \\ 0 & H_{fii} & 0 & H_{fic} \\ H_{pci} & 0 & H_{pcc} & 0 \\ 0 & H_{fci} & 0 & H_{fcc} \end{bmatrix} \begin{Bmatrix} f_{pi} \\ f_{fi} \\ f_{pc} \\ f_{fc} \end{Bmatrix} \quad (16.23)$$

Moreover the springs can be described by an impedance matrix as

$$\begin{Bmatrix} f_s^u \\ f_s^l \end{Bmatrix} = \begin{bmatrix} Z_{11} & Z_{12} \\ Z_{21} & Z_{22} \end{bmatrix} \begin{Bmatrix} x_s^u \\ x_s^l \end{Bmatrix} \quad (16.24)$$

where, $x_s^u = \{x_{s1}^u, x_{s1}^u, \dots, x_{sN3}^u\}$, $x_s^l = \{x_{s1}^l, x_{s1}^l, \dots, x_{sN3}^l\}$ denotes the displacement and slope vectors for the upper and lower end of the springs, respectively; $f_s^u = \{f_{s1}^u, f_{s1}^u, \dots, f_{sN3}^u\}$, $f_s^l = \{f_{s1}^l, f_{s1}^l, \dots, f_{sN3}^l\}$ denotes the force and moment vectors for the upper and lower end of the springs, respectively.

For the internal points, the displacement vectors and force vectors must also satisfy compatibility conditions. At the upper and lower connection points, the displacement vectors and force vectors must satisfy compatibility conditions as follows

$$\begin{Bmatrix} X_{pc} \\ X_{fc} \end{Bmatrix} = \begin{Bmatrix} x_{pc} \\ x_{fc} \end{Bmatrix} = \begin{Bmatrix} x_s^u \\ x_s^l \end{Bmatrix}, \begin{Bmatrix} f_{pc} \\ f_{fc} \end{Bmatrix} = \begin{Bmatrix} F_{pc} \\ F_{fc} \end{Bmatrix} - \begin{Bmatrix} f_s^u \\ f_s^l \end{Bmatrix} \quad (16.25)$$

where $\begin{Bmatrix} F_{pc} \\ F_{fc} \end{Bmatrix}$ is the external force.

Finally, the FRF matrix of the coupled system can be expressed as

$$\begin{Bmatrix} X_{pi} \\ X_{fi} \\ X_{pc} \\ X_{fc} \end{Bmatrix} = \begin{bmatrix} H_{pii} & H_{pfi} & H_{ppic} & H_{pfic} \\ & H_{fii} & H_{fpic} & H_{ffic} \\ & & H_{ppcc} & H_{pfcc} \\ sym & & & H_{ffcc} \end{bmatrix} \begin{Bmatrix} F_{pi} \\ F_{fi} \\ F_{pc} \\ F_{fc} \end{Bmatrix} \quad (16.26)$$

where the elements of the matrix denote the driving-point FRF and the transfer or cross FRF.

16.3 Simulation and Discussion

16.3.1 Numerical Validation

An example is presented here to illustrate the correction of the method. The numerical model is shown in Fig. 16.5. As shown in the figure, the pipe is supported by a plate-like foundation, and is divided into 4 segments, the length of each segment are 1, 1.251, 1.251 and 1 m, the inner radius is 0.02601 m, pipe wall thickness is 0.003945 m. The plate is simply supported at the edges and its size is 3 m × 7 m. The axial stiffness of the springs is 2e5 N/m. The material of the pipe and plate is steel, and the fluid is water, the properties are listed in Table 16.1.

Figure 16.6 illustrates the driving-point FRF at the left end of the pipe substructure and the transfer FRF between the right end of the pipe and the left end. It is shown that very good agreement has been obtained compared with the results by FEM. In what follows, the same definition for driving-point FRF and transfer FRF is adopted.

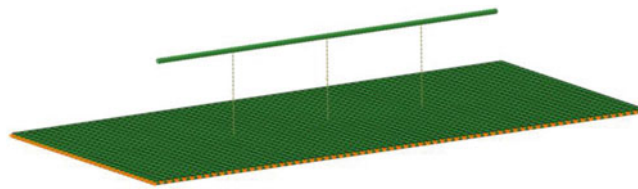


Fig. 16.5 Model of the coupled system

Table 16.1 Material properties

Steel	
Young's modulus	$E = 168 \text{ GPa}$
Mass density	$\rho_p = 7985 \text{ kg/m}^3$
Poisson's ratio	$\nu = 0.3$
Shear coefficient	$\kappa = 0.53$
Water	
Bulk modulus	$K = 2.14 \text{ GPa}$
Mass density	$\rho_f = 999 \text{ kg/m}^3$

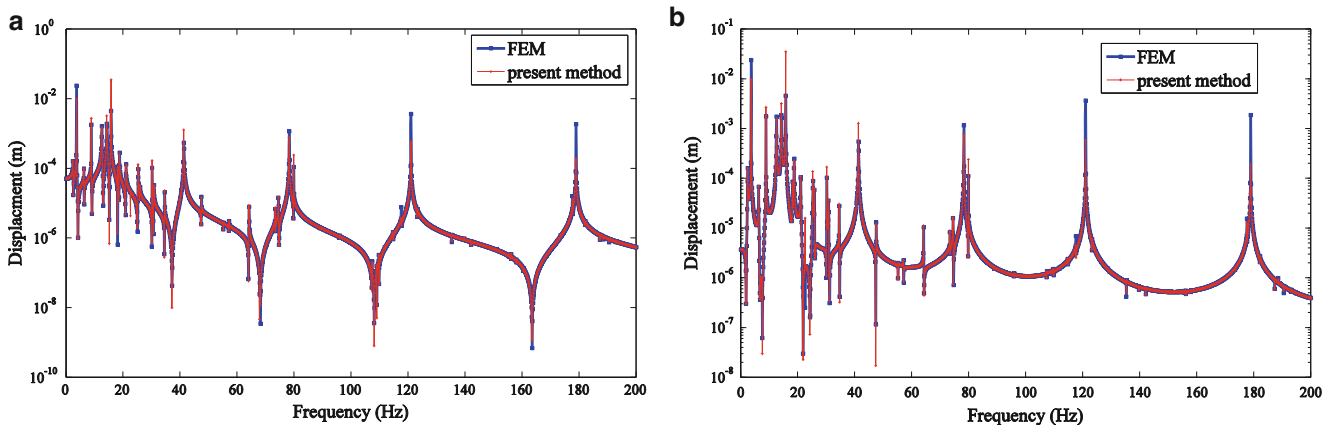


Fig. 16.6 Driving-point FRF and transfer FRF

16.3.2 Effect of the Stiffness of the Foundation and the Springs

In order to investigate the effect of the foundation and springs on the dynamic response of the pipe system, a parametric study is performed in this section.

16.3.2.1 Effect of the Stiffness of the Foundation

Figures 16.7 and 16.8 show the driving-point FRF and transfer FRF due to the change of the thickness of the plate, of which the thickness is 10, 20 and 30 mm, respectively. The results show that the stiffness of the plate plays an important role in the low frequency range and hardly change the response of the pipe system in the high frequency range. Through this numerical study, it shows that the flexible plate will influence the vibration of the pipe system.

16.3.2.2 Effect of the Flexibility of the Stiffness of the Springs

Figures 16.9 and 16.10 show the driving-point FRF and transfer FRF due to the change of the stiffness of the springs, of which the stiffness is $2e5$, $2e6$ and $2e7 \text{ N/m}$, respectively. The results show that the stiffness of the springs plays an important role in the high frequency range; however, there are few changes on the responses of the pipe system in the low frequency range.

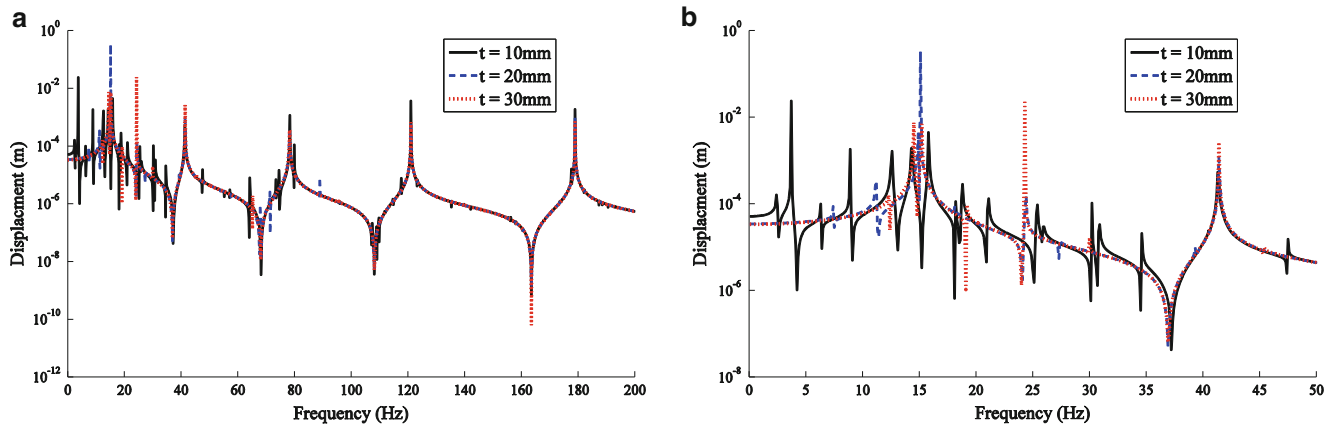


Fig. 16.7 Driving-point FRF. (a) 0–200 Hz; (b) 0–50 Hz

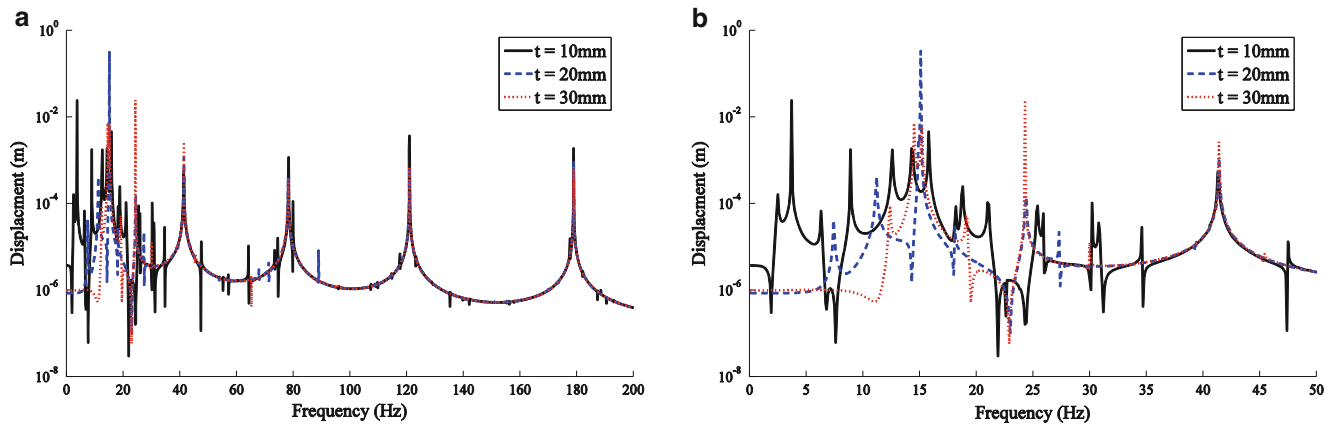


Fig. 16.8 Transfer FRF. (a) 0–200 Hz; (b) 0–50 Hz

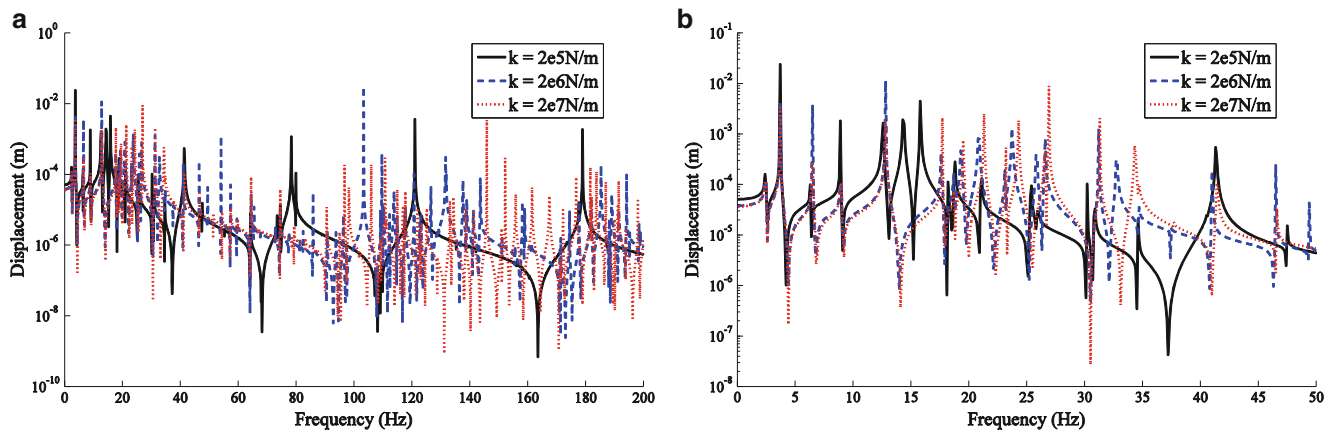


Fig. 16.9 Driving-point FRF. (a) 0–200 Hz; (b) 0–50 Hz

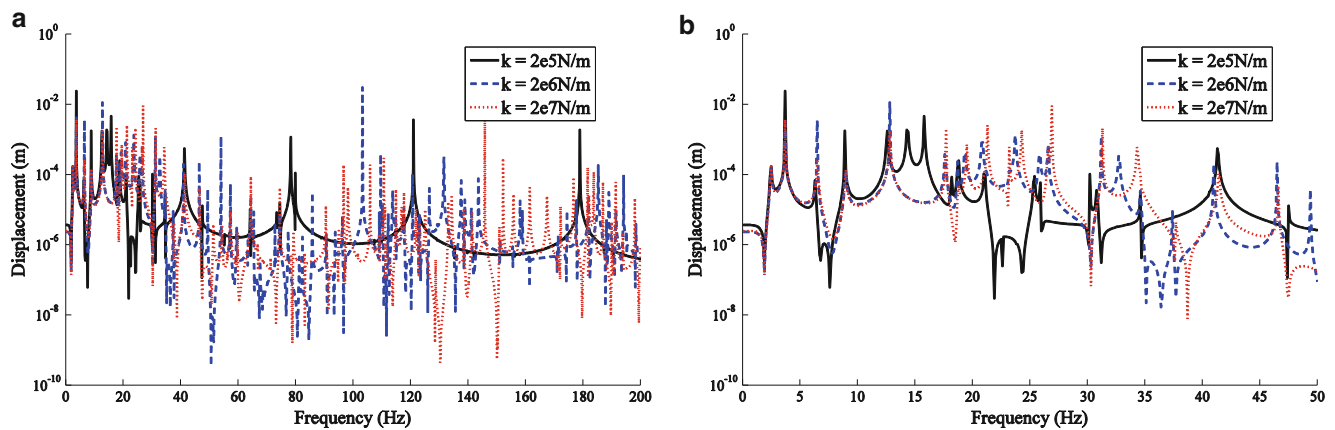


Fig. 16.10 Transfer FRF. (a) 0–200 Hz; (b) 0–50 Hz

16.4 Conclusions

A method by using the TMM and FRF-based substructure method is proposed to model the coupled pipe-springs-flexible foundation system. The proposed method is validated by FEM. A parametric study on the effect of the foundation and springs on the dynamic response of the pipe system is investigated. The results show that the flexible foundation will have influence on the dynamics of the pipe system. Therefore, it should take into consideration of the flexible foundation into consideration when designing the pipe system.

References

1. Tijsseling, A.S.: Fluid-structure interaction in liquid-filled pipe systems: a review. *J. Fluids Struct.* **10**(2), 109–146 (1996)
2. Li, S., Karney, B.W., Liu, G.: FSI research in pipeline systems—A review of the literature. *J. Fluids Struct.* **57**, 277–297 (2015)
3. Tijsseling, A.S., Vardy, A.E.: Twenty years of FSI experiments in Dundee. In: *Proceedings of the Third MIT Conference on Computational Fluid and Solid Mechanics*, Elsevier, Boston, USA, 1014–1017 2005
4. Walker, J.S., Phillips, J.W.: Pulse propagation in fluid-filled tubes. *J. Appl. Mech.* **44**(1), 31–35 (1977)
5. Valentin, R.A., Phillips, J.W., Walker, J.S.: Reflection and transmission of fluid transients at an elbow. In: *Argonne National Lab., IL (USA)*, 1979
6. Shuai-Jun, L.I., Gong-Min, L.I.U., Hao, C.: Pressure wave propagation characteristics in fluid-filled pipes with fluid-structure interaction. *J. Vib. Shock* **31**(24), 177–182 (2012)
7. Lee, D.M., Choi, M.J., Oh, T.Y.: Transfer matrix modelling for the 3-dimensional vibration analysis of piping system containing fluid flow. *KSME J.* **10**(2), 180–189 (1996)
8. Wiggert, D.C., Hatfield, F.J., Stuckenbruck, S.: Analysis of liquid and structural transients in piping by the method of characteristics. *J. Fluids Eng.* **109**(2), 161–165 (1987)
9. Dupuis, C., Rousselet, J.: Application of the transfer matrix method to non-conservative systems involving fluid flow in curved pipes. *J. Sound Vib.* **98**(3), 415–429 (1985)
10. Yang, K., Li, Q.S., Zhang, L.: Longitudinal vibration analysis of multi-span liquid-filled pipelines with rigid constraints. *J. Sound Vib.* **273**(1), 125–147 (2004)
11. Liu, G., Li, Y.: Vibration analysis of liquid-filled pipelines with elastic constraints. *J. Sound Vib.* **330**(13), 3166–3181 (2011)
12. Bonello, P., Brennan, M.J.: Modelling the dynamic behavior of a supercritical rotor on a flexible foundation using the mechanical impedance technique. *J. Sound Vib.* **239**(3), 445–466 (2001)
13. Zhang, Z., Huang, X., Zhang, Z., et al.: On the transverse vibration of Timoshenko double-beam systems coupled with various discontinuities. *Int. J. Mech. Sci.* **89**, 222–241 (2014)
14. Liu, W., Ewins, D.J.: Substructure synthesis via elastic media. *J. Sound Vib.* **257**(2), 361–379 (2002)
15. Huang, X.C., Zhang, Z.Y., Zhang, Z.H., et al.: Vibro-acoustic optimization of an immersed cylindrical structure with a floating-raft system inside by using frequency-response-function-based substructure sensitivity analysis. *Proc. Inst. Mech. Eng. Part M J. Eng. Maritime Environ.* **225**(2), 111–132 (2011)

Chapter 17

Incremental Dynamic Analyses of Steel Moment Resisting Frames with Superelastic Viscous Dampers

Baikuntha Silwal, Osman E. Ozbulut, and Robert J. Michael

Abstract This study aims to evaluate the seismic performance of steel moment resisting frames upgraded with shape memory alloy (SMA)-based self-centering viscous dampers. The superelastic viscous damper (SVD) relies on SMA cables for re-centering capability and employs viscoelastic (VE) damper that consists of two layers of a high damped (HD) blended butyl elastomer compound to augment its energy dissipation capacity. First, the design and mechanical behavior of SVDs are described. A nine-story steel frame building is selected for the numerical analyses. The building is analyzed as (1) a conventional special moment resisting frame (SMRF), (2) a dual SMRF-buckling restrained brace (BRB) system, and (3) a SMRF with SVDs. A model of the steel building for each configuration is developed to determine the dynamic response of the structure. The incremental dynamic analysis is used to evaluate the behavior of each building under seven ground-motion records. The analytical results indicate that the SVDs improve the response of steel frame buildings under different level of seismic hazards.

Keywords Shape memory alloys • Passive control • Viscoelastic damper • Earthquakes • Steel structures

17.1 Introduction

Conventional seismic design approaches rely on the ability of structures to dissipate the input earthquake energy through inelastic deformations in designed regions of the steel frames, implying substantial structural damage and potential extensive residual deformations after a major earthquake [1]. As performance-based earthquake engineering is becoming more prominent, it is important to minimize the damage at multiple seismic hazard levels to achieve the selected performance objectives. McCormick et al. [2] studied the effects of residual drifts on occupants and concluded that residual drifts greater than 0.5 % in buildings may suggest a complete loss of the structure from an economic point of view. In another study, Erochko et al. [3] examined the residual drift response of special moment-resisting frames (SMRFs) and buckling-restrained braced frames (BRBFs). It was found that both types of building systems experience significant residual drifts, with values between 0.8 and 1.5 % for the SMRFs and 0.8–2.0 % for the BRBFs under design-based excitations. By reducing residual drifts of a structure subjected to a seismic event, structural engineers can maximize post-event functionality, reduce the cost to repair the structures, and increase the public safety.

A number of studies have been carried out to develop new structural systems that can provide stable energy dissipation with full re-centering capabilities. Often referred to as self-centering or re-centering, these systems provide a restoring force which is either independent from or acts in addition to energy dissipation capabilities. Christopoulos et al. [4] developed a self-centering energy dissipative bracing system, which combines a friction dissipative mechanism and post-tensioning elements. Experimental tests on the proposed full-scale bracing system were conducted to confirm the repeatable flag-shape hysteretic response. Deierlein et al. [5] proposed a new seismic resisting system that includes controlled rocking, elastic post-tensioning, and replaceable fuses to minimize the damage after an earthquake. Kam et al. [6] studied the effectiveness of advanced flag-shaped systems, where self-centering elements were combined with alternative dissipation elements in series and/or in parallel. It was shown that a seismic-resistant system that consist of a combination of hysteretic and viscous energy

B. Silwal • O.E. Ozbulut (✉)

Department of Civil and Environmental Engineering, University of Virginia, Charlottesville, VA, USA

e-mail: ozbulut@virginia.edu

R.J. Michael

Department of Mechanical Engineering, Gannon University, Erie, PA, USA

dissipation achieve better performance. Eatherton and Hajjar [7] conducted a parametric study to evaluate the necessary maximum re-centering force relative to the yield strength of supplemental energy-absorbing devices as well as the ambient capacity of the structure.

Shape memory alloys (SMAs) have attracted a great deal of attention as a smart material that can be used in seismic protection systems for energy dissipating and re-centering purposes [8]. SMAs behave similarly to linear-elastic materials for small magnitude events, but for moderate and more severe strain levels, SMAs display superelastic behavior from which it can fully recover its original elastic shape. SMAs also exhibit self-centering behavior when permanent deformations in surrounding assemblies afflict the SMA installation; thus, the overall integrity of neighboring structural systems can be maintained. Due to strain hardening of SMA materials, the stiffness of the overall system increases during extreme deformations, which further alleviates deflections in surrounding structural systems. Because of their re-centering capability, SMAs can serve as a valuable component in a seismic control device. Previous studies on SMAs indicate that the quantity of equivalent viscous damping provided by superelastic SMA wires or bars is not sufficient to render the use of SMAs as the sole damping device implemented in a tall structure subjected to severe dynamic loadings [9]. Therefore, several researchers have explored the development of SMA-based control devices with supplemental energy dissipation capabilities [10–12].

This paper investigates the performance of an SMA-based control device, where SMA elements were used in combination with a viscoelastic element in parallel. Compared with conventional structural control devices, the proposed superelastic viscous damper (SVD) is an attractive alternative in both performance and design efficiency. First, a description of the SVDs is provided and the effect of different design parameters on the behavior of the device is studied. Then, a nine-story steel building is designed as conventional special moment resisting frame and with SVDs. For comparison purposes, the steel building is also designed with buckling restrained braces (BRB). Incremental dynamic analyses are conducted using seven ground motion records. The results are analyzed in terms of peak interstory drift, peak floor acceleration, and residual interstory drifts.

17.2 Superelastic Viscous Damper

The Superelastic Viscous Damper combines re-centering capabilities of shape memory alloys with the energy dissipation ability of viscoelastic devices. The 3D renderings of the SVD and schematic diagrams of the device in the undeformed and deformed positions are given in Fig. 17.1. The module comprises two high damped butyl elastomer compounds, sandwiched between and bonded to three identical steel plates and installed SMA cables. Each SMA cable forms a continuous loop; wrapping the loops around the outer two plates improves compactness and efficiency. Whether the device itself undergoes a compressive or tensile loading, the configuration ensures that the SMA elements will remain under tension. Along the top and bottom of the device, the wires are threaded through guides, which ensure that the wires remain parallel to the direction of shear deformation in the elastomer layers. As the device moves through its design displacements, the SMA cables apply a re-centering force to the center plate through a second set of wire guides. Composed of three C-channels, two angle brackets, and four crescent-shaped steel sections (one for each strand), each guide distributes the design loads over a longer length of wire (the arc-length of each crescent, compared to the thickness of the center plate) in order to eliminate problematic stress concentrations.

Figure 17.2 shows the typical force-deformation curves of the SVD and its subcomponents. In the SVD, SMA elements are mainly used for its re-centering capability and the viscoelastic device is mainly employed to dissipate seismic energy. By a judicious specification of design parameters of each individual component, a re-centering device with enhanced energy dissipation can be realized.

17.3 Building Description

To investigate the seismic performance of the SVD dampers, a nine-story building is selected from the SAC steel project for numerical simulations. The selected steel moment resisting frame is designed as an office building located on a stiff-soil site (Site Class D) in Seattle, Washington. It includes a basement level in addition to the nine stories above the ground level. A floor plan and elevation of the nine-story building are shown in Fig. 17.3. The elevation and floor plan, gravity loads, and seismic mass of the model are identical with the SAC Steel Frame Project [13]. The lateral force resisting system consists of

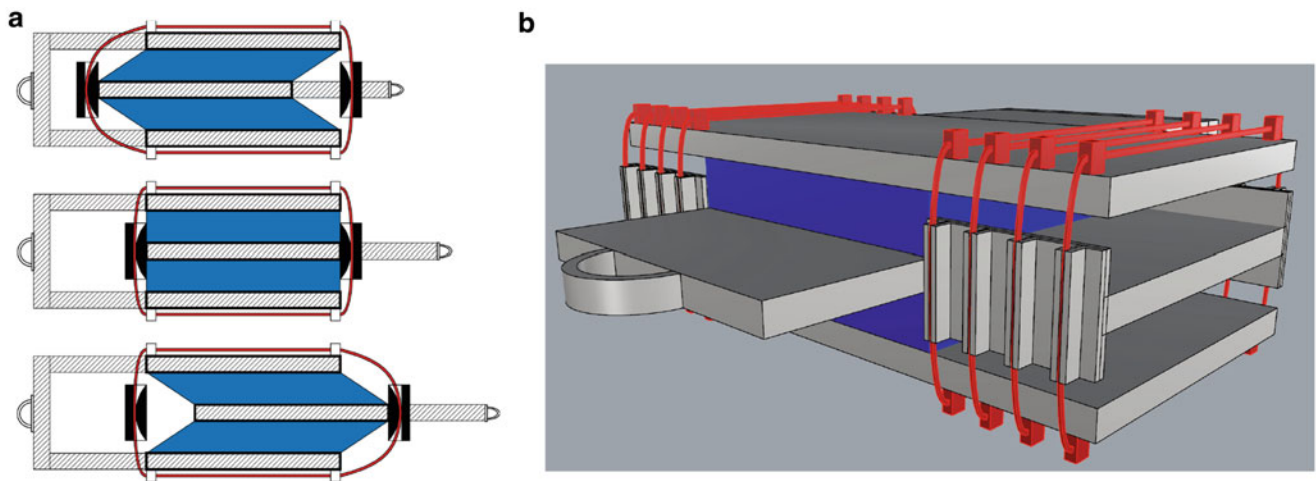


Fig. 17.1 (a) A schematic diagram of SVD at its undeformed and deformed positions, and (b) 3D Rendering of SVD

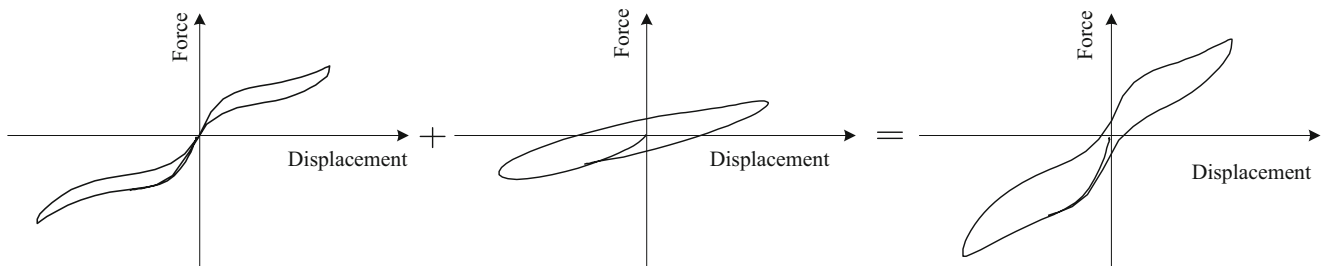


Fig. 17.2 Force-deformation curves of the SVD and its sub-components

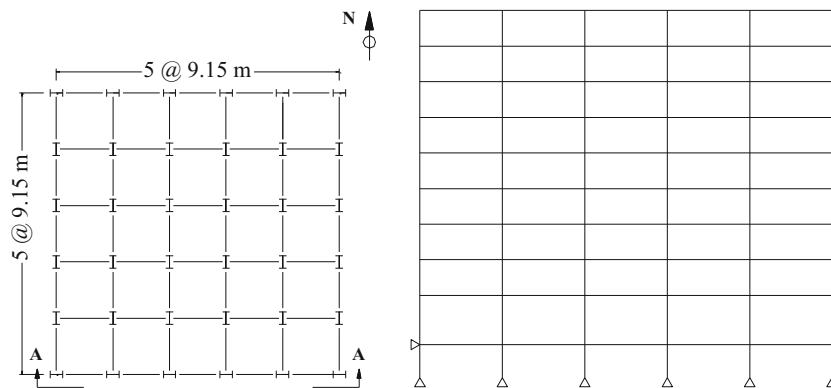


Fig. 17.3 Plan and elevation of the nine-story steel frame building

two code compliant special steel moment resisting frame in each direction. This study analyzes one of the moment resisting frames in the E-W direction. All columns are assumed to be pinned at the base and the exterior columns are also restrained laterally at the ground level.

The design of the Seattle nine-story moment resisting frame is governed by seismic loads and is compliant with ASCE/SEI 7–10 [14] to satisfy both the strength and drift requirements. The seismic masses used for the analysis of the structures are assigned as 1.01×10^6 , 9.89×10^5 , and 1.07×10^6 kg for floor level 2, floor levels 3–9, and roof level, respectively. Based on the Seismic Design Category (SDC) D, the following design response spectral values are assigned to the site: $S_{DS} = 0.912$ g and $S_{DI} = 0.530$ g for the design basic earthquake (DBE), and $S_{MS} = 1.368$ g and $S_{MI} = 0.795$ g for the maximum considered earthquake (MCE). ASCE/SEI 7–10 procedure is employed to develop target spectra for DBE and MCE levels. The response

Table 17.1 Seven ground motion records used in the design

No.	Earthquake	Station name	Magnitude (M_w)	Distance (km)	Peak ground acceleration (g)
1	San Fernando (1971)	LA-Hollywood	6.6	22.8	0.19
2	Imperial Valley-06 (1979)	Elcentro array	6.5	12.6	0.37
3	Loma Prieta (1989)	Gilroy array	6.9	12.2	0.37
4	Superstition Hills-02 (1987)	El Centro Imp.	6.5	18.2	0.26
5	Northridge (1994)	Canyon Country	6.7	12.4	0.40
6	Duzce, Turkey (1999)	Duzce	7.1	12.0	0.81
7	Kocaeli, Turkey (1999)	Bolu	7.5	15.4	0.36

Table 17.2 Members of steel moment resisting frames

Story	SMRF			SMRF with BRB			SMRF with SVDs		
	Exterior columns	Interior columns	Girders	Exterior columns	Interior columns	Girders	Exterior columns	Interior columns	Girders
1	W18 × 311	W18 × 311	W21 × 201	W18 × 311	W18 × 311	W21 × 201	W18 × 311	W18 × 311	W21 × 201
2	W18 × 311	W18 × 311	W21 × 201	W18 × 311	W18 × 311	W21 × 201	W18 × 311	W18 × 311	W21 × 201
3	W18 × 311	W18 × 311	W21 × 201	W18 × 258	W18 × 258	W21 × 166	W18 × 258	W18 × 258	W21 × 166
4	W18 × 311	W18 × 311	W21 × 201	W18 × 258	W18 × 258	W21 × 166	W18 × 258	W18 × 258	W21 × 166
5	W18 × 283	W18 × 283	W21 × 182	W18 × 192	W18 × 211	W21 × 132	W18 × 192	W18 × 211	W21 × 132
6	W18 × 283	W18 × 283	W21 × 182	W18 × 192	W18 × 211	W21 × 132	W18 × 192	W18 × 211	W21 × 132
7	W18 × 234	W18 × 234	W18 × 192	W18 × 130	W18 × 143	W18 × 106	W18 × 130	W18 × 143	W18 × 106
8	W18 × 234	W18 × 234	W18 × 192	W18 × 130	W18 × 143	W18 × 106	W18 × 130	W18 × 143	W18 × 106
9	W18 × 192	W18 × 192	W18 × 175	W18 × 86	W18 × 86	W18 × 65	W18 × 86	W18 × 86	W18 × 65
R	W18 × 192	W18 × 192	W18 × 175	W18 × 86	W18 × 86	W18 × 65	W18 × 86	W18 × 86	W18 × 65

history analysis is adopted to design the structure using a total of seven ground motions that are selected from PEER NGA database [15] as shown in Table 17.1 and scaled according to ASCE/SEI 7–10. The selected column and beam sections are given in Table 17.2. The fundamental period of the nine-story special moment resisting frame is 2.44 s.

In order to comparatively assess the seismic performance of superelastic viscous dampers (SVDs), the nine-story building is also designed with SVDs and traditional BRBs. First, the steel frame is designed to meet all strength and section property requirements by reducing stiffness of beam and columns as given in Table 17.2. This lighter frame design complies with the strength requirements but does not satisfy the prescribed story drift requirements. To comply with the current design requirements, the modified frame is retrofitted with SVDs to satisfy the story drift requirements set by the current design standards, prescribed in Chap. 18 of ASCE/SEI 7–10 for structures with a damping system. Each elastomer compound of the SVD has a dimension of $406 \times 406 \times 50$ mm. Each SVD employs a total of 8 SMA cables with a diameter of 8 mm and a length of 1210 mm. With these design parameters, the SVD has a displacement capacity of 100 mm and a maximum force capacity of 300 kN. The equivalent viscous damping ratio of a single damper is about 10 %. The SVDs are installed into the second and fourth bays of each story. A nonlinear response-history analysis procedure is adopted to design the frame with SVDs. From the nonlinear response history analyses, the number of dampers at each bay is selected to be 10. Similarly, the lighter frame is also retrofitted with the BRBs to meet story drift requirements as per ASCE/SEI 7–10. The BRB frame is designed using the nonlinear response-history analysis procedure considering the seven ground motion records shown in Table 17.1. The yield stress of the BRB used in the design is 260 MPa. The higher capacity of the BRB is used in the lower five floors above the ground level and the lower capacity is used in remaining top floors. The yield forces of the BRB are 550 kN up to fifth floor from the ground level and 365 kN capacity in the upper four floors. The fundamental periods of the nine-story frame upgraded with SVD and with BRB are 2.26 and 2.04 s, respectively.

17.4 Analytical Models

Individual analytical models for the nine-story frame with and without retrofitting devices are developed as two-dimensional frame in the Open System for Earthquake Engineering Simulation (OpenSees) [16]. Based on the concentrated plasticity concept, the beam and column elements are modeled with elastic beam column elements connected by zero-length inelastic plastic hinges employing the modified Ibarra-Krawinkler deterioration model [17]. The modified Ibarra-Krawinkler

deterioration model considers bilinear hysteric response behavior. The cyclic deterioration model parameters of the zero-length rotational springs are assigned based on the model parameters developed by Lignos and Krawinkler [18]. The deterioration characteristics of the rotational springs are indicated by yield strength, post-capping strength, unloading stiffness, and reloading stiffness. The moment-rotation curve is characterized by the elastic stiffness, plastic rotation, a post-capping plastic rotation capacity and the corresponding residual strength. To capture the important panel zone deformation modes, the panel zones are modeled considering the shear distortion in beam-column joints using Krawinkler model [19]. The Krawinkler model includes four rigid links and a rotational spring at the upper right corner to represent shear distortion in the panel zone. The nonlinear plastic hinges are created in beams at an offset from the interface of the panel zone and the beam element while the column plastic hinges are assigned at the face of the panel zone and the column element. To account for P-delta effects, a leaning column is linked to each model with elastic beam-column elements and connected to the model with an axially rigid truss element at each story level. The model assumes Rayleigh damping with a 2 % damping ratio for the first and second modes.

The superelastic viscous damper (SVD) is developed in OpenSees program by combining uniaxial self-centering material property to represent the SMAs and the Maxwell material property to model the elastomeric compound. The superelastic component of the SVD is represented by the finite length element with a uniaxial self-centering material property to capture the hysteric response of the NiTi SMA cable. The self-centering material exhibits flag-shaped hysteric response and also considers the post-transformation hardening behavior with a stiffness equals to the initial stiffness. The experimental test results of SMAs and HD butyl compound reported in Ozbulut et al. [20] are used to develop model parameters for the SMA and elastomeric compound. The model parameters selected for the self-centering material are initial stiffness $k_1 = 2.915$ kN/mm, post-activation stiffness $k_2 = 0.994$ kN/mm, forward activation force $SigAct = 53.047$ kN, post-transformation hardening stiffness = 2.915 kN/mm, and ratio of forward to reverse activation force $\beta = 1.0$. Similarly, the Maxwell model parameters are elastic spring coefficient $K = 1.43$ kN/mm, viscous damping coefficient $C = 1.00$ kN(s/mm), and nonlinear exponent coefficient $\alpha = 0.8$.

The buckling restrained braces are modeled in OpenSees software using inelastic corotTruss element which resists only axial force and deformation. The BRB commonly used in practice varies cross-section from small in the core section and large at the end connections. To reasonably represent the equivalent behavior of the braces, a constant cross-sectional area is employed to the entire length of the truss element. In the constant cross-section model, the modified elastic stiffness and the modified yield strength are assigned to account for the change in BRB area. The elastic stiffness of the BRB is modified according to Ozborrow [21]. The yield strength of the BRB in the truss element is modified to match experimental results by Coy [22]. A bilinear hysteric material model is incorporated using steel02 material to capture the yield behavior of BRB elements. The steel02 material model considers a uniaxial Giuffre-Menegotto-Pinto model with isotropic strain hardening behavior.

17.5 Incremental Dynamic Analyses

To evaluate the performance of the steel frames considered in this study up to collapse, incremental dynamic analyses are conducted using seven earthquake records given in Table 17.1. A scale factor of one indicates that the average spectra of seven ground motions are scaled to match the DBE level seismic hazard at the fundamental frequency of the steel moment resisting frame. Peak interstory drift and peak floor absolute acceleration are considered as performance measures. Figures 17.4 and 17.5 show IDA curves for the conventional moment resisting frame and BRB and SVD systems. The figures provide the traces for individual ground motions as well as an average of all ground motions considered here. It can be seen that the SVD system experiences considerably lower interstory drifts compared with other seismic force resisting systems, especially at higher seismic intensity levels. The peak floor acceleration responses of three systems are similar while the SMRF system possesses slightly larger values. The increase in the acceleration response at very high intensity levels for the SVD system can be attributed to the post-transformation hardening behavior of SMA elements.

In addition to IDA curves, the distribution of the peak interstory drift, peak residual story drift and peak floor acceleration over the height of the building are computed for three lateral systems. Figures 17.6 and 17.7 provide the response of each system to individual ground motion records at the DBE level and MCE level, respectively. To facilitate performance assessment of SMRF, BRB and SVD systems comparatively, average response of seven records for each system at the DBE level and MCE level is provided in Figs. 17.8 and 17.9, respectively. It can be seen that the SVD system has the lowest interstory drift and acceleration response values at the MCE level compared to other two lateral systems. The SVD system also has minimal residual drifts at both the DBE and MCE levels, whereas especially BRB system has significant residual deformations.

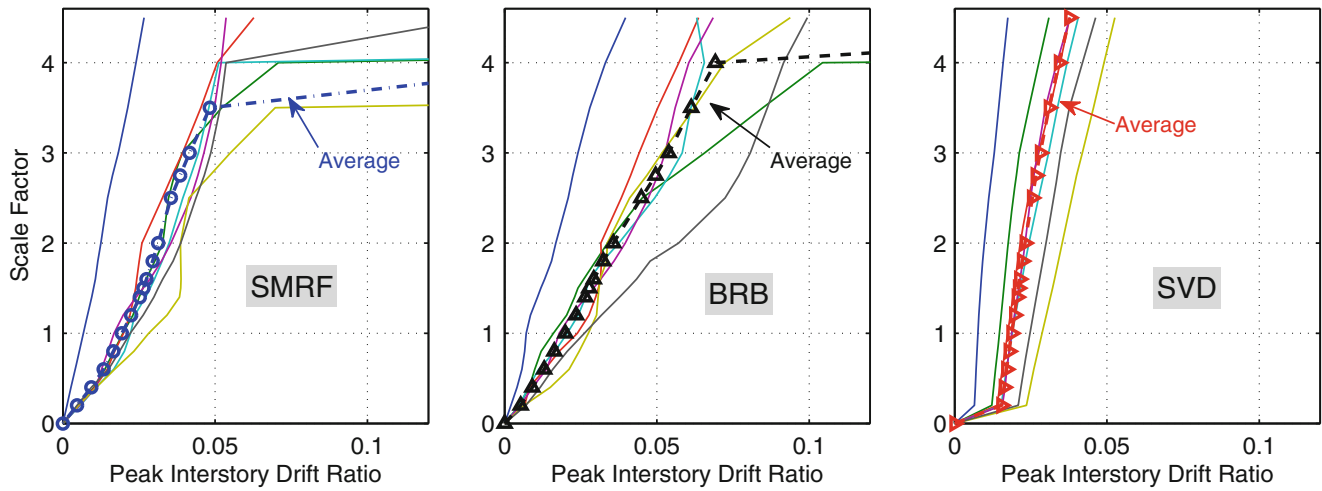


Fig. 17.4 IDA curves for SMRF, BRB and SVD systems at DBE level—peak interstory drift ratio

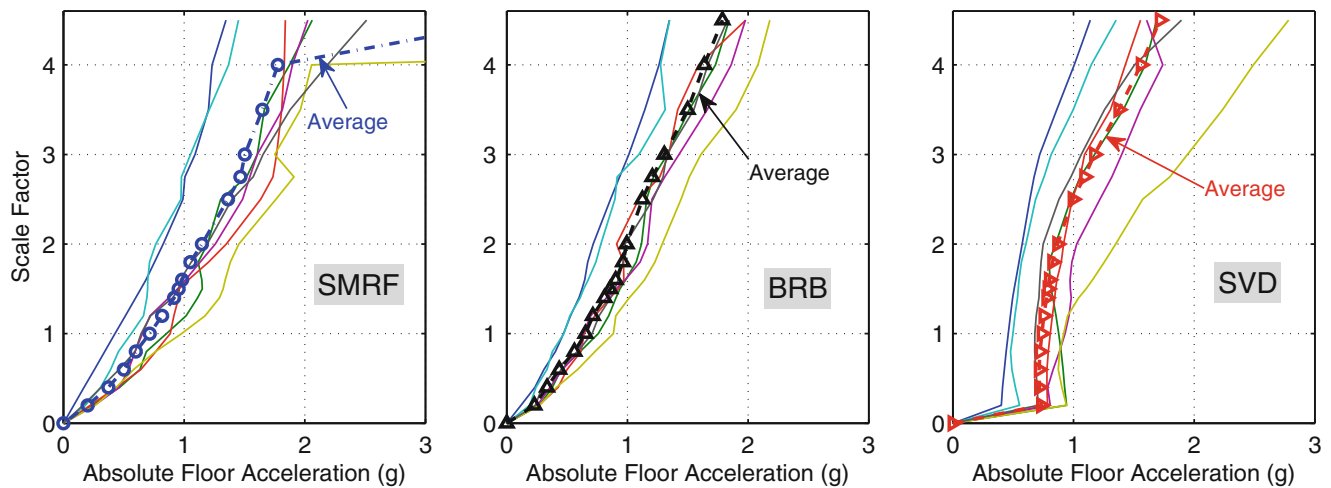


Fig. 17.5 IDA curves for SMRF, BRB and SVD systems at MCE level—peak absolute floor acceleration

17.6 Conclusions

In this study, comparative seismic performance assessment of a nine-story steel frame structure designed (1) as special moment resisting system, (2) with buckling restrained braces, and (3) with superelastic viscous devices is conducted. The superelastic viscous dampers leverage the inherent re-centering capability of shape memory alloys and energy dissipation ability of an elastomer compound for superior seismic performance. A heavily damped butyl compound, which provides high damping at low stiffness, is considered for the viscoelastic component of the hybrid damper. Incremental dynamic analysis approach is employed to explore the behavior of nine-story steel building with three different design configurations. Performance of each system in mitigating response of steel frame buildings under DBE and MCE level seismic loads is also assessed. Results show that the superelastic viscous dampers can effectively control the peak drift and acceleration response of steel frames at multiple seismic hazard levels while minimizing residual drifts.

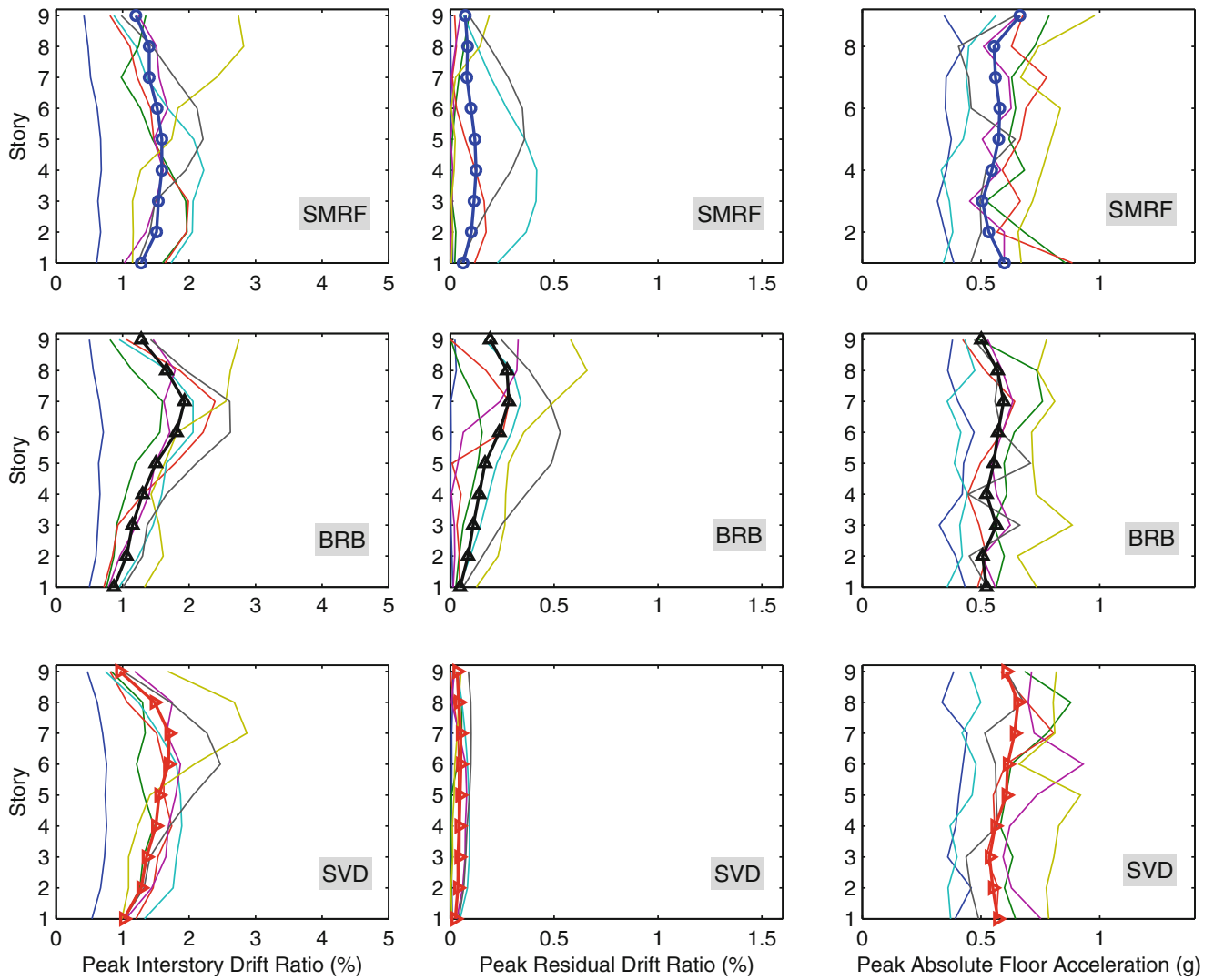


Fig. 17.6 Profiles of peak response quantities at DBE level for each frame under individual ground motion records

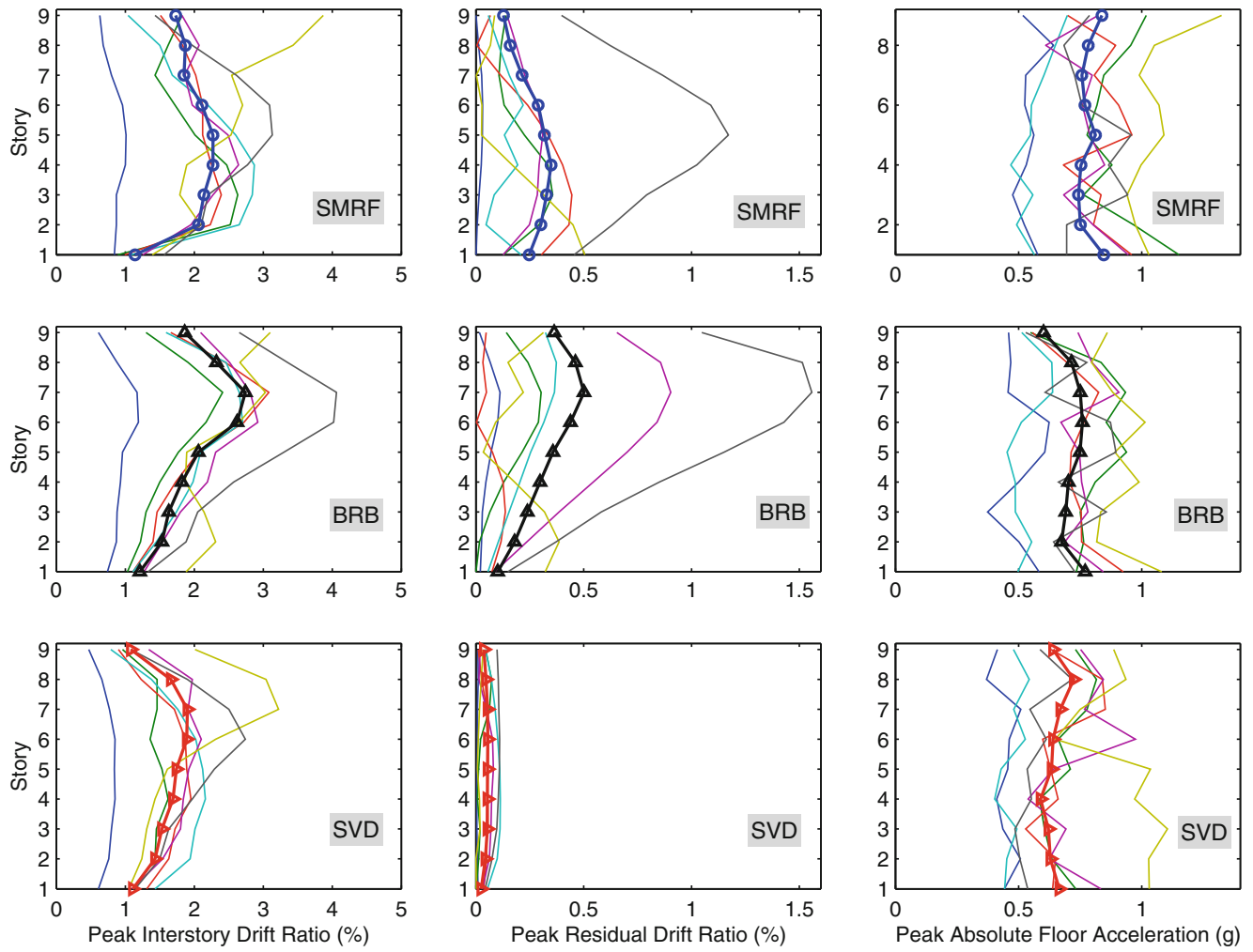


Fig. 17.7 Profiles of peak response quantities at MCE level for each frame under individual ground motion records

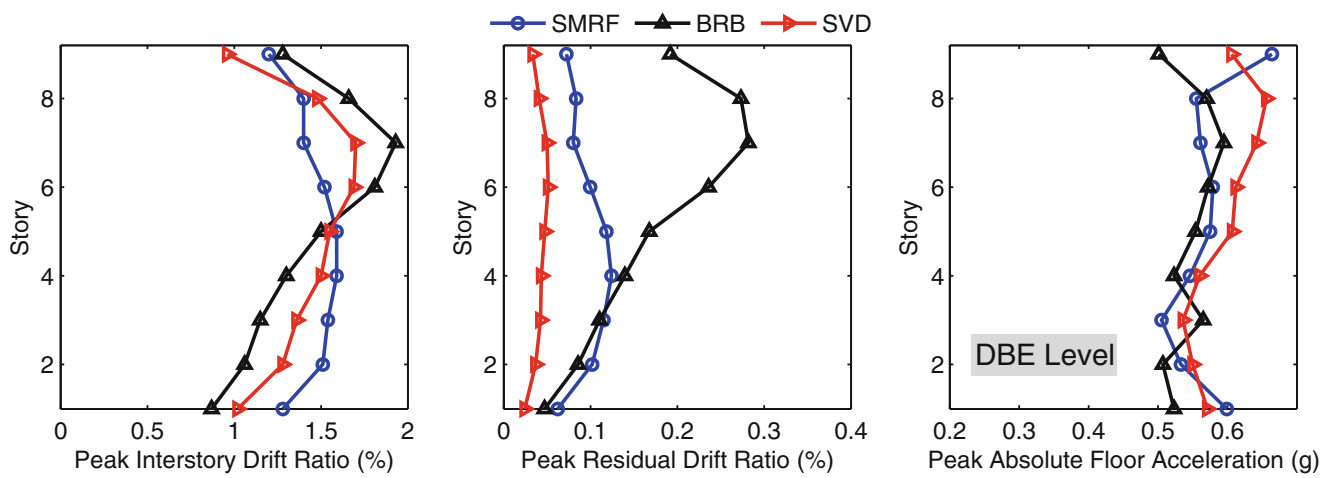


Fig. 17.8 Envelopes for average of peak response quantities for SMRF, BRB, and SVD systems at DBE level

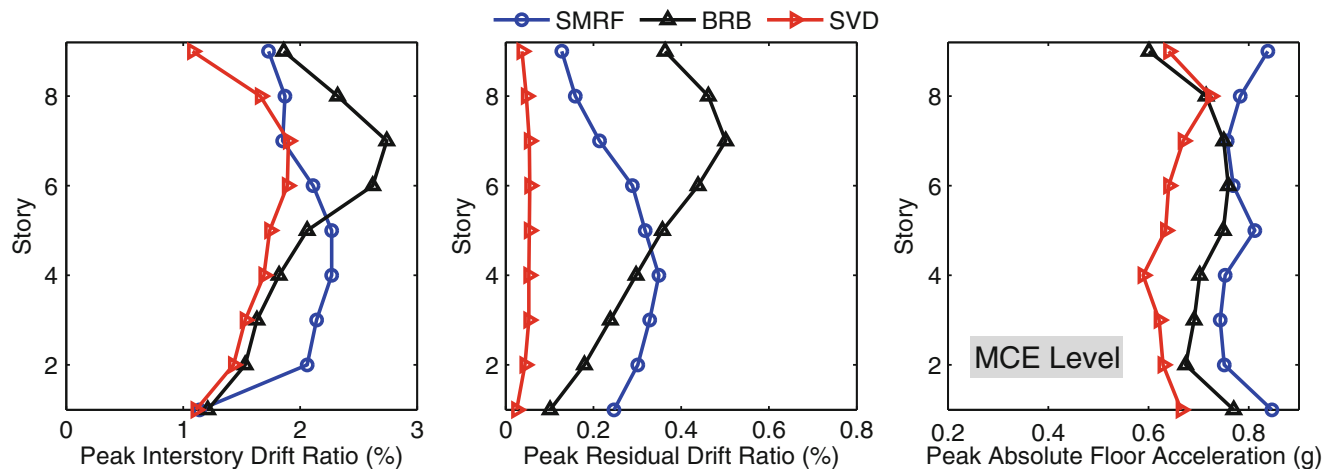


Fig. 17.9 Envelopes for average of peak response quantities for SMRF, BRB, and SVD systems at MCE level

References

1. Soong, T.T., Dargush, G.F.: *Passive Energy Dissipation System Structural Engineering*. Wiley, Chichester (1997)
2. McCormick, J., Aburano, H., Ikenaga, M., Nakashima, M.: Permissible residual deformation levels for building structures considering both safety and human elements. In: Proc. 14th World Conf. Earthquake Engineering, Seismological Press of China, Beijing, Paper ID 05-06-0071 2008
3. Erochko, J., Christopoulos, C., Tremblay, R., Choi, H.: Residual drift response of SMRFs and BRB frames in steel buildings designed according to ASCE 7–05. *J. Struct. Eng.* **137**(5), 589–599 (2010)
4. Christopoulos, C., Tremblay, R., Kim, H.J., Lacerte, M.: Self-centering energy dissipative bracing system for the seismic resistance of structures: development and validation. *J. Struct. Eng.* **134**(1), 96–107 (2008)
5. Deierlein, G., Krawinkler, H., Ma, X., Eatherton, M., Hajjar, J., Takeuchi, T., Midorikawa, M.: Earthquake resilient steel braced frames with controlled rocking and energy dissipating fuses. *Steel Const.* **4**(3), 171–175 (2011)
6. Kam, W.Y., Pampanin, S., Palermo, A., Carr, A.J.: Self-centering structural systems with combination of hysteretic and viscous energy dissipations. *Earthq. Eng. Struct. Dyn.* **39**(10), 1083–1108 (2010)
7. Eatherton, M.R., Hajjar, J.F.: Residual drifts of self-centering systems including effects of ambient building resistance. *Earthq. Spectra* **27**(3), 719–744 (2011)
8. Ozbulut, O.E., Hurlbauss, S., Desroches, R.: Seismic response control using shape memory alloys: a review. *J. Intell. Mater. Struct.*, **22**, 1531–1549 (2011)
9. Ozbulut, O.E., Hurlbauss, S.: Re-centering variable friction device for vibration control of structures subjected to near-field earthquakes. *Mech. Syst. Sig. Process.* **25**, 2849–2862 (2011)
10. Yang, C.S.W., DesRoches, R., Leon, R.T.: Design and analysis of braced frames with shape memory alloy and energy-absorbing hybrid devices. *Eng. Struct.* **32**, 498–507 (2010)
11. Zhu, S., Zhang, Y.: Seismic analysis of concentrically braced frame systems with self-centering friction damping braces. *J. Struct. Eng.* **134**, 121–31 (2008)
12. Ozbulut, O.E., Hurlbauss, S.: Application of an SMA-based hybrid control device to 20-story nonlinear benchmark building. *Earthq. Eng. Struct. Dyn.* **41**, 1831–1843 (2012)
13. FEMA: *State of the Art Report on Systems Performance of Steel Moment Frames Subject to Earthquake Ground Shaking (FEMA 355C)*. Federal Emergency Management Agency, Washington, DC (2000)
14. ASCE: *Minimum Design Loads for Buildings and Other Structures, ASCE 7–10*. American Society of Civil Engineers, Reston, Virginia (2010)
15. PEER NGA database. The Pacific Earthquake Engineering Research Center, <http://ngawest2.berkeley.edu>, Pacific Earthquake Engineering Research Center (PEER) (2014)
16. OpenSees. The Open System for Earthquake Engineering Simulation. <http://opensees.berkeley.edu> Pacific Earthquake Engineering Research Center (PEER) (2014)
17. Ibarra, L.F., Medina, R.A., Krawinkler, H.: Hysteretic models that incorporate strength and stiffness deterioration. *Int. J. Earthq. Eng. Struct. Dyn.* **34**(12), 1489–1511 (2005)
18. Lignos, D.G., Krawinkler, H.: A database in support of modeling of component deterioration for collapse prediction of steel frame structures. In: Proceedings, ASCE Structures Congress, Long Beach, California, 18–20 May 2007
19. Gupta, A., Krawinkler, H.: *Seismic Demands for Performance Evaluation of Steel Moment Resisting Frame Structures, Technical Report 132*. The John A. Blume Earthquake Engineering Research Center, Department of Civil Engineering, Stanford University, Stanford, CA (1999)

20. Silwal, B., Michael, R.J., Ozbulut, O.E.: A superelastic viscous damper for enhanced seismic performance of steel moment frames. *Eng. Struct.* **105**, 152–164 (2015)
21. Ozborrow, G.T.: Optimized distribution of strength in buckling-restrained brace frames in tall buildings. Masters Thesis, BYU, Provo, UT (2009)
22. Coy, B.B.: Buckling-restrained brace connection design and testing. M.S. Thesis, Brigham Young Univ., Provo, UT (2007)

Chapter 18

Structural Control Using a Semiactive Friction Damper

Juan S. Mantilla, Daniel Gómez, and Peter Thomson

Abstract All civil structures are prone to vibrations caused by external sources such as earthquakes, wind, mechanical loads and anthropogenic loads. However, structural control systems have proven to be effective in reducing excessive vibrations. This article describes a Semiactive-Variable-Friction-Damper that was designed for reducing the dynamic response of structures subject to seismic excitation. The structural control device, which consists of a hydraulic brake activated with a servomotor, was identified and characterized in order to design a decentralized control strategy. A small-scale benchmark structure was built and the structure with control system was tested on a shaking-table. Results of the structural response with and without the control system are compared, with the friction device reducing story drift by up to 90 %.

Keywords Semiactive control • Earthquake response • Shaking table • Variable friction • Damper

18.1 Introduction

In recent years, control systems has become a standard alternative to reduce excessive vibrations [1] especially in buildings and bridges [2]. Control systems are classified according to their energy requirements into four groups [1, 3]: passive, active, semiactive and hybrid systems. (1) Passive systems which do not require an external power source and are designed to have an optimum performance for a specific dynamic load. (2) Active systems are more effective than passives but need high energy requirements and are usually more expensive. (3) Semi-active systems have a similar or same effectiveness to the active systems but with lower energy consumption, therefore these systems require low power supplies such as batteries and (4) hybrid systems are a combination of the previous three, usually presented as a passive system plus an active or semi-active.

Friction dampers are usually used in buildings as passive structural control systems and add energy dissipation through damping mechanisms induced by sliding friction between their surfaces. Different studies has demonstrated the potential of these systems implemented as a passive device [4] on the diagonals of braced buildings, but such devices have the disadvantage that performance is only optimal for specific a range of force, but out of that range the efficiency decreases. The above is due to the fact that each damper is designed and built for a specific sliding force, that depends on the clamping force magnitude at which the damper changes from a state of slip to a locked state and does not dissipate energy through friction.

An alternative way to enhance the optimum efficiency range of friction dampers is to control the clamping force in real time, using Semiactive-Variable-Friction-Dampers (SAVFD). The SAVFD has shown to be more effective than Passive Friction Dampers (PFD) to reduce earthquake response of structures [5]. This article describes the development of a small scale SAVFD to reduce the dynamic response of buildings subject to seismic excitation.

J.S. Mantilla (✉) • D. Gómez • P. Thomson
Universidad del Valle, Cali, Colombia
e-mail: juan.salvador.mantilla@correounivalle.edu.co; daniel.gomez@correounivalle.edu.co; peter.thomson@correounivalle.edu.co

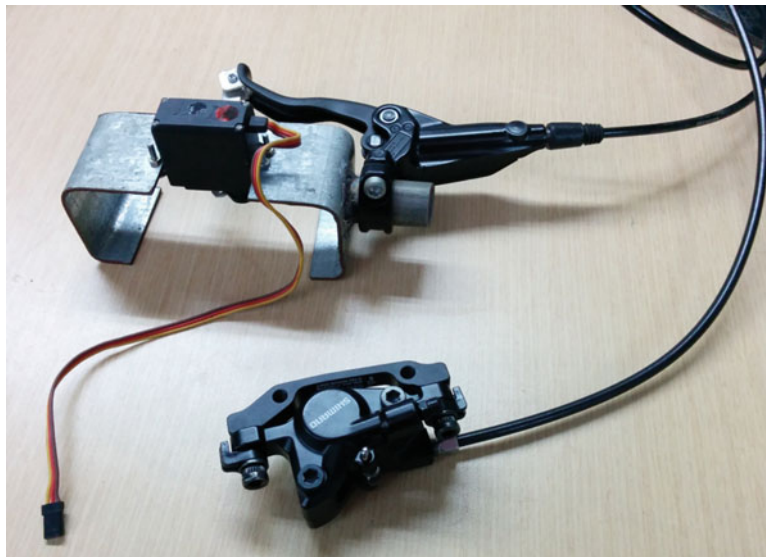


Fig. 18.1 Braking mechanism

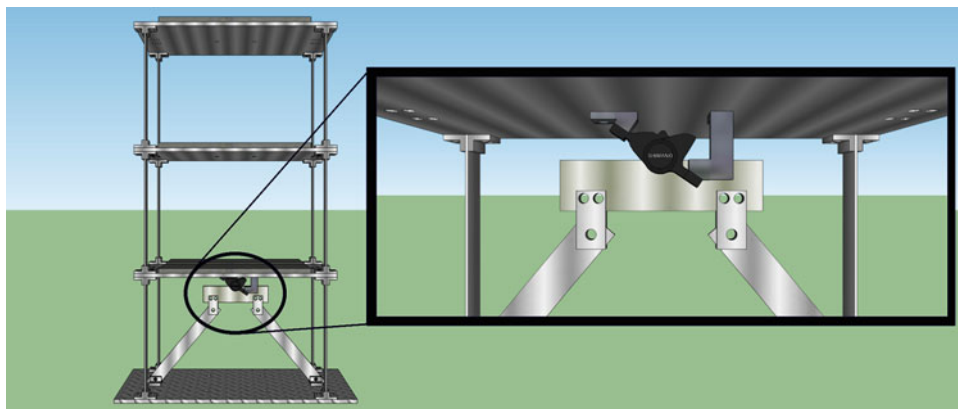


Fig. 18.2 Implementation of the SAVFD at the first floor of the structure

18.2 Methodology

18.2.1 Semiactive Variable Friction Damper (SAVFD)

The SAVFD uses hydraulic brakes that are activated with a servomotor (9 kg-cm torque) controlled by an Arduino board. The servomotor adjusts the brake lever, changing the normal force to a metal plate, which modifies the dry friction forces. Figure 18.1 shows a picture of the braking mechanism. The damper can be easily operated using common batteries.

In this research a benchmark structure is used, this structure has been implemented by different researchers in structural control field [6]. It is a modular steel structure made of columns, slabs and additional loads. Each story has a height of 30.5 cm, a width of 30.5 cm and a length of 50.8 cm. In this case the structure was assembled with three floors. The damper can be installed at the upper slab of each level and generates friction against a metal plate supported by a pair of eccentric diagonals, as shown in Fig. 18.2.

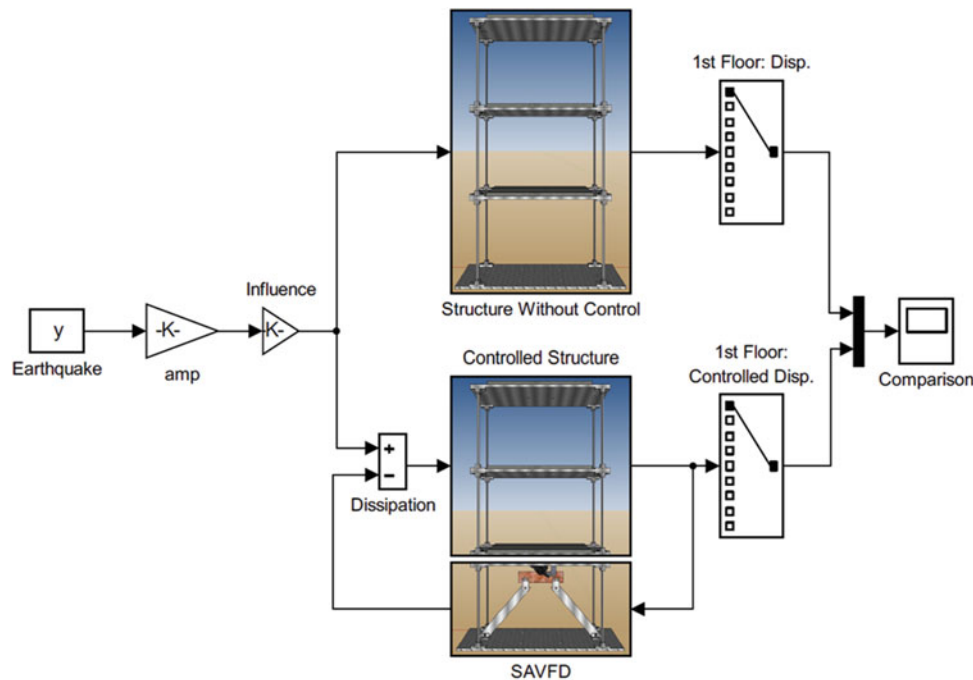


Fig. 18.3 General blocks diagram

18.2.2 Control Algorithm

The performance of semiactive structural control systems varies significantly depending on the control strategy [5]. Most of the control strategies implemented in semiactive friction dampers are decentralized. In this work a sliding mode strategy is implemented.

When relative movement between the damper and the metal plate exists, the damper is in the sliding phase and the cinematic friction force dissipates the energy, but when the damper is in sticking phase there is no energy dissipation by friction. The philosophy of the sliding mode strategy is to maintain the damper in the slipping phase as much as possible [7].

Relative displacement or acceleration of consecutive stories is used as the input. The strategy consists of saving information of relative displacement or acceleration during a period of decision (T_d) and at the end of this period the peak value (P_v) of the structural response is compared with a threshold of admitted response (A_0). If P_v is greater than A_0 , the system is in sliding phase, indicating that the system has the potential of dissipating more energy and thus the clamping force is increased one value of ΔP . On the other hand, if P_v is smaller than A_0 , the brake is locked and therefore the clamping force is reduced one value of ΔP .

18.2.3 Numerical Simulation

A numerical model of the structure with the SAVFD was developed using Simulink[®] [8] (Fig. 18.3) in order evaluate the control algorithm. The test structure was modelled with space state representation based on the results of experimental characterization tests using a shaking table. The SAVFD model was based on the experimental dynamic characterization of the damper. The algorithm was simulated and implemented using accelerations as input.

18.2.4 Experimental Test

Shaking table tests were used to determine the performance of the control system in terms of story drift. In this particular case the SAVFD was installed between the first and second floors only (Fig. 18.4), but multiple SAVFD can be used with the

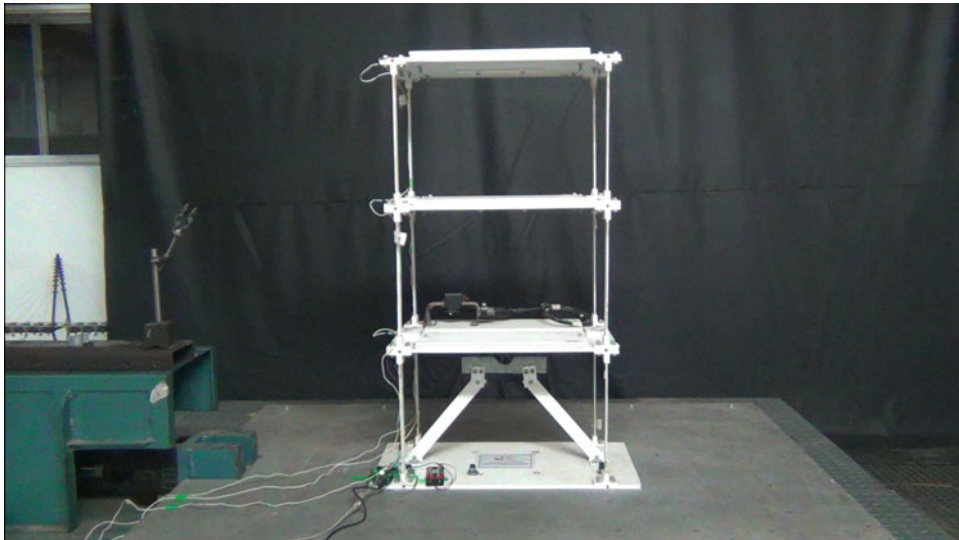


Fig. 18.4 Test structure on the shaking table

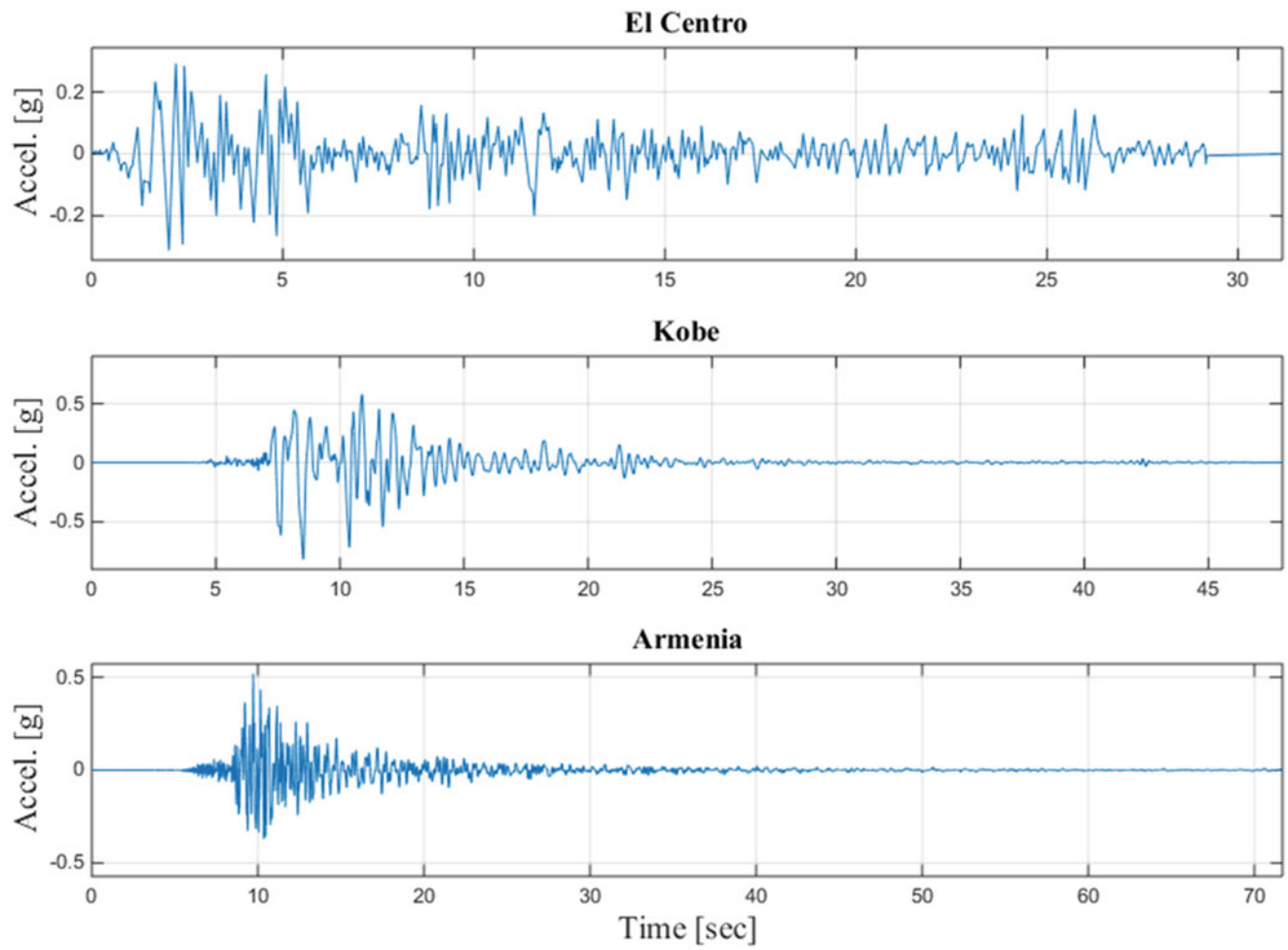


Fig. 18.5 Earthquake signals

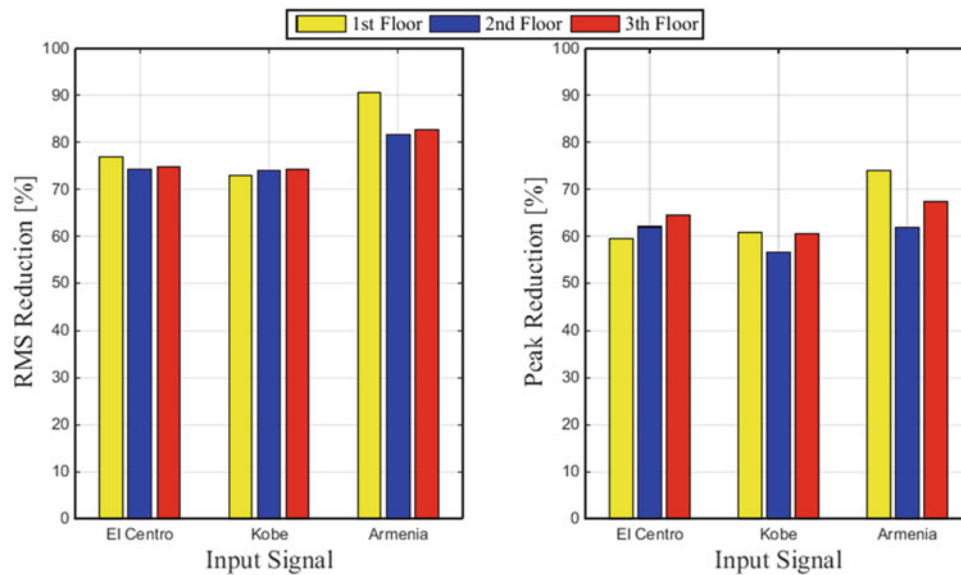


Fig. 18.6 Drift reduction

same control algorithm as it is a decentralized control strategy. Three accelerometers were installed at the test structure, one on each floor and an additional one on the shaking table.

The historical earthquake signals of: El Centro—USA (1940), Kobe—Japan (1995) and Armenia—Colombia (1999), were used in the tests. The time signals of those earthquakes are shown at Fig. 18.5. These signals were scaled (El Centro 50 %, Kobe 15 % and Armenia 25 %) such that they could be produced by the shaking table without exceeding its maximum displacement limits.

18.3 Results

Inter story drift for the three floors are compared in terms of reduction of peak and RMS (root mean square) values with respect to the structure without SAVFD. A summary of the results are shown in Fig. 18.6, and the time signals are compared in Figs. 18.7, 18.8, and 18.9.

18.4 Conclusions

The SAVFD is shown to be effective in reducing the structural response for seismic cases. The damper with sliding mode strategy, reduced the RMS value of interstory drift by over 70 %, with respect to that of the structure without SAVFD, for all three earthquake signals. For the Armenia earthquake, the system reduced RMS drift by over 90 %. Reduction of the peak values of drift for the floor where the damper is installed varies between 59 % and 74 %. As expected, the reduction are greater for the floor where the damper was installed.

Acknowledgments This research was developed by the G7 investigation group from the *Universidad del Valle*, Colombia. Funding of the research project “*Desarrollo tecnológico de sistemas de control estructural de bajo costo*”, contract number 1106-569-34424, by COLCIENCIAS through its program “*Programa nacional de ciencias del medio ambiente y hábitat*” is greatly appreciated.

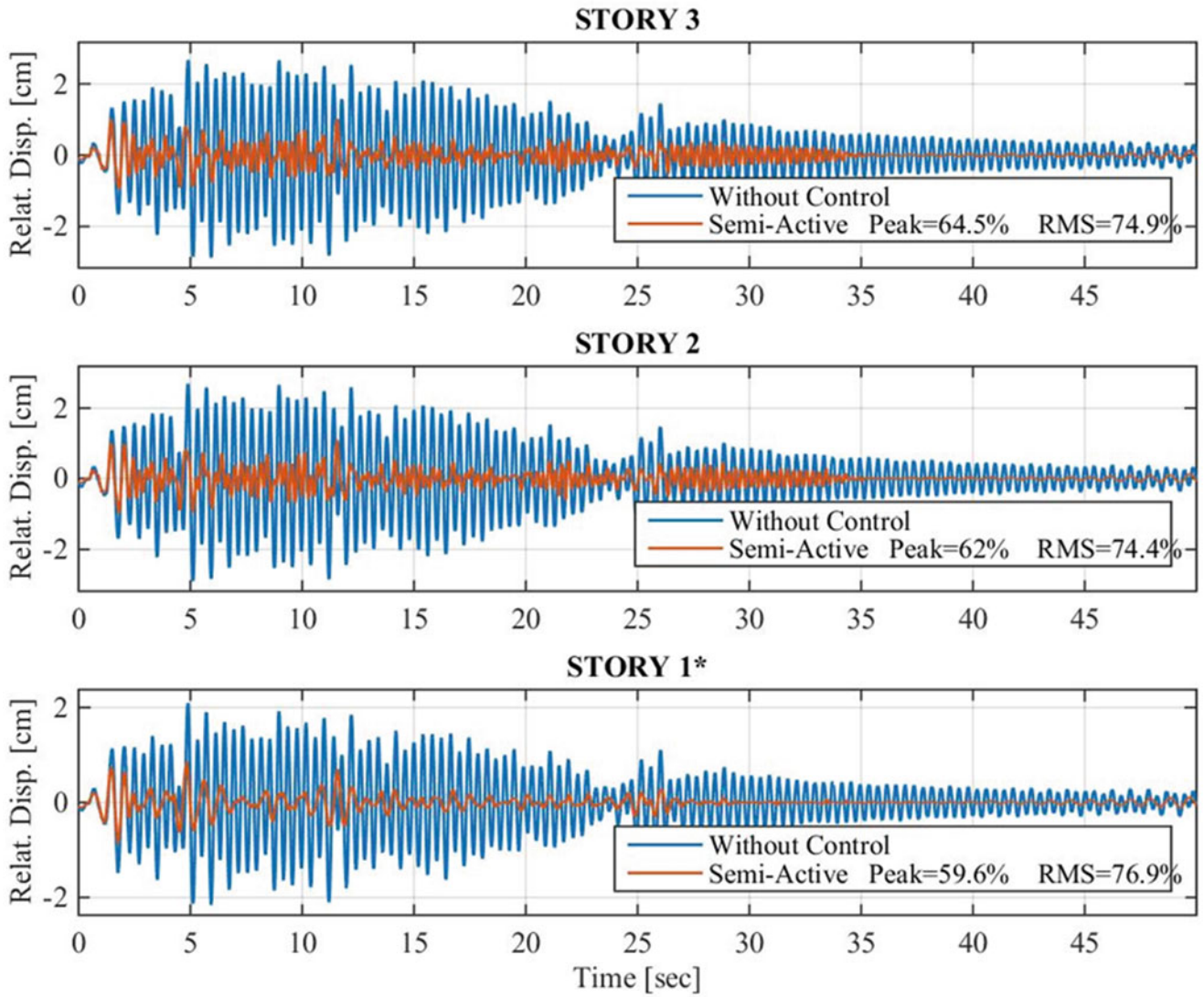


Fig. 18.7 Displacement reduction for El Centro earthquake

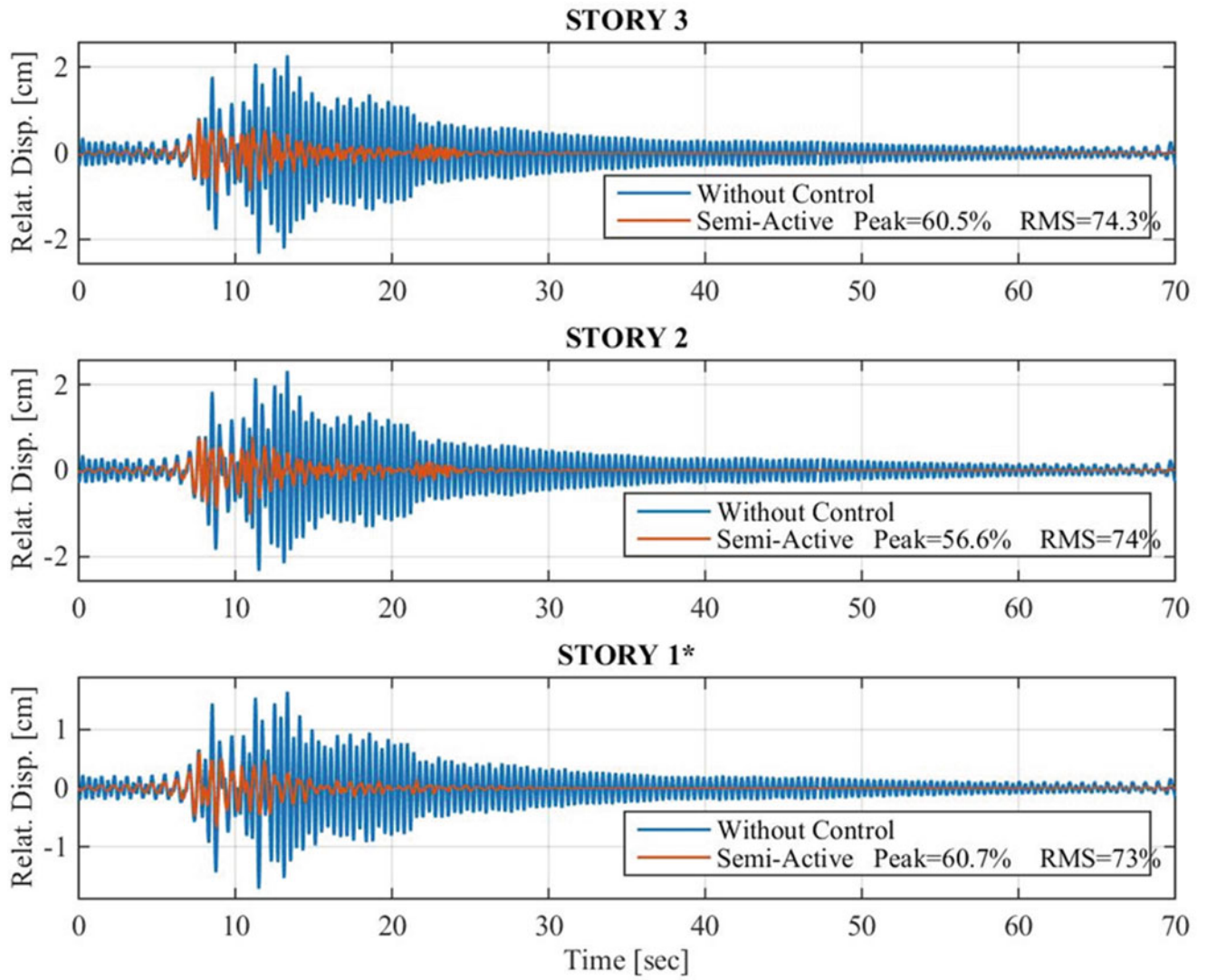


Fig. 18.8 Displacement reduction for the Kobe earthquake

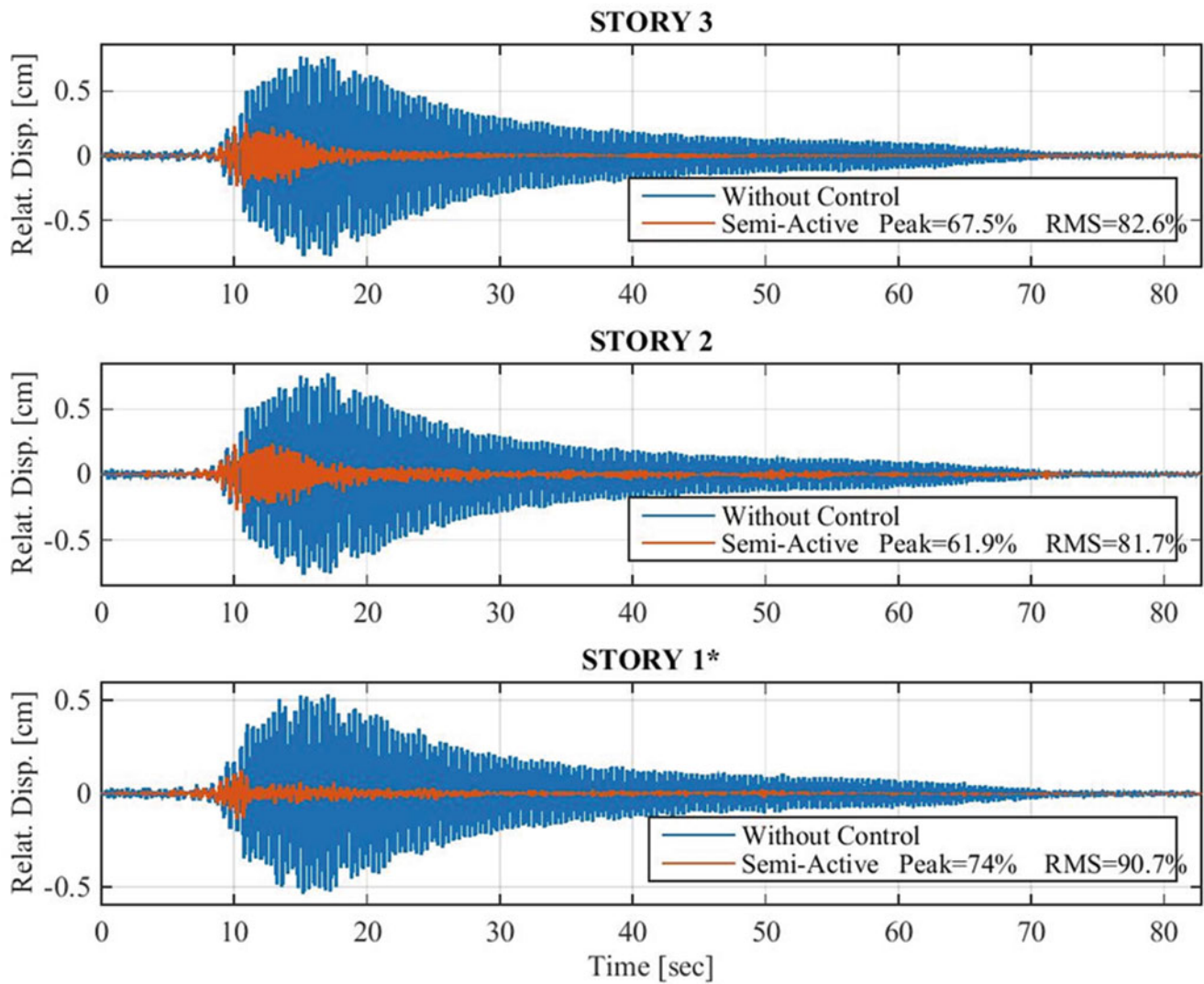


Fig. 18.9 Displacement reduction for the Armenia earthquake

References

1. Saaed, T.E., Nikolakopoulos, G., Jonasson, J.-E., Hedlund, H.: A state-of-the-art review of structural control systems. *J. Vib. Control* **21**(5), 919–937 (2015)
2. Soong, T.T., Spencer, J.B.F.: Active, semi-active and hybrid control of structures. In: 12th World Conference on Earthquake Engineering, Auckland, New Zealand, 2000
3. Housner, G., Caughey, L., Chassiakos, T., Claus, A., Skelton, R., Soong, T., Spencer, B., Yao, J.: Structural control: past, present and future. *Eng. Mech.* **123**, p. 899 (1997)
4. Pall, A.S., Marsh, C.: Response of friction damped braced frames. *J. Struct. Div.* **108**, 1–13 (1982)
5. He, W.L., Agrawal, A.K., Yang, J.N.: Novel semiactive friction controller for linear structures against earthquakes. *J. Struct. Eng.* **129**, 941–950 (2003)
6. Dyke, S., Veto, R., Wang, P., Sun, F., Lu, C.: Employing wireless sensing technology in smart structures. in The Proceeding of 4th China-Japan-US Symposium on Structural Control and Monitoring, Hangzhou, 2006
7. Yang, J.N., Wu, J.C., Li, Z.: Control of seismic-excited buildings using active variable stiffness systems. *Eng. Struct.* **18**(8), 589–596 (1996)
8. The MathWorks Inc., “MATLAB,” Natick, MA (2000)

Chapter 19

Seismic Response of SMA Reinforced Shear Walls

Marina Maciel, Dan Palermo, and Alaa Abdulridha

Abstract This paper presents the performance of concrete shear walls reinforced with Shape Memory Alloys (SMAs) using nonlinear numerical modelling. A hysteretic constitutive model for Superelastic (SE) SMA reinforcing bars that was recently implemented into a nonlinear finite element analysis package applicable to reinforced concrete membrane structures and compatible with a compression field approach is presented. The objective of the model is to provide simple formulations that satisfactorily capture the forward and reverse transformations phases that superelastic SMAs experience when subjected to mechanical loading. The finite element model was corroborated with experimental results of a slender SMA reinforced concrete shear wall subjected to reverse cyclic loading. The model captures salient features of behaviour, including strength, ductility, energy dissipation, load-displacement response, cracking patterns, and failure modes. Nonlinear static analyses are conducted on the SMA reinforced shear wall and assessed against a companion traditional reinforced concrete shear wall. The comparison includes strength, ductility, and displacement recovery capacities. In addition, the effect of increasing axial load on the performance of the SMA and traditional reinforced walls is presented.

Keywords Shape memory alloys • Shear walls • Nonlinear finite element analysis • Reinforced concrete • Axial load

19.1 Introduction

Shape Memory Alloys (SMAs) have been drawing the attention of researchers, primarily due to their potential as alternative reinforcement in concrete structures [1–4], as external retrofitting [5], and as pre-stressing materials [6], to name a few. Shape memory alloys have the ability to sustain large deformations and to return to their original undeformed shape upon removal of stress (superelastic SMA) or with the application of heat (shape memory effect). Concrete structural members reinforced internally with SE-SMAs can dissipate significant energy through hysteretic damping. The deformation recovery capacity of SE-SMAs is highly effective at controlling permanent deformation. Conversely, conventional steel exhibits significant permanent deformation; a disadvantage of using steel in construction. This unique property of superelasticity in SMAs promotes self-centering in structures, a concept that is garnering attention in the seismic community.

Presented herein are preliminary numerical results of a slender concrete shear wall reinforced with SE-SMA bars in the boundary elements. A companion steel reinforced wall is also investigated. The focus of this study is to evaluate the deformation recovery capacity of SMA and steel reinforced walls subjected to reverse cyclic loading and under axial loading of 0, 2.5, 5, 7.5, 10, 15, 20, and 25 % of the axial capacity of the wall (f'_{cg}). In addition, the study evaluates the displacement ductility of the walls under the range of axial loads studied.

M. Maciel
Universidade Federal de Santa Maria, Santa Maria, Brazil

D. Palermo (✉)
Department of Civil Engineering, York University, 4700 Keele Street, Toronto, ON, Canada M3J 1P3
e-mail: dan.palermo@lassonde.yorku.ca

A. Abdulridha
Department of Civil Engineering, University of Ottawa, 161 Louis Pasteur, Ottawa, ON, Canada K1V 1X3

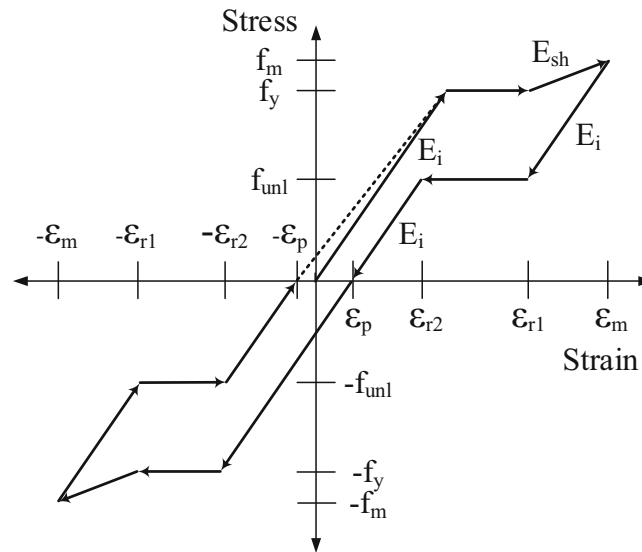


Fig. 19.1 SMA plastic offset constitutive model [1]

19.2 Constitutive Finite Element Model

Recently, a hysteretic constitutive model for superelastic Shape Memory Alloy (SMA) bars was developed by Abdulridha et al. [1] and implemented into program VecTor2 [7], a nonlinear analysis tool for two-dimensional reinforced concrete membrane structures. Figure 19.1 illustrates the constitutive model for the SMA bars, which is based on a trilinear backbone envelope that follows the monotonic response. The envelope includes the initial linear elastic behaviour, followed by yielding (forward transformation of the SMA), and finally strain hardening, which defines the stress-induced elastic response of Martensite phase of the SMA material. The model explicitly accounts for permanent strains that accumulate in the material for strains in excess of 6 %, degradation of the lower plateau stress (reverse transformation), and a trilinear unloading response. The constitutive model has been demonstrated to provide accurate simulations of behaviour for SMA reinforced slender beams, and a beam-column joint [1].

19.3 Finite Element Modelling

Two slender, reinforced concrete shear walls recently tested [8] provided benchmarks to corroborate the finite element model, which was used in the parametric study presented herein on the effect of axial load on the deformation recovery capacity of traditional and SMA reinforced walls.

19.4 Shear Walls

Two shear walls, W1-SR (steel reinforced) and W2-NR (hybrid-SMA reinforced), were tested under reverse cyclic lateral loading. The shear walls had a rectangular cross section with a thickness of 150 mm and length of 1000 mm. The height of the walls was 2200 mm. The walls were reinforced with two layers of steel reinforcement in the web section. The vertical reinforcement consisted of 10 M (100 mm² and 11.3 mm diameter) deformed bars spaced uniformly at 150 mm and the horizontal steel reinforcement consisted of 10 M deformed bars spaced uniformly at 150 mm. The walls had web vertical and horizontal reinforcement ratios of 0.88 %. The only difference between W1-SR and W2-NR was the longitudinal reinforcement used in the plastic hinge region within the end boundary zones. Four-12.7 mm-diameter superelastic SMA

(NiTi) smooth bars were used in Wall W2-NR; while four-10 M deformed steel bars were used in W1-SR. [NiTi refers to Nickel-Titanium.] Mechanical couplers were used in W2-NR to connect the SMA bars with 15 M (200 mm² and 16 mm diameter) deformed steel bars extending outside the plastic hinge region. The total length of the SMA bars was 1200 mm, of which 950 mm extended from the top of the foundation into the wall and the remaining 250 mm extended into the foundation. To prevent buckling of the longitudinal reinforcement in the end boundary zones, 10 M closed steel ties were used along the full height of the walls. The ties were spaced at 75 mm within the plastic hinge region and 150 mm above the plastic hinge region. In addition, four pairs of 10 M starter bars with a length of 300 mm extended into the wall above the foundation.

The finite element mesh of W2-NR shear was constructed with 506 plane stress rectangular elements to represent the concrete. The horizontal, boundary zone confinement and web starter bar reinforcements were smeared within the concrete elements. A total of 203 truss bar elements were used for the longitudinal reinforcement in the web and boundary zones. The finite element model was divided into five concrete zones. Zones 1 and 2 correspond to the foundation and top loading beam respectively; Zones 3 and 4 correspond to the boundary elements; and Zone 5 corresponds to the web section of the wall. The deformed steel reinforcement was assumed perfectly bonded to the surrounding concrete. Bond-slip elements were used at the interface of the SMA truss elements and the rectangular concrete elements to model the bond characteristics of the SMA. The base fixity of the wall was simulated by restraining, in the vertical and horizontal directions, the six nodes around the location of each tie rod used to clamp the foundation during testing. All other base nodes were free to move. The finite element model for W1-SR was similar to W2-NR. The only difference was the replacement of the SMA bars in the boundary zones with deformed reinforcement that was assumed fully bonded to the surrounding concrete elements. Additional information regarding the models is available elsewhere [9]. The default materials models of VecTor2 were selected for the analysis of the walls. The analyses followed the same loading protocol that was used during testing. Note that the analyses presented herein assumed that the shear walls did not include starter bars in the web. Figure 19.2 provides a representation of the finite element model developed for Wall W2-NR.

19.5 Finite Element Analyses

The analyses conducted in this study were intended to investigate the deformation recovery capacities of a slender shear wall reinforced with SMA bars relative to a companion shear wall reinforced with traditional deformed steel. As previously described, the SMA bars were only used in the plastic hinge region of the boundary elements to optimize the use of the SMA material. Both W1-SR and W2-NR were subjected to axial loads of 0, 2.5, 7.5, 10, 15, 20, and 25 %. Figure 19.3 provides the lateral load-lateral displacement responses of Wall W1-SR and W2-NR.

The results in Fig. 19.3 demonstrate that up to an axial load of 10 % the wall with SMA reinforcement is significantly more effective at controlling the permanent lateral displacements. Note that reinforced concrete shear walls in high-rise buildings typically carry approximately 10 % axial load. Above an axial load of 10 %, there is marginal improvement in using SMA to control the permanent displacement. The hysteretic responses of Walls W1-SR and W2-NR are similar for axial loads of 20 and 25 %. This level of axial load would be found in bridge pier walls. The axial load acts as a mechanism to restore the wall to its original position. Figure 19.4 provides the residual displacements as a function of imposed lateral displacements for each wall and were obtained from the responses in Fig. 19.3.

Figure 19.4 further illustrates the effectiveness of the SMA reinforced wall for axial loads not exceeding 10 %. It is evident, that for all axial load levels, the SMA wall experienced negligible residual displacements. The abrupt rise in residual displacements for the SMA wall with axial load arose at the end of the analyses when the wall had failed. For the steel reinforced wall, it is clear that the residual displacements are significant for axial load levels up to 10 %. Tables 19.1 and 19.2 provide the yield loads and displacements, the maximum loads, the ultimate displacements, and the displacement ductility (yield displacement divided by the ultimate displacement). The yield point was established using the equivalent elasto-plastic system with a secant stiffness passing through the load-displacement response at 75 % of the average nominal strength [10]. The ultimate displacement was taken as the penultimate displacement corresponding to the lateral load capacity of the wall dropping below 80 % of the maximum load capacity [10]. The penultimate displacement was also based on sustaining the lateral load for two repetitions of loading.

Tables 19.1 and 19.2 illustrate that: the walls experienced similar yield and maximum loads for the range of axial loads investigated; Wall W2-NR experienced notably higher yield displacements as a result of the lower modulus of elasticity of the SMA bars; and in general the ultimate displacements were similar while the walls sustained axial loading. As a result of the larger yield displacements, Wall W2-NR exhibited smaller displacement ductility. However, in this study with two walls using reinforcements with markedly different elastic moduli, combined with the analyses conducted under static loading, the ductility results should be judged with caution. Nonlinear dynamic time-history analysis should be conducted to assess these differences in reinforcement properties.

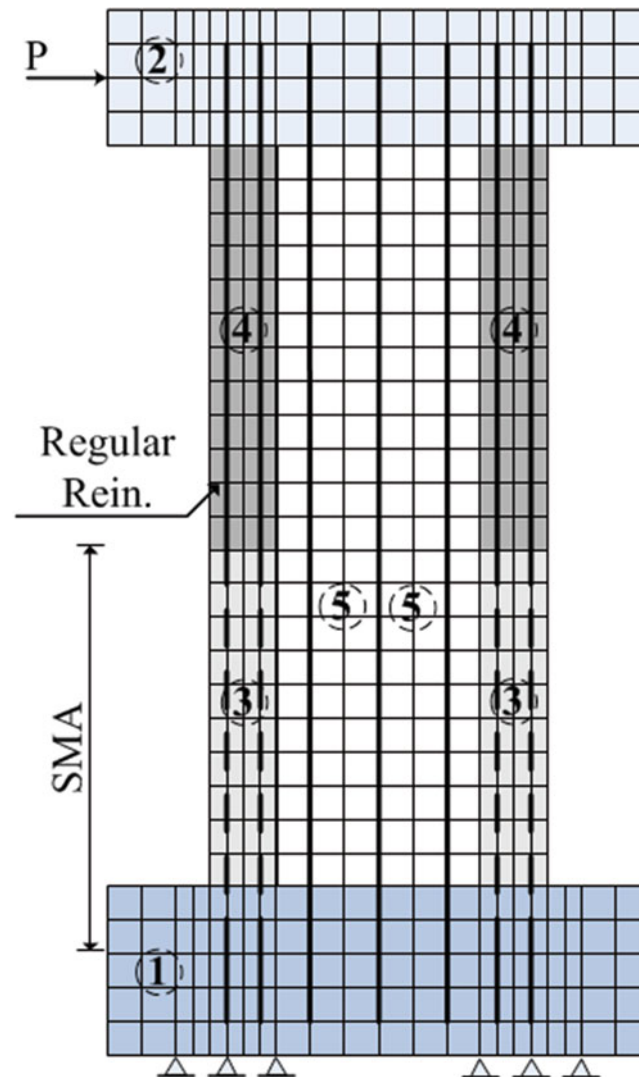


Fig. 19.2 Representation of finite element mesh for Wall W2-NR

19.6 Conclusions

This study presented preliminary results of numerical analyses of shear walls reinforced with either Shape Memory Alloy (SMA) bars or traditional deformed steel in the plastic hinge region within the end boundary elements of a rectangular section. Deformed steel reinforcement was used elsewhere in both walls. A recently developed hysteretic constitutive model for superelastic SMAs was used in this study. The numerical results demonstrated that the SMA reinforced wall was significantly more effective at controlling permanent displacements for axial loads not exceeding 10 % of the axial load capacity of the wall. However, for axial loads greater than 10 %, there was no clear advantage in using SMA. Notably, the hysteretic response of the SMA and steel reinforced walls were very similar for axial load levels of 20 and 25 %. The SMA and steel walls provided similar yield and maximum lateral load capacities, while the SMA walls experienced higher yield displacements due to the lower modulus of elasticity of the SMA. The ultimate displacements were, however, similar for both types of walls, indicating similar drift capacities.

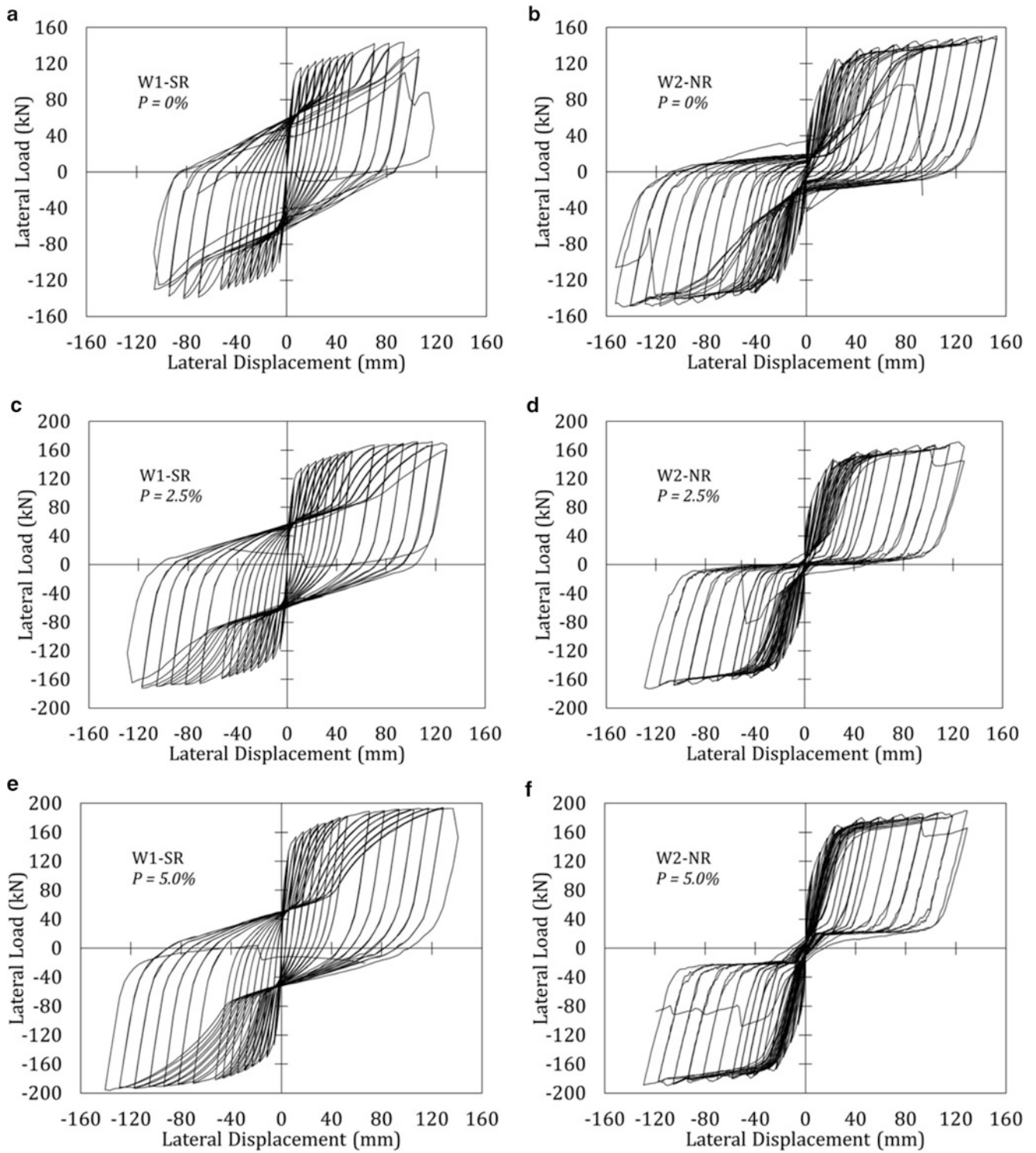


Fig. 19.3 Load-displacement responses: (a) W1-SR ($P = 0\%$); (b) W2-NR ($P = 0\%$); (c) W1-SR ($P = 2.5\%$); (d) W2-NR ($P = 2.5\%$); (e) W1-SR ($P = 5\%$); (f) W2-NR ($P = 5\%$); (g) W1-SR ($P = 7.5\%$); (h) W2-NR ($P = 7.5\%$); (i) W1-SR ($P = 10\%$); (j) W2-NR ($P = 10\%$); (k) W1-SR ($P = 15\%$); (l) W2-NR ($P = 15\%$); (m) W1-SR ($P = 20\%$); (n) W2-NR ($P = 20\%$); (o) W1-SR ($P = 25\%$); and (p) W2-NR ($P = 25\%$)

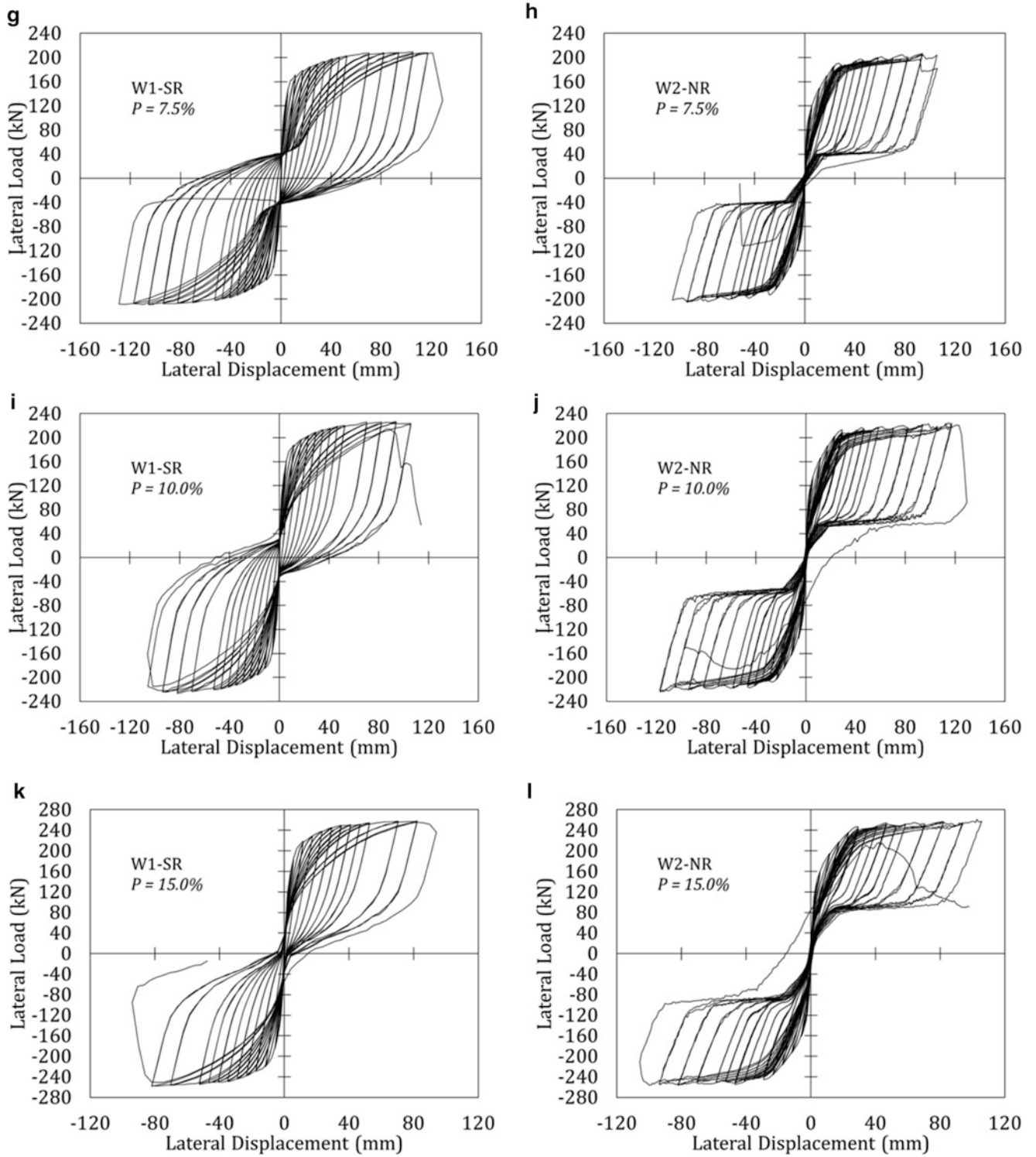


Fig. 19.3 (continued)

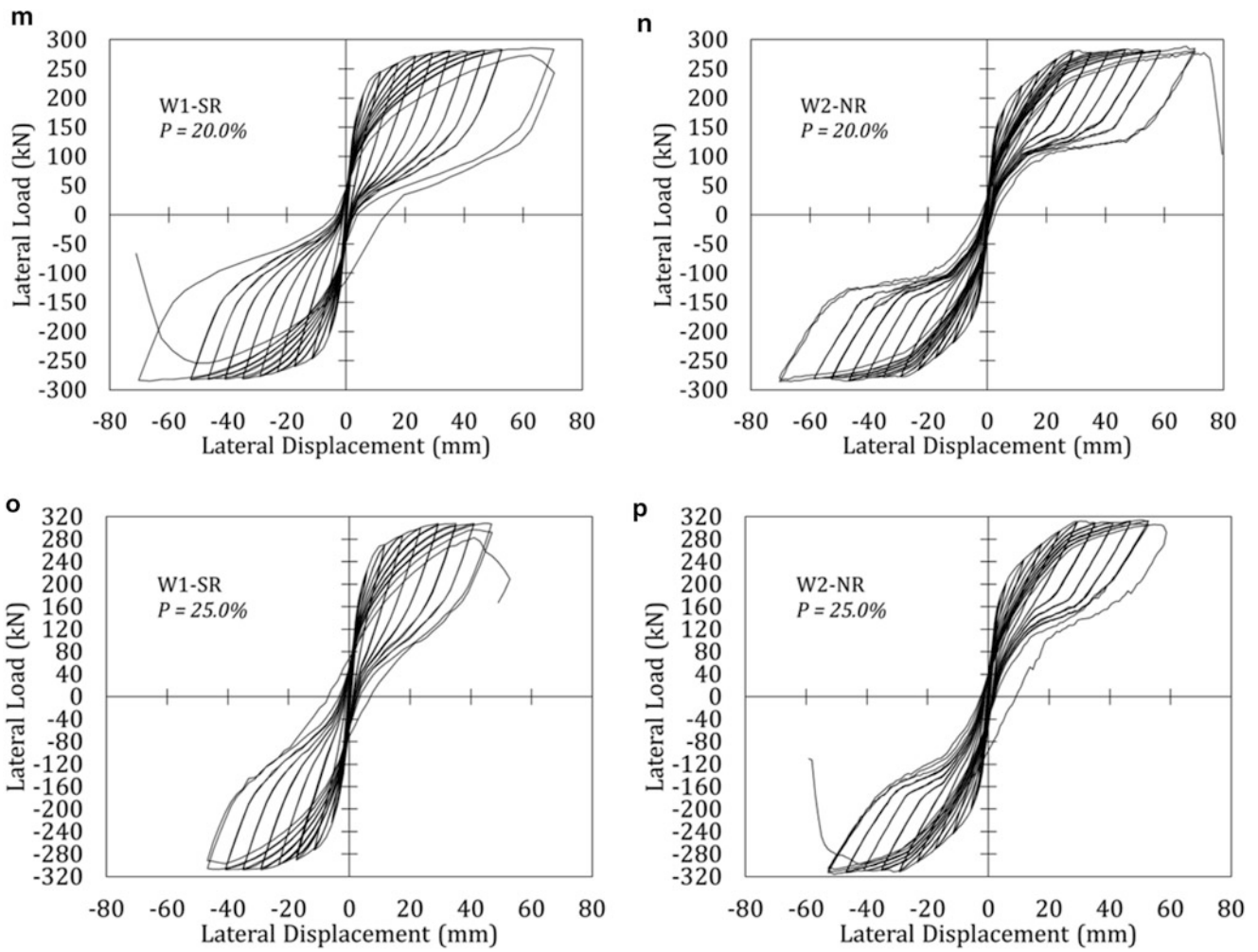


Fig. 19.3 (continued)

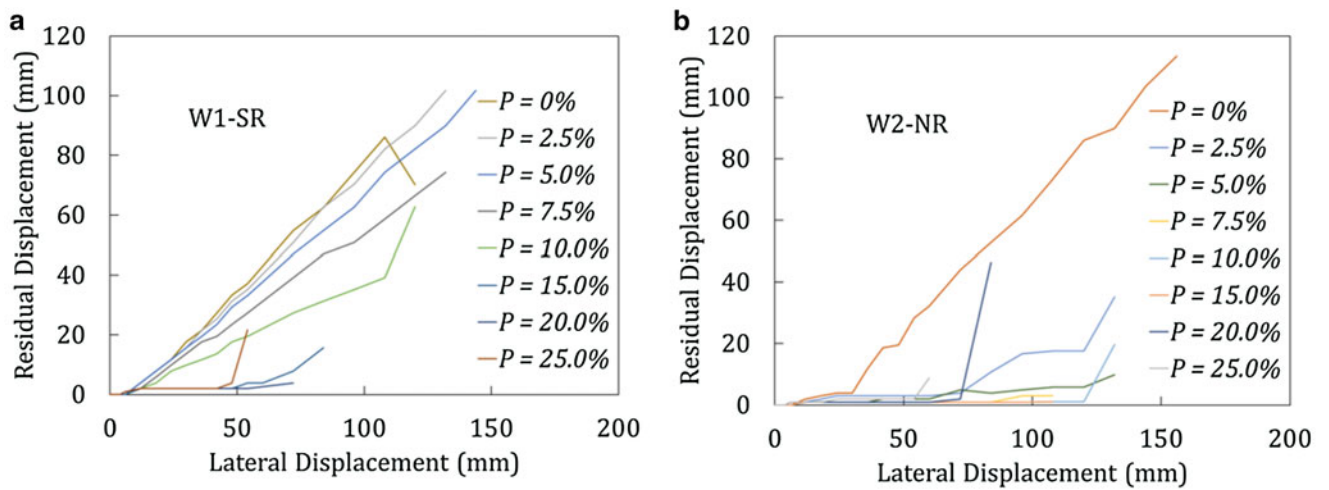


Fig. 19.4 Residual displacement responses: (a) W1-SR and; (b) W2-NR

Table 19.1 Loads and displacements for Wall W1-SR

Wall	Axial load level (%)	Py (kN)	Δy (mm)	Pmax (kN)	Δu (mm)	$\Delta u/\Delta y$
W1-SR	0	111	9.2	144	106	11.5
	2.5	135	11.5	172	129	11.2
	5	150	10	194	128.5	12.9
	7.5	166	9.4	209	117	12.4
	10	180	8.5	227	105.8	12.4
	15	208	8	258	82	10.3
	20	234	8.4	285	70.2	8.4
	25	258	8.3	308.4	46.8	5.6

Table 19.2 Loads and displacements for Wall W2-NR

Wall	Axial load level (%)	Py (kN)	Δy (mm)	Pmax (kN)	Δu (mm)	$\Delta u/\Delta y$
W2-NR	0	124	22.8	153	152.6	6.7
	2.5	142	21.5	171	129	6.0
	5	168	19.5	190	129	6.6
	7.5	169	17	207	106	6.2
	10	187	17	225	117.5	6.9
	15	211	15.8	262	94	5.9
	20	228	13.2	289	71	5.4
	25	253	13.5	315	53	3.9

References

1. Abdulridha, A., Palermo, D., Foo, S., Vecchio, F.J.: Behavior and modeling of superelastic shape memory alloy reinforced concrete beams. *Eng. Struct.* **49**, 893–904 (2013)
2. Ayoub, C., Saiidi, M., Itani, A.: A study of shape-memory-alloy reinforced beams and cubes. Center for Civil Engineering Earthquake Research, Department of Civil Engineering, University of Nevada, Reno, Nevada, Report No. CCEER-03-7, 2003
3. Saiidi, M.S., Wang, H.: Exploratory study of seismic response of concrete columns with shape memory alloys reinforcement. *ACI Struct. J.* **103**(3), 436–443 (2006)
4. Youssef, M., Alam, M., Nehdi, M.: Experimental investigation on the seismic behaviour of beam-column joints reinforced with superelastic shape memory alloys. *J. Earthq. Eng.* **12**, 1205–1222 (2008)
5. Cortés-Puentes, W.L., Palermo, D.: Tension-only SMA bracing for seismic retrofitting. In: Fifth International Conference on Construction Materials (CONMAT'15), Whistler, Canada, Paper 150, 12 August 2015
6. El-Tawil, S., Ortega-Rosales, J.: Prestressing concrete using shape memory-alloy tendons. *ACI Struct. J.* **101**, 846–851 (2004)
7. Wang, P.S., Vecchio, F.J., Trommels, H.: *VecTor2 and Formworks User's Manual*, 2nd edn. Department of Civil Engineering, University of Toronto, Canada, 347 pp (2013)
8. Abdulridha, A., Palermo, D.: Response of a Hybrid-SMA reinforced concrete shear wall. In: 10th US National Conference on Earthquake Engineering, Anchorage, USA, 10 July 2014
9. Abdulridha, A.: Performance of superelastic shape memory alloy reinforced concrete elements subjected to monotonic and cyclic loading. Ph.D thesis, Department of Civil Engineering, University of Ottawa, Ottawa, Canada, 346 (2013)
10. Park, R.: Ductility evaluation from laboratory and analytical testing. In: *Proceeding of Ninth World Conference on Earthquake Engineering*, 605–616, Tokyo-Kyoto, Japan, (1988)

Chapter 20

Stability of MIMO Controllers for Floor Vibration Control

Donald Nyawako, Paul Reynolds, and Emma Hudson

Abstract There are many research studies in the literature that have been devoted to active control of human-induced vibrations in civil engineering structures. This technology has been implemented in floors and footbridges in order to improve their vibration serviceability performance. Most of these works have focused on single-input single-output (SISO) controller schemes, i.e. comprising of a single sensor and actuator pair. Their closed-loop stability properties expressed in terms of the gain margin (GM) and phase margin (PM) can easily be evaluated from techniques such as root locus studies of the closed-loop systems and Nyquist contour plots.

For multiple-input multiple-output (MIMO) controller schemes, i.e. systems with multiple sets of actuators and sensors, evaluation of their stability properties is not so obvious and most past researches hardly show this although it is taken into account in one way or another. This is the focus of this work. It presents a study of MIMO stability of a control set-up comprising of two sensors and actuators and further reviews what might be regarded as the appropriate controller gains for velocity based controllers. The approaches used to evaluate the stability properties of this control scheme comprise of comparative studies covering the generalized Nyquist criterion, plots of eigenvalues of the closed-loop system and relative gain arrays (RGA). A limiter on the actuator displacement to disturbance loop both for SISO and MIMO studies is introduced to reduce potential stroke saturation.

Keywords Vibration • Control • Stability • Velocity feedback • Actuator

20.1 Introduction

There have been numerous studies in the literature that have been devoted to active control of human-induced vibrations in civil engineering structures, for example, in floors and footbridges [1–5]. For floor structures, the timeliness of such studies is imperative to ensure that future floor configurations or layouts arising from the advancements in materials and design technologies will possess enhanced vibration serviceability performances.

Most of the past studies on floor and footbridge vibration control have predominantly employed single-input single-output (SISO) collocated sensor and actuator pairs. By making use of simple and robust controller structures, for example, the direct velocity feedback (DVF) controller [6], they have been successfully implemented in augmenting damping of the desired structural vibration modes. Stability requirements for such systems have also been fairly well developed and have been carried out using procedures, for example, the Nyquist stability criterion [7]. Stability margins in terms of the gain margin (GM) and phase margin (PM) can be pre-set and appropriate controller gains designed to meet these requirements. Appropriate compensation for the actuator dynamics has also been considered to mitigate the potential for actuator stroke saturation [1].

Multi-SISO and MIMO controller schemes have been trialled in some past active control studies on human-induced vibrations [8], but a majority of studies have mainly been in other sectors, for example, the automatic control, electrical engineering, mechanical engineering and aerospace industries. In some studies [9, 10], it has been shown that in order to achieve considerable reductions in spatially averaged responses and sound radiation of panel units, dense arrays of decentralized control units should be used. Potentially this would also be beneficial for floor vibration control. It is important, however, to guarantee the stability of the resultant closed-loop systems. An evaluation of the stability properties of these systems is normally undertaken by the generalized Nyquist criterion [7, 11, 12]. It has been proposed in these past works that the control loops considered should implement the same feedback gain as this presents a clearer pattern of evaluating

D. Nyawako (✉) • P. Reynolds • E. Hudson

Vibration Engineering Section, College of Engineering, Mathematics and Physical Sciences, University of Exeter, Exeter, EX4 4QF, UK
e-mail: d.s.nyawako@exeter.ac.uk; p.reynolds@exeter.ac.uk; e.j.hudson@exeter.ac.uk

their stability properties. A further measure of MIMO system interaction is provided by the Relative Gain Array (RGA) procedure [13]. It provides a quantitative approach for analysing interactions between control and process outputs and thus provides a recommendation of appropriate pairings between manipulated and controlled variables, necessary for generating an appropriate control scheme [15]. It is, however, deemed to be more appropriate for MIMO systems that can be decoupled. RGA procedures have been applied to some MIMO processes [14].

Future floors will potentially require arrays of actuator and sensor pairs in multi-SISO or full MIMO configurations. This will be dependent of their dynamic properties which play a key role towards the achievable degrees of controllability and observability for different actuator and sensor combinations. With such controller structures, it will be necessary to guarantee the stability of the closed-loop system whilst maintaining desirable vibration mitigation performances. This is the primary focus of the work presented here, to review appropriate schemes that can be used in evaluating stability properties of multi-SISO/MIMO controller configurations used in floor vibration control.

Section 2 introduces the structure whose dynamic properties are used in the work presented here and develops some reduced order models (ROM) from experimental modal analysis (EMA) tests. A typical SISO controller scheme including some stability studies is outlined in Sect. 3, whilst Sect. 4 looks into stability studies with multi-SISO/MIMO controller configurations selected. Conclusions are presented in Sect. 5.

20.2 Structure and Actuator Dynamics

The structure whose dynamic properties are used in the analytical studies presented in this work is a walkway bridge in the University of Exeter’s Forum building shown in Fig. 20.1a. Figure 20.1b illustrates the plan view of the test points that are used for the experimental modal analysis (EMA) tests. Further details of the EMA tests are shown in [16], of which a summary of the estimated modal properties of the lowest two vibration modes are presented in Table 20.1. The actuator dynamic properties shown in Eqs. (20.1a) and (20.1b), i.e. the actuator force-voltage (N/V) and displacement-voltage characteristics (m/V) have also been obtained from [16].

$$G_{act}(s) = \frac{F(s)}{V(s)} = \frac{K_{act}s^2}{s^2 + 2\zeta_{act}\omega_{act}s + \omega_{act}^2} \tag{20.1a}$$

$$G_{actd}(s) = \frac{D(s)}{V(s)} = \frac{K_{actd}}{s^2 + 2\zeta_{act}\omega_{act}s + \omega_{act}^2} \tag{20.1b}$$

To study the stability properties of the SISO and/or multi-SISO/MIMO controllers, a lumped parameter model of the walkway bridge is derived that consists of ‘n’ modal co-ordinates in Eq. (20.2a). The state space representations in Eqs. (20.2b) and (20.2c) can be derived and tailored to provide outputs in modal or spatial velocities and accelerations. Appropriate reduced-order models (ROM) can be extracted for controller designs. M^* , C^* and K^* are the $n \times n$ modal mass, damping and stiffness matrices, whilst \varnothing is the $m \times n$ mass normalised modal transformation matrix. D is the $m \times m$ actuator location matrix and E

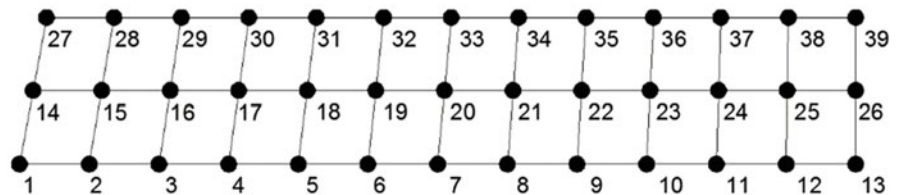


Fig. 20.1 Photo of walkway bridge in the forum building, University of Exeter and plan view for experimental modal analysis tests

Table 20.1 Summary of estimated modal properties from EMA [16]

Mode	Natural frequency (Hz)	Damping ratio (%)
1	6.34	1.0
2	10.50	0.9

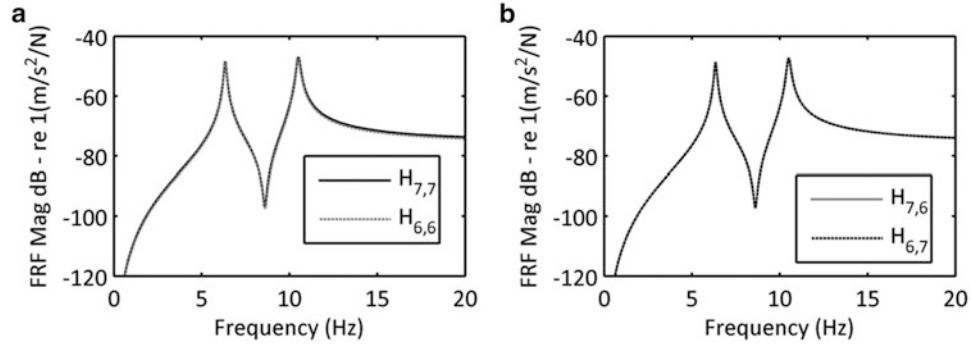


Fig. 20.2 Collocated actuator and sensor pair locations for stability studies of SISO and multi-SISO/MIMO configurations

is the $m \times m$ excitation force location matrix. ζ_i and ω_i are the modal damping ratio and circular natural frequency of the i th vibration mode. Classical control extensions of transfer function form can be derived from Eq. (20.2d) for SISO, multi-SISO and MIMO cases.

$$M^* \ddot{z} + C^* \dot{z} + K^* z = \varnothing^T D u + \varnothing^T E f \quad (20.2a)$$

$$\begin{Bmatrix} \dot{x}_1 \\ \dot{x}_2 \end{Bmatrix} = \begin{bmatrix} 0 & I \\ -\frac{K^*}{M^*} & -\frac{C^*}{M^*} \end{bmatrix} \begin{Bmatrix} x_1 \\ x_2 \end{Bmatrix} + \begin{bmatrix} 0 & 0 \\ \varnothing^T D & \varnothing^T E \end{bmatrix} \begin{Bmatrix} u \\ f \end{Bmatrix} \quad (20.2b)$$

$$\begin{Bmatrix} y_1 \\ y_2 \end{Bmatrix} = \begin{bmatrix} 0 & I \\ -\frac{K^*}{M^*} & -\frac{C^*}{M^*} \end{bmatrix} \begin{Bmatrix} x_1 \\ x_2 \end{Bmatrix} + \begin{bmatrix} 0 & 0 \\ \varnothing^T D & \varnothing^T E \end{bmatrix} \begin{Bmatrix} u \\ f \end{Bmatrix} \quad (20.2c)$$

$$G(s) = C(sI - A)^{-1} B + D \quad (20.2d)$$

where

$$K^* = \begin{bmatrix} \omega_1^2 & 0 & \cdots & 0 \\ 0 & \omega_2^2 & \cdots & 0 \\ \vdots & \vdots & \ddots & \vdots \\ 0 & 0 & \cdots & \omega_7^2 \end{bmatrix} \quad C^* = \begin{bmatrix} 2\zeta_1\omega_1 & 0 & \cdots & 0 \\ 0 & 2\zeta_2\omega_2 & \cdots & 0 \\ \vdots & \vdots & \ddots & \vdots \\ 0 & 0 & \cdots & 2\zeta_7\omega_7 \end{bmatrix}$$

$$M^* = \begin{bmatrix} 1 & 0 & \cdots & 0 \\ 0 & 1 & \cdots & 0 \\ \vdots & \vdots & \ddots & \vdots \\ 0 & 0 & \cdots & 1 \end{bmatrix} \quad \varnothing = \begin{bmatrix} \varnothing_{1,1} & \varnothing_{1,2} & \cdots & \varnothing_{1,7} \\ \varnothing_{2,1} & \varnothing_{2,2} & \cdots & \varnothing_{2,7} \\ \vdots & \vdots & \ddots & \vdots \\ \varnothing_{39,1} & \varnothing_{39,2} & \cdots & \varnothing_{39,7} \end{bmatrix}$$

Stability studies with SISO controllers comprise of independent and collocated actuator and sensor pairs implemented at TPs 6 and 7. Stability studies for multi-SISO/MIMO controllers consist of two pairs of collocated sensor and actuators pairs located at TPs 6 and 7 for the illustrations in this work. These are not regarded as the most optimal locations to any degree but are only used to develop the stability studies. The derived reduced order walkway bridge models at the above locations are shown in Fig. 20.2.

20.3 Stability of SISO Controllers

As noted in the previous section, two independent locations: TPs 6 and 7 are selected for siting a collocated sensor and actuator pair. Figure 20.3 shows a typical set-up that can be tailored for SISO control. $G_p(s)$, $G_{act}(s)$, $G_c(s)$, $G_{not}(s)$, $G_{bp}(s)$ represent the plant, actuator, controller, notch filter and bandpass filter dynamics. $d_i(t)$, $f_c(t)$, $y_a(t)$ and $r(t)$ are the disturbance input force, control force, structural acceleration response and reference input. $r(t)$, can be considered equal to zero.

For control of human-induced vibrations, disturbance rejection is the primary objective as human walking forces cannot easily be measured. This objective, derived from Fig. 20.3, is shown in Eq. (20.3), and the key parameter to be designed for is the controller, $G_c(s)$. In this work, $G_c(s)$ is a lossy integrator of the form in Eq. (20.4) that is designed to provide active damping to global structural vibration modes. k_g is the velocity feedback gain and ε is chosen to be very small, typically $\varepsilon < 0.01$. The sensitivity of the actuator stroke to human disturbance input can be monitored from Eq. (20.5), and the notch filter, $G_{not}(s)$, is introduced to compensate for the actuator dynamics.

$$Y_a(s) = \frac{G_p(s)}{1 + G_p(s)G_{act}(s)G_{not}(s)G_c(s)G_{bp}(s)} D_i(s) \quad (20.3)$$

$$G_c(s) = \frac{k_g}{s + \varepsilon} \quad (20.4)$$

$$Y_{actd}(s) = \frac{G_{actd}(s)G_{not}(s)G_c(s)G_{bp}(s)G_p(s)}{1 + G_{actd}(s)G_{not}(s)G_c(s)G_{bp}(s)G_p(s)} D_i(s) \quad (20.5)$$

Appropriate controller gains, k_g , are evaluated from the following two criteria:

1. System closed-loop stability using the classical Nyquist stability criterion. This considers the Nyquist contour plot of the open loop system $G_p(s)G_{act}(s)G_{not}(s)G_c(s)G_{bp}(s)$. Minimum stability margins can be specified, for example, gain (GM) and phase margins (PM) of 10 dB and 30°.
2. Actuator stroke to disturbance input relationship in Eq. (20.5) around the actuator resonant frequency ($k_1\omega_{act} < \omega_{act} < k_2\omega_{act}$). In this work, $k_1 = 0.2$, $k_2 = 2.0$ and a limit is placed on the absolute value of this equation within this frequency bandwidth, i.e. the selected gain, k_g , should guarantee that this does not exceed 0.05 mm/N for all frequencies in the bandwidth.

The lower of k_g from the above two conditions can be considered as the robust velocity feedback gain for the SISO velocity feedback controller. Typical gains, assuming a SISO controller implemented either at TP7 or TP6 that would meet requirements 1 and 2 above is shown in Table 20.2.

The Nyquist contour plot of $G_p(s)G_{act}(s)G_{not}(s)G_c(s)G_{bp}(s)$ for a SISO system with an actuator and sensor pair sited at TP7 is shown in Fig. 20.4a. The closed-loop system is stable as the Nyquist contour does not encircle the -1 point

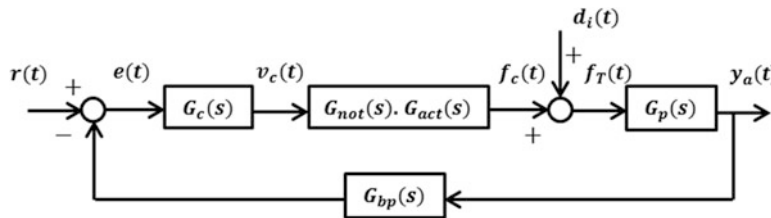


Fig. 20.3 Set-up that can be tailored for SISO, multi-SISO and MIMO controller schemes

Table 20.2 Control gains that meet required stability requirements (1) and (2) above

Test location	Velocity feedback gain (V/(m/s))	Stability margins (1)	Actuator stroke to disturbance input (2)
TP 7	735	GM = 14.4 dB, PM = 67.9°	0.05 mm/N
TP 6	775	GM = 14.4 dB, PM = 67.9°	0.05 mm/N

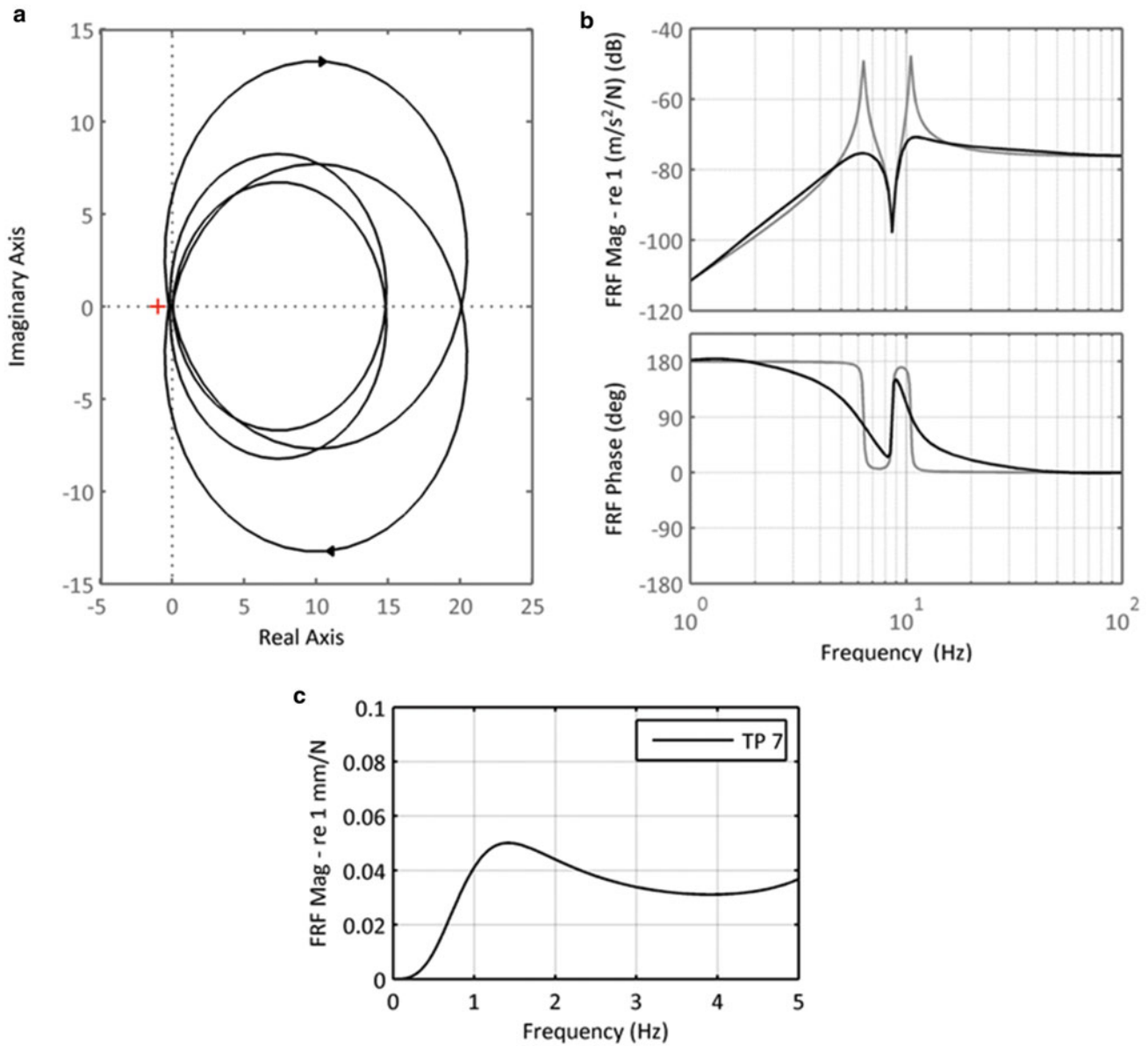


Fig. 20.4 Nyquist contour of open loop system $G_p(s)G_{act}(s)G_{not}(s)G_c(s)G_{bp}(s)$, actuator displacement to disturbance input relationship, and uncontrolled and controlled FRF at TP 7 for a general SISO collocated sensor and actuator pair

on the real-imaginary axis and also meets appropriate stability margins. Figure 20.4c illustrates the actuator stroke to disturbance input relationship around the actuator resonant frequency, and this meets requirement 2 above. A typical plot of an uncontrolled and controlled frequency response function (FRF) at TP7 is shown in Fig. 20.4b. Similar studies to evaluate robust feedback gains can be done for a SISO set-up at any other location on the walkway bridge structure.

20.4 Stability of Multi-SISO and MIMO Controllers

Only a 2×2 multi-SISO/MIMO system is considered in this work, and the respective control system components based on Fig. 20.3 are shown in Eqs. (20.6a)–(20.6c). Complex interactions can exist between controller and measurement locations even for a basic 2×2 system as demonstrated in Fig. 20.5. Considering Fig. 20.1b and the notations i and j , the combination $i, j = 7, 6$ refers to the locations of siting the collocated sensor and actuator pairs for these studies. The distinction between

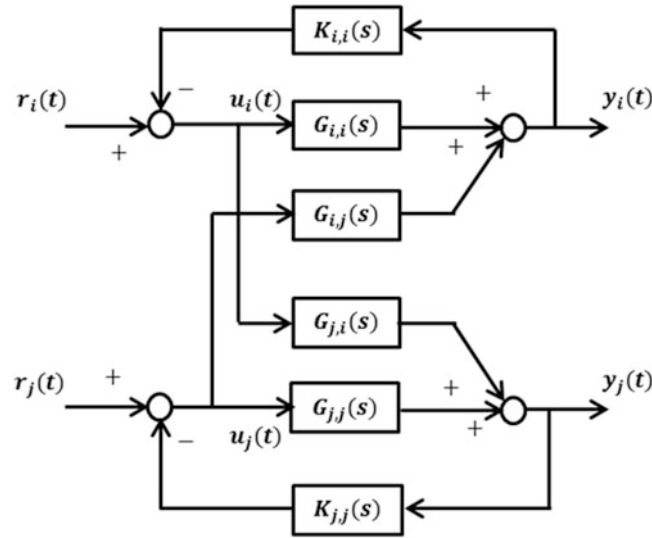


Fig. 20.5 Controller and sensor pairings for a 2×2 multi-SISO or MIMO set-up

a multi-SISO set-up and a full MIMO set-up can be made from the gain term in Eq. (20.6d) in which the off-diagonal terms b_{12} and b_{21} can be assumed as zero for the former.

$$G_p(s) = \underline{G}_p(s) = \begin{bmatrix} G_{p_{i,i}}(s) & G_{p_{i,j}}(s) \\ G_{p_{j,i}}(s) & G_{p_{j,j}}(s) \end{bmatrix}, \quad G_{bp}(\omega) = \underline{G}_{bp}(s) = \begin{bmatrix} G_{bp_{i,i}}(s) & 0 \\ 0 & G_{bp_{j,j}}(s) \end{bmatrix} \quad (20.6a)$$

$$G_c(s) = \underline{G}_c(s) = \begin{bmatrix} G_{c_{i,i}}(s) & 0 \\ 0 & G_{c_{j,j}}(s) \end{bmatrix}, \quad (20.6b)$$

$$G_{not}(s)G_{act}(s) = \underline{G}_{not}(s)\underline{G}_{act}(s) = \begin{bmatrix} G_{not}(s)G_{act_{i,i}}(s) & 0 \\ 0 & G_{not}(s)G_{act_{j,j}}(s) \end{bmatrix} \quad (20.6c)$$

$$K_{gain} = \begin{bmatrix} b_{11} & b_{12} \\ b_{21} & b_{22} \end{bmatrix} \quad (20.6d)$$

Following a similar procedure to that in the SISO studies section, disturbance rejection and actuator displacement-disturbance relationships can also be derived as shown in Eqs. (20.7) and (20.8).

$$\underline{Y}_a(s) = \left(I + \underline{G}_{cl1}(s) \right)^{-1} \underline{G}_p(s) \underline{D}_i(s) \quad (20.7)$$

$$\underline{Y}_{actd}(s) = \left(I + \underline{G}_{cl2}(s) \right)^{-1} \underline{G}_{cl2}(s) \underline{D}_i(s) \quad (20.8)$$

Where:

$$\underline{G}_{cl1}(s) = \underline{G}_p(s) \underline{G}_{act}(s) \underline{G}_{not}(s) \underline{G}_c(s) \underline{G}_{bp}(s) \quad (20.9)$$

$$G_{cl2}(s) = \underline{G}_{actd}(s)\underline{G}_{not}(s)\underline{G}_c(s)\underline{G}_{bp}(s)\underline{G}_p(s) \quad (20.10)$$

The stability properties of the multi-SISO/MIMO controller schemes can be evaluated from the generalized Nyquist criterion. As observed by [7, 11], stability analysis for multi-channel feedback systems can be determined graphically from a plot of the determinant of $\left(I + \underline{G}_{cl1}(s)\right)$. The system is stable if the plot of $\det\left(I + \underline{G}_{cl1}(s)\right)$ does not encircle the instability point $(0, j0)$. This, however, does not provide information about maximum gains that can be implemented before instability is reached, and implementing variable gains implies changes in the loci of $\det\left(I + \underline{G}_{cl1}(s)\right)$ making stability studies and derivation of optimal gains even more difficult. To get round this issue, it has been proposed by [7, 11] that a good approach to design is to implement similar gains for all control loops. Stability can then be assessed from polar plots of the eigenvalues of $\underline{G}_{cl1}(s)$ which is identical to Nyquist stability criterion for SISO set-ups. The closed-loop system is stable provided the eigenvalues do not enclose the instability point $(-1, j0)$.

For the present studies, velocity feedback gains of $k_g = 250$ and $k_g = 750$ that are implemented in both locations sequentially for both multi-SISO controllers at TPs 7 and 6 are used to highlight evolution of the stability properties. This approach can be applied to any multi-SISO/MIMO system. Figure 20.6a presents the polar plots of the eigenvalues of $\underline{G}_{cl1}(s)$ for the control gains considered and Fig. 20.6b illustrates the loci of $\det\left(I + \underline{G}_{cl1}(s)\right)$ for the two sets of velocity feedback gains. A pole-zero plot of $\det\left(I + \underline{G}_{cl1}(s)\right)$ is highlighted in Fig. 20.6c and this reflects that all zeros are in the left hand plane of the complex plane. The predicted vibration mitigation performances for these controller gains are shown in Fig. 20.7. It is seen that the controller gains selected for these studies do satisfy the stability requirements outlined above. The requirement outlined in the SISO design section that places a limiter on the actuator stroke to disturbance input relationship around the actuator resonant frequency is also met as illustrated in Fig. 20.8. Only the result from the actuator at location 7 is shown here as that at location 6 is nearly identical. For these particular locations for siting the collocated sensor and actuator pairs, the higher gains tending towards $k_g = 750$ at both locations might be considered as the appropriate gains as they just about meet the stability requirements as well as the required threshold for the actuator displacement to disturbance input.

Relative gain arrays (RGA) present a measure of MIMO system interactions and can provide a recommendation of the best pairing between controlled and manipulated variables in some process systems. This is useful for systems that can be decoupled [15], where it is noted that a good MIMO control scheme for a system that can be decoupled is one that can control a process variable without significantly influencing other process variables. It requires knowledge of steady-state gains and not process or system dynamics. The RGA gives a measure of the ratio shown in Eq. (20.11) [13, 15]. A detailed review of the derivation of the full system definitions outlined in Eqs. (20.12a) and (20.12b) is presented in [13]. It should be noted that if $\lambda_{ij} \approx 0$, then a change in input “j” does not influence output “i” and hence cannot be used to control it.

$$\lambda = \frac{\text{process gain as seen by a given controller with all other loops open}}{\text{process gain as seen by a given controller with all other loops closed}} \quad (20.11)$$

$$\Lambda = \begin{bmatrix} \lambda_{ii} & \lambda_{ij} \\ \lambda_{ji} & \lambda_{jj} \end{bmatrix} = \begin{bmatrix} \left. \frac{y_i}{u_i} \right|_{K_{jj,ol}} / \left. \frac{y_i}{u_i} \right|_{K_{jj,cl}} & \left. \frac{y_i}{u_j} \right|_{K_{ii,ol}} / \left. \frac{y_i}{u_j} \right|_{K_{ii,cl}} \\ \left. \frac{y_j}{u_i} \right|_{K_{jj,ol}} / \left. \frac{y_j}{u_i} \right|_{K_{jj,cl}} & \left. \frac{y_j}{u_j} \right|_{K_{ii,ol}} / \left. \frac{y_j}{u_j} \right|_{K_{ii,cl}} \end{bmatrix} \quad (20.12a)$$

$$\Lambda(G(j\omega)) = G(j\omega) \otimes (G^{-1}(j\omega))^T \quad (20.12b)$$

Considering the walkway bridge structure dynamics used in these studies, by virtue of the system mode shapes, and associated controllability and observability conditions of the locations, the frequencies of interest that are considered prone to human excitation can be controlled from either TP 6 or TP 7. This is because they are observable from the two locations, and complete decoupling of this multi-SISO/MIMO system is not possible for the selected locations. Figure 20.9 shows $\Lambda(j\omega)$ in Eq. (20.12b) over the frequency bandwidth 0.0–20.0 Hz highlighting strong coupling between these selected locations. A controller at any given location will significantly influence the performance at the other selected location and vice versa. The respective values around the resonant frequencies of the walkway bridge structure, i.e. at 6.34–10.5 Hz are shown in Eqs. (20.13a) and (20.13b).

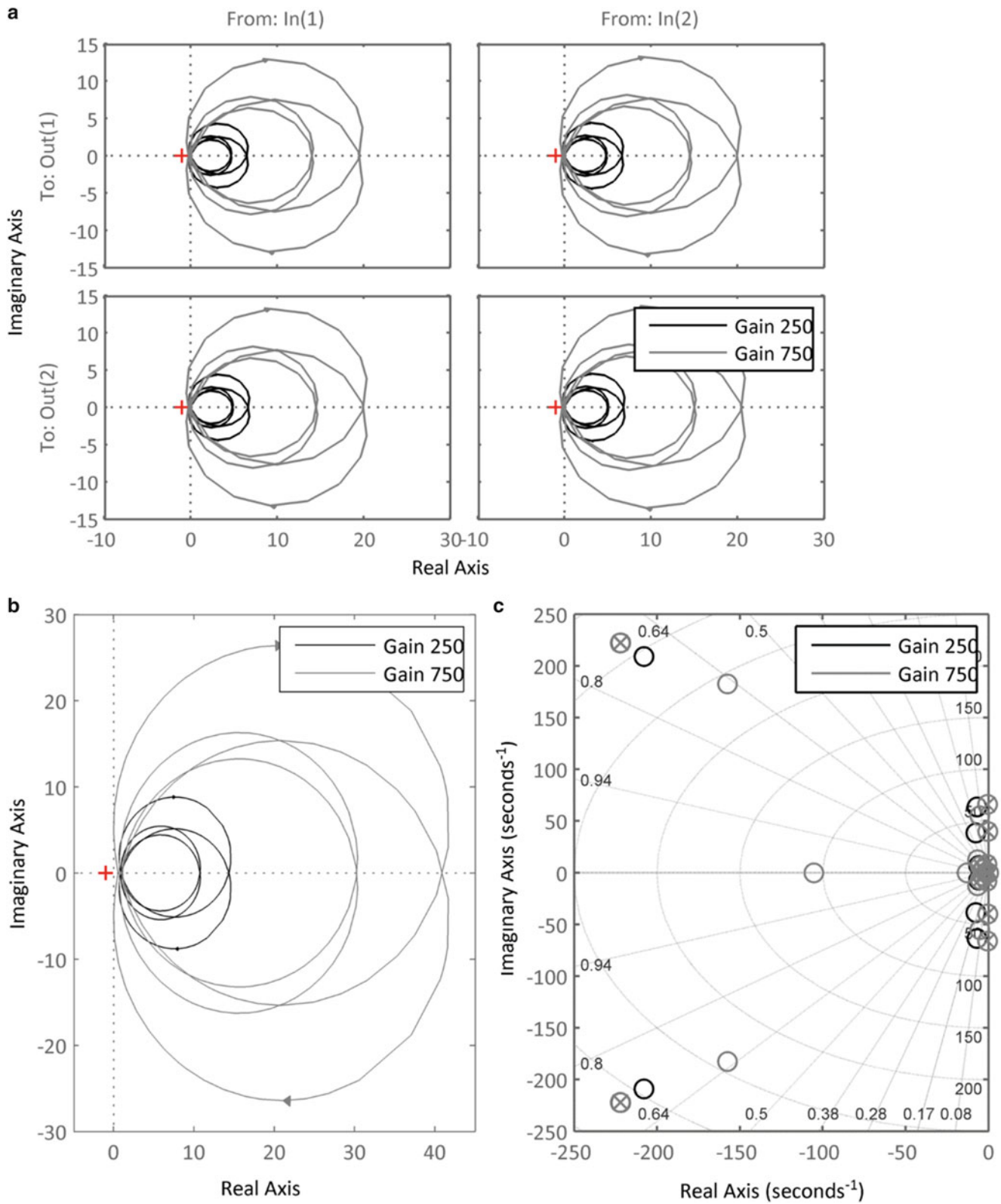


Fig. 20.6 Figures highlighting: (a) Polar plot of eigenvalues of $G_{cl1}(s)$, (b) Loci of $\det(I + G_{cl1}(s))$, and (c) Pole-zero plot of $\det(I + G_{cl1}(s))$ for velocity feedback gains $k_g = 250$ and $k_g = 750$

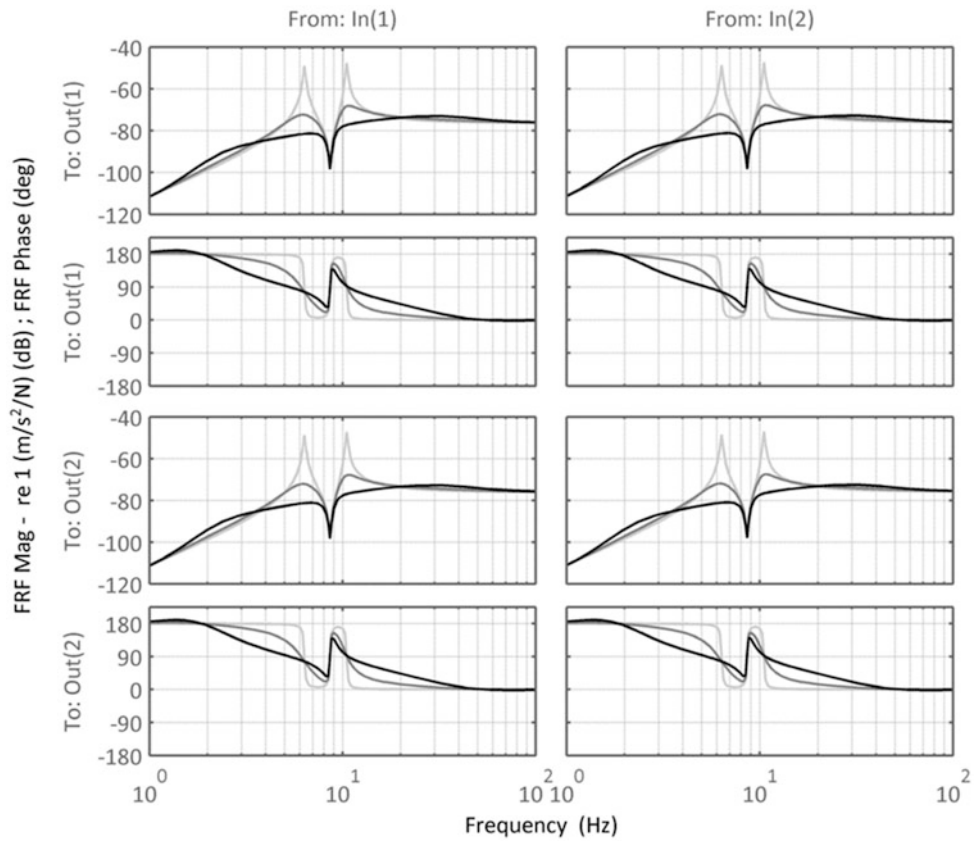
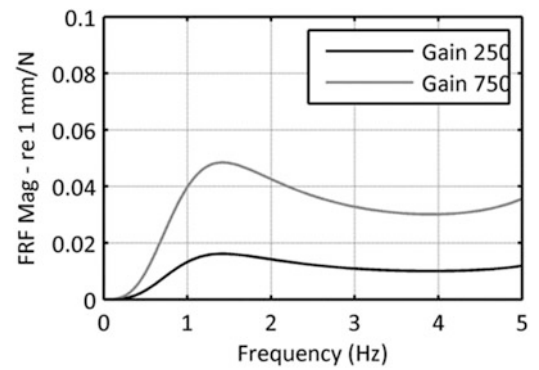


Fig. 20.7 Uncontrolled and controlled frequency response functions at TPs 6 and 7 (In this figure, In(1) and Out(1) refer to TP 7 and vice-versa)

Fig. 20.8 Actuator displacement to disturbance input relationship at TP 7 (relationship at TP 6 identical to that at TP 7)



$$\Lambda (G(j\omega_1)) = \begin{bmatrix} 7.4e5 & 7.4e5 \\ 7.4e5 & 7.4e5 \end{bmatrix}, = 39.8 \text{ rad/s} \tag{20.13a}$$

$$\Lambda (G(j\omega_2)) = \begin{bmatrix} 3.4e5 & 3.4e5 \\ 3.4e5 & 3.4e5 \end{bmatrix}, = 66.0 \text{ rad/s} \tag{20.13b}$$

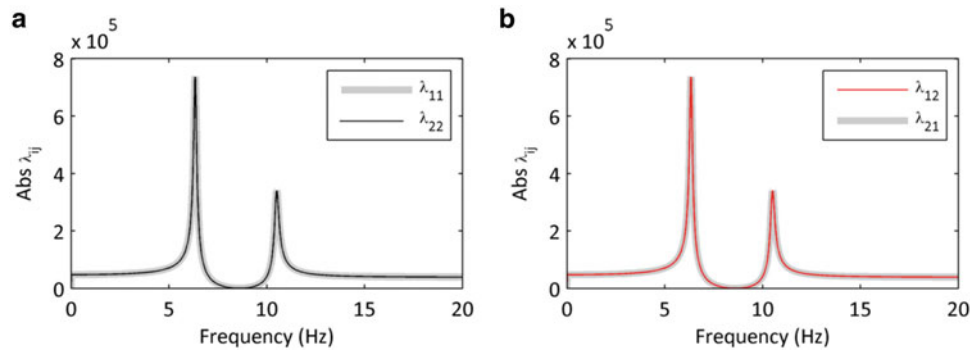


Fig. 20.9 RGA pairings $\Lambda(j\omega)$ in Eq. (20.13a) for the 2×2 system in Fig. 20.5

20.5 Conclusions

The work presented here has looked at stability properties of both SISO and multi-SISO/MIMO controller structures. For SISO controller schemes with collocated sensor and actuator pairs and implementing a basic controller like the velocity feedback scheme, stability properties are easily evaluated from the classical Nyquist stability criterion with specification of appropriate stability margins (gain and phase margins). An additional condition is imposed on the actuator stroke to disturbance input relationship around the actuator resonant frequency to reduce the potential for stroke saturation instability. This has been implemented on TP 7 of the walkway bridge structure.

For multi-SISO/MIMO controller structures, implemented at TPs 6 and 7, the generalized Nyquist criterion has been used to evaluate the closed-loop stability properties. A limiter is also introduced on the actuator stroke to disturbance input relationship. By implementing similar control gains at the control locations, it is seen that this gives a rather clear indication of maximum gains that can be implemented before instability is reached. Stability is evaluated from plots of $\det(I + G_{cl}(s))$ and polar plots of the eigenvalues of $G_{cl}(s)$. The actuator stroke to disturbance input relationship introduced ensures the limiter imposed is not exceeded for the selected feedback gains. These studies present avenues for evaluating stability properties of multi-SISO/MIMO controller structures that will be beneficial particularly for future floor vibration control applications.

The use of relative gain array approach (RGA) which finds greater application in processes that can be decoupled may not be appropriate for the present studies. Decoupling dynamic properties of civil structures, usually with dense resonant frequencies and associated mode shapes may not be easily done. Through modal testing, it is easy to derive the inter-relationships between different locations without necessarily resorting to using RGAs.

Acknowledgements The authors would like to acknowledge the financial assistance provided by the UK Engineering and Physical Sciences Research Council (EPSRC) through a responsive mode grant (Ref. EP/H009825/1), and a Leadership Fellowship Grant (Ref. EP/J004081/2).

References

- Díaz, I.M., Pereira, E., Hudson, M.J., Reynolds, P.: Enhancing active vibration control of pedestrian structures using inertial actuators with local feedback control. *Eng. Struct.* **41**, 157–166 (2012). doi:[10.1016/j.engstruct.2012.03.043](https://doi.org/10.1016/j.engstruct.2012.03.043)
- Hanagan, L.M.: Practical implications of optimizing an active floor vibration controller. In: IMAC XXVIII, Jacksonville, FL, 189–194 (2010) doi:[10.1007/978-1-4419-9831-6_20](https://doi.org/10.1007/978-1-4419-9831-6_20)
- Moutinho, C., Cunha, A., Caetano, E. Implementation of an active mass damper to control vibrations in a “lively” footbridge. In: III ECCOMAS Thematic Conference on Smart Structures and Materials, III ECCOMAS thematic conference on smart structures and materials, W.Ostachowicz, J. Molnicki–Szule, C. Mota Soares et al. (eds.) Gdansk, Poland, July 9–11, 2007
- Nyawako, D., Reynolds, P., Hudson, M.J.: Findings with AVC design for mitigation of human induced vibrations in office floors. In: IMAC XXXI, Society for Experimental Mechanics (SEM), Orange County, CA, 2013
- Pereira, E., Díaz, I.M., Hudson, E.J., Reynolds, P.: Optimal control-based methodology for active vibration control of pedestrian structures. *Eng. Struct.* **80**, 153–162 (2014). doi:[10.1016/j.engstruct.2014.08.046](https://doi.org/10.1016/j.engstruct.2014.08.046)
- Hanagan, L.M., Murray, T.M.: Active control approach for reducing floor vibrations. *J. Struct. Eng.* **123**(11), 1497–1505 (1997). doi:[10.1061/\(ASCE\)0733-9445\(1997\)123:11\(1497\)](https://doi.org/10.1061/(ASCE)0733-9445(1997)123:11(1497))

7. González Díaz, C., Gardonio, P.: Feedback control laws for proof-mass electrodynamic actuators. *Smart Mater. Struct.* **16**(5), 1766–1783 (2007). doi:[10.1088/0964-1726/16/5/031](https://doi.org/10.1088/0964-1726/16/5/031)
8. Diaz, I.M., Pereira, E., Zanuy, C., Alen, C.: A comparative study of SISO and MIMO control strategies for floor vibration damping. In: SMART2013, Torino, Italy, 2013
9. Gardonio, P., Elliot, S.J.: Smart panels for active structural acoustic control. *Smart Mater. Struct.* **13**, 1314–1336 (2004)
10. Elliot, S.J., Gardonio, P., Sors, T.C., Brennan, M.J.: Active vibroacoustic control with multiple local feedback loops. *J. Acoust. Soc. Am.* **111**(2), 908–915 (2002)
11. Desoer, C.A., Wang, Y.T.: On the generalized Nyquist stability criterion. *IEEE Trans. Autom. Control* **25**(2), 187–196 (1980)
12. Barmanj, J.F., Katzenelson, J.: A generalized Nyquist-type stability criterion for multivariable feedback systems. *Int. J. Control* **20**(4), 593–622 (1974). doi:[10.1080/00207177408932763](https://doi.org/10.1080/00207177408932763)
13. Skogestad, S., Postlethwaite, I.: *Multivariable Feedback Control: Analysis and Design*, 2nd edn. John Wiley and Sons publishers ISBN:978-0-470-01167-6 (2005)
14. Chen, D., Seborg, D.E.: Relative gain array analysis for uncertain process models. *AIChE J.* **48**(2), 302–310 (2002)
15. RGA (controls wiki). Accessed online at <https://controls.engin.umich.edu/wiki/index.php/RGA>
16. Nyawako, D.S., Reynolds, P.: Observer-based controller for floor vibration control with optimization algorithms. *J. Vib. Control* 1–16 (2015). doi:[10.1177/1077546315581229](https://doi.org/10.1177/1077546315581229)

Chapter 21

Extraction of Wave Dispersion Characteristics in a Discrete Chain Using Complex Modal Decomposition

Rickey A. Caldwell Jr., Smruti Panigrahi, and Brian F. Feeny

Abstract The dispersion relationship of a discrete chain of masses is extracted from numerically simulated data by applying complex modal decomposition. When an impulse excitation is applied to one end of a semi-infinite mass-spring chain, a wave is generated and propagates down the chain. This wave consists of various modes. The time record for the generated data is limited such that the wave reflection does not return to the “sensed” masses. For example, a 250-mass chain is simulated, and we consider (or sensed) the time record of the first 100 masses. The data collected from the numerical simulation consists of the displacements of each mass at each time step. This data is then used to extract complex modes using the complex orthogonal decomposition (COD) and smooth complex orthogonal decomposition. The extracted complex modes accommodate modal traveling waves. We then compute the frequencies and wave numbers from modal coordinates and mode shapes, respectively. The amplitudes and frequencies of the modes are also estimated using Rayleigh’s quotients. The COD extracted dispersion relationship matched the analytical prediction of the dispersion curve for the linear mass chain.

Keywords Complex orthogonal decomposition • Wave propagation • Dispersion relationship • Modal analysis • Complex modes

21.1 Introduction

We interact with waves everyday from the electromagnetic waves sent from our cellphones, bluetooth enable electronics and GPS navigation to mechanical waves used in electric toothbrushes or in the sound we hear. There are parameters used to describe these waves; in this paper we will focus on waves of the form $y(x, t) = A \sin(kx - \omega t)$ where A is the amplitude of the wave measured in meters, k is the wavenumber (spatial frequency) measured in rad/meter, and ω is temporal frequency measured in rad/sec. The velocity or frequency of a wave can be related to k when a wave travels through a medium. This relationship is called the dispersion relationship. For example, waves traveling through an Euler-Bernoulli beam have the relationship $\omega = \sqrt{EI/\rho Ak}$ [1]. If the waves have multiple frequency components then phase velocity c_p and group velocity c_g are used to describe the velocity of the wave form and wave envelope, respectively. There are several methods used to measure these parameters including MUSIC [2], ESPRIT [3], and wavelet transforms [4].

In this paper we will apply complex orthogonal decomposition (COD) [5, 6] and smooth complex orthogonal decomposition (SCOD) [7] for the purpose of extracting the parameters of harmonic complex structural waves traveling through a mass-chain system. When applied both methods use measurement ensembles to form correlation matrices. COD uses an ensemble of analytic displacement measurements to compute a correlation matrix $\mathbf{R} = \mathbf{Z}\mathbf{Z}^H/N$, where \mathbf{Z} is the analytic displacement ensemble, H is the Hermitian or conjugate transpose, and N is the number of time samples. Next the COD eigenvalue problem (EVP) is posed as $\lambda \mathbf{R}\underline{\phi} = \lambda \underline{\phi}$ or in the matrix form $\mathbf{R}\Phi\Lambda = \Phi\Lambda$. Wavenumbers are computed from the $\underline{\phi}$ such that $k_i = d\angle\phi_i/dx$ and the frequencies are computed from the modal coordinates, $\mathbf{Q} = \Phi^{-1}\mathbf{Z}$ and $\omega_i = d\angle q_i/dt$. Where q_i is a row of \mathbf{Q} .

R.A. Caldwell Jr.
Department of Mechanical Engineering, Michigan State University, East Lansing, MI 48824, USA
e-mail: caldwe20@msu.edu

S. Panigrahi
Research and Innovation Center, Ford Motor Company, 2101 Village Road, Dearborn, MI 48121, USA
e-mail: spanigr2@ford.com

B.F. Feeny (✉)
Department of Mechanical Engineering, Michigan State University, East Lansing, MI 48823, USA
e-mail: feeny@egr.msu.edu

When using SCOD a second correlation matrix, \mathbf{S} is built using an analytic ensemble matrix from velocities \mathbf{Z}_v , where $\mathbf{S} = \mathbf{Z}_v \mathbf{Z}_v^H / N$. A SCOD generalized EVP (GEVP) is posed as $\mathbf{R} \Phi \Lambda = \mathbf{S} \Lambda$, where Λ is a diagonal matrix whose elements are the frequencies squared, such that $\Lambda_{ii} = \omega_i^2$. The wavenumbers are computed similarly to COD, however, they are computed from Ψ the inverse conjugate transpose of Φ where $\Psi = \Phi^{-H}$. Now the gradient of the angle of each column of Ψ equal to the wavenumber.

This paper will focus on applying COD and SCOD to a disturbance propagating through a mass-chain system. In Sect. 21.2 the dynamics of the mass-chain system will be outlined. Section 21.3 will apply COD to a linear mass chain system Sect. 21.4 is a conclusion.

21.2 Analytical Model for Periodic Chain

The wave behaviors in an infinite uniform cubic nonlinear mass-spring chain with stiffness α has been studied in details in [8, 9]. Here, we show the derivation for a linear chain (Fig. 21.1).

The mass-spring chain is arranged in a fashion such that each mass is separated by a distance h from its nearest neighbor. h is also the relaxed length of each spring before any deformation occurs. We use the assumption that all the masses are equal, ($m_j = m$) and only the nearest neighbors have direct effects on each other. As such, we consider a linear spring force relative to the equilibrium state. The equations of motion (EOM) in physical coordinates can then be written as

$$m \ddot{u}_j = \tilde{\alpha} [(u_{j+1} - u_j) - (u_j - u_{j-1})] \quad (21.1)$$

for $j = \dots, -2, -1, 0, 1, 2, \dots$. Letting $\alpha = \frac{\tilde{\alpha}}{m}$ we get

$$\ddot{u}_j = \alpha [(u_{j+1} - u_j) - (u_j - u_{j-1})] \quad (21.2)$$

The non-dimensionalization is done by assuming $x = \frac{\tilde{x}}{h}$, which results in $x_j = j$ and $x_{j\pm 1} = j \pm 1$. The non-dimensional wave number is denoted by μ . We assume a traveling dispersive wave solution at frequency ω and wave number μ and substitute into the equations of motion. Let

$$u_j(t) = y_j + \bar{y}_j = A e^{i(\mu j - \omega t)} + \bar{A} e^{-i(\mu j - \omega t)}. \quad (21.3)$$

Substituting $u_{j\pm 1} = e^{\pm i\mu} A e^{i(\mu j - \omega t)}$ into the equations we get

$$\omega^2 = 2\alpha(1 - \cos \mu) \quad (21.4)$$

for the required relationship between ω and μ . This is the dispersion relationship for the linear chain. Thus for a linear chain, the dispersion is given as

$$\omega = \sqrt{2\alpha(1 - \cos \mu)} \quad (21.5)$$

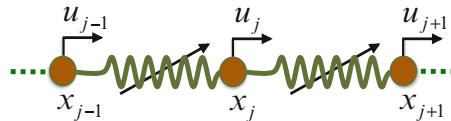


Fig. 21.1 Infinite mass chain. The relaxed position and displacement of mass m_j are denoted by x_j and u_j respectively. In this case the springs are linear with relaxed length h

21.3 Complex Orthogonal Decomposition

COD is a generalization of proper orthogonal decomposition (POD). POD was independently created by several people including Lumley [10], Berkooz [11], Kosambi [12], and others. In the application of POD sensed data is arranged in a measurement ensemble. Typically, each sensor is aligned in a row, and each column of that row is a time step. Where there are M sensors and N time steps such that $\mathbf{X} \in \mathcal{R}^{M \times N}$. The ensemble matrix \mathbf{X} is used to compute the correlation matrix \mathbf{R} which is defined as

$$\mathbf{R} = \frac{\mathbf{X}\mathbf{X}^T}{N}. \quad (21.6)$$

Typically the means are subtracted from \mathbf{R} in which case it is called a co-variance matrix. The co-variance matrix is used to formulate an eigenvalue problem (EVP). Defined as

$$\mathbf{R}\mathbf{v} = \lambda\mathbf{v}. \quad (21.7)$$

Where the eigenvector \mathbf{v} is called a proper orthogonal mode and in certain system corresponds to linear normal modes, and the eigenvalue λ is called proper orthogonal value and relates to spectral energy density. POD is great at extracting synchronous wave modes in lightly damped freely vibrating structures. Traveling waves can be extracted using COD. The mathematical framework for COD is similar to POD with the exception that the ensemble matrix is made into a analytic ensemble using the Hilbert Transform, or via a single-sided double magnitude fast Fourier transform (FFT) where the negative frequencies are zeroed out. These steps are outlined in the next section.

21.3.1 COD: Mathematical Development

First \mathbf{Z} is computed by taking the fast Fourier transform (FFT) of each row of \mathbf{X} to get $\tilde{\mathbf{X}}$. The FFT ensemble is in the discrete frequency domain, and can be defined to roughly cover the spectrum from $-\omega_{ny}$ to ω_{ny} , indexed from $-N/2$ to $N/2$ (for example in the case that N is even). Each row of $\tilde{\mathbf{X}}$ is the FFT of a sensor signal and each column is a frequency sample, and the elements of $\tilde{\mathbf{X}}$ are \tilde{X}_{ij} with $i = 1, \dots, M$ and $j = -N/2, \dots, N/2$. Then the negative spectrum is nullified, and the positive spectrum is doubled, such that the elements of $\tilde{\mathbf{Z}}$ of \mathbf{Z} are

$$\tilde{Z}_{ij} = \begin{cases} 0 & \text{if } j < 0 \\ 2\tilde{X}_{ij} & \text{if } j \geq 0 \end{cases} \quad (21.8)$$

for the j th columns of $\tilde{\mathbf{Z}}$ and $\tilde{\mathbf{X}}$. The complex analytic ensemble is obtained using the inverse FFT (IFFT), of each row, as $\mathbf{Z} = \text{IFFT}(\tilde{\mathbf{Z}})$.

Now that the measurement ensemble data has been converted to analytic signals, the correlation matrix \mathbf{R} is computed as $\mathbf{R} = \frac{\mathbf{Z}\mathbf{Z}^H}{N}$, where superscript H is the Hermitian operation (conjugate transpose). Once the correlation matrix is computed the eigenvalue problem is formulated such that $\mathbf{Z}\underline{\phi} = \lambda\underline{\phi}$. The eigenvector $\underline{\phi}$ is a complex orthogonal mode (COM) and the eigenvalue λ is the corresponding complex orthogonal value. Indeed, the correlation matrix can also be formed in the frequency domain as $\tilde{\mathbf{R}} = \tilde{\mathbf{Z}}\tilde{\mathbf{Z}}^H/N$, to produce the same COMs [5]. Note that \mathbf{R} is Hermitian, meaning $\mathbf{R}^H = \mathbf{R}$. As such, $\phi_i^H \phi_j = \delta_{ij}$, if the $\underline{\phi}$'s are normalized.

The complex modal coordinate (COC) ensemble, \mathbf{Q} , is computed such that $\mathbf{Q} = \Phi^H \mathbf{Z}$, where each column of Φ is an eigenvector $\underline{\phi}$. Each row \mathbf{q}_i^T of \mathbf{Q} is a sampled COC, such that $\mathbf{Q} = [\mathbf{q}_1 \ \mathbf{q}_2 \ \dots \ \mathbf{q}_M]^T$, $\mathbf{Q} \in \mathbb{C}^{M \times N}$. For nearly harmonic COCs, the rate of change of the phase with respect to the time sample is equal to the frequency, ω , such that $\omega_i = \frac{d}{dt} \{\angle \mathbf{q}_i\}$ where, in the sampled case, the time derivative is applied numerically. Similarly, the COMs are complex and the rate of change of the phase of nearly harmonic COMs with respect to the spatial position, x , defines a local wave number as $\mathbf{k}_i = \frac{d}{dx} \{\angle \phi_i\}$. Using the COMs, and \mathbf{Q} , the mean wave number, k , and frequency ω can be extracted for each mode.

21.3.2 COD Applied to a Linear Mass Chain

A 250 mass mass-spring chain was excited with an unit impulse on the left hand side. The disturbance propagated toward the right. The response of the first 100 masses were recorded as the disturbance passed the 100th mass but before reflections traveled backward to the 100th mass. Essentially, the time record was truncate at a time such that no reflections were recorded. The means were subtracted from the displacement. The displacements for four of the masses are shown in Fig. 21.2.

This can be seen here that the lower frequency waves travels faster than the higher frequency waves. The displacements are converted to complex analytic signals which are used compute the co-variance matrix, and the COD eigenvalue problem. The COV's are shown in the Fig. 21.3.

The COVs were used as a guide to discern which COMs contained extractable data [13]. Using the 30 highest COVs the dispersion relationship extracted is shown in Fig. 21.4. The COD extracted dispersion relationship correlates well to the

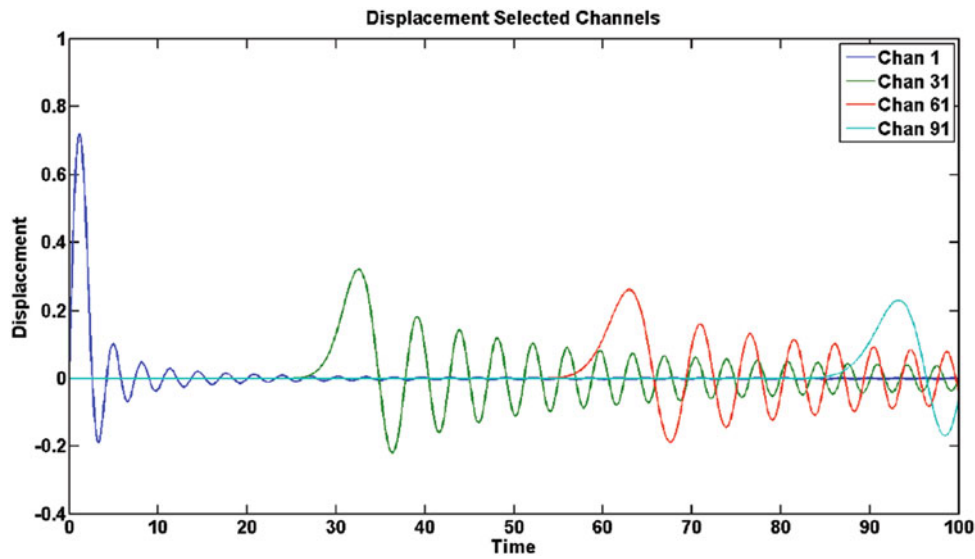


Fig. 21.2 Displacements for mass 1, 31, 61, and 91

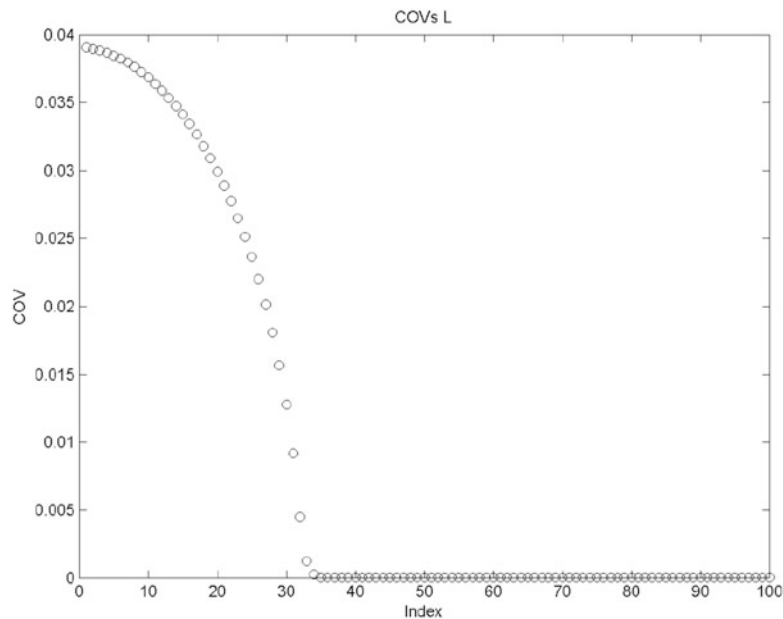


Fig. 21.3 Complex orthogonal values

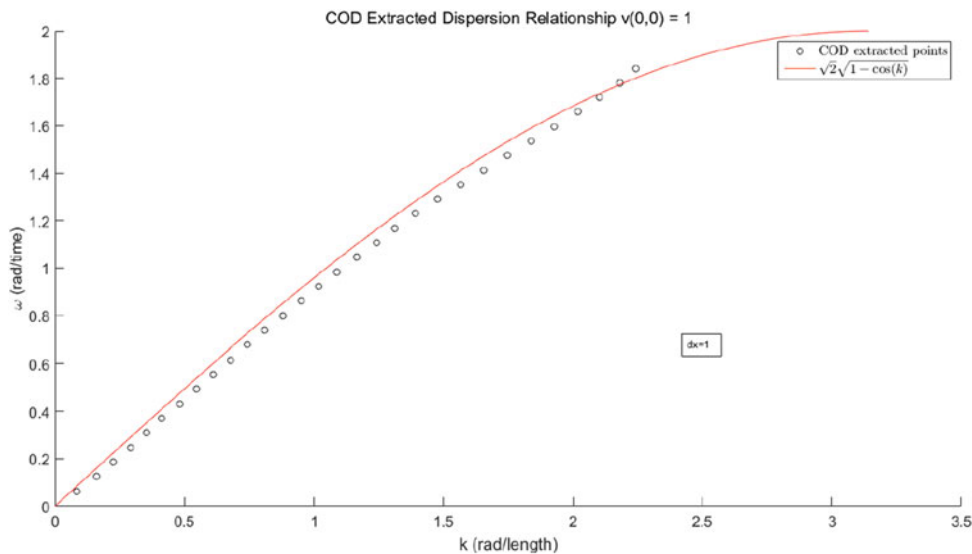


Fig. 21.4 Linear system’s geometric dispersion relationship using the mode from the 30 highest COVs initial velocity on the first mass = 1.0

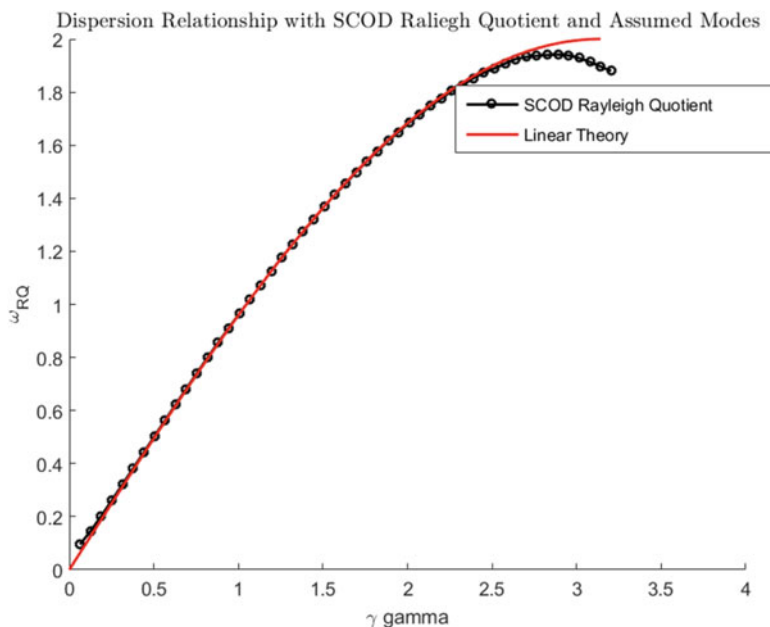


Fig. 21.5 Linear system’s geometric dispersion relationship using SCOD Rayleigh Quotients and assumed mode shape; initial velocity on the first mass = 1.0

theory qualitatively. COD like POD has a hard time extracting wavenumbers and frequencies when the constituent waves are close together. In order to improve on this we will use assumed modes and the generalize Rayleigh Quotient, where

$$\mathbf{RQ}(\lambda) = \frac{\phi_a^H \mathbf{R} \phi_a}{\phi_a^H \mathbf{S} \phi_a}. \tag{21.9}$$

\mathbf{R} and \mathbf{S} are the correlation matrices from SCOD, ϕ_a are assumed modes and the form $\phi_a = e^{ikx}$. The where k can be defined by the user and the Rayleigh Quotient will find the closest generalized eigenvalue in the eigenspace of \mathbf{R} and \mathbf{S} when ϕ_a used as eigenvector. SCOD correlation matrices were used because the square root of the SCOD eigenvalues are the frequencies of the traveling waves. The results of this can be seen in Fig. 21.5. The results of all three methods can be seen in Fig. 21.6.

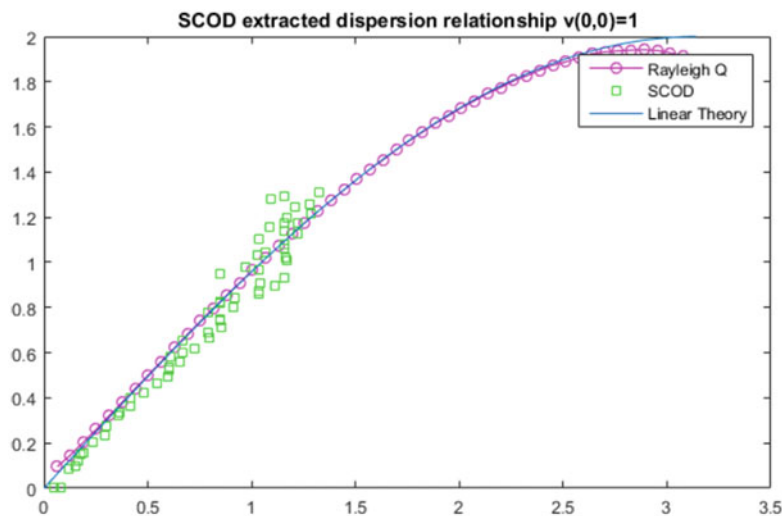


Fig. 21.6 Linear dispersion relationship using SCOD

21.4 Conclusions

The dynamics of an infinite mass-chain was derived and the dispersion relationship was solved using the method of multiple scales for a nonlinear mass-chain system. The efforts of this paper focused on the linear case where $\alpha = 1$. First, COD was applied to the analytic displacements of the masses. Since the individual waves that composed the traveling pulse were very similar in terms of k and ω , COD was able to extract a qualitatively good approximation to the dispersion relationship. Improvements were sought by using assumed modes and the generalized Rayleigh Quotient. The predicted dispersion relationship using Rayleigh Quotient was nearly exact. Slight deviation was seen near the origin and $k = \pi$. Current efforts are underway to apply this method to the linear cubic mass-chain system.

Acknowledgements This work is part of a project with the National Science Foundation, grant number CMII-1030337. Any results, findings, and opinions are those of the authors and do not necessarily reflect those of the NSF.

References

1. Graff, K.F.: Wave Motion in Elastic Solids. Dover, New York (1975)
2. Schmidt, R.: Multiple emitter location and signal parameter estimation. *IEEE Trans. Antennas and Propag.* **34**(3), 276–280 (1986)
3. Roy, R., Kailath, T.: Esprit-estimation of signal parameters via rotational invariance techniques. *IEEE Trans. Acoust. Speech Signal Process.* **37**(7) 984–995 (1989)
4. Önsay, T., Haddow, A.G.: Wavelet transform analysis of transient wave-propagation in a dispersive medium. *J. Acoust. Soc. Am.* **95**(3), 1441–1449 (1994)
5. Feeny, B.F.: Complex modal decomposition for estimating wave properties in one-dimensional media. *J. Vib. Acoust.* **135**(3), 031010 (2013)
6. Feeny, B.F.: A complex orthogonal decomposition for wave motion analysis. *J. Sound Vib.* **310**(1–2), 77–90 (2008)
7. Caldwell Jr. RA, Feeny B. Characterizing Wave Behavior in a Beam Experiment by Using Complex Orthogonal Decomposition. *ASME J. Vib. Acoust.* (2016). doi: [10.1115/1.4033268](https://doi.org/10.1115/1.4033268)
8. Narisetti, R.K., Leamy, M.J., Ruzzene, M.: A perturbation approach for predicting wave propagation in one-dimensional nonlinear periodic structures. *ASME J. Vib. Acoust.* **132**(3), 031001 (2010)
9. Narisetti, R., Ruzzene, M., Leamy, M.: A perturbation approach for analyzing dispersion and group velocities in two-dimensional nonlinear periodic lattices. *J. Vib. Acoust.* **133**(6), 061020 (2011)
10. Lumley, J.: Stochastic Tools in Turbulence. Academic, New York (1970)
11. Berkooz, G., Holmes, P., Lumley, J.L.: The proper orthogonal decomposition in the analysis of turbulent flows. *Annu. Rev. Fluid Mech.* **25**, 539–575 (1993)
12. Kosambi, D.: Statistics in function space. *J. Indian Math. Soc.* **7**, 76–88 (1943)
13. Feeny, B.F.: On proper orthogonal coordinates as indicators of modal activity. *J. Sound Vib.* **255**(5), 805–817 (2002)

Chapter 22

Approximate General Responses of Multi-Degree-of-Freedom Systems with Parametric Stiffness

Gizem Acar and Brian F. Feeny

Abstract In the work presented, the solutions and stability of multi-degree-of-freedom Mathieu-type systems are investigated. An approach combining Floquet theory with harmonic balance is used to find the system response. The assumed Floquet-type solution consists of a product between an exponential part and a periodic part. The periodic part is approximated with a finite number of harmonics, and without making further assumptions, this solution is directly applied to the original differential equations of motion. A harmonic balance analysis results in an eigenvalue problem. The characteristic exponents are the eigenvalues and the corresponding eigenvectors provide the Fourier coefficients of the harmonic part of the solution. By examining the solutions of the eigenvalue problem, the initial conditions response, frequency content, and stability characteristics can be determined. The approach is applied to two and three DOF examples. For a few parameter sets, the results obtained from this method are compared to the numerical solutions.

Keywords Parametric stiffness • Mathieu equation • Floquet theory • Harmonic balance • Stability

22.1 Introduction

Numerous mechanical systems have parametric excitation characteristics [1–4]. The Mathieu equation represents a single-degree-of-freedom (SDOF) system with parametric stiffness, and has been studied using a variety of methods. Perturbation methods, such as application of a second-order multiple scales [3], and the method of van der Pol [4] have been used to determine stability characteristics. Floquet theory has also been used to approach the Mathieu equation. It makes use of a solution separated into an exponential part and a periodic part, such as $x(t) = e^{\hat{\mu}t}p(t)$. The theory proves that the solution is periodic on the stability boundaries. Therefore, without solving for the general response itself, stability regions can be obtained by assuming a periodic solution [5–8]. System identification methods have been used to investigate the response characteristics of the time-periodic systems. Allen et al. used an output-only system identification method to find the Floquet exponents and the modal functions of the damped Mathieu equation [9].

In this study, general solutions to Mathieu-type multi-degree-of-freedom (MDOF) systems of the form

$$\mathbf{M}\ddot{\mathbf{x}} + \mathbf{K}(t)\mathbf{x} = \mathbf{0}, \quad (22.1)$$

are investigated, where \mathbf{x} is an $d \times 1$ vector of coordinate displacements, where d is the number of degrees of freedom, and \mathbf{M} and $\mathbf{K}(t)$ are the mass and time-varying stiffness matrices. The aim is to obtain a general initial condition response as well as the stability characteristics of the system. To this end, instead of assuming a periodic solution, a Floquet-type solution is assumed as

$$\underline{x}_r = e^{i\mu_r t} \sum_{k=-n}^n \underline{c}_k^{(r)} e^{ik\omega t}, \quad (22.2)$$

where the index r distinguishes between $2d$ independent Floquet solution terms for an d -degree-of-freedom system. The assumed solution is plugged into the equations of motion, and by applying harmonic balance, the characteristic exponents,

G. Acar (✉) • B.F. Feeny
Michigan State University, East Lansing, MI, USA
e-mail: dilbergi@egr.msu.edu; feeny@egr.msu.edu

μ_r and associated Fourier coefficients, $\underline{c}_k^{(r)}$, are determined. The response to an arbitrary initial condition can then be found by considering a linear combination of the \underline{x}_r . The same method was applied on the SDOF undamped and damped Mathieu equations [10].

22.2 Analysis

We demonstrate the response analysis procedure can be explained by going over example MDOF systems, namely a two DOF case and a three DOF system.

22.2.1 Two-Degree-of-Freedom Example

To this end, a mass-spring chain as shown in Fig. 22.1, with periodic stiffness is used. The equations of motion are

$$\ddot{x}_1 + k(2x_1 - x_2) = 0, \quad (22.3)$$

$$\ddot{x}_2 + k(2x_2 - x_1) = 0, \quad (22.4)$$

where $m = 1$ and $k = 1 + \delta \cos \omega t$. For the case of $\delta = 0$, the system has constant coefficients and the modal frequencies are well defined as $\omega_1 = 1$ and $\omega_2 = \sqrt{3}$, with mode shapes $\underline{u}_1 = (1 \ 1)^T$ and $\underline{u}_2 = (1 \ -1)^T$. To find the response, a Floquet type solution with finite harmonics, as given in Eq. (22.2), is assumed and plugged into the equations. Specifically, in this example, we seek $x_1(t) = e^{i\mu t} \sum_{k=-n}^n c_{1,k} e^{ik\omega t}$ and $x_2(t) = e^{i\mu t} \sum_{k=-n}^n c_{2,k} e^{ik\omega t}$. Applying harmonic balance, governing equations for $c_{j,k}$'s are found. In matrix form,

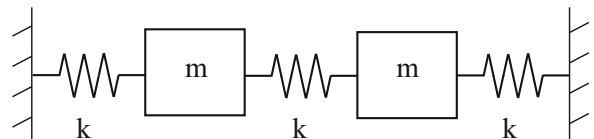
$$\mathbf{A}\underline{c} = \begin{bmatrix} A_{11} & A_{12} \\ A_{21} & A_{22} \end{bmatrix} \begin{pmatrix} \underline{c}_1 \\ \underline{c}_2 \end{pmatrix} = \begin{pmatrix} 0 \\ 0 \end{pmatrix}, \quad (22.5)$$

where $\underline{c}_j = [\dots c_{j,-1} \ c_{j,0} \ c_{j,1} \ \dots]^T$, and A_{ij} 's correspond to $(2n+1) \times (2n+1)$ block matrices. Since there is a structural symmetry in this example, the coefficient matrix is symmetric with $A_{11} = A_{22}$ and $A_{12} = A_{21}$ as given below.

$$A_{11} = A_{22} = \begin{bmatrix} \ddots & \ddots & 0 & \dots & 0 \\ \ddots & 2 - (\mu - \omega)^2 & \delta & \ddots & \vdots \\ 0 & \delta & 2 - \mu^2 & \ddots & \vdots \\ \vdots & \ddots & \ddots & 2 - (\mu + \omega)^2 & \delta \\ 0 & \dots & 0 & \delta & \ddots \end{bmatrix}, \quad (22.6)$$

$$A_{12} = A_{21} = \begin{bmatrix} -1 & -\delta/2 & 0 & \dots & 0 \\ -\delta/2 & -1 & -\delta/2 & \ddots & \vdots \\ 0 & \ddots & \ddots & \ddots & 0 \\ \vdots & \ddots & \ddots & \ddots & -\delta/2 \\ 0 & \dots & 0 & -\delta/2 & -1 \end{bmatrix}. \quad (22.7)$$

Fig. 22.1 A two DOF spring-mass chain



To have a nonzero \underline{c} solution, the determinant of the coefficient matrix, $A(\mu)$, must be zero. This constitutes a characteristic equation for μ , in terms of the parameters δ and ω . The characteristic equation yields $2d(2n + 1)$ roots for μ ($d = 2$ in this example), where n is the number of assumed harmonics. Yet, there are effectively $2d$ principal roots, and the other ones are related to the principal roots via the relation $\mu_i = \mu_j \pm k\omega$. Notice that these extra roots do not contribute to extra solutions, since the corresponding exponential part can be written as $e^{i\mu_j t} e^{ik\omega t}$ and the second part can be plugged into the periodic part.

By inserting $\mu_j \delta$ into the coefficient matrix, solutions for $\underline{c}^{(j)}$'s can be found as the null space of $A(\mu_j)$. The relations $A_{11} = A_{22}$ and $A_{12} = A_{21}$ lead to the relation $\underline{c}_1 = \underline{c}_2$. Furthermore, the principal roots come in pairs as $\mu_{j+1} = -\mu_j$, and this leads to the diagonal elements $A(\mu_{j+1})$ be the same as those of $A(\mu_j)$, but in reverse order. This relation results in a c_{j+1} having the same elements as c_j , in the reversed order.

The roots of the characteristic equation give information about both the stability and the frequency content of the solution. If any one of the roots has a negative imaginary part, the exponential part makes the solution grow unstable, whereas if all roots have a non-negative imaginary part, the solution is bounded. More specifically, if the roots are real, the solution is either periodic or quasi-periodic. The stability transition curves for the 2DOF mass-spring chain are plotted by evaluating the imaginary parts of the characteristic roots, as given in Fig. 22.2.

The frequency content can be determined by combining the frequencies of the exponential part and the periodic part, as $|Re(\mu) \pm k\omega|$. For this 2 DOF system, there are four distinct μ 's as $\mu_2 = -\mu_1$ and $\mu_4 = -\mu_3$. In the frequency response, half of the frequencies are determined by the first pair, and the other half are determined by the other pair. In this case, symmetric initial conditions (i.e. $x_1(0) = x_2(0)$, $\dot{x}_1(0) = \dot{x}_2(0)$) excite the frequencies associated with μ_1 and μ_2 , whereas anti-symmetric initial conditions (i.e. $x_1(0) = -x_2(0)$, $\dot{x}_1(0) = -\dot{x}_2(0)$) excite those associated with μ_3 and μ_4 . These two responses can be used to represent the response in terms of “modal components”, such as $\underline{x}(t) = a_1 \underline{x}^{(1)}(t) + a_2 \underline{x}^{(2)}(t)$, where a_1 and a_2 are to be determined from the initial conditions. As an example, for $\omega = 2.3$ and $\delta = 0.4$, the characteristic roots are $\mu_1 = -\mu_2 = 0.599$ and $\mu_3 = -\mu_4 = 1.035$. The symmetric initial conditions excite the frequencies $|1.035 \pm 2.3k|$ whereas the anti-symmetric initial conditions excite the frequencies $|0.599 \pm 2.3k|$, as shown in FFT plots of m_1 in Fig. 22.3. Arbitrary initial conditions produce responses with all of the frequencies contributing to the fast Fourier transforms (FFTs) plotted in Fig. 22.3. The eigenvectors are $\underline{c}^{(1)} = [0.03179 \quad 0.68947 \quad -0.1527 \quad -0.01701 \quad -0.000425]^T$ and $\underline{c}^{(3)} = [0.003834 \quad 0.22452 \quad 0.67037 \quad 0.013249 \quad 0.000086]^T$. Since the fifth elements in both vectors are small, the fifth frequencies ($\mu_j + 2\omega$) are not visible in the FFT plots.

The 2DOF spring-mass chain was analyzed with $n = 2$ harmonics, for different sets of parameters and initial conditions. The results were compared to those obtained from a numerical study, and the response and FFT plots are given in Figs. 22.4 and 22.5 for an example.

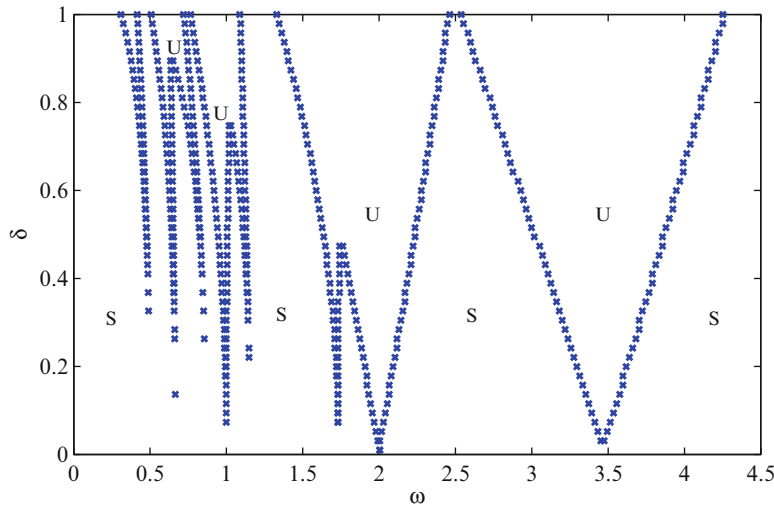


Fig. 22.2 Stability regions for the 2 DOF mass spring chain

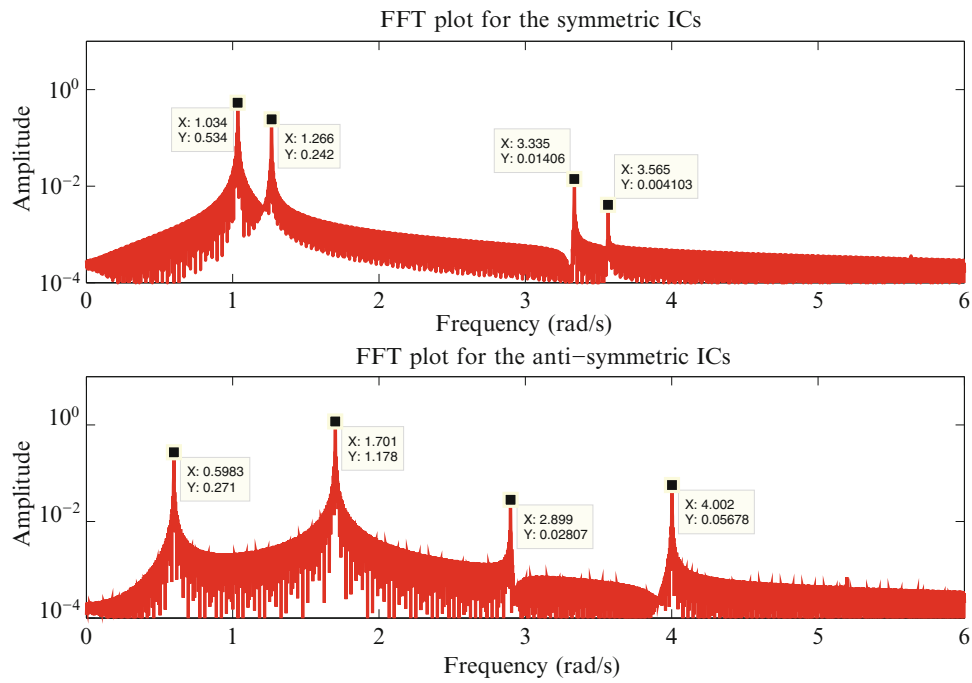


Fig. 22.3 Modes excited by the symmetric and the anti-symmetric initial conditions, for $\omega = 2.3$ and $\delta = 0.4$

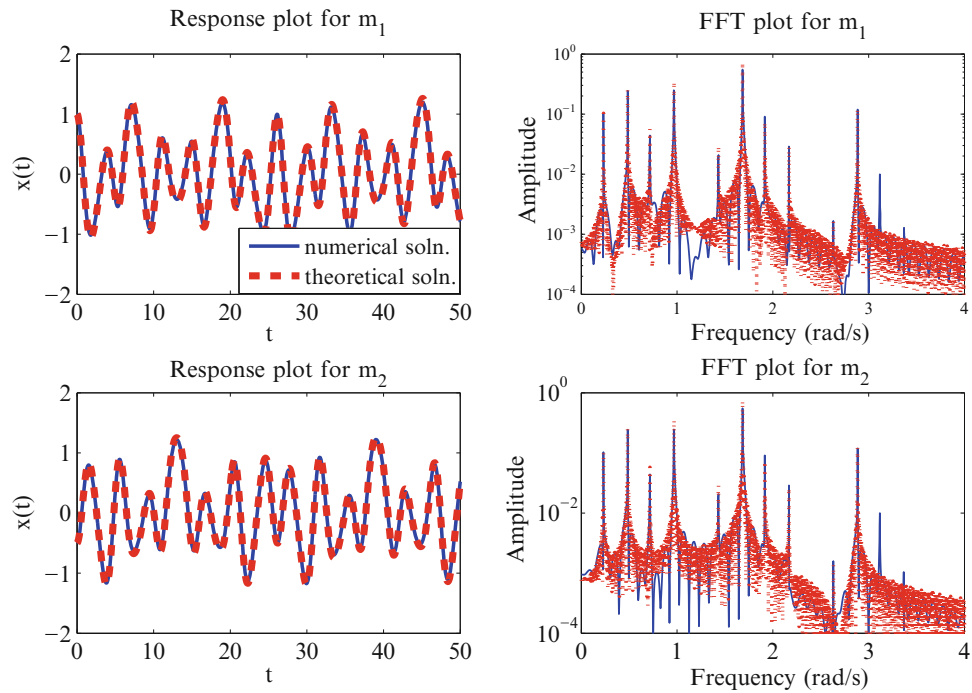


Fig. 22.4 Response and FFT plots for $n = 2$, $\omega = 1.2$, $\delta = 0.6$, $\mathbf{x}(0) = [1 \quad -0.5]^T$ and $\dot{\mathbf{x}}(0) = [0 \quad 0]^T$

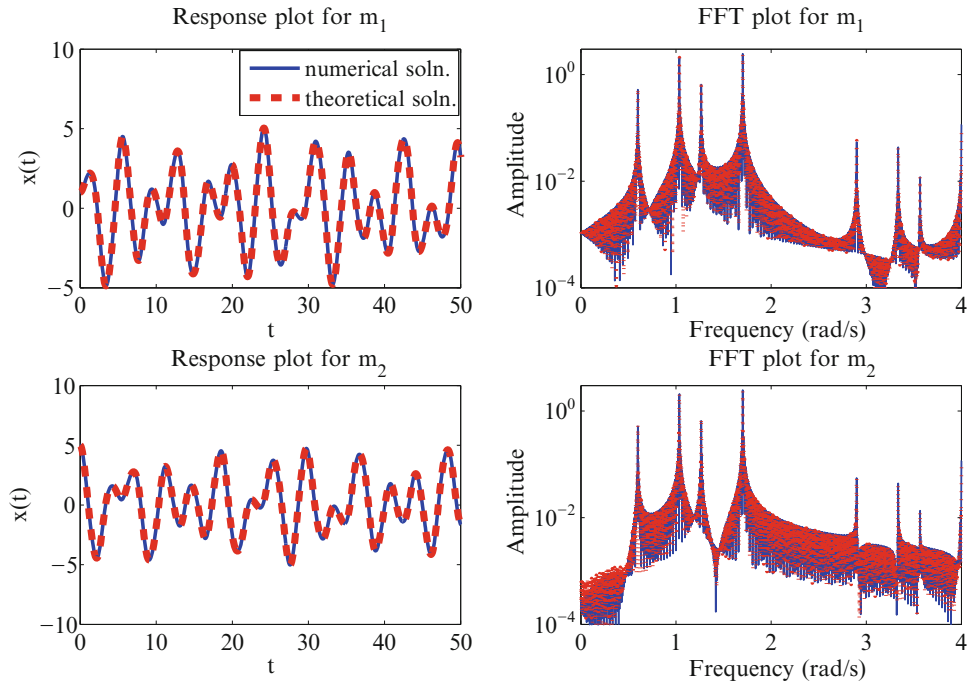


Fig. 22.5 Response and FFT plots for $n = 2$, $\omega = 2.3$, $\delta = 0.4$, $\mathbf{x}(0) = [1 \ 5]^T$ and $\dot{\mathbf{x}}(0) = [0 \ 0]^T$

22.2.2 Three-Degree-of-Freedom Example

Another MDOF system with parametric stiffness is given in Fig. 22.6. Two masses are connected to a main mass through parametric springs, which are driven out of phase, and the main mass is grounded with a regular spring. This system is analogous to a horizontal-axis turbine with two blades under a constant rotation rate, where the main mass represents the hub, and the other masses represent the blades.

For a normalized system, the parameters are assumed as $m_1 = m_2 = 1$, $M = \beta m_2$, $K = \gamma$, $k_1 = 1 - \delta \cos \omega t$ and $k_2 = 1 + \delta \cos \omega t$. Equations of motion representing this system are

$$\begin{aligned} \ddot{x}_1 + (1 - \delta \cos \omega t)(x_1 - X) &= 0 \\ \ddot{x}_2 + (1 + \delta \cos \omega t)(x_2 - X) &= 0 \\ \beta \ddot{X} - (1 - \delta \cos \omega t)x_1 - (1 + \delta \cos \omega t)x_2 + (2 + \gamma)X &= 0. \end{aligned} \quad (22.8)$$

Plugging the approximate solution given in Eq.(22.2) into the Eqs. (22.8), and applying the steps explained in the previous section, characteristic exponents and the corresponding eigenvectors are found. By examining the imaginary parts of the characteristic exponents, the stability regions of the 3DOF system are plotted for $\gamma = 1$, $\beta = 1$ in Fig. 22.7.

In order to find the “modal solutions”, as done in the previous section, the following procedure is applied.

There are six principal characteristic roots and so the general solution can be written as

$$\underline{\mathbf{x}}(t) = \sum_{j=1}^6 a_j \underline{\mathbf{x}}_j(t), \quad (22.9)$$

where

$$\underline{\mathbf{x}}_j(t) = \sum_{k=-n}^n c_{j,k} e^{ik\omega t}. \quad (22.10)$$

Fig. 22.6 A 3 DOF mass-spring system

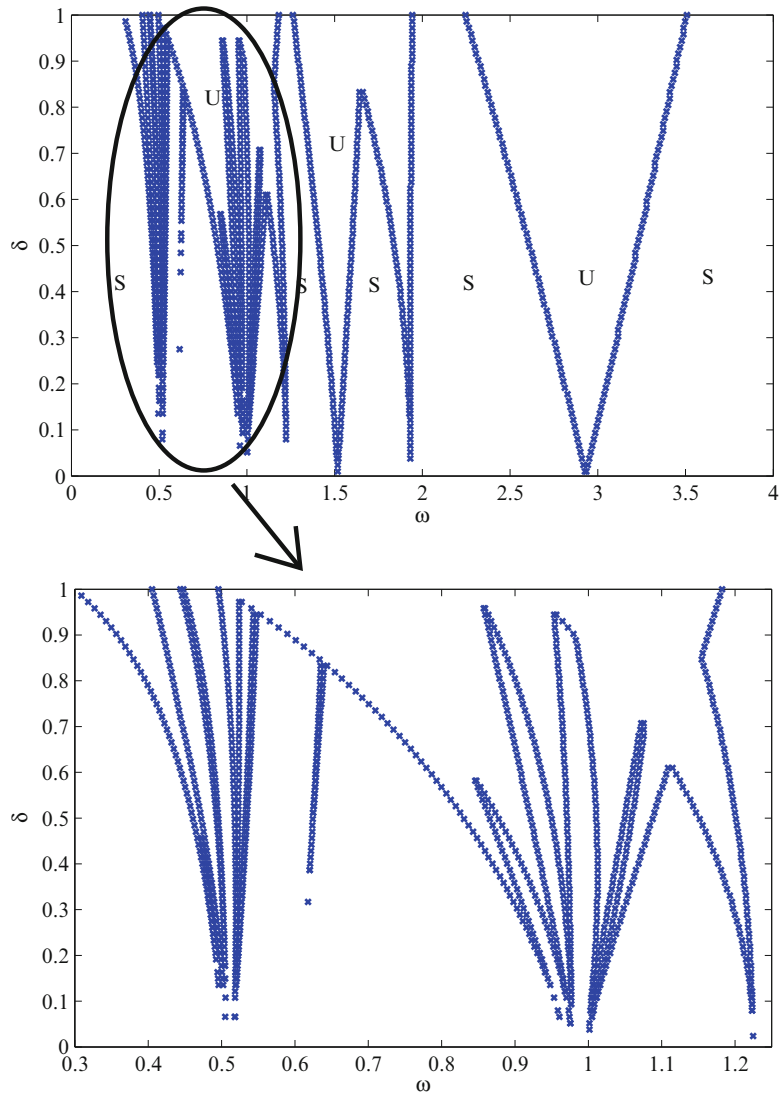
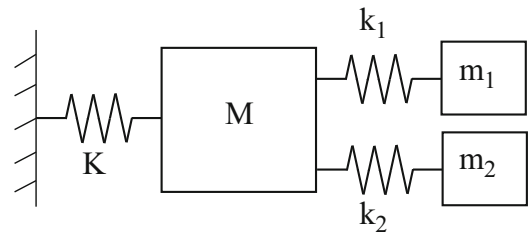


Fig. 22.7 Stability regions for the 3 DOF mass spring system, for $\beta = 1$ and $\gamma = 1$

Arbitrary initial conditions can be expressed as a set of linear equations in terms of the constants a_j , as

$$\begin{bmatrix} \underline{x}_0 \\ \underline{\dot{x}}_0 \end{bmatrix} = \begin{bmatrix} \underline{x}_1(0) & \dots & \underline{x}_6(0) \\ \underline{\dot{x}}_1(0) & \dots & \underline{\dot{x}}_6(0) \end{bmatrix} \begin{bmatrix} a_1 \\ \vdots \\ a_6 \end{bmatrix}. \tag{22.11}$$

Notice that the initial condition $\begin{bmatrix} \underline{x}_0^T & \underline{\dot{x}}_0^T \end{bmatrix}^T = \begin{bmatrix} \underline{x}_j(0)^T & \underline{\dot{x}}_j(0)^T \end{bmatrix}^T$ results in $a_j = 1$ and $a_{k \neq j} = 0$. Therefore a scalar multiple of each column can be used as an initial condition to find the separate modal functions. Then, by writing an initial condition as a linear combination of $\begin{bmatrix} \underline{x}_j(0)^T & \underline{\dot{x}}_j(0)^T \end{bmatrix}^T$'s, the response can be found as the same linear combination of the corresponding modal functions.

The initial condition responses and FFT plots were obtained assuming $n = 2$ harmonics, for various parameter sets, and were compared to those obtained from a numerical study, as given in Figs. 22.8 and 22.9.

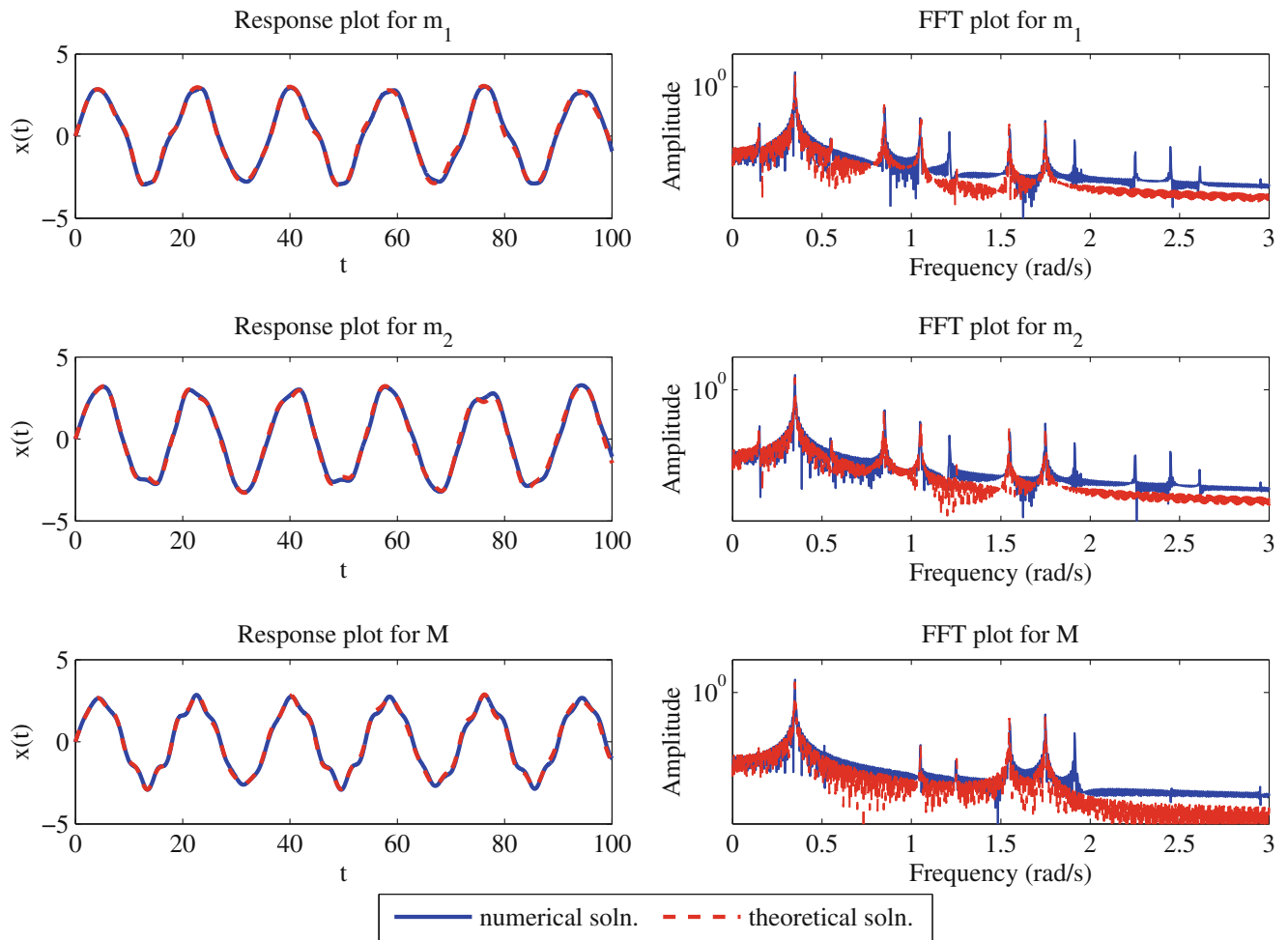


Fig. 22.8 Response and FFT plots for $n = 2$, $\omega = 0.7$, $\delta = 0.5$, $\gamma = 0.4$, $\mathbf{x}(0) = [0 \ 0 \ 0]^T$ and $\dot{\mathbf{x}}(0) = [1 \ 1 \ 1]^T$

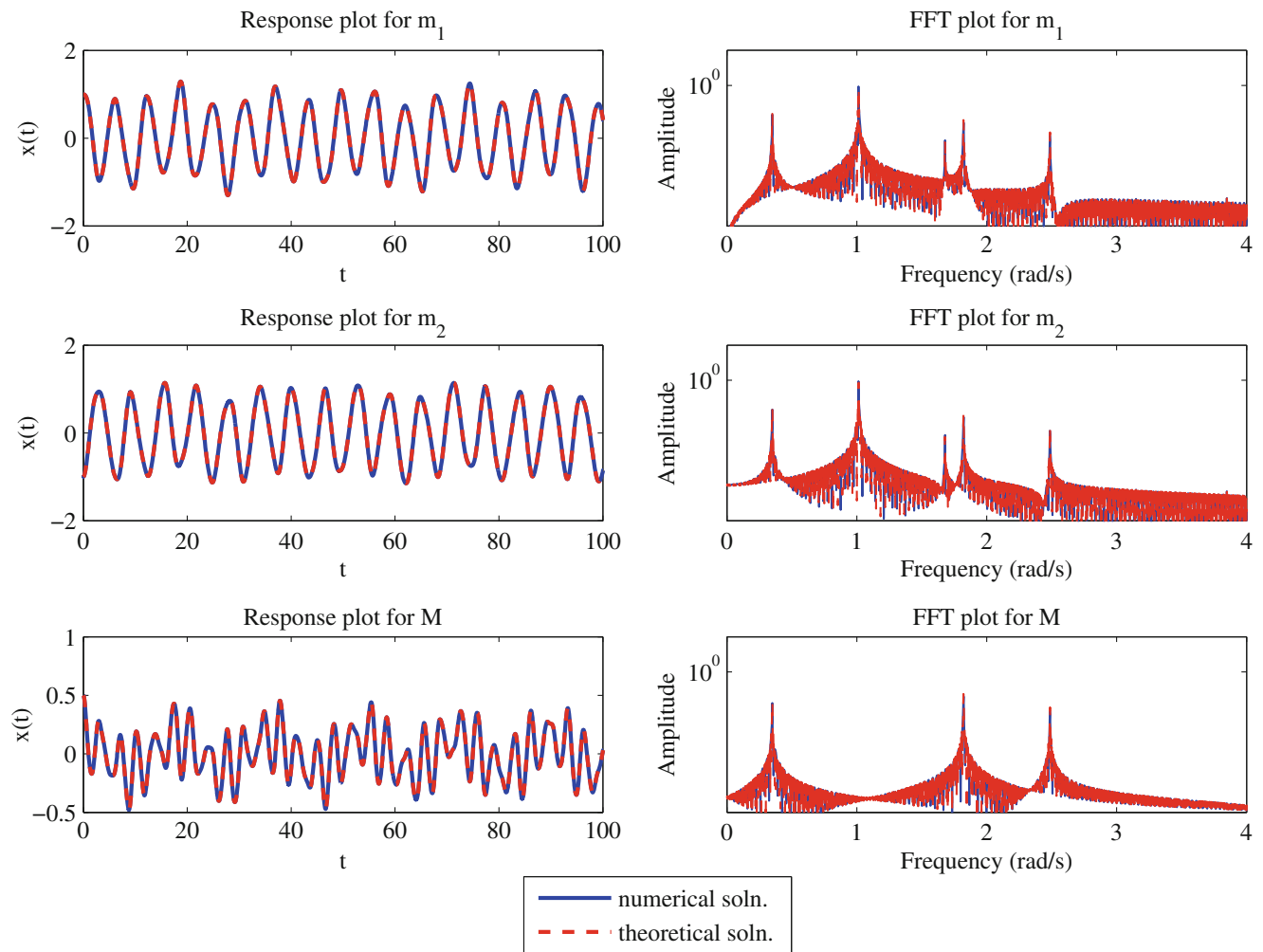


Fig. 22.9 Response and FFT plots for $n = 2$, $\omega = 3.5$, $\delta = 0.3$, $\gamma = 0.4$, $\mathbf{x}(0) = [1 \quad -1 \quad 0.5]^T$ and $\dot{\mathbf{x}}(0) = [0 \quad 0 \quad 0]^T$

22.3 Discussion

In the MDOF examples we presented, close examination of the stability wedges suggests that they may be based at $\omega = (\omega_i + \omega_j)/N$, where N is a positive integer. For the two-DOF case, with $\omega_1 = 1$ and $\omega_2 = \sqrt{3} = 1.73$, we see the major wedges at $2\omega_1 = 2$ and $2\omega_2 = 3.46$, representing the subharmonic instability of each “mode.” The symmetry in the two-DOF model drives the resonances such that $\omega_i = \omega_j$ (i.e. $i = j$) in the suggested instability condition. We also see the other slender instability wedges for mode one at $\omega = \omega_1$, $\omega = 2/3$, and even $\omega = 1/2$, and likewise for mode two at $\omega = \omega_2$, $\omega = 2\omega_2/3 \approx 1.15$, and $\omega = \omega_2/2 \approx 0.87$. In the three-DOF system, for $\beta = 1$ and $\gamma = 1$, the modal frequencies are $\omega_1 = 0.518$, $\omega_2 = 1$, $\omega_3 = 1.932$. We see two major subharmonic instability wedges originating at frequencies $\omega \approx \omega_2 + \omega_3 = 2.93$ and $\omega \approx \omega_2 + \omega_1 = 1.52$. Some of the superharmonic wedges are also based at frequencies that match the pattern, such as $\omega_3 = 1.93$, $(\omega_1 + \omega_3)/2 = 1.22$, $\omega_1 = 1$, $(\omega_2 + \omega_3)/3 = 0.98$, $\omega_3/2 = 0.97$, $(\omega_1 + \omega_3)/2 = 1.22$, $\omega_1 = 0.52$, and $(\omega_1 + \omega_2)/3 = 0.51$. Simulations were done at various parameter values to check consistency. For example, at $\delta = 0.3$ and $\omega = 3.1$, the simulation was unstable, while at $\omega = 3.2$, the simulation was stable, consistent with the stability wedge in Fig. 22.7. Resonance conditions based closely at 0.97 and 0.98 are consistent with the two slender wedges seen at that location in the figure. Similarly, resonance conditions based at 0.51 and 0.52 match a pair of slender wedges seen there. There is a second wedge near $\omega = 1$ that is unaccounted for. A third subharmonic instability seems not to be evident. Simulations of the three-DOF system with other values of γ (not shown) show the same kinds of trends.

Based on the Floquet solution as a linear combination of terms of the form $e^{i\mu t} \mathbf{p}(t)$, where $\mathbf{p}(t)$ is a periodic function, it is clear that initial conditions can be specified such that only one of these terms is active. In this sense, we can call them

“modal responses”. But the $\mathbf{p}(t)$ are not synchronous, and not described using shape vectors like traditional modes. We have demonstrated such independent oscillation solutions in the two examples given here. We might consider whether a coordinate transformation exists such that a given modal response can be isolated as a single degree of freedom, and then whether each modal degree of freedom is parametrically excited and follows the stability pattern of a Hill’s equation (or more generally an Ince equation, which has a periodic coordinate transformation between it and a Hill’s equation [11]). Complicating these speculations is the entanglement of the reference modal frequencies (those from the $\delta = 0$ system) in the excited system’s stability wedge patterns.

The analysis presented here involves the solution to a nonstandard eigenvalue problem in the form of Eq. (22.5), in which matrix \mathbf{A} includes elements with quadratic μ terms. The resulting characteristic equation is a polynomial of degree $2d(2n+1)$ in μ . There may be computational limits on finding symbolic solutions for the μ as the degree of freedom, d , or the number of harmonics, n , increases. Though $n = 2$ harmonics was able to predict the response for the systems analyzed above.

22.4 Conclusions

In this work, a procedure for finding an approximate solution to a MDOF system with parametric stiffness has been represented. A Floquet-type solution composed of an exponential and a periodic part was assumed, and applying harmonic balance to the system equations, an eigenvalue problem resulted, with eigenvalues that provide the Floquet characteristic exponents and the eigenvectors that provide the Fourier coefficients. The initial-conditions response was expressed in terms of independent modal components, which were demonstrated by separating the initial conditions exciting the modes associated with separate characteristic exponents. The stability transition curves were obtained by examining the imaginary parts of the characteristic exponents. The response and FFT plots were generated for various parameters and initial conditions, and compared to numerical results for validation.

The method used in this study was applied to determine the initial condition response as well as the stability of the system, whereas the common analyses reflect interest only in the latter. The procedure is to be applied on three-blade wind turbine models to find the response characteristics.

Acknowledgements This project is funded by the National Science Foundation, under grant CMMI-1335177.

References

1. Ruby, L.: Applications of the Mathieu equation. *Am. J. Phys.* **64**(1), 39–44 (1996)
2. Li, Y., Fan, S., Guo, Z., Li, J., Cao, L., Zhuang, H.: Mathieu equation with application to analysis of dynamic characteristics of resonant inertial sensors. *Commun. Nonlinear Sci. Numer. Simul.* **18**(2), 401–410 (2013)
3. Ramakrishnan, V., Feeny, B.F.: Resonances of a forced Mathieu equation with reference to wind turbine blades. *J. Vib. Acoust.* **134**(6), 064501 (2012)
4. Inoue, T., Ishida, Y., Kiyohara, T.: Nonlinear vibration analysis of the wind turbine blade (occurrence of the superharmonic resonance in the out of plane vibration of the elastic blade). *J. Vib. Acoust.* **134**(3), 031009 (2012)
5. Ishida, Y., Inoue, T., Nakamura, K.: Vibration of a wind turbine blade (theoretical analysis and experiment using a single rigid blade model). *J. Environ. Eng.* **4**(2), 443–454 (2009)
6. McLachlan, N.W.: *Theory and Application of Mathieu Functions*. Dover, New York (1961)
7. Peterson, A., Bibby, M.: *Accurate Computation of Mathieu Functions*. Morgan & Claypool, San Rafael (2013)
8. Hodge, D.B.: *The Calculation of the Eigenvalues and Eigenfunctions of Mathieu’s Equation*, vol. 1937. National Aeronautics and Space Administration, Washington (1972)
9. Allen, M.S., Sracic, M.W., Chauhan, S., Hansen, M.H.: Output-only modal analysis of linear time-periodic systems with application to wind turbine simulation data. *Mech. Syst. Signal Process.* **25**(4), 1174–1191 (2011)
10. Acar, G., Feeny, B.: Floquet-based analysis of general responses of the Mathieu equation. *J. Vib. Acoust.* (2015, under review)
11. Rand, R.: Lecture notes on nonlinear vibrations. Published online (2012). <http://www.math.cornell.edu/~rand/randdocs/nlvibe52.pdf>

Chapter 23

Harmonic Forcing of a Two-Segment Elastic Rod

Arnaldo J. Mazzei Jr. and Richard A. Scott

Abstract This work is on the motions of non-homogeneous elastic rods. In a previous work the natural frequencies and associated mode shapes were determined for a two-segment rod, in which the geometric and material properties were constant in each segment. Here the steady state response due to harmonic forcing is investigated using two strategies. The first employs the exact displacement equations. For harmonic forcing in time, the response is periodic and general solutions to the resulting differential equations can, in principle, be found for each segment. The constants involved are found from boundary and interface conditions and then response, as a function of forcing frequency, can be obtained. The procedure is cumbersome and problematic if the forces vary spatially, due to difficulties in finding “particular integrals”. An alternative method is developed in which geometric and material discontinuities are modeled by continuously varying functions (here logistic functions). This leads to a single differential equation with variable coefficients, which is solved numerically using MAPLE®’s PDE solver. For free-fixed boundary conditions and spatially constant force good agreement is found between the two methods, lending confidence to the continuous varying approach, which is then used to obtain response for spatially varying forces.

Keywords Non-homogeneous rods • Layered structures • Logistic functions • Rod vibrations

Nomenclature

A	Cross-section area (A_i , cross-section area for i -th material)
A_r	Non-dimensional parameter $A_r = A_2/A_1$
B_i	Constants of integration
c_i	Wave speed $c_i = \sqrt{E/\rho_i}$
c_r	Non-dimensional parameter $c_r = c_1/c_2$
E	Young’s modulus (E_i Young’s modulus for i -th material)
E_r	Non-dimensional parameter $E_r = E_2/E_1$
F_i	Spatial functions
f_i	Forcing functions (force per unit length q_i in the continuously varying approach)
g_i	Non-dimensional functions for material/geometrical properties
L	Length of rod, $L = L_1 + L_2$
Q_0	Non-dimensional parameter $Q_0 = F_0L/A_1E_1$
R_i	Spatial functions
t	Time
u	Longitudinal displacement of the rod
w	Non-dimensional longitudinal displacement of the rod, $w = u/L$
x	Longitudinal coordinate
x_D	Non-dimensional longitudinal coordinate, $x_D = x/L$
α	Numerical parameter for length of individual cell components of the layered rod, $L = (1 + \alpha)L_1$

A.J. Mazzei Jr. (✉)
Department of Mechanical Engineering, C. S. Mott Engineering and Science Center, Kettering University, 1700 University Avenue,
Flint, MI 48504, USA
e-mail: amazzei@kettering.edu

R.A. Scott
University of Michigan, Herbert H. Dow Building, 2300 Hayward, Ann Arbor, MI 48109, USA

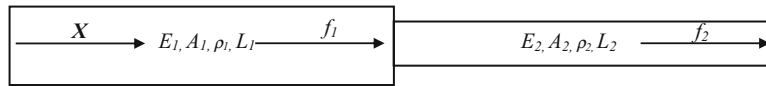


Fig. 23.1 Two-segment rod

β	Non-dimensional parameter, $\beta = \sqrt{L^2 \Omega_0^2 \rho_1 / E_1}$
ρ	Mass density (ρ_i , density value for i -th material)
τ	Non-dimensional time, $\tau = \Omega_0 t$
ω	Natural frequency of longitudinal vibrations for the rod
ω_d	Non dimensional natural frequency of longitudinal vibrations for the rod (ν), $\nu = \omega / \Omega_0$
Ω_0	Reference frequency

23.1 Introduction

This work is the second one of a series [1] on longitudinal vibrations of layered solids. Of primary interest is the analysis, both theoretical and numerical, of layered solids, for vibration and wave control. The media of interest include solids with continuous variation of properties, such as Functionally Graded Materials (FGM), and those with discrete layering. Examples of studies dealing with solids composed by discrete layers can be found in [2–5]. A larger number of references can be found in a recent review article [6]. Numerical approaches to waves in non-homogeneous media can be found in [7]. The current work treats a one-dimensional uniaxial problem composed of two layers of different materials bonded together. The main objective is the determination of frequency response functions (FRFs) when the solid is exposed to different types of forcing functions and boundary conditions. Analytical solutions can be found via a transfer matrix method, requiring solutions for each layer and matching these across interfaces. Also, particular integrals for the complete solution must be obtained. This approach can be lengthy and sometimes mathematically untraceable. Here an alternate method is used, in which the layered profile is modeled by continuously varying functions. The resulting partial differential equation is solved via direct numerical analysis using MAPLE[®] software. Maximum amplitudes are monitored and respective numerical FRFs are generated. For cases where analytical solutions can be obtained, numerical results are in excellent agreement with those.

23.2 Basic Problem

Shown in Fig. 23.1 is a two-segmented elastic rod with properties as indicated. Consider this layered structure in which E , ρ , and A vary in a discontinuous fashion. The segments are under loads f_1 and f_2 (force per unit length).

In the following strategies for obtaining the steady state response due to harmonic forcing are investigated.

23.3 Analytic Solutions

In this section analytic solutions are derived using standard rod theory.

Consider the two-segmented rod shown in Fig. 23.1. In general the axial displacement $u(x, t)$ of a segment must satisfy the equation:

$$\frac{\partial}{\partial x} \left(A(x)E(x) \frac{\partial u(x, t)}{\partial x} \right) + f(x, t) = A(x)\rho(x) \frac{\partial^2 u(x, t)}{\partial t^2} \quad (23.1)$$

where $E(x)$, $A(x)$ and $\rho(x)$ are functions describing the longitudinal variations of Young's modulus, cross-sectional area and mass density, respectively.

The longitudinal displacement equation of motion for each segment (“i-th” segment) is:

$$\frac{\partial}{\partial x} \left(A_i E_i \frac{\partial u_i(x, t)}{\partial x} \right) + f_i(x, t) = A_i \rho_i \frac{\partial^2 u_i(x, t)}{\partial t^2}, \quad i = 1, 2, \dots \quad (23.2)$$

where f_i are forces per unit length.

For harmonic forcing with frequency ω :

$$f_i(x, t) = F_i(x) \sin(\omega t) \quad (23.3)$$

Assuming solutions of the form:

$$u_i(x, t) = R_i(x) \sin(\omega t) \quad (23.4)$$

leads to

$$\frac{d}{dx} \left(A_i E_i \frac{dR_i(x)}{dx} \right) + F_i(x) = -A_i \rho_i \omega^2 R_i(x) \quad (23.5)$$

or for A_i, E_i constant in each segment:

$$\frac{d^2 R_i(x)}{dx^2} + \frac{\omega^2}{c_i^2} R_i(x) = -\frac{F_i(x)}{A_i E_i} \quad (23.6)$$

where $c_i = \sqrt{\frac{E_i}{\rho_i}}$.

General solutions to the linear differential equation (23.6) can be written as:

$$R_i(x) = R_{ih}(x) + R_{ip}(x) \quad (23.7)$$

where $R_{ih}(x)$ are the general solutions to the homogeneous equations and $R_{ip}(x)$ are “particular integrals”.

For Eq. (23.6),

$$R_{1h}(x) = B_1 \cos\left(\frac{\omega}{c_1} x\right) + B_2 \sin\left(\frac{\omega}{c_1} x\right) \quad (23.8)$$

$$R_{2h}(x) = B_3 \cos\left(\frac{\omega}{c_2} x\right) + B_4 \sin\left(\frac{\omega}{c_2} x\right) \quad (23.9)$$

For arbitrary forcing $F_i(x)$, finding tractable particular integrals can pose a problem. In the following several examples are considered.

23.3.1 Constant Spatial Force

Here attention is restricted to constant spatial forcing: $F_1(x) = F_{1,0}$, $F_2(x) = F_{2,0}$; $F_{1,0}, F_{2,0}$ constants.

Then

$$R_{1p}(x) = -\frac{F_{1,0} c_1^2}{A_1 E_1 \omega^2} = -\frac{F_{1,0}}{A_1 \rho_1 \omega^2} \quad (23.10)$$

$$R_{2p}(x) = -\frac{F_{2,0}}{A_2\rho_2\omega^2} \quad (23.11)$$

Now the general solutions can be written:

$$R_1(x) = B_1 \cos\left(\frac{\omega}{c_1}x\right) + B_2 \sin\left(\frac{\omega}{c_1}x\right) - \frac{F_{1,0}}{A_1\rho_1\omega^2} \quad (23.12)$$

$$R_2(x) = B_3 \cos\left(\frac{\omega}{c_2}x\right) + B_4 \sin\left(\frac{\omega}{c_2}x\right) - \frac{F_{2,0}}{A_2\rho_2\omega^2} \quad (23.13)$$

The overall analytic solution requires that the boundary conditions be defined. Two sets are considered below.

23.3.1.1 Free-Fixed Boundary Conditions

For these conditions the stress-free end at $x = 0$ gives: $\left.\frac{dR_1(x)}{dx}\right|_{x=0} = 0$, which leads to $B_2 = 0$. Then Eq. (23.8) becomes:

$$R_{1h}(x) = B_1 \cos\left(\frac{\omega}{c_1}x\right) \quad (23.14)$$

The procedure now is as follows. There are three constants involved in the solutions, namely, B_1 , B_3 and B_4 . These can be determined in terms of the applied forces on applying the boundary conditions: $R_2(x) = 0$, $x = L$ ($L = L_1 + L_2$) and the interface continuity conditions: $R_1(x) = R_2(x)$, $x = L_1$ (displacement continuity), $A_1E_1\frac{dR_1(x)}{dx} = A_2E_2\frac{dR_2(x)}{dx}$, $x = L_1$ (force continuity). The conditions lead to a system of algebraic equations in B_1 , B_2 , B_3 and B_4 (setting $F_{1,0} = F_{2,0} = F_0$):

$$\begin{aligned} B_2 &= 0 \\ B_3 \cos\left(\frac{\omega}{c_2}L\right) + B_4 \sin\left(\frac{\omega}{c_2}L\right) &= \frac{F_0c_2^2}{A_2E_2\omega^2} \\ B_1 \cos\left(\frac{\omega}{c_1}L_1\right) - \frac{F_0c_1^2}{A_1E_1\omega^2} &= B_3 \cos\left(\frac{\omega}{c_2}L_1\right) + B_4 \sin\left(\frac{\omega}{c_2}L_1\right) - \frac{F_0c_2^2}{A_2E_2\omega^2} \\ -\frac{B_1}{c_1} \sin\left(\frac{\omega}{c_1}L_1\right) &= \frac{A_2E_2}{A_1E_1} \left(-\frac{B_3}{c_2} \sin\left(\frac{\omega}{c_2}L_1\right) + \frac{B_4}{c_2} \cos\left(\frac{\omega}{c_2}L_1\right)\right) \end{aligned} \quad (23.15)$$

from which B_1 , B_2 , B_3 and B_4 can be determined.

In non-dimensional matrix form:

$$\begin{bmatrix} 0 & 0 & \cos\left(\frac{\omega_d}{c_r}\right) & \sin\left(\frac{\omega_d}{c_r}\right) \\ 0 & 1 & 0 & 0 \\ \cos\left(\frac{\omega_d}{(1+\alpha)}\right) & 0 & -\cos\left(\frac{\omega_d}{c_r(1+\alpha)}\right) & -\sin\left(\frac{\omega_d}{c_r(1+\alpha)}\right) \\ -\sin\left(\frac{\omega_d}{(1+\alpha)}\right) & 0 & \frac{A_rE_r}{c_r} \sin\left(\frac{\omega_d}{c_r(1+\alpha)}\right) & -\frac{A_rE_r}{c_r} \cos\left(\frac{\omega_d}{c_r(1+\alpha)}\right) \end{bmatrix} \begin{bmatrix} b_1 \\ b_2 \\ b_3 \\ b_4 \end{bmatrix} = \begin{bmatrix} \frac{c_r^2}{A_rE_r} \\ 0 \\ 1 - \frac{c_r^2}{A_rE_r} \\ 0 \end{bmatrix} \frac{Q_0}{\omega_d^2} \quad (23.16)$$

$$\equiv [A] \{B\} = \{F\}$$

where $b_i = \frac{B_i}{L}$, $L_2 = \alpha L_1$, $\omega_d = \frac{\omega}{c_1}L$, $c_r = \frac{c_2}{c_1}$, $A_r = \frac{A_2}{A_1}$, $E_r = \frac{E_2}{E_1}$, $Q_0 = \frac{F_0L}{A_1E_1}$, with $L = (1 + \alpha)L_1$.

Note that natural frequencies can be found on setting the determinant of $[A]$ to zero.

23.3.1.2 Fixed-Fixed Boundary Conditions

For these conditions $R_1(x) = 0$, $x = 0$. This leads to $B_1 = \frac{F_{1,0}}{A_1\rho_1\omega^2} = \frac{F_{1,0}c_1^2}{A_1E_1\omega^2}$. The procedure now is similar to the one given above. There are three constants involved in the solutions, which can be determined from: $R_2(x) = 0$, $x = L$ ($L = L_1 + L_2$),

$R_1(x) = R_2(x)$, $x = L_1$ and $A_1E_1 \frac{dR_1(x)}{dx} = A_2E_2 \frac{dR_2(x)}{dx}$, $x = L_1$. These conditions lead to the following system of algebraic equations ($F_{1,0} = F_{2,0} = F_0$):

$$\begin{aligned} B_1 &= \frac{F_0 c_1^2}{A_1 E_1 \omega^2} \\ B_3 \cos\left(\frac{\omega}{c_2} L\right) + B_4 \sin\left(\frac{\omega}{c_2} L\right) &= \frac{F_0 c_2^2}{A_2 E_2 \omega^2} \\ B_1 \cos\left(\frac{\omega}{c_1} L_1\right) + B_2 \sin\left(\frac{\omega}{c_1} L_1\right) &= B_3 \cos\left(\frac{\omega}{c_2} L_1\right) + B_4 \sin\left(\frac{\omega}{c_2} L_1\right) - \left[\frac{F_0 c_2^2}{A_2 E_2 \omega^2} - \frac{F_0 c_1^2}{A_1 E_1 \omega^2} \right] \\ -B_1 \sin\left(\frac{\omega}{c_1} L_1\right) + B_2 \cos\left(\frac{\omega}{c_1} L_1\right) &= \frac{A_2 E_2}{A_1 E_1} \left(-\frac{c_1 B_3}{c_2} \sin\left(\frac{\omega}{c_2} L_1\right) + \frac{c_1 B_4}{c_2} \cos\left(\frac{\omega}{c_2} L_1\right) \right) \end{aligned} \quad (23.17)$$

In non-dimensional matrix form:

$$\begin{bmatrix} 1 & 0 & 0 & 0 \\ 0 & 0 & \cos\left(\frac{\omega_d}{c_r}\right) & \sin\left(\frac{\omega_d}{c_r}\right) \\ \cos\left(\frac{\omega_d}{(1+\alpha)}\right) & \sin\left(\frac{\omega_d}{(1+\alpha)}\right) & -\cos\left(\frac{\omega_d}{c_r(1+\alpha)}\right) & -\sin\left(\frac{\omega_d}{c_r(1+\alpha)}\right) \\ -\sin\left(\frac{\omega_d}{(1+\alpha)}\right) & \cos\left(\frac{\omega_d}{(1+\alpha)}\right) & \frac{A_r E_r}{c_r} \sin\left(\frac{\omega_d}{c_r(1+\alpha)}\right) & -\frac{A_r E_r}{c_r} \cos\left(\frac{\omega_d}{c_r(1+\alpha)}\right) \end{bmatrix} \begin{bmatrix} b_1 \\ b_2 \\ b_3 \\ b_4 \end{bmatrix} = \begin{bmatrix} 1 \\ \frac{c_r^2}{A_r E_r} \\ 1 - \frac{c_r^2}{A_r E_r} \\ 0 \end{bmatrix} \frac{Q_0}{\omega_d^2} \quad (23.18)$$

$$\equiv [\mathbf{A}] \{\mathbf{B}\} = \{\mathbf{G}\}$$

23.3.2 Variable Spatial Force

For this case take, for example, $F_1(x) = F_{1,0} x^2$ and $F_2(x) = F_{2,0} x^2$. Furthermore take $F_{1,0} = F_{2,0} = F_1$ (all constants). Then

$$R_{1p}(x) = -\frac{F_1 c_1^2 (\omega^2 x^2 - 2c_1^2)}{A_1 E_1 \omega^4} \quad (23.19)$$

$$R_{2p}(x) = -\frac{F_1 c_2^2 (\omega^2 x^2 - 2c_2^2)}{A_2 E_2 \omega^4} \quad (23.20)$$

The general solutions are:

$$R_1(x) = B_1 \cos\left(\frac{\omega}{c_1} x\right) + B_2 \sin\left(\frac{\omega}{c_1} x\right) - \frac{F_1 c_1^2 (\omega^2 x^2 - 2c_1^2)}{A_1 E_1 \omega^4} \quad (23.21)$$

$$R_2(x) = B_3 \cos\left(\frac{\omega}{c_2} x\right) + B_4 \sin\left(\frac{\omega}{c_2} x\right) - \frac{F_1 c_2^2 (\omega^2 x^2 - 2c_2^2)}{A_2 E_2 \omega^4} \quad (23.22)$$

23.3.2.1 Free-Fixed Boundary Conditions

Similar to the constant force case, the stress-free end at $x = 0$ leads to $B_2 = 0$. Following the procedure discussed above one obtains the matrix equation given below.

$$\begin{bmatrix} 0 & 0 & \cos\left(\frac{\omega_d}{c_r}\right) & \sin\left(\frac{\omega_d}{c_r}\right) \\ 0 & 1 & 0 & 0 \\ \cos\left(\frac{\omega_d}{(1+\alpha)}\right) & 0 & -\cos\left(\frac{\omega_d}{c_r(1+\alpha)}\right) & -\sin\left(\frac{\omega_d}{c_r(1+\alpha)}\right) \\ -\sin\left(\frac{\omega_d}{(1+\alpha)}\right) & 0 & \frac{A_r E_r}{c_r} \sin\left(\frac{\omega_d}{c_r(1+\alpha)}\right) & -\frac{A_r E_r}{c_r} \cos\left(\frac{\omega_d}{c_r(1+\alpha)}\right) \end{bmatrix} \begin{bmatrix} b_1 \\ b_2 \\ b_3 \\ b_4 \end{bmatrix} = \begin{bmatrix} \frac{c_r^2}{A_r E_r} \left(1 - \frac{2c_r^2}{\omega_d^2}\right) \\ 0 \\ \frac{1}{(1+\alpha)^2} - \frac{2}{\omega_d^2} + \frac{2c_r^4}{\omega_d^2 A_r E_r} - \frac{c_r^2}{A_r E_r (1+\alpha)^2} \\ \frac{2(1-c_r^2)}{(1+\alpha)\omega_d} \end{bmatrix} \frac{Q_1}{\omega_d^2} \quad (23.23)$$

$$\equiv [\mathbf{A}] \{\mathbf{B}\} = \{\mathbf{H}\}$$

where $Q_1 = \frac{F_0 L^3}{A_1 E_1}$.

23.3.2.2 Fixed-Fixed Boundary Conditions

For fixed-fixed conditions, $R_1(x) = 0$, $x = 0$. In this case, $B_1 = -\frac{2F_1 c_1^4}{A_1 E_1 \omega^4}$ and the approach gives:

$$\begin{bmatrix} 1 & 0 & 0 & 0 \\ 0 & 0 & \cos\left(\frac{\omega_d}{c_r}\right) & \sin\left(\frac{\omega_d}{c_r}\right) \\ \cos\left(\frac{\omega_d}{(1+\alpha)}\right) & \sin\left(\frac{\omega_d}{(1+\alpha)}\right) & -\cos\left(\frac{\omega_d}{c_r(1+\alpha)}\right) & -\sin\left(\frac{\omega_d}{c_r(1+\alpha)}\right) \\ -\sin\left(\frac{\omega_d}{(1+\alpha)}\right) & \cos\left(\frac{\omega_d}{(1+\alpha)}\right) & \frac{A_r E_r}{c_r} \sin\left(\frac{\omega_d}{c_r(1+\alpha)}\right) & -\frac{A_r E_r}{c_r} \cos\left(\frac{\omega_d}{c_r(1+\alpha)}\right) \end{bmatrix} \begin{bmatrix} b_1 \\ b_2 \\ b_3 \\ b_4 \end{bmatrix} = \begin{bmatrix} -\frac{2}{\omega_d^2} \\ \frac{c_r^2}{A_r E_r} \left(1 - \frac{2c_r^2}{\omega_d^2}\right) \\ \frac{1}{(1+\alpha)^2} - \frac{2}{\omega_d^2} + \frac{2c_r^4}{\omega_d^2 A_r E_r} - \frac{c_r^2}{A_r E_r (1+\alpha)^2} \\ \frac{2(1-c_r^2)}{(1+\alpha)\omega_d} \end{bmatrix} \frac{Q_1}{\omega_d^2}$$

$$\equiv [A] \{B\} = \{K\} \quad (23.24)$$

23.3.3 Numerical Example

Consider the rod shown in Fig. 23.1 and assume the following materials: Aluminum ($E_1 = 71$ GPa, $\rho_1 = 2710$ Kg/m³) and Silicon Carbide ($E_2 = 210$ GPa, $\rho_2 = 3100$ Kg/m³). Note that these values are taken from a basic paper in the field [8].

For the free-fixed case and taking $\alpha = 1$, the determinant of $[A]$ in Eq. (23.16) leads to the following values for the first two non-dimensional natural frequencies: $\omega_{d,1} = 2.2725$ and $\omega_{d,2} = 5.6338$. (The following parameters apply: $c_1 = 5118.52$, $c_2 = 8230.55$, $c_r = 1.61$, $E_r = 2.96$, $A_r = 1.00$, $Q_0 = 1.00$.)

For this case the non-dimensional version of Eq. (23.12) is given by ($x_D = x/L$):

$$R_1(x_D) = b_1 \cos(\omega_d x_D) - \frac{Q_0}{\omega_d^2} \quad (23.25)$$

Setting $x_D = 0.50$ (rod mid-span) and using b_1 from Eq. (23.16), amplitudes can be calculated for different values of the non-dimensional frequency ω_d .

The frequency response function spanning the first two natural frequencies for the mid-point of the rod is shown in Fig. 23.2.

For the fixed-fixed case (same numerical parameters as above), the determinant leads to: $\omega_{d,1} = 4.1326$ and $\omega_{d,2} = 7.3837$.

Here the non-dimensional version of Eq. (23.12) is:

$$R_1(x_D) = b_1 \cos(\omega_d x_D) + b_2 \sin(\omega_d x_D) - \frac{Q_0}{\omega_d^2} \quad (23.26)$$

For $x_D = 0.50$, with b_1 and b_2 from Eq. (23.18), amplitudes can be calculated for different values of the non-dimensional frequency ω_d .

The frequency response function for the mid-point of the rod is shown in Fig. 23.3.

23.4 Continuous Variation Model

The following dimensionless variables are introduced: $w = \frac{u}{L}$, $\tau = \Omega_0 t$, $\nu = \frac{\omega}{\Omega_0}$.

For the continuously varying functions:

$$\frac{\partial}{\partial x} \left(A(x) E(x) \frac{\partial u(x, t)}{\partial x} \right) + q(x, t) = A(x) \rho(x) \frac{\partial^2 u(x, t)}{\partial t^2} \quad (23.27)$$

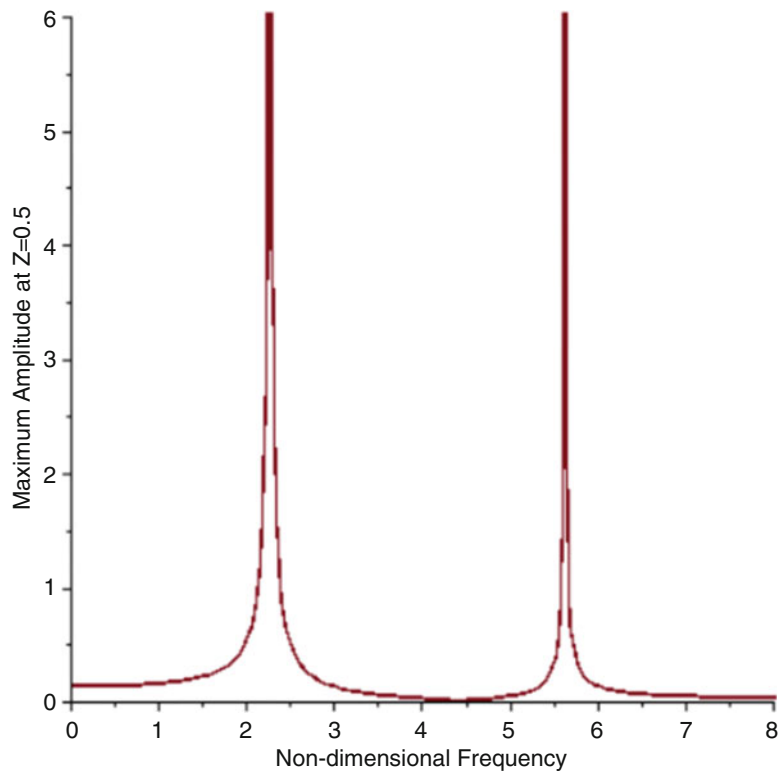


Fig. 23.2 FRF for non-homogeneous rod mid-point—free/fixed

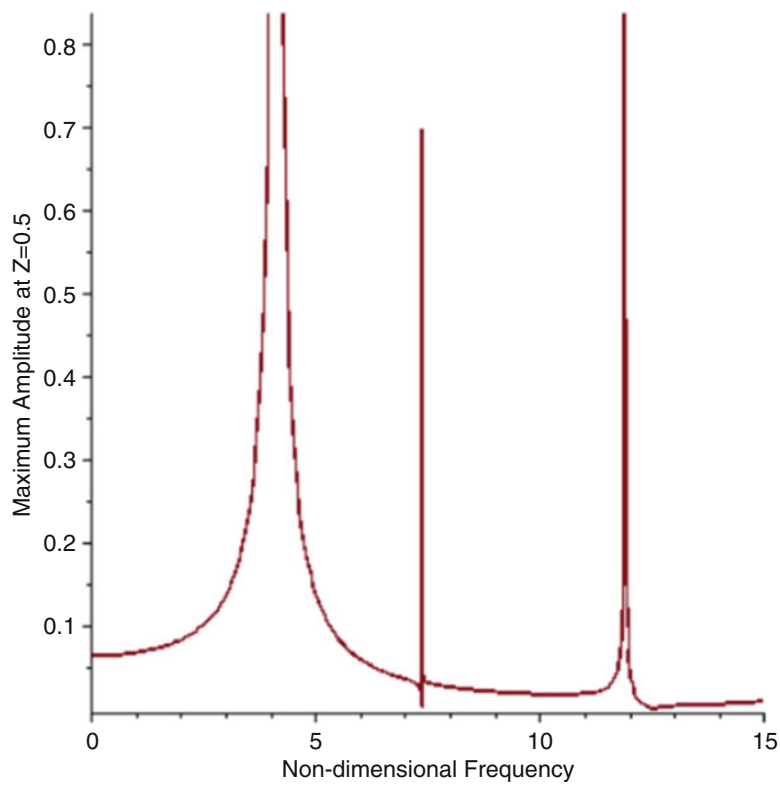


Fig. 23.3 FRF for non-homogeneous rod mid-point—fixed/fixed

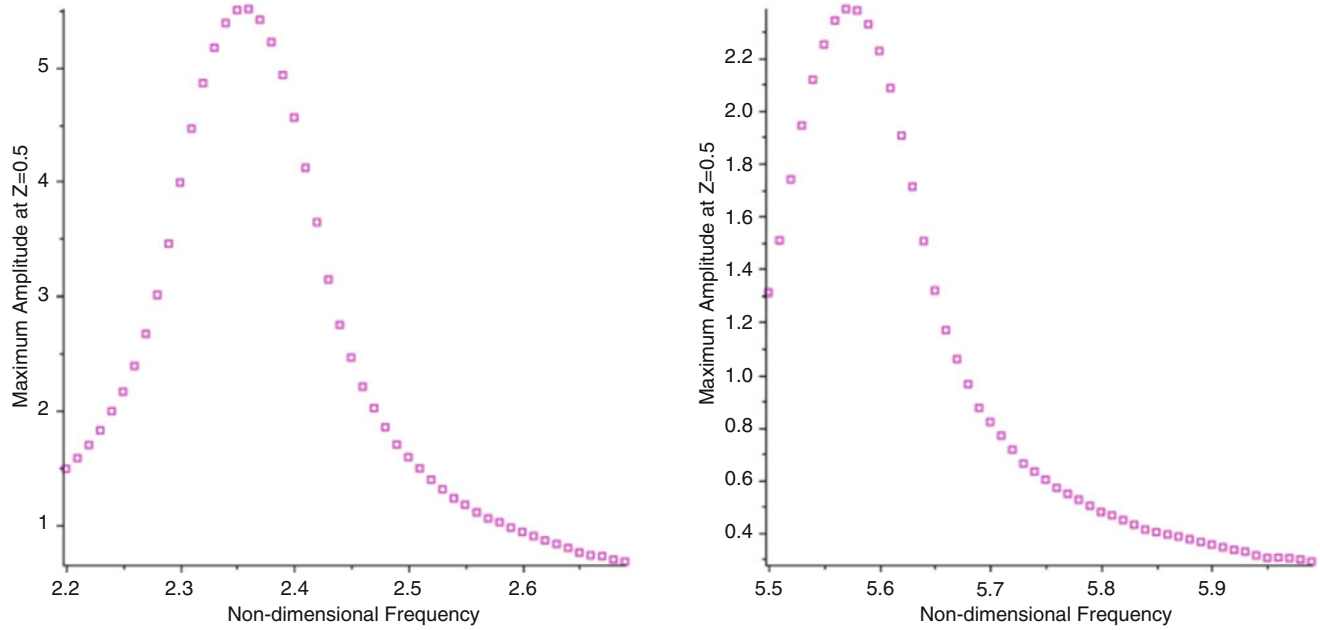


Fig. 23.4 FRF for non-homogeneous rod mid-point—numerical approach

Set:

$$E(x) = g_1(x_D) E_1, \quad \rho(x) = g_2(x_D) \rho_1, \quad A(x) = g_3(x_D) A_1, \quad \beta = \sqrt{\frac{L^2 \Omega_0^2 \rho_1}{E_1}}$$

$$q(x, t) = F(x) \sin(\omega t) \rightarrow \frac{F(x)L}{A_1 E_1} \sin\left(\nu \Omega_0 \frac{\tau}{\Omega_0}\right) = Q(x_D) \sin(\nu \tau)$$

$$\frac{\partial}{\partial x_D} \left(g_3(x_D) g_1(x_D) \frac{\partial w(x_D, \tau)}{\partial x_D} \right) + Q(x_D) \sin(\nu \tau) = \beta^2 g_2(x_D) g_3(x_D) \frac{\partial^2 w(x_D, \tau)}{\partial \tau^2} \quad (23.28)$$

Note that Ω_0 is arbitrary, so it is set to: $\Omega_0 = \sqrt{\frac{E_1}{\rho_1 L^2}}$, which gives $\beta = 1$. Also, $\nu = \sqrt{\frac{L^2 \rho_1}{E_1}} \omega = \omega_d$

The numerical FRF for this case is shown in Fig. 23.4, spanning the first two natural frequencies. These were obtained using MAPLE®'s PDE solver. For the case of constant body force, an overlap of the results from the analytical and numerical approaches is given in Fig. 23.5, for the free-fixed case. For the fixed-fixed case, the overlap is given in Fig. 23.6. It is seen that the numerical approach gives a very good approximation of the mid-point FRF.

Analytical results for the variable force are obtained in a similar manner as the ones for constant force. In this case Eqs. (23.21) and (23.23) are utilized for the free-fixed conditions and Eqs. (23.21) and (23.24) for the fixed-fixed (note: $Q_1 = 1.00$). Amplitudes at the rod-mid span are investigated.

Analytical and numerical comparisons for this case can be seen in Fig. 23.7 (free-fixed) and Fig. 23.8 (fixed-fixed). As in the constant case good agreement is observed.

The good agreement for the variable force gives confidence to the approach. An example is now given in which the spatial force variation is such that the particular integral is intractable analytically. However the results can be found using the continuous variation model. Consider, for example, a variable force given by an exponential function: $F(x) = F_0 e^{-[(x/L)^2]}$. The frequency response functions for this case are seen in Fig. 23.9 (the continuous lines are trend lines connecting the points obtained via the simulation).

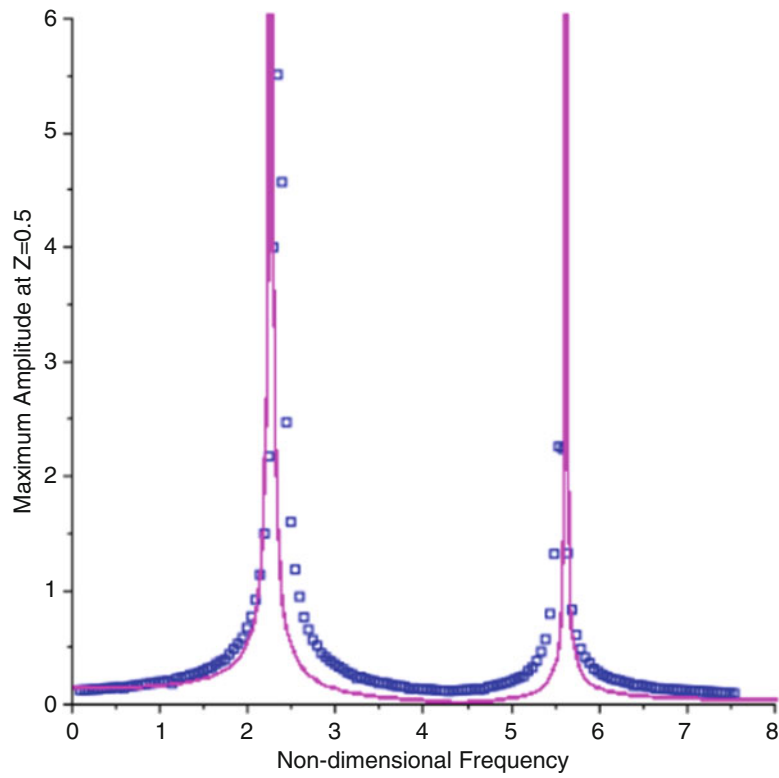


Fig. 23.5 Results comparison—numerical and analytical approaches—free/fixed

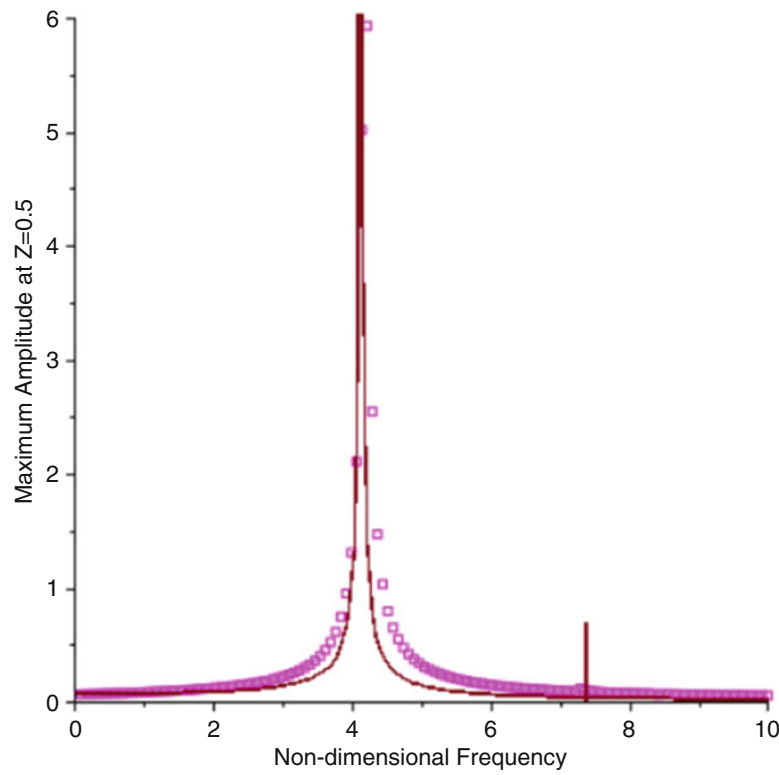


Fig. 23.6 Results comparison—numerical and analytical approaches—fixed/fixed

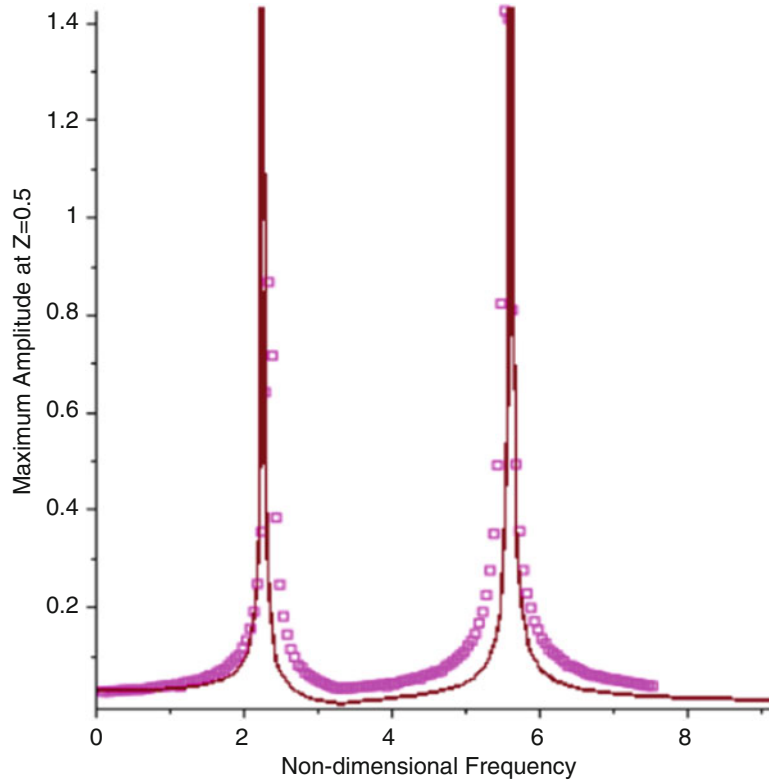


Fig. 23.7 Results comparison—numerical and analytical approaches—free/fixed (variable force)

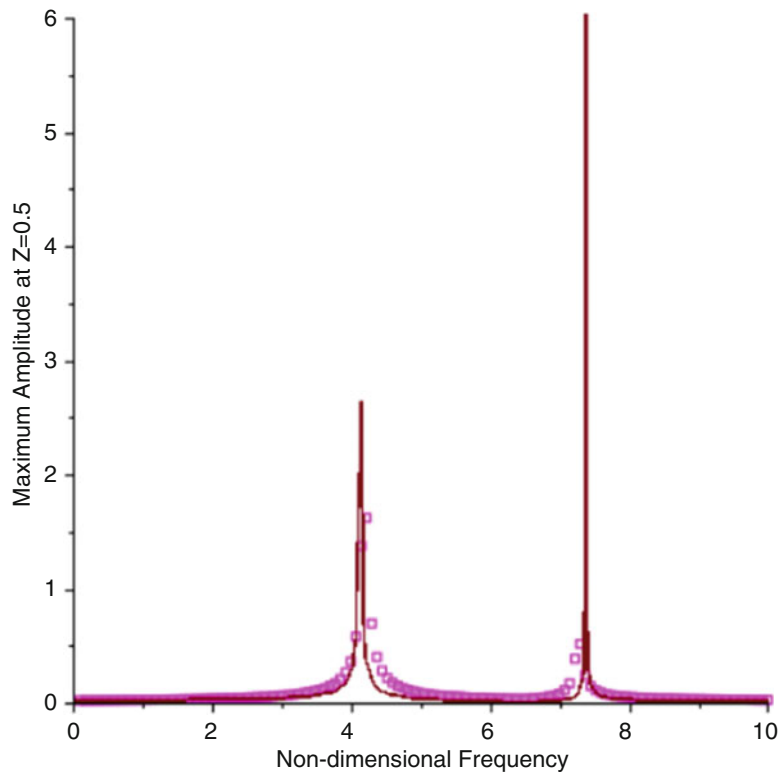


Fig. 23.8 Results comparison—numerical and analytical approaches—fixed/fixed (variable force)

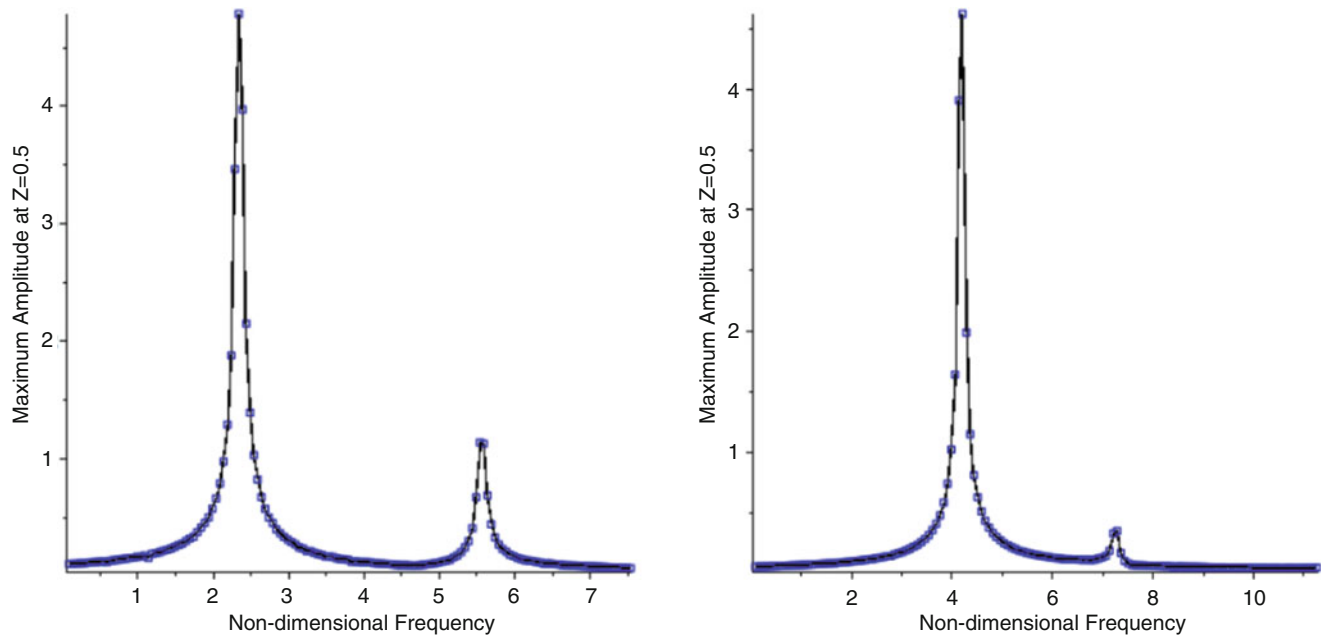


Fig. 23.9 FRF for exponential force—free/fixed (a), fixed/fixed (b)

23.5 Conclusions

Harmonic forcing of a two-layer elastic rod was examined. Spatial variations of the forcing functions were allowed. Analytic solutions using rod theory were developed, from which the FRFs at the rod mid-point, for example, could be found numerically. These were compared with ones obtained using a continuous variation model and MAPLE[®]'s numerical PDE solver. Three cases of external forcing were examined (constant, polynomial and exponential variation) and excellent agreement between the two methods was found.

References

- Mazzei, A.J., Scott, R.A.: Vibrations of Discretely Layered Structures Using a Continuous Variation Model, in: R. Allemang (Ed.) Topics in Modal Analysis II, Volume 8: Proceedings of the 32nd IMAC, A Conference and Exposition on Structural Dynamics, 2014, Springer International Publishing, Cham, 2014, pp. 385—396. http://link.springer.com/chapter/10.1007/978-3-319-04774-4_36, <http://link.springer.com/book/10.1007/978-3-319-04774-4>
- Lee, E.H., Yang, W.H.: On waves in composite materials with periodic structure. *SIAM J. Appl. Math.* **25**(3), 492–499 (1973)
- Hussein, M.I., Hulbert, G.M., Scott, R.A.: Dispersive elastodynamics of 1D banded materials and structures: analysis. *J. Sound Vib.* **289**(4–5), 779–806 (2006)
- Hussein, M.I., Hulbert, G.M., Scott, R.A.: Dispersive elastodynamics of 1D banded materials and structures: design. *J. Sound Vib.* **307**(3–5), 865–893 (2007)
- Hussein, M.I., Hulbert, G.M., Scott, R.A.: Dispersive elastodynamics of 1D banded materials and structures: design. *J. Sound Vib.* **307**(3–5), 865–893 (2007)
- Vasseur, J.O., Deymier, P., Sukhovich, A., Merheb, B., Hladky-Hennion, A.C., Hussein, M.I.: Phononic band structures and transmission coefficients: methods and approaches. In: Deymier, P.A. (ed.) *Acoustic Metamaterials and Phononic Crystals*, vol. 173, pp. 329–372. Springer, Heidelberg (2013)
- Hussein, M.I., Leamy, M.J., Ruzzene, M.: Dynamics of phononic materials and structures: historical origins, recent progress, and future outlook. *Appl. Mech. Rev.* **66**(4), 040802-1–040802-38 (2014)
- Berezovski, A., Engelbrecht, J., Maugin, G.A.: *Numerical Simulation of Waves and Fronts in Inhomogeneous Solids*. World Scientific Publishing Co. Pte. Ltd. (2008)
- Chiu, T.C., Erdogan, F.: One-dimensional wave propagation in a functionally graded elastic medium. *J. Sound Vib.* **222**(3), 453–487 (1999)

Chapter 24

An Unified Framework for Studying Gear Dynamics Through Model Reduction Techniques

Carlo Rosso and Elvio Bonisoli

Abstract Contribution of gear, shaft and bearing stiffnesses to the gear dynamics is an important aspect that can affect the gearbox behavior. Nowadays, it is possible to simulate the gear mating with a very accurate numerical approach, but with the drawback of very huge computational effort. Gear designers in first design steps need instruments able to give good description of gear dynamics without spending much time in high performance numerical simulations. They need an easy instrument for making decisions in a short time. In this paper, an unified framework for studying gear dynamics is proposed. The gears and mechanical elements are modeled in a very simple way, reducing as much as possible the number of dofs, but maintaining the highest fidelity and with different complexity levels. This is reached using MoGeSeC master dofs selection and building a reduced parametric LTI model of each element. The gear mating model is the interface and it is handled with different nonlinear Maxwell models. By using block-oriented approach, it is possible to have a library of increasing complexity elements that depict the gear dynamics and share the same platform, so it is possible to increase the model complexity simply changing a block in the simulation framework and to compare the different approaches.

Keywords Nonlinear interaction • Gear dynamics • Model order reduction

24.1 Introduction

There is a wide number of publications in literature related to the engagement dynamics and the gear dynamics [1–3]. This great amount is due to the various outputs the engineers are interested in, starting from the stress in the gears, the damage cumulated, the transmission efficiency, the noise and vibration emission, the load on the bearings, coming to the rotor dynamics of the geared shafts and the life assessment of the entire gearbox. The first scientific analyses of the gear dynamics were established in the Twenties and Thirties of the twentieth century and they were related to the evaluation of the dynamic overload due to the teeth mating. In the Fifties of the twentieth century, the first studies based on the dynamic models were conducted, with the aim to understand the overload in the engagement.

More recently, in the Seventies and Eighties, complex models were introduced in order to improve the accuracy of the developed models considering the effect of the tooth tridimensionality, the non-linearities in the principal elements and the friction and lubrication effects. From Nineties up to now, the wide diffusion and the increasing computation capabilities of the computers enriches the literature of complex Finite Element and Multibody models for taking into account the macro and micro geometrical features of the gears, the complex deformation of the gearbox components and the time evolution of the engagement. The wide number of studies has different goals, in fact, some of them, the earlier, are oriented to evaluate the Dynamic Factor, i.e. the load increment due to the dynamics. Others are related to the engagement dynamics and for this they focalize their attention on the tooth compliance. For studying the effects of the gear dynamics on the system, complex models that consider the shaft and bearing compliances are proposed. For high spin speed system, the gyroscopic effects are also taken into account by complex rotor dynamics model of geared system, and other models study the noise and vibration of gearboxes by means of Multibody and Finite Element techniques. The common line of all the literature models and techniques is the evaluation of the dynamic behavior of geared system. The aim of this paper is to describe the possibility to create a common framework for studying all those problems.

C. Rosso (✉) • E. Bonisoli
Politecnico di Torino, Corso Duca degli Abruzzi, 24 – 10129 Torino, Italy
e-mail: carlo.rosso@polito.it

24.2 Gear Mating Models

In the present paper, the models used for the description of gear mating dynamics are monodimensional and originate from the literature and in particular the 1D model proposed by Kahraman and Singh [4] and by Parker et al. [5].

The first work that tried to consider the gear manufacturing error was performed by Tuplin [6]. The model proposed in that paper is simple, but it well expresses the fundamental of gears mating. In fact, considering an easy two-masses-one-spring model, Tuplin defines the natural frequency of the resonance phenomenon that could occur in a gear pair when a pitch error is present and the maximum external load that the gear pair could experience. By defining the two gear teeth displacements x_1 and x_2 a motion equation can be written, where k is the stiffness of the engagement and m_1 and m_2 are the two gear masses referred to the line of action ($s + vt$ represents the external error variation):

$$\left(\frac{d^2}{dt^2} + k\left(\frac{1}{m_2} + \frac{1}{m_1}\right)\right)(x_2 - x_1) = k\left(\frac{1}{m_2} + \frac{1}{m_1}\right)(s + vt) \tag{24.1}$$

As a consequence, the natural frequency of the gear mating dynamics is:

$$2\pi f = \sqrt{k\left(\frac{m_1 + m_2}{m_2 m_1}\right)} = \sqrt{k\left(\frac{J_1 r_{b,2}^2 + J_2 r_{b,1}^2}{J_1 J_2}\right)} \tag{24.2}$$

where J_1 and J_2 are the gear inertias and $r_{b,i}$ are the gear base radii.

Using the same single degree of freedom model proposed by of Özgüven and Houser [7], Kahraman and Singh [4] study the dynamic behavior of a gear pair. This model is quite similar to the previous one, but it simplifies some aspects. In this model the sources are the Static Transmission Error (STE), modeled as a sinusoidal quantity that varies with its own frequency, and the fluctuation of the torque, that is characterized by a fundamental frequency different from the STE frequency. The model sketch is analogous to the Özgüven and Houser’s one, Fig. 24.1, and the differences are concentrated in the elastic force contribution and in the sources.

The elastic contribution to the force equilibrium is considered non linear and it has a trends as in Fig. 24.2, it is equal to zero when the displacement q measured along the line of contact is between the backlash values, it becomes linear and with the same angular slope when the teeth are moving in contact.

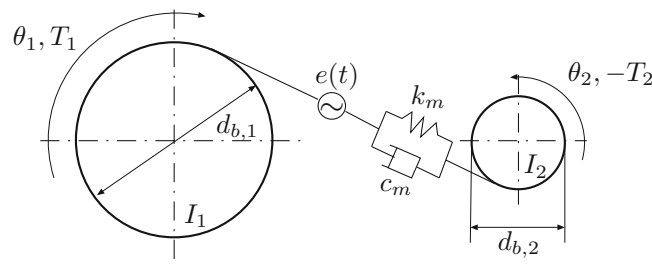
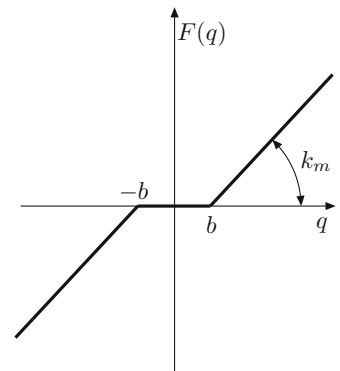


Fig. 24.1 1D model used by Kahraman and Singh [4]

Fig. 24.2 Elastic force non-linearity used by Kahraman and Singh [4]



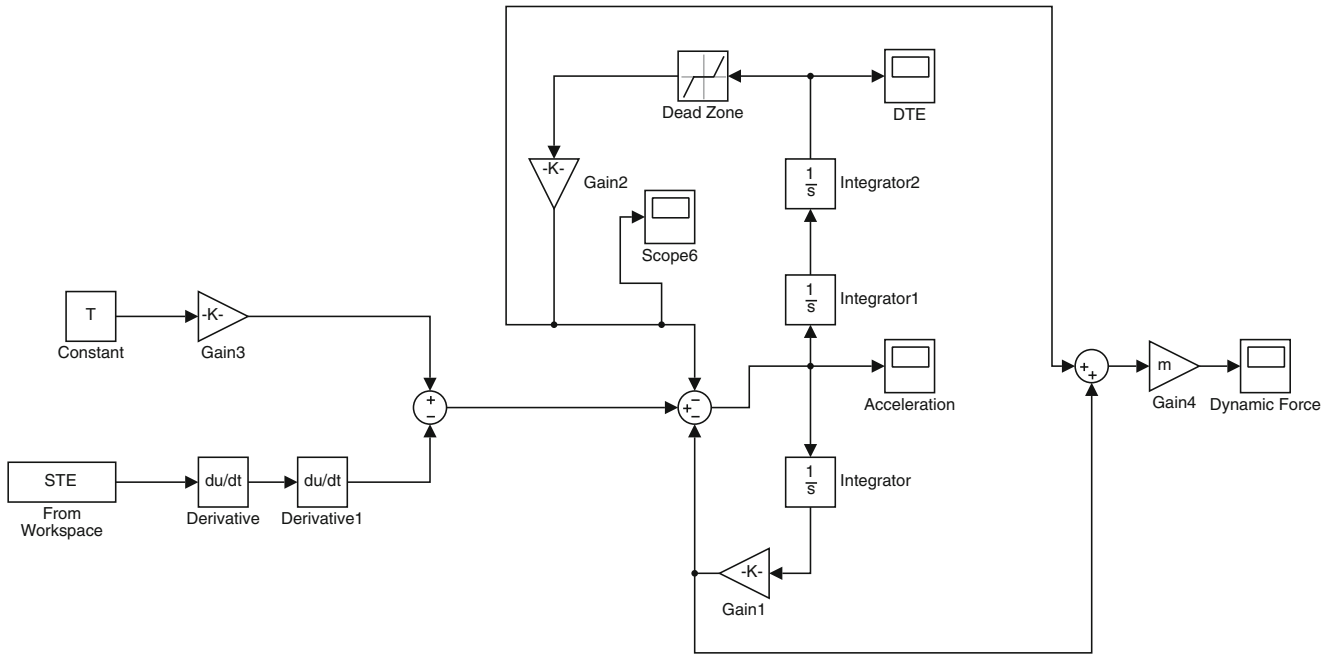


Fig. 24.3 Implementation of Eq. (24.4) in Matlab/Simulink

The equation proposed by Kahraman can be expressed as:

$$m_e \ddot{q} + c_m \dot{q} + F(q) = P_{r,b} + P_{a,b}(t) - m_e e(\ddot{i}) \tag{24.3}$$

where $P_{r,b}$ represents the mean value of force exchanged by teeth in contact along the line of action, $P_{a,b}(t)$ is the alternate component of the force exchanged by teeth, m_e is the equivalent mass computed as in (24.2), $e(t)$ is the STE and c_m is the viscous damping in the teeth mating.

In Matlab/Simulink, Eq. (24.3) is rewritten as Eq. (24.4), and implemented as depicted in Fig. 24.3.

$$\ddot{q} = \frac{T}{r_b \cdot m_e} - \ddot{e}(t) - 2\zeta \omega_n \dot{q} - \frac{F(q)}{m_e} \tag{24.4}$$

where T is the transmitted torque, r_b is the base radius and the alternate part of the exchanged force $P_{a,b}(t)$ is null.

Parker’s approach is a little bit different. Parker et al. [5] consider the STE as an intrinsic characteristic of the model and not as input. In fact, the STE is generated by the natural variation of the meshing stiffness, so Parker’s model considers the meshing stiffness variable in time [8]. The fundamental equation is not so different from Kahraman’s one, the differences are located in the definition of the meshing stiffness. In Kahraman’s approach the stiffness is constant apart the dead zone due to backlash. In Parker’s methodology the stiffness varies with the engagement and the non linearity due to the backlash is represented by a simple condition: elastic force is equal to zero when the teeth are not in contact and it varies according to the engagement when the two mating teeth are in contact. In that way the motion equation is simple and it can be written as:

$$m_e \ddot{q} + c_m \dot{q} + F(t, q) = P_b \tag{24.5}$$

In order to connect the mating models to the rest of the system, the two Matlab/Simulink implementations have to share the same inputs and the same outputs. This reasoning leads to arrange the Parker’s approach in order to consider torque as input and STE an external elements of the model useful for computing the stiffness variation. The stiffness variation can be derived using the STE and the force along the line of action, in formula:

$$k(t) = \frac{T}{r_b \cdot \text{STE}} \tag{24.6}$$

Doing so, the Matlab/Simulink model of Parker’s approach is depicted in Fig. 24.4.

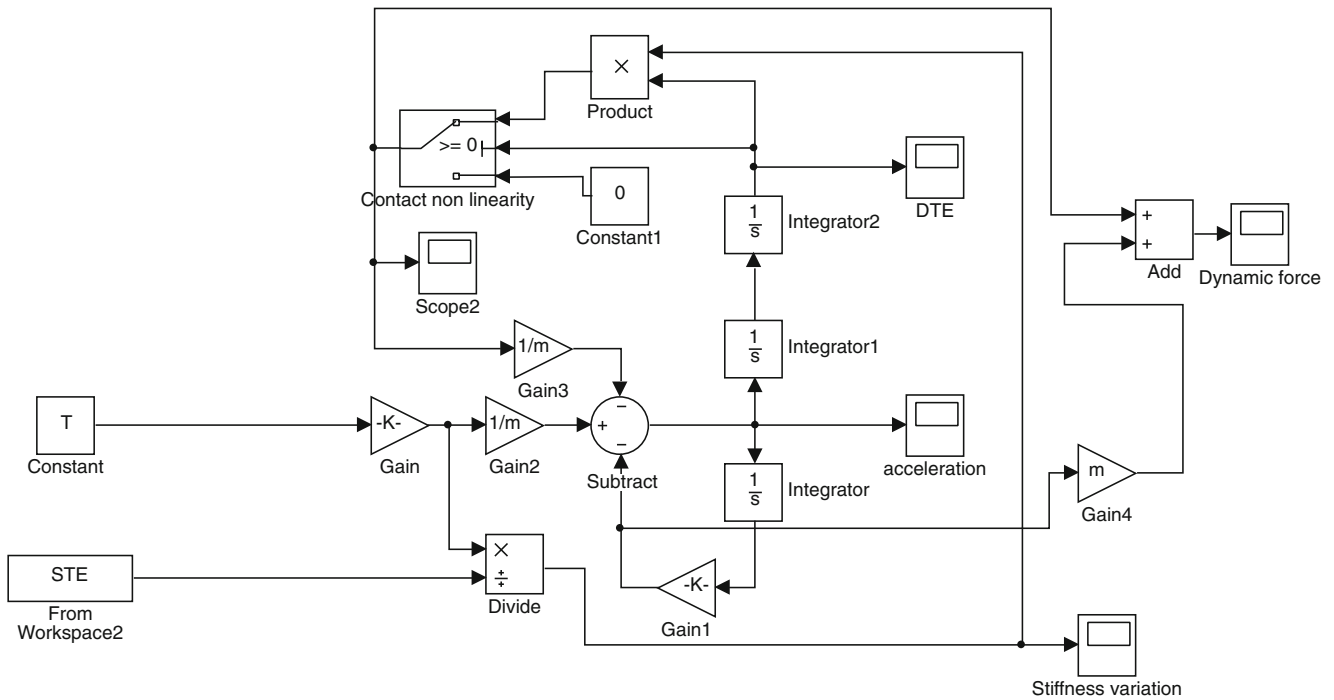


Fig. 24.4 Implementation of Eq. (24.6) in Matlab/Simulink

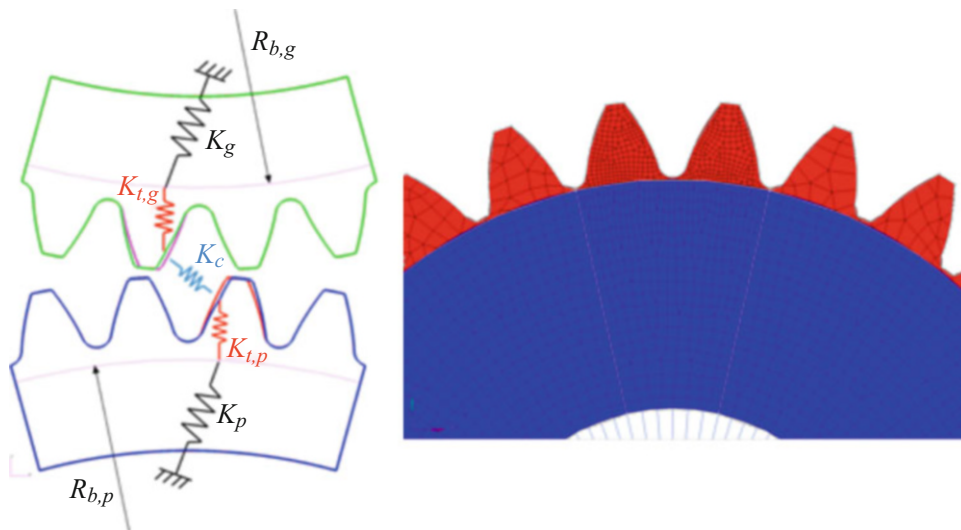


Fig. 24.5 Simplified stiffness model, on the left, and FE simplification on the right. In red the tooth model for computing tooth compliance, and in blue the gear wheel for body stiffness. The cut line corresponds to the base diameter

24.3 Geared Wheels Models

In order to simulate the geared wheel compliance, an assumption is made: a geared wheel can be described in three elements and, for that, its compliance can be described with at least three components, as depicted in Fig. 24.5.

The first one is the tooth-to-tooth contact K_c , i.e. the Hertzian stiffness of the two mating teeth. In this case the stiffness is an overall value that takes into account the contribution of the two mating gears. The second compliance element, K_t , is the tooth flexibility, in other words, the tooth can be considered as a cantilever that is in the same time compressed and bended. According to [9], the tooth stiffness is defined on the basis of two contributions, one is given by the cantilever shape of the tooth, the second one is given by the rim compliance. This approach is used when the gear is not physically drawn,

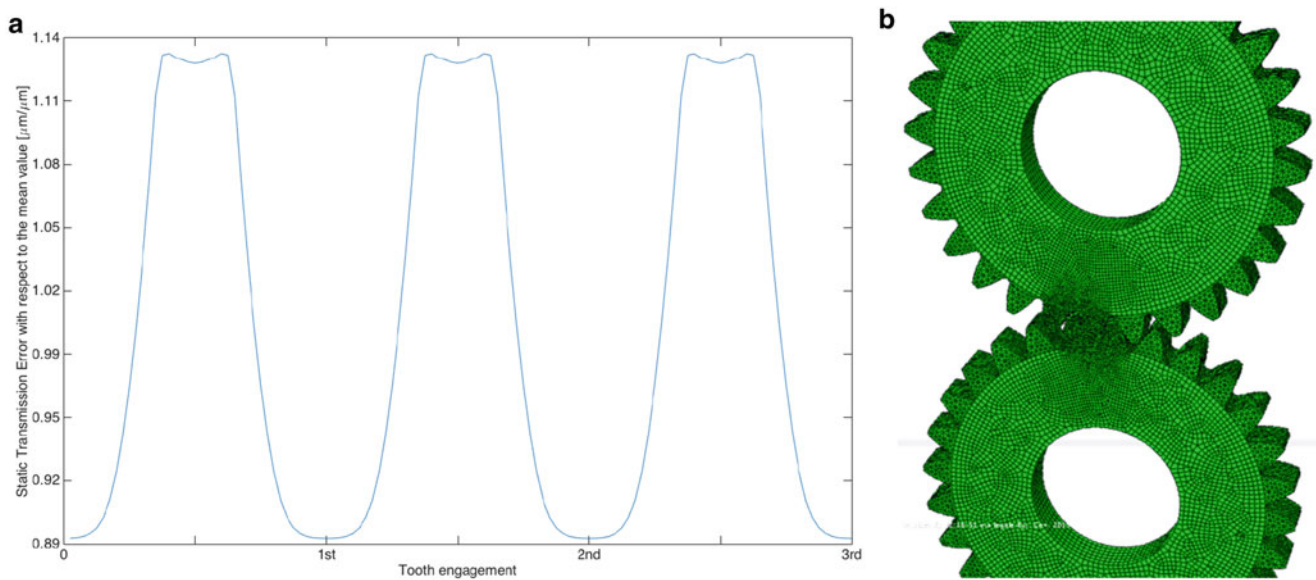


Fig. 24.6 Static transmission error (a) computed by means of numerical model (b)

otherwise, if a CAD model is present, the stiffness can be computed using Finite Element Methodology. In [9], the tooth stiffness is computed with respect to the base radius, so the graphical representation of gear model can be shown in Fig. 24.5 on the right.

Finally, the third element of the geared wheel is the compliance of its body, K_p or K_g . Also in this case, stiffness contribution of gear body can be defined using analytical method (when no drawings are present) or by FEM (when a CAD model is present, Fig. 24.5). Using that approach, a gear pair can be described by at least five elements: two gear bodies, two teeth stiffness and a contact stiffness. Other dynamic elements have to be considered, such as the inertia and the damping. In particular the body inertia is easily computable, and in a first analysis the tooth inertia can be neglected because it is very little with respect to the body one. For the damping, according to the literature, a viscous model is considered and the damping ratio is set to 0.08. Additional elements can be used for describing gear shafts, bearings and casing.

24.4 Results Obtained by 1D Model

As first step in this work, an analysis of standard 1D models of Figs. 24.3 and 24.4 are performed. For doing that a gear pair is considered. The gear stiffness is set higher than the meshing frequency, in order to take the normal modes due to the gear bodies outside the working condition. The gear ratio is set equal to 1. A Static Transmission Error, computed by engaged model depicted in Fig. 24.6b, is used as input in both the Kahraman's and Parker's models.

A typical output of the two different models, compared in the same condition using a speed sweep from 0 to more than 3 times the natural frequency n_{res} of the engagement resonance, can be seen in Fig. 24.7. The chart represents the output of Kahraman's model (red) and Parker's one (blue). The resonance condition is clearly highlight by both the models, but in this case the contact non linearity are not excited because the level of torque is high. Non linearity effect of the contact can be visible at low level of transmitted torque, in Fig. 24.8. In that case, both the models highlight softening jump phenomenon in the neighbourhood of the theoretical resonance value.

24.5 Block Oriented (Bond Graph) Approach

Block Oriented (Bond Graph) [10] strategy is the philosophy that aims this paper. For each element considered into the model, the same communication ports are defined, the single element exchanges with the others state conditions and generalized forces. The single element receives in input the position and speed conditions together with the force applied on it. As an example, consider the block in Fig. 24.9a. This image depicts the engagement block, where the inputs are the relative

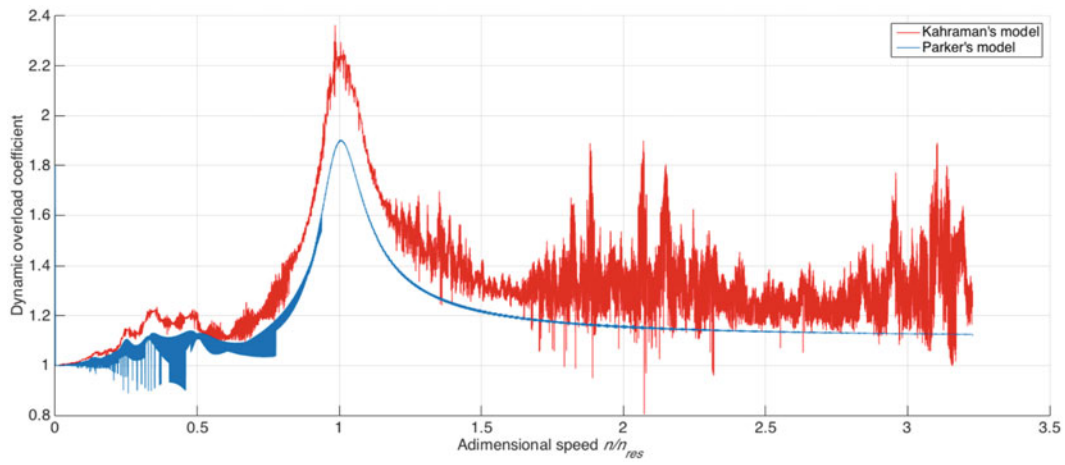


Fig. 24.7 Overload coefficient due to dynamic effect comparing Kahraman and Parker's models at the same condition

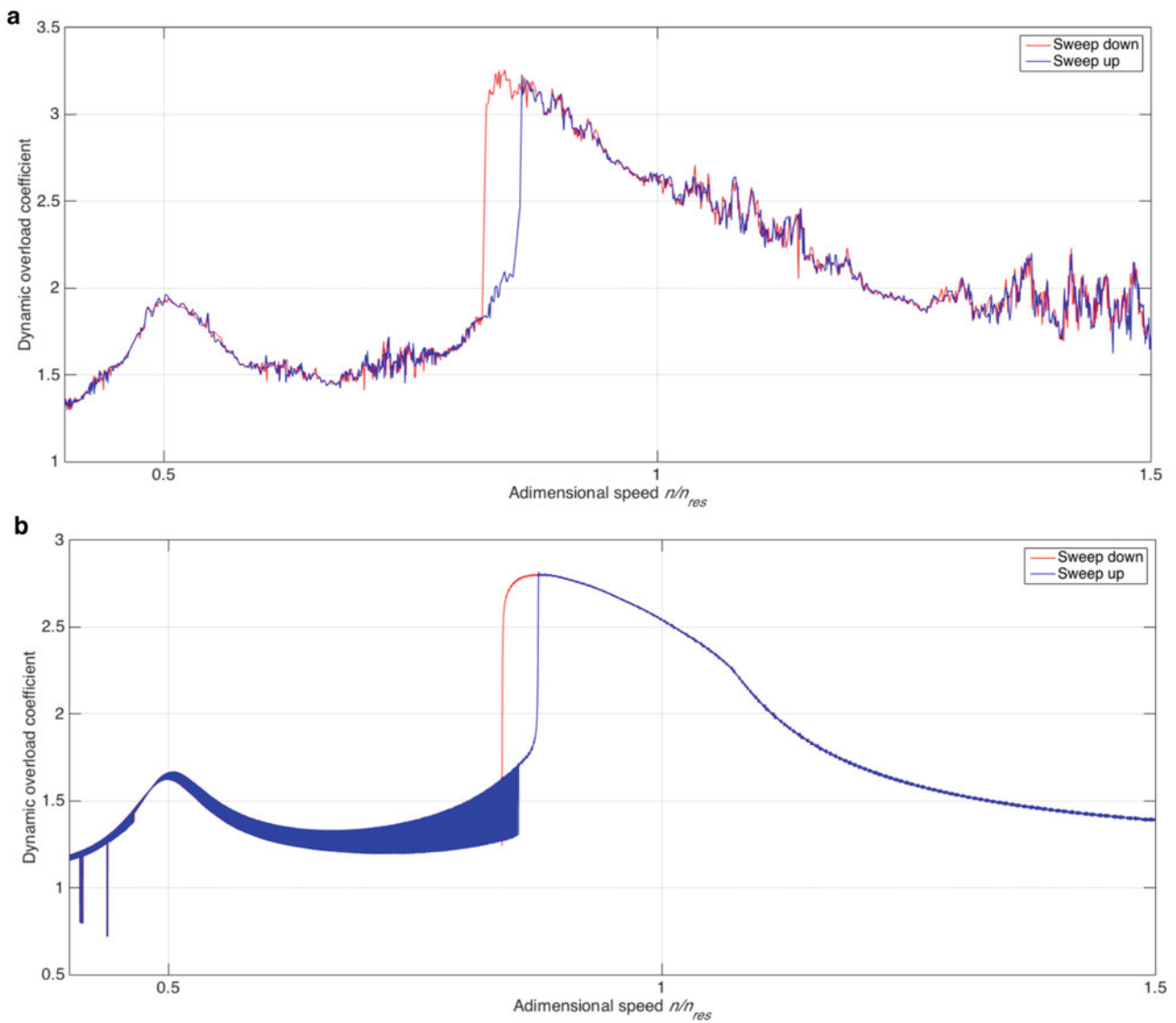


Fig. 24.8 Overload coefficient due to dynamic effect comparing Kahraman (a) and Parker's (b) models at the same condition and the presence of contact non linearity

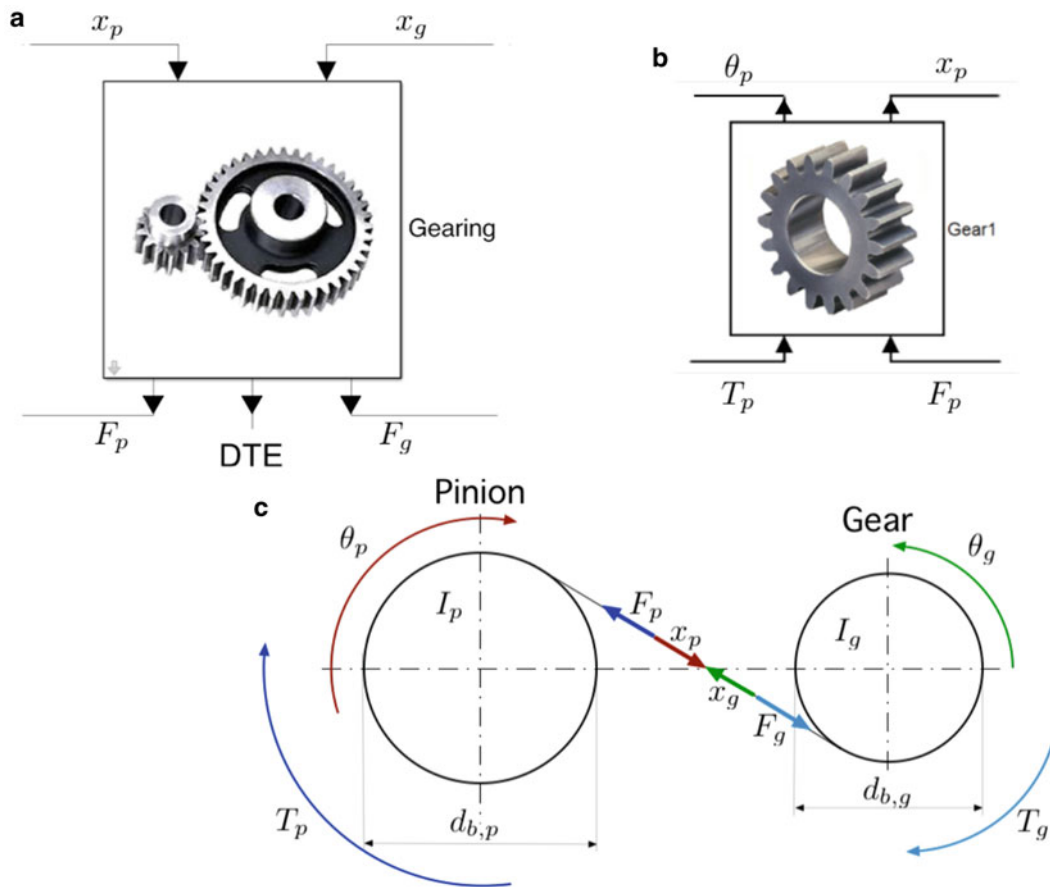


Fig. 24.9 Block oriented philosophy and conventional definitions

displacements along the line of action related to the two mating teeth and the outputs are the forces exchanged in the gear contact. In Fig. 24.9c the conventional directions of displacements and forces are shown. In the same manner the block that depicts the gear compliance receives as input the forces (input and feedback) and gives as output the displacements, Fig. 24.9b.

The authors decide to use that approach because it allows to define a unique framework for the system analysis, as a matter of fact, the blocks are always defined in the same manner but the number of degree of freedom can change, so the authors have the possibility to change the model complexity just changing the model order. For reaching that goal and for testing the approach, the authors use the block oriented approach for rewriting the Kahraman’s and Parker’s models. Using such approach, the Kahraman’s model can be described as in Fig. 24.10.

It can be seen in Fig. 24.10 the dead zone element that represents the non linear contact behaviour. The element called Model is useful for selecting linear or non-linear behaviour. Inputs of the block are the teeth positions and speeds whereas the outputs are the exchanged forces between teeth.

Also for Parker’s approach the block oriented methodology is used. In Fig. 24.11 it is possible to see the equivalent diagram.

Using that method, the model of powertrain is divided in subsystems and represented as in Fig. 24.12. Using the same data and the same integration conditions, outputs of the two Block Oriented models are practically the same of Figs. 24.7 and 24.8. The difference becomes appreciable when the gear body compliance is considered. For doing that, gears dynamic features are reduced to equivalent few degrees of freedom by using the methodology explained in [11]. In Fig. 24.13 the selected master nodes are shown. The black points represent the selected nodes, that are a combination of master nodes imposed as default for taking into account the boundary conditions, the zone where forces are exchanged, the kinematics is highlighted and the added degrees of freedom for taking into account the gear dynamics.

The Block Oriented method applied in Matlab/Simulink allows to share the same framework between 1-D to n -D models. So the scheme created in Fig. 24.12 is simply extended to manage matrices. In other words, the scheme remains the same, but the quantities pass from lumped values to matrix values.

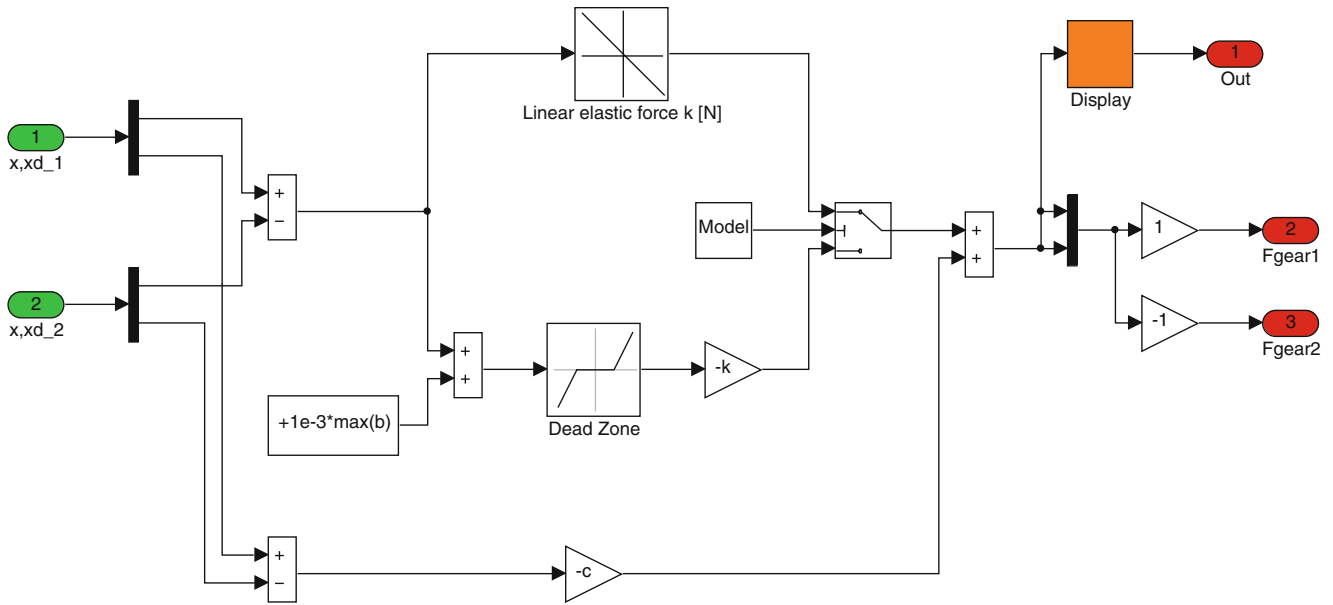


Fig. 24.10 Kahraman’s model in block oriented methodology

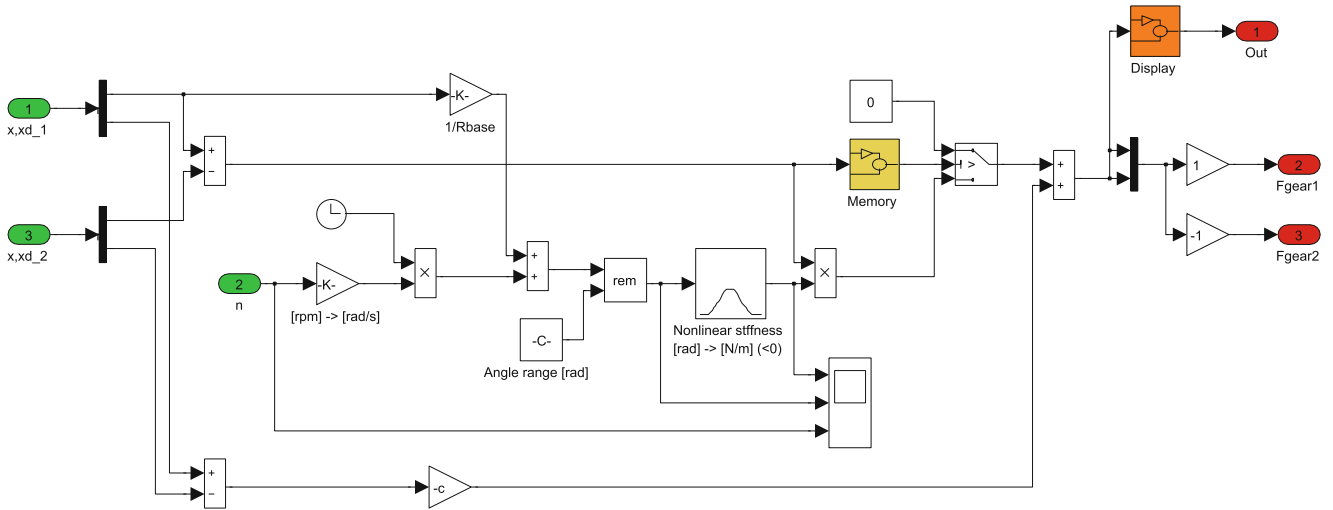


Fig. 24.11 Parker’s model in block oriented methodology

In that way the block that depicts gear body dynamics is modified as in Fig. 24.14. The interface nodes remain the same of the 1D model, but the authors insert additional degrees of freedom in order to take into account the gear contribution to the dynamic response. In that way the quantities that “walk” along the block lines are vectors (displacements, speeds and accelerations) and the gains are the dynamic matrices. The outputs are, as a consequence, vectors of generalized forces corresponding to the selected node degrees of freedom.

24.6 Results

The main goal of this paper is to set up a model that can be modified in complexity without changing the basis. In order to test the increment of model complexity using the same blocks of the 1D model, just extended to n dimensions, the authors test the same gear pair used for the 1-D model. This is the reason why the gear body is chosen with high stiffness, so it is possible to uncouple the meshing frequency and the gear body frequency and understand the correct working of the procedure. The results obtained are shown in Fig. 24.15. As it can be noted, the behaviour is the same of Fig. 24.7, but a sort of noise is present. This is due to the high harmonics of gear bodies and to a damping matrix that is arbitrary set proportionally to the mass and stiffness matrices.

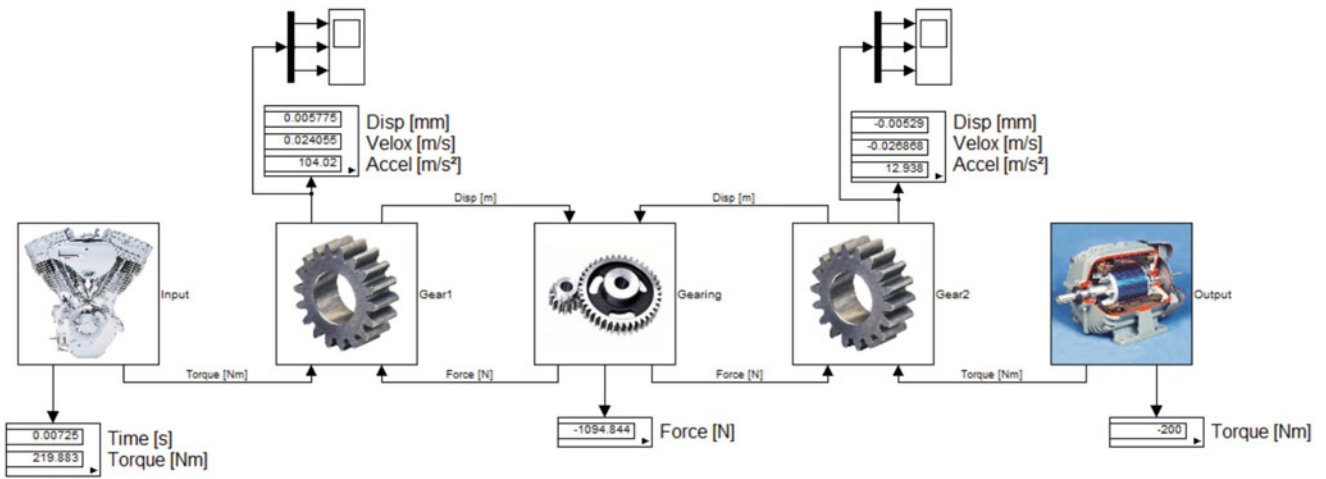


Fig. 24.12 Block oriented model of a gearbox

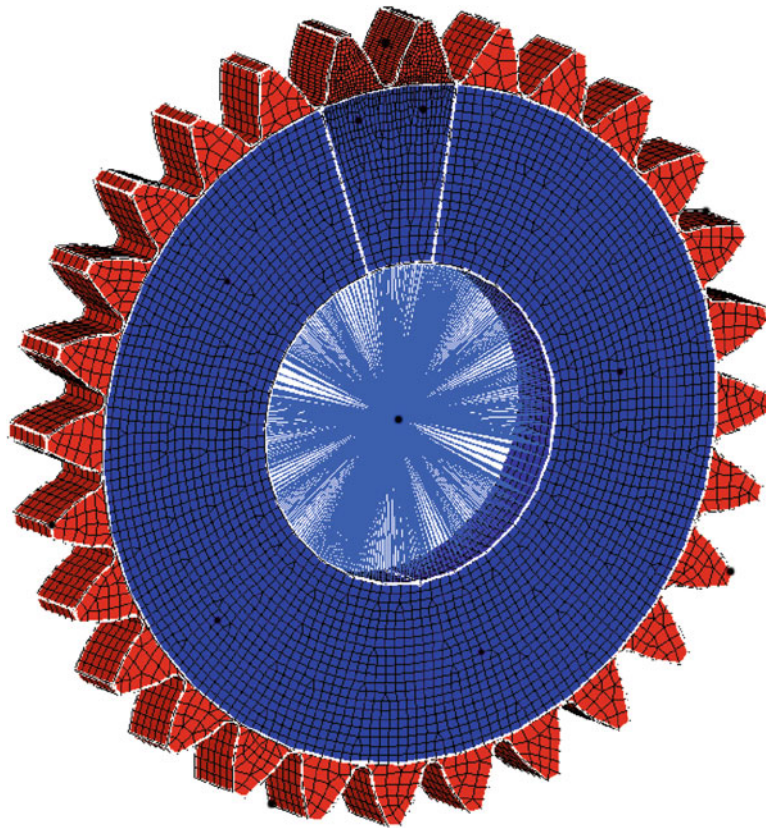


Fig. 24.13 Selected master nodes on a gear, the black points represent the master nodes selected by MoSeGeC procedure

24.7 Conclusions

The aim of this paper is to present the idea and to test it applied to a simple model. As described in the previous sections, the methodology proves to be effective and easy to manage. The power of this method is the possibility to easily increase the model complexity just changing the number of degrees of freedom. Obviously, this is the starting point, many improvements have to be implemented. The authors want to take into account a 3D engagement model and gear bodies with natural frequencies placed inside the working conditions.

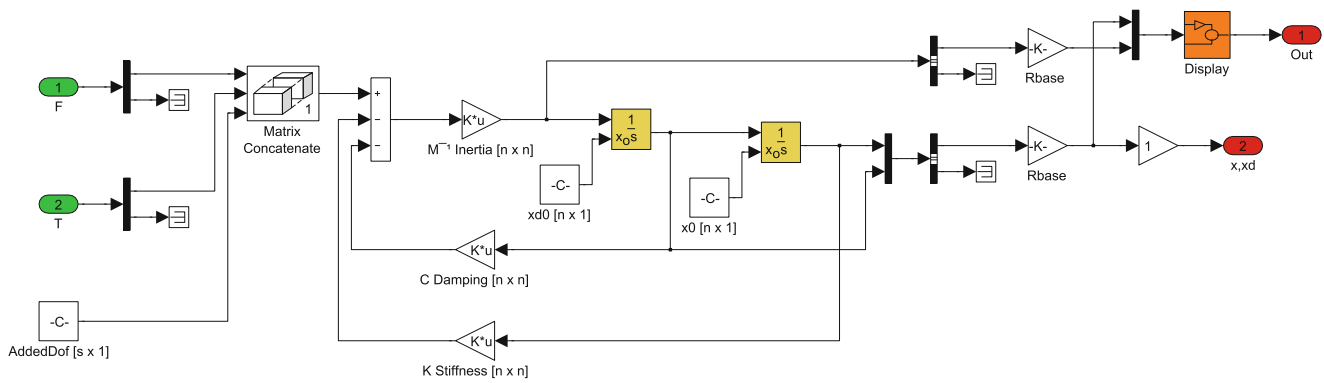


Fig. 24.14 Block oriented model of a gear considered as a reduced dynamic model

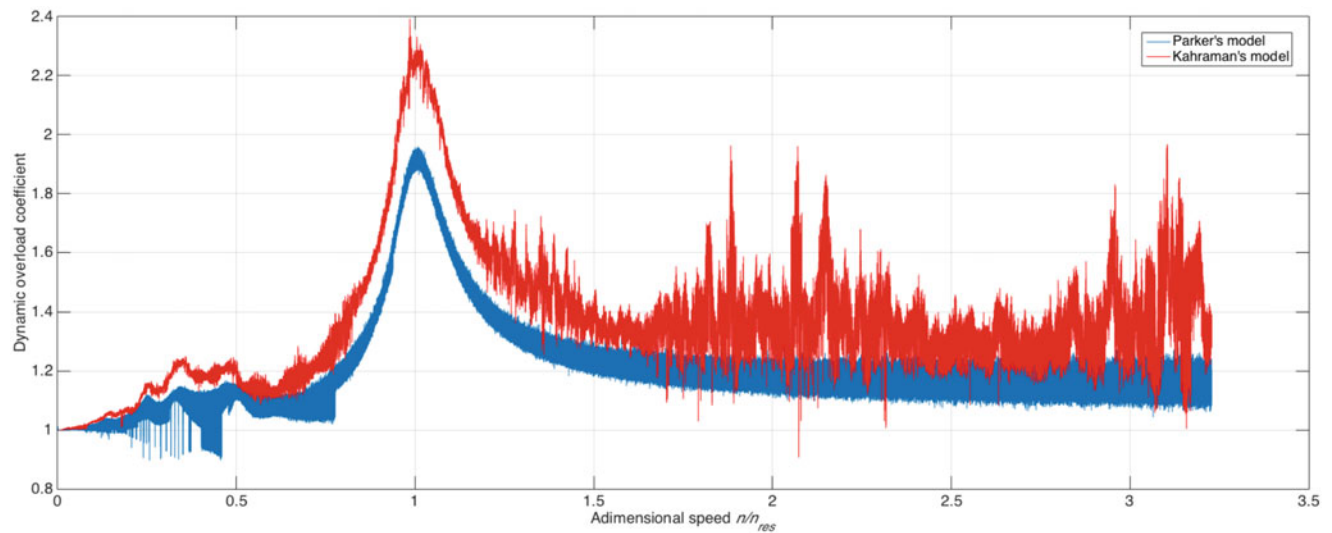


Fig. 24.15 Block oriented model results: the dynamics proves to be the same of the 1D equivalent model

References

1. Nevzat Ozguven, H., Houser, D.R.: Mathematical models used in gear dynamics—a review. *J. Sound Vib.* **121**(3), 383–411 (1988)
2. Abersek, B., Flasker, J., Glodez, S.: Review of mathematical and experimental models for determination of service life of gears. *Eng. Fract. Mech.* **71**, 439–453 (2004)
3. Prasil, L., Mackerle, J.: Finite element analyses and simulations of gears and gear drives a bibliography 1997–2006. *Int. J. Comput. Aided Eng. Softw.* **25**(3), 196–219 (2008)
4. Kahraman, A., Singh, R.: Non-linear dynamics of a spur gear pair. *J. Sound Vib.* **142**(1), 45–79 (1990)
5. Parker, R.G., Vijayakar, S.M., Imajo, T.: Non-linear dynamic response of a spur gear pair: Modelling and experimental comparisons. *J. Sound Vib.* **237**(3), 435–455 (2000)
6. Tuplin, W.A.: Gear tooth stresses at high speed. *Proc. Inst. Mech. Eng.* **16**, 162–167 (1950)
7. Nevzat Ozguven, H., Houser, D.R.: Dynamic analysis of high speed gears by using loaded static transmission error. *J. Sound Vib.* **125**(1), 71–83 (1988)
8. T.I. Fossen, H. Nijmeijer, *Parametric Resonance in Dynamical Systems*, ISBN: 978-1-4614-1042-3 (Print) 978-1-4614-1043-0 (Online), 2012, Springer New York, DOI 10.1007/978-1-4614-1043-0
9. Cornell, R.W.: Compliance and stress sensitivity of spur gear teeth. *J. Mech. Des.* **103**(2), 447–459 (1981)
10. Velardocchia, M., D'Alfo, N., Bonisoli, E., Galvagno, E., Amisano, F., Sorniotti, A.: Block-oriented models of torque gap filler devices for AMT transmissions, SAE Technical Paper 2008-01-0631. doi:10.4271/2008-01-0631, 2008
11. Bonisoli, E., Delprete, C., Rosso, C.: Proposal of a modal-geometrical based master nodes selection criterion in modal analysis. *Mech. Syst. Sig. Process.* **23**(3), 606–620 (2009)
12. Umezawa, K., Suzuki, T., Sato, T.: Vibration of power transmission helical gears (approximate equation of tooth stiffness). *Bull. JSME* **29**(251), 1605–1611 (1986)
13. Kahraman, A., Singh, R.: Interactions between time-varying mesh stiffness and clearance non-linearities in a geared system. *J. Sound Vib.* **146**(1), 135–156 (1991)

Chapter 25

Application of the Harmonic Balance Method to Centrifugal Pendulum Vibration Absorbers

Mustafa A. Acar and Steven W. Shaw

Abstract The harmonic balance method (HBM) is a powerful analysis tool for nonlinear vibrating systems, provided that the forms of the nonlinearities of the system result in a manageable algebraic system of equations. The authors of Cochelin and Vergez (J Sound Vib 324(1):243–262, 2009) created a framework that modifies the structure of the equations of motion involving a wide variety of nonlinearities into a quadratic form, which then can be approximated with HBM with as many assumed harmonics the problem needs for a satisfactory accuracy. In this work, we employ this framework for the analysis of centrifugal pendulum vibration absorbers (CPVA). The crucial step of this framework is the recasting of the variables into the required form. It has been shown that the dimensionless equations of motion for point mass CPVAs with general paths fitted to a rigid rotor can be put into the quadratic polynomial form. Two benchmark problems with known dynamical characteristics are investigated and the results show that this approach provides a powerful tool for investigating steady-state responses of these absorber systems. This will be very beneficial for design evaluations of CPVA systems where parameter values do not allow for the application of perturbation methods and/or make direct simulations very time consuming.

Keywords Order-tuned vibration absorbers • Harmonic balance method • Nonlinear dynamical system simulation • Continuation of solution branches • MANLAB

25.1 Introduction

Centrifugally driven pendulum vibration absorbers (CPVA) are used to reduce engine-order torsional vibrations in rotating systems [1]. They are widely used in light aircraft piston engines (see Fig. 25.1) and have recently been introduced for smoothing torsional vibrations in automotive powertrain applications [1–3]. These absorbers make use of the centrifugal field due to rotation, rather than elastic elements, so that they can be tuned to a particular engine order, rather than a fixed frequency.

A CPVA is composed of a mass that moves relative to the supporting rotor, supported by some type of hinge, typically of a bifilar type using two rollers, as shown in Fig. 25.2. Traditional absorber designs have the absorber center of mass following a circular path [5], but more modern designs use other paths, generally epicycloids, to better handle large amplitude responses [1, 6, 7]. The response of these systems are well captured by models with degree(s) of freedom for the rotor (one for nonresonant tuning, more if one considers torsional modes of the shaft), and one degree of freedom for each absorber. The governing equations are highly nonlinear and have complicated expressions (involving polynomial and square root terms) resulting from the CPVA path kinematics as it moves with respect to the host rotor. Time integration approaches are easy to apply to this system, yet conducting parameter studies this way requires extensive computational time, since the systems are lightly damped, leading to long transients. Moreover, it is not possible to gather information about unstable responses using time simulations. Perturbation methods, on the other hand, are quite powerful in terms of obtaining insight about the response characteristics with respect to system parameters, as well as stability characteristics, and these can be applied in some practical parameter ranges. However, they require careful application of parameter scaling and their error bounds are linked to the values of physical parameters that are assumed to be small. In addition, in some practical systems the parameter values do not satisfy the required conditions for using perturbation methods. Thus, there is a need for more general and powerful numerical tools for investigating these systems.

M.A. Acar (✉)
Michigan State University, East Lansing, MI, USA
e-mail: acarmust@msu.edu

S.W. Shaw
Florida Institute of Technology

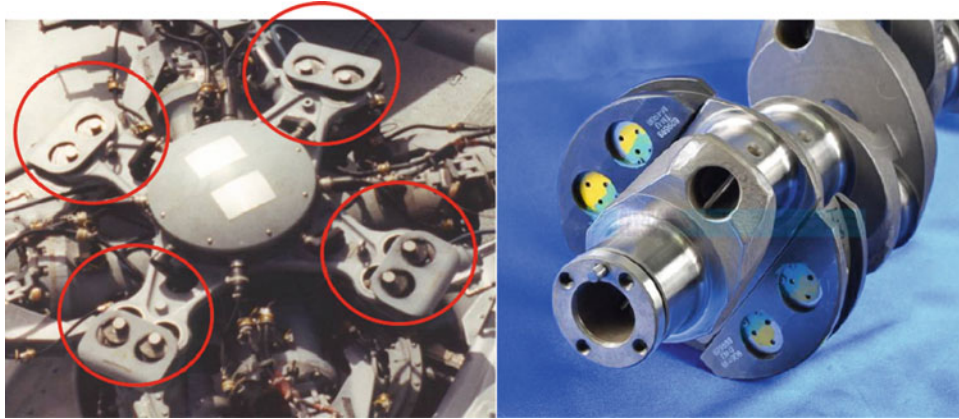


Fig. 25.1 *Left:* CPVAs installed on an helicopter rotor; photo, S.W. Shaw. *Right:* CPVAs on a light aircraft engine crankshaft, from [4]

Fig. 25.2 The bifilar suspension of a CPVA used as a test specimen at MSU



In this work we adapt the harmonic balance method (HBM) proposed in [8], which recasts the nonlinear terms in the equations of motion into a quadratic polynomial form of differential and algebraic equations by introducing new variables. In this way, application of the HBM, which normally requires cumbersome algebraic operations in systems with non-polynomial nonlinearities and/or with a high number of assumed harmonics, becomes straightforward even when the number of assumed harmonics is large.

The method aims to transform the model of interest into a system of the form

$$m(\dot{Z}) = c + l(Z) + q(Z, Z) \quad Z \in \mathbb{R}^{N_{\text{eq}}} \quad (25.1)$$

where Z is the vector of unknowns of the set of equations, c is a constant vector, m and l are linear operators, and q is a quadratic operator. Application of the HBM involves expressing Z in a Fourier series as

$$Z(t) = Z_0 + \sum_{k=1}^H Z_{c,k} \cos(k\omega t) + \sum_{k=1}^H Z_{s,k} \sin(k\omega t) \quad (25.2)$$

and substituting this form into Eq. (25.1). Solving the resulting algebraic system of equations for the Fourier coefficients of each harmonic approximates a periodic solution to the original system. In order to systematically obtain the algebraic equations, the coefficients are collected in a single vector

$$U = [Z_0^\top, Z_{c,1}^\top, Z_{s,1}^\top, Z_{c,2}^\top, Z_{s,2}^\top, \dots, Z_{c,H}^\top, Z_{s,H}^\top]^\top. \quad (25.3)$$

The algebraic system of coefficients then takes the form

$$\omega M(U) = C + L(U) + Q(U, U) \tag{25.4}$$

where the operators $M(\cdot)$, C , $L(\cdot)$ and $Q(U, U)$ depend only on the original operators $m(\cdot)$, c , $l(\cdot)$, $q(\cdot, \cdot)$ and the number of harmonics assumed in Eq. (25.2), H . The details of the relation between these set of operators are derived in [8]. This means, as long as the original system can be put into form of Eq. (25.1), the system of equations resulting from the application of the HBM can be automatically generated. Numerical solutions to this system of quadratic algebraic equation can be obtained using one of many available algorithms. The algorithm used in [8] is a pseudo-arclength continuation method, codes of which are freely available to public under the package name called *MANLAB* [9], where one of the system parameters is chosen as a free variable and periodic solutions are obtained by solving the Fourier coefficients as a function of this parameter. Moreover, the stability information of these periodic orbits can be obtained through the methodology used in [10], which employs Hill’s method to calculate Floquet exponents by expressing the Jacobian of the original equation of motion with the newly defined set of system variables.

25.2 Dynamical Model

The system illustrated in Fig. 25.3, incorporates point mass CPVAs prescribed to move along indicated paths with respect to the rotor. The excitation torque applied to the rotor has order-domain characteristics, namely the frequency of the excitation is a function of rotor angular position, $\theta(t)$. This system is modeled using Lagrange’s equations for a rigid rotor with N CPVAs, that is, with $N + 1$ degrees of freedom. The equations of motion of the system are given by

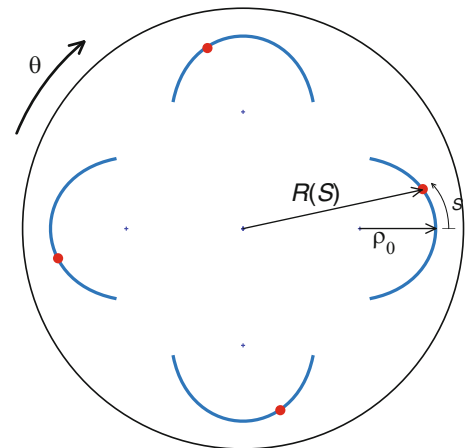
$$J\ddot{\theta} + \sum_{j=1}^N m_j \left(R_j^2(S_j)\ddot{\theta} + G_j(S_j)\ddot{S}_j + \frac{dG_j(S_j)}{dS_j}\dot{S}_j^2 + \frac{dR_j^2(S_j)}{dS_j}\dot{S}_j\dot{\theta} \right) = T(\theta) + T_0 - c_0\dot{\theta} \tag{25.5}$$

$$m_j\ddot{S}_j + m_jG_j(S_j)\ddot{\theta} + \frac{1}{2}m_j\dot{\theta}^2\frac{dR_j^2(S_j)}{dS_j} = -c_{a,j}\dot{S}_j \quad \text{where } j = 1 : N \tag{25.6}$$

where S_j is the (arc length) displacement of the j th absorber COM relative to the vertex on its path, m_j is the mass of absorber j , $R_j(S_j)$ is the distance from the rotor center of rotation to the absorber mass, the function

$$G_j(S_j) = \sqrt{R_j^2(S_j) - \frac{1}{4} \left(\frac{d(R_j^2(S_j))}{dS_j} \right)^2} \tag{25.7}$$

Fig. 25.3 Schematic of a rotor fitted with CPVAs



relates to a projection of the tangent of the path onto the moment arm to the center of rotor at S , J is the moment of inertia of the rotor, $T(\theta)$ is the applied torque acting on the rotor, $c_{a,j}$ represents the equivalent viscous damping coefficient for absorber j as it moves along its path, T_0 is the constant torque applied to the rotor in order to maintain a mean operating rotational speed Ω , by counteracting viscous rotor damping modeled by coefficient c_0 .

The forcing term $T(\theta)$ in Eq. (25.5) has the form of engine order excitation, so that rather than explicitly depending on time it is a function of rotor position. It is reasonable to assume that the rotor angle $\theta(t)$ can be used as the independent variable in the forcing term, as

$$T(t) = T \sin(n\theta) \quad (25.8)$$

where n is the engine excitation order. For example, in four-stroke piston engines, n is equal to one half the number of cylinders.

25.2.1 Non-dimensionalization

The set of equations are non-dimensionalized using the definitions listed in Table 25.1. As time does not appear explicitly in the equations, it is convenient to replace time as the independent variable with the rotor position θ . This results in the following definition for the dimensionless speed of the rotor position:

$$v(\theta) = \frac{\dot{\theta}}{\Omega}. \quad (25.9)$$

These operations and definitions, along with use of the chain rule, yield the following dimensionless set of equations that govern the behavior of the rotor speed and the absorber displacements

$$vv' = - \sum_{j=1}^N \alpha_j \left\{ g_j(s_j) (vv's'_j + v^2s''_j) + r_j^2(s_j)vv' + v^2s'_j \frac{d(r_j^2(s_j))}{ds_j} + v^2s'^2 \frac{d(g_j(s_j))}{s_j} - vs'_j g_j(s_j) \mu_{a,j} \right\} + \Gamma \sin(n\theta) + \Gamma_0 - \mu_0 v \quad (25.10)$$

$$vs''_j + v'(s'_j + g_j(s_j)) - \frac{1}{2}v \frac{d(r_j^2(s_j))}{ds_j} = -s'_j \mu_{a,j} \quad (25.11)$$

Table 25.1 Definition of dimensionless variables

Variables	Definitions
α_j	$\frac{m_j R_j^2(0)}{J}$
$\mu_{a,j}$	$\frac{c_{a,j}}{m_j \Omega}$
μ_0	$\frac{c_0}{J \Omega}$
s_j	$\frac{S_j}{R_j(0)}$
$g_j(s_j)$	$\frac{G_j(S_j)}{R_j(0)}$
$r_j^2(s_j)$	$\frac{R_j^2(S_j)}{R_j^2(0)}$
Γ	$\frac{T}{J \Omega^2}$
Γ_0	$\frac{T_0}{J \Omega^2}$

where $()' = \frac{d()}{d\theta}$. Note that these equations now have the familiar form of periodic excitation, where $n\theta$ plays the role usually taken by ωt .

25.2.2 The Absorber Path

Until this point, terms depending on the absorber path have been kept general, specifically, $r(s)$ (and noting that $r(s)$ specifies $g(s)$). In [6], these paths are formulated as a family of paths with two parameters which control the linear and nonlinear tuning of the CPVA. Since the behavior of the CPVA is order tuned and generally nonlinear, this motion has a small amplitude frequency given by $\tilde{n}\Omega$ where \tilde{n} is the linear tuning order, and this frequency maintains for all amplitudes when the path is a tautochronic epicycloid [1, 6]. The deviation from this path allows for nonlinear order tuning, and is conveniently defined by approximating the path function $r^2(s)$ as

$$r^2(s) = 1 - \tilde{n}^2 s + \phi s^4 + \mathcal{O}(s^6), \quad (25.12)$$

where the (small) nonlinear tuning parameter ϕ captures hardening/softening when it is negative/positive [1]. The tautochronic epicycloid, corresponding to $\phi = 0$, generates simple harmonic motion of order \tilde{n} at all amplitudes up to the cusp on the epicycloidal path, which can be determined by the condition $g(s_{\text{cusp}}) = 0$. For the $\phi = 0$ case the cusp (maximum possible) absorber amplitude is given by [1]

$$s_{\text{cusp}} \approx \frac{1}{\tilde{n}\sqrt{1 + \tilde{n}^2}}. \quad (25.13)$$

25.2.3 Reforming the Equations for HBM

In order to put the non-dimensional equations of motion, given in Eqs. (25.10) and (25.11), into the form described in Eq. (25.1), a large number of new variable definitions are required. This change of variables is described in the Appendix. These operations result in the following set of differential and algebraic equations that govern the new unknown vector, $Z \in \mathbb{R}^{N_{\text{eq}}}$, where $N_{\text{eq}} = 2 + 13N$. Note that, the terms in these equations are at most quadratic in the components of Z . Thus, application of the HBM as described in [8] becomes possible.

$$z'_{(1)} = z_{(2)} \quad (25.14)$$

$$z'_{(3j)} = z_{(3j+1)} \quad (25.15)$$

$$z'_{(3j+1)} = z_{(3j+2)} \quad (25.16)$$

$$0 = -\Gamma_0 - \Gamma \sin(n\theta) + \mu_0 z_{(1)} + z_{(1)} z_{(2)} + z_{(1)} \sum_{j=1}^N \alpha_j z_{(10N+2+j)} \quad (25.17)$$

$$0 = \mu_{a,j} z_{(3j+1)} + z_{(1)} \left(z_{(3j+2)} - \frac{1}{2} z_{(3N+3j+1)} \right) + z_{(2)} (z_{(3j+1)} + z_{(8N+2j+1)}) \quad (25.18)$$

$$0 = 1 - z_{(3N+3j)} - \tilde{n}_j^2 z_{(6N+2j+1)} + \phi_j z_{(6N+2j+1)}^2 \quad (25.19)$$

$$0 = -2\tilde{n}_j^2 z_{(3j)} + 4\phi_j z_{(3j)} z_{(6N+2j+1)} \quad (25.20)$$

$$0 = -2\tilde{n}_j^2 + 12\phi_j z_{(6N+2j+1)} \quad (25.21)$$

$$0 = -z_{(6N+2j+1)} + z_{(3j)}^2 \quad (25.22)$$

$$0 = -z_{(6N+2j+2)} + z_{(3j+1)}^2 \quad (25.23)$$

$$0 = z_{(3N+3j)} - \frac{1}{4} z_{(3N+3j+1)}^2 - z_{(8N+2j+1)}^2 \quad (25.24)$$

$$0 = z_{(3N+3j+1)} - \frac{1}{2}z_{(3N+3j+1)}z_{(3N+3j+2)} - z_{(8N+2j+1)}z_{(8N+2j+2)} \quad (25.25)$$

$$0 = -z_{(10N+j+2)} - \mu_{aj}z_{(3j+1)}z_{(8N+2j+1)} + z_{(1)}z_{(11N+2j+2)} + z_{(2)}z_{(11N+2j+1)} \quad (25.26)$$

$$0 = z_{(3N+3j)} - z_{(11N+2j+1)} + z_{(3j+1)}z_{(8N+2j+1)} \quad (25.27)$$

$$0 = -z_{(11N+2j+2)} + z_{(3j+1)}z_{(3N+3j+1)} + z_{(3j+2)}z_{(8N+2j+1)} + z_{(6N+2j+2)}z_{(8N+2j+2)} \quad (25.28)$$

25.3 Case Studies

In order to test the capabilities of this new solution approach, certain configurations of the system described above that are known to produce rich dynamical behavior are analyzed. Perturbation methods such as the method of averaging can accurately predict the dynamical behavior of these systems, provided assumptions about small values of certain non-dimensional parameters for the analysis hold [11]. Specifically, it is common to choose the ratio of the total rotational inertia of the absorbers to the rotor inertia as the main small parameter, since it is typically less than 0.15 in practice. Other parameters, such as the absorber damping and its detuning away from the engine order, and the excitation torque amplitude, must also be small when scaled appropriately. However, in systems with an inertia ratio that is not small, one generally relies on time integration of the equations of motion, which, as mentioned before, are time consuming and cumbersome for carrying out parameter studies. Also, perturbation methods assume single harmonic response of the absorbers, which is a good approximation in many cases, but is known to break down, for example, when the absorbers move at amplitudes near the cusp of the epicycloidal path. Here, we show case studies for system where the parameter values do not permit the use of perturbation methods, and also generate solutions that capture several harmonics. Furthermore, the harmonic balance approach captures unstable responses that cannot be found by time simulations.

The first case considered is a rotor equipped with a single circular path CPVA whose inertia is not small compared with that of the rotor. It is well known [12, 13] that circular path CPVAs tuned close to the excitation order will undergo a jump instability at a critical excitation torque amplitude. These jumps do not occur in CPVAs with paths such as tautochronic epicycloids or cycloids. This renders the use of circular path CPVAs impractical at close tunings to the excitation order, as this jump instability basically causes the CPVA to amplify the rotor torsional vibrations. Therefore, such absorbers are generally overtuned, which reduces their effectiveness. In the present model, we consider with single harmonic engine excitation of order $n = 2$ and a rotor/CPVA system for which the inertia ratio is $\alpha = 0.9$, which is far too large for the application of perturbation methods. The steady-state response characteristics of this system as a function of the excitation torque amplitude are given in Fig. 25.4, for both the dimensionless rotor speed (left panel) and the absorber displacement (right panel) response. Amplitudes for several harmonics are shown. Of course, the total response is a combination of these harmonics, and the response waveform depends also on the phases of these harmonics (not shown). The overall response as a function has the classic form for a softening nonlinear system, that is, as the torque increases the amplitude increases until it hits a turning point (a saddle-node bifurcation), and then there exists another, larger amplitude saddle-node bifurcation, such that there are three branches of response, the upper and lower of which are generally dynamically stable and the middle of which is unstable. (We do not consider stability analysis here; it is left for future work.) In fact, on the upper branch, the CPVA acts like a vibration amplifier, so this response must be avoided in practice. As can be seen from the harmonic amplitudes, on the lower response branch the absorber is dominated by the $n = 2$ harmonic, although other harmonics contribute significantly to the response on the upper branch. On the other hand, the harmonic content of the rotor response is dominated by higher order harmonics, specifically, $n = 4, 6, 8, \dots$, since the $n = 2$ harmonic is very small, as it should be when the absorber are operating to reduce the order n rotor response. Overall, the higher harmonic amplitudes do not sequentially diminish, for instance, harmonic amplitudes of the rotor response at orders $n = 6$ and $n = 8$ are higher than the amplitude at order $n = 4$ for certain torque ranges.

In general, balancing and space restrictions in applications force designers to distribute the absorber inertia into several absorbers placed around and along the rotor. The response characteristics of such groups of CPVAs are of importance, since the maximum torque range can be achieved when the CPVAs move in a synchronous manner, that is, all absorbers respond with equal amplitude and phase. In [1], it was shown that sets of multiple identical CPVAs with tautochronic paths undergoing a synchronous response can undergo an instability to a non-synchronous response at a certain torque amplitude that depends on the system parameters. (These tautochronic paths render the absorber essentially linear out to large amplitudes, such that the dominant system nonlinearity comes from the interactions between the rotor and the absorbers, rather than from the absorber path, as in the previous case.) To consider systems of this type, the response of a rotor subjected to order $n = 1.5$

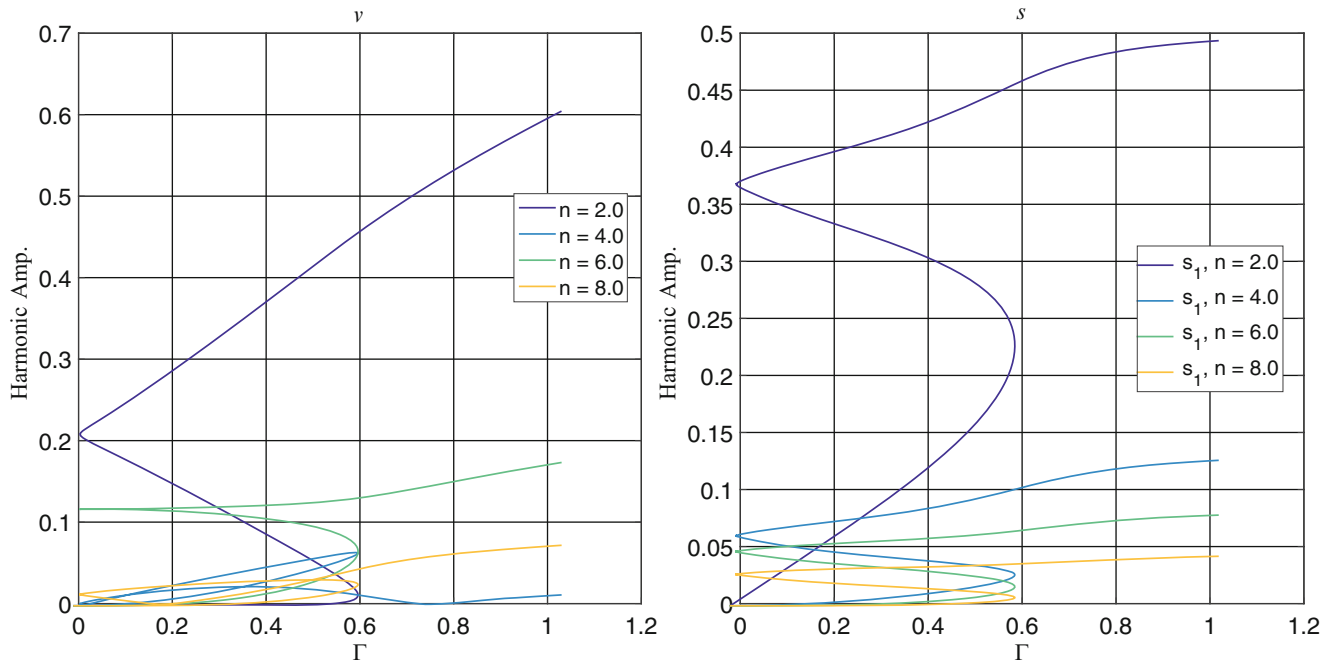


Fig. 25.4 Harmonic amplitudes of the response characteristics of a circular CPVA system, where $N = 1$, $\tilde{n}_1 = 2.01$, $\alpha_1 = 0.9$, $\mu_{a,1} = 0.005$, $H = 25$, $n = 2$ and the order of the first assumed harmonic is 1. *Left*: rotor speed, v . *Right*: absorber displacement, s_1

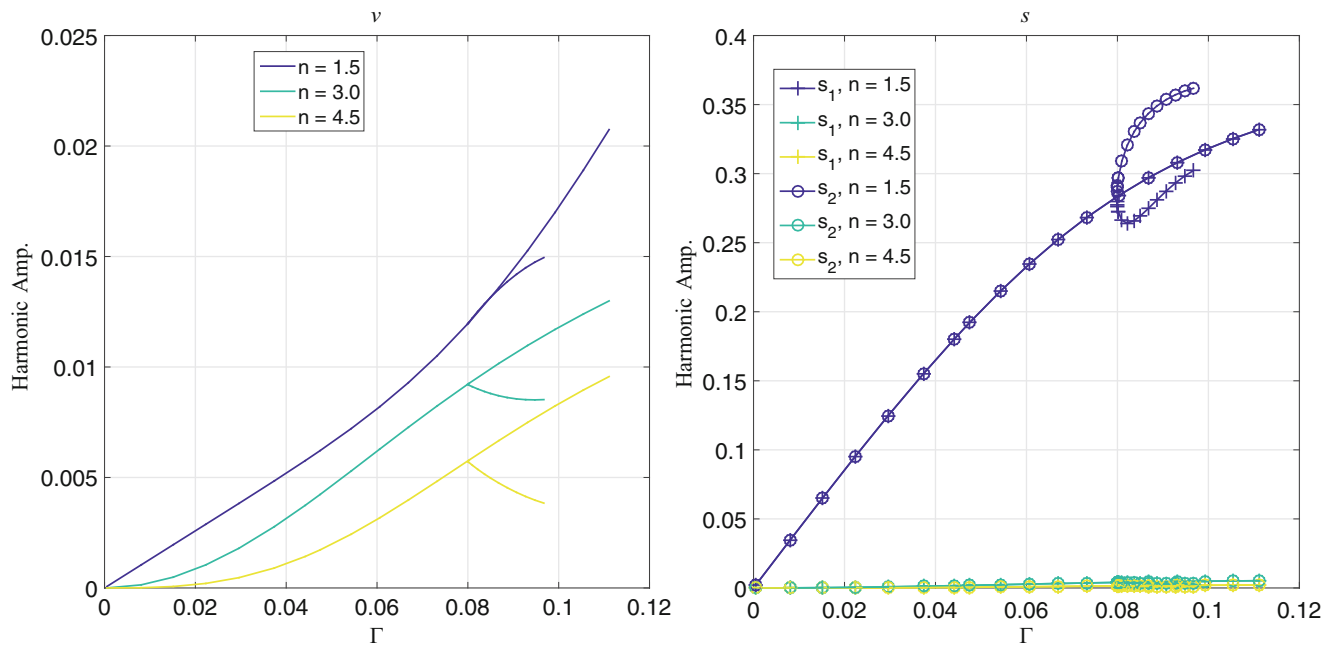


Fig. 25.5 Harmonic amplitudes of the response characteristics of the rotor with two identical tautochronic CPVAs, where $N = 2$, $\tilde{n}_{1,2} = 1.50$, $\alpha_{1,2} = 0.05$, $\mu_{a,1,2} = 0.003$, $H = 16$, $n = 1.5$ and the order of the first assumed harmonic is 0.5. *Left*: rotor speed, v . *Right*: absorber displacement, $s_{1,2}$

torque, fitted with two identical absorbers with tautochronic paths, and a small inertia ratio so that the perturbation results of [1] can be verified. The purpose of this case study is to check the ability of the HBM to capture bifurcations to non-synchronous responses. The parameters used are identical to those considered in [1], with the intention of replicating those results. The solution branches for the amplitudes of several harmonics obtained by the HBM are presented in Fig. 25.5, for both the dimensionless rotor speed (left panel) and the absorber displacement (right panel). At low torques the two absorbers

respond in a synchronous way and the rotor responds to this motion accordingly, as can be identified in the plots. As the torque is increased there is a splitting of the absorber response, where the synchronous response becomes unstable and two branches of absorber response emerge, one for each absorber, which now are moving distinctly from one another. Note that, surprisingly, the rotor torsional vibrations are lowered when the absorbers undergo the non-synchronous response, most probably due to the higher amplitude of one of these absorbers. However this response also causes that absorber to reach its cusp (maximum possible response amplitude) at a lower torque, leaving the available amplitude range of the second absorber unused and limiting the feasible operating torque range. Finally, we note that the value of Γ at which this bifurcation occurs matches almost exactly the value predicted using perturbation methods in [1].

25.4 Conclusion

In this study we present application of a harmonic balance method for determining the steady-state response of rotor systems equipped with centrifugal pendulum vibration absorbers. These nonlinear equations are generally analyzed either with time integration or using perturbation methods, which have limitations in terms of speed or applicability. The current method is adopted from the study described in [8], with which the nonlinearities are put into a quadratic polynomial form and the equations obtained this way are expressed in a Fourier series for application of the harmonic balance method with a relatively high number of assumed harmonics.

This solution framework is put to test in two different system configurations that are known to show significant qualitative changes in their response characteristic as the excitation conditions are varied. The result showed that this approach can effectively be used in the analysis of such systems. This will allow for the rapid study of absorber systems with parameter values that render analytical tools inapplicable and/or direct numerical simulations too slow. Such a tool will be very useful for design purposes.

The stability evaluation capabilities of this framework are known [10] and are essential for evaluating proposed designs. This is under study and will be integrated into the HB tool for these CPVA systems.

Acknowledgements This work is supported by the US National Science Foundation under grant CMMI-1100260 as well as by Fiat Chrysler Automobiles (FCA) US LLC. The authors are grateful to Brendan Vidmar, Abhisek Jain, Ming Mu of MSU, Johannes Mayet of Technische Universität München, and Bruce Geist of FCA, and Sami Karkar, member of development team of MANLAB, for helpful discussions.

Appendix: Variable Recasting

The procedure starts by inserting the coordinates and their derivatives of the original equations into the new unknown vector, Z .

$$z_1 = v \quad (25.29)$$

$$z_2 = v' \quad (25.30)$$

$$z_{(3j)} = s_j \quad (25.31)$$

$$z_{(3j+1)} = s'_j \quad (25.32)$$

$$z_{(3j+2)} = s''_j \quad (25.33)$$

The next step is to define variables to represent the radial position of the absorber mass and its first and second derivatives as shown

$$z_{(3N+3j)} = r_j^2(s_j) \quad (25.34)$$

$$z_{(3N+3j+1)} = \frac{d(r_j^2(s_j))}{ds_j} \quad (25.35)$$

$$z_{(3N+3j+2)} = \frac{d^2(r_j^2(s_j))}{ds_j^2}. \quad (25.36)$$

Such that

$$z_{(3N+3j)} = 1 - \tilde{n}_j^2 z_{(3j)}^2 + \phi_j z_{(3j)}^4 \quad (25.37)$$

$$z_{(3N+3j+1)} = -2\tilde{n}_j^2 z_{(3j)} + 4\phi_j z_{(3j)}^3 \quad (25.38)$$

$$z_{(3N+3j+2)} = -2\tilde{n}_j^2 + 12\phi_j z_{(3j)}^2. \quad (25.39)$$

In order to account for powers of absorber position and velocity coordinates that are higher than quadratic, another set of variables are defined as

$$z_{(6N+2j+1)} = z_{(3j)}^2 \quad (25.40)$$

$$z_{(6N+2j+2)} = z_{(3j+1)}^2. \quad (25.41)$$

The most problematic terms in the equations of motion stem from the function $g(s)$ and its derivative, as the definition of the former involves the square root of an expression [see Eq. (25.7)]. To handle this we define a new set of variables and form a set of quadratic algebraic equations as follows

$$z_{(8N+2j+1)} = g_j(s_j) \quad (25.42)$$

$$z_{(8N+2j+2)} = \frac{d(g_j(s_j))}{s_j} \quad (25.43)$$

to obtain

$$z_{(8N+2j+1)}^2 = z_{(3N+3j)} - \frac{1}{4} z_{(3N+3j+1)}^2 \quad (25.44)$$

$$z_{(8N+2j+2)} z_{(8N+2j+1)} = z_{(3N+3j)} - \frac{1}{2} z_{(3N+3j+1)} z_{(3N+3j+2)}. \quad (25.45)$$

Using these definitions, we can express the terms in the equations of motion using yet another variable definition

$$\begin{aligned} z_{(10N+j+2)} = & -\mu_{a,j} z_{(3j+1)} z_{(8N+2j+1)} + z_{(2)} \left(z_{(3N+3j)} + z_{(3j+1)} z_{(8N+2j+1)} \right) \\ & + z_{(1)} \left(z_{(3j+1)} z_{(3N+3j+1)} + z_{(3j+2)} z_{(8N+2j+1)} + z_{(6N+2j+2)} z_{(8N+2j+2)} \right) \end{aligned} \quad (25.46)$$

Finally, as the last layer of the recasting process, we define

$$z_{(11N+2j+1)} = z_{(3N+3j)} + z_{(3j+1)} z_{(8N+2j+1)} \quad (25.47)$$

$$z_{(11N+2j+2)} = z_{(3j+1)} z_{(3N+3j+1)} + z_{(3j+2)} z_{(8N+2j+1)} + z_{(6N+2j+2)} z_{(8N+2j+2)}. \quad (25.48)$$

References

1. Shaw, S.W., Geist, B.: Tuning for performance and stability in systems of nearly tautochronic torsional vibration absorbers. *J. Vib. Acoust.* **132**(4), 041005 (2010)
2. Shaw, S.W., Schmitz, P.M., Haddow, A.G.: Tautochronic vibration absorbers for rotating systems. *J. Comput. Nonlinear Dyn.* **1**(4), 283–293 (2006)
3. Geist, B., Barron, C.S., Resh, W.F., Hossain, M.I., Patyi, M.P., Mashkevich, S.M.: Pendulum vibration absorber on a crankshaft. US Patent 8,813,604, 26 Aug 2014
4. Tsio360 Crankshaft: <http://www.aircraft-specialties.com/tsio360-crankshaft-653139/>. Accessed 24 Oct 2015
5. Wilson, W.K.: *Practical Solution of Torsional Vibration Problems*, Chap. 30. Chapman & Hall, London (1968)
6. Denman, H.H.: Tautochronic bifilar pendulum torsion absorbers for reciprocating engines. *J. Sound Vib.* **159**(2), 251–277 (1992)
7. Alsuwaiyan, A.S., Shaw, S.W.: Performance and dynamic stability of general-path centrifugal pendulum vibration absorbers. *J. Sound Vib.* **252**(5), 791–815 (2002)
8. Cochelin, B., Vergez, C.: A high order purely frequency-based harmonic balance formulation for continuation of periodic solutions. *J. Sound Vib.* **324**(1), 243–262 (2009)

9. Manlab: An interactive path-following and bifurcation analysis software. <http://manlab.lma.cnrs-mrs.fr/>. Accessed 24 Oct 2015
10. Thomas, O., Lazarus, A., Touzé, C.: A harmonic-based method for computing the stability of periodic oscillations of non-linear structural systems. In: ASME 2010 International Design Engineering Technical Conferences and Computers and Information in Engineering Conference, pp. 883–892. American Society of Mechanical Engineers, Montreal (2010)
11. Sanders, J.A., Verhulst, F., Murdock, J.A.: Averaging Methods in Nonlinear Dynamical Systems, vol. 59. Springer, New York (2007)
12. Den Hartog, J.P.: Tuned pendulums as torsional vibration absorbers. S. Timoshenko 60th Anniversary Volume, pp. 17–26 (1938)
13. Newland, D.E.: Nonlinear aspects of the performance of centrifugal pendulum vibration absorbers. J. Manuf. Sci. Eng. **86**(3), 257–263 (1964)

Chapter 26

Development of Multi-Physics Dynamics Models for High-Frequency Large-Amplitude Structural Response Simulation

Armen Derkevorkian, Lee Peterson, Ali R. Kolaini, Terry J. Hendricks, and Bill J. Nesmith

Abstract An analytic approach is demonstrated to reveal potential pyroshock-driven dynamic effects causing temporary power losses in the Thermo-Electric (TE) module bars of the Mars Science Laboratory (MSL) Multi-Mission Radioisotope Thermoelectric Generator (MMRTG). This study utilizes high-fidelity finite element analysis with SIERRA/PRESTO codes to estimate wave propagation effects due to large-amplitude suddenly-applied pyroshock loads in the MMRTG. A high fidelity model of the TE module bar was created with ~ 30 million degrees-of-freedom (DOF). First, a quasi-static preload was applied on top of the TE module bar, then transient tri-axial displacement inputs were simultaneously applied on the preloaded module. The applied displacement inputs were derived from measured acceleration signals during MMRTG shock qualification tests performed at the Jet Propulsion Laboratory. An explicit finite element solver in the SIERRA/PRESTO computational environment, along with a 3000 processor parallel super-computing framework at NASA-AMES, was used for the simulation. The simulation results were investigated both qualitatively and quantitatively. The predicted shock wave propagation results provide detailed structural responses throughout the TE module bar, and key insights into the dynamic response (i.e., loads, displacements, accelerations) of critical internal spring/piston compression systems, TE materials, and internal component interfaces in the MMRTG TE module bar. They also provide confidence on the viability of this high-fidelity modeling scheme to accurately predict shock wave propagation patterns within complex structures. This analytic approach is envisioned for modeling shock sensitive hardware susceptible to intense shock environments positioned near shock separation devices in modern space vehicles and systems.

Keywords Computational modeling • Nonlinear dynamics • Shock waves • Multi-physics simulation • Parallel computing

26.1 Introduction

Severe pyroshock environments due to several shock separation devices in the close proximity of the Multi-Mission Radioisotope Thermoelectric Generator (MMRTG) were derived for the Mars Science Laboratory (MSL) project. A series of pyroshock tests was performed as part of the multi-mission qualification testing using an Engineering Unit (EU). During the MMRTG engineering unit's pyroshock test, the power output from the system temporarily decreased, but fully recovered after the shock signature subsided. Additional Qualification Unit (QU) testing was performed as part of standard MSL flight readiness preparations. The QU test was performed at JPL by mounting it on the flight MSL rover chassis, where flight-like separation nuts were fired. The results from the QU pyroshock test confirmed that the generator would respond to a flight level pyroshock event with a temporary power drop, although significantly less severe than that experienced by the EU shock test. An effort is underway to understand the root causes of the RTG temporary power losses, and a detailed system fault tree and associated system analyses have been developed to establish specific root-cause and recovery pathways. As part of this effort, the shock-induced structural response within Thermo-Electric (TE) module bars of the system has been modeled, and the results are presented and discussed in this study.

The activation of pyro-shock devices such as separation nuts, pin-pullers, etc., produces high-frequency transient structural inputs and responses to spacecraft power units, typically from a few tens of Hz to several tens of kHz. Lack of reliable analytical tools makes the prediction and interpretation of appropriate design and qualification test levels a challenge. In the past decades, several attempts have been made to develop methodologies that predict the structural responses to shock environments. However, there is no validated approach that is viable to capture the full frequency range of interest (i.e.,

A. Derkevorkian (✉) • L. Peterson • A.R. Kolaini • T.J. Hendricks • B.J. Nesmith
Jet Propulsion Laboratory, California Institute of Technology, 4800 Oak Grove Dr., Pasadena, CA 91109, USA
e-mail: Armen.Derkevorkian@jpl.nasa.gov

100 Hz to 10 kHz). Some of the important studies include works by [1–7], amongst others. Conventional modal analysis tools that are used to predict structural responses are applicable only to low-frequency regions (i.e., a few-hundreds of Hz). In order to capture the structural response due to high-frequency wave propagation in electronics components positioned near separation devices, advanced high-fidelity, wave propagation modeling and analysis methods are needed. Shock analysis techniques can broadly be categorized into three approaches: (1) Empirical Models and Scaling Laws, (2) Statistical Energy Analysis, and (3) Finite Element Analysis. Since the approach used in this study is based on finite element analysis, the discussion will focus on finite-element based approaches.

Finite Element Analysis can be used to predict structural response to transient full-frequency dynamic loads. However, in order to capture the high-frequency shock wave propagation, the model has to be meshed into very small elements. Large numbers of elements can lead to computational challenges and long model run times. More importantly, simulating the correct physics for high-frequency wave propagation is a daunting task, and most classical finite element approaches are not feasible to solve this problem [8]. In the recent years, important studies have been published relevant to FEA-based modeling. Ramajeyathilagam et al. studied the non-linear transient dynamic response of rectangular plates under shock loading [9]. Qiu et al. investigated the finite element analysis of the dynamic response of clamped sandwich beams subject to shock loading [10]. Lee et al. analyzed a finite element response of a rotor-bearing system to base shock excitations using the space Newmark scheme and compared it with experiments [11]. Kalman et al. published on the numerical analysis of the dynamic effects in shock-load-induced ice shedding on overhead ground wires [12]. Mace and Manconi modeled wave propagation in 2-dimensional structures using finite element analysis [13]. Liu et al. studied the impact of sand slugs against beams and plates using coupled discrete particle and finite element simulations [14]. Pagani et al. simulated the dynamic response of aerospace structures by means of refined beam theories [15]. Derkevorkian et al. investigated the viability of using advanced computational modeling approaches for shock response prediction [16].

However, there is paucity of high-fidelity computational tools, and corresponding explicit finite element solvers that can potentially be utilized for shock simulation problems of complex structures. One such numerical tool (i.e., SIERRA/Presto) is used in this study to model the TE module bar within a MMRTG structure, and to predict its response to pyro-shock-induced dynamic loads.

26.2 Modeling Methodology

An explicit finite element solver, called Presto (part of the SIERRA—Solid Mechanics suite), was used to simulate the dynamic effects due to shock wave propagation in the TE module bar. The SIERRA suite is a Lagrangian, three-dimensional numerical tool developed for finite-element analysis of large-scale multi-physics phenomena. Its explicit dynamics features are designed to solve models that have various contact surfaces and are subjected to large, suddenly applied loads, such as the model and structures under investigation in this paper. Further details on SIERRA’s technical multi-physics capabilities can be found in [17, 18]. The Cubit mesh generation environment, which meshes volumes and solid models for finite element analysis, was used to generate three-dimensional finite element mesh of the TE module bar. Some of the algorithms embedded in Cubit include paving, mapping, and sweeping, to discretize a given geometry into a finite element mesh. More information on Cubit’s features is available in [19].

A top view of the TE module bar is shown in Fig. 26.1. The bar is made of various materials and it consists of multiple springs, contact surfaces, and joint discontinuities. Using Cubit, the module bar was discretized into ~ 11.5 million elements.

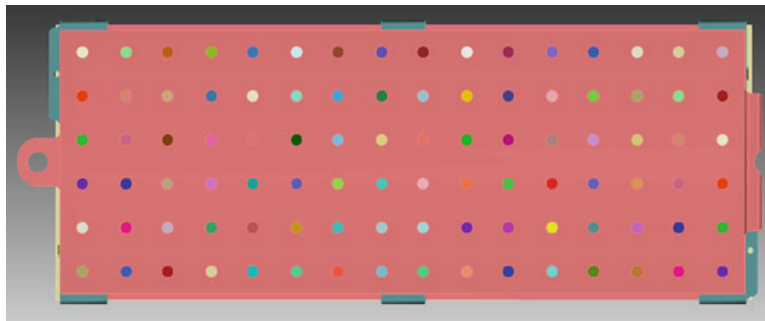


Fig. 26.1 Top view of the TE module bar

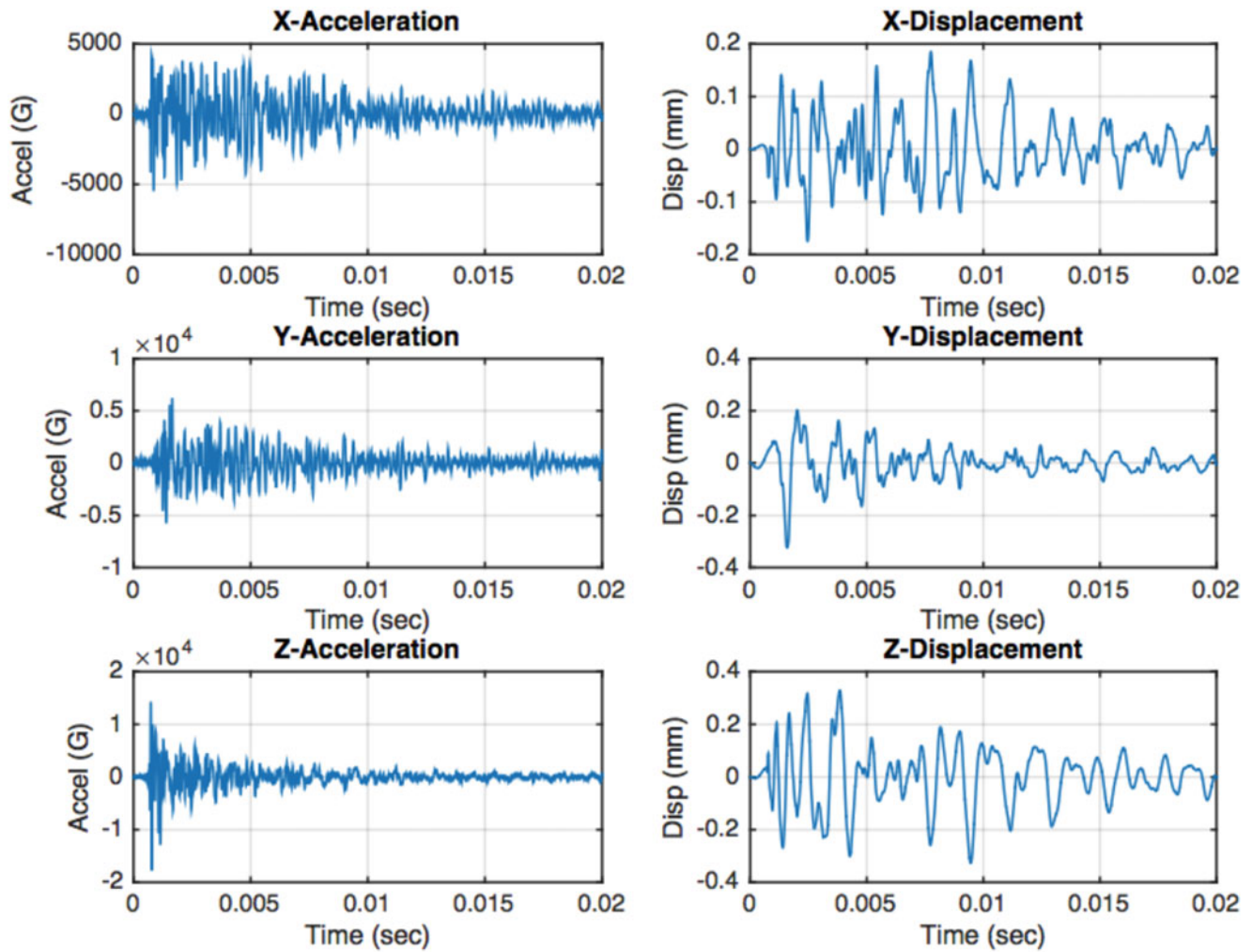


Fig. 26.2 Measured shock acceleration signatures in X, Y, and Z directions (*left column*), and the displacement signatures obtained by numerical integration (*right column*)

About 30 % of the elements are tetrahedral elements (used to mesh the interior springs), and the rest are hexahedral elements used to discretize and mesh the rest of the components. The finite element model size was chosen to maximize detail to capture the right physics within reasonable CPU time on the supercomputers at the NASA AMES Research Center. The system loading was applied in two analytic steps. The springs within the model were compressed in the vertical direction by applying a quasi-static pre-load in the gravity direction, before the shock environment was applied as an input to the model. Then, a displacement time-history, derived from a measured 3-dimensional shock acceleration record from a previous qualification test was applied to the model (in all three direction, simultaneously). The acceleration record was measured during the shock qualification test of the Engineering Unit (EU) mentioned earlier. The shock input signatures obtained from EU pyro-firing test were band-pass filtered using Finite Impulse Response (FIR) filter of 20th order to include shock signatures between 500 and 10,000 Hz. The frequencies below 500 Hz were filtered to concentrate on the high-frequency wave propagation aspect of the model, as well as to eliminate the low-frequency dynamic effects of supporting structures, such as the steel plate on which the MMRTG was mounted during the shock qualification test. The acceleration time-histories and the corresponding displacements in all three directions are shown in Fig. 26.2. The displacement time-histories were applied as inputs to the FE model at the short edge of an interface plate located on top of the module bar, to predict the nonlinear dynamic response of the module bar's inner components. The short edge, where the shock displacement record was applied, is shown in Fig. 26.4b. Non-reflecting surface boundary conditions were applied on the other sides of the

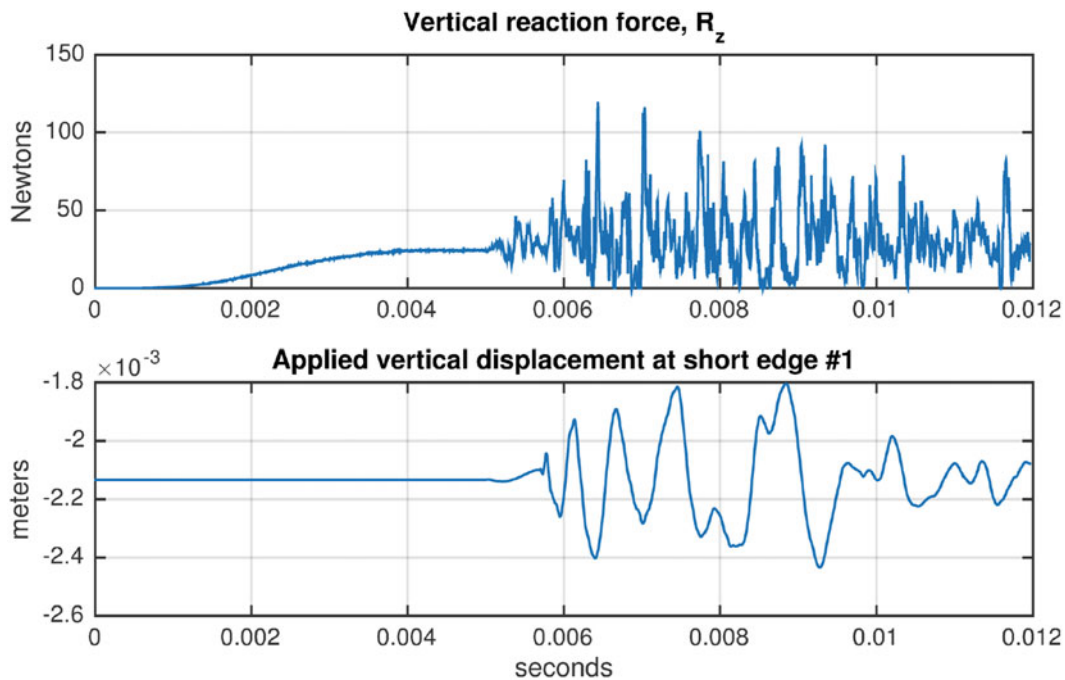


Fig. 26.3 The reaction force (Newton) at the *bottom* of a sample section shown in Fig. 26.4 (first subfigure). The displacement (meters) applied during the preload and the pyroshock, at the edge of the interface plate (second subfigure)

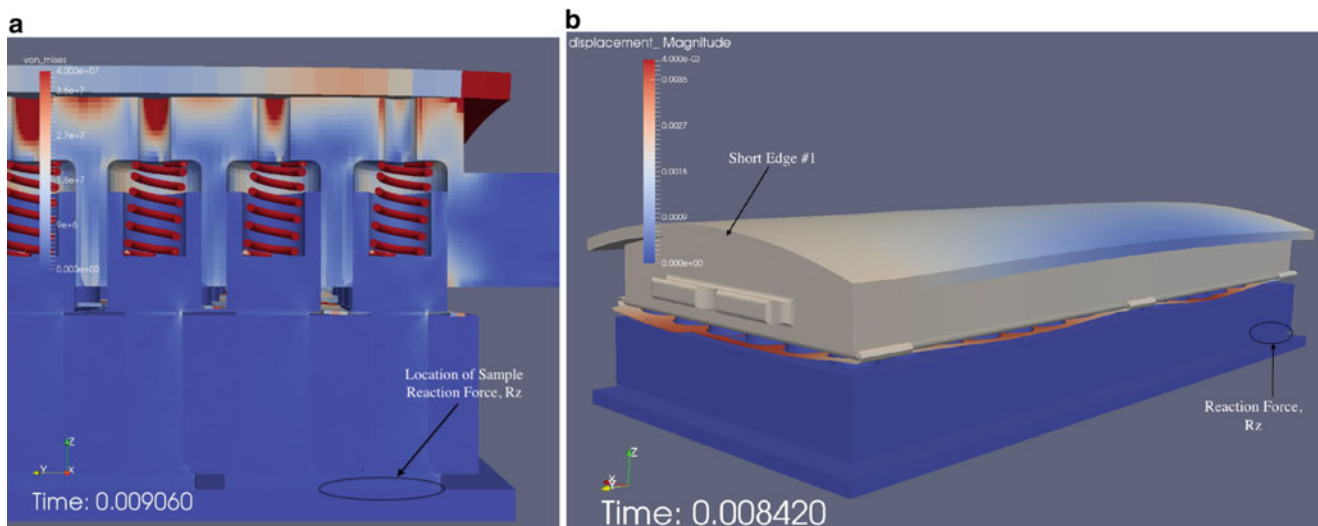


Fig. 26.4 Von Mises stresses and displacements results from the numerical simulation. (a) Von Mises stresses at a sample cross-section in the module bar; (b) The displacements at the various sections of the module bar

top interface plate. The module bar model was placed in between two interface plates at the top and the bottom. The bottom plate was fixed in all directions with no slippage allowed. Several contact surfaces were modeled with frictional force applied within the inner components of the system. A coefficient of friction of 0.5 was assumed. The assumed coefficient of friction will be experimentally verified and will be reported in the upcoming papers. The quasi-static pre-load was applied for the first 5 ms. Then the shock displacement inputs (shown in Fig. 26.2) were applied. The reaction forces at the bottom of the FE model, as well as the Von Mises stresses at various locations were recovered at the end of the simulation. The total running time was about 60 h using 3000 processors.

26.3 Numerical Results

The first row in Fig. 26.3 shows the reaction force in the vertical direction at the bottom of a sample location in the module bar. The second row in Fig. 26.3 shows the applied vertical displacement at one of the short edges of the interface plate located on top of the module bar (i.e., short edge #1 shown in Fig. 26.4b). The locations of the retrieved reaction force and the applied displacement signature are shown in Fig. 26.4. In the first row of Fig. 26.3, it is shown that a preload of ~ 25 Newton is applied as a slowly varying cosine function during the first 5 ms of the simulation. Then, the shock signature is applied as a prescribed displacement, resulting in a maximum reaction force of ~ 120 Newton at about 6.5 ms. The maximum reaction force corresponds to more than 4 times increase in the initial preload. Another very important observation is that the reaction force becomes zero at multiple instances throughout the simulation (i.e., the spring/piston system in the module bar unloads). This phenomenon was observed in other locations throughout the TE module bar as well, and may potentially be one of the significant reasons that contribute to the overall power drop in the MMRTG. The second row of Fig. 26.3 shows the applied vertical displacement at one of the short edges of the interface plate on the top of the module bar. The two plots in Fig. 26.3 are placed after each other to detect potential correlation between the peaks of the applied displacement and the unloading that occurs at the bottom. It is seen that most of the peaks in the pyroshock displacement signature are correlated, relatively well, with the instances where the reaction force is zero. This observation supports the argument that the spring/piston unloading at the bottom is due to high intensity waves in the input shock signature.

The numerical results were further processed using a powerful postprocessing tool called, Paraview. Sample results are shown in Fig. 26.4. Figure 26.4a shows the Von Mises stresses at a sample cross-section in the module bar. The springs shown in the figure are modeled to have friction contacts at the top and the bottom. After applying the quasi-static preload, the springs tilt sideways and contact the interior sidewalls at the top and the bottom. The tilting is due to the asymmetric nature of the springs' ends. The contact of the springs' coils with the surrounding walls during pyroshock dynamic loading/unloading can affect the thermal properties of the TE module bar, which in turn might affect the corresponding power output. The animation of Fig. 26.4a also reveals that after applying the shock signatures, the springs exhibit a strong response at a frequency of ~ 3 kHz. Figure 26.4b shows the displacement of the overall module bar with the top and the bottom interface plates. The figure shows significant amount of displacements along the insulation sheet in the middle of the bar. It is seen that the high-fidelity modeling approach adopted in this study reveals important information about the nonlinear dynamic behavior of the inner components of the TE module bar and provides critical insights into potential causes of MMRTG power losses during pyroshock events.

26.4 Conclusion

This work is part of a large ongoing effort in understanding the risks associated with the output power drop and recovery observed during various levels of MMRTG pyroshock testing. In this study, a finite-element based high fidelity modeling approach is adopted to simulate shock wave propagation in a relatively complex structural system (i.e., the MMRTG TE module bar). The complexity of the system underlies in its multiple contact mechanisms and interfaces and the preloaded interior springs. A sophisticated explicit solver (i.e., Presto) is utilized to estimate the response of the system to transient shock signatures measured from system level shock qualification tests. It is shown that the proposed approach can provide valuable information regarding the structural behavior as shock waves propagate through the system's various components and interfaces. Some of the important findings from this study include the unloading of the reaction force multiple times during the pyroshock event, tilting of the springs during the preload, the unexpected contact between the springs and the sidewalls of the bar during the pyroshock event, and the strong oscillation of the springs at about 3 kHz. These findings were not obvious before the shock qualification test and could not be obtained from traditional modal-based low-frequency finite element transient analysis approaches. These findings are crucial and provide guidance for potential improvements and refinements to the existing design of the MMRTG system and its TE module bars. Performing large-scale multi-physics numerical simulations is associated with certain challenges. Some of these challenges include the physical interpretation of the results (i.e., distinguishing between potential numerical errors and actual physical responses), sensitivity to uncertain input parameters, and the need for significant computational capabilities and run time. Hence, verification and validation is needed to evaluate the efficacy of such tools. A tunable-beam shock simulation testing is currently being planned at JPL to validate the numerical results presented in this paper. Currently, there is a paucity of viable approaches to predict shock wave propagation and the corresponding structural response of complex structures. The approach presented in this study provides an improved method to be considered for high-frequency shock wave propagation predictions.

Acknowledgments The authors would like to thank June Zakrajsek, NASA-Glenn Research Center, RPS Program Planning & Assessment Manager, and Dave Woerner, NASA-Jet Propulsion Laboratory, RTG Integration Manager, RPS Program. The research was carried out at the Jet Propulsion Laboratory, California Institute of Technology, under a contract with the National Aeronautics and Space Administration.

References

1. Lih, S.-S., Mal, A.K.: Elastodynamic response of a unidirectional composite laminate to concentrated surface loads: Part II. *J. Appl. Mech.* **59**(4), 887–892 (1992)
2. Mal, A.K., Lih, S.-S.: Elastodynamic response of a unidirectional composite laminate to concentrated surface loads: Part I. *J. Appl. Mech.* **59**(4), 878–886 (1992)
3. Kotzias, B.: Shock simulation for truss coupled shell structures. In: 55-th International Astronautical Congress, 2004, Vancouver, Canada
4. Kotzias, B.: Projection method in structural dynamics in application to shock propagation simulation for truss coupled shell structures. In: Proc. European Conference on Spacecraft Structures, Materials and Mechanical Testing 2005, Noordwijk, The Netherlands. vol 581, p. 121, 2005
5. Kotzias, B., Albus, J.: Pyrotechnique shocks in launch vehicles. In: Proc. 5th European Conference for Aerospace Sciences (EUCASS), Munich, Germany, 2013
6. Botta, F., Cerri, G.: Shock response spectrum in plates under impulse loads. *J. Sound Vib.* **308**(3), 563–578 (2007)
7. Duran, A., Hwang, H.-J.: Stochastic shock response spectrum decomposition method. In: Proceedings of the Spacecraft and Launch Vehicle Dynamic Environments Workshop, El Segundo, CA, May 2015
8. Hamelblau, H., Kern, D.L., Manning, J.E., Pierson, A.G., Rubin, S.: Dynamics environmental criteria. In: NASA Technical Handbook, NASA-HDBK-7005, 4 December 2000
9. Ramajeyathilagam, K., Vendhan, C.P., Bhujanga Rao, V.: Non-linear transient dynamic response of rectangular plates under shock loading. *Int. J. Impact Eng.* **24**(10), 999–1015 (2000)
10. Qiu, X., Deshpande, V.S., Fleck, N.A.: Finite element analysis of the dynamic response of clamped sandwich beams subject to shock loading. *Eur. J. Mech. A. Solids* **22**(6), 801–814 (2003)
11. Lee, A.S., Kim, B.O., Kim, Y.-C.: A finite element transient response analysis method of a rotor-bearing system to base shock excitations using the state-space newmark scheme and comparisons with experiments. *J. Sound Vib.* **297**(3), 595–615 (2006)
12. Kalman, T., Farzaneh, M., McClure, G.: Numerical analysis of the dynamic effects of shock-load-induced ice shedding on overhead ground wires. *Comput. Struct.* **85**(7), 375–384 (2007)
13. Mace, B.R., Manconi, E.: Modelling wave propagation in two-dimensional structures using finite element analysis. *J. Sound Vib.* **318**(4), 884–902 (2008)
14. Liu, T., et al.: The impact of sand slugs against beams and plates: coupled discrete particle/finite element simulations. *J. Mech. Phys. Solids* **61**(8), 1798–1821 (2013)
15. Pagani, A., et al.: Dynamic response of aerospace structures by means of refined beam theories. *Aerosp. Sci. Technol.* **46**, 360–373 (2015)
16. Derkevorkian, A., Kolaini, A.R., Peterson, L.: Advanced computational modeling approaches for shock response prediction. In: Proceedings of the 29th Aerospace Testing Seminar, Los Angeles, CA, 2015
17. Crane, N.K.: Sierra/SM Theory Manual. No. SAND2013-4615. Sandia National Laboratories (SNL-NM), Albuquerque, NM (United States), 2013
18. Thomas, J.D.: Sierra/Solid Mechanics 4.22 User's Guide. No. SAND2011-7597. Sandia National Laboratories, 2011
19. Blacker, T.D., Bohnhoff, W.J., Edwards, T.L.: CUBIT Mesh Generation Envi0072onment, vol. 1: Users Manual. No. SAND-94-1100. Sandia National Labs, Albuquerque, NM (1994)

Chapter 27

An Efficient Simulation Method for Large-Scale Systems with Local Nonlinearities

Yousheng Chen, Andreas Linderholt, and Thomas Abrahamsson

Abstract In practice, most mechanical systems show nonlinear characteristics within the operational envelope. However, the nonlinearities are often caused by local phenomena and many mechanical systems can be well represented by a linear model enriched with local nonlinearities. Conventional nonlinear response simulations are often computationally intensive; the problem which becomes more severe when large-scale nonlinear systems are concerned. Thus, there is a need to further develop efficient simulation techniques. In this work, an efficient simulation method for large-scale systems with local nonlinearities is proposed. The method is formulated in a state-space form and the simulations are done in the Matlab environment. The nonlinear system is divided into a linearized system and a nonlinear part represented as external nonlinear forces acting on the linear system; thus taking advantage in the computationally superiority in the locally nonlinear system description compared to a generally nonlinear counterpart. The triangular-order hold exponential integrator is used to obtain a discrete state-space form. To shorten the simulation time additionally, auxiliary matrices, similarity transformation and compiled C-codes (mex) to be used for the time integration are studied. Comparisons of the efficiency and accuracy of the proposed method in relation to simulations using the ODE45 solver in Matlab and MSC Nastran are demonstrated on numerical examples of different model sizes.

Keywords Efficient time integration • Triangular-order hold • State-space • Locally nonlinear systems • C-code/mex

27.1 Introduction

Forced responses of a nonlinear system are essential for the understanding of its nonlinear dynamic characteristics. This generally requires significant computational effort, especially when large-scale systems are concerned. If steady-state responses are searched for, frequency domain methods which do not include the transient part of the solution, such as the harmonic balance method [1, 2], are considered to be more efficient than time domain methods. However, to include the transient part of a solution, a time domain method has to be utilized. When tackling a stiff problem, which is often encountered in a large-scale model, traditional time domain methods such as the Runge-Kutta [3] and Newmark method [4] may be considered as inefficient because they require small time step sizes to maintain stability and accuracy. Many research papers deal with the development of fast nonlinear simulation methods. In [5–7], model reduction of nonlinear structures is applied in order to shorten the simulation times. In [8], a digital filter based method is used to efficiently simulate the forced response of a locally nonlinear structure. The approach was applied and further developed in [9, 10].

Nonlinearity can be considered as being either global or local. If a large portion of the structure shows nonlinear characteristics, the nonlinear sources can be considered as global, e.g. when a structure is exposed to an excessively large loading. In contrast, a structure with local nonlinearities is characterized as being mainly linear while with limited areas showing strong nonlinear behavior. Common sources for local nonlinearities are large displacements, contacts and dry friction. The simulation method developed in this paper is for structures with local nonlinearities.

A fast simulation method which utilizes a discrete state-space form to describe the linear part and treat the nonlinear restoring forces as pseudo forces acting on the linear part was proposed in [11, 12]. The method includes two stages. In the first stage, the whole time sequence is adaptively splitted into equal duration time blocks with length nh , where h is the time step. The responses are then found using an n -step ahead implicit integrator in the second stage. Such an n -step ahead

Y. Chen (✉) • A. Linderholt
Department of Mechanical Engineering, Linnaeus University, 35195 Växjö, Sweden
e-mail: yousheng.chen@lnu.se

T. Abrahamsson
Department of Applied Mechanics, Chalmers University of Technology, 41296 Gothenburg, Sweden

prediction results in a loss of accuracy to some extent. It may require a lot of computationally effort to decide the length of the time block to be used for updating of the nonlinearities and it may suffer from convergence problems when the nonlinearities are strong or non-smooth.

In this paper, the accuracy and efficiency of the state-space based method are improved by using one-step ahead instead of n -step ahead prediction. One-step ahead prediction enables the improved method to utilize the superiority of the discrete state-space representation built by the non-causal triangular-order hold to update nonlinear forces more efficiently. To further shorten the simulation time, an auxiliary matrix (AM), matrix diagonalization (MD) and compiled C-codes are applied. Comparisons of the efficiency and accuracy of the proposed method in relation to simulations using the ODE45 solver in Matlab and MSC Nastran are demonstrated on a bouncing ball problem which is modelled using different model sizes.

27.2 Theory

For a general nonlinear mechanical system, the governing equation of motion can be expressed as

$$M\ddot{q} + V\dot{q} + Kq + u^{\text{NL}}(q, \dot{q}) = u \quad (27.1)$$

in which M , V , K are the mass, damping and stiffness matrices respectively, while \ddot{q} , \dot{q} , q , u^{NL} and u are the acceleration, velocity, displacement, nonlinear function of the displacement and velocity and applied external force vector respectively.

To simulate the response of a locally nonlinear system, a one-step linear implicit integrator which takes advantage of the superiority of the triangular-order hold is proposed in this paper. The proposed method mainly consists of two parts; modelling and time integration, which is illustrated in Fig. 27.1.

The fundamental idea is to model a locally nonlinear system as an underlying linear system and a nonlinear part which is treated as a feedback force acting on the underlying linear system. The underlying linear system is first written in a continuous state-space form. A discrete state-space form is obtained using an exponential integrator together with a non-causal triangular-order hold which is used for interpolation of the external force and the nonlinear forces. The nonlinear forces are obtained through iterations.

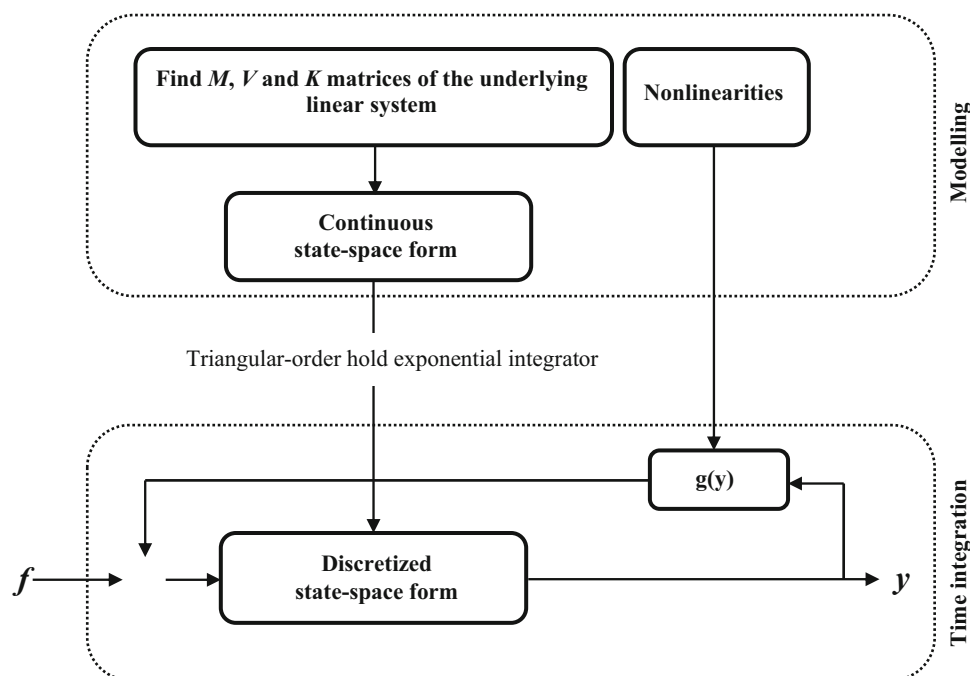


Fig. 27.1 An overview of the proposed simulation method. The nonlinear system is separated into a linear part and nonlinear feedback forces. A triangular-order hold exponential integrator is used to obtain a discrete state-space form of the linear part

27.2.1 Exponential Integrator

A state vector composed by the displacement \mathbf{q} and velocity $\dot{\mathbf{q}}$ such that $\mathbf{x}^T = [\mathbf{q}^T \dot{\mathbf{q}}^T]$ is defined. Equation (27.1) can be recast into a state-space form as

$$\dot{\mathbf{x}} = \mathbf{A}_c \mathbf{x} + \mathbf{B}_c \mathbf{u}(t) + \mathbf{B}_c^{\text{NL}} \mathbf{u}^{\text{NL}}(\mathbf{q}, \dot{\mathbf{q}}) \quad (27.2a)$$

$$\mathbf{y} = \mathbf{C}_c \mathbf{x} + \mathbf{D}_c \mathbf{u}(t) + \mathbf{D}_c^{\text{NL}} \mathbf{u}^{\text{NL}}(\mathbf{q}, \dot{\mathbf{q}}) \quad (27.2b)$$

where $\mathbf{x} \in \mathbb{R}^{N \times 1}$, $\mathbf{A}_c \in \mathbb{R}^{N \times N}$, $\mathbf{B}_c \in \mathbb{R}^{N \times ni}$, $\mathbf{B}_c^{\text{NL}} \in \mathbb{R}^{N \times nnl}$, $\mathbf{C}_c \in \mathbb{R}^{no \times N}$, $\mathbf{D}_c \in \mathbb{R}^{no \times ni}$, and $\mathbf{D}_c^{\text{NL}} \in \mathbb{R}^{no \times nnl}$. The matrices \mathbf{A}_c , \mathbf{B}_c , \mathbf{B}_c^{NL} , \mathbf{C}_c , \mathbf{D}_c and \mathbf{D}_c^{NL} are the continuous state-space matrices which are constant. N is twice of the number of degrees of freedom of the system, ni the number of external inputs, no the number of outputs and nnl the number of nonlinear forces. The external forces are projected into the state-space through the input matrix \mathbf{B}_c . The residual term $\mathbf{B}_c^{\text{NL}} \mathbf{u}^{\text{NL}}(\mathbf{q}, \dot{\mathbf{q}})$, represents the internal nonlinear forces. The \mathbf{A}_c matrix can be written as:

$$\mathbf{A}_c = \begin{bmatrix} 0 & \mathbf{I} \\ -\mathbf{M}^{-1} \mathbf{K} & -\mathbf{M}^{-1} \mathbf{V} \end{bmatrix} \quad (27.3)$$

Subtracting $\mathbf{A}_c \mathbf{x}$ from both side of Eq. (27.2a) gives a quasi-linear form,

$$\dot{\mathbf{x}} - \mathbf{A}_c \mathbf{x} = \mathbf{B}_c \mathbf{u}(t) + \mathbf{B}_c^{\text{NL}} \mathbf{u}^{\text{NL}}(\mathbf{q}, \dot{\mathbf{q}}) \quad (27.4)$$

Premultiplying both sides of Eq. (27.4) with $e^{-\mathbf{A}_c t}$, the left hand side of the equation can then be written as a derivate which yields

$$\frac{d(e^{-\mathbf{A}_c t} \mathbf{x}(t))}{dt} = e^{-\mathbf{A}_c t} (\mathbf{B}_c \mathbf{u}(t) + \mathbf{B}_c^{\text{NL}} \mathbf{u}^{\text{NL}}(\mathbf{q}, \dot{\mathbf{q}})) \quad (27.5)$$

The analytical solution can be obtained through integration and decomposition

$$\mathbf{x}(t) = e^{\mathbf{A}_c(t-t_0)} \mathbf{x}(t_0) + \mathbf{B}_c \int_{t_0}^t e^{\mathbf{A}_c(t-\tau)} \mathbf{u}(\tau) d\tau + \mathbf{B}_c^{\text{NL}} \int_{t_0}^t e^{\mathbf{A}_c(t-\tau)} \mathbf{u}^{\text{NL}}(\tau) d\tau \quad (27.6)$$

This approach utilizes matrix exponential functions and is therefore known as an exponential integrator [13]. To obtain a numerical solution, Eq. (27.6) needs to be converted into a time discrete form with time step T_s

$$\mathbf{x}(nT_s + T_s) = e^{\mathbf{A}_c T_s} \mathbf{x}(nT_s) + \mathbf{B}_c \int_{nT_s}^{nT_s+T_s} e^{\mathbf{A}_c(nT_s+T_s-\tau)} \mathbf{u}(\tau) d\tau + \mathbf{B}_c^{\text{NL}} \int_{nT_s}^{nT_s+T_s} e^{\mathbf{A}_c(nT_s+T_s-\tau)} \mathbf{u}^{\text{NL}}(\tau) d\tau \quad (27.7)$$

The first term at the right hand side of Eq. (27.7) can be calculated exactly. However, the remaining terms have to be calculated approximately for time-discrete forces.

27.2.2 System Discretization

Different discretization methods can be used to numerically interpolate the external and the nonlinear forces. In this paper, a triangular-order hold discretization method is applied to Eq. (27.7), which results in the following discrete form

$$\mathbf{x}(nT_s + T_s) = \mathbf{A}_d \mathbf{x}(nT_s) + \mathbf{B}_d \mathbf{u}(nT_s) + \mathbf{B}_d^{\text{NL}} \mathbf{u}^{\text{NL}}(\mathbf{q}(nT_s), \dot{\mathbf{q}}(nT_s)) \quad (27.8)$$

$$\mathbf{y}(nT_s + T_s) = \mathbf{C}_d \mathbf{x}(nT_s + T_s) + \mathbf{D}_d \mathbf{u}(nT_s + T_s) + \mathbf{D}_d^{\text{NL}} \mathbf{u}^{\text{NL}}(\mathbf{q}(nT_s + T_s), \dot{\mathbf{q}}(nT_s + T_s)) \quad (27.9)$$

in which

$$\left\{ \begin{array}{l} \mathbf{A}_d = e^{\mathbf{A}_c T_s} \\ \mathbf{B}_d = \frac{1}{T_s} \mathbf{A}_c^{-2} (e^{\mathbf{A}_c T_s} - \mathbf{I})^2 \mathbf{B}_c \\ \mathbf{B}_d^{\text{NL}} = \frac{1}{T_s} \mathbf{A}_c^{-2} (e^{\mathbf{A}_c T_s} - \mathbf{I})^2 \mathbf{B}_c^{\text{NL}} \\ \mathbf{C}_d = \mathbf{C}_c \\ \mathbf{D}_d = \mathbf{D}_c + \mathbf{C}_c \left(-\mathbf{A}_c^{-1} + \frac{1}{T_s} \mathbf{A}_c^{-2} (e^{\mathbf{A}_c T_s} - \mathbf{I}) \right) \mathbf{B}_c \\ \mathbf{D}_d^{\text{NL}} = \mathbf{D}_c^{\text{NL}} + \mathbf{C}_c \left(-\mathbf{A}_c^{-1} + \frac{1}{T_s} \mathbf{A}_c^{-2} (e^{\mathbf{A}_c T_s} - \mathbf{I}) \right) \mathbf{B}_c^{\text{NL}} \end{array} \right. \quad (27.10)$$

The formulas shown in Eq. (27.10) can be found in [14].

27.2.3 Time Integration

As shown in Eq. (27.8), $\mathbf{x}(nT_s + T_s)$ can be determined using the information from the previous time step. Therefore, only Eq. (27.9) needs to be balanced to compute the nonlinear forces. To reduce the computational effort, the output states corresponding to the nonlinear forces are used to update the nonlinear forces, which results in a smaller set of balancing equations compared with using the entire discrete state-space representation. The balancing equations can then be expressed as

$$\mathbf{y}_n(nT_s + T_s) = \mathbf{C}_{\text{dn}} \mathbf{x}(nT_s + T_s) + \mathbf{D}_{\text{dn}} \mathbf{u}(nT_s + T_s) + \mathbf{D}_{\text{dn}}^{\text{NL}} \mathbf{u}^{\text{NL}}(\mathbf{q}(nT_s + T_s), \dot{\mathbf{q}}(nT_s + T_s)) \quad (27.11)$$

in which subscript including n means the states in which nonlinear elements are involved. When the nonlinear forces are known, the input and output relationship of the underlying linear system can be used to obtain any states of the system. Rearranging Eq. (27.11) so that all the unknowns are at the left hand side and all the knowns are at the right hand side gives

$$\mathbf{y}_n(nT_s + T_s) - \mathbf{D}_{\text{dn}}^{\text{NL}} \mathbf{u}^{\text{NL}}(\mathbf{q}(nT_s + T_s), \dot{\mathbf{q}}(nT_s + T_s)) = \mathbf{R} \quad (27.12)$$

in which $\mathbf{R} = \mathbf{C}_{\text{dn}} (\mathbf{A}_d \mathbf{x}(nT_s) + \mathbf{B}_d \mathbf{u}(nT_s) + \mathbf{B}_d^{\text{NL}} \mathbf{u}^{\text{NL}}(\mathbf{q}(nT_s), \dot{\mathbf{q}}(nT_s))) + \mathbf{D}_{\text{dn}} \mathbf{u}(nT_s + T_s)$. \mathbf{R} is completely determined by the past values together with the currently applied force. Equation (27.12) is solved by the fixed point iteration method in this work.

27.2.4 Auxiliary Matrix

For some problems, the Jacobian matrix \mathbf{A}_c may be ill-conditioned. Then, it is worth to use an auxiliary matrix (damping/stiffness matrix) to improve the condition number of the \mathbf{A}_c matrix. The \mathbf{A}_c matrix can be written as

$$\mathbf{A}_c = (\mathbf{A}_c + \Delta \mathbf{A}) - \Delta \mathbf{A} \quad (27.13)$$

in which $\Delta \mathbf{A} \ll \mathbf{A}_c$. The $\Delta \mathbf{A}$ is selected, so that

$$\text{cond}(\mathbf{A}_c + \Delta \mathbf{A}) \ll \text{cond}(\mathbf{A}_c) \quad (27.14)$$

in which cond represents the condition number operator. A new underlying linear system is built with the modified Jacobian matrix $(\mathbf{A}_c + \Delta \mathbf{A})$. The dynamic properties are preserved by treating the $\Delta \mathbf{A} \mathbf{x}$ term as an external force acting on the new underlying linear system.

27.2.5 Matrix Diagonalization

To make the simulation even faster, the modified Jacobian matrix $\mathbf{A}_d + \Delta\mathbf{A}_d$, where $\Delta\mathbf{A}_d = \mathbf{e}^{\Delta\mathbf{A}T_s}$, can be transformed into a complex diagonal matrix

$$\tilde{\mathbf{A}}_d = \text{diag}[\lambda_1, \lambda_2, \dots, \lambda_N] \quad (27.15)$$

where $[\lambda_1, \lambda_2, \dots, \lambda_N]$ are complex eigenvalues of the modified Jacobian matrix $\mathbf{A}_d + \Delta\mathbf{A}_d$. This is done by using a transformation matrix which consists of the corresponding linearly independent complex eigenvectors of the $\mathbf{A}_d + \Delta\mathbf{A}_d$ matrix. The complex diagonal matrix and complex transformation may lead to some numerical error. Therefore, the Matlab function ‘cdf2rdf’ is used to convert the complex diagonal form $\tilde{\mathbf{A}}_d$ and the complex eigenvectors to a real block diagonal form and real eigenvectors. $\tilde{\mathbf{A}}_d$ is hereafter referred as the real block diagonal matrix calculated by

$$\tilde{\mathbf{A}}_d = \mathbf{T}^{-1}\mathbf{A}_d\mathbf{T} \quad (27.16)$$

where \mathbf{T} is a matrix containing the real valued eigenvectors. Using the transformation matrix \mathbf{T} , the discrete state-space form can be recast into

$$\tilde{\mathbf{x}}(nT_s + T_s) = \tilde{\mathbf{A}}_d\mathbf{x}(nT_s) + \mathbf{T}^{-1}\mathbf{B}_d\mathbf{u}(nT_s) + \mathbf{T}^{-1}\mathbf{B}_d^{\text{NL}}\mathbf{u}^{\text{NL}}(\mathbf{q}(nT_s), \dot{\mathbf{q}}(nT_s)) \quad (27.17)$$

$$\mathbf{y}_n(nT_s + T_s) = \mathbf{C}_{\text{dn}}\mathbf{T}\mathbf{x}(nT_s + T_s) + \mathbf{D}_{\text{dn}}\mathbf{u}(nT_s + T_s) + \mathbf{D}_{\text{dn}}^{\text{NL}}\mathbf{u}^{\text{NL}}(\mathbf{q}(nT_s + T_s), \dot{\mathbf{q}}(nT_s + T_s)) \quad (27.18)$$

in which the new state vector $\tilde{\mathbf{x}}(nT_s + T_s)$ equals $\mathbf{T}^{-1}\mathbf{x}(nT_s + T_s)$. Most elements of the $\tilde{\mathbf{A}}_d$ matrix are zeros and it has nonzero values only in the main diagonal terms and in the first upper and lower diagonal terms. The matrix multiplication $\tilde{\mathbf{A}}_d\mathbf{x}(nT_s)$ in Eq. (27.17), can therefore be replaced by vectors multiplications which reduce the computational cost.

27.2.6 C Code

The simulation scheme is written in a Matlab environment. It has many routines that are highly optimized and give good performance and many researchers in the structural dynamic community use it as their program language of choice. However, for some specific feature calculations the speed of Matlab may be slower than a C code which is first compiled into the computer’s native language. Using a C code to execute the time integration may improve the efficiency of the simulation code drastically compared with performing the calculation in Matlab. Thus, the strategy here is to combine the superiority of Matlab’s libraries with a C code. The system matrices of the discrete state-space model are obtained using the Matlab system identification toolbox and the time integration part is written using C code. The C code source file is built into an executable Matlab subroutine as a so-called mex function.

27.3 Numerical Examples

To investigate the accuracy and efficiency of the proposed method, the dynamic properties of a vertically dropped hollow ball is studied. The ball has thickness 0.001 m, radius 0.05 m, density 7850 kg/m³ and Young’s modulus 210 GPa. The ball, which is initially at rest, is released from a height d_0 onto a trampoline, see Fig. 27.2. The bounce dynamic behaviour of the ball is modelled both as a Single-Degree-of-Freedom (SDOF) system and a Multiple-Degree-of-Freedom (MDOF) system.

For the SDOF system, the simulated response using the proposed method is compared to the Matlab adaptive time-step Runge-Kutta (RK) method (ODE45) here used as a reference solution. The reference solution, which is regarded as ‘the correct’ solution, is computed using the fourth order RK (RK4) with a very small fixed time step. For the MDOF system, the simulated response is compared with the RK45 method as well as a solution made using the commercial finite element software MSC Nastran. All the simulations are done in a computer with a 2.6 GHz processor and 32 GB RAM

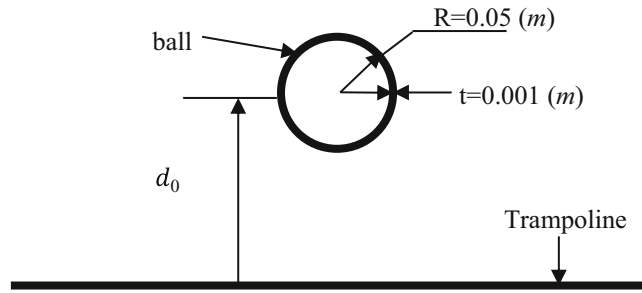


Fig. 27.2 Schematic representation of the studied contact problem

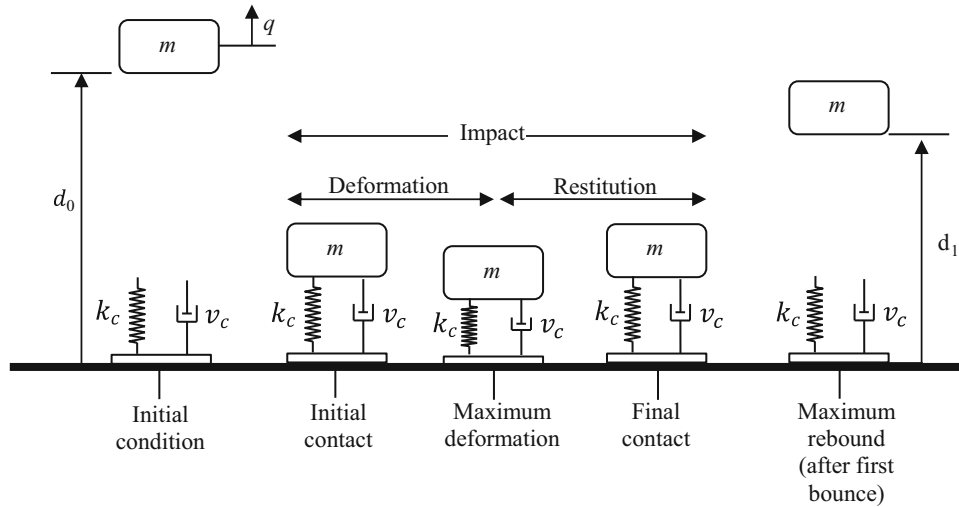


Fig. 27.3 A mass-spring-damper model of a bouncing ball showing phases of the first cycle

27.3.1 An SDOF System

The dynamic properties of a vertically dropped ball are represented by a single degree of freedom (SDOF) model, shown in Fig. 27.3, using mass m , viscous damping v_c , and Hertzian contact stiffness k_c . Assuming no aerodynamic drag, the governing equations of motion can then be expressed as

$$\begin{cases} m\ddot{q} = -mg & \text{(no contact)} \\ m\ddot{q} = -mg - v_c\dot{q} + k_c(-q - d_0)^{1.5} & \text{(in contact)} \end{cases} \quad (27.19)$$

with initial conditions $q(0) = d_0$, and $\dot{q}(0) = 0$. In order to illustrate the accuracy and efficiency of the proposed method, the simulated responses of the proposed method are compared with the adaptive RK45 method (Matlab’s ODE45). A fixed time step RK4 method with a time step equals 1×10^{-6} is used as a reference. Comparison of the results of the simulated responses of the SDOF system solved by the proposed method, Matlab ODE45 solver and the RK4 method are shown in Fig. 27.4.

The deviation of these methods compared with the reference solution is defined as

$$dev (\%) = \frac{q - q_{Ref}}{q_{Ref}} \times 100 \quad (27.20)$$

in which q is the responses from different simulation methods and q_{Ref} is the reference solution. It is difficult to compare efficiency and accuracy alone because they are coupled. Therefore, the methods are tuned by using different step sizes and convergence criterions to obtain the responses which have about 0.01 % deviation from the reference solution and the required computational times are then compared. The results are shown in Table 27.1.

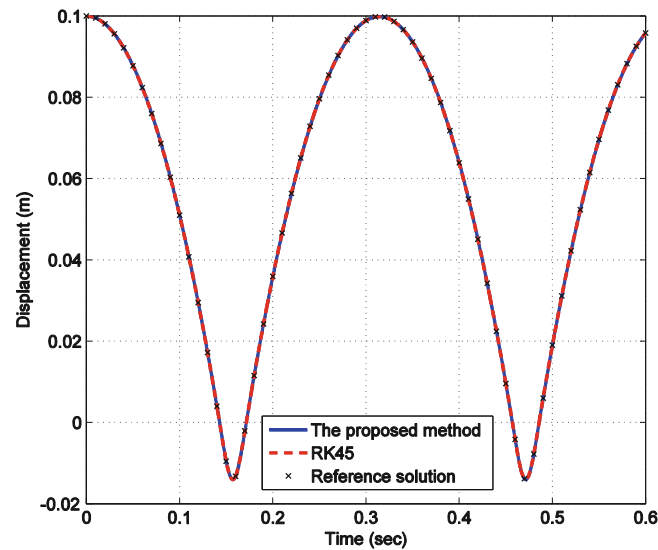


Fig. 27.4 Time responses of the SDOF system computed using different methods. The response simulated using the proposed method is plotted in *blue*; the adaptive time step RK45 method is plotted in *dashed red* and the reference solution from the fixed time step RK4 is plotted using crosses

Table 27.1 Required times to find the time responses of the SDOF system and the deviations of the methods

Methods	Proposed simulation method	Proposed simulation method with C code	RK45
Simulation time (s)	6.4	0.2	134
Deviation	0.0050 %	0.0050 %	0.0083 %

The simulations are made for the time interval [0 100] s. and the simulations are done using $m=0.25$ kg, $\nu_c=0.01$ Ns/m, $k_c=3 \times 10^4$ N/m and $d_0=0.1$ m

Table 27.1 shows that the proposed method is more efficient and accurate compared with the Matlab ODE45 solver. The implementation of the time integration part in a C code makes the simulation 32 times faster than the proposed method without using C code.

27.3.2 An MDOF System

To show the superiority of the proposed simulation method when tackling a large-scale system, the ball is modelled using MSC Nastran shell elements; 588 CQUAD4 and 16 CTRIA3 shell elements (the modelling was made using MSC SimXpert). The ball is constrained so that some nodes of it can only move along the z axis, which has 3858 degrees-of-freedom. The contact surface is represented by 85 discrete independent linear springs which have the same stiffness. The springs have the same initial length and are at rest on the same horizontal surface which is 0.15 m offset (in the z-direction) from the centre of gravity of the ball. The springs are in contact with the ball in different time steps due to the shape of the ball. The spring forces representing contact, constitute the nonlinear forces acting on the ball. The simulation model is visualized in Fig. 27.5.

The aim of this case study is twofold. Firstly, to illustrate how much the MD and AM algorithms can further shorten the computational time of the proposed simulation method. The required simulation time of the proposed method with and without MD to simulate the forced time responses for different time intervals are shown in Table 27.2. Secondly, the efficiency and accuracy of the proposed method are shown by comparing the simulated responses with the corresponding responses simulated from the RK45 method and MSC Nastran. In Nastran, Sol 400 together with the equivalent gap contact element (CGAP) are used to conduct the simulation. An example of the time responses of the node 1, which is shown in Fig. 27.5 calculated by the different methods are shown in Fig. 27.6.

Table 27.2 shows that the MD algorithm can speed up the simulation of the MDOF system when longer than 1 s of simulation is required and its excellence becomes more significant for simulating a longer time period data. The reason is that it takes a certain time to compute the MD. However, it computed only once independently of the simulation time. As illustrated in Table 27.3, the proposed method, with a good accuracy, is about 425 times faster than the RK45 method and 41 times faster than the MSC Nastran software in this case study.

Fig. 27.5 An MDOF model of the bouncing ball, in which the contact surface is modelled by 85 discrete independent linear springs with equal spring constants. Four out of the 85 springs are shown. The lowest node of the ball (Node 1) is illustrated by a red dot

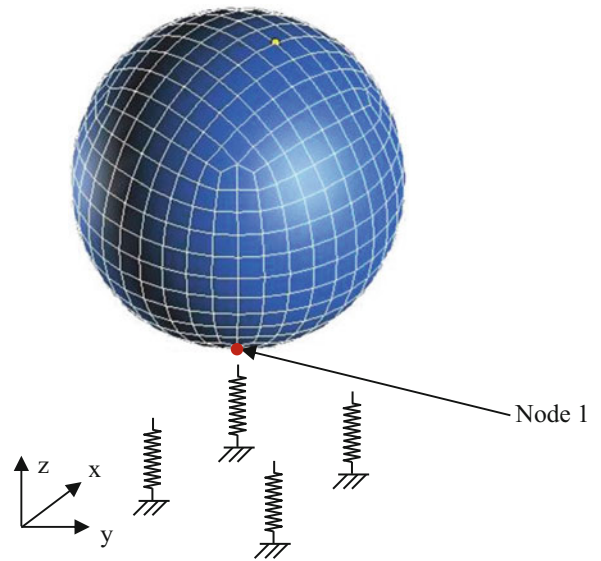


Table 27.2 Required time for simulating the response of the MDOF system for different time intervals using the proposed method with and without the MD algorithm are shown

Simulation time				
Time intervals (s)	1	2	20	100
Without MD (s)	126	218	954	9234
With MD (s)	153	159	207	747

The simulations are done using a fixed time step of 1×10^{-4} s. Here, the AM algorithm is applied for all the simulations of different time intervals

Table 27.3 Required time for different methods to find the response of the MDOF system for the time interval [0 2] s, with a time step equals 1×10^{-4} s are listed and the deviations are calculated using Eq. (27.20), in which the Nastran solution is considered as the reference solution

Method	Proposed simulation method with MD and AM	Proposed simulation method with MD	RK45	Nastran
Required simulation time (s)	159	220	67500	6480
Deviation (%)	0.15 %	0.15 %	0.11 %	0.00 %

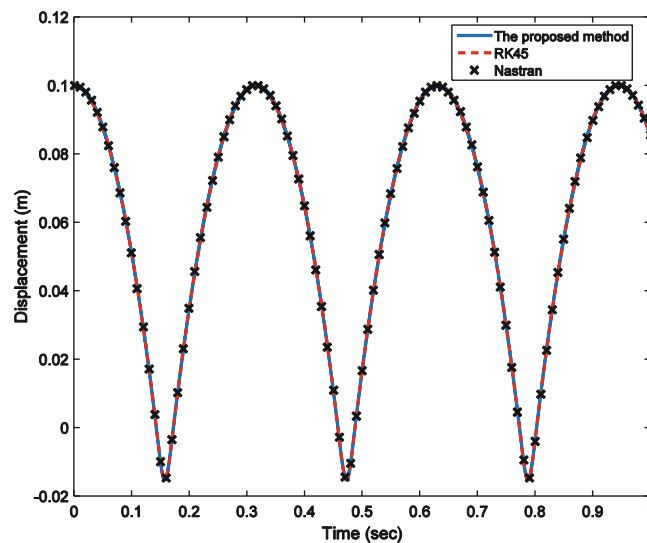


Fig. 27.6 Time response of node 1 of the MDOF system computed using the proposed method (solid blue line), the adaptive time step RK45 method (dashed red line) and MSC Nastran (black crosses)

27.4 Conclusion

In this paper, an improved state-space based simulation approach is proposed. The method can be presented in two subparts; modelling and time integration. In the modelling part, a continuous state-space model of the underlying linear system is made. An exponential integrator combined with a triangular-order hold discretization method is used to obtain a discrete state-space form which is then used in the time integration part. In the time integration part, the nonlinear forces are treated as external forces acting on the discrete state-space model. The implementation of C codes, matrix diagonalization and auxiliary matrices can be applied in the time integration part to speed up the simulation additionally. The efficiency and accuracy of the proposed method are illustrated using a contact problem which is modelled using an SDOF system and an MDOF system. In the SDOF case study, with the same accuracy the proposed method is more efficient than the RK45 and the efficiency can be improved 32 times by using the C code. For the MDOF case study, the superiority of using matrix diagonalization and auxiliary matrices is shown. In this case, the RK45 method and Nastran solver are time consuming compared with the proposed method.

References

1. Ren, Y., Beards, C.F.: A new receptance-based perturbative multi-harmonic balance method for the calculation of the steady state response of non-linear systems. *J. Sound Vib.* **172**(5), 593–604 (1994)
2. Ferreira, J.V., Ewins, D.J.: Algebraic nonlinear impedance equation using multi-harmonic describing function. In: *Processing of International Modal Analysis Conference*, Orlando, 1997
3. Carnahan, B., Luther, H.A., Wilkes, J.O.: *Applied Numerical Methods*. Wiley, Newyork (1969)
4. Géradin, M., Rixen, D.J.: *Mechanical Vibrations: Theory and Application to Structural Dynamics*. Wiley, Chichester (1997)
5. Friswell, M.I., Penny, J.E.T., Garvey, S.D.: Using linear model reduction to investigate the dynamics of structures with local non-linearities. *Mech. Syst. Sig. Process.* **9**(3), 317–328 (1995)
6. Petrov, E.P., Ewins, D.J.: Method for analysis of nonlinear multiharmonic vibrations of mistuned bladed disks with scatter of contact interface characteristics. *J. Turbomach.* **127**(1), 128–136 (2005)
7. Avitabile, P., O’Callahan, J.: Efficient techniques for forced response involving linear modal components interconnected by discrete nonlinear connection elements. *Mech. Syst. Sig. Process.* **23**(1), 45–67 (2009)
8. Ahlin, K., Magnevall, M., Josefsson, A.: Simulation of forced response in linear and nonlinear mechanical systems using digital filters. In: *Proceedings of the International Conference on Noise and Vibration Engineering (ISMA)*, Leuven, 2006
9. Josefsson, A.: Identification and simulation methods for nonlinear mechanical systems subjected to stochastic excitation. Ph.D. Thesis, Blekinge Institute of Technology, Karlskrona (2011)
10. Magnevall, M.: Simulation and experimental methods for characterization of nonlinear mechanical systems. Ph.D. Thesis, Blekinge Institute of Technology, Karlskrona (2011)
11. Rahrovani, S., Abrahamsson, T., Modin, K.: An efficient exponential integrator for large nonlinear stiff systems part 1: theoretical investigation. In: *Conference Proceedings of the Society for Experimental Mechanics*, Orlando, 2014
12. Rahrovani, S., Abrahamsson, T., Modin, K.: Stability limitations in simulation of dynamical systems with multiple time-scales. In: *Conference Proceedings of the Society for Experimental Mechanics*, Orlando, 2015
13. Hochbruck, M., Ostermann, A.: Exponential integrators. *Acta Numer.* **19**, 209–286 (2010)
14. Franklin, G.F., Powell, J.D., Workman, M.: *Digital control of dynamic systems*. Ellis-Kagle Press, Half Moon Bay, CA (2006)

Chapter 28

A Modal Superposition Method for the Analysis of Nonlinear Systems

Erhan Ferhatoğlu, Ender Cığeroğlu, and H. Nevzat Özgüven

Abstract In the determination of response of nonlinear structures, computational burden is always a major problem even if frequency domain methods are used. One of the methods used to decrease the computational effort is the modal superposition method for nonlinear systems where the modes of the linear system are used in the calculation. However, depending on the type of the nonlinearity, in order to obtain an accurate response, the number of modes retained in the response calculations needs to be increased, which increases the number of nonlinear equations to be solved. In this study, a method is proposed to decrease the number of modes used for systems having nonlinearities where the equivalent stiffness varies between two limiting values. For such systems, one can define different linear systems for each value of the limiting equivalent stiffness. In this study, it is proposed to use a combination of these linear mode shapes in the modal superposition method. It is shown that proper combination of mode shapes of different linear systems provides satisfactory results by keeping the number of modes used at a minimum. The method is demonstrated on case studies where describing function method is used in the analysis of the nonlinear system.

Keywords Modal superposition method • Hybrid mode shapes • Nonlinear vibration • Describing function method • Newton's method

28.1 Introduction

Most of the engineering structures show nonlinear behavior. Determination of dynamic response of large nonlinear structures can be troublesome in terms of computational time even though frequency domain methods are used. In modal superposition method, decreasing the number of modes used in the solution procedure reduces number of nonlinear equations; hence, the computational effort as well. On the other hand, in order to obtain an accurate response, the number of modes used should be increased. Finding the optimum number of modes required in solution of nonlinear systems has always been a challenge.

In literature, various frequency domain solution methods have been proposed in order to have accurate response with reduced computational effort. Menq et al. [1] proposed receptance method, which decreases the total number of nonlinear equations to be solved. Chen and Menq [2] also worked on prediction of the resonant response of frictionally constraint blade systems by using receptance method. Authors used different mode shapes for different cases to decrease the computational time. For the nonlinear vibration analysis of structures with frictional contact interfaces, Petrov [3] considered the effect of number of modes retained in the receptance method. It is observed from their results that the error outside of the resonance regions is higher than the error around it. Moreover, accuracy of the resonance frequencies and the frequency response function increases as the number of modes used increases. Kuran and Özgüven [4] proposed a modal superposition method for nonlinear systems and they showed that using even one mode at the resonance region for local nonlinearities gives satisfactory results. However, this condition may hold if the natural frequencies of the linear structure are sufficiently away from each other and if the nonlinear element does not excite the higher modes of the linear system. In such cases, the number

E. Ferhatoğlu

Department of Mechanical Engineering, Middle East Technical University, 06800 Ankara, Turkey

Turkish Aerospace Industries, Inc., 06980 Ankara, Turkey

e-mail: erhan.ferhatoglu@metu.edu.tr

E. Cığeroğlu (✉) • H.N. Özgüven

Department of Mechanical Engineering, Middle East Technical University, 06800 Ankara, Turkey

e-mail: ender@metu.edu.tr; ozguven@metu.edu.tr

of modes used need to be increased in order to capture the dynamic behavior of the system. Cigeroglu et al. [5, 6] proposed a modal superposition method for the nonlinear forced response analysis of bladed disk systems where authors employed multiple modes of the system in order to obtain sufficient accuracy.

In this paper, the concept of hybrid modes for certain nonlinearity types is introduced. For some nonlinearities, such as piecewise linear stiffness, dry friction, etc., equivalent stiffness of the nonlinearity has limiting values depending on the vibration amplitude. In such cases equivalent stiffness of the nonlinearity varies from one limit to the other, where linear systems are obtained at these limiting cases neglecting the equivalent damping of the nonlinearity. Instead of using the mode shapes of the linear system without the nonlinearities, proper combination of the mode shapes of the linear systems corresponding to these limiting cases can provide a better basis for the nonlinear solution. Therefore, less number of modes can be used in the nonlinear response calculations. A similar approach is used by Cigeroglu and Özgüven [7], where authors decompose the simplified microslip element into a linear stiffness and a nonlinear element, and include the linear part into the original stiffness matrix which simplifies the solution process. In this paper hybrid modes composed of these limiting linear systems is proposed for the solution of the nonlinear system. It is observed from the case studies performed that hybrid mode shapes composed of proper combination of linear modes of these limiting cases provide satisfactory results by keeping the number of modes used in the solution at a minimum.

28.2 Theory

Hybrid mode shapes proposed in this study can be used in both solution methods, i.e. modal superposition method or receptance method. In this study modal superposition method (MSM) is used in the solution of the case studies considered. Consider a nonlinear system defined by the following matrix equation

$$\mathbf{M} \cdot \ddot{\mathbf{x}} + \mathbf{C} \cdot \dot{\mathbf{x}} + i\mathbf{H} \cdot \mathbf{x} + \mathbf{K} \cdot \mathbf{x} + \mathbf{f}_N = \mathbf{f}, \quad (28.1)$$

where \mathbf{M} , \mathbf{C} , \mathbf{H} and \mathbf{K} represent the mass, viscous damping, structural damping, and stiffness matrices of the linear system, respectively. \mathbf{f}_N represents the internal nonlinear force vector, i is the unit imaginary number. Here, \mathbf{x} is the vector of displacements and dot denotes differentiation with respect to time. \mathbf{f} represents the external harmonic forcing vector. The nonlinear internal forcing vector, \mathbf{f}_N can be written as follows by using describing function method (DFM) with single harmonic [8]

$$\mathbf{f}_N = \Delta \cdot \mathbf{x} = (\Delta_{re} + i\Delta_{im}) \cdot \mathbf{x}, \quad (28.2)$$

where Δ is displacement (velocity, etc.) dependent complex nonlinearity matrix, Δ_{re} and Δ_{im} are real and imaginary parts. Therefore, the nonlinear equation of motion can be written as follows

$$\mathbf{M} \cdot \ddot{\mathbf{x}} + \mathbf{C} \cdot \dot{\mathbf{x}} + i(\mathbf{H} + \Delta_{im}) \cdot \mathbf{x} + (\mathbf{K} + \Delta_{re}) \cdot \mathbf{x} = \mathbf{f}, \quad (28.3)$$

It can be seen from Eq. (28.3) that real part of the nonlinearity matrix changes the overall stiffness matrix of the system whereas the imaginary parts modifies the overall structural damping matrix. Therefore, at the limiting cases the equivalent linear systems with modified stiffness and structural damping matrices can be defined where the new stiffness matrix of the system can be written as

$$\mathbf{K}_l = \mathbf{K} + \Delta_{re,l}, \quad (28.4)$$

where \mathbf{K}_l is the new stiffness matrix and $\Delta_{re,l}$ is the real part of the nonlinearity matrix of the l^{th} limiting case. For the sake of simplicity the number of limiting cases considered in the rest of the study is taken as 2. A new eigenvalue problem can be defined as

$$(\mathbf{K}_l - \lambda_l \mathbf{M}) \cdot \mathbf{x}_l = \mathbf{0}, \quad l = 1, 2 \quad (28.5)$$

Solution of the eigenvalue problem gives eigenvalues λ_l , which are the squares of the natural frequencies, and mass normalized mode shape matrix Φ_l .

Elements of the nonlinearity matrix, Δ can be written as follows [8]

$$\Delta_{kk} = v_{kk} + \sum_{\substack{j=1 \\ j \neq k}}^n v_{kj} \quad \text{and} \quad \Delta_{kj} = -v_{kj}, \quad (28.6)$$

where v_{kj} is the harmonic input describing function of a nonlinear element in the system and can be described as equivalent complex stiffness for the internal nonlinear force, f_N^{kj} acting between the k^{th} and the j^{th} coordinates. Single harmonic describing function, v_{kj} can be obtained as [9, 10]

$$v_{kj} = \frac{i}{\pi |X_k - X_j|} \int_0^{2\pi} f_N^{kj}(\psi) e^{-i\psi} d\psi, \quad \psi = \omega t, \quad (28.7)$$

where X_k is the complex amplitude of the k^{th} degree of freedom. Describing function value, v , is decomposed into real and imaginary parts as

$$v = v_{re} + i v_{im}, \quad (28.8)$$

During the solution process, describing function for each nonlinearity is recalculated at every iteration step. Comparing the real part of the describing function, i.e. equivalent stiffness, with respect to the limiting value of the real part of the describing function, k^* , a ratio is defined

$$\alpha = \frac{v_{re}}{k^*}, \quad (28.9)$$

where $0 \leq \alpha \leq 1$ and k^* is selected as the maximum of the limiting equivalent stiffnesses. Assuming the maximum of the limiting equivalent stiffness is for limiting case 2, i.e. maximum value of α becomes 1, hybrid mode shape matrix can be obtained as a linear combination of the mode shapes of both limiting cases as

$$\Phi = [\phi_1 \ \phi_2 \ \cdots \ \phi_n] = \alpha \Phi_2 + (1 - \alpha) \Phi_1, \quad (28.10)$$

Response of the system can be written in terms of hybrid mode shapes as

$$\mathbf{x}(t) = \sum_{r=1}^{N_m} a_r \phi_r e^{i\omega t}, \quad (28.11)$$

where ϕ_r is the r^{th} mode shape, a_r is the complex coefficient of the r^{th} mode shape and N_m is the number of modes considered in the expansion. Substituting Eq. (28.11) into Eq. (28.3) the following result is obtained

$$-\omega^2 \Phi^T \mathbf{M} \Phi \cdot \mathbf{a} + i\omega \Phi^T \mathbf{C} \Phi \cdot \mathbf{a} + \Phi^T (\mathbf{K} + i\mathbf{H}) \Phi \cdot \mathbf{a} + \Phi^T \Delta(\mathbf{a}) \Phi \cdot \mathbf{a} = \Phi^T \cdot \mathbf{f}, \quad (28.12)$$

where \mathbf{a} is the vector of complex amplitudes of modal coefficients. In this nonlinear equation set, the unknowns are the modal coefficients given in vector \mathbf{a} , which are complex.

Numerical solution of the set of nonlinear algebraic equation given by Eq. (28.12) can be obtained by using Newton's method with Arc-length continuation. Detailed information about Newton's method with Arc-length continuation can be found in [11, 12].

Computational time is directly related to the number of modes used in Eq. (28.12). Although small number of modes is sufficient for some systems in which natural frequencies of the structure are well separated, it should be increased in order to get accurate response for highly nonlinear systems which increases the computational load. However, using hybrid mode shapes as explained above decreases the number of modes required in the analysis and hence, the computational time. In the following section, proposed approach is demonstrated on cases studies.

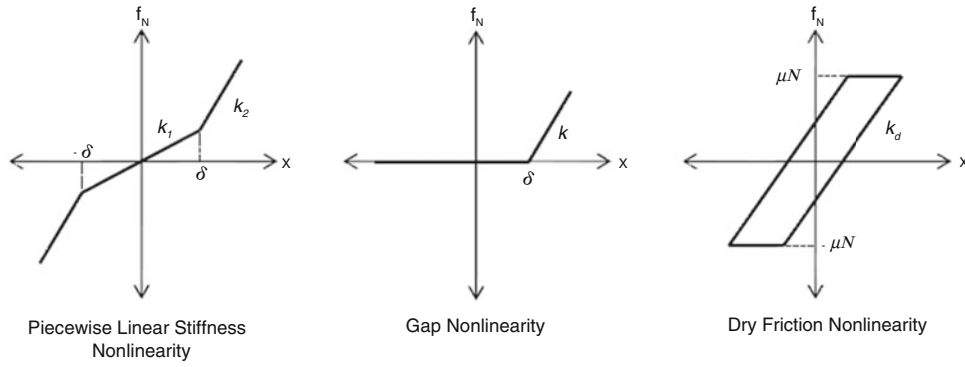


Fig. 28.1 Internal nonlinear force of nonlinearities with respect to displacement

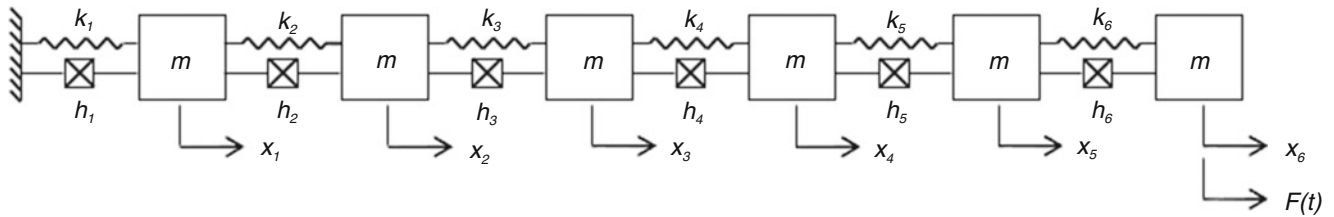


Fig. 28.2 Six-DOF linear system

28.3 Case Studies

In this section, proposed method is presented on several case studies having different nonlinearities. In order to apply proposed approach, nonlinearities in the system should have equivalent stiffness which does not change at least at one limiting value of the vibration amplitude. For instance, as vibration amplitude (displacement, velocity etc.) increases equivalent stiffness converges to a specific value. Piecewise linear stiffness, gap and dry friction nonlinearities (Fig. 28.1) show this kind of behavior and they are used in the following case studies.

Validation of the proposed method is demonstrated on a system in which natural frequencies are close to each other. Utilizing a system like this, it is provided that contribution of other modes to the response at the resonance region is comparable and the effect of other modes cannot be neglected. Therefore, the effect of using hybrid mode shapes can be clearly demonstrated on such a system. The underlying linear system used in the case study is a 6-degree-of-freedom (DOF) system given in Fig. 28.2.

The values of the parameters of this 6-DOF linear system are given as follows

$$m = 3kg \quad , \quad k_1 = 7500N/m \quad , \quad k_2 = k_5 = 2500N/m \quad , \quad k_3 = k_4 = k_6 = 5000N/m \quad , \quad F = 10N \quad , \quad \gamma = 0.01$$

28.3.1 Case Study 1: Piecewise Linear Stiffness Element

This nonlinear element is connected between the 6th mass and ground. The parameters of the nonlinear element are $k_1 = 2000N/m$, $k_2 = 10000N/m$, $\delta = 0.015m$. Figure 28.3 shows response of the 6th DOF for linear (i.e., there is no nonlinear element) and nonlinear systems. Hardening effects and jump phenomena are seen at the resonance regions as expected. In the response calculation of the nonlinear system all the modes of the linear system are used; hence, no reduction is done. Studying the piecewise nonlinear element, it can be concluded that, two limiting equivalent stiffness values can be defined. The first one is k_1 , which is the case if the vibration amplitude is small than the break away amplitude (limiting case 1) and the second one is k_2 , which is the case if the vibration amplitude is very large (limiting case 2). Therefore, adding these equivalent stiffness values to the original system it is possible to define two additional linear systems. After solving the eigenvalue problems, hybrid mode shapes are obtained by using Eqs. (28.8), (28.9), and (28.10).

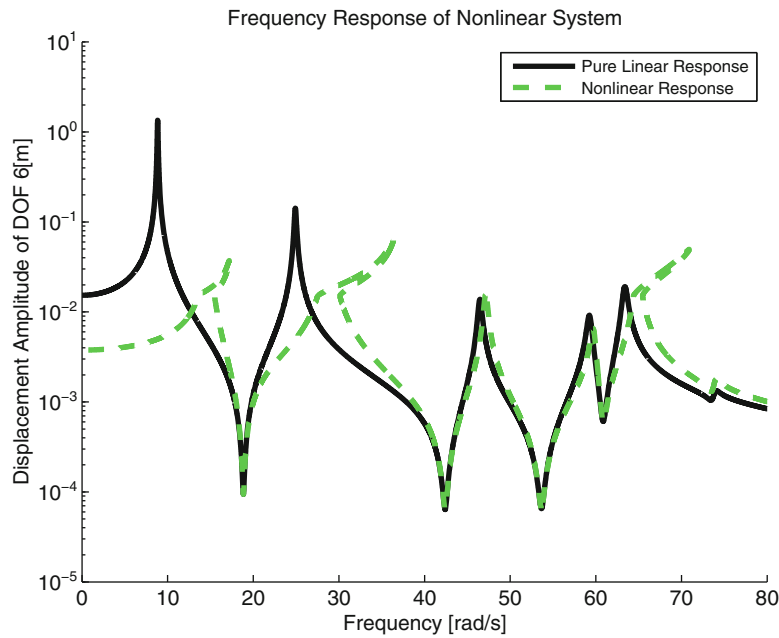


Fig. 28.3 Displacement amplitude of the 6th mass with respect to frequency

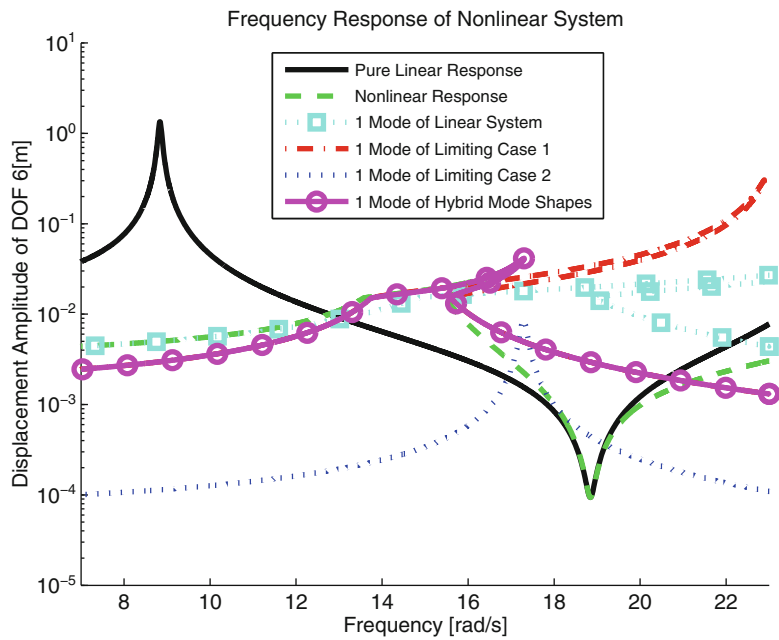


Fig. 28.4 Effect of linear modes used on the displacement amplitude of the 6th mass around the first resonance

In Figs. 28.4 and 28.5, response of the 6th mass is given by using one mode of the linear system without nonlinearities, one mode of linear system corresponding to limiting case 1, one mode of the linear system corresponding to limiting case 2, and one mode of the hybrid mode shapes. It is observed from the results that one mode of hybrid mode shapes gives very accurate results throughout the frequency range considered. It should be noted that the difference observed at the off-resonance region is due to the fact that vibration amplitudes at off-resonance region are very small compared to those at resonance.

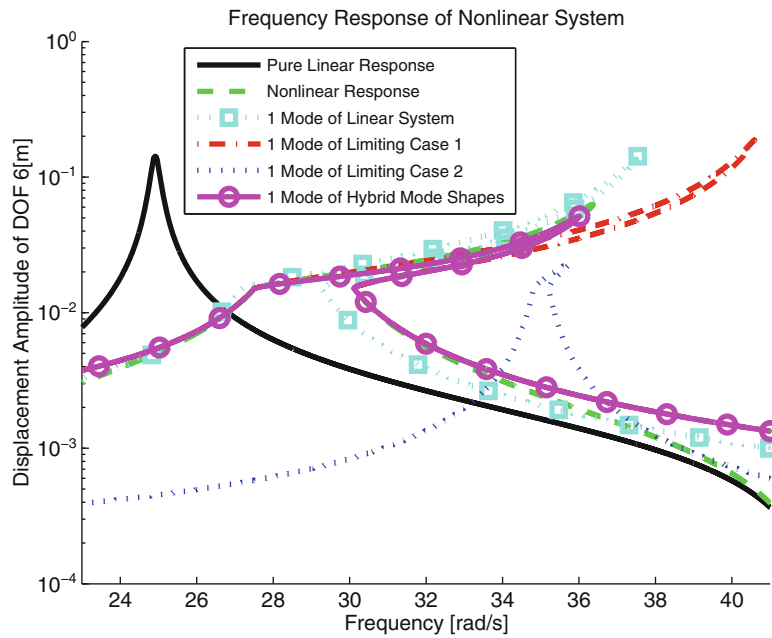


Fig. 28.5 Effect of linear modes used on the displacement amplitude of the 6th mass around the second resonance

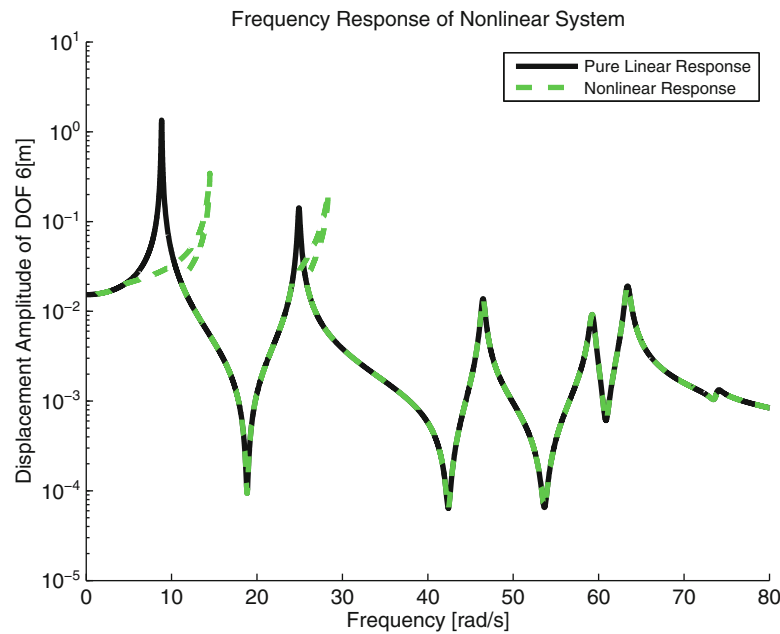


Fig. 28.6 Displacement amplitude of the 6th mass with respect to frequency

28.3.2 Case Study 2: Gap Element

In this case, the nonlinear element, i.e. gap element, is connected between the 6th mass and ground, as in the Case Study 1. The values of the parameters of the nonlinearity are $k = 4000N/m$, $\delta = 0.02m$. Figure 28.6 shows the displacement amplitude of the 6th mass as a function of frequency for the linear and nonlinear systems. For gap nonlinearity, there exists one limiting equivalent stiffness, which is referred to as limiting case 2. For limiting case 1, limiting equivalent stiffness is taken as zero which corresponds to the case with no nonlinear element.

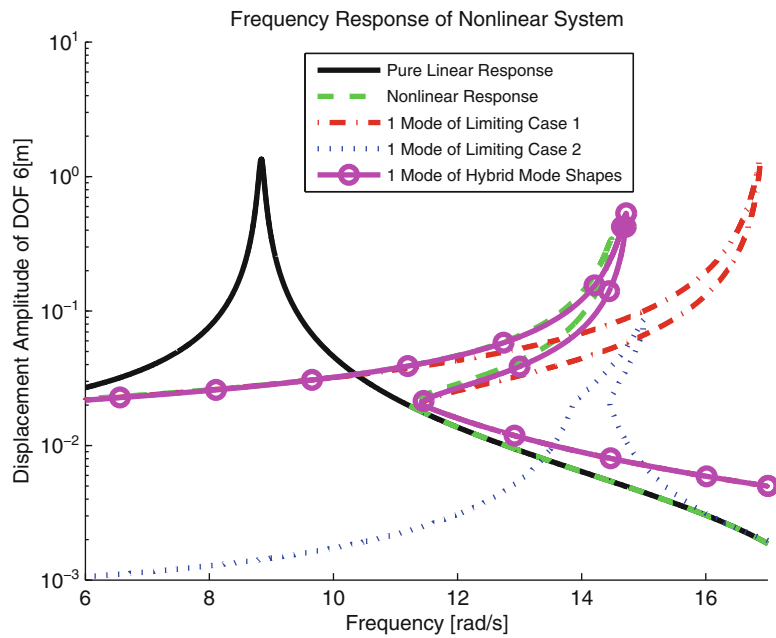


Fig. 28.7 Effect of linear modes used on the displacement amplitude of the 6th mass around the first resonance

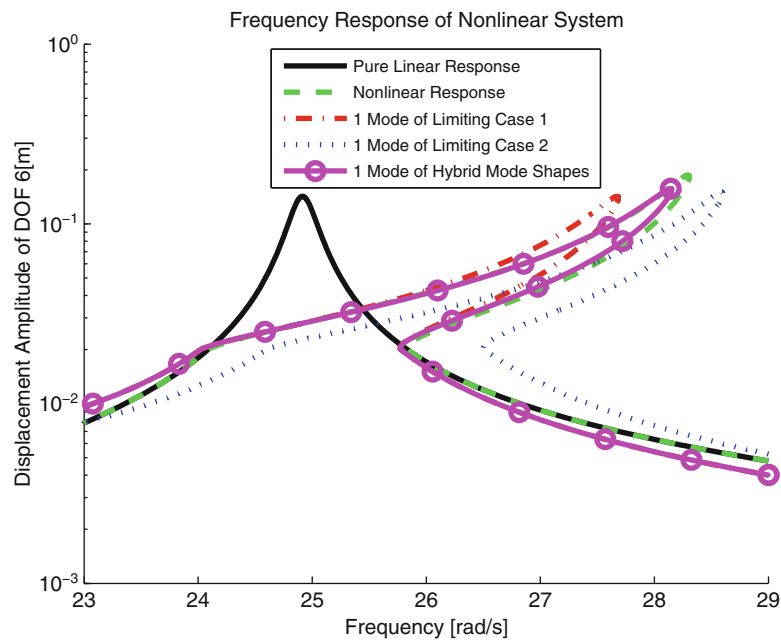


Fig. 28.8 Effect of linear modes used on the displacement amplitude of the 6th mass around the second resonance

Displacement amplitude of the 6th mass with respect to frequency is given in Figs. 28.7 and 28.8. It is observed from the results obtained that hybrid mode shape outperforms the other cases. Accuracy of the method can be increased further if two modes are used instead of a single mode.

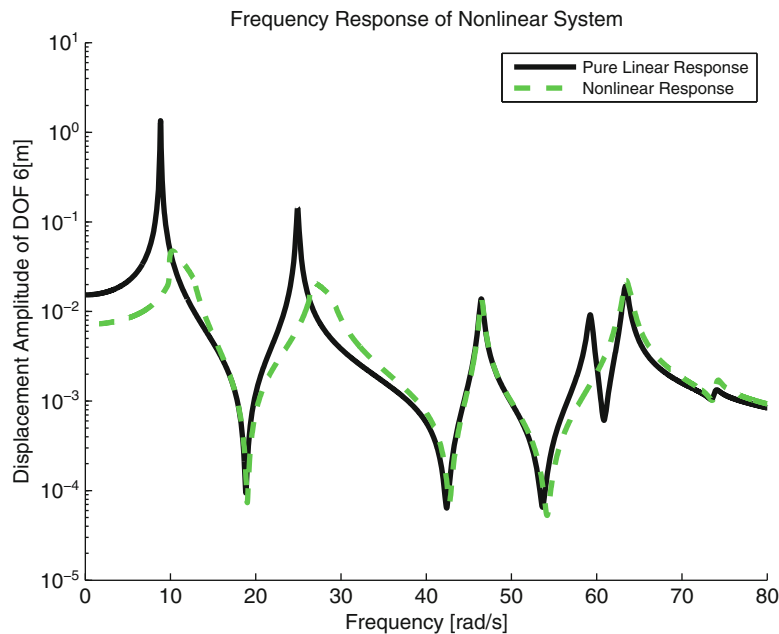


Fig. 28.9 Displacement amplitude of the 6th mass with respect to frequency

28.3.3 Case Study 3: Dry Friction Element

In this case study, the nonlinear element, i.e. dry friction, is connected between the 1st mass and the 6th mass. Parameters of the dry friction nonlinearity are $k_d = 1000\text{N/m}$, $\mu N = 15\text{N}$. Comparison of the linear and nonlinear responses for the 6th mass are given in Fig. 28.9 where the effect of dry friction nonlinearity is very clear at the first and second resonances. Studying dry friction nonlinearity, two limiting cases can be defined. For very large displacement amplitudes, since majority of a cycle is covered by slip state, limiting equivalent stiffness is zero which is referred to as limiting case 1. On the other hand, if the displacement amplitude is very small, dry friction element stays always in stick state which results in a limiting equivalent stiffness of k_d and this case is considered as limiting case 2. It should be also noted that limiting case 1 corresponds to the linear system without the dry friction element.

In Figs. 28.10 and 28.11, response of the 6th mass is calculated by using one mode of linear system corresponding to limiting case 1, one mode of the linear system corresponding to limiting case 2 and one mode of the hybrid mode shapes. It is seen from the results obtained that using hybrid mode shapes gives more accurate results.

28.4 Discussion and Conclusion

In this study, a new approach based on hybrid mode shapes defined in this study is proposed to obtain dynamic response of nonlinear structures. For systems with nonlinear elements where the equivalent stiffness has limiting values, hybrid mode shapes composed of mode shapes of the linear systems corresponding to each limiting equivalent stiffness value can be defined. Hybrid mode shapes are obtained by a linear combination of mode shapes of the limiting linear cases by monitoring the equivalent stiffness of nonlinear elements in the iterative solution process. Using these hybrid mode shapes in the forced response prediction of nonlinear structures leads to accurate solution of system by keeping the number of mode shapes at a minimum. This results in a significant reduction in computational time, which is very important for large nonlinear systems.

In the case studies presented in this study, piecewise linear stiffness, gap element and dry friction element are the nonlinearities used which show the aforementioned limiting behaviors. A 6-DOF lumped parameter model with a single nonlinear element attached is considered in all case studies. It is observed that hybrid mode shapes proposed in this study give very satisfactory results compared to the mode shapes of the linear system obtained by disregarding the nonlinear elements.

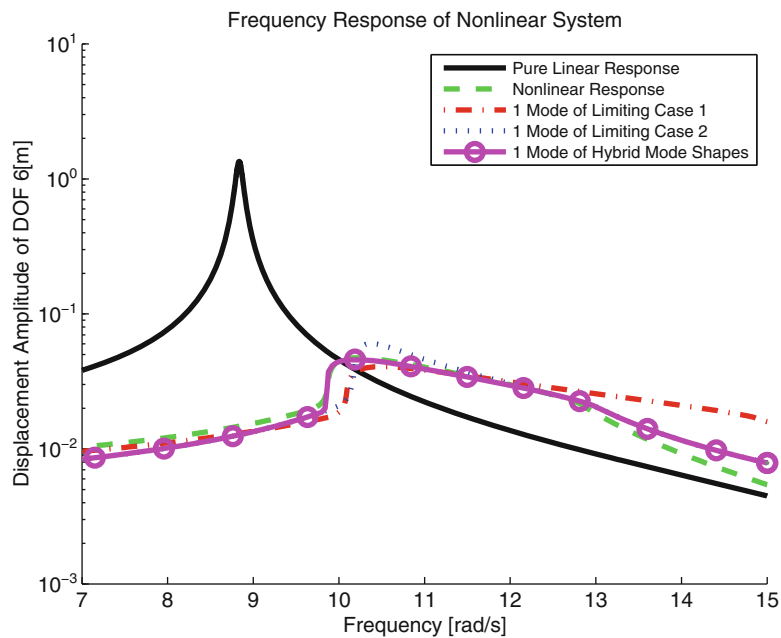


Fig. 28.10 Effect of linear modes used on the displacement amplitude of the 6th mass around the first resonance

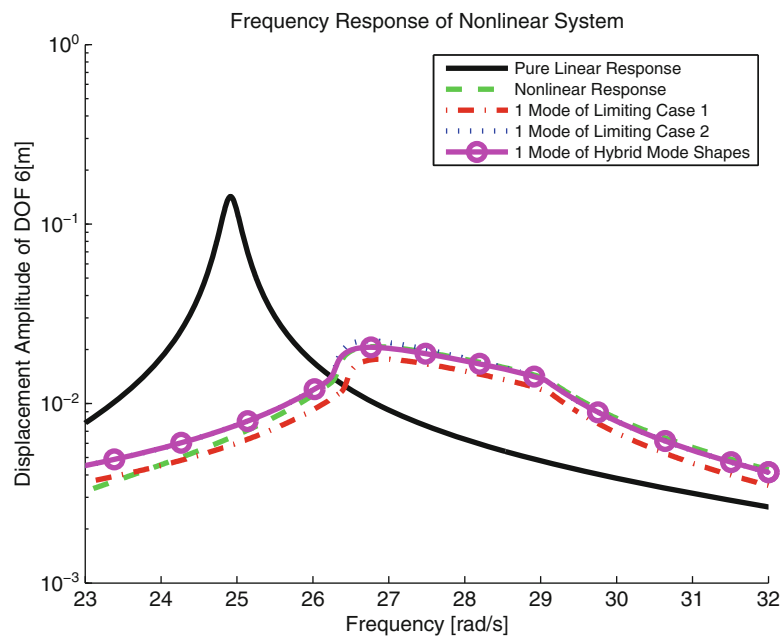


Fig. 28.11 Effect of linear modes used on the displacement amplitude of the 6th mass around the second resonance

References

1. Menq, C.H., Griffin, J.H., Bielak, J.: The influence of microslip on vibratory response, Part II: a “comparison with experimental results”. *J. Sound Vib.* **107**(2), 295–307 (1986)
2. Chen, J.J., Menq, C.H.: Prediction of the resonant response of frictionally constrained blade systems using constrained mode shapes. In: *Proceedings of the International Gas Turbine & Aero Engine Congress & Exhibition*, Stockholm, Sweden, 1998
3. Petrov, E.P.: A high-accuracy model reduction for analysis of nonlinear vibrations in structures with contact interfaces. *J. Eng. Gas Turb. Power* **133**(10), 102503/1–102503/10 (2011)
4. Kuran, B., Özgüven, H.N.: A modal superposition method for nonlinear structures. *J. Sound Vib.* **189**(3), 315–339 (1996)
5. Cigeroglu, E., An, N., Menq, C.H.: A microslip friction model with normal load variation induced by normal motion. *Nonlinear Dyn.* **50**(3), 609–626 (2007)

6. Cigeroglu, E., An, N., Menq, C.H.: Forced response prediction of constrained and unconstrained structures coupled through frictional contacts. *J. Eng. Gas Turb. Power* **131**(2), 11 (2009)
7. Cigeroglu, E., Özgüven, H.N.: Non-linear vibration analysis of bladed disks with dry friction dampers. *J. Sound Vib.* **295**, 1028–1043 (2006)
8. Tanrikulu, O., Kuran, B., Özgüven, H.N., Imregun, M.: Forced harmonic response analysis of non-linear structures using describing functions. *AIAA J.* **31**(7), 1313–1320 (1993)
9. Gelb, A., Vander Velde, W.E.: Multiple-input describing functions and nonlinear system design. McGraw-Hill, New York (1968)
10. Atherton, D.P.: Nonlinear control engineering: Describing Function Analysis and Design. Van Nostrand Reinhold, London, 627 (1975)
11. Cigeroglu, E., Samandari, H.: Nonlinear free vibration of double walled carbon nanotubes by using describing function method with multiple trial functions. *Phys. E* **46**, 160–173 (2012)
12. Groll, G.V., Ewins, D.J.: The harmonic balance method with arc-length continuation in rotor/stator contact problems. *J. Sound Vib.* **241**(2), 223–233 (2001)

Chapter 29

Adaptive Harmonic Balance Methods, A Comparison

Onur Sert and Ender Cigeroğlu

Abstract Harmonic balance method (HBM) is one of the most popular and powerful methods, which is used to obtain response of nonlinear vibratory systems in frequency domain. The main idea of the method is to express the response of the system in Fourier series and converting the nonlinear differential equations of motion into a set of nonlinear algebraic equations. System response can be obtained by solving this nonlinear equation set in terms of the unknown Fourier coefficients. The accuracy of the solution is greatly affected by the number of harmonics included in the solution; hence, increasing the number of harmonics increases the accuracy of the solution at the expense of computational effort. Therefore, it is desirable to use an adaptive algorithm where the number of harmonics can be optimized in terms of both accuracy and computational effort. Until now, various adaptive harmonic balance methods have been formulated to perform this task. This paper presents an overview and a comparison of these adaptive harmonic balance methods in terms of their effectiveness.

Keywords Harmonic balance method • Adaptive harmonic balance method • Harmonic selection • Nonlinear vibrations • Nonlinear dynamics

29.1 Introduction

Mathematical methods of solving nonlinear equation systems are an essential part of nonlinear vibrations research. Most common methods for solving nonlinear differential equations are dependent on performing numerical integration in time domain. However, these time marching methods are known to require a great deal of computational effort [1, 2]. For vibration problems, most of the time the amplitude of steady-state response over a certain frequency spectrum is sought. In this case, time marching methods require even more computational time to reach and identify the steady-state response. Hence, when one is after the steady-state response, methods that can operate directly in the frequency domain are computationally favorable.

Harmonic Balance Method (HBM) is a frequency domain method which is used to determine the steady-state response. The mathematical basis of the method is to represent time periodic phenomena as truncated Fourier series with a finite number of harmonics. It reduces a set of nonlinear ordinary differential equations (ODEs) into a set of nonlinear algebraic equations, leaving the Fourier coefficients as the only unknowns to be determined. Therefore, HBM is computationally more efficient than time integration methods and it is capable of representing very strong nonlinearities with sufficient accuracy [3]. Therefore, HBM is extensively used in the literature and many different variants of HBM have been developed over the time [3–8].

Despite its advantages, for large scale applications, multi harmonic HBM can produce an excessive number of equations to be solved simultaneously and extensive computational time spent for unnecessary precision. In order to eliminate the use of unnecessary harmonics and increase the computational efficiency of HBM even more, Adaptive Harmonic Balance Methods (AHBMs), come into the picture. Together with a condensation method [2, 9], AHBMs have the potential to drastically decrease the computational time and the storage space required to solve a nonlinear system. For this purpose numerous AHBMs are introduced in the literature by different researchers in the recent years [9–14].

O. Sert • E. Cigeroğlu (✉)
Middle East Technical University, 06800 Ankara, Turkey
e-mail: ender@metu.edu.tr

In this paper, it is aimed to compare the AHBM which are developed for structural dynamics. In the following sections, firstly, the basics of HBM is explained in detail. Secondly, the methods taken from the literature and their selection algorithms are summarized. Finally, a case study is conducted in order to compare these methods. The methodology of the method is explained and using that methodology, the same nonlinear system is analyzed separately by all of the studied AHBM and the obtained results are compared in terms of computational time and accuracy.

29.2 Theory

29.2.1 Multi Harmonic HBM

The most general form of the equation of motion for an n degree of freedom (DOF) nonlinear vibratory system can be written as

$$[M] \{\ddot{q}(t)\} + [D] \{\dot{q}(t)\} + [K] \{q(t)\} + \{f_N(t, q, \dot{q})\} = \{F_{ext}(t)\}, \quad (29.1)$$

where $\{q(t)\}$ is the displacement vector, $[M]$ is the mass matrix, $[D]$ is the damping matrix (including damping and gyroscopic effects), $[K]$ is the stiffness matrix which may include structural damping, $\{f_N(t, q, \dot{q})\}$ is the nonlinear internal forcing vector and $\{F_{ext}(t)\}$ is the external forcing vector. If the external forcing is assumed to be periodic, then it can be represented as an infinite Fourier series. However, since using infinite number of terms is not practical, an m -harmonic representation can be used. In this case, the external forcing can be written as

$$\{F_{ext}(t)\} = \{F_0\} + \sum_{k=1}^m \{F_{sk}\} \sin(k\theta) + \sum_{k=1}^m \{F_{ck}\} \cos(k\theta), \quad (29.2)$$

where $\theta = \omega \cdot t$, $\{F_0\}$, $\{F_{sk}\}$ and $\{F_{ck}\}$ are $(n \times 1)$ vectors containing the known time independent bias terms and k^{th} harmonic coefficients of the sine and cosine components of the external forcing, respectively. For periodic excitation, the response of the system is as well expected to be periodic. Therefore, periodic response of the nonlinear system can be represented as:

$$\{q(t)\} = \{q_0\} + \sum_{k=1}^m \{q_{sk}\} \sin(k\theta) + \sum_{k=1}^m \{q_{ck}\} \cos(k\theta), \quad (29.3)$$

where $\{q_0\}$, $\{q_{sk}\}$ and $\{q_{ck}\}$ are $(n \times 1)$ unknown Fourier coefficient vectors of the bias component, sine and cosine components of the k^{th} harmonic, respectively and $\{q_0\}$ corresponds to the bias term. Similarly, the nonlinear forcing vector can be expressed as follows

$$\{f_N(t, q, \dot{q})\} = \{f_{N0}\} + \sum_{k=1}^m \{f_{Nsk}\} \sin(k\theta) + \sum_{k=1}^m \{f_{Nck}\} \cos(k\theta), \quad (29.4)$$

where, $\{f_{Nsk}\}$ and $\{f_{Nck}\}$ are $(n \times 1)$ vectors containing sine and cosine component of the k^{th} harmonic of the nonlinear internal forcing vector, respectively and $\{f_{N0}\}$ corresponds to the bias term. However, the nonlinear internal forces are not only dependent on time but also the response and its derivatives. Therefore, $\{f_{N0}\}$, $\{f_{Nsk}\}$ and $\{f_{Nck}\}$ are functions of $\{q_0\}$, $\{q_{sk}\}$ and $\{q_{ck}\}$. The Fourier coefficients of the internal nonlinear forces can be calculated as follows [2]:

$$\begin{aligned} \{f_{N0}\} &= \frac{1}{2\pi} \int_0^{2\pi} f_N(t, q, \dot{q}) d\theta \\ \{f_{Nsk}\} &= \frac{1}{\pi} \int_0^{2\pi} f_N(t, q, \dot{q}) \sin(k\theta) d\theta \\ \{f_{Nck}\} &= \frac{1}{\pi} \int_0^{2\pi} f_N(t, q, \dot{q}) \cos(k\theta) d\theta. \end{aligned} \quad (29.5)$$

For the cases where the internal nonlinear forces at steady-state cannot be represented analytically, Cameron and Griffin introduced an alternate frequency time (AFT) method in order to calculate nonlinear forcing coefficients [2, 15].

Substituting Eqs. (29.2), (29.3), and (29.4) into Eq. (29.1), equating the coefficients of like terms on both sides to each other, one obtains $n(2m + 1)$ nonlinear algebraic equations with $n(2m + 1)$ unknowns in terms of frequency, ω , which can be put in matrix form as follows:

$$\begin{bmatrix} [K] & [0] & [0] & \dots & [0] \\ [0] & [\Lambda(\omega)] & [0] & \dots & [0] \\ [0] & [0] & [\Lambda(2\omega)] & \dots & [0] \\ \vdots & \vdots & \vdots & \ddots & \vdots \\ [0] & [0] & [0] & \dots & [\Lambda(m\omega)] \end{bmatrix} \begin{Bmatrix} \{q_0\} \\ \{q_{s1}\} \\ \{q_{c1}\} \\ \{q_{s2}\} \\ \{q_{c2}\} \\ \vdots \\ \{q_{sm}\} \\ \{q_{cm}\} \end{Bmatrix} + \begin{Bmatrix} \{f_{N0}\} \\ \{f_{Ns1}\} \\ \{f_{Nc1}\} \\ \{f_{Ns2}\} \\ \{f_{Nc2}\} \\ \vdots \\ \{f_{Nsm}\} \\ \{f_{Ncm}\} \end{Bmatrix} = \begin{Bmatrix} \{F_0\} \\ \{F_{s1}\} \\ \{F_{c1}\} \\ \{F_{s2}\} \\ \{F_{c2}\} \\ \vdots \\ \{F_{sm}\} \\ \{F_{cm}\} \end{Bmatrix}, \quad (29.6)$$

where

$$[\Lambda(\omega)] = \begin{bmatrix} [K] - \omega^2 [M] & -\omega [D] \\ \omega [D] & [K] - \omega^2 [M] \end{bmatrix}. \quad (29.7)$$

Equation (29.6) can be solved by using a nonlinear equation solver. In order to obtain the frequency response of a dynamic system over a certain frequency range $[\omega_1, \omega_2]$, one needs to solve Eq. (29.6) for different values of $\omega \in [\omega_1, \omega_2]$. In order to select these frequency values and generate initial guesses in a systematic way, and to obtain the frequency response curve in full, a path following method can be combined with a suitable predictor [2]. Newton's Method and arc length continuation are utilized for the solution of the resulting set of nonlinear algebraic equations in this paper.

29.2.2 Adaptive Harmonic Balance Methods

In the previous section, it is indicated that application of the classical multi harmonic HBM method yields $n(2m + 1)$ algebraic equations. For precision, keeping m high is desirable; however, it is computationally expensive. Therefore, using an algorithm that can predict and neglect the harmonics which do not contribute significantly to the total solution is favorable. The basis of adaptive harmonic balance methods (AHBMs) depends on this idea. In the following sections, the AHBMs available in the field of structural dynamics are discussed.

29.2.2.1 Jamouillé, Sinou and Petitjean's Method

In 2010, Jamouillé, Sinou and Petitjean [9] introduced an AHBM (Jamouillé's method) which is originally intended to be used in analyzing nonlinear bolted joint models. In order to identify the harmonics that are to be used, the method uses the concept of approximate strain energy. It is basically equal to the mean potential energy stored in the linear springs during one period of vibratory motion. At every frequency point, a k -harmonic response is calculated. Then, by using this response, the corresponding approximate strain energy is obtained. For the same frequency point, the number of harmonics is increased by 1 to $k + 1$, the response and the approximate strain energy is computed once more. This process continues until the relative approximate strain energy ratio given below falls down a certain threshold value:

$$\varepsilon = \frac{U_m^{k+1} - U_m^k}{U_m^k} \quad (29.8)$$

where U_m^k is the approximate strain energy calculated from the response containing k harmonics and U_m^{k+1} is the approximate strain energy calculated with $k + 1$ harmonics and m stands for mean. When ε becomes less than the threshold value, it means that the contribution from the last added harmonic is small enough. In such a case, no more harmonics are added, the solution is stored and the starting value of k is set to 1 for the next frequency step. The whole algorithm is summarized in Fig. 29.1.

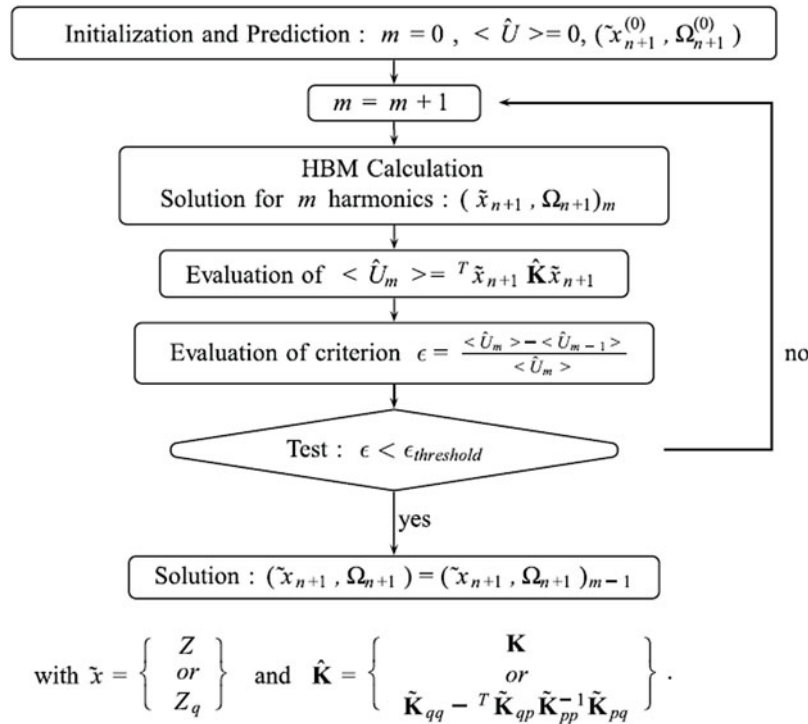


Fig. 29.1 Algorithm for the method presented by Jamouillé et al. [9]

Since this method assigns the same number of harmonics for all DOFs and increases the number of harmonics one by one, it is referred as a global method and an incremental method, respectively [10].

29.2.2.2 Yümer’s Method

In 2010, Yümer [11] presented an AHBM (Yümer’s method), which is initially intended to be used in vibration analysis of bladed disks. Like the method presented by Jaumoillé et al., it is a global and an incremental method. But different from the previous method, the harmonic selection criterion does not require repeated computation of system response for the same frequency point. Instead, at each frequency point, it tests the nonlinear forcing vector according to the following criterion:

$$|f_0| + |f_{s1}| + |f_{c1}| + \dots + |f_{sk}| + |f_{ck}| \geq a (|f_{s(k+1)}| + |f_{c(k+1)}| + \dots + |f_{sN_h^m}| + |f_{cN_h^m}|), \tag{29.9}$$

where the subscripts 0, s and c indicate the bias term, sine and cosine components of the nonlinear forcing, respectively. Subscript k stands for the harmonic number, N_h^m is the maximum number of harmonics allowed in the solution, a is an accuracy parameter set by the user. Initially, k is taken as 1. Then, k is increased one by one until the criterion given in Eq. (29.9) is satisfied. It can be seen from the equation that, increasing a forces the algorithm to increase k closer to N_h^m , whereas doing the opposite keeps k closer to 1, leading to a more coarse solution. Another implication of Eq. (29.9) is that, one needs to compute a N_h^m nonlinear forcing vector for every solution point, even when the response representation has less harmonics. This can be achieved by taking the unused harmonics in the response as zero and evaluating the integrals given in Eq. (29.5) for $k = 1, 2, \dots, N_h^m$.

29.2.2.3 Grolet and Thouverez’s Method

In 2012, Grolet and Thouverez proposed a new AHBM (Grolet and Thouverez’s method) [10]. Unlike the method described above; this method is local, that is, the number of harmonics is arranged separately for each DOF. In addition, the method is not incremental.

The harmonic selection process of the method is based on the tangent predictor. Assume that the Fourier coefficients are solved for the solution point i . At that point, due to the nature of AHBM, some harmonics are neglected and the resulting Fourier coefficient vector $\{q\}_r^i$ has less than the maximum number of harmonics, N_h^m , which is defined by the user. It is assumed that the neglected harmonics at the current solution step are so small that, they can be assumed zero. An $n(2N_h^m + 1) \times 1$ vector, $\{q\}_r^i$, is formed by adding zeros into $\{q\}_r^i$. From this new vector, by using the tangent predictor, an initial guess, $\{q\}_p$, having N_h^m harmonics is computed for the next solution point. After that, $\{q\}_p$ is divided into n sub-vectors having $2N_h^m + 1$ elements, each of which associated to a different DOF. The harmonic selection is performed through these vectors.

Considering the sub-vector of DOF d , $\{u\}_p^d$. The fraction of spectral energy for the k^{th} harmonic of DOF d is defined as:

$$\varepsilon_k^d = \frac{(u_{p_{sk}}^d)^2 + (u_{p_{ck}}^d)^2}{\|\{u\}_p^d\|}, \quad (29.10)$$

where $\|\cdot\|$ is the Euclidean norm, $u_{p_{sk}}^d$ and $u_{p_{ck}}^d$ are the sine and cosine coefficients of the k^{th} harmonic, respectively. Then, the total spectral energy ratio of the harmonics that are retained at the i^{th} solution point can be calculated as:

$$E_r^d = \sum_{k \in H_r^d} \varepsilon_k^d, \quad (29.11)$$

where $[H]_r^d$ is the row matrix, in which the retained harmonic indices of DOF d , at the solution point i are stored. If $[H]_r^d$ is equal to $\begin{bmatrix} 0 & 1 & 2 & \dots & N_h^m \end{bmatrix}$, E_r^d becomes 1. This leads to the definition of the fraction of residual energy:

$$\rho_d = 1 - E_r^d. \quad (29.12)$$

During the harmonic selection procedure, ρ_d is compared to two thresholds ρ_f and ρ_b , which are defined by the user such that, they satisfy the inequality $0 \leq \rho_b \leq \rho_f \leq 1$. If ρ_d is greater than ρ_f , it means that the amount of energy contained in the neglected harmonics is very large. Therefore the neglected harmonics with largest spectral energy values are added one by one into $[H]_r^d$ until ρ_d becomes less than ρ_f . If ρ_d turns out to be less than ρ_b this means that the error obtained is much smaller than the allowable error. Therefore the harmonics with minimum spectral energy values are deleted one by one from $[H]_r^d$ until ρ_d becomes larger than ρ_b . If ρ_d lies between two threshold values, the solution scheme continues with the current harmonics. This process is repeated for every DOF in the system. The algorithm for harmonic selection process is summarized in Fig. 29.2.

29.3 Comparison

29.3.1 Methodology

The aim of this study is to compare the AHBM in terms of solution accuracy and computational time. Naturally, the methods which obtain the same accuracy using the shortest time are regarded as the most effective ones.

In structural dynamics, one of the most important concerns is the magnitude of oscillations throughout a certain frequency spectrum. Therefore, in the case of a nonlinear frequency response obtained by HBM, it is natural for one to be interested in the total response rather than the harmonics themselves. Therefore, for this study, the accuracy measurements are all based on the total response.

In the case study, the discrete nonlinear dynamic system to be analyzed is firstly solved by a 10-harmonic classical HBM script. After the amplitudes of each harmonic are examined, it is decided that a 10 harmonic solution is sufficient to express the system response with an acceptable degree. The total response curve obtained from this solution, is assumed to be correct and is taken as a reference in the error calculations.

Afterwards, the same dynamic system is analyzed by using the AHBM. In order to form a data repository for each method, analyses are done for a wide range of harmonic selection parameters. Accuracies of the response curves obtained from AHBM are evaluated by how much they deviate from the 10-harmonic solution curve at the chosen frequencies. Since it is very difficult to measure the distance between points inside the unstable region and also it is difficult to observe the unstable region in a real-life experiment, the frequency points inside that part are excluded.

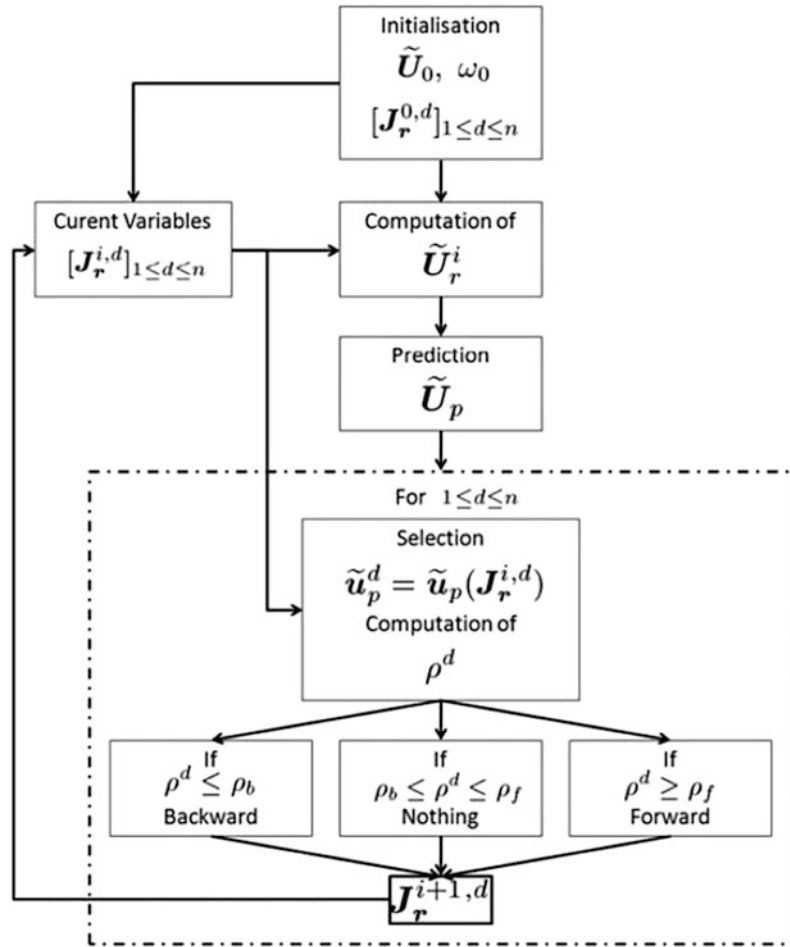


Fig. 29.2 The algorithm for Grolet and Thouverez's method [10]

When comparing two different total response values, one taken from the classical solution curve and the other from an AHBM solution curve, it has to be guaranteed that the two points are located at the same frequency. In order to make the frequencies correspond, the step sizes are taken as constant in the path following schemes. If some of the chosen frequencies do not overlap, linear interpolation is performed. For the purpose of preventing the interpolation from being inaccurate, the step size is chosen as a small value. After the error values are obtained for all of the chosen frequency points, integral error values are calculated. For computing the integral error, the trapz function of MATLAB[®] is used. Since the step size is chosen as a small value, it is considered that the number of partitions to be used in the trapezoidal rule and the accuracy obtained are sufficient to give a good idea about the order of integral error.

The time spent during the solutions are measured by the tic-toc function of MATLAB[®]. All of the analyses are run on the same Dell XPS 15-L502X laptop computer having a 2.0 Intel Core i7-2630 (quad core) processor and 4 GB of 667 MHz DDR3 RAM.

29.3.2 The Analyzed System

The studied system is illustrated in Fig. 29.3. Parameters of the system and parameters of the gap nonlinearities are given in Tables 29.1 and 29.2, respectively.

When the linear system is studied, it can be seen that the natural frequencies are located at 48.21 and 119.76 rad/s. The frequency range in consideration is [35, 65] rad/s, which covers the first resonance frequency. Since the external forcing contains three harmonics, two super-harmonic resonances, located at 39.92 and 59.88 rad/s, the points where 2ω and 3ω are equal to the second natural frequency, are expected. Also, one more resonance must appear at the first natural frequency.

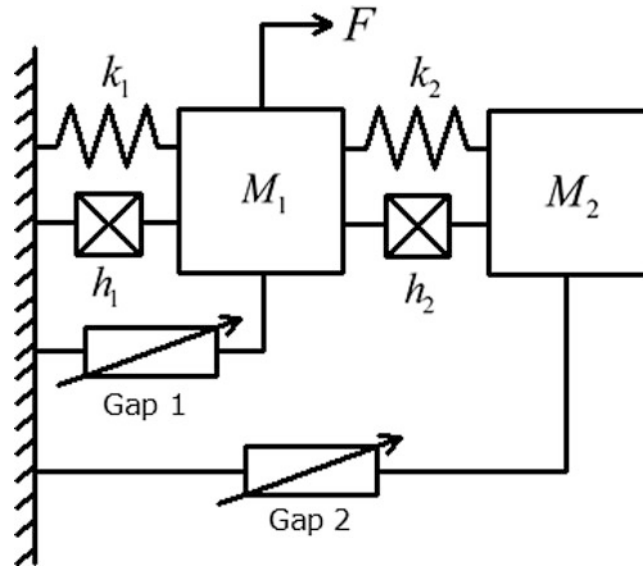


Fig. 29.3 A 2-DOF system with gap nonlinearity

Table 29.1 Parameters for the 2-DOF System

M_1 (kg)	M_2 (kg)	k_1, k_2 (N/m)	h_1, h_2 (N/m)	F (N)
1	0.75	5000	50	$30 \sin(\theta) + 30 \sin(2\theta) + 30 \sin(3\theta)$

Table 29.2 Parameters of Gap Elements

Nonlinear element	δ (m)	k_g (N/m)
Gap 1	0.05	500
Gap 2	0.1	500

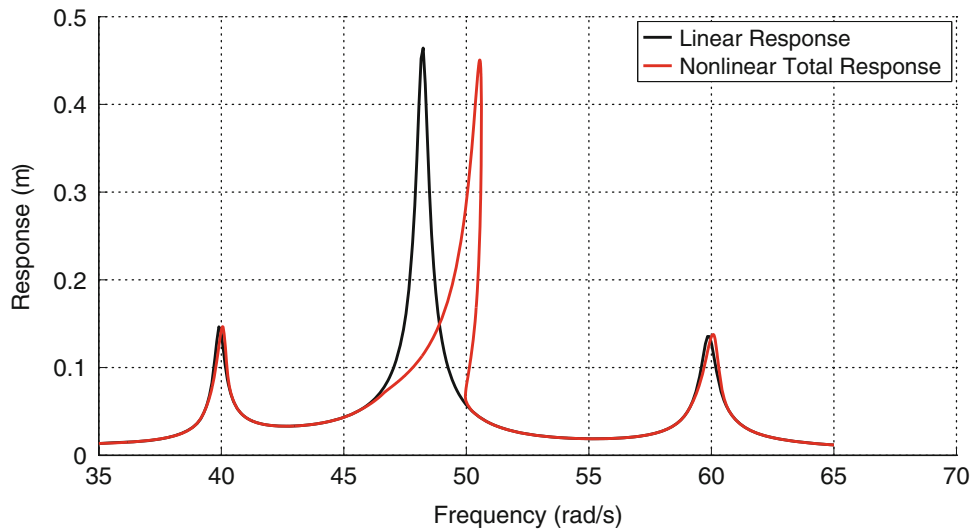


Fig. 29.4 Total Response of the first DOF

Gap nonlinearity is chosen for this study, since it excites higher harmonics when the system makes large oscillations; whereas for small oscillations, the system acts as a linear structure. Therefore adaptive algorithms analyzing systems with gap nonlinearity are forced to change the harmonic content often. The total response and contribution of each harmonic obtained by using a 10-harmonic solution, i.e. baseline solution for error calculations, are given in Figs. 29.4 and 29.5 for the first DOF, respectively.

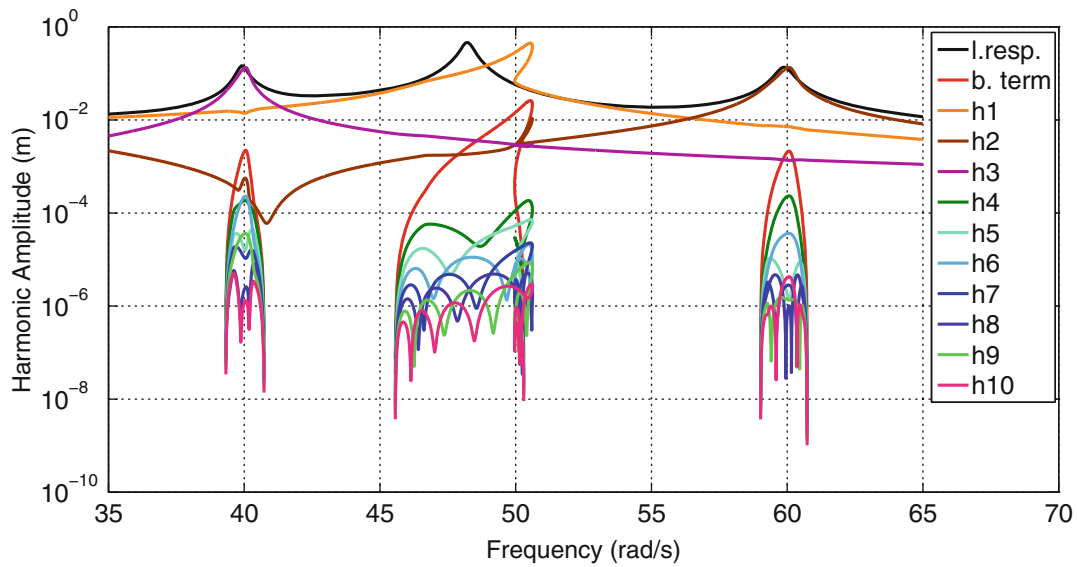


Fig. 29.5 Amplitudes of harmonics for the first DOF

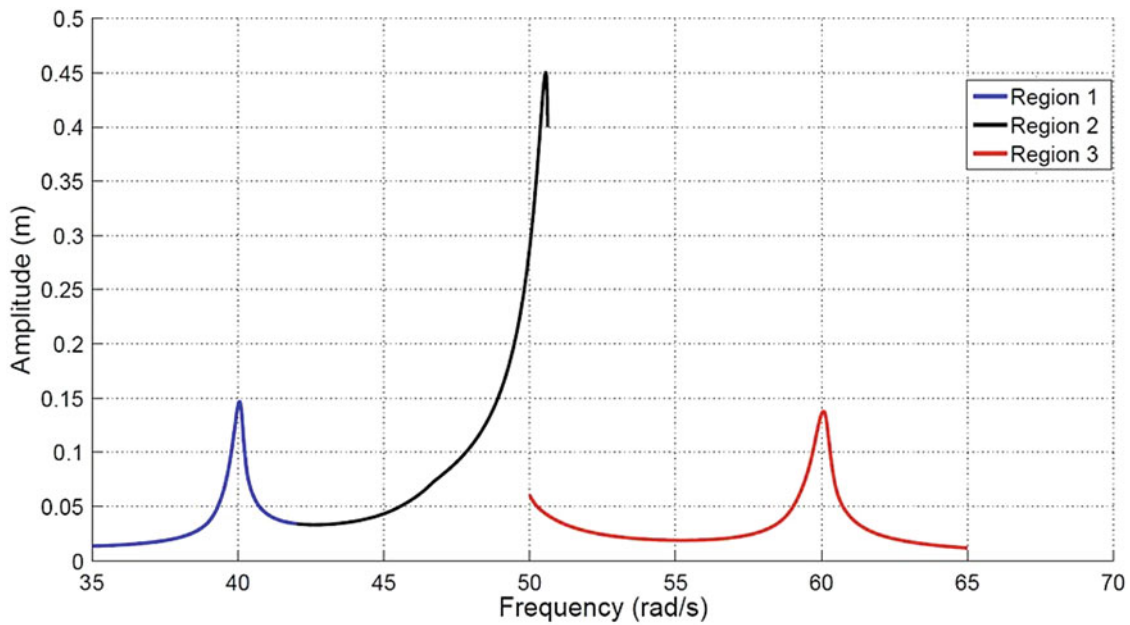


Fig. 29.6 Regions defined for error analysis

For the error analysis, the total response curve is divided into three parts. As explained in the previous section, the unstable region is excluded and the resulting regions are shown in Fig. 29.6.

29.3.3 Results

In this section, two criteria used for evaluation are presented in graphical form. In these plots, the horizontal axis is the computational time, and the vertical axis is the error. Every point on the given curve corresponds to an analysis performed by one of the AHBMs, with a different harmonic selection parameter set. The methods for which the points lie closest to the lower left corner are more favorable methods, since they manage to achieve greater accuracy in a shorter time. Results are presented in Figs. 29.7 and 29.8.

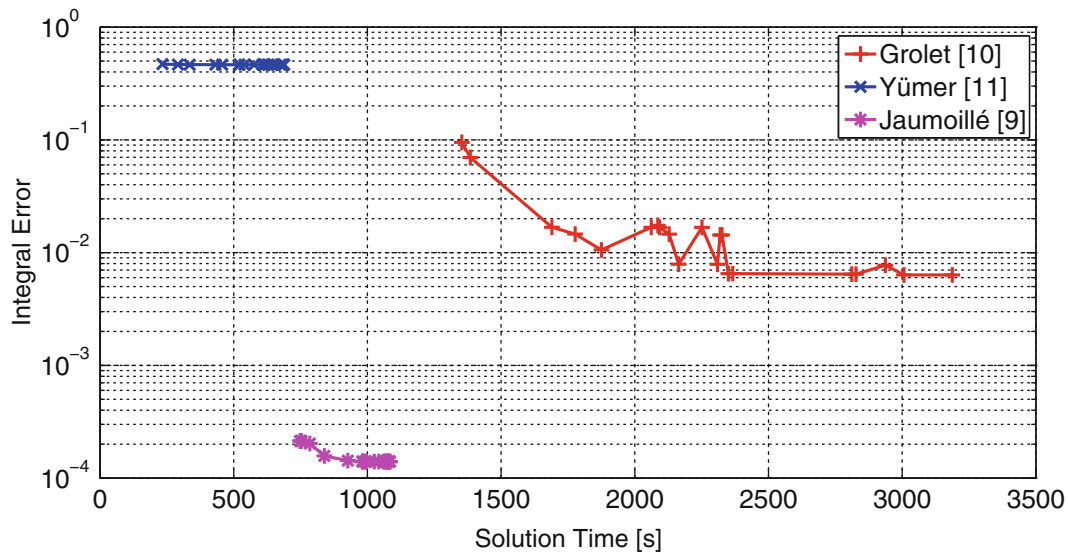


Fig. 29.7 Computational time vs integral error

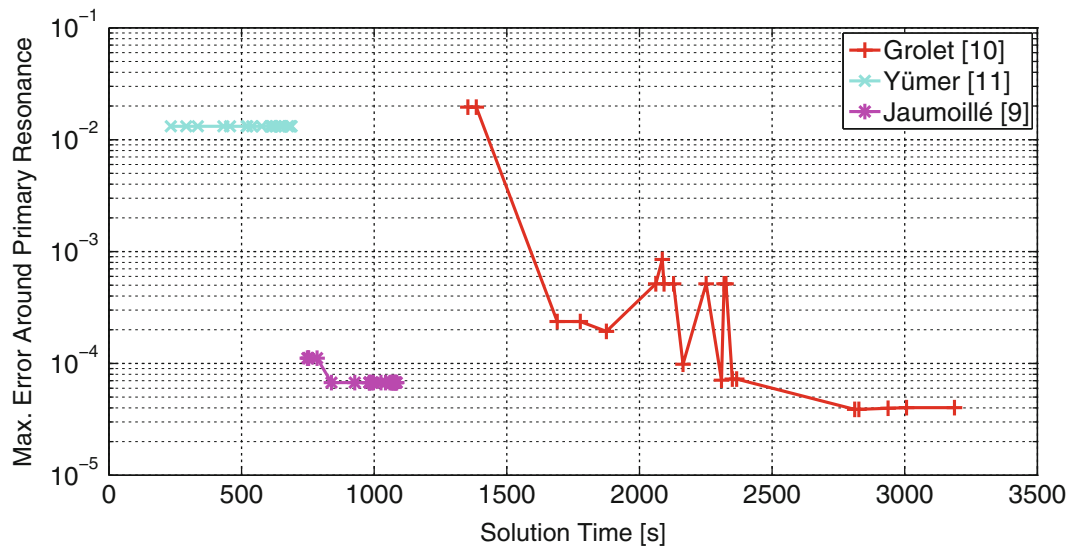


Fig. 29.8 Computational time vs maximum error around the first natural frequency

The results indicate that the computational times are relatively low, as desired for Yümer’s method. However the error values are significantly high and they tend to stay constant, although the control parameter changes. It is observed that the method failed to increase the number of harmonics around the super-harmonic resonances. Therefore, the error values around those regions are high even though they are quite low near the first natural frequency. However, since Region 2 starts from 42 rad/s, the error values corresponding to region 2 turn out to be high as well. Around the secondary resonances, a single harmonic representation is used regardless of the value of a and the same amount of error is introduced, in almost every analysis. This phenomenon can be clearly seen in the overlapping absolute error plots given in Fig. 29.9.

The results also show that, even though the harmonic selection parameters change, the error obtained by Jaumoillé et al.’s method does not vary greatly. In Fig. 29.10, the number of harmonics for two different threshold parameters are shown. For $\varepsilon = 10^{-20}$, the algorithm is expected to retain much more harmonics than the case where $\varepsilon = 10^{-2}$. It can be seen from the figure that, this result occurs only in the neighborhood of the resonances. In other regions, the harmonic contents are almost the same. In addition to this in Figs. 29.10 and 29.11 one can see that, around 40 rad/s one can see that the algorithm increases the number of harmonics rapidly at first. Then a sudden drop occurs until the number of harmonics starts to rise again. The same behavior happens at other resonances as well. When the drop in the retained harmonics occurs, as expected, the error increases rapidly and reaches to a maximum. The algorithm shows this behavior for every value of ε considered in

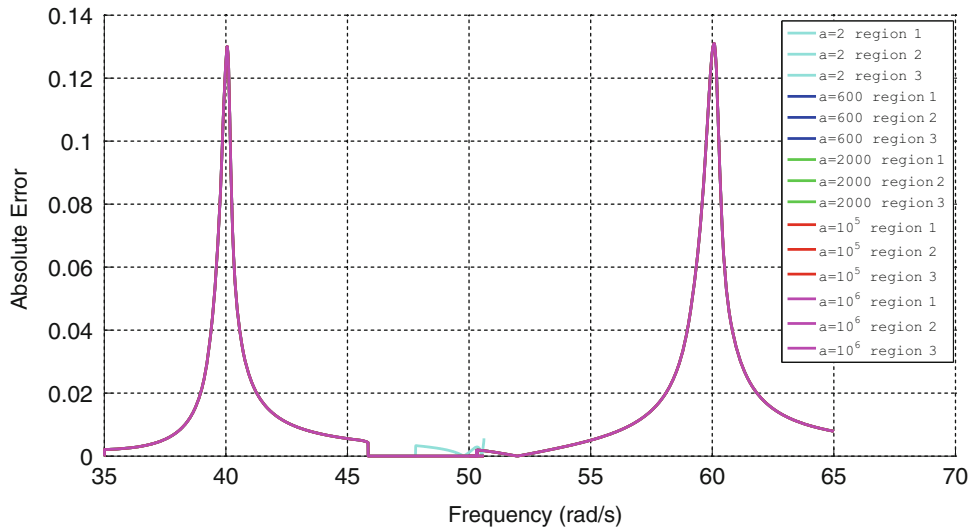


Fig. 29.9 Error plots for Yümer's method

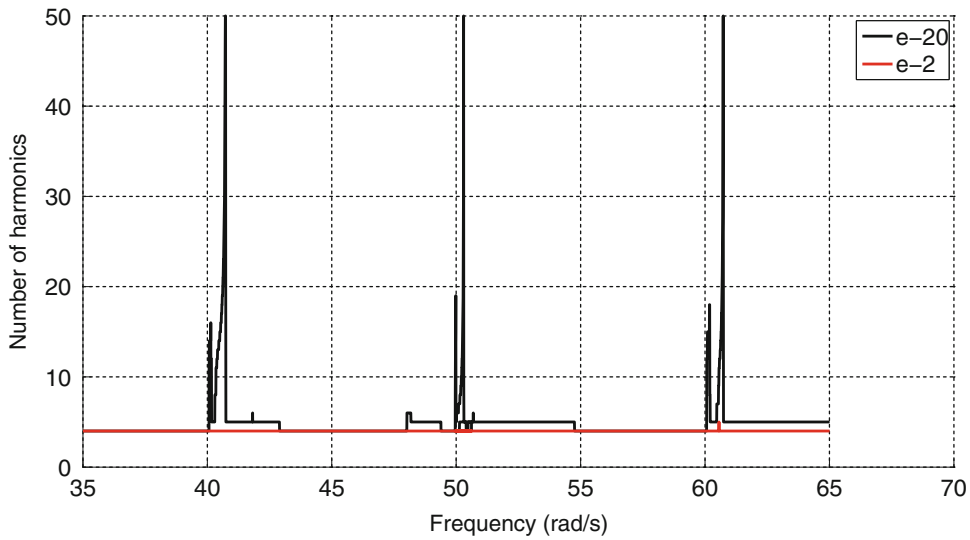


Fig. 29.10 Number of retained Harmonics for Jaumoillé's method

this study, therefore the maximum error values do not change significantly. For the case where $\varepsilon = 10^{-20}$, the number of harmonics reach up to 50 at 3 points however, since this number is extremely high for the current nonlinear system under study, its contribution to the accuracy is very low.

The method developed by Grolet and Thouverez obtains higher integral error values than Jaumoillé et al.'s method; however, it is more responsive to the changes in harmonic selection parameters. The method is actually accurate around the primary resonance; however, the higher integral error shows that the method is somewhat less accurate around the superharmonic resonances.

29.4 Discussion and Conclusion

In this paper, a short summary on AHBM's currently available in the field of structural dynamics are presented. Using a two-DOF lumped parameter model with gap nonlinearities, AHBM's are compared with each other in terms of computational time and accuracy. For comparison purposes, 10-harmonic solution is used as the baseline. It is observed, that the AHBM's

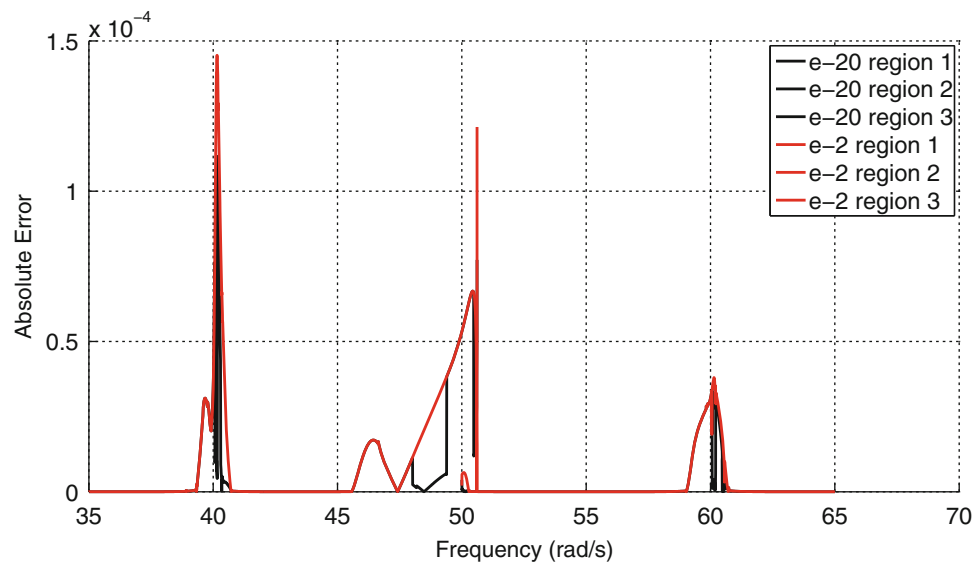


Fig. 29.11 Error plots for Jaumoillé's method

considered are perform better around the primary resonance whereas their performance around the superharmonic resonances are limited. Yümer's method is the fastest; however, its accuracy very limited. In terms of computational time and accuracy, Jaumoillé's method is better than the other two methods.

References

1. LaBryer, A., Attar, P.J.: A harmonic balance approach for large-scale problems in nonlinear structural dynamics. *Comput. Struct.* **88**(17–18), 1002–1014 (2010)
2. Sarrouy, E., Sinou, J.: Non-linear periodic and quasi-periodic vibrations in mechanical systems-on the use of the harmonic balance methods. In: Ebrahimi, D.F. (ed.) *Advances in Vibration Analysis Research InTech*, Rijeka, Croatia, pp. 419–434. (2011)
3. Kim, Y., Choi, S.: A multiple harmonic balance method for the internal resonant vibration of a non-linear Jeffcott rotor. *J. Sound Vib.* **208**, 745–761 (1997)
4. von Groll, G., Ewins, D.J.: The harmonic balance method with arc-length continuation in rotor/stator contact problems. *J. Sound Vib.* **241**(2), 223–233 (2001)
5. Lau, S.L., Cheung, Y.K.: Amplitude incremental variational principle for nonlinear vibration of elastic systems. *J. Appl. Mech.* **48**(4), 959 (1981)
6. Yuste, B.S.: Comments on the method of harmonic balance in which Jacobi elliptic functions are used. *J. Sound Vib.* **145**(3), 381–390 (1991)
7. Kim, Y., Noah, S.: Quasi-periodic response and stability analysis for a non-linear Jeffcott rotor. *J. Sound Vib.* **190**, 239–253 (1996)
8. Kim, T.C., Rook, T.E., Singh, R.: Super- and sub-harmonic response calculations for a torsional system with clearance nonlinearity using the harmonic balance method. *J. Sound Vib.* **281**(3–5), 965–993 (2005)
9. Jaumoillé, V., Sinou, J.-J., Petitjean, B.: An adaptive harmonic balance method for predicting the nonlinear dynamic responses of mechanical systems—application to bolted structures. *J. Sound Vib.* **329**(19), 4048–4067 (2010)
10. Grolet, A., Thouverez, F.: On a new harmonic selection technique for harmonic balance method. *Mech. Syst. Sig. Process.* **30**, 43–60 (2012)
11. Yümer, M.E.: *On the Non-Linear Vibration and Mistuning Identification of Bladed Disks*. Middle East Technical University, Ankara, Turkey (2010)
12. Zhu, L., Christoffersen, C.E.: Adaptive harmonic balance analysis of oscillators using multiple time scales. In *IEEE-NEWCAS Conference, 2005. The 3rd International*, Quebec City, 187–190 (2005), doi: [10.1109/NEWCAS.2005.1496738](https://doi.org/10.1109/NEWCAS.2005.1496738)
13. Gourary, M.M., Rusakov, S.G., Ulyanov, S.L., Zharov, M.M., Gullapalli, K.K., Mulvaney, B.J.: A New Computational Approach to Simulate Highly Nonlinear Systems by Harmonic Balance Method. In *16th IMACS WORLD CONGRESS 2000 on Scientific Computation, Applied Mathematics and Simulation*. Lausanne, 366 (2000)
14. Maple, R.C., King, P.I., Orkwis, P.D., Mitch Wolff, J.: Adaptive harmonic balance method for nonlinear time-periodic flows. *J. Comput. Phys.* **193**(2), 620–641 (2004)
15. Cameron, T.M., Griffin, J.H.: An alternating frequency/time domain method for calculating the steady-state response of nonlinear dynamic systems. *J. Appl. Mech.* **56**(1), 149 (1989)